Development of Functional Binders and Li_2S@Carbon Nanocomposites for High-Performance Lithium Sulfide Batteries

by

Zhe Huang

A thesis

presented to the University of Waterloo

in fulfillment of the

thesis requirement for the degree of

Doctor of Philosophy

in

Chemical Engineering (Nanotechnology)

Waterloo, Ontario, Canada, 2025

© Zhe Huang 2025

Examining Committee Membership

The following served on the Examining Committee for this thesis. This decision of the Examining Committee is by majority vote.

External Examiner	Prof. Yang Zhao (Western University)
Supervisor	Prof. Yuning Li (University of Waterloo)
Internal Members	Prof. Xianshe Feng (University of Waterloo) Prof. Michael Pope (University of Waterloo)
Internal-External Member	Prof. Xianguo Li (University of Waterloo)

Author's Declaration

This thesis consists of material all of which I authored or co-authored: see Statement of Contributions included in the thesis. This is a true copy of the thesis, including any required final revisions, as accepted by my examiners.

I understand that my thesis may be made electronically available to the public.

Statement of Contributions

Chapter 1 forms the foundation of a review manuscript currently in progress. I conducted the majority of the work, including conceptualization, comprehensive literature review, reference synthesis, figure design, and manuscript drafting. Yixuan Zhao contributed to reference collection and assisted in preparing several illustrative figures, while Yonglin Wang provided additional support with reference collection.

Chapter 2 was written entirely by me and describes the materials, synthesis procedures, and characterization techniques used throughout this thesis.

Chapter 3 is based on a published manuscript. I was the primary author and contributed to conceptualization, methodology development, investigation, experiments, formal analysis, and preparation of both the original draft and revised versions. Xiguang Gao contributed to methodology, investigation, and experimental work. Yonglin Wang assisted with investigation and experiments. Prof. Yuning Li contributed to conceptualization, investigation, supervision, project administration, funding acquisition, and writing – review & editing. This work was published as: **Zhe Huang**, Xiguang Gao, Yonglin Wang, Yuning Li, Mitigating first charge overpotential of Li_2S-based lithium-sulfur batteries by leveraging PVDF reaction with the LiOH/Li_2O layer. *Journal of Power Sources*, **2023**, 582: 233530. https://doi.org/10.1016/j.jpowsour.2023.233530.

Chapter 4 is based on a published manuscript. I served as the primary author, contributing to conceptualization, data curation, formal analysis, investigation, methodology, validation, visualization, and writing – original draft and review & editing. Yonglin Wang contributed to data curation, formal analysis, investigation, methodology, and performed the SEM characterization. Yixuan Zhao contributed data curation, formal analysis, investigation, and methodology. Prof. Yuning Li contributed to conceptualization, formal analysis, investigation, methodology, visualization, supervision, project administration, funding acquisition, resources, and writing – review & editing. No conflicts of interest were declared. This work was published as: **Zhe Huang**, Yonglin Wang, Yixuan Zhao, Yuning Li, Zinc complex-based multifunctional binders for lithium sulfide-based lithium–sulfur batteries. *Nanoscale*, **2025**, 17, 18744-18755. https://doi.org/10.1039/D5NR01950H.

Chapter 5 is based on a published manuscript. I was the primary author and contributed to conceptualization, data curation, formal analysis, investigation, methodology development, validation, visualization, and writing – original draft and review & editing. Yonglin Wang contributed to data curation, formal analysis, investigation, methodology, and performed the SEM characterization. Prof. Yuning Li contributed to conceptualization, formal analysis, investigation, methodology, visualization, supervision, project administration, funding acquisition, resources, and writing – review & editing. This work was published as: **Zhe Huang**, Yonglin Wang, Yuning Li, Facile Synthesis of Lithium Sulfide@Carbon Nanocomposite via Precursor Solution Infiltration-Decomposition for High-Performance Lithium Sulfide Batteries. *ACS Applied Energy Materials*, **2025**, 8, 5759-5769. https://doi.org/10.1021/acsaem.5c00102.

Chapter 6 is based on a submitted manuscript that is currently under review. I served as the primary author and contributed to conceptualization, data curation, formal analysis, investigation, methodology development, validation, visualization, and manuscript preparation and revision. Yonglin Wang contributed to data curation, formal analysis, investigation, methodology, and performed the SEM characterization. Yixuan Zhao contributed to data curation, formal analysis, investigation, and methodology. Prof. Yuning Li contributed to conceptualization, formal analysis, investigation, methodology, visualization, supervision, project administration, funding acquisition, resources, and writing – review & editing.

Chapter 7 is based on a completed manuscript that is not yet published and is intended for future publication. This work is currently in preparation for submission. I was the primary author and contributed to conceptualization, data curation, formal analysis, investigation, methodology development, validation, visualization, and manuscript preparation and revision. Yonglin Wang contributed to data curation, formal analysis, investigation, methodology, and performed the SEM characterization. Yixuan Zhao contributed to data curation, formal analysis, investigation, and methodology. Prof. Yuning Li contributed to conceptualization, formal analysis, investigation, methodology, visualization, supervision, project administration, funding acquisition, resources, and writing – review & editing.

Chapter 8 presents the full-cell demonstration work and includes selected content adapted from the manuscripts prepared in **Chapter 6** and **Chapter 7**. I was the principal and primary contributor, responsible for conceptualization, experimental design, electrode fabrication, cell assembly, data collection, formal analysis, and preparation of the written chapter. This work was conducted under the supervision of Prof. Yuning Li, who provided guidance on experimental direction, data interpretation, and manuscript review.

Chapter 9 was written entirely by me. I synthesized the key findings from all research chapters, developed the overall conclusions, and proposed future research directions. This chapter was written under the supervision and guidance of Prof. Yuning Li.

Abstract

Lithium sulfide (Li_2S) is a promising cathode material for lithium-sulfur batteries (LSBs) owing to its high theoretical capacity (1166 mA h g^{-1}) and potential for safer, scalable battery architectures. In contrast to sulfur cathode, Li_2S enables direct pairing with commercial anode materials, avoiding the safety risks of lithium metal. Despite these merits, practical application of Li_2S is challenged by its hygroscopic nature, which forms insulating LiOH/Li_2O surface layers that cause a large first-charge overpotential; its high melting point (~938 °C), which prevents melt infiltration into carbon frameworks; sluggish redox kinetics; severe polysulfide dissolution; poor conductivity. Addressing these challenges requires integrated advances in binder design, electrode engineering, and cathode nanostructuring.

The large first-charge overpotential due to the insulating LiOH/Li_2O surface layer in Li_2S-LSBs hinders activation and induces irreversible side reactions. **Chapter 3** proposes mitigating the activation barrier by exploiting the reaction between polyvinylidene fluoride (PVDF) binder and LiOH/Li_2O through dehydrofluorination. The overpotential was successfully reduced from 3.74 V with 30 min slurry grinding to 2.75 V by extending slurry stirring to 48 h. However, PVDF was also found to react with Li_2S itself, partially consuming active material and lowering discharge capacity. Overall, this study provides mechanistic insights into the origin of Li_2S activation overpotential and demonstrates the dual role of conventional PVDF binders, where slurry processing with PVDF can effectively reduce the first-charge barrier, while also highlighting the limitations of PVDF as a binder for Li_2S electrodes.

Since PVDF proved unsuitable for Li_2S electrodes, **Chapter 4** investigates alternative binders capable of enhancing the electrochemical performance of Li_2S-LSBs. A binder based on a zinc acetate triethanolamine ($Zn(OAc)_2$·TEA) complex was developed, which not only provides strong polysulfide-trapping ability but also exhibits redox catalytic activity, leading to markedly improved capacity, rate capability, and cycling stability compared with PVDF. To further reinforce electrode integrity and improve dispersion stability, polyethylenimine (PEI) was incorporated to form a $Zn(OAc)_2$·TEA/PEI hybrid binder. Electrochemical testing showed that Li_2S cathodes employing $Zn(OAc)_2$·TEA/PEI with 10 wt.% PEI achieved superior rate performance, high discharge capacity,

and excellent long-term cycling stability. An additional advantage of these binders is their fluorine-free composition, which aligns with sustainability goals and complying with emerging regulations, including EU restrictions on per- and polyfluoroalkyl substances (PFAS).

In **Chapter 5**, an efficient precursor solution infiltration-decomposition strategy was invented to synthesize Li_2S@Carbon nanocomposites under mild conditions, overcoming the challenges of Li_2S's high melting point, poor solubility, and the large particle size of commercial Li_2S. In this approach, Li_2S was first reacted with carbon disulfide (CS_2) in ethanol at ambient temperature to form a highly soluble lithium trithiocarbonate (Li_2CS_3) precursor, which was readily infiltrated into mesoporous Super P carbon (SP). Subsequent thermal decomposition of Li_2CS_3@SP at 400 °C produced Li_2S@SP-400 nanocomposites with a Li_2S:SP mass ratio of 60:40, containing finely dispersed Li_2S particles (~11 nm) uniformly confined within the Super P matrix. Electrochemical testing demonstrated that these nanocomposites delivered a high discharge capacity of 821 mA h g^{-1} (Li_2S) at 0.1 C, equivalent to 1190 mA h g^{-1} (S), and exhibited superior rate capability and cycling stability compared to commercial Li_2S, non-infiltrated Li_2S nanoparticles, and melt-infiltrated sulfur composites (S@SP).

The thermal decomposition of Li_2CS_3 precursor releases a large amount of CS_2 gas (~62 wt.% of the precursor), which creates internal voids and limits the in-pore Li_2S loading. To address this, **Chapter 6** builds upon precursor infiltration-decomposition method with a multi-cycle strategy, enabling higher Li2S content and in-pore loading. Using mesoporous Super P as the conductive host and Li_2CS_3 as the precursor, repeated infiltration-decomposition cycles progressively increased the pore filling factor (FF) and in-pore Li_2S loading (IPL), from FF = 38% and IPL = 30% for Li_2S@SP-1 (one cycle) to FF = 91% and IPL = 73% for Li_2S@SP-5 (five cycles), while also raising the overall Li_2S content to 70 wt.%. Direct structural evidence from XRD and SEM confirmed reduced crystallite size, suppressed external deposition, and uniform Li_2S distribution in the optimized Li_2S@SP-5. Electrochemical tests demonstrated that Li_2S@SP-5 delivered an initial discharge capacity of 807 mA h g^{-1} (Li_2S) at 0.1 C, 598 mA h g^{-1} (Li_2S) in the first cycle at 1.0 C, and retained 376 mA h g^{-1} (Li_2S) after 500 cycles at 1.0 C.

To construct high-performance cathodes, the functional binder from **Chapter 4** was combined with the high in-pore loading Li_2S@SP from **Chapter 6**. This attempt failed because $Zn(OAc)_2$·TEA/PEI-based binders exhibited limitations with highly reactive nanoscale Li_2S, resulting in diminished binding effectiveness. **Chapter 7** therefore introduces a series of polyethylenimine-epoxy resin (PEI-ER) binders, where high-molecular-weight PEI anchors and catalyzes polysulfides while epoxy crosslinking reinforces mechanical stability, making this strategy particularly effective for stabilizing nanoscale Li_2S composites. The *in-situ* crosslinking method further improved processing by removing the short crosslinking time window and enabling uniform networks without altering Li_2S@SP morphology. Electrochemical tests showed the optimized *in-situ* crosslinked PEI-$ER_{1:1}$ binder achieved 928 mA h g^{-1} at 0.05 C, 688 mA h g^{-1} in the first cycle at 0.5 C and retained 325 mA h g^{-1} after 1000 cycles at 0.5 C with stable Coulombic efficiency. SEM confirmed its compact structure, establishing *in-situ* PEI-ER crosslinking as a robust binder strategy for nanoscale, high-loading Li_2S cathodes.

Chapter 8 serves as the culmination of these research projects, combining the optimized Li_2S@Carbon cathodes from **Chapter 6** and functional binders developed from **Chapter 7** with commercial Si/C anodes to successfully assemble and evaluate lithium-anode-free full cells, with PVP used as a baseline comparison, thereby demonstrating their practical feasibility. The *in-situ* crosslinked PEI-$ER_{1:1}$-based full cell batteries delivered 670 mA h g^{-1} at 0.1 C and retained 304 mA h g^{-1} after 100 cycles (~45% retention), outperforming PVP-based full cell batteries (582 to 250 mA h g^{-1}, ~43%). At 0.5 C, the *in-situ* crosslinked PEI-$ER_{1:1}$-based full cell batteries achieved 564 mA h g^{-1} after activation and maintained 377 mA h g^{-1} after 500 cycles (66.8% retention), while the PVP counterparts fell from 573 to 176 mA h g^{-1} (30.7%). These results underscore the binder's role in stabilizing cathodes and mark the successful assembly of lithium-free-anode Li_2S full cells with commercial Si/C anodes.

In summary, this thesis addresses the critical challenges of Li_2S cathodes, including the large first-charge overpotential, the drawback of PVDF consuming Li_2S, the large particle size of commercial Li_2S, the high melting point and poor solubility that hinder conventional Li_2S@Carbon composite fabrication, and the limitations of binders when applied to nanoscale Li_2S, each identified in the process of resolving the preceding issue. By systematically investigating these problems, this

thesis advances functional binder design, exploits precursor chemistry, and engineers nanostructured composites, concluding with the successful demonstration of lithium-anode-free full cell batteries. Further improvements could be achieved by employing more efficient carbon hosts with tailored structures, developing high-loading electrodes, integrating solid-state electrolytes to mitigate polysulfide dissolution, and incorporating catalytic components to accelerate Li_2S redox kinetics, thereby pushing Li_2S-LSBs closer to practical, high-energy-density applications.

Acknowledgements

First and foremost, I would like to express my deepest gratitude to my supervisor, Prof. Yuning Li, for his outstanding mentorship throughout my Ph.D. journey. His enthusiasm for scientific research has been a constant source of inspiration, and his patience in supervising students has created an encouraging environment where ideas can grow. With his broad knowledge across multiple disciplines, he guided me to approach challenges with both depth and breadth. I am especially grateful for his continuous encouragement in every application for scholarships and research funding, which greatly strengthened my confidence and professional development.

I am sincerely grateful to the Waterloo Institute for Nanotechnology (WIN) for providing world-class experimental facilities and a vibrant academic platform that has greatly enriched my Ph.D. experience. WIN has fostered a wonderful and supportive community for students in nanotechnology, where frequent seminars, workshops, and networking activities broaden both scientific knowledge and professional connections. I am especially honored to have been awarded the WIN Nanofellowship twice, in 2020 and 2024—a highly competitive and prestigious distinction regarded as a valuable honor for every University of Waterloo graduate student working in nanotechnology-related fields—and I am profoundly grateful for the financial support and personal motivation it has provided.

I also wish to thank the Department of Chemical Engineering and the University of Waterloo for their constant support. The Department provided me with valuable teaching assistantship positions that not only allowed me to share knowledge with students but also gave me the opportunity to refine my teaching, communication, and leadership skills. I owe special thanks to my course instructor, Jennifer Moll, for her confidence in my abilities and for selecting me as her TA on four occasions. Her trust provided me with invaluable teaching experience and greatly enhanced my confidence as an academic. I am also sincerely grateful to Judy Caron for her kind and consistent assistance in all aspects of graduate affairs in Chemical Engineering; her efficiency and generosity have made many parts of my Ph.D. journey much smoother. Finally, I thank the University of Waterloo for providing essential funding support during the pandemic and throughout my Ph.D. extension period.

My gratitude extends to my colleagues and group members, whose collaboration, insightful discussions, and friendship have made research more meaningful and enjoyable. I would like to especially thank Dr. Xiguang Gao for his guidance during the early stage of my Ph.D. studies, Yonglin Wang for his microscopy support in each project, Dr. Razieh Fazaeli for both her experimental support and her thoughtful care in daily life, and Yixuan Zhao for her consistent experimental assistance. I am also grateful to all of my group members, past and present, including Dr. Yi Yuan, Naixin Zhao, Songbo Cui, Jimmy Papazotos, Xin Jin, Yunxiang Tan, Dr. Jenner Ngai, Dr. Yaoyao Li, Dr. Guoliang Zhang, Dr. Fangqing Ge, Dr. Chengcheng Wang, Dr. Jun Peng, Dr. Lin Zhang, Dr. Venkateswarlu Samala, Scott Flynn, Andrew Stella, Zhaoyi Yin, Yunsheng Jiang, Daniel Afzal, Haoyu Fu, Merlan Nurzhanov, and Chenyang Guo. Their companionship and support have made my graduate journey both productive and enjoyable, and I truly believe that each encounter has been meaningful and has contributed to my growth.

I am deeply appreciative of my committee members for dedicating their valuable time to reviewing my comprehensive proposal, thesis, and defense. Their constructive feedback and guidance have significantly improved the quality of my work. I would like to thank Prof. Xianshe Feng and Prof. Michael Pope from the Department of Chemical Engineering, Prof. Xianguo Li from the Department of Mechanical and Mechatronics Engineering, and Prof. Yang Zhao from Western University, who served as my external examiner. Their collective expertise and thoughtful suggestions have been invaluable in shaping the final outcome of this dissertation.

To my friends and mentors, both near and far, I am truly grateful for their unwavering support. In Toronto, I have been fortunate to stay connected with Maoyu Zhu, Jiaqi Wu, and Youwei Li, friends I have known since middle school, whose companionship has been a constant source of joy and comfort and who always make me feel at home. In Wuhan, although separated by distance, I am deeply thankful to Jia Ye, Sitong Liu, Xueyin Fang, and You Tang, who always send me messages of encouragement and care, reminding me that their support is never far away. I would like to thank Shengfeng Xue for his generous help in daily life, which made many moments of this journey easier and brighter. Finally, I also owe special thanks to my high school Chinese literature teacher, Junling Xin; we were fortunate enough to gather together in Vancouver and Toronto in two consecutive years, an experience that brought warmth and inspiration during my doctoral journey.

To my family, I owe my deepest gratitude for their unconditional love, patience, and encouragement not only throughout my doctoral journey but also throughout my whole life. In particular, I would like to thank my father, who has always believed in me and supported me without pressure, giving me the freedom to pursue my own path with confidence. I am also grateful to all my uncles and aunts, who have each shown support and care in their own ways, reminding me that I have a strong family foundation behind me. I especially miss my grandparents, who raised me with love and guidance but passed away before I entered university as an undergrad; their memory continues to inspire me and give me strength. The unwavering support of my family has carried me through the most challenging moments and has been the source of my perseverance.

As a final reflection, I would like to share some words that have touched me deeply since the very beginning of my determination to pursue a Ph.D. It captures the many encounters that have shaped the journey of my life, during which I learned to study, I learned to teach, and eventually I learned to grow:

Someone comes to my life and quickly goes.

Someone moves my soul to dance with the passing whisper of their wisdom.

Someone makes the sky more beautiful to gaze upon.

They stay in my life for a little while, leaving footprints in my hearts.

And then I'll never ever be the same.

Zhe Huang

Waterloo, ON, Canada

September 2025

Dedication

To Wuhan, my birthplace and my home, where I lived, learned, and dreamed until the day my Ph.D. journey was to begin.

In early 2020, as I prepared to set out, the world paused. My departure was delayed, my city was tested, and life was forever changed.

This work is for the memory of those we lost, the strength of those who endured, and the resilience that carried me from the first days of lockdown to this final page.

Table of Contents

Examining Committee Membership ii
Author's Declaration iii
Statement of Contributions iv
Abstract vii
Acknowledgements xi
Dedication xiv
List of Figures xxi
List of Tables xxxvi
List of Abbreviations xxxix
Chapter 1 Introduction 1
1.1 Lithium-Ion Batteries (LIBs) 1
1.2 Lithium-Sulfur (Li-S) Batteries 6
1.2.1 Electrochemical Reactions in Li-S Batteries 8
1.2.2 Effects of Soluble Lithium Polysulfides (LPSs) 10
1.2.3 Main Problems and Challenges in Li-S Batteries 11
1.2.4 Enhancement Strategies for Li-S Batteries 15
1.3 Lithium Sulfide (Li_2S)-Based Li-S Batteries 16
1.3.1 Activation of Li_2S 18
1.3.2 Nanostructure Engineering: Li_2S@Carbon Nanocomposites 31
1.3.3 Binder Materials in Li_2S-Based Batteries 45
1.3.4 Li_2S-Based Full Cells 52
1.4 Objective and Structure of This Thesis 63
Chapter 2 Experimental Materials and Characterization Methods 66
2.1 Chemicals and Materials 66
2.2 Experimental Instruments and Equipment 68
2.3 Phase and Elemental Analysis 69
2.3.1 Powder X-ray Diffraction (XRD) 69
2.3.2 Fourier Transform Infrared Spectroscopy (FTIR) 71

2.3.3 Ultraviolet-Visible Spectroscopy 72
2.4 Morphological and Structural Analysis 73
2.4.1 Scanning Electron Microscope (SEM) 73
2.4.2 High-Resolution Transmission Electron Microscopy (HRTEM) 73
2.5 Electrochemical Performance Analysis 74
2.5.1 Electrode Processing 74
2.5.2 Coin Cell Assembly 75
2.5.3 Electrochemical Impedance Spectroscopy (EIS) 76
2.5.4 Cyclic Voltammetry (CV) 77
2.5.5 Galvanostatic Charge and Discharge 79
Chapter 3 Mitigating First Charge Overpotential of Li_2S-Based Lithium-Sulfur Batteries by Leveraging PVDF Reaction with the LiOH/Li_2O Layer 81
3.1 Introduction 81
3.2 Experimental Section 85
3.2.1 Materials 85
3.2.2 Reactions between Lithium Compounds and Binders 85
3.2.3 Fabrication of Lithium Sulfide Electrodes 85
3.2.4 Electrochemical Measurements 86
3.2.5 Characterization 86
3.3 Results and Discussion 87
3.3.1 Reaction between PVDF and LiOH or Li_2O 87
3.3.2 First Charge/Discharge Cycle of Li_2S Cathodes 89
3.3.3 Reaction of Li_2S with PVDF 93
3.3.4 Effects of Stirring on the Crystallinity of the Li_2S Particles 96
3.3.5 Impacts of the Reaction of PVDF with Commercial Li_2S on the First Cycle of Li_2S-LSBs 98
3.4 Conclusions 104
3.5 Supporting Information 105
Chapter 4 Zinc Complex-Based Multifunctional Binders for Lithium Sulfide-Based Lithium-Sulfur Batteries 113

4.1 Introduction 113
4.2 Experimental Section 116
4.2.1 Materials 116
4.2.2 Synthesis of $Zn(OAc)_2$·DEA, $Zn(OAc)_2$·TEA and $Zn(OAc)_2$·TEA/PEI Complex Solution 116
4.2.3 Synthesis of Li_2S_6 117
4.2.4 Fabrication of Lithium Sulfide Electrodes 117
4.2.5 Electrochemical Measurements 117
4.2.6 Characterization 118
4.3 Results and Discussion 119
4.3.1 Preparation of $Zn(OAc)_2$·TEA Complex 119
4.3.2 Electrochemical Performance of $Zn(OAc)_2$·TEA-Based Li_2S Electrode 121
4.3.3 Modification of $Zn(OAc)_2$·TEA with PEI 126
4.3.4 Electrochemical Performance of $Zn(OAc)_2$·TEA/PEI-Based Li_2S Electrodes 127
4.3.5 Mechanical Integrity and Structural Evolution of PVDF-, $Zn(OAc)_2$·TEA-, and $Zn(OAc)_2$·TEA/PEI (10%)-Based Li_2S Electrodes 131
4.4 Conclusions 133
4.5 Supporting Information 134
Chapter 5 Facile Synthesis of Li_2S@Carbon Nanocomposite via Precursor Solution Infiltration-Decomposition for High-Performance Lithium Sulfide Batteries 144
5.1 Introduction 144
5.2 Experimental Section 148
5.2.1 Materials 148
5.2.2 Preparation of Li_2CS_3 148
5.2.3 Preparation of Nano Li_2S 148
5.2.4 Preparation of Li_2CS_3@SP Precursor Composite 148
5.2.5 Preparation of Li_2S@SP Precursor Nanocomposite 148
5.2.6 Preparation of S@SP Nanocomposite 149
5.2.7 Fabrication of Cathodes 149
5.2.8 Electrochemical Measurements 149

5.2.9 Characterizations 149
5.3 Results and Discussion 150
5.3.1 Preparation and Characterization of Li_2CS_3 and Nano Li_2S 150
5.3.2 Preparation and Characterization of Li_2CS_3@SP Precursor and Li_2S@SP Nanocomposite 152
5.3.3 Electrochemical Performance of Li_2S@SP Nanocomposites 154
5.3.4 Performance comparison of Li_2S@SP Nanocomposite with Commercial Li_2S and Nano Li_2S 157
5.3.5 Performance comparison of Li_2S@SP Nanocomposite with S@SP Nanocomposite 161
5.4 Conclusions 165
5.5 Supporting Information 166
Chapter 6 Multi-Cycle Precursor Infiltration-Thermal Decomposition Achieves High In-Pore Li_2S Loading in Mesoporous Carbon for High-Performance Lithium Sulfide Batteries 173
6.1 Introduction 173
6.2 Experimental Section 177
6.2.1 Materials 177
6.2.2 Preparation of Li_2CS_3 Solution 177
6.2.3 Preparation of Li_2S@SP-1 Nanocomposite 177
6.2.4 Preparation of Li_2S@SP-3 and Li_2S@SP-5 Nanocomposites 177
6.2.5 Synthesis of S@SP Nanocomposite 178
6.2.6 Fabrication of Cathodes 178
6.2.7 Electrochemical Measurements 178
6.2.8 Characterizations 178
6.3 Results and Discussion 179
6.3.1 Synthesis of Li_2S@SP Nanocomposites 179
6.3.2 Characterization of Li_2S@SP Nanocomposites 181
6.3.3 Electrochemical Performance of Li_2S@SP Nanocomposites 183
6.3.4 Performance Comparison of Li_2S@SP-5 and S@SP Nanocomposites 187
6.4 Conclusions 192

6.5 Supporting Information 193

Chapter 7 Crosslinked Polyethylenimine-Epoxy Resin Binder for High-Performance Li_2S@C Nanocomposite Cathodes 200

7.1 Introduction 200

7.2 Experimental Section 203

7.2.1 Materials 203

7.2.2 Preparation of Li_2S@SP Nanocomposite 203

7.2.3 Preparation of PEI Solutions and an ER Solution in NMP 204

7.2.4 Preparation of Pre-crosslinked PEI-ER Binder-based Li_2S Electrodes 204

7.2.5 Preparation of *In-Situ*-Crosslinked PEI-ER Binder-based Li_2S Electrodes 204

7.2.6 Preparation of PVDF- and PVP-based Li_2S Electrodes 205

7.2.7 Electrochemical Measurements 205

7.2.8 Characterizations 205

7.3 Results and Discussion 206

7.3.1 Selection of PEI and ER as Binder Raw Materials 206

7.3.2 Impact of PEI Molecular Weight on the Electrochemical Performance of PEI-ER Binders in Li_2S@SP Cathode 208

7.3.3 Optimization of PEI-ER Mass Ratio and Development of *In-Situ* Crosslinking Strategy 212

7.3.4 Performance Benchmarking: *In-Situ* Crosslinked PEI-$ER_{1:1}$ Binder versus Conventional PVDF and PVP Binders 216

7.4 Conclusions 228

7.5 Supporting Information 229

Chapter 8 Integration of High In-Pore Li_2S Loading Li_2S@Carbon Cathode with Si/C Anode for Lithium-Metal-Free Full Cells 233

8.1 Introduction 233

8.2 Experimental Section 235

8.2.1 Materials 235

8.2.2 Preparation of Li_2S@SP Nanocomposite 235

8.2.3 Preparation of PEI solutions and an ER solution in NMP 236

8.2.4 Preparation of *In-situ* crosslinked PEI-ER binder-based Li_2S electrode 236

8.2.5 Preparation of PVP-based Li_2S electrodes 236
8.2.6 Preparation of Si/C Anode 236
8.2.7 Electrochemical Measurements 236
8.3 Results and Discussion 238
8.4 Conclusions 244
Chapter 9 Conclusions and Outlook 245
9.1 Conclusions 245
9.2 Outlook 250
References 253

List of Figures

Figure 1.1 Schematic diagram of the structure of a typical Li-ion battery.[19] Copyright © 2024 Elsevier Ltd. All rights are reserved, including those for text and data mining, AI training, and similar technologies. 2

Figure 1.2 Four types of Li-ion battery configurations: (a) cylindrical, (b) coin, (c) prismatic, and (d) pouch cell.[47] Copyright © 2001, Springer Nature Limited. 4

Figure 1.3 Brief timeline of important events in the development of Li-S batteries.[86] Adapted from Ref. 86 with permission from Copyright © 2023, Shanghai University and Periodicals Agency of Shanghai University. 7

Figure 1.4 Comparison of (a) capacity density and energy density.[94] Reproduced from Ref. 94. Copyright © 2021 The Authors. Advanced Science published by Wiley-VCH GmbH, under the Creative Commons Attribution (CC BY) license. (b) Massive stockpiles of sulfur at an oil refinery in Vancouver, Canada.[95] Copyright © 2016 Wiley-VCH Verlag GmbH & Co. KGaA, Weinheim. 8

Figure 1.5 (a) Schematic of Li-S batteries.[87] Copyright © 2014, American Chemical Society. (b) The discharge/charge curves and multi-step reaction of Li-S batteries.[98] Copyright © 2017 WILEY-VCH Verlag GmbH & Co. KGaA, Weinheim. 9

Figure 1.6 The formation of soluble lithium polysulfides (LPSs).[101] Copyright © 2022 The Korean Society of Industrial and Engineering Chemistry. Published by Elsevier B.V. All rights reserved. 10

Figure 1.7 Main problems and challenges in Li-S batteries.[111] Copyright © 2019 WILEY-VCH Verlag GmbH & Co. KGaA, Weinheim. 12

Figure 1.8 The "shuttle effect" of soluble lithium polysulfides (LPSs).[113] Copyright © 2020, The Author(s), under exclusive license to Springer Nature Limited. 13

Figure 1.9 Schematic of the main issues with lithium metal anode: (a) short circuit introduced by Li dendrites, (b) formation of inactive/dead Li, and (c) development of thick and mechanically unstable SEI.[119] Copyright © 2020 Elsevier B.V. All rights reserved. 15

Figure 1.10 The challenges faced by the sulfur (S_8) and lithium sulfide (Li_2S) batteries.[140] Copyright © 2022 The Authors. Published by American Chemical Society. 17

Figure 1.11 (a) A typical initial charging curve of Li_2S cathodes.[145] Copyright © 2017, Springer Nature Limited. (b) Crystal structure and activation barrier of Li_2S.[168] Copyright © 2020, American Chemical Society. 19

Figure 1.12 (a) The initial potential barrier of Li_2S cathode material at C/8, C/50, C/200, and C/1000. (b) Relationship between the logarithm of the current rate and the overpotential of Li_2S cathode. (c) The model for the initial charging of Li_2S.[104] Adapted from Ref. 104. Copyright © 2012, American Chemical Society. 21

Figure 1.13 (a) Proposed reaction mechanism of Li_2S initial charge by Vizintin *et al.*[174] Copyright © 2017 Elsevier B.V. All rights reserved. (b) *In situ* S K-edge XAS spectra. (c) Proposed reaction scheme of the Li_2S electrode during the initial charge and discharge processes by Zhang *et al*.[175] Copyright © 2017, American Chemical Society. 22

Figure 1.14 (a) *In situ* time-lapse XRD patterns and (b) its enlarged plot. (c) *Ex situ* XANES of S K-edge for Li_2S@graphene electrodes at different charge/discharge states. (d) *Ex situ* XANES of S K-edge for Li_2S@graphene electrodes at certain states of charge/discharge during the first cycle.[145] Copyright © 2017, Springer Nature Limited. 24

Figure 1.15 (a) Degradation region of common ether-based electrolyte in the initial charging process of Li_2S batteries.[177] Copyright © 2014, American Chemical Society. (b) The corrosion mechanism of Al as the current collector in the Li-S batteries.[178] Copyright © 2023 Published by Elsevier Ltd. 25

Figure 1.16 (a) Schematic diagram of the activation process of Li_2S (upside) without ethanol and (downside) with ethanol added in the electrolyte. (b) The initial charge/discharge curves of Li_2S batteries based on electrolytes with different amount addition of ethanol.[188] Copyright © 2019 Royal Society of Chemistry. 28

Figure 1.17 (a) Schematic of high-energy ball milling process for preparing Li_2S-C nanocomposites.[160] Copyright © 2012 American Chemical Society. (b) Schematic of the

approach for synthesizing the Li_2S/C composite particles encapsulated by a nitrogen-doped carbon shell.[199] Copyright © 2013 Royal Society of Chemistry. (c) Schematic illustration of the fabrications of Li_2S and the Li_2S/C hybrid.[200] Copyright © 2013 Royal Society of Chemistry. 32

Figure 1.18 (a) *In situ* synthesis scheme for a Li_2S@Carbon composite.[206] Copyright © 2013 Royal Society of Chemistry. (b) Ellingham diagram for different carbothermal reductions. Numbers at the end of the lines are DGR values at 820 °C.[207] Reproduced from Ref. 207 under a Creative Commons Attribution–NonCommercial 3.0 Unported License. Copyright © 2015 The Authors. Published by Royal Society of Chemistry. (c) Schematic of the fabrication process of Li_2S@C strips and structural evolution of PVA during its assisted carbothermal reduction of Li_2SO_4.[204] Copyright © 2013 Royal Society of Chemistry. 34

Figure 1.19 (a) Schematic illustration of the production of freestanding flexible Li_2S@NCNF paper electrodes via Ar-protected carbothermal reduction of Li_2SO_4@PVP fabrics made by electrospinning at ambient conditions.[209] © 2017 WILEY-VCH Verlag GmbH & Co. KGaA, Weinheim (b) Illustrative process of magnesothermal synthesis of Li_2S and purification.[213] Copyright © 2022 American Chemical Society..... 36

Figure 1.20 (a) X-ray diffraction characterization of Li_2S/mesoporous carbon nanocomposite particles.[157] Copyright © 2010 American Chemical Society. (b) Schematic illustration of the synthesis of Li_2S/GO@C nanospheres.[214] Copyright © 2015 American Chemical Society. 38

Figure 1.21 (a) Schematics of routes to prepare Li_2S/C composite and electrodes.[219] Copyright © 2016 Elsevier B.V. All rights reserved. (b) Li_2S@graphene capsules by burning lithium in CS_2.[145] Copyright © 2017, Springer Nature Limited. (c) Schematic illustration of the synthesis procedure of Li_2S@PC-CNT.[220] Copyright © 2013 Royal Society of Chemistry. 40

Figure 1.22 Schematic of the Li_2S and Li_2S-graphene composite synthesis process.[224] Copyright © 2014 WILEY-VCH Verlag GmbH & Co. KGaA, Weinheim. 41

Figure 1.23 (a) Schematic illustration of the material preparation processes of the nano-Li_2S/rGO paper and structure changes during cycling of nano-Li_2S/rGO paper.[225] Copyright © 2015, American Chemical Society. (b) Synthetic procedure of the 3DCG–Li_2S composite.[226] Copyright © 2016, American Chemical Society. 42

Figure 1.24 (a) Cycling stability of the graphene-nano Li_2S@C electrode at 0.5 C and its morphological characterization.[227] Copyright © 2016, American Chemical Society. (b) Cycling stability of free-standing Li_2S electrodes at 0.5 C and its schematic illustration by using infiltration of active materials into porous carbonized biomass sheets.[228] Copyright © 2016 WILEY-VCH Verlag GmbH & Co. KGaA, Weinheim. 43

Figure 1.25 The functions of polymer binders in Li-S batteries.[253] Adapted from Ref. 253. Copyright © 2023 Wiley-VCH GmbH. 47

Figure 1.26 Schematic of the architecture of the Li_2S-LSB full cell composed of Cu foil/Li metal/organic electrolyte-1/ceramic separator (LATP)/organic electrolyte-2/Li_2S cathode/carbon/Ti foil.[173] Copyright © 2008 Royal Society of Chemistry. 54

Figure 2.1 Schematic of Bragg's Law.[284] Copyright © 2010 Elsevier Ltd. All rights reserved. 69

Figure 2.2 XRD patterns of (a) Kapton tape and (b) Kapton tape-covered commercial Li_2S powders obtained by Bruker D8 Discover X-ray Diffraction Spectrometer. 71

Figure 2.3 Schematics of (a) Transmission FTIR and (b) Attenuated total reflectance (ATR)-FTIR.[286] Adapted from Ref. 286. Copyright © 2015 by the authors, licensed under CC BY. 72

Figure 2.4 Schematic of the assembly of a coin cell.[287] Adapted from Ref. 287. Copyright © 2023, The Author(s), under exclusive license to Springer-Verlag GmbH Germany, part of Springer Nature. 76

Figure 2.5 (a) Representation of Randles circuit, and (b) its characteristic Nyquist plot. (c) Randles circuit with Warburg element and (d) its characteristic Nyquist plot.[288]

Reproduced from Ref. 288, used under the Creative Commons Attribution (CC BY) license. 76

Figure 2.6 (a) A schematic CV curve for a simple reversible reaction, with the inserted showing the voltage change during the CV scan. (b) CV curves of a typical Li-S battery at a scanning rate of 0.1 mV s^{-1}.[289] Copyright © 2019 WILEY-VCH Verlag GmbH & Co. KGaA, Weinheim. 78

Figure 2.7 The typical discharge/charge curve of Li-S batteries.[290] Copyright © The Royal Society of Chemistry. Licensed under CC BY 3.0. 79

Figure 3.1 The first cycle galvanostatic charge/discharge characteristics of a typical Li_2S-LSB and the first discharge-charge cycle of a typical S-LSB, where the specific capacities were normalized to be based on sulfur for a clearer comparison. Data for the S-LSB are reproduced with permission.[295] Copyright © 2021 American Chemical Society..... 82

Figure 3.2 (a) Dehydrofluorination of PVDF in the presence of a base to form unsaturated C=C bonds. FTIR spectra of (b) commercial PVDF, (c) PVDF reacted with LiOH (n_{Li}:n_F = 1:1) in NMP for 24 and 48 h, and (d) PVDF reacted with Li_2O (n_{Li}:n_F = 1:1) in NMP for 24 and 48 h..... 87

Figure 3.3 First charge/discharge curves of (a) PVDF-0h, PVDF-24h and PVDF-48h, and (b) PVDF-0h-A, PVDF-24h-A, and PVDF-48h-A batteries. Inserts are the zoomed initial charging stage of the batteries. All the electrochemical tests were carried out at 0.1 C (1 C = 1166 mA g^{-1} (Li_2S)) with an upper cut-off voltage of 3.6 V. 89

Figure 3.4 ATR-FTIR spectra of (a) PVDF treated Li_2S (molar ratio n_{Li}:n_F =1:1) in in anhydrous NMP by stirring for 24 h and (b) PVDF samples treated with Li_2S (molar ratio n_{Li}:n_F = 10:1 or mass ratio m_{Li2S}:m_{PVDF}=70:10) in anhydrous NMP by grinding for 30 min (and 12 h drying at 50 °C under vacuum) and stirring for 24 h and 48 h, respectively.. 94

Figure 3.5 XRD patterns of (a) commercial Li_2S powders, (b) commercial Li_2S ground for 2 h, (c) commercial Li_2S powders stirred in NMP for 24 h, dried electrode slurries based on (d) PVDF-0h, (e) PVDF-24h and (f) PVDF-48h. The average Li_2S crystal size (D) values

of the samples calculated using XRD data with the *Scherrer* equation are shown in the graphs. Peak (111) was excluded for the average crystal size calculation since this peak overlaps with one of the peaks from the Kapton tape. 97

Figure 3.6 First charge/discharge curves of (a) PVP-48h and (b) PVDF5%-48h-5% batteries. Inserts are the zoomed initial charging stage of the batteries. The first charge/discharge curves of PVDF-0h and PVDF-48h are incorporated for comparison. All the electrochemical tests were carried out at 0.1 C (1 C = 1166 mA g^{-1} (Li_2S)) with an upper cut-off voltage of 3.6 V. 99

Figure 3.7 Schematic first charging processes of Li_2S particles in different Li_2S-LSBs at a rate of 0.1 C. ΔE (Li_2S) and ΔE (LiOH/Li_2O) are the overpotentials contributed by the pure crystalline Li_2S (~0.4 V) and the LiOH/Li_2O layer (~1.2 V for the PVP-48h cell with the pristine commercial Li_2S), respectively..... 102

Figure 4.1 (a) $Zn(OAc)_2$·TEA prepared by mixing anhydrous $Zn(OAc)_2$ and TEA mixed in NMP. (b) XRD pattern of vacuum-dried $Zn(OAc)_2$·TEA. (c) XRD pattern of Kapton tape-covered dried Li_2S/SP/$Zn(OAc)_2$·TEA mixture. (d) Reaction between $Zn(OAc)_2$·TEA and lithium polysulfides (Li_2S_x, where x = 4–8), with photographs showing a Li_2S_6 solution before and after the addition of 0.5 molar equivalents of $Zn(OAc)_2$·TEA inside a glove box. The dark red Li_2S_6 solution turned into a suspension with brown precipitates, indicating complete reaction..... 120

Figure 4.2 Electrochemical performance of Li_2S electrodes using PVDF and $Zn(OAc)_2$·TEA as binders. (a) First-cycle charge/discharge curves at 0.05 C. (b, c) Initial five charge/discharge cycles of PVDF- and $Zn(OAc)_2$·TEA-based electrodes, respectively. (d) Cycling performance at 0.1 C. (e) Rate performance at various current densities. (f, g) Cyclic voltammetry (CV) curves of PVDF- and $Zn(OAc)_2$·TEA-based electrodes, respectively. Electrodes were scanned from 1.7 to 4.0 V for the first cycle, and from 1.7 to 2.8 V for subsequent cycles at a scan rate of 0.025 mV s^{-1}. 122

Figure 4.3 (a) Proposed polysulfide trapping cycles of $Zn(OAc)_2$·TEA during the initial charge and subsequent discharge/charge processes in the $Zn(OAc)_2$·TEA-based Li_2S

electrode ([red]: reduction; [ox]: oxidation). (b) Schematic representation of the structural evolution of Li_2S particles during the first charge/discharge cycle, corresponding to the stages illustrated in (a). 125

Figure 4.4 Schematic illustration of the formation of the $Zn(OAc)_2$·TEA/PEI binder, where the addition of PEI enables the establishment of a three-dimensional (3D) network through coordination between Zn^{2+} ions in $Zn(OAc)_2$·TEA and nitrogen atoms in PEI. 127

Figure 4.5 Electrochemical performance of Li_2S electrodes using PVDF and various $Zn(OAc)_2$·TEA/PEI binders. (a) Initial five charge/discharge curves of $Zn(OAc)_2$·TEA/PEI (10%)-based electrode. (b) Initial five charge/discharge curves of $Zn(OAc)_2$·TEA/PEI (15%)-based electrode. (c) Initial charge/discharge curves $Zn(OAc)_2$·TEA/PEI (25%)-based electrode. (d) Cycling performance of the $Zn(OAc)_2$·TEA/PEI (10%)- and $Zn(OAc)_2$·TEA/PEI (15%)-based electrodes at 0.1 C. (e) Rate performance of the $Zn(OAc)_2$·TEA/PEI (10%)- and $Zn(OAc)_2$·TEA/PEI (15%)-based electrodes at various rates. (f) Long-term cycling performance of PVDF-, $Zn(OAc)_2$·TEA-, and $Zn(OAc)_2$·TEA/PEI (10%)-based electrodes at 0.5 C, which were all activated at 0.05 C in the first cycle. 128

Figure 4.6 SEM images of (a, d) PVDF-, (b, e) $Zn(OAc)_2$·TEA-, and (c, f) $Zn(OAc)_2$·TEA/PEI (10%)-based electrodes before and after 100 cycles. 132

Figure 5.1 (a) Conversion of Li_2CS_3 to Li_2S over time at 150 and 200 °C under vacuum. The inset shows the corresponding weight change of Li_2CS_3 samples as a function of time at different temperatures. (b) XRD patterns of cLi_2S, Li_2CS_3, Li_2S-200, and Li_2S-400. (c) SEM images of cLi_2S, Li_2CS_3 and Li_2S-400. 151

Figure 5.2 (a) Conversion of Li_2CS_3@SP precursor to Li_2S@SP nanocomposites over time at 150 and 200 °C in vacuo. (b) XRD patterns of Li_2S@SP-200, Li_2S@SP-350, Li_2S@SP-400 and Li_2S@SP-450. (c) SEM images of cLi_2S/SP (commercial Li_2S mixed with SP at a 6:4 mass ratio), Li_2S@SP-200, Li_2S@SP-400 and Li_2S@SP-450..... 153

Figure 5.3 Initial charge/discharge curves at 0.1 C for batteries with PVP binder and cathode materials of (a) Li_2S@SP-200, (b) Li_2S@SP-350, (c) Li_2S@SP-400, and (d) Li_2S@SP-450. The voltage range was set to 1.7–4.0 V for the first cycle and 1.7–2.8 V for subsequent cycles. (e) Cycling performance of the batteries at 0.1 C. 155

Figure 5.4 (a) Schematic illustration of the cathode structures for cLi_2S/SP/PVP, Li_2S-400/SP/PVP, and Li_2S@SP-400/SP/PVP. Initial charge/discharge curves at 0.1 C for batteries with the active material of: (b) cLi_2S, (c) Li_2S-400, and (d) Li_2S@SP-400. The first charge voltage was set to 4.0 V and the following electrochemical processes were in the voltage window between 1.7 and 2.8 V. (e) Cycling performance of batteries based on cLi_2S, Li_2S-400, and Li_2S@SP-400 at 0.1 C. (f) Rate performance of batteries based on cLi_2S, Li_2S-400, and Li_2S@SP-400. (g) Cycling performance of batteries based on Li_2S@SP-400 at 2 C. 158

Figure 5.5 CV of (a) Li_2S@SP-400 and (b) S@SP with a scanning rate of 0.1 mV s^{-1}. (c) Initial charge/discharge curves of batteries based on Li_2S@SP-400-PVP and S@SP-PVP at 0.1 C. The first charge voltage of Li_2S@SP-400 was set to 4.0 V and the following electrochemical processes were in the voltage window between 1.7 and 2.8 V. (d) Rate performance of batteries based on Li_2S@SP-400 and S@SP. (e) Cycling performance of batteries based on S@SP and Li_2S@SP-400 at 1 C. 162

Figure 6.1 Schematic illustration of the synthesis of Li_2S@C nanocomposites with high in-pore Li_2S loading via multi-cycle Li_2CS_3 infiltration-decomposition strategy..... 180

Figure 6.2 (a) XRD patterns of cLi_2S/SP (manually ground mixture, 70:30 wt.%), Li_2S@SP-1, Li_2S@SP-3, and Li_2S@SP-5. (b) Crystallite sizes derived from XRD. (c) Schematic illustration of sulfur species evolution and volume change during charging process of Li_2S@SP-1 and Li_2S@SP-5. SEM images of charged electrodes: (d) Li_2S@SP-1/SP/PVP, (e) Li_2S@SP-3/SP/PVP, and (f) Li_2S@SP-5/SP/PVP (Li_2S@SP:SP:PVP = 8:1:1 by weight), each charged from open circuit voltage (OCV) to 4.0 V..... 182

Figure 6.3 Cyclic voltammetry (CV) profiles of freshly assembled Li_2S-LSBs based on (a) Li_2S@SP-1, (b) Li_2S@SP-3, and (c) Li_2S@SP-5 nanocomposites, recorded at a scan rate

of 0.025 mV s^{-1}. The initial CV scan was performed anodically from open-circuit voltage (OCV) to a cutoff of 4.0 V, followed by cyclic scans within the voltage window of 1.7–2.8 V. 184

Figure 6.4 Galvanostatic charge-discharge (GCD) performance of Li_2S@SP electrodes. (a–c) Initial charge/discharge profiles; (d) long-term cycling at 0.1 C; (e) rate performance; and (f) long-term cycling at 1.0 C. The initial charge was performed at 0.1 C to 4.0 V, followed by cycling within 1.7–2.8 V. 185

Figure 6.5 CV profiles of (a) Li_2S@SP-5 and (b) S@SP at a rate of 0.1 mV s^{-1}. (c) Initial charge/discharge curves of Li_2S@SP-5 and S@SP cells at 0.1 C. The first charge of Li_2S@SP-5 was carried out to 4.0 V, followed by cycling within 1.7–2.8 V. (d) Rate performance of Li_2S@SP-5 and S@SP cells. (e) Long-term cycling performance of Li_2S@SP-5 and S@SP cells at 0.5 C. 188

Figure 6.6 SEM images of (a) fresh S@SP electrode, (b) cycled S@SP electrode in the charged state after 100 cycles at 0.5 C, (c) fresh Li_2S@SP-5 electrode after initial charging, and (d) cycled Li_2S@SP-5 electrode in the charged state after 100 cycles at 0.5 C. 190

Figure 7.1 Schematics of reaction between polyethylenimine (PEI) and epoxy resin (ER). 207

Figure 7.2 Charge/Discharge curves of (a) PEI(LM)-$ER_{1:2}$-based and (b) PEI-$ER_{1:2}$-based electrodes at 0.05 C for the initial cycle and 0.1 C for the following ones. (c) Long-term cycling comparison between these two electrodes at 0.5 C. 210

Figure 7.3 Initial charge/discharge curves of (a) PEI-$ER_{1:0.5}$- (b) PEI-$ER_{1:1}$- (c) PEI-$ER_{1:4}$-, and (d) *in-situ* crosslinked PEI-$ER_{1:1}$-based electrodes at 0.05 C for the initial cycle and 0.1 C for the following ones. 213

Figure 7.4 Schematic illustration of (a) Li_2S@SP/SP/PVDF (b) Li_2S@SP/SP/PVP and (c) Li_2S@SP/SP/*in-situ* crosslinked PEI-$ER_{1:1}$ electrodes. Initial charge/discharge curves of (d) PVDF- (e) PVP- and (f) *in-situ* crosslinked PEI-$ER_{1:1}$-based electrodes. (g) Rate

performance comparison among PVDF-, PVP- and *in-situ* crosslinked PEI-$ER_{1:1}$-based electrodes. (h) Long-term cycling performance comparison among PVDF-, PVP- and *in-situ* crosslinked PEI-$ER_{1:1}$-based electrodes at 0.1 C. (i) Long-term cycling performance comparison between PVP- and *in-situ* crosslinked PEI-$ER_{1:1}$-based electrodes at 0.5 C. 219

Figure 7.5 Cyclic voltammetry (CV) of (a) PVP- and (b) *in-situ* crosslinked PEI-$ER_{1:1}$-based electrodes at a scan rate of 0.025 mV s^{-1}. The initial upper scan was set to 4.0 V and the following was set between 1.7–2.8 V. 223

Figure 7.6 SEM images of (a) fresh PVP-based Li_2S@SP electrode after initial charging, (b) cycled PVP-based Li_2S@SP electrode in the charged state after 500 cycles at 0.5 C, (c) fresh *in-situ* crosslinked PEI-$ER_{1:1}$-based Li_2S@SP electrode after initial charging, and (d) cycled *in-situ* crosslinked PEI-$ER_{1:1}$-based Li_2S@SP electrode in the charged state after 500 cycles at 0.5 C. 225

Figure 8.1 Activation of Si/C anode via discharge-charge-discharge processes at 0.25 mA between 0.01–2.0 V. 238

Figure 8.2 Initial charge/discharge curves of Li_2S@SP||Si/C full cells using (a) PVP and (b) *in-situ* crosslinked PEI-$ER_{1:1}$ binders in the cathodes. 239

Figure 8.3 Electrochemical performance of Li_2S@SP||Si/C full cell: (a) Rate performance. (b) Cycling performance at 0.1 C. (c) Long-term cycling performance at 0.5 C. The voltage range was set to 1.5–3.0 V after the initial activation to 4.0 V. 241

Figure S 3.1 The mixture of PVDF with (a and d) LiOH, (b and e) Li_2O and (c and f) Li_2S in molar ration n_{Li}:n_F = 1:1 in NMP in the beginning and after 24 h. The white particles in (a), (b), and (c) are the unreacted LiOH, Li_2O, and Li_2S, respectively, while the unreacted PVDF dissolved in NMP is colorless. 105

Figure S 3.2 Full ATR-FTIR spectra of (a) the commercial PVDF sample without treatment and PVDF samples treated (b) LiOH, (c) Li_2O, and (d) Li_2S (molar ratio n_{Li}:n_F=1:1) in anhydrous NMP by stirring for 24 h. 106

Figure S 3.3 Progress of the reaction between Li_2S powders and PVDF (m_{Li2S}:m_{PVDF} = 70:10 or n_{Li}:n_F = 10:1) with NMP as the solvent by hand grinding for 30 min. Experiments were carried out in an Ar-filled glove box. (a) The mixture of Li_2S and PVDF before being ground, (b) the mixture after being ground for 30 min, and (c) the mixture after being vacuum dried for 12 h at 50 °C. 107

Figure S 3.4 The Nyquist plots of experimentally measured data (dots) and fitting results (lines) of (a) PVDF-0h, (b) PVDF-24h, and (c) PVDF-48h. (d) shows the equivalent Randles circuit used for the fitting, where R_e is the resistance of the electrolyte solution, R_{ct} is the charge transfer resistance, *CPE* is the capacitance, and W_o is the Warburg impedance. 108

Figure S 3.5 The charge/discharge curves of the first five cycles of (a) PVDF-0h, (b) PVDF-24h, (c) PVDF-48h and (d) a battery using Li_2S ground for 2 h. All the electrochemical tests were carried out at 0.1 C (1 C = 1166 mA g^{-1} (Li_2S)) with upper cut-off voltage of 3.6 V for the first charge process and voltage window of 1.7–2.8 V for the following cycles. 109

Figure S 3.6 Cycling performance of cathodes at 0.1 C over 100 cycles: (a) PVDF-0h, (b) PVDF-24h, and (c) PVDF-48h. 110

Figure S 3.7 The charge/discharge curves of the first five cycles of (a) PVP-48h and (b) PVDF5%-48h-5%. All the electrochemical tests were carried at 0.1 C (1 C = 1166 mA g^{-1} (Li_2S)) with upper cut-off voltage of 3.6 V for the first charge process and voltage window of 1.7–2.8 V for the following cycles. 111

Figure S 3.8 Cycling performance of cathodes at 0.1 C over 100 cycles: (a) PVP-48h and (b) PVDF5%-48h-5%..... 112

Figure S 4.1 UV-vis spectroscopy analysis of LPS trapping by $Zn(OAc)_2$·TEA using Li_2S_6 as a representative polysulfide species, following a previously reported procedure.[282] (a) UV-vis spectra of Li_2S_6 in DME at various known concentrations. (b) Calibration curve of absorbance at 420 nm *vs.* Li_2S_6 concentration, with a linear fit given by Equation S4.1: 135

Figure S 4.2 Tafel plots derived from CV data at Peak A, B and C for Li_2S cathode using (a,b,c) PVDF and (d,e,f) $Zn(OAc)_2$·TEA, based on the CV curves shown in **Figure 4.2** (f) and (g)..... 137

Figure S 4.3 $Zn(OAc)_2$·TEA and different $Zn(OAc)_2$·TEA/PEI solutions after storage at room temperature for 12 h following preparation. 138

Figure S 4.4 Charge/discharge curves of $Zn(OAc)_2$·TEA-based electrodes corresponding to their rate performance data in **Figure 4.2** (g). 138

Figure S 4.5 Charge/discharge curves of the PEI-based electrode during the initial five cycles: the first cycle at 0.05 C and subsequent cycles at 0.1 C. 139

Figure S 4.6 Charge/discharge curves of (a) $Zn(OAc)_2$·TEA/PEI (10%)- and (b) $Zn(OAc)_2$·TEA/PEI (15%)-based electrodes corresponding to their rate performance data in **Figure 4.5** (e). 139

Figure S 4.7 Coulombic efficiencies of the electrodes corresponding to the rate performance tests presented in **Figure 4.2** (e) and **Figure 4.5** (e). 140

Figure S 4.8 Electrochemical performance of $Zn(OAc)_2$·TEA/PEI (10%)-based Li_2S cathodes with high areal loadings (3.72 and 4.51 mg cm^{-2}) on carbon paper current collectors at 0.5 C. The initial cycle was activated at 0.05 C. 140

Figure S 4.9 Nyquist plots from electrochemical impedance spectroscopy (EIS) of freshly prepared electrodes using PVDF, $Zn(OAc)_2$·TEA, $Zn(OAc)_2$·TEA/PEI (10%), $Zn(OAc)_2$·TEA/PEI (15%), $Zn(OAc)_2$·TEA/PEI (25%) binders. The inset shows the equivalent Randles circuit used for fitting, where R_e is the resistance of the electrolyte

solution, R_{ct} is the charge transfer resistance, *CPE* is the capacitance, and W_o is the Warburg impedance..... 141

Figure S 4.10 Nyquist plots from electrochemical impedance spectroscopy (EIS) of freshly prepared electrodes using PVDF, $Zn(OAc)_2$·TEA, $Zn(OAc)_2$·TEA/PEI (10%) binders. The inset shows the equivalent Randles circuit used for fitting, where R_e is the resistance of the electrolyte solution, R_{ct} is the charge transfer resistance, R_{int} is the interphase resistance, *CPE* is the capacitance, and W_o is the Warburg impedance. 142

Figure S 4.11 Tape peeling test results of Li_2S cathodes with different binders. Photographs showing the electrode surfaces and corresponding adhesive tapes after peeling: (a) PVDF, (b) $Zn(OAc)_2$·TEA, and (c) $Zn(OAc)_2$·TEA/PEI (10%). Tests were conducted inside an argon-filled glovebox by firmly pressing adhesive tape onto the electrode surface, then slowly peeling it off to assess adhesion and cohesion. 143

Figure S 5.1 Photos of (a) Commercial Li_2S powders, (b) Li_2S powders in EtOH (mixed in 60 mg_{Li2S}/1 mL_{EtOH}), (c) Li_2CS_3/EtOH solution (mixed in 60 mg_{Li2S}/100 μL_{CS2}), (d) Concentrated Li_2CS_3/EtOH solution, (e) Completely dried Li_2CS_3 powders, and (f) Li_2S-400. 166

Figure S 5.2 Solubility tests of as-prepared Li_2CS_3 powders in (a) 1,3-dioxolane (DOL), (b) dimethoxyethane (DME), and (c) *N*-methyl-2-pyrrolidone (NMP). 166

Figure S 5.3 SEM images of (a) Li_2CS_3 and (b) Super P. 168

Figure S 5.4 EIS of batteries based on Li_2S@SP nanocomposites using PVP as the binder. Inserted is the equivalent Randles circuit used for the fitting, where R_e is the resistance of the electrolyte solution, R_{ct} is the charge transfer resistance, *CPE* is the capacitance, and W_o is the Warburg impedance. 168

Figure S 5.5 LSV at 1.0 mV s^{-1} of battery based on carbon paper and lithium metal anode using liquid electrolyte containing 1.0 M LiTFSI in DOL/DME (*v*/*v*=1:1) with 2 wt.% $LiNO_3$ as additive. 169

Figure S 5.6 TEM images of (a) cLi_2S, (b) Li_2S-400, and (c) Li_2S@SP-400..... 170

Figure S 5.7 EIS of batteries based on cLi_2S, Li_2S-400 and Li_2S@SP-400. Inserted is the equivalent Randles circuit used for the fitting, where R_e is the resistance of the electrolyte solution, R_{ct} is the charge transfer resistance, *CPE* is the capacitance, and W_o is the Warburg impedance..... 170

Figure S 5.8 EIS of batteries based on charged Li_2S@SP-400 and S@SP. Inserted is the equivalent Randles circuit used for the fitting, where R_e is the resistance of the electrolyte solution, R_{ct} is the charge transfer resistance, *CPE* is the capacitance, and W_o is the Warburg impedance..... 171

Figure S 5.9 Picked charge/discharge curves from the rate performance in **Figure 5.5** (d). The picked cycles were 4th, 9th, 14th, 19th, and 24th (the third cycle of each C-rate). 172

Figure S 6.1 SEM images of the as-prepared nanocomposites: (a) cLi_2S/SP (b) Li_2S@SP-1, (c) Li_2S@SP-3, and (d) Li_2S@SP-5. 196

Figure S 6.2 EIS Nyquist plots of fresh Li_2S@SP-1, Li_2S@SP-3, and Li_2S@SP-5 electrodes. The inset shows the equivalent Randles circuit used for fitting, where R_e is the electrolyte resistance, R_{ct} is the charge transfer resistance, *CPE* is the capacitance, and W_o is the Warburg impedance..... 197

Figure S 6.3 EIS Nyquist plots of fresh S@SP and initially charged Li_2S@SP-5 electrodes. The inset shows the equivalent Randles circuit used for fitting, where R_e is the electrolyte resistance, R_{ct} is the charge transfer resistance, *CPE* is the capacitance, and W_o is the Warburg impedance..... 198

Figure S 7.1 EIS of fresh pre-mixed PEI(LM)-$ER_{1:2}$- and PEI-$ER_{1:2}$-based Li_2S@SP electrodes. Inserted is the equivalent Randles circuit used for the fitting, where R_e is the resistance of the electrolyte solution, R_{ct} is the charge transfer resistance, *CPE* is the capacitance, and W_o is the Warburg impedance. 229

Figure S 7.2 EIS of fresh pre-mixed PEI-$ER_{1:0.5}$-, PEI-$ER_{1:1}$-, PEI-$ER_{1:2}$-, PEI-$ER_{1:4}$- and *in-situ* crosslinked PEI-$ER_{1:1}$-based Li_2S@SP electrodes. Inserted is the equivalent Randles circuit used for the fitting, where R_e is the resistance of the electrolyte solution, R_{ct} is the

charge transfer resistance, *CPE* is the capacitance, and W_o is the Warburg impedance. 230

Figure S 7.3 Tape peeling test comparison of Li_2S@SP electrodes using different binders: (a) PVDF, (b) PVP, and (c) In-situ crosslinked PEI-$ER_{1:1}$ 231

Figure S 7.4 EIS of fresh PVDF-, PVP- and *in-situ* crosslinked PEI-$ER_{1:1}$-based Li_2S@SP electrodes. Inserted is the equivalent Randles circuit used for the fitting, where R_e is the resistance of the electrolyte solution, R_{ct} is the charge transfer resistance, *CPE* is the capacitance, and W_o is the Warburg impedance. 232

List of Tables

Table 1.1 Electrochemical characteristics of typical cathode materials. 5

Table 1.2 Low electronic and ion conductivities of Li_2S and S_8.[112] 13

Table 1.3 Molar mass and density of Li_2S and S..... 14

Table 1.4 Chemical Lithiation Agents for Elemental Sulfur. 36

Table 1.5 Chemical Sulfuration Agents for Lithium-Rich Precursors. 39

Table 1.6 A summary of commonly used binders based on their primary roles in S-LSBs.[262] Adapted from Ref. 262. Copyright © 2018 WILEY-VCH Verlag GmbH & Co. KGaA, Weinheim. 48

Table 1.7 Binder materials applied in Li_2S-LSBs and their representative battery performances. 50

Table 1.8 Representative Li_2S-LSB full cell performance with graphite as anodes. 55

Table 1.9 Representative Li_2S-LSB full cell performance with different types of Si anodes. 58

Table 1.10 Representative Li_2S-LSB full cell performance with different types of Sn anodes. 59

Table 1.11 Parameter comparison of anode materials. 60

Table 1.12 Representative Li_2S-LSB full cell performance with Si/C as anodes. 62

Table 1.13 Representative Li_2S-LSB full cell performance with other types of anodes. 62

Table 2.1 Chemicals and Materials for Experimental Designs 66

Table 2.2 Experimental Instruments and Equipment. 68

Table S 3.1 Resistances of cathodes calculated from the EIS data in **Figure S 3.4**. 108

Table S 3.2 Summary of first cycle capacity breakdown for different batteries. 112

Table S 4.1 Different binder materials applied in Li_2S-based Li-S batteries. 134

Table S 4.2 Summary of LPS trapping experiment results corresponding to **Figure S 4.1**. 136

Table S 4.3 Tafel slopes (mV dec^{-1}) extracted from the second-cycle CV curves at Peak A, B and C for Li_2S cathode using PVDF and $Zn(OAc)_2$·TEA complex..... 137

Table S 4.4 Resistances of cathodes calculated from the EIS data in **Figure S 4.9**..... 141

Table S 4.5 Resistances of cathodes calculated from the EIS data in **Figure S 4.10**.... 142

Table S 5.1 Crystallite sizes of different Li_2S samples calculated using the *Scherrer* equation. 167

Table S 5.2 Resistances of cathodes calculated from the EIS data in **Figure S 5.4**..... 168

Table S 5.3 Summary of the Initial Charge Capacity, Discharge Capacity, and 1st Discharge Plateau in **Figure 5.3**..... 169

Table S 5.4 Resistances of cathodes calculated from the EIS data in **Figure S 5.7**..... 170

Table S 5.5 Summary of the Initial Charge Capacity, Discharge Capacity, and 1st Discharge Plateau in **Figure 5.4**..... 171

Table S 5.6 Resistances of cathodes calculated from the EIS data in **Figure S 5.8**..... 171

Table S 6.1 Reported methods for synthesizing Li_2S@C nanocomposites..... 193

Table S 6.2 Calculated parameters for multi-cycle precursor infiltration-decomposition processes to make Li_2S@C nanocomposites at different cycle number..... 194

Table S 6.3 Crystallite sizes of Li_2S in different samples determined by the *Scherrer* equation. 195

Table S 6.4 Cathode resistances derived from the EIS data in **Figure S 6.2**. 197

Table S 6.5 Cathode resistances derived from the EIS data in **Figure S 6.3**. 198

Table S 6.6 Performance of representative Li_2S-LSB full cells reported in the literature. 199

Table S 7.1 Resistances of cathodes calculated from the EIS data in **Figure S 7.1**..... 229

Table S 7.2 Resistances of cathodes calculated from the EIS data in **Figure S 7.2**..... 230

Table S 7.3 Resistances of cathodes calculated from the EIS data in **Figure S 7.4**..... 232

List of Abbreviations

Abbreviation	Definition
AC	Alternating current
ALD	Atomic layer deposition
ALLRP	NSERC Alliance Grants program code
Å	Angstrom (10^{-10} m)
BLIB	Beyond lithium-ion battery
C-rate	Charge/discharge current normalized to theoretical capacity
CE	Coulombic efficiency
Celgard 2400	Polypropylene battery separator
CMC	Carboxymethyl cellulose
CMK-3	Ordered mesoporous carbon CMK-3
CNT	Carbon nanotubes
CPE	Constant phase element
CR2032	Coin-type cell format
C/S	Carbon/sulfur composite
CVD	Chemical vapor deposition
CV	Cyclic voltammetry
DEC	Diethyl carbonate
DFT	Density Functional Theory
DMC	Dimethyl carbonate
DME	1,2-Dimethoxyethane
DMF	Dimethylformamide

DMAc	Dimethylacetamide
DOL	1,3-Dioxolane
EC	Ethylene carbonate
EES	Electrochemical energy storage
EIS	Electrochemical impedance spectroscopy
ER	Epoxy resin
EtOH	Ethanol
EVs	Electric vehicles
FF	Pore filling factor
FTIR	Fourier-transform infrared spectroscopy
GCD	Galvanostatic charge and discharge
GO	Graphene oxide
GPC	Gel permeation chromatography
GS60	Silicon–carbon anode powder
HRTEM	High-resolution transmission electron microscopy
ICDD	International Centre for Diffraction Data
LATP	Lithium aluminum titanium phosphate
LCO	Lithium cobalt oxide
$LiEt_3BH$	Lithium triethylborohydride
LiEX	Lithium ethyl xanthate
Li_2S-LSBs	Lithium sulfide–based lithium sulfur batteries
Li_2S@C	Lithium sulfide@carbon nanocomposite
Li_2S@SP	Lithium sulfide@Super P

Li_2S@SP-1	Li_2S@SP prepared with 1 infiltration cycle
Li_2S@SP-3	Li_2S@SP prepared with 3 cycles
Li_2S@SP-5	Li_2S@SP prepared with 5 cycles
LiTFSI	Lithium bis(trifluoromethanesulfonyl)imide
LFP	Lithium iron phosphate
LIBs	Lithium-ion batteries
LIMO	Lithium manganese oxide
LISICON	Lithium superionic conductor
LMO	Lithium manganese oxide
LNO	Lithium nickel oxide
LPS	Lithium polysulfide
LSBs	Lithium–sulfur batteries
MP	Melting point
MWCNTs	Multi-walled carbon nanotubes
M_w	Weight-average molecular weight
M_n	Number-average molecular weight
NCA	Nickel cobalt aluminum oxide
NMC	Nickel manganese cobalt oxide
NMP	*N*-Methyl-2-pyrrolidone
NPC	N,P-doped carbon nanoflakes
NSERC	Natural Sciences and Engineering Research Council
OCP	Open-circuit potential
OCV	Open-circuit voltage

PAN	Polyacrylonitrile
PAA	Poly(acrylic acid)
PDF	Powder diffraction file
PEI	Polyethylenimine
PEO	Poly(ethylene oxide)
PFAS	Per- and polyfluoroalkyl substances
PFSA	Perfluorosulfonic acid
PIB	Polyisobutylene
PTFE	Polytetrafluoroethylene
PVA	Poly(vinyl alcohol)
PVDF	Poly(vinylidene fluoride)
PVP	Polyvinylpyrrolidone
rGO	Reduced graphene oxide
RM	Redox mediator
RT	Room temperature
SBR	Styrene butadiene rubber
S@C	Sulfur@carbon
S@SP	Sulfur@Super P
SEI	Solid electrolyte interphase
SEM	Scanning electron microscope
SHE	Standard hydrogen electrode
Si/C	Silicon–carbon composite
SLGO	Single-layer graphene oxide

S-LSBs	Sulfur-based lithium–sulfur batteries
SP	Super P
TEGDME	Tetraethylene glycol dimethyl ether
TEM	Transmission electron microscopy
TEA	Triethanolamine
THF	Tetrahydrofuran
TMCs	Transition metal carbides
TMDs	Transition metal dichalcogenides
TMPs	Transition metal phosphides
UV-Vis	Ultraviolet-Visible
V_{pore}	Pore volume
VSP	Versatile Potentiostat, mode name
Wo	Warburg impedance
wt.%	Weight percent
XANES	X-ray absorption near-edge structure
XAS	X-ray absorption spectroscopy
XPS	X-ray photoelectron spectroscopy
XRD	X-ray diffraction

Chapter 1 Introduction

The demand for energy escalates daily, with fossil fuels such as coal, gasoline, and natural gas remaining the primary sources of energy.[1–3] The ongoing extraction and use of fossil fuels has led to decreasing reserves while emitting significant quantities of greenhouse gases,[4,5] contributing to global warming and severe climate change. Consequently, the advancement of sustainable clean energy technologies aimed at decreasing dependence on fossil fuels is recognized as the most effective approach to attain a low-carbon economy, ensure a healthy environment, and avert energy crises.[6–8] Sunlight,[9,10] wind,[1,11] and tides[12] represent clean and renewable energy sources that can be transformed into electricity and have seen extensive utilization in recent years. Nonetheless, these energy sources exhibit an intermittent nature.[13,14] Therefore, the development of efficient, safe, and reliable electrochemical energy storage (EES) systems, including grids and batteries, is essential for the effective utilization of these energy sources.[15–19]

Utilizing clean energy has emerged as a crucial approach for nations globally to address the widespread challenges of energy scarcity and environmental degradation.[20,21] In the field of emerging clean energy technologies, secondary batteries represent a crucial element of energy storage systems.[16,22,23] Rechargeable lithium-ion batteries (LIBs) are the preferred electrochemical energy storage system in electric vehicles (EVs), due to their extended cycle life and elevated energy density.[24–26] In recent years, there has been a pressing demand for LIBs with higher energy density to ensure an extended driving range for electric vehicles.[27,28] Consequently, "beyond lithium-ion battery" (BLIB) technologies may offer innovative solutions to tackle these issues.[29,30]

1.1 Lithium-Ion Batteries (LIBs)

LIBs have significantly transformed contemporary society, energizing the devices and technologies that characterize our everyday experiences.[31] Their impressive energy density, ability to be recharged, and lightweight construction have facilitated remarkable progress in various industries, including personal electronics, transportation, and renewable energy storage.[32,33] Renewable energy sources such as solar and wind power exhibit intermittent characteristics,

generating electricity solely during periods of sunlight or wind activity, and LIBs offer a dependable method for energy storage, enabling the capture of surplus energy for later use.[31,34]

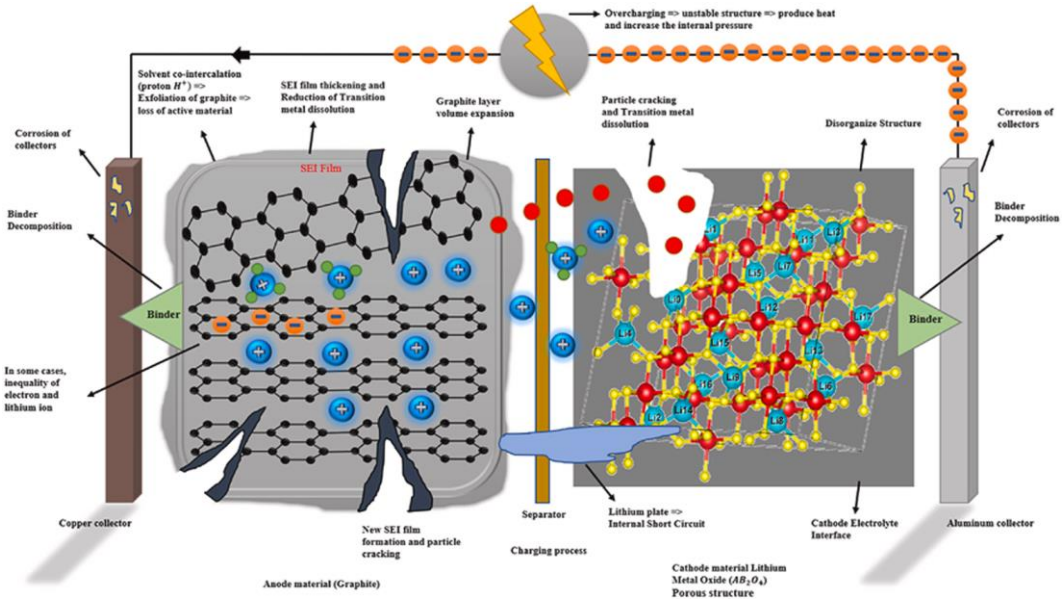


Figure 1.1 Schematic diagram of the structure of a typical Li-ion battery.[19] Copyright © 2024 Elsevier Ltd. All rights are reserved, including those for text and data mining, AI training, and similar technologies.

In 1817, Berzelius and Arfwedson identified lithium while studying $LiAlSi_4O_{10}$,[35–37] but it was not until 1821 that Brande and Davy successfully isolated the elemental lithium through the electrolysis of lithium oxide.[38] A century later, Lewis began an exploration of its electrochemical properties.[39] Given the remarkable physical characteristics of lithium metal, including its low density (0.534 g cm^{-3}), high specific capacity (3860 mA h g^{-1}), and low redox potential (-3.04 V *vs.* SHE), it became evident that lithium could effectively function as a battery anode. In the early 1990s, Sony Corporation made the initial introduction of LIBs.[22]

Figure 1.1 illustrates the four essential components of LIBs: the cathode, anode, separator, and electrolyte.[19] The charging carriers involved in the energy storage and release of LIBs are cathodes and anodes. The separator serves to physically divide the electrodes, thereby preventing internal short-circuits while allowing the flow of Li^+ ions.[40] The electrolyte facilitates the transport of ions, such as Li^+.[41] The anode, which serves as the negative electrode, consists of graphitic carbon capable of housing Li^+ within its layers.[42] In contrast, the cathode, functioning as the positive

electrode, is typically a Li-intercalation compound, often an oxide, chosen for its higher potential and frequently arranged in stacks.[43] Both electrodes allow for the reversible insertion and extraction of Li^+ from their respective structures.[44] During the charging process, Li^+ ions are removed from the layered oxide structure and inserted into the graphite layers. Upon discharge, the procedure is inverted. The electrochemical reactions, exemplified by the $LiCoO_2$/graphite battery, are outlined as follows.[45,46]

The reaction in the cathode is:

$$LiCoO_2 \underset{\text{Discharge}}{\overset{\text{Charge}}{\rightleftharpoons}} Li_{(1-x)}CoO_2 + xLi^+ + xe^- \qquad \textbf{Equation 1.1}$$

The reaction in the anode is:

$$6C + xLi^+ + xe^- \underset{\text{Discharge}}{\overset{\text{Charge}}{\rightleftharpoons}} Li_xC_6 \qquad \textbf{Equation 1.2}$$

The overall reaction is:

$$LiCoO_2 + 6C \underset{\text{Discharge}}{\overset{\text{Charge}}{\rightleftharpoons}} Li_{(1-x)}CoO_2 + Li_xC_6 \qquad \textbf{Equation 1.3}$$

LIBs come in four primary configurations as shown in **Figure 1.2**: cylindrical, coin, prismatic, and pouch cells.[47] Each type presents unique benefits and limitations. Cylindrical cells, including the commonly utilized model 18650 and 21700, provide significant mechanical stability, effective thermal management, and economical manufacturing processes, rendering them suitable for applications in EVs, power tools, and consumer electronics.[48] Nonetheless, the inflexible structure and reduced packing efficiency may constrain design adaptability. Coin cells, which are small and button-shaped, find widespread applications in watches, medical devices, and memory backup systems.[49,50] Their compact size, long lifespan, and low self-discharge rate make them ideal for these uses; however, they do not possess high energy capacity and are not suitable for high-power applications. Prismatic cells, contained within sturdy rectangular enclosures, offer improved space efficiency and enhanced energy density relative to cylindrical cells, which contributes to their widespread adoption in electric vehicles and energy storage solutions.[51,52] Nonetheless, the intricate nature of their manufacturing processes and reduced mechanical stability cause them to become increasingly susceptible to swelling as time progresses. Pouch cells, characterized by their flexible,

lightweight, and customizable design, provide the highest energy density relative to weight and volume, making them particularly suitable for smartphones, drones, and next-generation electric vehicles.[53,54] While these benefits are notable, the absence of a sturdy casing makes them more susceptible to swelling and physical harm. Each of these configurations is designed for particular applications, optimizing energy density, safety, cost, and durability to satisfy the requirements of contemporary technology.[55]

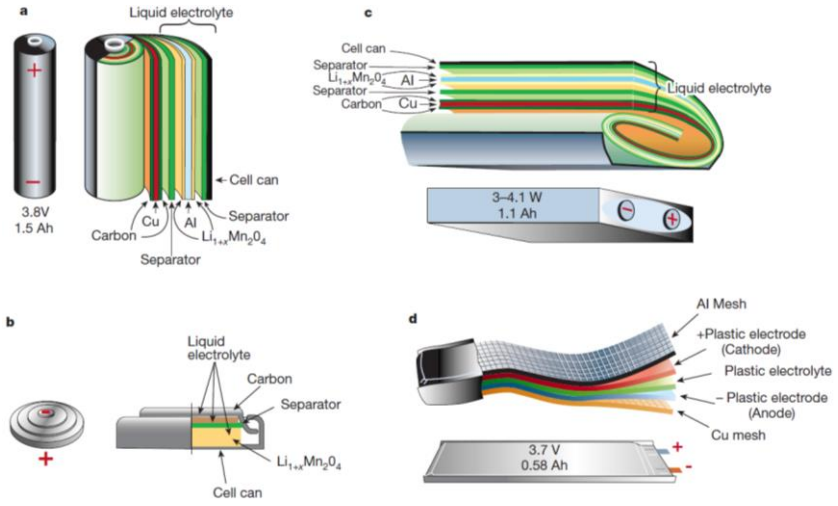


Figure 1.2 Four types of Li-ion battery configurations: (a) cylindrical, (b) coin, (c) prismatic, and (d) pouch cell.[47] Copyright © 2001, Springer Nature Limited.

LIBs rely on various cathode materials, each with distinct structural, electrochemical, and performance characteristics that determine their suitability for different applications, summarized in **Table 1.1**. Lithium cobalt oxide (LCO), with its layered α-$NaFeO_2$ structure, offers high energy density (~150–200 W h kg^{-1}) but has a relatively short cycle life, making it good for consumer electronics like smartphones and laptops.[46,56] Lithium iron phosphate (LFP), featuring an olivine structure, provides excellent thermal stability and long cycle life (2000–5000 cycles) but has a lower energy density (~90–160 W h kg^{-1}), making it popular in electric vehicles and energy storage systems.[57,58] Lithium nickel manganese cobalt oxide (NMC) and lithium nickel cobalt aluminum oxide (NCA), both layered materials, balance high energy density (~150–260 W h kg^{-1}) with a moderate cycle life (1000-3000 cycles), making them the dominant choices for electric vehicles (EVs).[59,60] Meanwhile, lithium manganese oxide (LMO), with its spinel structure, delivers good thermal stability and fast charging capability but lower capacity (~100–120 mA h g^{-1}), making it

suitable for hybrid electric vehicles and power tools.[61,62] As the demand for high-performance, cost-effective, and sustainable battery technologies grows, ongoing research is focused on optimizing these cathode materials to enhance safety, lifespan, and energy efficiency.

Table 1.1 Electrochemical characteristics of typical cathode materials.

Cathode Material	**$LiCoO_2$ (LCO)**	**$LiNi_xMn_yCo_zO_2$ (NMC)**	**$LiFePO_4$ (LFP)**	**$LiMn_2O_4$ (LMO)**	**$LiNi_xCo_yAl_zO_2$ (NCA)**
Structure	Layered α-$NaFeO_2$	Layered α-$NaFeO_2$	Olivine	Spinel	Layered
Theoretical Capacity (mA h g^{-1})	274	~280	170	148	~278
Available Capacity (mA h g^{-1})	~140–160	~160–220	~150–165	~100–120	~180–220
Operating Voltage (V *vs.* Li^+/Li)	3.7–3.9	3.6–3.8	3.2–3.3	3.8–4.1	3.6–3.9
Energy Density (W h kg^{-1})	~150–200	~150–250	~96–160	~100–150	~180–260
Cycle Life (cycles)	500–1000	1000–3000	2000–5000	500–2000	1000–2000
Ref.	56	63,64	65,66	67,68	68,69

Although the actual energy density of commercial LIBs is approaching its theoretical limit, it remains insufficient for many practical applications.[70] Further significant improvements are challenging due to the limited number of lattice sites available for Li^+ ion intercalation and deintercalation.[71] This constraint hampers their ability to meet the growing demands of emerging fields such as electric vehicles and smart grid energy storage. To address these limitations, researchers are exploring "beyond lithium-ion battery (BLIB)" technologies that offer higher energy density, enhanced safety, lower costs, and greater sustainability.[72]

Among the most widely explored directions are polyvalent metal-ion batteries, which employ elements such as magnesium,[73] aluminum,[74] calcium,[75] and zinc,[76] are attractive for their low cost, inherent safety, and potential multi-electron storage.[30] However, their progress remains limited: polyvalent cations diffuse sluggishly through solid hosts, suitable cathode materials are scarce, and electrode-electrolyte compatibility is often poor.[77] These fundamental challenges have so far prevented them from achieving practical performance despite their theoretical promise.[30]

Another major direction is metal-air batteries,[78] such as lithium-air,[79] zinc-air,[80] and aluminum-air systems.[81] By using oxygen from ambient air as the cathode active material, they can minimize cell weight and theoretically deliver exceptionally high specific energies.[78] However, their practical development is severely constrained by poor reversibility of oxygen reactions, rapid degradation of the air electrode, and instability of both liquid and solid electrolytes.[78]

A third direction is sodium-ion[82,83] and potassium-ion batteries,[84] which offer cost-effective alternatives to lithium-ion technology.[85] They operate through similar intercalation chemistry but use more abundant and evenly distributed elements, making them attractive for large-scale stationary storage.[85] However, their significantly lower energy density compared with lithium systems limits their suitability for applications where compactness and lightweight design are essential.

Within this diverse landscape of beyond-lithium-ion systems, lithium-sulfur (Li-S) batteries have emerged as a particularly promising alternative, boasting an ultra-high theoretical energy density (~2600 W h kg^{-1}), the natural abundance of sulfur, and environmental benefits.[86,87] Unlike conventional LIBs, which depend on expensive and resource-limited metals like cobalt and nickel, Li-S batteries utilize elemental sulfur, a widely available and cost-effective material, making them a more sustainable and scalable solution for future energy storage needs.[88]

1.2 Lithium-Sulfur (Li-S) Batteries

Figure 1.3 briefly describes the timeline of development of Li-S batteries. Li-S batteries were first proposed in the 1960s.[86] Nonetheless, the investigation into Li-S batteries experienced limited advancement in the subsequent decades, primarily attributed to their low actual specific capacity and rapid capacity decline. In 2009, Nazar and colleagues achieved significant breakthroughs by employing highly ordered mesoporous nanostructured carbon as a carrier for encapsulating sulfur.[89] This innovative approach effectively confines the active sulfur species within its conductive channels, leading to enhanced specific capacity and cycle stability. Since then, a vast number of researchers have made substantial contributions to their development and resulting in significant advancements.[90–92]

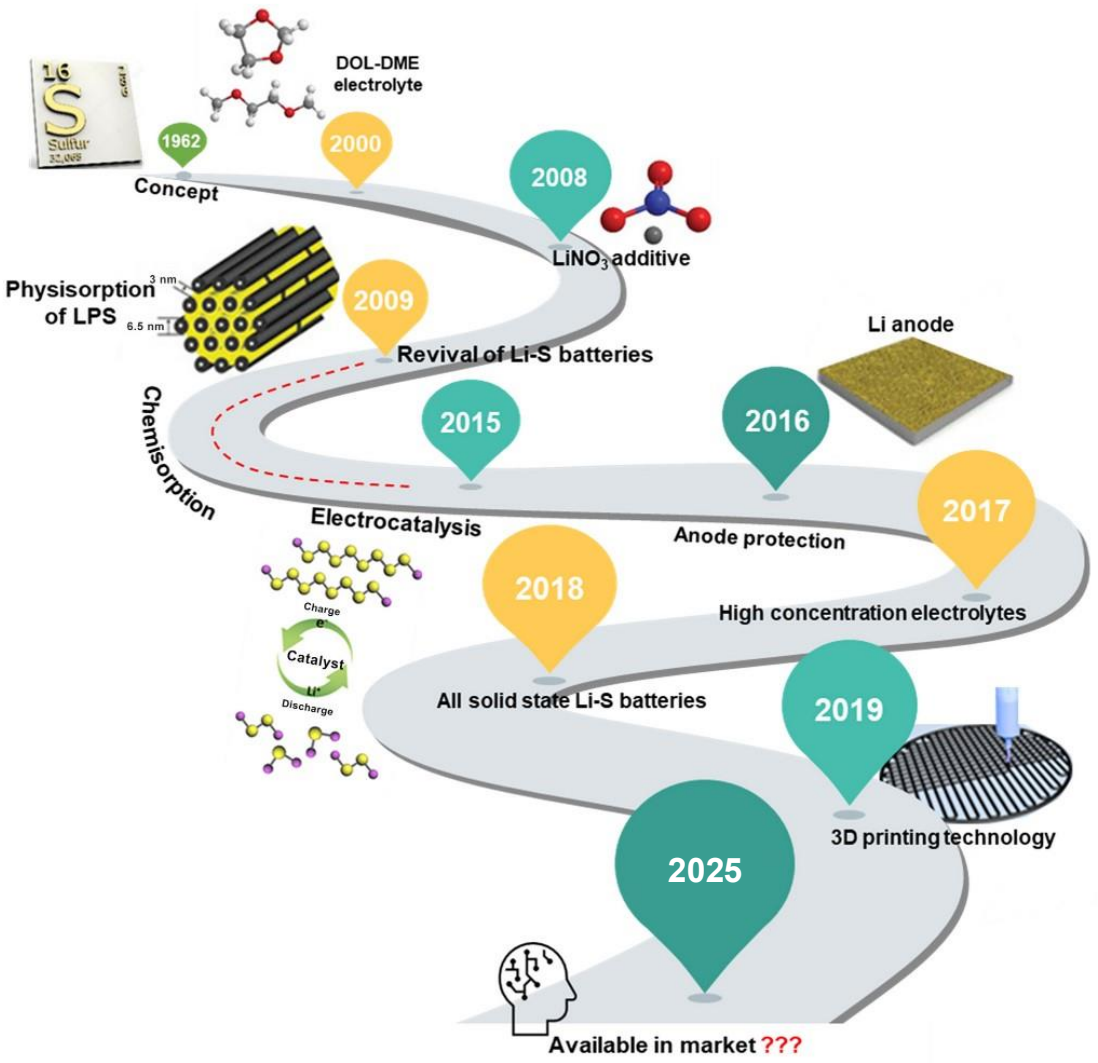


Figure 1.3 Brief timeline of important events in the development of Li-S batteries.[86] Adapted from Ref. 86 with permission from Copyright © 2023, Shanghai University and Periodicals Agency of Shanghai University.

Sulfur, when utilized as a cathode material, renders a theoretical specific capacity of 1672 mA h g^{-1}, marking it as the highest among the solid-state cathode materials presently accessible.[87] **Figure 1.4** illustrates the comparison of capacity and energy density between commercialized batteries and Li-S batteries. The use of lithium metal as an anode, boasting a theoretical capacity of 3860 mA h g^{-1}, results in theoretical volumetric and mass energy densities of 2800 W h L^{-1} and 2500 W h kg^{-1}, respectively.[87,93,94] When considering inactive components such as current collectors, electrolytes, and conductive agents, the actual energy density can achieve levels of 400–600 W h kg^{-1}, approximately three times greater than that of current LIBs.[87,93] Sulfur is plentiful on Earth, usually the byproduct of oil refinery as shown in **Figure 1.4** (b), and offers benefits such as low

cost, non-toxicity, and environmental friendliness.[95] The Li-S battery emerges as a compelling candidate for the next generation of secondary batteries, boasting a high specific energy that is anticipated to supplant the existing LIBs system.[96]

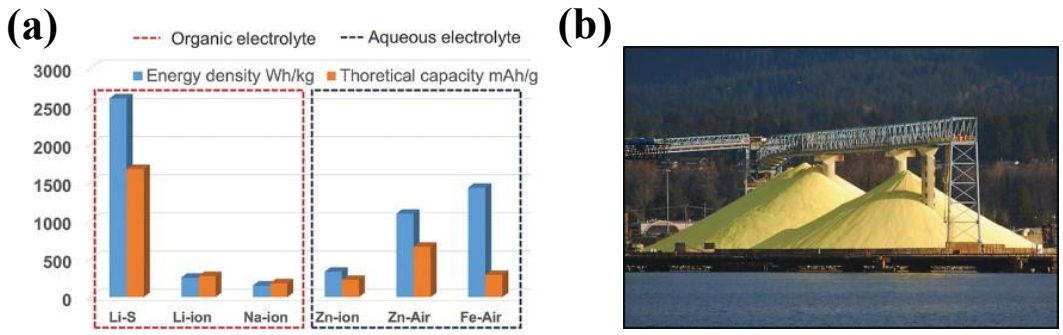


Figure 1.4 Comparison of (a) capacity density and energy density.[94] Reproduced from Ref. 94. Copyright © 2021 The Authors. Advanced Science published by Wiley-VCH GmbH, under the Creative Commons Attribution (CC BY) license. (b) Massive stockpiles of sulfur at an oil refinery in Vancouver, Canada.[95] Copyright © 2016 Wiley-VCH Verlag GmbH & Co. KGaA, Weinheim.

1.2.1 Electrochemical Reactions in Li-S Batteries

Figure 1.5 (a) illustrates a typical structure of Li-S batteries.[87] The cathode in Li-S batteries typically consists of a composite material made from elemental sulfur and conductive carbon, while the anode is composed of lithium metal. At ambient temperature, elemental sulfur exhibits an orthorhombic crystal structure, where each sulfur molecule is interconnected with eight sulfur atoms, resulting in the formation of a cyclic S_8 molecule.[97] In the discharge process, lithium metal undergoes oxidation to generate Li^+ ions while releasing electrons. These electrons are subsequently transferred to the sulfur cathode through the external circuit. Meanwhile, Li^+ ions move from the anode to the cathode through the separator via electrolyte. Upon accepting electrons, sulfur reacts with Li^+ ions to produce lithium polysulfides and then lithium sulfide. The capacity of sulfur is significantly greater than that of conventional materials used in LIBs, as one sulfur atom can accommodate two electrons, while typical materials have limited lattice sites for the deintercalation of lithium ions.[96]

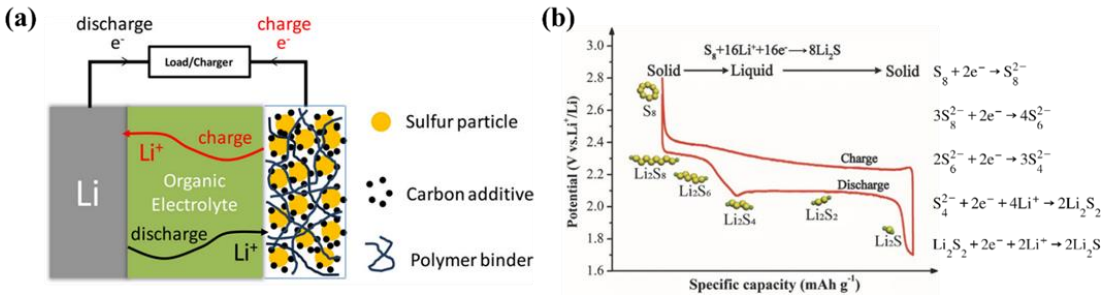


Figure 1.5 (a) Schematic of Li-S batteries.[87] Copyright © 2014, American Chemical Society. (b) The discharge/charge curves and multi-step reaction of Li-S batteries.[98] Copyright © 2017 WILEY-VCH Verlag GmbH & Co. KGaA, Weinheim.

The reaction in the cathode is:

$$S_8 + 16e^- + 16Li^+ \underset{\text{Charge}}{\overset{\text{Discharge}}{\rightleftharpoons}} 8Li_2S \qquad \textbf{Equation 1.4}$$

The reaction in the anode is:

$$16Li \underset{\text{Charge}}{\overset{\text{Discharge}}{\rightleftharpoons}} 16Li^+ + 16e^- \qquad \textbf{Equation 1.5}$$

The overall reaction is:

$$S_8 + 16Li \underset{\text{Charge}}{\overset{\text{Discharge}}{\rightleftharpoons}} 8Li_2S \qquad \textbf{Equation 1.6}$$

The aforementioned generic reaction serves as a basis for calculating the theoretical capacity of Li-S batteries; however, the electrochemical process involved in Li-S batteries encompasses a complex multi-step and multi-phase transformation process. **Figure 1.5** (b) illustrates the standard discharge and charge curves observed in Li-S batteries.[98] The discharge curves of Li-S batteries can be divided into two parts, with each one representing distinct electrode reaction processes. The solid-state S_8 molecules experience a transition reaction to Li_2S_8 within the high plateau range of 2.15–2.40 V, followed by the transformation of Li_2S_8 into Li_2S_6, and subsequently into Li_2S_4. The specific capacity of this plateau is 418 mA h g^{-1}, with each sulfur atom receiving an average of 0.5 electrons. Lithium polysulfides (LPSs), including Li_2S_8, Li_2S_6, and Li_2S_4, produced in this process can be dissolved in the electrolyte, resulting in the formation of chain polysulfide ions, as the sulfur cathode transitions from a solid phase to a liquid phase. At voltages lower than 2.15 V, liquid Li_2S_4 undergoes a transformation into solid Li_2S_2, ultimately resulting in solid Li_2S as the final discharged

product. During the second plateau, the sulfur cathode transitions from the liquid phase to the solid phase, theoretically providing a specific capacity of 1254 mA h g^{-1}. Throughout the charging process, the sulfur cathode experiences a transformation from solid-phase Li_2S to liquid-phase LPSs (Li_2S_x, where $4 \leqslant x \leqslant 8$), and subsequently to solid-phase S_8 molecules.

To be noted, the boundaries between the electrode processes are not entirely distinct, as these polysulfide ions are susceptible to disproportionation and neutralization reactions.[99] Various sulfur ions, such as polysulfide ions like S_7^{2-} and S_5^{2-}, can also be identified in each stage of the reaction process, adding complexity to the electrode reaction.[100]

1.2.2 Effects of Soluble Lithium Polysulfides (LPSs)

Figure 1.6 illustrates the process by which lithium polysulfide is formed through the ring opening of S_8.[101] Typically, the conversion reaction during discharge at the sulfur cathode follows a progressive "solid-liquid-solid" transition process ($S_8 \rightarrow Li_2S_8 \rightarrow Li_2S_6 \rightarrow Li_2S_4 \rightarrow Li_2S_2 \rightarrow Li_2S$). These LPSs are highly soluble in commonly used organic electrolytes, such as dioxolane (DOL) and dimethoxy ethane (DME).[102] However, the influence of soluble LPSs on the performance of Li-S batteries presents both advantageous and disadvantageous effects.

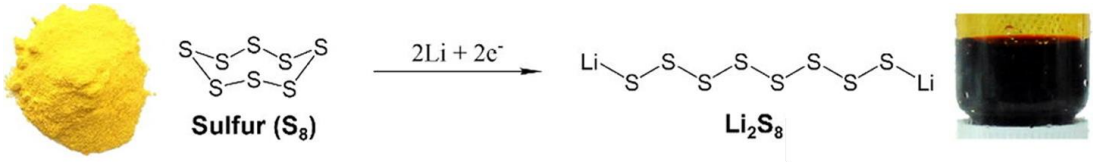


Figure 1.6 The formation of soluble lithium polysulfides (LPSs).[101] Copyright © 2022 The Korean Society of Industrial and Engineering Chemistry. Published by Elsevier B.V. All rights reserved.

Viewing it positively: (1) The dissolution of LPSs as intermediate products ensures that elemental sulfur remains unobstructed by reaction products, thereby allowing full exposure of the sulfur to the electrolyte and enhancing the reduction process of the sulfur cathode.[87,96] (2) Polysulfide ions exhibit greater electrochemical activity compared to solid-state elemental sulfur, resulting in an accelerated reaction rate on the electrode.[99] (3) The distribution of sulfur is uneven on the conductive framework in newly prepared sulfur cathodes, particularly those with high sulfur content, frequently. The dissolution and redeposition of LPSs within the cathode during the initial cycles facilitate the redistribution of sulfur, resembling an activation process of the electrode, which

can enhance sulfur utilization.[103] (4) LPSs have the capability to lower the activation energy required for the reaction of Li_2S, thereby facilitating the oxidation process of Li_2S during charging.[104]

LPSs negatively impact battery performance as well. (1) Due to the concentration gradient, some of the dissolved LPSs will naturally move from the cathode region to the anode, where they will react with lithium metal to produce Li_2S, subsequently covering the surface of anode. This process leads to the depletion of elemental sulfur and the passivation of the lithium anode, resulting in a decline in battery capacity and an increase in polarization.[105] (2) Throughout the charging process, the long-chain LPSs produced by oxidation on the cathode can readily diffuse to the anode, where they are reduced to short-chain LPSs. Subsequently, the short-chain LPSs will migrate back due to the influence of the electric field force, undergoing oxidation and reformation into long-chain LPSs once more. The movement of polysulfide ions back and forth between the cathode and anode is referred to as "shuttle effect," which leads to reduced Coulombic efficiency and significant self-discharge issues.[106] (3) The continuous shuttle, dissolution, diffusion, and deposition processes of LPSs lead to an uneven distribution of sulfur on the conductive framework of the cathode, ultimately resulting in the accumulation of large sulfur particles anywhere else rather than inside the framework. Such sulfur without doubt is distanced from the conductive framework, will exhibit limited reactivity, and present challenges in recycling, ultimately leading to a decline in capacity.[107]

To attain a high-performance sulfur cathode, it is essential to address the issue of the "shuttle effect" of LPSs while also strategically leveraging their beneficial aspects for enhanced battery performance.[108–110]

1.2.3 Main Problems and Challenges in Li-S Batteries

Although Li-S batteries exhibit high energy density, several notable challenges need to be addressed to enhance their performance and achieve commercialization. **Figure 1.7** provides a comprehensive summary of the key problems and challenges associated with Li-S batteries, detailing four major topics in depth.[111]

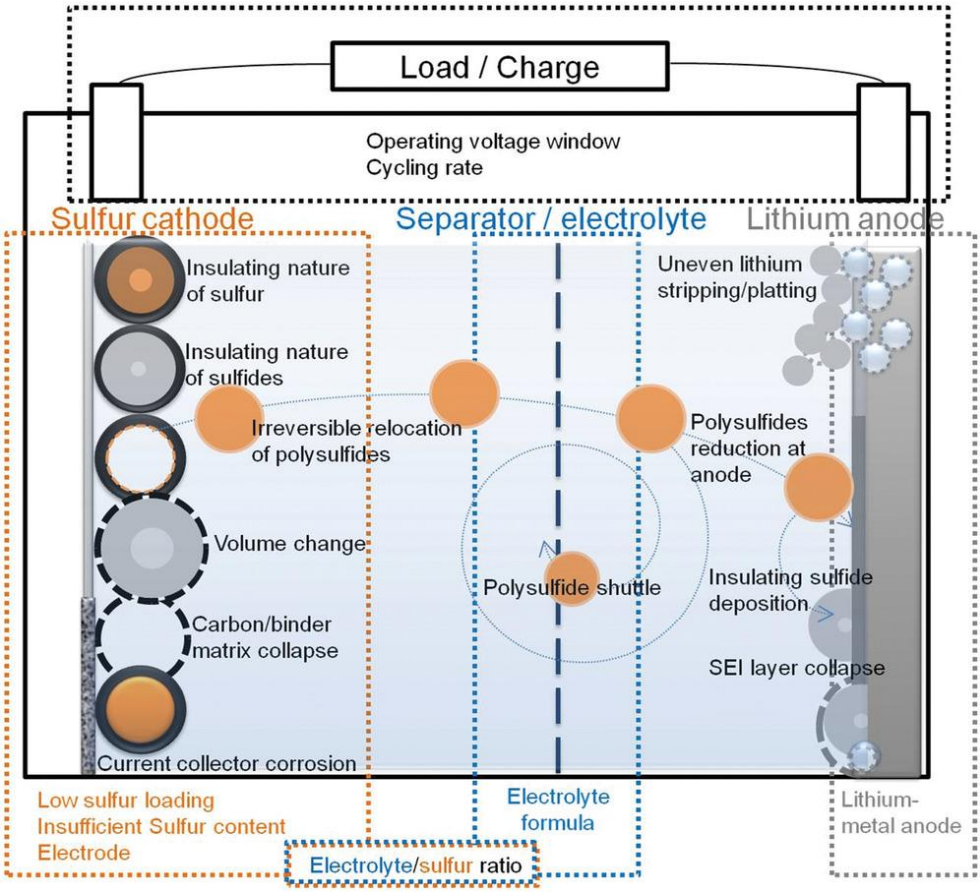


Figure 1.7 Main problems and challenges in Li-S batteries.[111] Copyright © 2019 WILEY-VCH Verlag GmbH & Co. KGaA, Weinheim.

1.2.3 a) Extremely Low Conductivities of Sulfur and Insulating Nature of Lithium Sulfide

To enable adequate electrode reactivity, it is essential that electrode materials possess high electrical conductivity. The electronic and ionic conductivities of elemental sulfur (S_8) and its discharged product Li_2S are notably low, as listed in **Table 1.2**.[112] The direct application of sulfur as electrode materials results in sluggish electrode reaction kinetics and restricted active material utilization, which has been reported to lead to incomplete conversion reactions within the battery. Consequently, following multiple cycles, there may still be unreacted sulfur species present on the cathode. The rate performance is inadequate, and the specific capacity is insufficient. While incorporating conductive materials with sulfur can enhance the conductivity of the electrode, this may lead to a decrease in sulfur content, which could ultimately diminish the overall energy density of the electrode.

Table 1.2 Low electronic and ion conductivities of Li_2S and S_8.[112]

Materials	Electronic Conductivity (S cm^{-1})	Ionic Conductivity (S cm^{-1}, at RT)
Lithium Sulfide (Li_2S)	$\sim 10^{-13}$	$10^{-14} \sim 10^{-10}$
Elemental Sulfur (S_8)	$\sim 10^{-28}$	--

Li_2S: Poor electronic conductor but slightly better ionic conductor.

S_8: Extremely poor electronic and ionic conductor in solid form.

1.2.3 b) The Notorious "Shuttle Effect" of Soluble Polysulfide Intermediates

While the aforementioned benefits of LPSs are noteworthy, their significant mobility and electrochemical activity lead to the rapid and irreversible diffusion of dissolved polysulfides from the cathode region as shown in **Figure 1.8**.[113] The uncontrolled diffusion of polysulfides can compromise the electrochemical stability of batteries, leading to a significant capacity loss exceeding 50% within merely 50 cycles.[100] The disproportionation reaction involves lithium metal reducing migrating polysulfides, leading to the formation of insoluble Li_2S_2/Li_2S.[114] This process contributes to the loss of active material and the passivation of the anode. The lithium metal anode facilitates the reduction of certain migratory polysulfides during the charging process, resulting in the formation of short chain polysulfides that are driven back to the cathode by the electric field generated between the anode and cathode. The polysulfide shuttle that emerges is acknowledged as the cause of the low electrochemical efficiency observed in Li-S batteries.

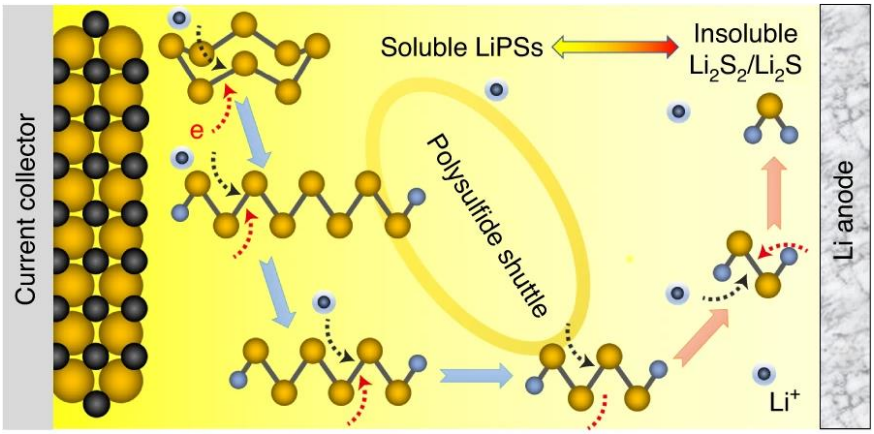


Figure 1.8 The "shuttle effect" of soluble lithium polysulfides (LPSs).[113] Copyright © 2020, The Author(s), under exclusive license to Springer Nature Limited.

1.2.3 c) Dramatic Volume Expansion of the Sulfur Cathode

The volume change of the sulfur cathode during cycling is a significant factor contributing to poor battery performance. The lithiation process leads to an increase in molar mass (45.95 g mol^{-1}) and a decrease in density (1.66 g cm^{-3}) of Li_2S when compared to elemental sulfur (32.07 g mol^{-1} and 2.07 g cm^{-3}). This results in a significant volume expansion of up to 78%, which causes the separation of elemental sulfur or Li_2S from the conductive framework.[115,116] The cathode materials undergo pulverization due to the significant volumetric changes that occur during cycling. When the integrity of a sulfur cathode is compromised, the insulating sulfur disconnects from the conductive agents.[117] The isolated sulfur loses access to electrons, rendering it an inactive component of the cathode due to weak electrical conductivity. This situation increases the batteries' impedance and leads to a decline in capacity. Nevertheless, the enhanced porosity of the electrode can provide additional buffer space, effectively addressing this issue; however, it results in a decrease in the volumetric energy density of the electrode. Consequently, achieving an improved equilibrium between electrode porosity and energy density is essential.

Table 1.3 Molar mass and density of Li_2S and S.

Materials	Molar Mass (g mol^{-1})	Density (g cm^{-3})
Li_2S	45.95	1.66
S	32.07	2.07

1.2.3 d) Issues with Lithium Metal Anode

The safety concerns associated with the use of lithium metal as a negative electrode must be taken seriously. Li-S battery anodes generally utilize lithium metal, which boasts a high specific capacity of 3860 mA h g^{-1}, in contrast to the more secure commercial graphite anode with a capacity of 372 mA h g^{-1}, in order to align with the sulfur cathode.[118] The ongoing processes of lithium metal dissolution and deposition throughout the cycling contribute to the formation of high-surface-area mosses and dendrites, as illustrated in **Figure 1.9**.[119] The process of lithium metal plating and stripping leads to cracking in the anode and the formation of inactive regions due to significant and uneven volume changes.[120] Short circuits resulting from lithium dendrites can arise under these conditions, presenting both performance and safety challenges.[121,122] The high reactivity of lithium

metal leads to its rapid interaction with organic electrolytes, resulting in the formation of a solid electrolyte interphase (SEI) on the surface of the reacted lithium anode.[123] The SEI layer passivates the lithium metal, offering both electrochemical and chemical stability. The instability of the SEI layer arises from the interaction of uneven lithium plating and stripping, along with the growth of dendrites, which leads to the exposure of fresh lithium within the cracks.[124] With each re-formation of the SEI layer through repeated cycling, these processes lead to an irreversible loss of active lithium and electrolyte, resulting in a decrease in Coulombic efficiency and cycle life of the battery.[125] The reaction also generates gas, which can result in safety concerns like flatulence and potential battery damage.[126]

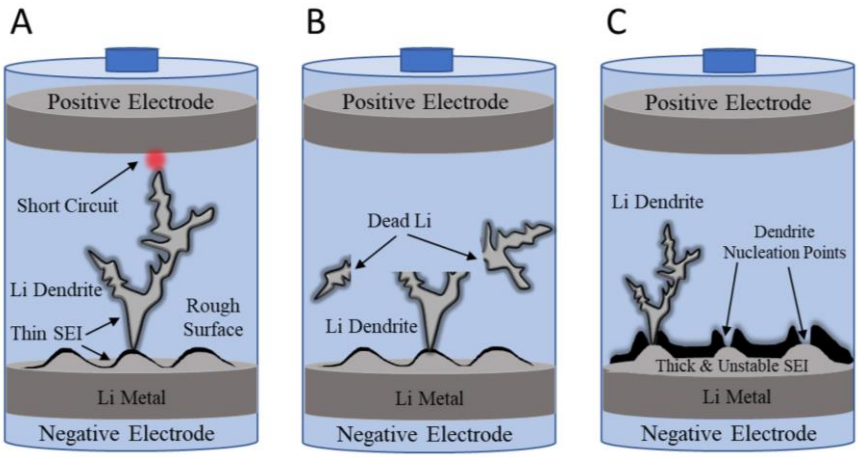


Figure 1.9 Schematic of the main issues with lithium metal anode: (a) short circuit introduced by Li dendrites, (b) formation of inactive/dead Li, and (c) development of thick and mechanically unstable SEI.[119] Copyright © 2020 Elsevier B.V. All rights reserved.

1.2.4 Enhancement Strategies for Li-S Batteries

To address these challenges in sulfur cathode, considerable efforts have been dedicated to trapping sulfur and its derivative species within various porous hosts[127,128] (e.g., carbonaceous materials,[129] metal oxides[130] and sulfides,[131] conductive polymers,[132,133] etc.) or binding elemental sulfur to create sulfurized polymers (e.g., sulfurized polyacrylonitrile[134]). Various approaches for inhibiting the movement of LPSs between the cathode and anode have been investigated, including the use of artificial interlayers and functionalized separators.[135] The cycling stability of Li-S batteries has significantly improved due to these efforts, achieving thousands of cycles.

Advancements have also been achieved in the rate performance and specific capacity of sulfur cathodes.

To enhance the stability of the lithium metal anode, two main approaches have been put forward: the first involves interfacial engineering of lithium metal to establish a stable solid electrolyte interphase (SEI) on its surface,[136] while the second focuses on distributing lithium metal within hosts that have a large surface area to effectively manage the current density.[137] Although considerable advancements have been made, the lithium metal anode remains uncommercialized. The incorporation of $LiNO_3$ into the electrolyte to establish a dynamically stable SEI on the lithium metal surface remains the prevailing method for protecting the lithium metal anode in Li-S batteries.[138,139] However, $LiNO_3$ is progressively depleted during cycling, resulting in the release of excessive gases that present a safety hazard.

To sum up, the sulfur cathode in traditional Li-S battery systems continues to face many obstacles. Although sulfur remains stable in air, typical techniques for generating sulfur cathodes require elevated temperatures and/or vacuum drying processes, which can readily result in the vaporization and loss of sulfur because of its low melting point.[140] This affects the actual sulfur loading in the cathode and its practically available capacity, leading to uncertainties in experiments and the investigation process. During the discharge process, the significant expansion of the sulfur cathode may lead to mechanical damage to the electrodes. The employment of lithium metal as anodes is essential; however, it may result in dendrite growth and associated safety concerns. Nonetheless, owing to its impressive theoretical specific capacity (1166 mA h g^{-1}) and the usage of lithium-metal-free anode, fully lithiated sulfur, lithium sulfide (Li_2S), presents a favorable option in this context.[141–143] Additionally, the extraction of lithium out of the structure of Li_2S leads to the shrinkage of electrode during delithiation, which creates sufficient space for sulfur to expand during lithiation, thereby enhancing the cycle performance of Li-S batteries.

1.3 Lithium Sulfide (Li_2S)-Based Li-S Batteries

The use of Li_2S as a cathode presents numerous advantages: (1) Li_2S is the fully lithiated form of elemental sulfur and has the potential to serve as a lithium-containing cathode in Li-S batteries as a viable alternative. (2) Li_2S exhibits a substantial specific capacity up to 1166 mA h g^{-1}. (3) In

contrast to elemental sulfur, Li_2S cathode is compatible with non-metallic anodes like graphite,[144–153] silicon,[154–160] and tin,[161–163] enabling it to circumvent the challenges associated with lithium metal. (4) Additionally, in comparison to the density of elemental sulfur (2.07 g cm^{-3}), Li_2S, which is the least dense form of active sulfur species, exhibits a lower density of 1.66 g cm^{-3}. This characteristic helps to prevent structural collapse of the cathode during the volume expansion that occurs during discharge and charge processes involving elemental sulfur. (5) Due to its high melting point (938 °C), Li_2S exhibits remarkable thermal stability, enabling the synthesis of diverse nanostructured Li_2S cathode composites at high temperatures (> 500 °C), a process that is unsuitable for elemental sulfur because of its thermal instability. Considering these benefits, Li_2S could possess greater potential as the cathode for practical Li-S batteries compared to elemental sulfur.

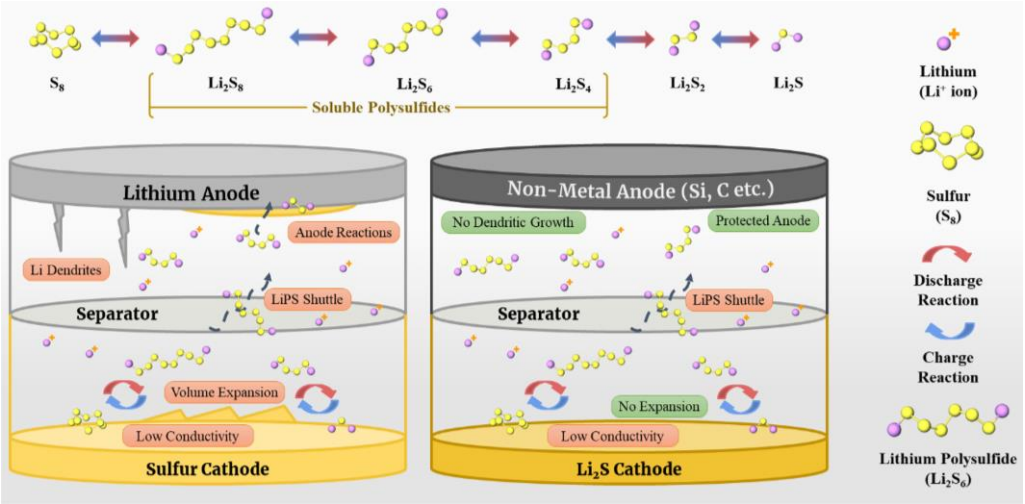


Figure 1.10 The challenges faced by the sulfur (S_8) and lithium sulfide (Li_2S) batteries.[140] Copyright © 2022 The Authors. Published by American Chemical Society.

Employing Li_2S as the starting material does not resolve ongoing issues as shown in **Figure 1.10**, including the low electrical and ionic conductivities of the active materials, along with the infamous polysulfide "shuttle effects", since the mechanism continues to rely on the conversion between Li_2S and S.[140] The utilization of Li_2S as the starting cathode material presents a unique array of challenges. (1) An inadequately constructed cathode structure presents a significant challenge during the initial charging phase, as it leads to a substantial overpotential required for the activation of Li_2S. The overpotential has been influenced by the particle size, morphology, and crystallinity of the Li_2S used. The commercially available Li_2S, with a particle size in the range of

tens of micrometers, exhibits weak electrochemical properties, making it an unsuitable candidate. (2) Due to the high sensitivity of Li_2S to moisture and its tendency to undergo hydrolysis, it is necessary to modify the conventional slurry-casting method used for cathode production to avoid exposing Li_2S to ambient air. It is noteworthy that it remains unreactive with O_2 at temperatures below 300 °C. Consequently, the production of unprotected Li_2S cathodes would only require a moisture-free environment.

To achieve high-performance and cost-effective Li-S batteries, addressing the challenges presented by Li_2S necessitates a thoughtful approach to the design and fabrication of Li_2S composites and cathode architectures.[112] The Li_2S-based cathode is expected to operate in a manner akin to the sulfur-based cathode following the activation process, where Li_2S is fully converted to elemental sulfur.

1.3.1 Activation of Li_2S

The first study of Li_2S as a cathode occurred in 2002,[164] however, the development of Li_2S has been notably less rapid compared to that of the sulfur cathode. Despite Li_2S exhibiting electrical conductivity an order of magnitude greater than that of elemental sulfur,[165] it remains mostly an insulator, and pure Li_2S has long been regarded as electrochemically inactive.

The size of commercially available Li_2S particles varies from several micrometers to several tens of micrometers.[166,167] In the typical operating voltage window of Li-S batteries (1.7–2.8 V), these Li_2S particles exhibit little capacity. A significant working potential (~4 V *vs.* Li^+/Li) is required during the initial charge cycle to overcome its charging overpotential.[104,164] Such a high overpotential is naturally believed to be associated with the crystal structure and the delithiation mechanism of Li_2S. **Figure 1.11** (a) illustrates a typical initial charging curve. The substantial activation barrier restricts the charging depth, leading to inefficient utilization of active materials.[145]

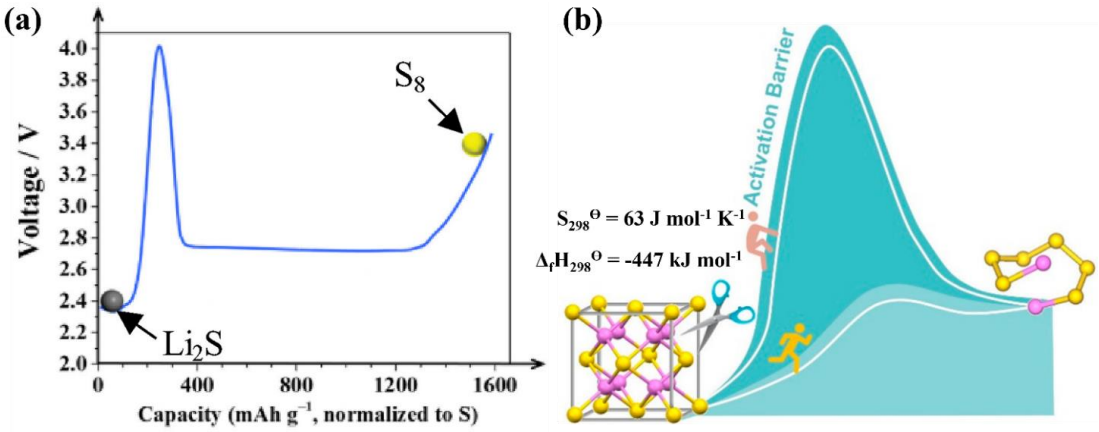


Figure 1.11 (a) A typical initial charging curve of Li_2S cathodes.[145] Copyright © 2017, Springer Nature Limited. (b) Crystal structure and activation barrier of Li_2S.[168] Copyright © 2020, American Chemical Society.

Figure 1.11 (b) illustrates that Li_2S possesses a very stable antifluorite (cubic) structure, characterized by greater bond energy and a higher standard enthalpy of formation than the cyclic molecular structure of elemental sulfur.[168] Thus, the delithiation of crystalline Li_2S is exceedingly challenging.[169,170] The elevated oxidation overpotential of Li_2S is largely ascribed to its distinctive reaction pathway in the first charge. Producing soluble polysulfides during the initial delithiation of Li_2S will be exceedingly challenging, unlike the lithiation of sulfur, which swiftly generates soluble polysulfides, transforming the slow solid-solid ($S \leftrightarrow Li_2S$) conversion into the more rapid solid-liquid-solid ($S \leftrightarrow LPSs \leftrightarrow Li_2S$) reaction pathway.[171]

1.3.1 a) Factors Contributing to the Charging Barrier/Overpotential

The prolonged plateau and substantial charging barrier observed in the typical initial charging curve of Li_2S (**Figure 1.11** (a)) signify that the first charging process could be a two-phase reaction, with the barrier associated with phase nucleation, necessitating an extra driving force. Such phenomenon can also be observed in other materials with a two-phase reaction, such as $LiFePO_4$.[172] Therefore, it has been confirmed by Yang *et al.* via adding polysulfide solution into the electrolyte that the reaction in the plateau region in the initial charge is a two-phase reaction between Li_2S and polysulfides and the origin of the initial barrier is phase nucleation, because the initial barrier disappeared as polysulfide nuclei had already been provided.[104]

Kinetic factors, such as ionic transport, electronic conductivity, and charge transfer, may also concur during the phase nucleation process in the overpotential spike.[104] To determine the variables contributing to the barrier, Yang *et al.* also examined the correlation between charge rates and barrier heights as illustrated in **Figure 1.12** (a) and (b).[104] The overpotential is almost constant and small when the current is very low (C/2000–C/500). At such extremely low current rates (≤ C/500, nearly approaching zero-current limit) where kinetic factors have little effect on the electrochemical process, the appearance of the initial overpotential spike indicates its thermodynamic origin from phase nucleation. Accompanying the current rate increase, the overpotential associated with kinetics also increases exponentially and dominates the height of the total barrier. So, a linear relation between the overpotential height and the logarithm of the current rate at high current rate (> C/200). In conclusion, it is kinetics rather than thermodynamics that govern the height of overpotential at practical rates.

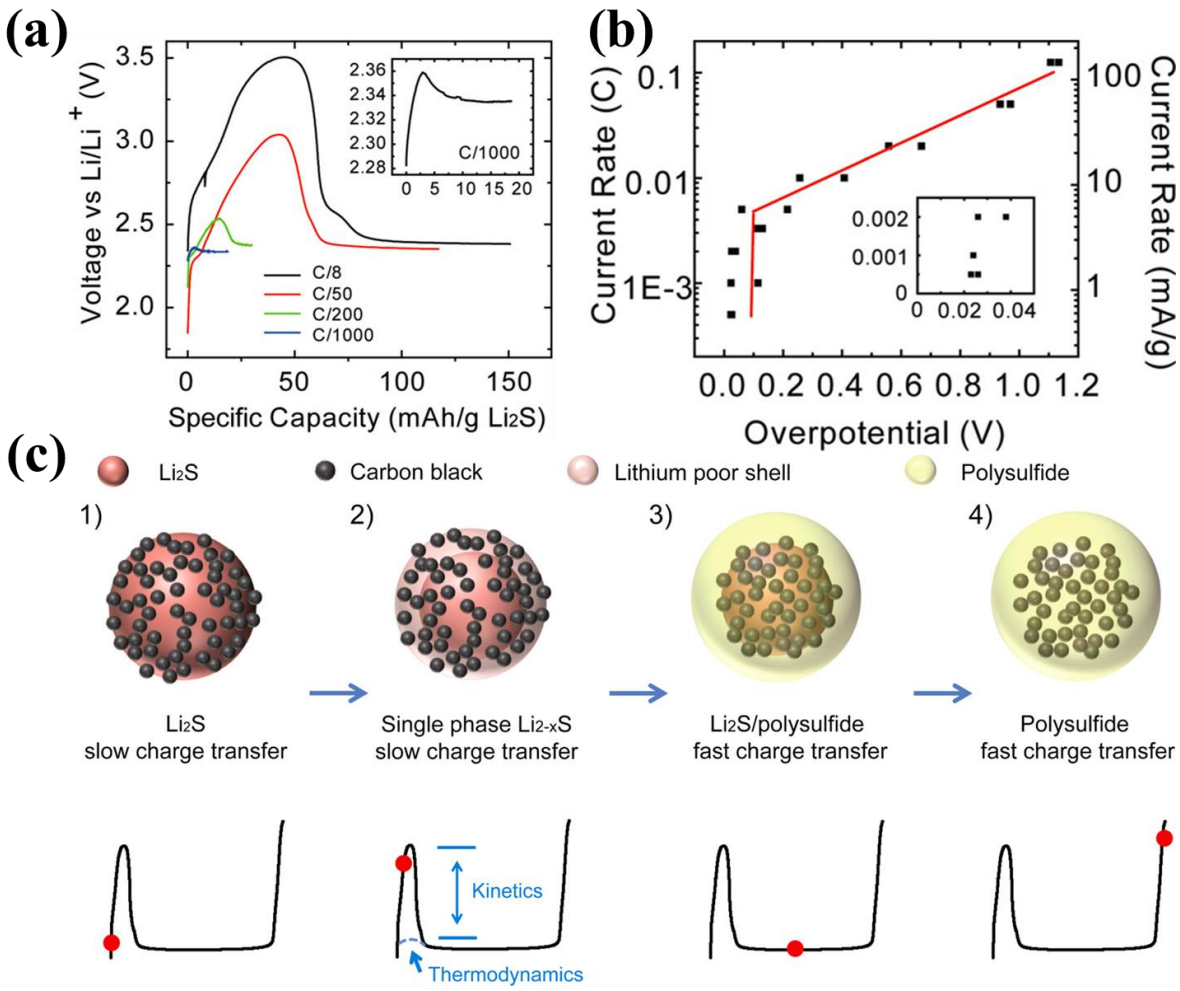


Figure 1.12 (a) The initial potential barrier of Li_2S cathode material at C/8, C/50, C/200, and C/1000. (b) Relationship between the logarithm of the current rate and the overpotential of Li_2S cathode. (c) The model for the initial charging of Li_2S.[104] Adapted from Ref. 104. Copyright © 2012, American Chemical Society.

Subsequent research, especially that based on the Butler-Volmer model, indicates that among the three kinetic factors—electronic conductivity of Li_2S, diffusivity of Li^+ in Li_2S, and charge transfer at the surface of Li_2S—the latter two, particularly the charge transfer process, predominantly influence the barrier height, whereas the impact of electronic conductivity is minimal. To be specific, charge transfer between Li_2S and polysulfides is much faster than between Li_2S and an electrolyte without polysulfides, and thus the initial charging barrier was dramatically reduced or even eliminated when lithium polysulfides were introduced to the electrolyte as additives. This rationale can also explain two additional observations: for sulfur-based Li-S batteries, there is no visible first charging barrier, and for Li_2S-based cathodes, the barrier vanishes after initial

charging process. LPSs emerge in the electrolyte once the sulfur- or Li_2S-based cathodes are discharged, promoting the charge transfer between Li_2S and electrolyte, which is also one of the aforementioned advantages of soluble LPSs. In short, the inability to produce soluble LPSs was the was the cause of the high overpotential in the initial stage. Therefore, Yang *et al.* proposed "nucleation of polysulfide" as shown in **Figure 1.12** (c), where the crystal Li_2S is very difficult to transform to polysulfide owing to the huge difference of bonding environment between the solid Li_2S and the liquid electrolyte unless the voltage reaches a certain potential. And these soluble LPSs intermediates can act as redox mediators to facilitate charge transfer on the Li_2S surface and reduce the charging overpotential. A similar activation mechanism was also proposed by Wang and colleagues, which involves two-step electrochemical oxidation of Li_2S on the surface.[173] The large potential disappears when the surface Li_2S is oxidized to short-chain LPSs and then to long-chain LPSs, which is due to the dissolved long-chain LPSs that can be directly oxidized to solid Li_2S.

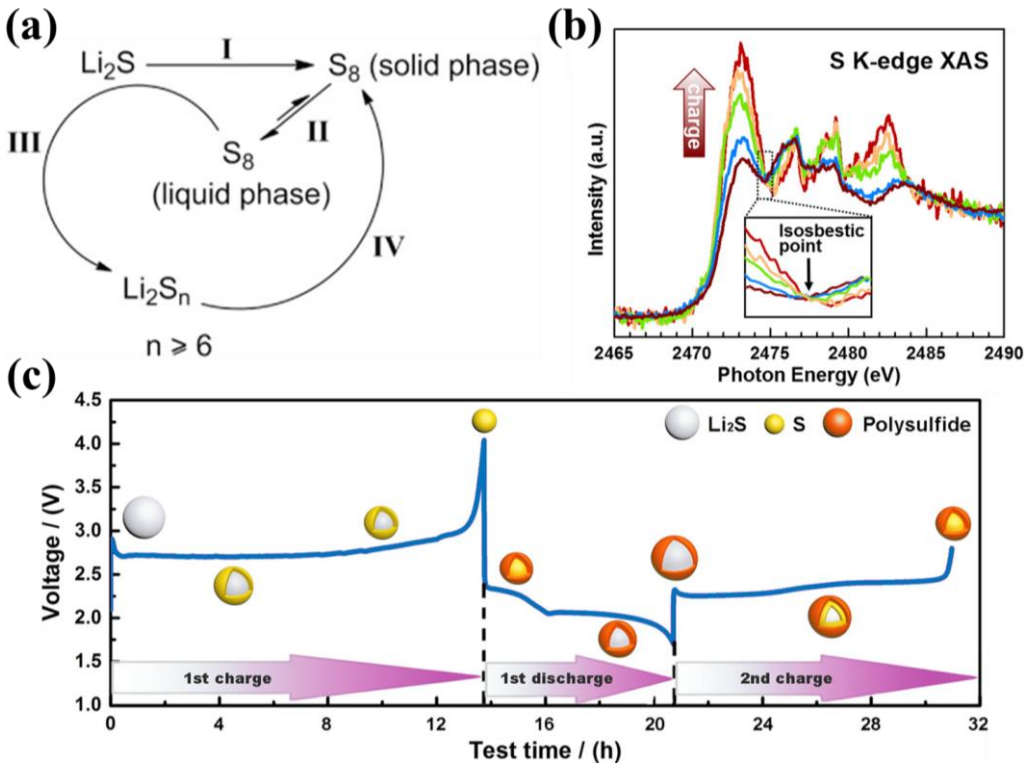


Figure 1.13 (a) Proposed reaction mechanism of Li_2S initial charge by Vizintin *et al.*[174] Copyright © 2017 Elsevier B.V. All rights reserved. (b) *In situ* S K-edge XAS spectra. (c) Proposed reaction scheme of the Li_2S electrode during the initial charge and discharge processes by Zhang *et al.*[175] Copyright © 2017, American Chemical Society.

There are varying perspectives on the first charging overpotential. Vizintin *et al.* applied two independent *operando* analytical tools (UV/Vis and X-ray absorption spectroscopy), suggesting that a little proportion of Li_2S is directly transformed into elemental sulfur by **Reaction I**, as shown in **Figure 1.13** (a), and the required overpotential arises from variations in crystallization enthalpy.[174] Then, the resultant sulfur is partly solubilized in the electrolyte to generate a liquid phase (**Reaction II**). The soluble sulfur interacts with Li_2S via **Reaction III** to produce long-chain LPSs. The oxidation of soluble LPSs to solid-state sulfur is much easier, which favors long-chain LPSs reducing back to elemental sulfur (**Reaction IV**). Finally, the amount of elemental sulfur dissolved in the electrolyte affects whether LPSs form during the initial charging stage.

Analogous to the activation mechanism put forward by Vizintin *et al.*, Zhang *et al.* used *in situ* X-ray absorption spectroscopy (XAS) to reveal the presence of an isosbestic point in the stack plot as shown in **Figure 1.13** (b), which implies a two-phase transformation in the first charging process, and also proposed that Li_2S was directly converted to elemental sulfur without producing polysulfides.[175] The distinction between the initial two charging processes arises from the residual LPSs remaining after the first discharging phase as illustrated in **Figure 1.13** (c). These residuals not only engage in chemical reactions with Li_2S, serving as a facilitator for the electrochemical oxidation of Li_2S, but they also enhance charge transfer at the Li_2S/electrolyte interface. In addition, the findings of Tan *et al*., derived from *in situ* synchrotron high-energy X-ray diffraction (XRD) and *ex situ* X-ray absorption near edge structure spectroscopy (XANES) in **Figure 1.14**, also agreed with theory on the direct transformation from Li_2S to elemental sulfur, since no polysulfides were detected.[145] Furthermore, sulfur emerged promptly upon the disappearance of Li_2S during the first charging step.

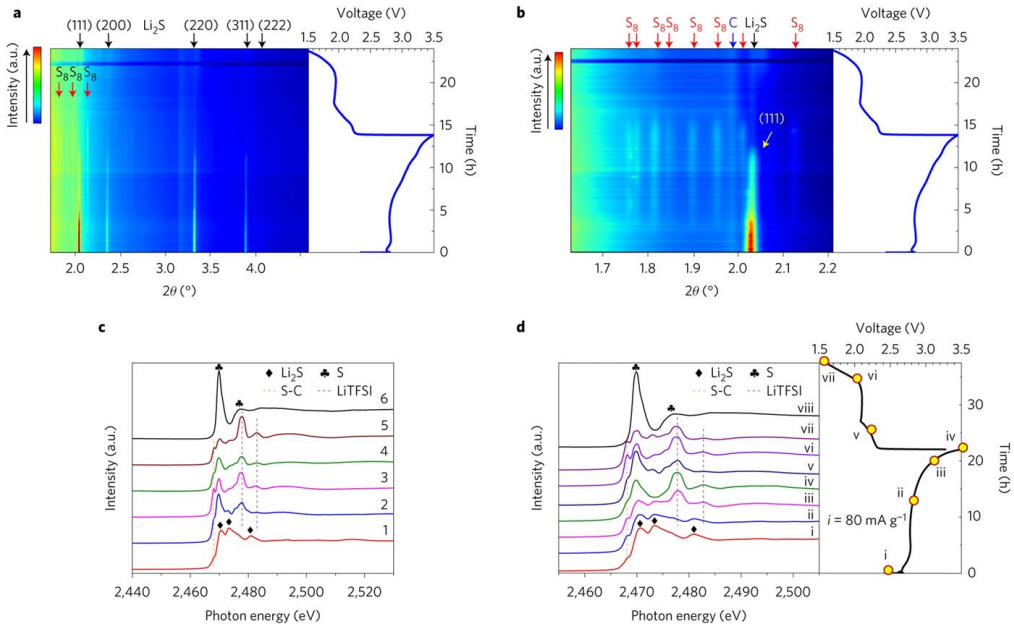


Figure 1.14 (a) *In situ* time-lapse XRD patterns and (b) its enlarged plot. (c) *Ex situ* XANES of S K-edge for Li_2S@graphene electrodes at different charge/discharge states. (d) *Ex situ* XANES of S K-edge for Li_2S@graphene electrodes at certain states of charge/discharge during the first cycle.[145]

Copyright © 2017, Springer Nature Limited.

Different views on the initial overpotential were also brought about when Jung *et al.* examined commercial Li_2S powders through X-ray photoelectron spectroscopy (XPS) measurements and electrochemical evaluations, believing that the large potential barrier of the initial charging process results from the contaminants (insulting oxidized products such as Li_2SO_3 or Li_2SO_4) on the surface and can be alleviated by washing its surface.[176] Bare sample, synthesized sample and acetonitrile-washed sample all have similar bulk structure but quite different potential barriers, suggesting that the bulk structure of Li_2S has little effect on the height of overpotential spike.

In summary, the elevated voltage barrier/overpotential observed during the initial phase of a Li_2S battery is mostly attributable to the following factors:

(1) The insulation of Li_2S (large resistance to charge transfer between Li_2S and the electrolyte).

(2) The highly stable antifluorite (cubic) structure of Li_2S with a strong bond energy and a high standard enthalpy of formation.

(3) The energy required for phase nucleation process of polysulfides.

(4) The energy required for Li_2S directly converted into sulfur.

(5) Contaminants (Li_2SO_3, Li_2SO_4, Li_2O, LiOH, *etc.*) present on the surface of Li_2S.

Certain explanations of the initial high overpotential are contradictory. The paradox shown by previous studies indicates the existence of a potentially more complex charging process for Li_2S.

1.3.1 b) Alleviation of the Charging Barrier

The high overpotential during the initial charge of Li_2S cathodes poses several challenges for battery performance, as it results in considerable energy loss and diminished efficiency while also hastening adverse side reactions that can irreversibly deplete a significant quantity of active electrode materials and/or electrolytes. Although the commercial microscale Li_2S particles can be activated at elevated cutoff voltages (~4 V *vs.* Li^+/Li), such high potentials would lead to the decomposition of the ether-based electrolyte (**Figure 1.15** (a))[177] and the corrosion of the aluminum current collector in Li-S battery system (**Figure 1.15** (b)),[178] ultimately causing rapid deterioration of electrochemical performance. Consequently, lowering the initial charge overpotential is therefore essential to improve energy efficiency, facilitating completer and more uniform Li_2S activation, and enhancing the reversibility of the redox process. Moreover, a reduced overpotential is particularly important in the context of practical battery configurations involving lean electrolyte and high sulfur loading, where energy losses and interfacial instability are further exacerbated. Tackling this problem is a key step toward advancing Li-S batteries for commercial applications.[179]

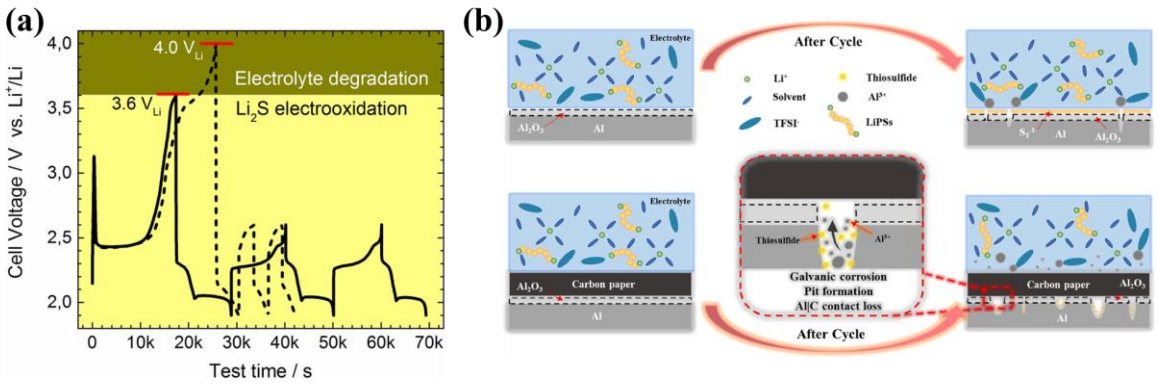


Figure 1.15 (a) Degradation region of common ether-based electrolyte in the initial charging process of Li_2S batteries.[177] Copyright © 2014, American Chemical Society. (b) The corrosion mechanism of Al as the current collector in the Li-S batteries.[178] Copyright © 2023 Published by Elsevier Ltd.

To address the challenges associated with the high initial charge overpotential of Li_2S cathodes, various strategies have been developed to facilitate Li_2S activation and enhance overall electrochemical performance. These approaches primarily aim to improve the conductivity of the cathode, lower the energy barrier for Li_2S oxidation, and stabilize the electrode-electrolyte interface during cycling. Here, several representative strategies are introduced and discussed, including elemental doping, cathode electrocatalysts, electrolyte additives and redox mediators.

Elemental Doping. Early findings by adding a small amount of transition metal (*e.g.* Co, Fe) into Li_2S lattice demonstrated a significantly reduced activation potential.[164,180] Since then, elemental doping has proven to be an efficient method for enhancing the ionic and electronic transport characteristics of Li_2S, which intrinsically exhibits low conductivity and slow Li^+ diffusion. Luo *et al.* first conducted a theoretical investigation on the lithium storage properties of Li_2S using DFT calculations.[181] The effects of doping transition metals (Fe, Co, Ni, Cu) on the lithiation/delithiation behavior and electrode potential of Li_2S have been examined, revealing a reduction in Li vacancy formation energy from 3.37 to 1.11 eV, indicating an increased tendency for defect generation following transition metal doping.[181] Apart from cation doping, the anion doping of Li_2S can also significantly improve its charge-transfer kinetics. According to Hong *et al.*, the incorporation of Se and Te into Li_2S can elongate and diminish the strength of the Li-S bond, as evidenced by the redshift of Li-S binding energy detected in XPS.[182] The Te-doped Li_2S exhibited a reduced energy barrier for phase transition and accelerated solid-state transformation kinetics, aligning with the mixing enthalpy values derived from DFT simulations. Combining cation and anion doping, Gao *et al.* reported a Cu^+, I^- co-doped Li_2S, which exhibited enhanced conductivity and Li^+ diffusion coefficient, increasing by five and two orders of magnitude, deriving advantages from Cu^+ as a redox mediator.[183] In summary, doping can generate structural defects, such lithium vacancies or interstitials, facilitating Li^+ migration and lowering the energy barriers for diffusion. Certain dopants have catalytic activity or enhance the polarizability of the host material, hence promoting surface charge transfer and expediting the redox kinetics of Li_2S and polysulfide intermediates.

Cathode Electrocatalysts. Electrocatalysts can enhance reaction kinetics by reducing activation energy, offering active sites, modifying reaction routes, and stabilizing intermediates,

which have been extensively investigated in Li-S batteries utilizing sulfur cathodes. Accordingly, with fast S-Li_2S conversion, the cyclability of the battery can be improved by the accelerated direct solid-solid conversion and the reduced dwelling time of soluble LPSs, hence suppressing the shuttle effect that nonpolar carbon hosts are susceptible to. Early study reported by Babu *et al.* suggests that the polysulfide shuttle effect can be mitigated by employing transition metal dichalcogenides (TMDs) as electrocatalysts.[184] Subsequently, Zhou *et al.* carried out systematic investigation into a series of metal sulfides as polar hosts, revealing that the energy barrier shows a pattern according to the first-principle simulations in terms of binding strengths between Li_2S_6 and electrocatalysts: Ni_3S_2 < SnS_2 < FeS < CoS_2 < TiS_2 < VS_2, which are consistent with the measured polysulfide adsorption capability.[185] Compared with TMDs, transition metal phosphides (TMPs) possess notable advantages serving as electrocatalysts, for they can demonstrate metallic properties or even superconductivity, which are beneficial to the electrochemical reaction in Li-S batteries, and their fabrication is straightforward and mild.[186] Yuan *et al.* devised a one-pot chelation approach for the synthesis of ultrafine TMP nanoparticles modified with N- and P-doped carbon nanoflakes (TMPs@NPC). The overpotential in the initial charging process of Li_2S has been reduced to 2.59, 2.51, and 2.44 V by employing Fe_2P@NPC, Co_2P@NPC, and Ni_2P@NPC as host materials in contrast with merely active carbon (3.50 V) or NPC (2.80 V) involved. The lower activation barriers and the extended voltage plateaus signify less charge-transfer resistance, attributed to the high reactivity of TMPs in decomposition of Li_2S.[186] Besides, transition metal carbides (TMCs) are also studied as electrocatalysts for the activation of Li_2S cathode. The multi-layered Ti_3C_2/Li_2S applied as cathode proposed by Liang *et al.* revealed a decreased activation barrier of 2.85 V, which is 0.6 V lower than that of graphene/Li_2S composite cathode, and additionally the "shuttle effect" could be effectively suppressed through both chemisorption and physisorption.[187] Overall, integrating cathode electrocatalysts is an effective approach to reduce overpotential, mitigate the shuttle effect, and enhance the energy efficiency and cycle stability of Li_2S batteries.

Electrolyte Additives. The stable crystal structure of Li_2S is one of the reasons that the high activation barrier arises from. Enhancing the solvation of Li_2S in the electrolyte through the use of appropriate additives turned out to be an effective strategy. The improved solvation can partially convert the original solid-solid reaction pathway into a solid-liquid process, thereby significantly

accelerating reaction kinetics and lowering the overpotential during the initial charge. As previously discussed, the incorporation of LPSs into the electrolyte has emerged as an effective approach to mitigate the initial overpotential. These polysulfide additives can undergo a comproportionation reaction with Li_2S, leading to partial dissolution of the Li_2S surface and promoting a phase transition that accelerates charge transport. Furthermore, the additional LPSs can also compensate for the loss of active material caused by side reactions at the lithium metal anode, thereby improving sulfur utilization and overall battery performance. In addition to polysulfide additives, solvent-mediated dissolution of Li_2S offers another viable approach. For example, Liang *et al.* as illustrated in **Figure 1.16** (a) exploited the solubility of Li_2S in ethanol and demonstrated that trace amounts of ethanol in the electrolyte can effectively reduce the activation overpotential.[188] The introduction of 250 ppm ethanol, as shown in **Figure 1.16** (b), led to a notable decrease in the overpotential spike from 3.4 V to 2.9 V. This effect is attributed to the transition to a liquid-solid phase reaction that enhances both electron and lithium-ion transport. The optimal ethanol content was found to be 500 ppm, achieving a high initial discharge capacity of 1144 mA h g^{-1} with a reduced overpotential of 3.1 V. Similarly, Lin *et al.* found that introducing a little quantity of P_2S_5 into the electrolyte could enhance the solubility of Li_2S in the tetraethylene glycol dimethyl ether (TEGDME) solvent by creating a soluble Li_2S-P_2S_5 complex in the electrolyte.[189] Building on this approach, Zu *et al.* applied the strategy to Li_2S cathodes and observed that the charging overpotential was minimized to when the molar ratio between Li_2S and P_2S_5 was optimized at 7:1.[190]

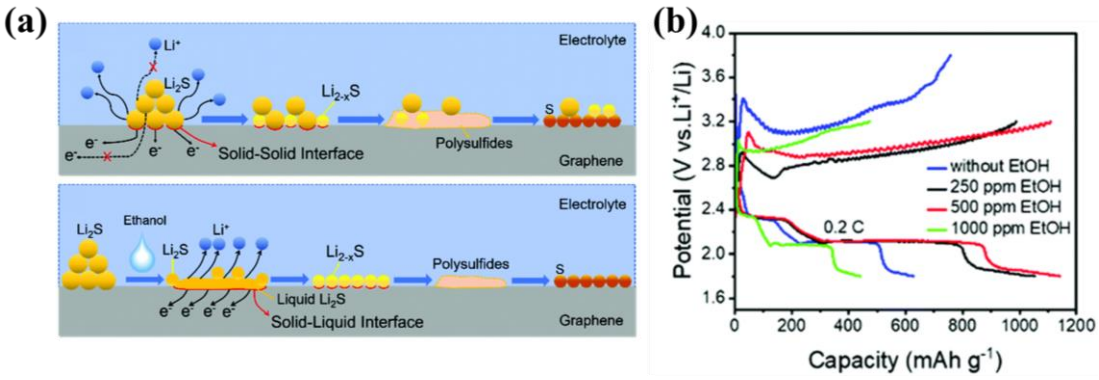


Figure 1.16 (a) Schematic diagram of the activation process of Li_2S (upside) without ethanol and (downside) with ethanol added in the electrolyte. (b) The initial charge/discharge curves of Li_2S batteries based on electrolytes with different amount addition of ethanol.[188] Copyright © 2019 Royal Society of Chemistry.

Redox Mediators. Redox mediators (RMs) are a specific type of electrolyte additives, which are substances that are electrochemically active and are applied to the electrolyte to help redox processes take place by moving electrons around in a roundabout way. These can help move charges between current collectors and electrode materials by acting as a charge shuttle. The first application of RMs to decrease the overpotential barrier of Li_2S battery was reported by Meini *et al.*, where the addition of RMs into the normally used electrolyte solution realized a lowered activation potential at 2.9 V using decamethylferrocene and a near-theoretical capacity.[177] Typically, when an RM is added to the electrolyte, at the electrode, the original form of RM (e.g., I^- or Fc) is electrochemically oxidized to its oxidized form (e.g., I_3^- or Fc^+).[191–193] This oxidized form is soluble, so it diffuses through the electrolyte. It will reach Li_2S particles that are not in direct electrical contact with the electrode. Then it chemically reacts with Li_2S to extract lithium and oxidize sulfur as **Equation 1.7** demonstrates:

$$RM^+ + Li_2S \rightarrow RM + 2Li^+ + S_x^{2-} \qquad \textbf{Equation 1.7}$$

It is a chemical redox reaction rather than an electrochemical reaction. In this way, Li_2S is oxidized without being at the electrode surface. In summary, the RMs selected for employment need to meet several criteria: 1) They should have lower oxidation potential than the onset potential of Li_2S oxidation; 2) They should be soluble and mobile in the electrolyte; 3) They can undergo fast and reversible redox reactions; 4) The oxidized form can chemically oxidize Li_2S without direct contact with the electrode.

Amorphization. Crystalline Li_2S has a well-defined cubic antifluorite structure, whereas amorphous Li_2S lacks long-range order, which modifies its electronic structure, bonding, and transport properties. Amorphous Li_2S shows slightly better electronic conductivity than crystalline Li_2S, which has a very poor value of approximately 10^{-13} S cm^{-1}, enabling easier initial charge. Through density functional theory (DFT) carried out by Ye *et al.* on the relationship between the crystallinity of Li_2S and the initial activation potential, the delithiation energy for amorphous Li_2S is significantly lower at 2.16 eV compared to 3.21 eV for crystalline Li_2S, effectively reducing the activation overpotential.[150] Additionally, the amorphous form allows for conformal coating rather than discrete particles, enhancing interfacial contact with conductive matrices and improving

charge transfer efficiency. Preparing amorphous substances generally involves methods that prevent crystallization or disrupt the long-range order of a material, such as rapid quenching, mechanical milling, sol-gel processing, thermal decomposition of precursors and vapor deposition. Meng *et al.* developed a vapor-phase atomic layer deposition (ALD) method for the atomically precise synthesis of Li_2S, which delivered stable capacities of ~800 mA h g^{-1}, a very low activation potential at ~2.38 V, nearly 100% Coulombic efficiency, and excellent rate capability.[194] This approach utilizes vapor deposition to enable atom-by-atom growth under controlled vacuum or plasma conditions. Huang *et al.* developed a simple thermal decomposition approach using a lithium trithiocarbonate (Li_2CS_3) precursor, which was easily synthesized at room temperature and subsequently decomposed at 200 °C to produce amorphous nano-sized Li_2S (Li_2S-200) and Li_2S@SP-200 nanocomposites.[195] XRD analysis of both Li_2S-200 and Li_2S@SP-200 revealed only broad, weak diffraction peaks characteristic of Li_2S, indicating their amorphous nature, while the initial charging curves displayed significantly reduced activation voltages.

Various strategies have been developed to reduce the high initial charge overpotential of Li_2S cathodes. Elemental doping improves conductivity and ion transport; electrocatalysts lower activation energy by enhancing redox kinetics; electrolyte additives and redox mediators facilitate Li_2S oxidation via solvation and remote redox pathways; and amorphization reduces the delithiation energy by disrupting crystallinity. While each method offers unique benefits based on different mechanisms, challenges remain in terms of complexity, scalability, and long-term stability

Among the strategies explored, nanostructure engineering—especially in the form of Li_2S@Carbon nanocomposites—offers a more comprehensive solution to overcome the intrinsic drawbacks of Li_2S.[112] By integrating nanosized Li_2S with conductive carbon frameworks, these composites simultaneously address electronic insulation, sluggish kinetics, and interfacial instability. The nanoconfinement effect, enhanced surface contact, and synergistic interactions between Li_2S and carbon significantly lower the activation energy for delithiation and improve electrochemical reversibility.

1.3.2 Nanostructure Engineering: Li_2S@Carbon Nanocomposites

Cathodes made from commercially available Li_2S often suffer from high initial charge overpotentials, limited rate capability, and poor cycling stability, primarily due to the large particle size of Li_2S (10–20 μm),[166,167] which hampers Li^+ diffusion and charge transport. In contrast, nanostructured Li_2S-based cathodes—particularly Li_2S@Carbon nanocomposites—have shown significantly improved electrochemical performance. This enhancement arises from the nanoscale dispersion of Li_2S within a conductive carbon matrix, which not only increases surface area and shortens ion diffusion pathways but also ensures intimate interfacial contact for efficient charge transfer.[112] Uniform distribution and strong connectivity between Li_2S and carbon are critical for lowering activation overpotentials, accelerating redox kinetics, and maximizing active material utilization. To achieve such structures, a variety of synthetic strategies have been developed, including solid-state methods like high-energy ball milling, carbothermal reduction, and thermal decomposition, as well as liquid-phase approaches involving chemical precipitation, infiltration, and subsequent conversion. Continued innovation in these synthesis routes is essential to further improve the structural and electrochemical characteristics of Li_2S@Carbon nanocomposites and to advance their practical implementation in high-performance LSBs.

The following section presents an overview of the synthesis strategies, structural designs, and electrochemical advantages of Li_2S@Carbon nanocomposites, highlighting their pivotal role as the most promising approach for realizing high-performance and commercially viable Li-S batteries.

1.3.2 a) High-Energy Ball Milling

High-energy ball milling is a mechanical technique that utilizes repeated collisions between powder particles and milling media to induce structural changes and reduce particle size.[196,197] This solvent-free (or using very small amount) method facilitates uniform mixing, solid-state reactions, and defect formation, while also breaking the Li_2S crystal lattice to enhance its electrochemical reactivity. Ball milling has been widely employed in the early development of Li_2S cathodes, primarily to reduce the particle size of commercial Li_2S (typically 10–20 μm) and enhance its electrochemical performance by improving contact with conductive carbon materials such as carbon black and multi-walled carbon nanotubes (MWCNTs).[198] High-energy ball milling typically reduces the particle size to the submicron range (0.2–2 μm), improving Li^+ diffusion and electron

transport. For example, Cai *et al.* prepared a nanostructured Li_2S-carbon composite by ball milling commercial Li_2S with carbon black at 1060 rpm for 2 hours, resulting in particles ranging from 200 to 500 nm as shown in **Figure 1.17** (a).[160] This composite exhibited a reduced activation potential of 2.6 V; however, full charging still required voltages up to 4.0 V. In another study, Chen *et al.* (**Figure 1.17** (b)) used high-energy ball milling to combine Li_2S and carbon black, followed by carbonization with pyrrole to form Li_2S/C composite particles (~400 nm) encapsulated within a nitrogen-doped carbon shell.[199] This core–shell structure retained a capacity of 652 mA h g^{-1} after 100 cycles, indicating improved cycling stability.[199] Additionally, some studies by Li *et al.* in **Figure 1.17** (c) employed ball milling not on commercial Li_2S directly but on precursors, enabling the synthesis of nanosized Li_2S particles.[200] These were subsequently embedded into mesoporous carbon matrices by milling with carbonizable polymers such as polyacrylonitrile (PAN), followed by high-temperature carbonization (~1000 °C), forming robust nanocomposites with enhanced conductivity and structural stability. It is important to note that hydrogen gas (H_2) generation during the ball milling process can lead to a significant increase in internal pressure and must be carefully vented to ensure safety. The major limitation of high-energy ball milling is the lack of precise control over particle size and morphology, often leading to broad size distributions and structural nonuniformities.[201] Furthermore, this technique is prone to inducing undesired particle agglomeration, which can negatively affect the dispersion and electrochemical performance of the resulting composite.[202]

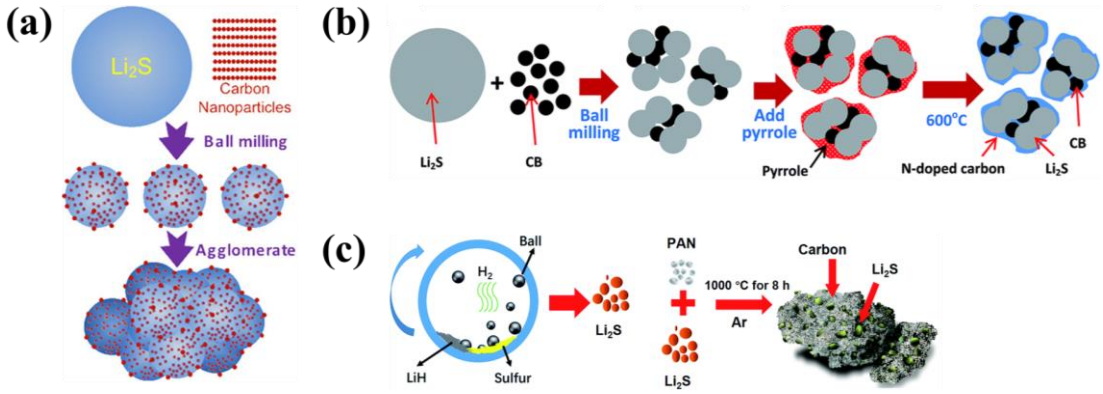


Figure 1.17 (a) Schematic of high-energy ball milling process for preparing Li_2S-C nanocomposites.[160] Copyright © 2012 American Chemical Society. (b) Schematic of the approach for synthesizing the Li_2S/C composite particles encapsulated by a nitrogen-doped carbon shell.[199]

Copyright © 2013 Royal Society of Chemistry. (c) Schematic illustration of the fabrications of Li_2S and the Li_2S/C hybrid.[200] Copyright © 2013 Royal Society of Chemistry.

1.3.2 b) Carbothermal Reduction

Carbothermal reduction is a high-temperature process where carbon serves as a reducing agent to convert metal oxides, sulfates, or similar precursors into lower-valence products like metals, sulfides, or carbides.[203] Typically conducted under inert or reducing atmospheres (e.g., Ar, N_2, or H_2), the method exploits carbon's strong affinity for oxygen. Besides traditional carbon sources like graphite or carbon black, carbon-rich polymers such as glucose, polyvinyl alcohol (PVA), polyvinylpyrrolidone (PVP), and polyacrylonitrile (PAN) can also be used.[204,205] These decompose during heating to generate carbon *in situ*, promoting effective reduction. In 2013, Yang *et al.* pioneered a cost-effective carbothermal technique for synthesizing Li_2S@Carbon composites from Li_2SO_4 via the following mechanism as **Equation 1.8**:[206]

$$Li_2SO_4\ (s) + xC\ (s) \rightarrow Li_2S\ (s) + xCO_y\ (g)\ ((x,y) = (1,1) \text{ or } (4,2)) \qquad \textbf{Equation 1.8}$$

As shown in **Figure 1.18** (a), the carbon framework is formed by pyrolyzing a resorcinol-formaldehyde (RF) gel, which is synthesized via condensation polymerization.[206] Due to its high surface area, porosity, and conductivity, the abundant oxygen groups in the RF gel may coordinate with Li^+ in Li_2SO_4, aiding its uniform distribution in the carbon matrix.

The temperature used in carbothermal reduction plays a crucial role in determining the crystallinity and particle size of Li_2S. As indicated by the Ellingham diagram in **Figure 1.18** (b), the reduction of Li_2SO_4 by carbon becomes thermodynamically feasible above 300 °C.[207] However, many studies conduct this process at around 800 °C, which tends to promote grain growth and leads to larger, highly crystalline particles. In contrast, Ye *et al.* demonstrated in **Figure 1.18** (c) that conducting the reaction using PVA as carbon source below the melting point of Li_2SO_4 (635 °C) helps preserve its original morphology and yields smaller Li_2S particles (10–20 nm) due to gradual oxygen removal.[204] The use of unsaturated carbon bonds (C=C and C=O) derived from partially carbonized polymers allows the carbothermal reduction of Li_2SO_4 to take place at a considerably low temperature. Notably, Li_2S@Carbon synthesized at this lower temperature exhibited a reduced

activation potential (2.63 V) and a higher initial discharge capacity (805 mA h g^{-1}), compared to 3.2 V and 760 mA h g^{-1} for material produced at 900 °C.

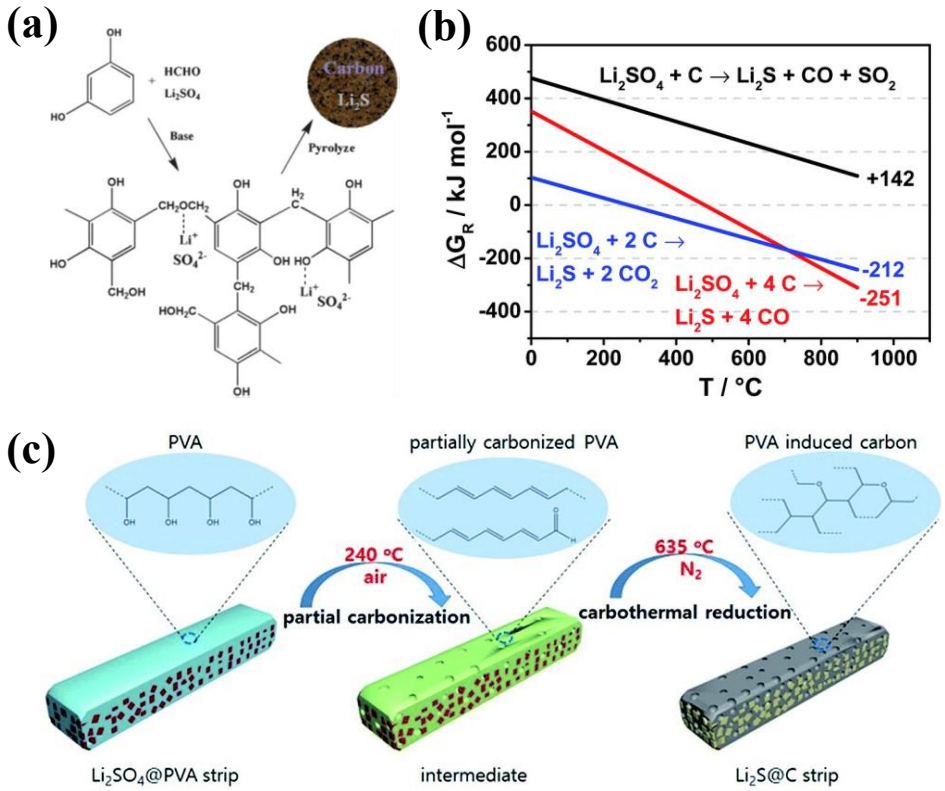


Figure 1.18 (a) *In situ* synthesis scheme for a Li_2S@Carbon composite.[206] Copyright © 2013 Royal Society of Chemistry. (b) Ellingham diagram for different carbothermal reductions. Numbers at the end of the lines are DGR values at 820 °C.[207] Reproduced from Ref. 207 under a Creative Commons Attribution–NonCommercial 3.0 Unported License. Copyright © 2015 The Authors. Published by Royal Society of Chemistry. (c) Schematic of the fabrication process of Li_2S@C strips and structural evolution of PVA during its assisted carbothermal reduction of Li_2SO_4.[204] Copyright © 2013 Royal Society of Chemistry.

One limitation of the carbothermal reduction method for low-cost Li_2S-carbon composite synthesis is the formation of excessive porosity in the carbon matrix, caused by the evolution of CO and CO_2 gases.[203,207] This increased porosity can lower the volumetric capacity of Li_2S cathodes. Additionally, the process may release toxic byproducts such as SO_2, SO_3, and H_2S.[208] Furthermore, controlling the morphology of Li_2S produced at high temperatures remains challenging.

1.3.2 c) Carbothermal Reduction-Derived Method

PVP serves as both a carbon source and structural template in the carbothermal reduction of Li_2SO_4 to Li_2S, forming Li_2S@Carbon composites. However, conventional solid-state mixing yields poor dispersion and irregular morphology. To address this, electrospinning, as shown in **Figure 1.19** (a), is used to fabricate uniform Li_2SO_4/PVP nanofibers as structured precursors.[209] These fibers enable nanoscale dispersion and form an interconnected architecture. After annealing under a reducing atmosphere, Li_2SO_4 is converted into finely distributed Li_2S within conductive carbon nanofibers. The resulting Li_2S@Carbon fibers can be collected as free-standing, binder-free electrodes. However, the resulting fiber mats often suffer from low mass loading, which restricts their areal capacity unless multiple layers are stacked. Scaling up the process remains challenging due to the limited throughput of traditional electrospinning setups. Additionally, the choice of solvent is constrained by the need to balance PVP solubility, Li_2SO_4 dispersion, and electrospinnability.[210] The final fiber morphology is highly sensitive to processing parameters and ambient conditions, requiring precise control.[211,212]

Also inspired by the traditional carbothermal reduction method, the magnesothermal synthesis of Li_2S replaces carbon with magnesium (Mg) as the reducing agent as shown in **Figure 1.19** (b).[213] While both approaches aim to reduce lithium-containing precursors such as Li_2SO_4 to Li_2S, Mg offers a significantly stronger reduction potential and enables the reaction to proceed at lower temperatures with greater thermodynamic favorability. Unlike carbothermal methods, which often generate gaseous byproducts like CO and CO_2 and leave behind porous carbon residues, magnesothermal synthesis produces solid MgO as a valuable byproduct with zero greenhouse-gas emissions. To obtain high-purity Li_2S after reduction and purification, the resulting product is often dissolved in ethanol, where Li_2S is moderately soluble, and then recrystallized to achieve uniform particle size and improved purity—an essential step for achieving consistent electrochemical performance in battery applications. Magnesothermal synthesis, while effective, faces several drawbacks. Highly exothermic reaction poses challenges in heat control and scalability. Mg powder is pyrophoric and requires careful handling under inert conditions. Post-reaction, MgO byproducts must be fully removed, and an additional ethanol-based recrystallization step is often needed to purify Li_2S. The method also offers little control over morphology and uniformity.

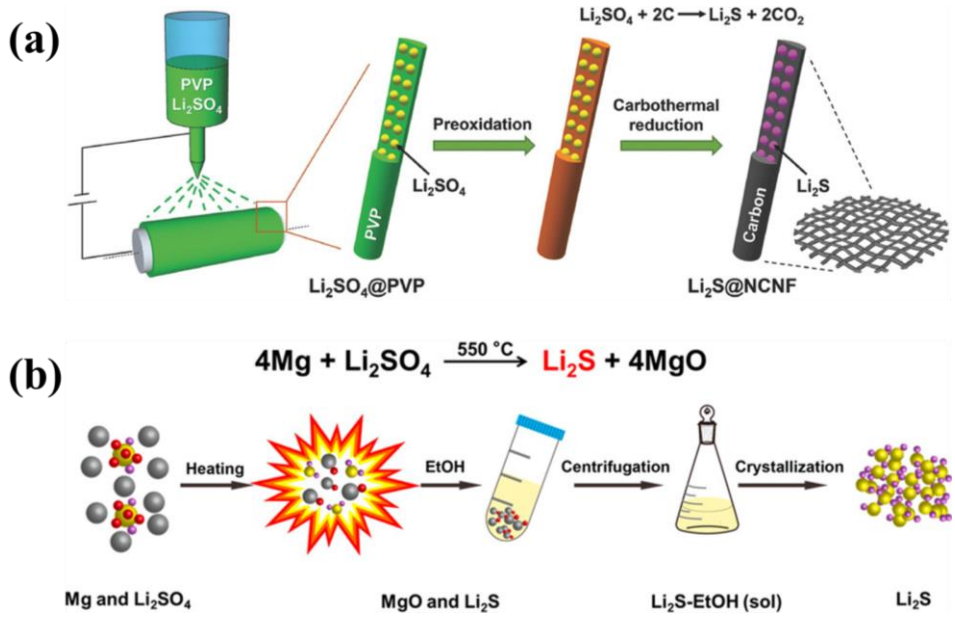


Figure 1.19 (a) Schematic illustration of the production of freestanding flexible Li_2S@NCNF paper electrodes via Ar-protected carbothermal reduction of Li_2SO_4@PVP fabrics made by electrospinning at ambient conditions.[209] © 2017 WILEY-VCH Verlag GmbH & Co. KGaA, Weinheim (b) Illustrative process of magnesothermal synthesis of Li_2S and purification.[213] Copyright © 2022 American Chemical Society.

1.3.2 d) Chemical Lithiation of Sulfur-Rich Precursors

The sulfur cathode has been extensively studied, and the synthesis of S@Carbon nanocomposites is now a well-established technique. Therefore, a logical approach is to first utilize sulfur to prepare either sulfur nanoparticles or S@Carbon nanocomposites, and then chemically lithiate them to obtain Li_2S@Carbon nanostructures. The most commonly used lithiation agents include organolithium compounds such as lithium triethylborohydride ($LiEt_3BH$)[214,215] and lithium naphthalenide ($[Li^+][Naph^-]$).[216] Representative examples and their corresponding synthesis reactions are summarized in the following **Table 1.4**.

Table 1.4 Chemical Lithiation Agents for Elemental Sulfur.

Lithiation Agent	Formula	Conditions	Reaction	Ref.
Lithium metal	Li	50-70 °C, inert gas, dry ether solvent	$S + 2Li \rightarrow Li_2S$	153

n-Butyllithium	C_4H_9Li	Room temp., dry THF or hexane, inert atmosphere	$S + 2C_4H_9Li \rightarrow Li_2S + C_4H_9\text{-}C_4H_9$	157
Lithium hydride	LiH	High-energy ball milling	$S + 2LiH \rightarrow Li_2S + H_2$	200
Lithium naphthalenide	$LiC_{10}H_8$	In THF, under Ar	$S + 2LiC_{10}H_8 \rightarrow Li_2S + 2C_{10}H_8$	216
Lithium triethylborohydride	$LiBEt_3H$	Anhydrous ether solvents, ambient conditions	$S + 2LiBEt_3H \rightarrow Li_2S + H_2 + 2BEt_3$	214,215

In 2010, Yang *et al.* utilized the well-studied CMK-3 mesoporous carbon as a host matrix and infiltrated its nanoscale pores with molten sulfur at 155 °C.[157] The resulting S/CMK-3 composite was lithiated with *n*-butyllithium at 65 °C for 2 hours and then at 105 °C for 18 hours. XRD was carried out toward samples before and after treatment as exhibited in **Figure 1.20** (a). XRD analysis showed no detectable peaks of sulfur or Li_2S, attributed to the confinement of Li_2S within the sub-5 nm pores of CMK-3, which limited crystallite size. To confirm Li_2S formation, lithiation was repeated using macroporous carbon (200–300 nm pores), where clear Li_2S diffraction peaks appeared, supporting that Li_2S also formed in S/CMK-3 but remained XRD-invisible due to its nanoscale dimensions. Other reagents, such as $LiEt_3BH$, have also been explored for lithiation, as shown in **Figure 1.20** (b).[214] Sulfur was first dissolved in toluene and then combined with a dispersion of single-layer graphene oxide (SLGO) in tetrahydrofuran (THF) to obtain a homogeneous S/SLGO mixture. This mixture was subsequently introduced into a THF solution of $LiEt_3BH$ and gently heated under stirring to evaporate the solvent, leading to the formation of well-defined Li_2S/GO spherical structures.

The chemical lithiation method offers the advantage of low-temperature synthesis compared to carbothermal approaches and improved dispersion of Li_2S within a conductive carbon matrix, especially when using nanostructured carbon hosts.[217] However, the major drawbacks of this approach stem from the highly reactive and unstable nature of the lithiation agents. Common reagents like *n*-butyllithium and $LiEt_3BH$ are hazardous—*n*-butyllithium is pyrophoric, while $LiEt_3BH$ is highly flammable, and both are corrosive or decompose into corrosive byproducts. These safety concerns make handling difficult and pose significant challenges for scalability and commercial application. Additionally, the degree of lithiation and crystallinity of Li_2S can be

difficult to verify via XRD in highly porous or nanoscale systems due to peak broadening or suppression.

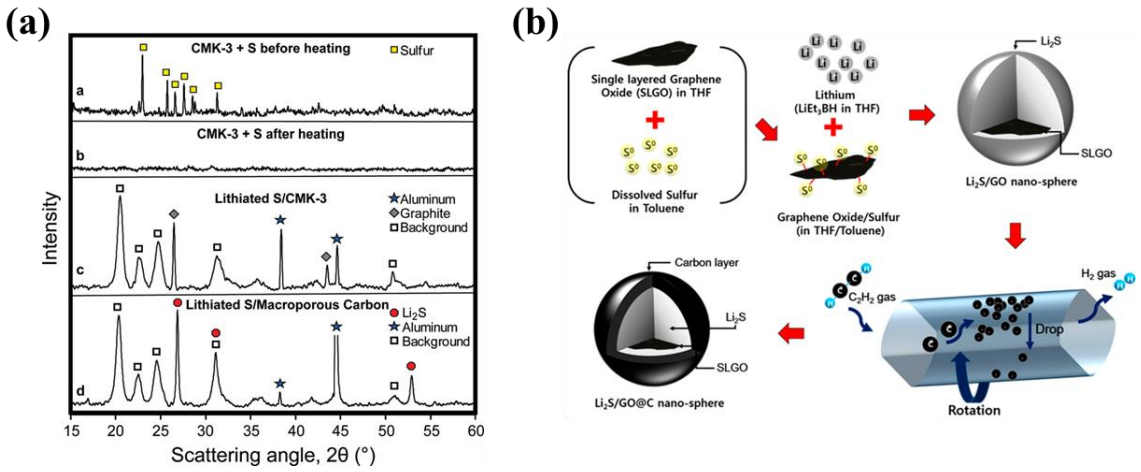


Figure 1.20 (a) X-ray diffraction characterization of Li_2S/mesoporous carbon nanocomposite particles.[157] Copyright © 2010 American Chemical Society. (b) Schematic illustration of the synthesis of Li_2S/GO@C nanospheres.[214] Copyright © 2015 American Chemical Society.

1.3.2 e) Sulfuration of Lithium-Rich Precursors

The sulfuration method, primarily based on vapor-phase reactions, has emerged as a versatile and scalable approach for synthesizing Li_2S from various lithium-containing precursors. This method leverages the high reactivity of sulfur-containing gases—including hydrogen sulfide (H_2S), carbon disulfide (CS_2), and sulfur vapor—to transform solid, liquid, or vapor-phase lithium precursors into Li_2S under controlled thermal and atmospheric conditions.

Air-stable lithium salts such as LiOH, Li_2CO_3, $LiNO_3$, and LiOEt are attractive starting materials due to their ease of handling and ambient stability.[218] Similarly, the relatively low melting points (MP) of certain lithium salts—such as lithium nitrite ($LiNO_2$, MP 222 °C) and lithium acetate (CH_3COOLi, MP 286 °C)—make them suitable for widely-applied melt-infiltration into carbon matrix to form Li-salt@Carbnon composites, which can then be transformed to Li_2S@Carbon composites through subsequent sulfurization. The conversion mechanism to Li_2S through reactions is shown in **Table 1.5**. The reacting temperature depends on the lithium precursor: strong Brønsted base salts (e.g., LiOH, LiH, $LiNH_2$) begin reacting at ~100 °C, while Li_2CO_3 and CH_3COOLi require higher temperatures of ~400–725 °C. Lower conversion temperatures are generally

preferred as they help preserve the original morphology, minimize Li_2S particle coarsening, and reduce energy consumption. Processing methods may include ball milling and recrystallization to tailor particle size prior to sulfuration. Dressel *et al.* first used high-energy ball milling to reduce the particle size of LiOH crystals, then blended the resulting powder with carbon black as shown in **Figure 1.21** (a).[219] This LiOH/C mixture, combined with a binder, was cast onto an aluminum current collector to form the electrode. Sulfuration was finally carried out by exposing the electrodes to a continuous H_2S gas flow at 100 or 150 °C. Due to the generation of H_2O, temperatures above 100 °C are recommended. The batteries based on sulfurized LiOH/C (i.e. Li_2S/C) show discharge capacities of up to 770 mA h g^{-1} and retained > 410 mA h g^{-1} after 100 cycles at 0.2 C.

CS_2 can be used as an alternative to H_2S in gas-solid reactions for synthesizing Li_2S and its composites. For example, as shown in **Figure 1.21** (b), combustion of lithium foils in CS_2 vapor carried out by Tan *et al.* produced Li_2S nanocrystals of 50–80 nm encapsulated in few-layer graphene (Li_2S@graphene). Notably, at a Li_2S loading of 10 mg cm^{-2}, the electrode delivers a high reversible capacity of 1,160 mA h g^{-1}.[145] In **Figure 1.21** (c) Liang *et al.* also used CS_2 to convert LiH to Li_2S at temperatures below 250 °C.[220] The resulting Li_2S particles, sized 5–15 nm, were embedded in porous carbon and interconnected by a CNT network, enhancing conductivity. As a result, the electrode delivers a high specific capacity of 820 mA h g^{-1} at 0.1 A g^{-1} after 10 cycles, along with excellent cycling stability, retaining 502 mA h g^{-1} at 0.5 A g^{-1} after 300 cycles.

Table 1.5 Chemical Sulfuration Agents for Lithium-Rich Precursors.

Sulfuration Agent	Reaction	Ref.
H_2S	$2ROLi\ (sol) + H_2S\ (g) \rightarrow 2Li_2S\ (s) + H_2\ (g)$	218
	$2LiX\ (s) + H_2S\ (g) \rightarrow 2Li_2S\ (s) + 2HX\ (g)$	219
CS_2	$4Li\ (l) + CS_2\ (g) \rightarrow 2Li_2S\ (s) + C\ (s)$	145
	$2LiOH\ (s) + CS_2\ (g) \rightarrow Li_2S\ (s) + CO_2\ (g) + H_2S\ (g)$	221
	$4LiH\ (s) + CS_2\ (g) \rightarrow 2Li_2S\ (s) + C\ (s) + 2H_2\ (g)$	220
S (gas)	$2Li + S\ (g) \rightarrow Li_2S\ (s)$	222
	$6LiOH\ (s) + 3S\ (g) \rightarrow 2Li_2S\ (s) + Li_2SO_3\ (g) + 3H_2O\ (g)$	208

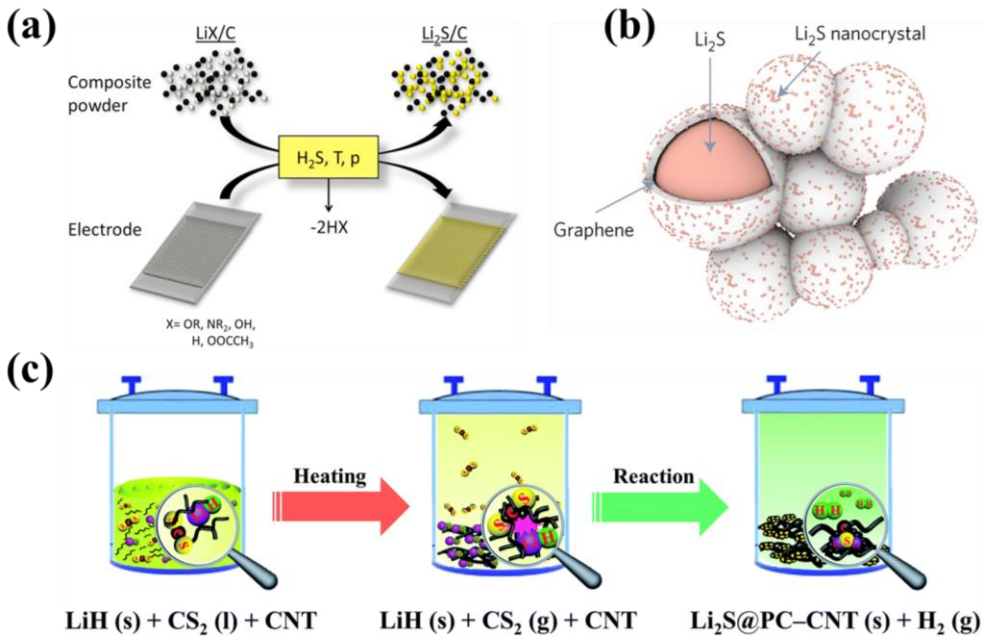


Figure 1.21 (a) Schematics of routes to prepare Li_2S/C composite and electrodes.[219] Copyright © 2016 Elsevier B.V. All rights reserved. (b) Li_2S@graphene capsules by burning lithium in CS_2.[145] Copyright © 2017, Springer Nature Limited. (c) Schematic illustration of the synthesis procedure of Li_2S@PC-CNT.[220] Copyright © 2013 Royal Society of Chemistry.

The reaction between lithium and sulfur would be the direct method to obtain Li_2S. Though less commonly used due to handling difficulty and low product yield, sulfur gas can react with Li metal in a sealed vacuum vessel at ~300 °C to produce Li_2S. The resulting materials can inherit the precursor's morphology but suffer from lower purity and yielding.[223]

The sulfuration method offers certain advantages, such as compatibility with air-stable lithium precursors, tunable synthesis conditions, and the ability to produce Li_2S with controlled particle size and crystal structure. It also supports integration with conductive carbon frameworks and shows potential for scale-up. However, the use of toxic and flammable gases like H_2S and CS_2 introduces serious safety and environmental hazards, demanding complex and costly reactor setups with rigorous gas handling systems. High-temperature processing is often required, which can lead to particle agglomeration and coarsening, compromising electrochemical performance. Incomplete conversion and the presence of unreacted precursors or byproducts can further reduce material quality and sulfur utilization. Additionally, post-processing steps are often necessary to purify the

product and address structural instability during cycling. These limitations pose significant barriers to commercialization, despite its synthetic flexibility.

1.3.2 f) Li_2S-Ethanol Solution-Assisted Infiltration

Crystalline Li_2S, with its high melting point of 938 °C, is incompatible with the conventional melt-infiltration technique widely used to produce S@Carbon composites. This fundamental limitation hinders the direct application of sulfur-based infiltration strategies to Li_2S cathodes. Nonetheless, incorporating Li_2S into conductive carbon matrix remains a critical objective, as it could help overcome key challenges such as its large particle size, poor conductivity, and high activation overpotential. Unlike sulfur, Li_2S does not suffer from severe volume expansion upon cycling—in fact, it undergoes volume contraction during delithiation, which can help maintain the structural integrity of the electrode. To address its processing limitations, a solution-assisted infiltration method has emerged as a viable alternative. Leveraging the fact that Li_2S is soluble in solvents like absolute ethanol, this technique involves dissolving commercial Li_2S in ethanol, infiltrating the solution into porous carbon hosts, and then recrystallizing the Li_2S through solvent evaporation. This process enables uniform distribution of Li_2S within the conductive matrix and has led to the successful development of a range of Li_2S@Carbon nanocomposites with improved electrochemical performance.

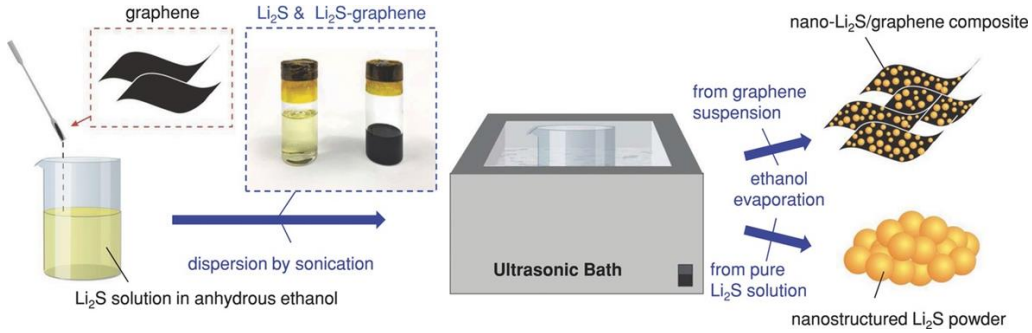


Figure 1.22 Schematic of the Li_2S and Li_2S-graphene composite synthesis process.[224] Copyright © 2014 WILEY-VCH Verlag GmbH & Co. KGaA, Weinheim.

Wu *et al.* in 2014 were the first to report a simple and versatile solution-based method for synthesizing nanosized Li_2S and graphene-Li_2S composites.[224] This approach is environmentally friendly and does not generate any hazardous gases, making it a green and safe process. As illustrated in **Figure 1.22**, commercial Li_2S powders can be dissolved or uniformly dispersed in

anhydrous ethanol. By introducing graphene powders into the suspension and allowing the solvent to evaporate under continuous mixing, Li_2S particles are effectively deposited onto the graphene sheets, forming well-integrated composites. XRD analysis confirmed that no chemical reaction occurs between Li_2S and ethanol during this process, ensuring the chemical integrity of the active material is preserved.

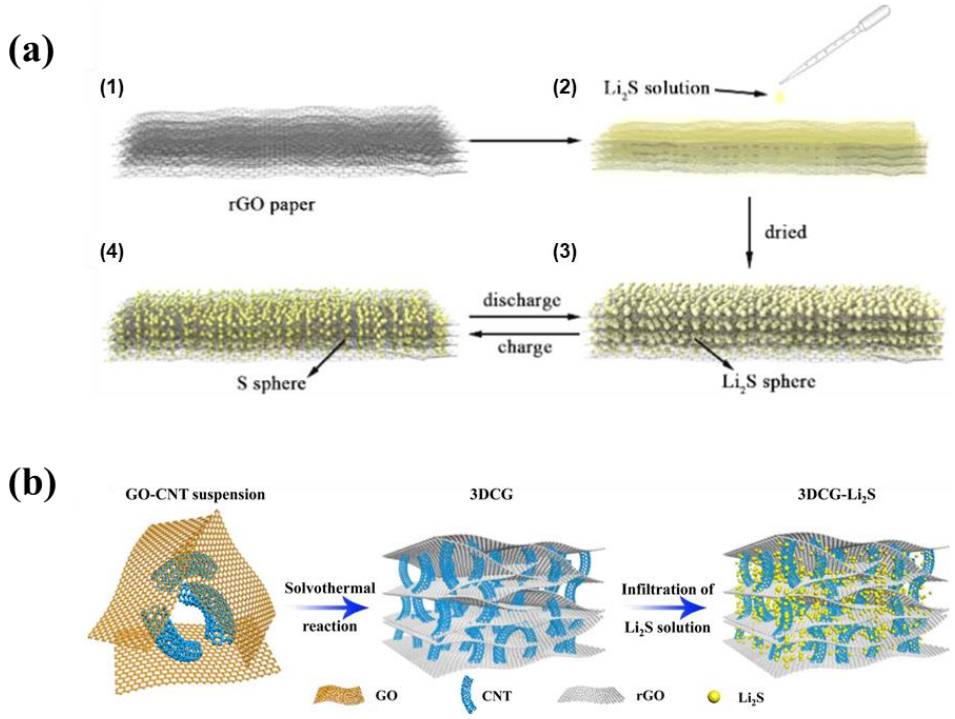


Figure 1.23 (a) Schematic illustration of the material preparation processes of the nano-Li_2S/rGO paper and structure changes during cycling of nano-Li_2S/rGO paper.[225] Copyright © 2015, American Chemical Society. (b) Synthetic procedure of the 3DCG–Li_2S composite.[226] Copyright © 2016, American Chemical Society.

Building on the Li_2S-ethanol solution-assisted infiltration method, the development of Li_2S@Carbon nanocomposites—particularly Li_2S-graphene systems—has progressed rapidly. Wang *et al.* employed reduced graphene oxide (rGO) as a flexible and conductive host.[225] In their approach as shown in **Figure 1.23** (a), a Li_2S-ethanol solution was drop-cast onto rGO paper, which exhibited strong solvent absorbency. This allowed the Li_2S solution to thoroughly infiltrate the rGO structure. Upon vacuum-assisted solvent evaporation, nanosized Li_2S particles precipitated uniformly throughout the rGO matrix. The flexibility of the rGO paper not only prevented particle agglomeration but also helped accommodate volume changes during cycling, thereby enhancing

structural stability and electrochemical performance. To construct a three-dimensional conductive network and enhance interlayer connectivity, He *et al.* incorporated carbon nanotubes (CNTs) into a graphene oxide (GO) suspension.[226] In this design as exhibited in **Figure 1.23** (b), the one-dimensional CNTs acted as nanoscale pillars, supporting and spacing the two-dimensional graphene sheets to form robust 3D architecture with improved electrical conductivity and mechanical stability. Li_2S nanoparticles were then introduced into this framework by infiltrating a Li_2S-ethanol solution, followed by vacuum-assisted solvent evaporation, which enabled uniform recrystallization of Li_2S within the interlayer spaces of the 3D structure.

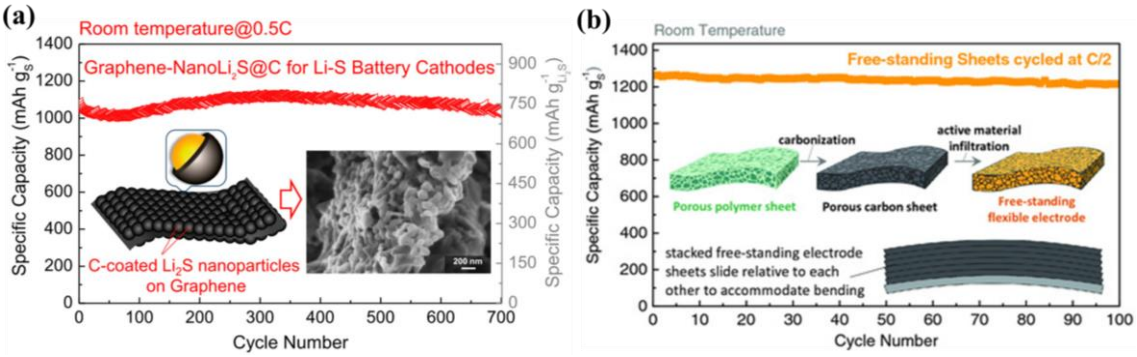


Figure 1.24 (a) Cycling stability of the graphene-nano Li_2S@C electrode at 0.5 C and its morphological characterization.[227] Copyright © 2016, American Chemical Society. (b) Cycling stability of free-standing Li_2S electrodes at 0.5 C and its schematic illustration by using infiltration of active materials into porous carbonized biomass sheets.[228] Copyright © 2016 WILEY-VCH Verlag GmbH & Co. KGaA, Weinheim.

Beyond two-dimensional graphene-based structures, a variety of Li_2S-based nanocomposites with diverse morphologies have been developed using this solution-assisted approach. Wu *et al.* advanced the method by applying carbon chemical vapor deposition (CVD) to coat Li_2S nanoparticles supported on graphene, successfully producing a core–shell structured Li_2S–C nanocomposite (**Figure 1.24** (a)).[227] The highly conductive graphene framework enhanced the rate capability of the cell, while the combination of a vapor-deposited carbon shell and an *in-situ* formed surface passivation layer provided robust protection during cycling. As a result, the composite cathode retained approximately 97% of its initial capacity (~1040 mA h g^{-1} at 0.5 C in terms of S) after more than 700 cycles, demonstrating exceptional long-term stability. Wu *et al.* further extended this method to fabricate freestanding Li_2S electrodes as shown in **Figure 1.24** (b).[228] One

of the key advantages of this approach is its versatility, allowing a wide range of conductive carbon matrices to be employed. In this case, porous cellulose sheets were selected as the structural framework and subsequently carbonized at 500 °C. This carbonization step not only prevented the hydrolysis of Li_2S during processing but also introduced additional porosity, enhancing the overall surface area and facilitating better Li_2S loading and ion transport. Minimal capacity degradation per cycle was observed in the battery tested at 0.5 C.

Among the various synthesis strategies for Li_2S-based cathodes, the Li_2S-ethanol solution-assisted infiltration method is arguably the closest analogue to the melt-infiltration approach commonly used in Li-S batteries. Both techniques share the fundamental objective of uniformly embedding the active material—either sulfur or Li_2S—into a conductive carbon matrix to enhance electrical contact and overall electrochemical performance. They similarly depend on capillary action and pore wetting to facilitate deep infiltration of the active material into the porous host structure. In the melt-infiltration method, sulfur is infused in its molten state and solidifies upon cooling, whereas in the ethanol-assisted approach, Li_2S is introduced via a solution and subsequently recrystallizes as the solvent evaporates by vacuuming. Owing to this method's simplicity and effectiveness, a wide variety of Li_2S@Carbon nanocomposites with diverse architectures have been successfully developed, significantly advancing the design and performance of Li_2S cathodes.

Despite its advantages, the Li_2S-ethanol solution-assisted infiltration method also faces several notable limitations that constrain its broader applicability. One major drawback is the very limited solubility of Li_2S in ethanol. According to reported studies, the concentration of Li_2S in ethanol is typically maintained at around 0.5–0.55 M (equivalent to roughly 25 mg mL^{-1}).[224–226,228–234] This low solubility significantly restricts the amount of active material that can be introduced into the carbon host in a single infiltration step, often requiring large volumes of solvent to achieve meaningful Li_2S loading. Moreover, even trace amounts of water in the ethanol can trigger undesirable side reactions, primarily the formation of LiOH, which compromises the purity and electrochemical activity of the final product. As such, the ethanol must be strictly anhydrous, adding to the handling complexity and cost. Another limitation lies in the structural compatibility between Li_2S and the carbon matrix. Most Li_2S@Carbon nanocomposites prepared via this method rely on

two-dimensional materials like graphene as the host.[224–228] This is likely due to the tendency of Li_2S to recrystallize into nano-spherical particles that are more easily dispersed on flat, sheet-like surfaces. As a result, the method appears biased toward specific carbon architectures, potentially limiting its adaptability to other morphologies such as 3D porous frameworks or bulk structures.

In **Chapter 5** and **Chapter 6** of this thesis, we introduce a novel approach that has markedly improved the solubility of Li_2S-based compounds in ethanol, even achieving a fully miscible solution. Building upon the conventional Li_2S-ethanol solution-assisted infiltration method, we developed a Li_2S-precursor solution infiltration strategy. In this method, a Li_2S-containing compound is both formed and fully dissolved in ethanol and then infiltrated into a carbon host, followed by vacuum drying. Subsequent thermal decomposition of the resulting Li_2S-precursor@Carbon composite leads to the formation of uniform Li_2S@Carbon nanostructures. Compared to the traditional method, this strategy, which will be elaborated in **Chapter 5** and **Chapter 6**, significantly reduces ethanol consumption while enabling much higher in-pore Li_2S loading in composites, improved dispersion, and enhanced scalability—making it more suitable for practical battery applications.

1.3.3 Binder Materials in Li_2S-Based Batteries

To overcome the inherent challenges associated with LSBs, significant research efforts have been devoted to optimizing various battery components, including the cathode,[89,235] anode,[236,237] separator,[238–241] and electrolyte.[138] However, many of these modifications involve the introduction of inactive materials, which increase the overall mass and volume of the electrode. This not only reduces the proportion of active material but also compromises the energy density of the cell—posing a critical trade-off between enhanced performance and practical implementation.

In addition to the active materials in the cathode, the so-called “inactive” components—especially binders—have emerged as important contributors to the structural and electrochemical stability of Li-S batteries. While active materials are directly responsible for storing and releasing Li^+ ions during cycling, binders play a pivotal role in maintaining electrode integrity by physically securing the active material and conductive additives to the current collector. To support the structural cohesion and ensure a percolated conductive network during repeated charge–discharge

cycles, a small amount of binder (typically 1–20 wt.%) is incorporated into the cathode slurry.[242–245] Among the available binder candidates, polyvinylidene fluoride (PVDF) remains the most widely used and traditional option with its widespread adoption in LIBs, LSBs, and Li-air batteries owing to its favorable electrochemical and thermal stability and decent adhesion to current collectors.[82,246,247]

Despite its widespread use, PVDF exhibits several critical drawbacks that limit its suitability for practical high-performance S-LSBs. Its interaction with active materials and polysulfides is governed mainly by weak van der Waals forces due to the cancellation of its dipole moment from the symmetric -CF_2- groups.[248,249] This results in poor adhesion to polar LPSs, weak binding with sulfur and carbon particles, and limited ability to suppress shuttle-induced losses.[250,251] In addition, PVDF is brittle and lacks sufficient elasticity to accommodate the severe volume expansion (~80%) that occurs during sulfur lithiation, especially in cathodes with high sulfur loading. Its high crystallinity also contributes to the agglomeration of active materials and uneven dispersion within the electrode.[252] Moreover, PVDF is electronically and ionically insulating, increasing the internal resistance of the cathode and impeding charge transport.[253]

Although traditionally viewed as electrochemically inert, recent studies have demonstrated that binders can serve multifunctional roles in Li-S batteries.[254–256] By introducing polar functional groups or redox-active moieties, functional binders can provide strong mechanical support, improve ionic or electronic conductivity, and chemically anchor polysulfides through hydrogen bonding or electrostatic interactions.[257] These multifunctional effects help buffer mechanical strain, accelerate reaction kinetics, and mitigate polysulfide shuttling. As shown in **Figure 1.25**, the design of advanced binder systems for S-LSBs has generally focused on three critical properties: (i) strong mechanical strength to withstand structural stress and volume change, (ii) ionic or electronic conductivity to overcome the insulating nature of elemental sulfur and Li_2S, and (iii) high affinity or redox activity toward LPSs to suppress shuttle effects.

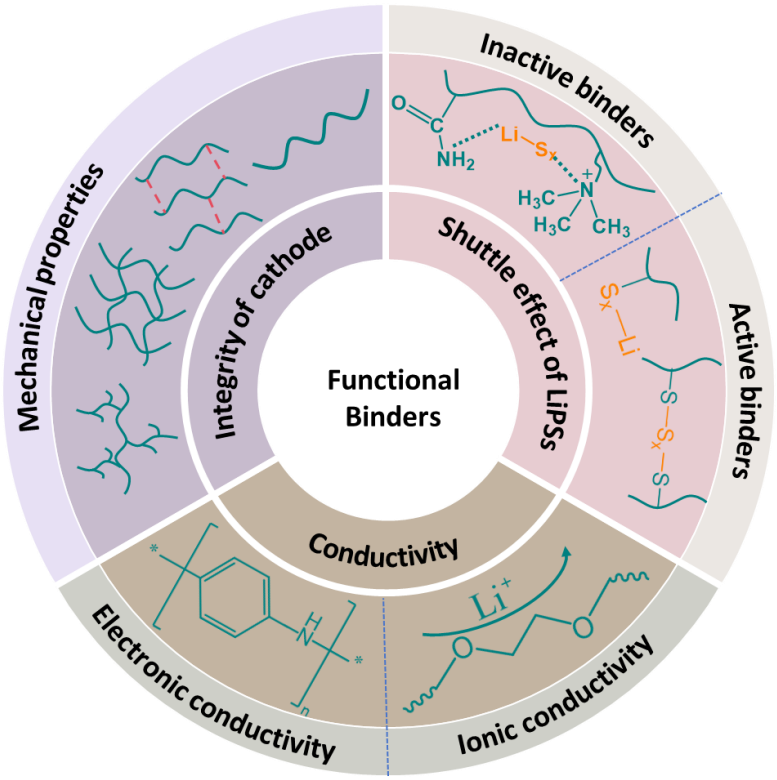


Figure 1.25 The functions of polymer binders in Li-S batteries.[253] Adapted from Ref. 253. Copyright © 2023 Wiley-VCH GmbH.

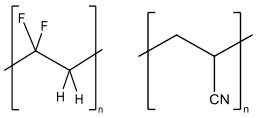
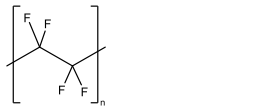
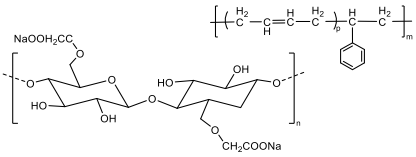
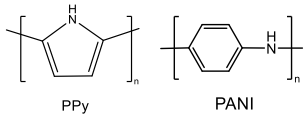
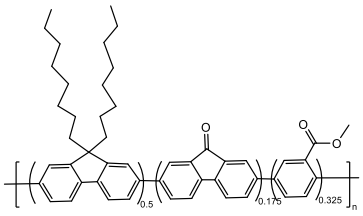
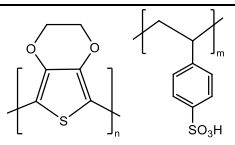
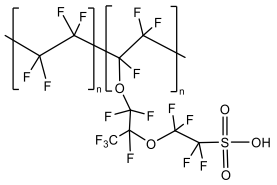
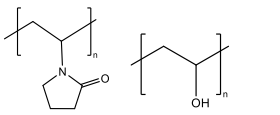
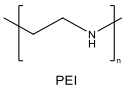
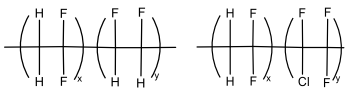
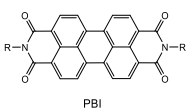
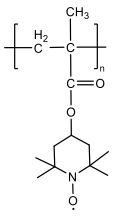
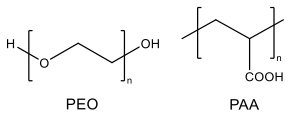
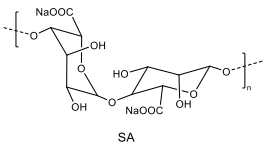
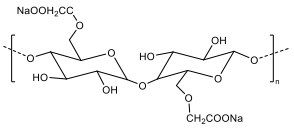
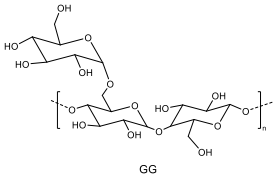
First, strong mechanical properties are vital because sulfur cathodes undergo significant volume changes during cycling, which can cause electrode cracking and delamination from the current collector—especially in high-loading designs.[258] Binders with robust mechanical strength and elasticity are essential for maintaining structural integrity and prolonging the cycle life of such electrodes.[259,260] Second, enhancing electronic and/or ionic conductivity is equally important, as both elemental sulfur and Li_2S are insulators. Functional binders can be tailored with conductive backbones or ionically active groups that facilitate charge transport, enabling better rate performance and utilization of active materials.[261] Third, the notorious polysulfide shuttle effect leads to capacity fading, lithium anode corrosion, and poor Coulombic efficiency.[99] Functional binders that can chemically trap or catalytically convert LPSs are highly beneficial for stabilizing the cathode-electrolyte interface and suppressing side reactions.[254]

Based on these critical roles, a broad range of binder materials have been reported, and they can be categorized by their dominant function (mechanical support, conductivity enhancement, or

shuttle suppression) as well as their processability (aqueous or organic solvents). Representative examples of functional binders and their associated properties are summarized in **Table 1.6**.

Table 1.6 A summary of commonly used binders based on their primary roles in S-LSBs.[262]

Adapted from Ref. 262. Copyright © 2018 WILEY-VCH Verlag GmbH & Co. KGaA, Weinheim.

Function	Nonaqueous Binders	Aqueous Binders
Mechanical Properties	 PVDF PAN	 PTFE  CMC/SBR
Conductivity	 PPy PANI  PFM	 PEDOT:PSS  Nafion
Polysulfide Regulation	 PVP PVA  PEI  P[VDF-co-TRFE] P[VDF-co-CTF]  PBI  PTMA	 PEO PAA  SA  CMC  GG

The development of binder materials for S-LSBs has been significantly more advanced than for Li_2S-LSB systems, due to differences in material properties, cell chemistry, and processing requirements. In S-LSBs, binders play a well-recognized role in addressing challenges such as polysulfide shuttling and large volume expansion, and a wide range of aqueous-processable binders (e.g., CMC, SBR, PEO) can be readily used in slurry preparation, enabling safer, cost-effective, and environmentally friendly electrode fabrication. In contrast, Li_2S is highly reactive, particularly with moisture, and must be processed in inert atmospheres with non-aqueous solvents such as *N*-methyl-2-pyrrolidone (NMP). This constraint means that only binders soluble or dispersible in organic solvents can be used for Li_2S cathode fabrication, excluding many water-soluble candidates that have shown promise in sulfur cathodes. Additionally, Li_2S is an ionic and highly polar compound, requiring strong interfacial binding and high conductivity to overcome its insulating nature and high activation overpotential. Despite its growing relevance, the binder's role in Li_2S-LSBs remains underexplored, as research has traditionally focused more on conductive host design and redox catalysts. These combined factors highlight the need for tailored binder development specifically designed to operate in Li_2S systems and compatible with organic processing environments.

As summarized in **Table 1.7**, the development of binder materials for Li_2S cathodes remains relatively underexplored compared to the extensive progress made in S-LSBs. The majority of reported Li_2S-based studies continue to rely on PVDF as the primary binder, followed by occasional use of polyvinylpyrrolidone (PVP). This limited diversity in binder selection highlights the early stage of binder research in Li_2S battery systems. In contrast to S-LSBs, where numerous functional and aqueous-processable binders have been developed to address issues like polysulfide shuttling and mechanical instability, similar advancements have not yet been translated to Li_2S systems. Notably, a few studies report the use of poly(acrylic acid) (PAA) as a binder for Li_2S cathodes; however, this is an exceptional case. In those instances, the Li_2S particles were coated with a protective layer such as lithium ethyl xanthate (LiEX), which isolates the active material from direct contact with PAA.[263] Without such surface modification, PAA is chemically incompatible with Li_2S due to its reactivity with the ionic surface of the sulfide particles. Therefore, PAA should not be considered a general-purpose binder for Li_2S electrodes. Overall, these observations reinforce the

need for dedicated binder design tailored specifically to the unique chemical and processing constraints of Li_2S-based cathodes.

Table 1.7 Binder materials applied in Li_2S-LSBs and their representative battery performances.

Binder	Li_2S Materials	Initial Capacity	Stability	Ref.
PVDF	Ball-milled Li_2S	950 mA h g^{-1}@0.1C	85%@40	[104]
PVDF	C-Li_2S nanoparticles	1069 mA h g^{-1}@0.05C	~90%@100	[229]
PVDF	Carbon-coated Li_2S	1029 mA h g^{-1}@0.2C	~63%@100	[199]
PVDF	Li_2S-graphene	759 mA h g^{-1}@0.05C	92%@200	[224]
PVDF	Li_2S@C-Co-N	1137.1 mA h g^{-1}@0.2C	81.7%@300	[234]
PVDF	Li_2S/N-doped graphene	801 mA h g^{-1}@0.3C	79%@100	[230]
PVDF	Li_2S-graphene	812 mA h g^{-1}@1/12C	~71%@20	[144]
PVDF	Li_2S@Ni-P-S@G cage	980 mA h g^{-1}@0.1C	77.3%@300	[232]
PVDF	Li_2S@graphene	1104 mA h g^{-1}@0.1C	60%@200	[145]
PVDF	Li_2S/FWNTs@rGO NBF	975 mA h g^{-1}@0.2C	~85%@300	[264]
PVDF	Co_9S_8/Li_2S@G	739 mA h g^{-1}@2C	~65%@900s	[265]
PVDF	Li_2S-C	~700 mA h g^{-1}@0.1C	~54%@200	[213]
PVP	Li_2S/C	~880 mA h g^{-1}@0.05C	73%@100	[266]
PVP	Holey-Li_2S	712 mA h g^{-1}@0.2C	75.6%@100	[267]
PVP	Li_2S/HNG	1067 mA h g^{-1}@0.05C	~45.8%@500	[268]
PVP	Ball-milled Li_2S	760 mA h g^{-1}@0.2C	69%@500	[257]
PVP	Li_2S@Super P	821 mA h g^{-1}@0.1C	82.5%@400	[195]
PVP	KB-Li_2S	693 mA h g^{-1}@1/12C	73.3%@40	[269]
PTFE	KB-Li_2S	~545 mA h g^{-1}@0.1C	~55%@100	[207]
PTFE	Commercial Li_2S	~500 mA h g^{-1}@0.1C	N/A	[176]
PIB, BASF	Carbon-coated Li_2S	~825 mA h g^{-1}@0.1C	~35%@100	[270]
$PEO_{20}LiCF_3SO_3$	Li_2S-C	600 mA h g^{-1}@0.05C	~100%@80	[161]
PAA	Li_2S-LiEX	1100 mA h g^{-1}@0.2 mA cm^{-2}	73%@1400	[263]
CMC	Li_2S-PAN	675.4 mA h g^{-1}@100 mA g^{-1}	90.6%@250	[271]

Our own findings, as presented in **Chapter 3** of this thesis, further demonstrate that PVDF is a poor choice for Li_2S-based systems. While PVDF may reduce the charging overpotential by reacting with Li_2O or LiOH on the surface of Li_2S particles, it also causes irreversible consumption of active material, leading to significant capacity loss. These reactions are associated with dehydrofluorination, where PVDF loses fluorine atoms and forms reactive -C=C- species, generating HF and compromising electrode stability. This degradation not only reduces electrochemical performance but also creates corrosive environments that further deteriorate the electrode-electrolyte interface. Moreover, this issue is not confined to Li_2S cathodes; similar dehydrofluorination has been observed in S-LSBs under high voltage and high sulfur loading, indicating that PVDF may be intrinsically unstable across both systems.

In addition to these electrochemical concerns, broader environmental and regulatory issues are beginning to cast doubt on the long-term viability of PVDF. As a fluorinated polymer, PVDF belongs to the class of materials often grouped under PFAS (per- and polyfluoroalkyl substances), which are currently under scrutiny due to their environmental persistence and potential health risks.[272] Emerging regulations in multiple countries are proposing restrictions or outright bans on PFAS-containing substances, further emphasizing the urgency for the battery community to develop fluorine-free alternatives.[273] Taking together, these chemical, electrochemical, and regulatory challenges strongly motivate the search for more stable, reactive-compatible, and environmentally benign binder materials for Li_2S cathodes.

To address these challenges, this thesis presents a development of novel fluorine-free binder systems specifically designed for Li_2S-based cathodes. In **Chapter 4**, a new functional binder is introduced, which demonstrates strong adhesion, polysulfide anchoring capability, and electrochemical compatibility with Li_2S cathodes. Building upon this, **Chapter 7** describes the further advancement of fluorine-free binder strategies for high in-pore Li_2S loading Li_2S@SP nanocomposite cathodes, focusing on achieving robust electrode stability, improved capacity retention, and enhanced reaction kinetics. These binder systems offer promising pathways toward scalable, high-performance, and environmentally responsible Li_2S battery technologies.

1.3.4 Li_2S-Based Full Cells

Traditional S-LSBs typically employ elemental sulfur as the cathode and lithium metal as the anode. This configuration offers extremely high theoretical energy density due to the high capacity of both sulfur (1672 mA h g^{-1}) and lithium metal (3860 mA h g^{-1}), making it attractive for advanced energy storage applications. However, the use of lithium metal introduces significant challenges that hinder practical deployment. Lithium tends to form dendrites during repeated charge/discharge cycles, which can penetrate the separator and lead to internal short circuits and thermal runaway. Moreover, lithium's high reactivity with conventional electrolytes results in the continuous breakdown and regeneration of the solid electrolyte interphase (SEI), consuming active lithium and electrolyte and leading to low Coulombic efficiency, poor cycle life, and safety risks. These issues are compounded by lithium's low melting point (180 °C) and instability in ambient conditions, which complicate manufacturing and storage.

To overcome these limitations, Li_2S-LSBs have gained increasing attention. Unlike sulfur, Li_2S is a fully lithiated cathode material, enabling the use of lithium-metal-free anodes such as graphite, silicon, or tin. This not only improves safety by eliminating lithium dendrite formation but also enhances compatibility with existing LIB manufacturing infrastructure. Furthermore, Li_2S can be processed under inert or even ambient conditions, offering better material stability and scalability. As a result, Li_2S-based full cells represent a promising path toward safer, high-energy-density LSBs suitable for practical applications.

To construct a practical and safe Li_2S-based full cell, careful selection of a suitable lithium-free anode is essential. Among the available options, graphite, silicon, and tin are three of the most widely studied anode materials due to their high theoretical capacities and compatibility with LIB technology.

1.3.4 a) with Graphite Anode

The commercially mature graphite anode is widely used in LIBs due to its excellent structural stability, low volume expansion (approximately 9–13%), and long cycle life. It accommodates Li^+ ion intercalation and deintercalation reversibly, making it a stable and reliable anode material. In LSBs, graphite also presents a safer and more stable alternative to lithium metal, reducing the risk

of dendrite formation and enhancing cycling stability. However, graphite is highly sensitive to electrolyte composition, and its compatibility is largely limited to carbonate-based electrolytes, such as ethylene carbonate (EC) and dimethyl carbonate (DMC), commonly used in commercial LIBs. In such electrolytes, graphite can form a stable solid electrolyte interphase (SEI) during initial cycling, which protects the graphite structure from continuous solvent co-intercalation and prevents exfoliation of graphene layers.

While graphite exhibits excellent performance in half-cell configurations using carbonate electrolytes, its application in LSB full cells is severely limited by electrolyte incompatibility. When graphite is paired with Li_2S cathode in a carbonate-based electrolyte, severe side reactions occur. This is due to the formation of reactive LPSs during discharge, which can chemically react with carbonate solvents. In particular, sulfur radicals or S^{2-} anions generated during the redox processes can attack alkyl carbonates like EC, leading to the formation of irreversible byproducts that degrade both the electrolyte and active materials. These side reactions render the battery non-rechargeable, making carbonate electrolytes fundamentally incompatible with conventional LSB chemistry. These approaches remain challenging and are not yet viable for commercial applications.

In contrast, ether-based electrolytes (e.g., DOL/DME mixtures) are widely used in LSBs due to their chemical stability with polysulfides, high ionic conductivity, and favorable solvation properties. However, ether solvents are not very suitable but still in use for graphite anodes because they tend to co-intercalate into the graphite structure, causing exfoliation and structural breakdown. This mutual exclusivity between graphite and ether electrolytes creates a fundamental challenge in designing LSB full cells with graphite anodes.

Therefore, while graphite is an ideal anode for conventional LIB systems, its application in Li_2S-LSBs is severely constrained by electrolyte incompatibility, motivating the search for alternative anodes such as silicon and tin that are better suited to ether electrolyte environments.

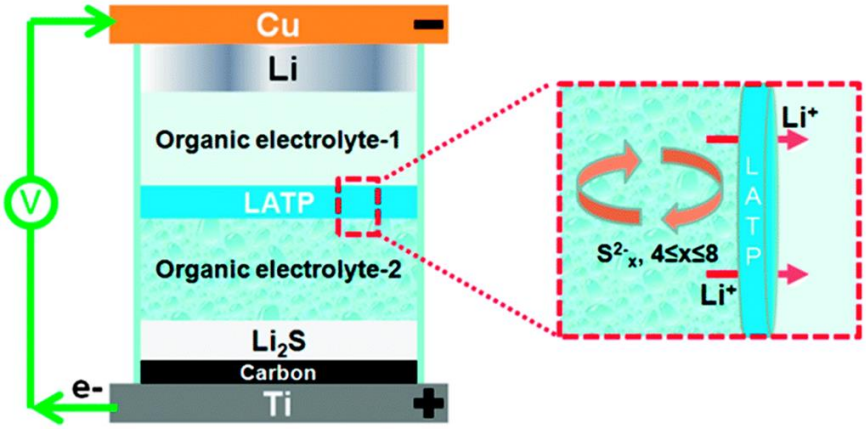


Figure 1.26 Schematic of the architecture of the Li_2S-LSB full cell composed of Cu foil/Li metal/organic electrolyte-1/ceramic separator (LATP)/organic electrolyte-2/Li_2S cathode/carbon/Ti foil.[173] Copyright © 2008 Royal Society of Chemistry.

To address the fundamental incompatibility between graphite anodes and ether-based electrolytes, as well as the chemical instability between polysulfide species and ester-based electrolytes, Wang *et al.* proposed an innovative two-phase electrolyte system for Li_2S-LSB full cells as shown in **Figure 1.26**.[173] In this design, a ceramic lithium superionic conductor (LISICON) separator was employed to spatially divide the electrolyte environment within the cell. On the anode side, a carbonate-based ester electrolyte, which is compatible with graphite and supports stable SEI formation, was used. On the cathode side, an ether-based electrolyte, chemically stable against polysulfides and sulfur radicals, was selected to support Li_2S redox reactions. The LISICON ceramic acts as a lithium-ion-conducting but solvent-blocking membrane, allowing only Li^+ ions to pass between the two compartments while preventing the direct interaction of incompatible species (e.g., LPSs and carbonates). The cell demonstrated a reversible specific capacity of 700 mA h g^{-1} (based on S) at 0.05 C after 20 cycles under a voltage window of 1.0-3.5 V.

The performance of Li_2S-SLB full cells can be significantly enhanced through electrolyte optimization, particularly by modifying ether-based electrolytes, which are widely used due to their compatibility with sulfur species and high ionic conductivity. One effective strategy involves increasing the salt concentration to suppress LPS dissolution and stabilize interfacial reactions. For example, in the absence of any additives, increasing the concentration of LiTFSI to 5 M in pure

DOL resulted in notable improvements: a full cell assembled with a pre-lithiated graphite anode and a sulfur cathode delivered a high reversible specific capacity of 980 mA h g^{-1} at 0.1 C, with a capacity retention of 81.3% after 100 cycles.[274] This is because the superconcentrated ether electrolyte forms a unique network structure of Li^+, $TFSI^-$, and solvating solvents, distinct from conventional dilute systems. This structure promotes the formation of a stable, TFSI-derived SEI on the graphite surface, preventing graphite exfoliation and solvent co-intercalation. As a result, it enables reversible lithium intercalation and suppresses continuous electrolyte decomposition. Similarly, Lv *et al.* developed a super-concentrated ether electrolyte composed of 5 M LiTFSI in DME/DOL (*v*/*v*, 1:1).[275] The full cell using a sulfur cathode and a lithium-preloaded graphite anode exhibited a stable cycling performance, maintaining a specific capacity of 686 mA h g^{-1} after 105 cycles at 0.1 C. These results demonstrate that high-concentration ether electrolytes not only improve the reversibility and stability of LSB full cells but also facilitate their integration with graphite anodes by enhancing interfacial compatibility and suppressing parasitic reactions.

Table 1.8 Representative Li_2S-LSB full cell performance with graphite as anodes.

Cathode	Electrolyte	Voltage Range	Initial Capacity	Stability	Ref.
Li_2S/CNT	1 M LiTFSI in DOL/DME (*v*/*v*, 1:1) + 1wt.% $LiNO_3$	1.3–2.8 V	900 mA h g^{-1}@0.1C	67%@150	[150]
Li_2S@PC	1 M LiTFSI in DOL/DME (*v*/*v*, 1:1) + 1wt.% $LiNO_3$	1.3–2.8 V	772 mA h g^{-1}@0.05C	49%@252	[151]
Li_2S@graphene	1 M LiTFSI in D2/DME (*v*/*v*, 2:1)	0–3.5 V	1047 mA h g^{-1}@0.1C	57%@200	[145]
Li_2S/Gr/CNT	2.5 M LiTFSI in DOL/DME (*v*/*v*, 1:1) + 0.4 M $LiNO_3$	1.6-2.8 V	5.3 mA h cm^{-2}@0.2C	~50%@800	[152]
Li_2S/MC	1 M $LiPF_6$ in EC/DEC (*v*/*v*, 1:1)	0.01–2.5 V	~700 mA h g^{-1}@0.1C	~84%@150	[147]
l-Li_2S/KB	LiTFSI in G1/G3 (*v*/*v*, 1:1)	1.0–3.3 V	~600 mA h g^{-1}@0.1C	~100%@30	[148]
Li_2S/KB	1 M LiTFSI in DOL/DME (*v*/*v*, 1:1)	0.5–3.0 V	700 mA h g^{-1}@0.1C	N/A	[153]
Li_2S/Graphene	1 M LiTFSA in TEGDME/HFE	0.5–3.5 V	809 mA h g^{-1}@1/12C	50%@100	[144]
Li_2S-Cu	5 M LiTFSI in DOL/DME (*v*/*v*, 1:1)	1.2–3.0 V	870 mA h g^{-1}@100 mA g^{-1}	~100%@800	[146]

Li_2S@Li_4SnS_4	1 M LiTFSI in DOL/DME (*v*/*v*, 1:1) + 1wt.% $LiNO_3$ + AN + TTE	1.0–3.5 V	634 mA h g^{-1}@0.05C	N/A	[149]

A variety of Li_2S-based cathodes paired with graphite anodes have been investigated in full-cell configurations as listed in **Table 1.8**, with performance largely influenced by cathode structure, electrolyte composition, and cycling conditions. Most studies utilize ether-based electrolytes such as 1 M LiTFSI in DOL/DME (*v*/*v*, 1:1), often with $LiNO_3$ as an additive. These systems commonly deliver high initial specific capacities in the range of 600–1000 mA h g^{-1} at low C-rates, with materials such as Li_2S@graphene[145] and Li_2S-Cu[146] reaching up to 1047 and 870 mA h g^{-1}, respectively. In terms of cycling stability, Li_2S-Cu[146] and *l*-Li_2S/KB[148] exhibit excellent capacity retention close to 100%, though over different cycling windows (800 and 30 cycles, respectively), indicating room for further improvement in long-term durability. Notably, a Li_2S/MC cathode[147] using a carbonate-based electrolyte (1 M $LiPF_6$ in EC/DEC) achieved ~700 mA h g^{-1} at 0.1 C with ~84% capacity retention after 150 cycles, suggesting that under certain conditions, carbonate electrolytes may be made compatible with Li_2S-based systems. Advanced formulations such as high-concentration electrolytes, mixed solvents, and functional interfacial layers (e.g., Li_4SnS_4 coatings[149]) are increasingly employed to enhance ionic conductivity, suppress polysulfide dissolution, and stabilize cycling. These findings underscore the critical role of electrolyte engineering and cathode design in enabling high-performance, lithium-metal-free Li_2S-LSB full cells suitable for practical applications.

1.3.4 b) with Silicon (Si) Anode

Silicon (Si) has been widely regarded as one of the most promising anode materials for next-generation LIBs due to its extraordinarily high theoretical specific capacity, reported to be between 3,579 and 4,200 mA h g^{-1}, which is nearly an order of magnitude greater than that of commercial graphite (372 mA h g^{-1}). In addition to its high capacity, silicon offers several advantages, including resource abundance, low cost, and a low lithiation potential (~0.4 V *vs.* Li^+/Li), all of which contribute to achieving high energy density in full-cell configurations.

However, the practical application of silicon is significantly hindered by its extreme volume expansion, which can reach up to 300–420%. This drastic change in volume induces severe mechanical stress, leading to cracking, pulverization, and delamination of the active material from the current collector, thereby disrupting electrical contact. Additionally, the continuous formation and rupture of the solid electrolyte interphase (SEI) on newly exposed silicon surfaces consume large amounts of lithium and electrolyte, resulting in irreversible capacity loss and poor initial Coulombic efficiency.

To address these challenges, strategies such as nanostructuring silicon, reserving internal free volume, and surface engineering have been developed to accommodate volume changes, reduce mechanical degradation, and improve the cycling stability of Si-based anodes in high-performance LIB systems.

Table 1.9 summarizes recent advancements in Li_2S-LSB full cells incorporating various Si-based anodes, including bulk silicon, silicon thin films, nanowires, nanoparticles, and silicon–oxygen–carbon composites. Across these studies, most full cells also employed ether-based electrolytes (typically 1 M LiTFSI in DOL/DME with $LiNO_3$ additives). The reported full cell performance demonstrated a wide range of initial discharge capacities, from 423 mA h g^{-1} (Si nanowire[157]) to as high as 953.3 mA h g^{-1} (bulk Si with Li_2S-PDTe cathode[154]), depending on electrode structure, electrolyte formulation, and testing conditions. In terms of cycling stability, performance varied considerably: while the Si-Li_2S-MCMB cell using a TEGDME-based electrolyte retained ~89% of its capacity after 50 cycles,[159] other systems showed moderate to poor retention—for example, only ~20% capacity retention was observed after 200 cycles in the Si-TiN/PHC@Li_2S system.[155] Several studies utilized nanoengineered silicon, such as Si nanowires or nanoparticles embedded in porous carbon frameworks, to alleviate mechanical degradation and accommodate volume changes, though improvements in long-term cycling remain a challenge. Overall, the results highlight the potential of silicon anodes for high-capacity, lithium-metal-free Li_2S-LSB full cells, but also underscore the importance of electrode design, electrolyte compatibility, and interfacial engineering to ensure stable and reversible cycling.

Table 1.9 Representative Li_2S-LSB full cell performance with different types of Si anodes.

Si Anode	Cathode	Electrolyte	Voltage Range	Initial Capacity	Stability	Ref.
Si	Li_2S-PDTe	1 M LiTFSI in DOL/DME (*v*/*v*, 1:1) + 1wt.% $LiNO_3$	1.5–2.5 V	953.3 mA h g^{-1}@0.2C	80@100	[154]
Si	TiN/PHC@Li_2S	1 M LiTFSI in DOL/DME (*v*/*v*, 1:1) + 2wt.% $LiNO_3$	1.3–3.8 V	702 mA h g^{-1}@0.5C	20%@200	[155]
Si thin film	*in situ* TG-Li_2S	1 M LiTFSI in DOL/DME (*v*/*v*, 1:1) + LPSs + $LiNO_3$	1.2–2.5 V	900 mA h g^{-1}@0.05C	N/A	[156]
Si nanowire	Li_2S/C	1 M LiTFSI in DOL/DME (*v*/*v*, 1:1)	1.7–2.6 V	423 mA h g^{-1}@0.1C	~59%@20	[157]
Si-NP@HCF	Li_2S-ZnS@NC	1 M LiTFSI in DOL/DME (*v*/*v*, 1:1) + 2wt.% $LiNO_3$	1.2–2.5 V	710 mA h g^{-1}@0.2C	57.7%@200	[158]
Si-O-C	Li_2S-MCMB	$LiCF_3SO_3$ in TEGDME (1:4 molar ratio)	0.1–2.8 V	~490 mA h g^{-1}@0.2C	~89@50	[159]
Gt-SiNW	Li_2S-CoFeP-CN	1 M LiTFSI in DOL/DME (*v*/*v*, 1:1) + 0.2 M $LiNO_3$	1.5–2.8 V	805.6 mA h g^{-1}@0.1C	64%@80	[160]

1.3.4 c) with Tin (Sn) Anode

Tin (Sn) is considered a promising anode material for LIBs due to its high theoretical specific capacity of 994 mA h g^{-1}, which is also substantially higher than that of commercial graphite (372 mA h g^{-1}). Tin stores Li^+ ions by forming $Li_{4.4}Sn$ alloy during lithiation and offers additional advantages, including good electrical conductivity, a moderate lithiation potential (~0.6 V *vs.* Li^+/Li), and abundant natural reserves, making it both cost-effective and scalable. However, like silicon, tin undergoes large volume expansion (~260%) during lithiation and delithiation, leading to mechanical degradation, pulverization, and instability of the SEI. These effects cause capacity fading and poor cycling stability, limiting its practical application. To overcome these challenges, several strategies have been explored. One common approach is to reduce the particle size to the nanoscale, which helps accommodate volume changes; however, nano-tin tends to agglomerate

over repeated cycles, diminishing its effectiveness. Designing hollow or porous structures or reserving internal buffer space can further alleviate mechanical stress. Among these strategies, incorporating an inert buffer matrix, particularly conductive carbon, has proven highly effective. The carbon matrix not only buffers volume expansion but also enhances electrical conductivity and structural integrity.

Table 1.10 Representative Li_2S-LSB full cell performance with different types of Sn anodes.

Sn Anode	Cathode	Electrolyte	Voltage Range	Initial Capacity	Stability	Ref.
SnO_2	Carbonized wipes/Li_2S	1 M LiTFSI in DOL/DME (*v*/*v*, 1:1) + 1wt.% $LiNO_3$ + 150 mM LiI + 50 mM InI_3	0.5–3.0 V	983 mA h g^{-1}@0.2C	N/A	[162]
Sn-C	Li_2S-C	$PEO_{20}LiCF_3SO_3$-10%S-ZrO_2 membrane + 1 M $LiPF_6$ in EC/DMC (*v*/*v*, 1:1)	1.5–4.1 V	600 mA h g^{-1}@0.05C	N/A	[161]
Sn/C	Li_2S/C	$PEO_{20}LiCF_3SO_3$-10%S-ZrO_2 membrane + 1 M $LiPF_6$ in EC/DMC (*v*/*v*, 1:1)	0.2–4 V	600 mA h g^{-1}@0.003C	66%@32	[163]

Table 1.10 summarizes representative studies on Li_2S-LSB full cells incorporating various Sn-based anodes, including SnO_2,[162] Sn-C composites,[161] and Sn/C materials.[163] These systems employed both liquid and solid-state hybrid electrolytes, combining ether- or carbonate-based solutions with polymer or ceramic membranes to enhance stability and suppress polysulfide migration. The reported initial capacities range from 600 to 983 mA h g^{-1}, with the highest value achieved by a SnO_2 anode paired with a carbonized wipe/Li_2S cathode and an ether-based electrolyte containing multiple additives ($LiNO_3$, LiI, InI_3) designed to stabilize the SEI and inhibit shuttle effects.[162] Sn-C and Sn/C composite anodes demonstrated initial capacities of 600 mA h g^{-1} at low rates, using hybrid electrolytes with polymer membranes (PEO-based) and carbonate solvents.[161,163] In terms of cycling stability, limited data are available, though one Sn/C system retained 66% of its capacity after 32 cycles.[163] Overall, these results highlight the potential of Sn-based anodes to deliver high capacity in Li_2S full cells, while also emphasizing the need for further

optimization of electrolyte design, interfacial stability, and cycling durability to realize their full potential in practical applications.

In summary, the successful commercialization of Li_2S-LSB full cells requires careful matching of the anode and cathode materials, along with the selection of electrolytes compatible with both electrodes and polysulfide species. The comparative parameters of the three most studied anode materials—graphite, silicon, and tin—are summarized in **Table 1.11**. As shown, graphite offers excellent structural stability and minimal volume change during cycling, but its low theoretical specific capacity limits the overall energy density of the full cell. In contrast, silicon and tin exhibit much higher theoretical capacities, which can significantly boost cell energy density. However, their practical application is severely hindered by large volume expansion during lithiation, leading to mechanical degradation, loss of electrical contact, unstable SEI formation, and rapid capacity fading over cycling.

Table 1.11 Parameter comparison of anode materials.

Anode Material	Graphite	Silicon	Tin
Density (g cm^{-3})	~2.26	~2.33	~7.31
Theoretical Capacity (mA h g^{-1})	372	3579-4200	994
Voltage Flat (V *vs.* Li$^+$/Li)	~0.1	~0.4	~0.6
Volume Change (%)	9~13	~300-420	~260
Fully Alloyed Material	LiC_6	$Li_{4.4}Si$	$Li_{4.4}Sn$

Notes:

Density values are approximate for the bulk material.

Theoretical Capacity is calculated based on the full lithiation product (**Fully Alloyed Material**).

Voltage Flat refers to the average lithiation potential versus Li$^+$/Li during alloying.

Volume Change reflects expansion upon full lithiation.

To address these challenges, research has increasingly focused on composite and engineered anode materials that combine high capacity with improved structural resilience. Among these, silicon/carbon (Si/C) composites have emerged as a particularly promising solution, as the carbon

matrix helps buffer silicon's volume change while enhancing electrical conductivity and SEI stability. In addition to Si/C, other advanced anode designs, such as Sn/C, metal oxide composites, and novel nano materials, are being explored to enable stable, high-capacity, lithium-metal-free full cells.

1.3.4 d) with Silicon/Carbon (Si/C) and Other Anodes

Si/C composites combine the high theoretical capacity of silicon with the excellent electrical conductivity, mechanical flexibility, and structural stability of carbon. The carbon matrix acts as a conductive network that not only facilitates electron transport but also serves as a mechanical buffer, effectively accommodating silicon's large volume changes during lithiation and delithiation. This design significantly reduces the risk of particle pulverization, loss of electrical contact, and continuous SEI rupture. Additionally, the carbon component helps suppress silicon nanoparticle agglomeration during cycling and contributes to forming a more stable SEI layer, improving Coulombic efficiency and cycle life.

The representative studies on Li_2S-LSB full cells employing Si/C composite anodes are presented in **Table 1.12**, highlighting the versatility and potential of these materials in lithium-metal-free configurations. The reported full cell systems utilize electrolytes predominantly based on ether solvents (DOL/DME) with LiTFSI and $LiNO_3$ additives, although carbonate electrolytes (e.g., $LiPF_6$ in EC/DMC) have also been explored. Initial specific capacities vary across the studies, ranging from approximately 540 mA h g^{-1} (Li_2S+C cathode[276]) to as high as 1100 mA h g^{-1} (Li_2S-LiEX cathode[263]) at low to moderate rates (0.1–1 C). In terms of cycling stability, the Mo-Li_2S-graphene cathode coupled with a Si/C anode demonstrated excellent durability, retaining 82.4% of its capacity after 500 cycles at 1 C.[277] Similarly, the Li_2S-LiEX system achieved 73% capacity retention over 1400 cycles, indicating remarkable long-term stability.[263] By contrast, cells with conventional Li_2S+C or Mo/Li_2S cathodes typically exhibited more modest capacity retention (~50–61%) over 70-150 cycles.[278,276] These results underscore the significant promise of Si/C anodes for enabling high-capacity, long-life Li_2S full cells, while also highlighting the importance of cathode architecture, electrolyte formulation, and electrode interface engineering in achieving optimal performance.

Table 1.12 Representative Li_2S-LSB full cell performance with Si/C as anodes.

Cathode	Electrolyte	Voltage Range	Initial Capacity	Stability	Ref.
Mo/Li_2S	1 M $LiPF_6$ in EC/DMC (*v*/*v*, 1:1)	0.2–2.5 V	788 mA h g^{-1}@0.1C	52%@150	[278]
Li_2S+C	1 M LiTFSI in DOL/DME (*v*/*v*, 1:1) + 0.5 M $LiNO_3$	1.3–2.8 V	~540 mA h g^{-1}@0.1C	~50%@70	[276]
Li_2S/C/G	1 M LiTFSI in DOL/DME (*v*/*v*, 1:1) + 1wt.% $LiNO_3$	1.2–3.5 V	593 mA h g^{-1}@100 mA g^{-1}	61%@30	[279]
Li_2S-LiEX	1 M LiTFSI in DOL/DME (*v*/*v*, 1:1) + 0.2 M $LiNO_3$	1.8–3.0 V	1100 mA h g^{-1}@0.17C	73%@1400	[263]
Mo-Li_2S-graphene	1 M LiTFSI in DOL/DME (*v*/*v*, 1:1) + 1wt.% $LiNO_3$	1.5–3.5 V	815 mA h g^{-1}@1C	82.4%@500	[277]

Beyond graphite, silicon, and tin, alternative anode materials have also been utilized in Li_2S-LSB full cells as listed in **Table 1.13**. These include metallic current collectors (e.g., Cu, Cu/Au)[280,281] as bare or modified substrates for *in situ* lithium plating, as well as conversion-type or composite anodes such as Fe_3O_4[282] and MnO_2-rGO.[283] Initial capacities reported for these systems vary widely, with values ranging from approximately 576 mA h g^{-1} (Fe_3O_4/CNs anode)[209] to 919 mA h g^{-1} (Cu anode paired with Li_2S/MWCNT cathode)[280] at low rates (typically 0.1–0.2 C). In terms of cycling stability, performance remains mixed: while some systems, such as MnO_2-rGO||Li_2S-rGO, achieved capacity retention of over 80% after 150 cycles,[283] others, particularly bare Cu-based anodes, showed more rapid capacity decay (e.g., ~51.5% after 100 cycles).[280]

Table 1.13 Representative Li_2S-LSB full cell performance with other types of anodes.

Anode	Cathode	Electrolyte	Voltage Range	Initial Capacity	Stability	Ref.
Cu	Li_2S/MWCNT	2 M $LiCF_3SO_3$ in DOL/DME (1:1) + 0.2 M $LiNO_3$	1.8–2.8 V	919 mA h g^{-1}@0.1C	51.5%@100	[280]
Cu	Li_2S/CFs	1 M LiTFSI in DOL/DME (1:1) + 0.75 M $LiNO_3$	1.7–2.8 V	639 mA h g^{-1}@0.1C	40%@150	[281]

Cu/Au	Li_2S/CFs	1 M LiTFSI in DOL/DME (1:1) + 0.75 M $LiNO_3$	1.7–2.8 V	770 mA h g^{-1}@0.1C	53%@150	[281]
Fe_3O_4	Li_2S@MXene/graphene	1 M LiTFSI in DOL/DME (1:1) + 2wt.% $LiNO_3$	1.7–2.8 V	600 mA h g^{-1}@0.2C	78%@50	[282]
Fe_3O_4/CNs	Li_2S@NCNF	1 M LiTFSI in DOL/DME (1:1) + 2wt.% $LiNO_3$	1.5–2.8 V	576 mA h g^{-1}@0.2C	60%@50	[209]
MnO_2-rGO	Li_2S-rGO	1 M LiTFSI in DOL/DME (1:1)	0.2–2.6 V	587.5 mA h g^{-1}@0.2C	80.5%@150	[283]

Considering the need to balance high capacity, structural integrity, cycle life, and compatibility with Li_2S cathodes, this thesis focuses on the use of commercial Si/C composite anodes as the most promising candidate for Li_2S-LSB full cells. Specifically, **Chapter 8** presents a detailed evaluation of full-cell performance based on the pairing of commercial Si/C anodes with our designed high in-pore loading Li_2S@SP nanocomposites (developed in **Chapter 6**) and optimized functional binders (developed in **Chapter 7**). This integrated design not only addresses the key challenges of Li_2S cathode activation, polysulfide management, and anode stability but also demonstrates significant potential for the commercial application of Li_2S-LSBs. The full-cell systems explored in this work provide a pathway toward safe, high-energy-density, and scalable Li_2S-LSB technologies suited for practical use in fields such as electric vehicles and grid energy storage.

1.4 Objective and Structure of This Thesis

The overarching objective of this thesis is to investigate the design and optimization of functional binders and Li_2S@Carbon nanocomposite engineering strategies to address critical challenges in Li_2S batteries. These challenges include the large first-charge overpotential and the drawback of PVDF consuming Li_2S. In addition, the large particle size of commercial Li_2S, the high melting point and poor solubility hinder conventional Li_2S@Carbon composite fabrication, while the limitations of binders also appear when applied to nanoscale Li_2S. Each of these issues is identified and addressed sequentially in the course of this research, ultimately paving the way toward the realization of practical lithium-anode-free full cells. This thesis is organized into nine chapters, each progressively building toward the objective.

Chapter 1 introduces the background of lithium-sulfur batteries, the unique advantages of Li_2S cathodes, and the fundamental challenges associated with their development. It also reviews state-of-the-art strategies for mitigating these challenges, with emphasis on binder materials, and nanostructured Li_2S composite, while also considering different anode materials as examples to illustrate the feasibility of full-cell configurations.

Chapter 2 summarizes the materials, chemicals, and equipment used in this research, and outlines the general experimental methods.

Chapter 3 proposes mitigating the activation barrier due to the insulating $LiOH/Li_2O$ surface layer by exploiting the reaction between polyvinylidene fluoride (PVDF) binder and $LiOH/Li_2O$ through dehydrofluorination. However, PVDF was also found to react with Li_2S, providing new insights into its dual role in Li_2S cathode.

Chapter 4 investigates alternative binders capable of enhancing the electrochemical performance of Li_2S-LSBs. A binder based on a zinc acetate triethanolamine ($Zn(OAc)_2$·TEA) complex was developed, exhibiting superior performance to PVDF. To further reinforce electrode integrity and improve dispersion stability, polyethylenimine (PEI) was incorporated to form a $Zn(OAc)_2$·TEA/PEI hybrid binder.

In **Chapter 5** , an efficient precursor solution infiltration-decomposition strategy was invented to synthesize Li_2S@Carbon nanocomposites under mild conditions, overcoming the challenges of Li_2S's high melting point, poor solubility, and the large particle size of commercial Li_2S.

The thermal decomposition of Li_2CS_3 precursor in **Chapter 5** releases a large amount of CS_2 gas (~62 wt.% of the precursor), which creates internal voids and limits the in-pore Li_2S loading. To address this, **Chapter 6** builds upon precursor infiltration-decomposition method with a multi-cycle strategy, enabling higher Li_2S content and in-pore loading.

An attempt to combine the functional binder from **Chapter 4** and optimized Li_2S@SP nanocomposites from **Chapter 6** manifested the limitations of $Zn(OAc)_2$·TEA/PEI-based binders on highly reactive nanoscale Li_2S. **Chapter 7** therefore introduces a series of polyethylenimine-epoxy resin (PEI-ER) binders with applicability to nanostructured Li_2S materials. The *in-situ*

crosslinking method further improved processing by removing the short crosslinking time window and enabling uniform networks without altering Li_2S@SP morphology.

Chapter 8 serves as the culmination of these research projects, integrating the optimized Li_2S@SP cathodes and functional binders developed in earlier chapters to successfully assemble and evaluate lithium-anode-free full cells. Using PVP as a benchmark binder and a commercial Si/C composite as the anode, this chapter demonstrates the practical feasibility of the proposed strategies.

Chapter 9 provides the overall conclusions and outlook, reflecting on the mechanistic insights, scalable strategies, and device demonstrations developed in this work, and highlighting future directions toward practical Li_2S-based LSBs.

Chapter 2 Experimental Materials and Characterization Methods

This chapter begins by presenting a comprehensive table of the chemicals and materials used for experimental designs, followed by a summary table of the required equipment. These resources provide a clear overview of the essential components and tools employed throughout the experimental work. Subsequently, the chapter introduces the fundamental principles and key instrumentation of the primary characterization techniques used to evaluate the physical, chemical, and electrochemical properties of electrode materials.

2.1 Chemicals and Materials

A variety of chemicals and materials were employed in the experimental work described in this thesis, ranging from precursors and solvents to conductive additives and binders. The selection of these substances was based on their compatibility with Li_2S-based LSB systems and their functional roles in material synthesis, electrode fabrication, and battery assembly. **Table 2.1** below provides a detailed list of all chemicals and materials used, including their names, formular, purities and suppliers.

Table 2.1 Chemicals and Materials for Experimental Designs

Chemicals/Materials	Formula/Structure	Purity (%)	Supplier
Lithium sulfide	Li_2S	99.98% trace metals basis	Sigma-Aldrich
Reagent alcohol	CH_3CH_3OH	⩽ 0.003% water	Sigma-Aldrich
Carbon disulfide	CS_2	⩾ 99.9%	Sigma-Aldrich
Sulfur	S_8	⩾ 99.0%	Sigma-Aldrich
N-Methyl-2-pyrrolidone (NMP)	C_5H_9NO	⩾ 99.5%	Sigma-Aldrich
Polyvinylpyrrolidone (PVP)	$(C_6H_9NO)_n$	M_w~1,300,000	Sigma-Aldrich
Lithium hydroxide monohydrate	$LiOH·H_2O$	99.95% trace metals basis	Sigma-Aldrich
Lithium oxide	Li_2O	99.5% metals basis	Alfa Aesar

Poly(vinylidene fluoride) (PVDF)	$(CH_2CF_2)_n$	M_w~1,000,000	Kynar
Carbon black (Super P)	C	> 96%	IMERYS
Zinc acetate dihydrate	$Zn(CH_3COO)_2 \cdot 2H_2O$	≥ 98%	Sigma-Aldrich
Diethanolamine (DEA)	$NH(CH_2CH_2OH)_2$	≥ 98.5%	Sigma-Aldrich
Triethanolamine (TEA)	$N(CH_2CH_2OH)_3$	≥ 99.5%	Sigma-Aldrich
Polyethylenimine, branched (PEI)	$H(NHCH_2CH_2)_nNH_2$	M_w~25,000	Sigma-Aldrich
Polyethylenimine (PEI) solution, ~50% in H_2O	$H(NHCH_2CH_2)_nNH_2$	M_r 600,000-1,000,000	Sigma-Aldrich
1,2-Dimethoxyethane (DME)	$CH_3OCH_2CH_2OCH_3$	99.5%	Sigma-Aldrich
1,3-Dioxolane (DOL)	$C_3H_6O_2$	99.8%	Sigma-Aldrich
Lithium bis(trifluoromethanesulfonyl)imide (LiTFSI)	$CF_3SO_2NLiSO_2CF_3$	99.99% trace metals basis	Sigma-Aldrich
Si/C Anode	Si and C	GS60	Shanshan Technology
Compressed argon gas	Ar	100%	Linde Canada Inc.
Battery grade lithium chips	Li	≥ 99.9%	China Energy Lithium Co., Ltd
Double Sides Conductive Carbon Coated Aluminum Foil-CCAL-18u	Al and C	Al Foil Purity >99.9%	MTI Corporation
Molecular sieves, 3 Å	$K_nNa_{12-n}[(AlO_2)_{12}(SiO_2)_{12}] \cdot xH_2O$	N/A	Sigma-Aldrich
Polypropylene separator (Celgard 2400)	$(C_3H_6)n$	N/A	Celgard LLC.
CR2032 coin cells	N/A	N/A	MTI Corporation

2.2 Experimental Instruments and Equipment

The successful execution of the experimental procedures in this thesis required the use of a wide range of laboratory equipment, encompassing synthesis tools, material processing instruments, and electrochemical workstations. Each piece of equipment was selected to meet the specific requirements of material preparation, battery fabrication, and performance evaluation. The following **Table 2.2** summarizes the key equipment used, along with their model numbers and manufacturers.

Table 2.2 Experimental Instruments and Equipment.

Instrument/Equipment	Model/Specification	Manufacturer
Analytical balance	VWRU10204-966	VWR International
Doctor blade coater	250/500/750/1000 μm	MTI Corporation
Blast oven	ED056	Binder Inc
Vacuum oven	Model 281A	Fisher Scientific
Ultrasonic cleaner	97043-964	VWR International
Glovebox	Standard Dual Module 4 ports	Virgo Technologies Inc
Battery testing system	Land 2001A	Wuhan Land Electronics Co., Ltd.
Electrochemical workstation	Biologic VMP-3	BioLogic

2.3 Phase and Elemental Analysis

2.3.1 Powder X-ray Diffraction (XRD)

X-ray diffraction (XRD) is one of the most powerful and widely used techniques for determining the crystal structure of materials. The most commonly applied XRD technique, known as powder X-ray diffraction, uses a monochromatic X-ray beam to examine specimens. The principle of XRD is based on wave interference as shown in **Figure 2.1**: when two waves with the same wavelength travel in the same direction, they can constructively interfere (in-phase, $n\lambda$) or destructively interfere (out-of-phase, $n\lambda/2$) depending on their phase difference.

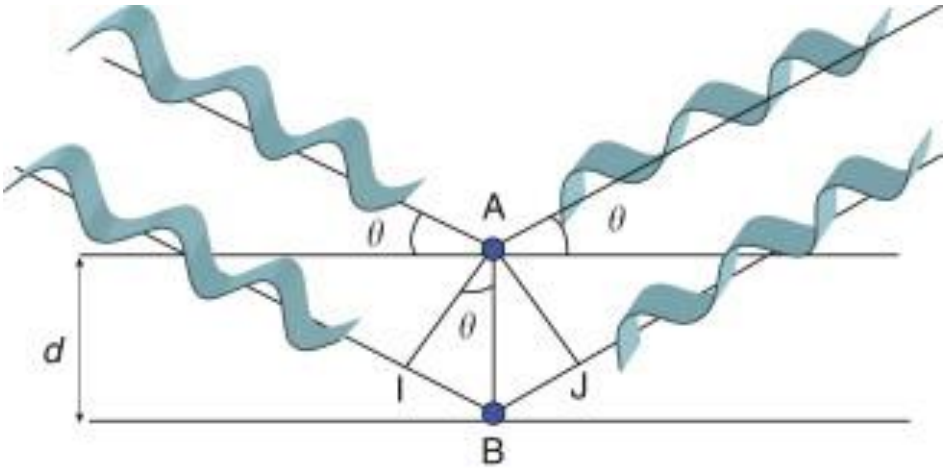


Figure 2.1 Schematic of Bragg's Law.[284] Copyright © 2010 Elsevier Ltd. All rights reserved.

In crystalline materials, this interference leads to diffraction patterns that are characteristic of the atomic arrangement, which meets with Bragg's Law (**Equation 2.1**). The diffraction patterns are then compared to standard reference data, such as the Powder Diffraction File (PDF) cards provided by the International Centre for Diffraction Data (ICDD).

$$n\lambda = 2d\sin\theta \qquad \textbf{Equation 2.1}$$

Where:

λ = wavelength of the X-ray sources

d = distance between planes

θ = the incident angle (Bragg angle)

n = an integer

In theory, diffraction peaks—according to Bragg's Law—are sharp and narrow; however, in real samples, the peaks exhibit finite widths. These broadened peaks arise from instrumental factors and, importantly, from the finite size of crystallites in the sample. Smaller crystal domains cause broader peaks due to incomplete destructive interference, with peak width inversely related to crystal size. Thus, *Scherrer* equation is introduced to estimate the average size of crystalline domains (also referred to as crystallite size) in a material.[285] This method is particularly valuable for analyzing nanostructured or fine-grained materials, where peak broadening in the diffraction pattern occurs due to small crystallite dimensions.

Scherrer equation is expressed as in **Equation 2.2**

$$D = \frac{K\lambda}{\beta \cos\theta} \qquad \textbf{Equation 2.2}$$

Where:

D = crystallite size (nm)

K = 0.89 (*Scherrer* constant, shape factor for spherical particles)

λ = 0.154184 nm (wavelength of the X-ray source used in this thesis)

β = FWHM (full width at half maximum of the diffraction peak, in radians)

θ = Bragg angle

The *Scherrer* equation is applicable when the crystallite size is below ~100 nm and based on XRD peak broadening. It also assumes that the observed broadening is caused solely by small crystallite size, with contributions, such as lattice strain and instrumental effects, negligible or corrected for.

Particularly for Li_2S research in this thesis, Kapton tape has been applied in the XRD analysis to protect materials from moisture in the air or humidity during measurement. Kapton tape is chemically inert, thermally stable, and X-ray transparent, making it ideal for sealing samples without affecting data quality. Importantly, the weak and broad background peaks from Kapton as shown in **Figure 2.2** (a) do not overlap with the characteristic diffraction peaks of Li_2S (**Figure 2.2** (b)), allowing accurate phase identification in Li_2S research.

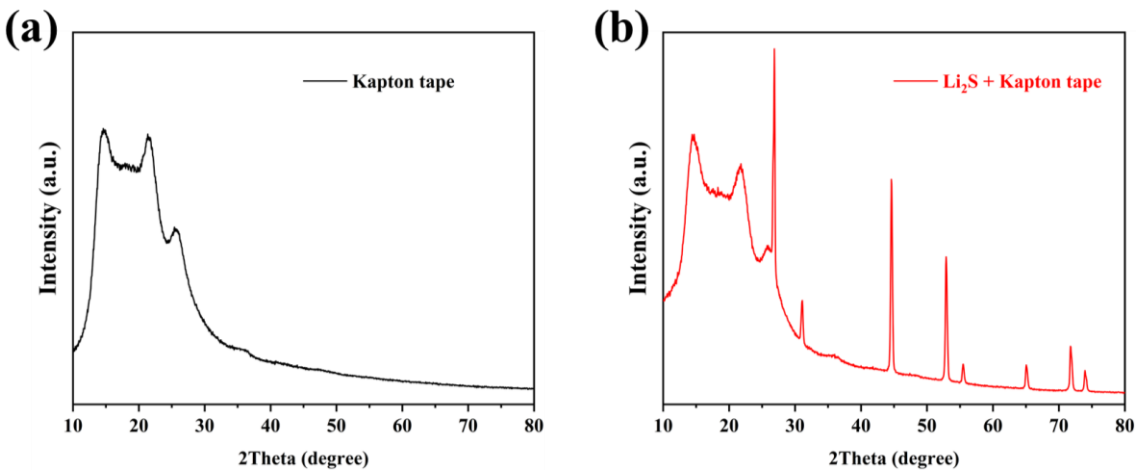


Figure 2.2 XRD patterns of (a) Kapton tape and (b) Kapton tape-covered commercial Li_2S powders obtained by Bruker D8 Discover X-ray Diffraction Spectrometer.

In this thesis, the XRD patterns were collected by Bruker D8 Discover X-ray Diffraction Spectrometer using Cu Kα radiation with a wavelength of 0.154184 nm. All samples containing Li_2S were placed onto the sample holder and covered with Kapton tape to avoid air.

2.3.2 Fourier Transform Infrared Spectroscopy (FTIR)

Fourier transform infrared (FTIR) spectroscopy is a widely used analytical technique for identifying organic, polymeric, and some inorganic materials by measuring how they absorb infrared (IR) light.[286] Molecules naturally vibrate in specific modes, such as stretching or bending, and absorb IR radiation at specific frequencies that correspond to the vibrational modes of their chemical bonds, like C=C, O–H, or C–H. In FTIR, the IR beam interacts with the sample—either passing through or reflecting off it—and the absorbed wavelengths are recorded. The raw data is then mathematically converted using a Fourier Transform into a spectrum that plots absorbance or transmittance (%) versus wavenumber (cm^{-1}). The resulting spectrum, with its characteristic peaks, serves as a molecular fingerprint for identifying chemical bonds by comparison with reference database.

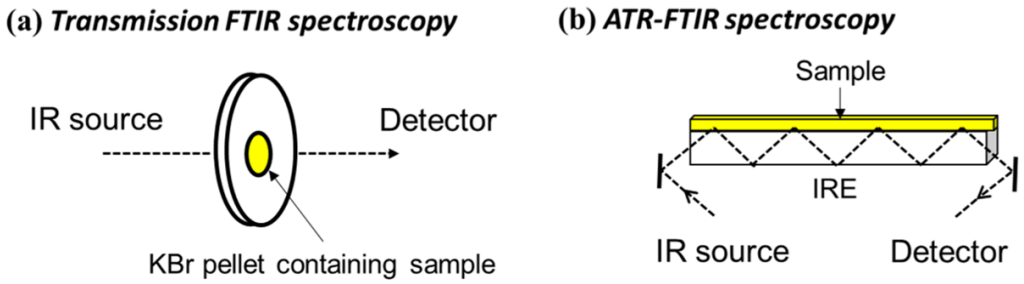


Figure 2.3 Schematics of (a) Transmission FTIR and (b) Attenuated total reflectance (ATR)-FTIR.[286]

Adapted from Ref. 286. Copyright © 2015 by the authors, licensed under CC BY.

FTIR analysis can be conducted using two main approaches: Transmission FTIR and Attenuated total reflectance FTIR (ATR-FTIR). In the transmission setup, illustrated in **Figure 2.3** (a), infrared light is directed through a sample that is usually prepared as a thin film or compressed into a pellet, such as with KBr. This technique captures spectral information reflective of the material's overall bulk composition but demands meticulous preparation and is susceptible to moisture interference. Alternatively, ATR-FTIR, shown in **Figure 2.3** (b), employs a specialized crystal that internally reflects the IR beam, generating an evanescent wave that interacts with only the surface layer of the sample—typically a few microns deep. Due to its ease of use, fast measurement capability, and suitability for various sample forms (including solids, liquids, and semi-solids), ATR-FTIR has become a preferred method in many practical applications.

In this thesis, attenuated total reflectance Fourier transform infrared (ATR-FTIR) spectroscopy measurements were performed on a Bruker VERTEX 70 FT-IR Spectrometer.

2.3.3 Ultraviolet-Visible Spectroscopy

UV-Vis spectroscopy has been extensively employed in the study of lithium-sulfur batteries (LSBs) due to its capability to probe soluble species and track dynamic electrochemical processes. A major application lies in the identification and quantification of lithium polysulfides (LPS) in the electrolyte, which is essential for elucidating reaction pathways and understanding the underlying degradation mechanisms. UV-Vis absorption spectra were measured on a Cary 7000 universal measurement spectrophotometer (UMS).

2.4 Morphological and Structural Analysis

2.4.1 Scanning Electron Microscope (SEM)

Scanning electron microscopy (SEM) is an effective analytical method for examining a material's surface morphology and composition by directing a focused beam of electrons onto the sample. When a sample is bombarded with a focused electron beam, a variety of signals are generated as a result of interactions between the incident electrons and the atoms in the sample. These signals include secondary electrons, backscattered electrons, absorbed electrons, Auger electrons, transmitted or projected electrons, cathodoluminescence (cathode rays), and characteristic X-rays. Each signal provides distinct information about the sample's surface and subsurface properties. Among these, secondary electrons are most commonly used to produce high-resolution images of the sample's surface morphology.

In this thesis, all the Li_2S samples for SEM were prepared in Ar-filled glovebox and samples were transferred to the sample chamber very swiftly to avoid the moisture contamination. The SEM images were taken using a Zeiss Sigma HD microscope.

2.4.2 High-Resolution Transmission Electron Microscopy (HRTEM)

High-resolution transmission electron microscopy (HRTEM) is an advanced characterization technique capable of achieving magnifications up to several million times. Unlike SEM, which primarily reveals surface morphology, HRTEM enables direct visualization of the internal atomic structure of materials. It operates by directing a high-energy electron beam through an ultrathin sample. As the electrons transmit through the material, they interact with the atomic lattice, and the resulting phase contrast allows the formation of lattice-resolved images. In addition to imaging, HRTEM can capture electron diffraction patterns, which offer complementary information on the material's crystal symmetry, orientation, and degree of crystalline.

The drop casting method was used to prepare TEM samples from powdered materials. A small amount of the sample is typically dispersed in a volatile, low-boiling-point solvent using ultrasonication to achieve a uniform suspension and minimize particle agglomeration. However, ethanol, commonly used for dispersion, is unsuitable because Li_2S can partially dissolve in ethanol, potentially altering its composition and morphology. To address this, 1,2-dimethoxyethane (DME) is preferred due to its compatibility with Li_2S and its ability to evaporate cleanly. After dispersion,

a small droplet of the suspension is carefully deposited onto a TEM grid. The sample is then dried under vacuum conditions to remove residual solvent and to minimize hydrolysis. It is critical to transfer the dried grid rapidly into the TEM sample chamber, preferably using a sealed or inert gas-transfer holder.

In this thesis, DME was used as the solvent to disperse Li_2S samples. Transferring procedures should be fast to avoid the moisture contamination. The TEM images were obtained by JEM-F200.

2.5 Electrochemical Performance Analysis

Electrochemical performance analysis plays a vital role in battery research, as they provide direct insight into the practical behavior and efficiency of battery materials under operating conditions. These tests not only validate the structural and chemical advantages of the designed components but also reveal critical parameters such as overpotential, specific capacity, cycling stability, and rate capability. To accurately evaluate the performance of the developed electrode materials, a systematic and rigorous approach is required. In the following sections, the entire process—from electrode processing to various battery testing methods—will be introduced in detail.

2.5.1 Electrode Processing

In laboratory-scale coin cell fabrication, electrode processing is a crucial step that significantly influences cell performance and reproducibility. The general procedures for electrode preparation involve the following key steps:

Slurry Preparation. A homogeneous slurry is prepared by mixing active materials (e.g., commercial Li_2S or Li_2S@Carbon nanocomposites), conductive additives (e.g., Super P), and a binder material (e.g., PVDF, PVP, or other functional binders) in an appropriate solvent (e.g., NMP). The typical weight ratio is 70:20:10 (active materials : conductive carbon : binder materials), but it varies depending on the lab design.

Coating. The prepared slurry is uniformly coated onto a current collector (e.g., carbon-coated Al foil or carbon paper) using a doctor blade. The coating thickness and uniformity must be well controlled.

Drying. The coated electrode is then dried followed by vacuum drying at elevated temperature (e.g., 50–120 °C) for several hours to ensure complete removal of the solvent.

Punching. After drying, the electrode film is cut into circular discs (e.g., 12 mm in diameter) using a coin cell punch.

Weighing. The punched electrodes are weighed to calculate the active material loading (controlled at 1.0–1.2 mg cm^{-2}).

In this thesis, the whole electrode processing was carried out in an Ar-filled glovebox with O_2 and H_2O < 0.5 ppm.

2.5.2 Coin Cell Assembly

Coin cell assembly is a critical step in evaluating electrochemical performance of battery materials. **Figure 2.4** illustrates the components required for a coin cell constructure[287]:

Cathode. A composite of active material (e.g., Li_2S or Li_2S@Carbon nanocomposites), conductive carbon (e.g., Super P), and binder (e.g., PVDF, PVP) on the carbon-coated Al foil discs.

Separator. Commonly Celgard 2400 or polypropylene (PP) membrane is used.

Electrolyte. Ether-based electrolyte (e.g., 1 M LiTFSI in DOL/DME *v*/*v*=1:1 with 2 wt.% $LiNO_3$ as an additive) is employed in Li-S batteries.

Anode. Lithium metal foils or Si/C composites on Cu foil discs.

Cell casing. CR2032 stainless steel coin cell cases (cathode and anode), spacers, and cone spring.

The assembly of a coin cell is conducted in an Ar-filled glovebox (O_2 and H_2O < 0.5 ppm) to prevent moisture and oxygen contamination, which is especially critical for moisture-sensitive materials like Li_2S and lithium metal. The process begins by placing the stainless-steel cathode casing of a CR2032 coin cell, followed by the prepared cathode disc composed of Li_2S-based composite. A precise volume of electrolyte is then added to fully wet the cathode. A separator (Celgard 2400) is placed on top, and more electrolyte is added to ensure complete saturation. A lithium metal foil (or Si/C composite on Cu foil) is then carefully placed as the anode, followed by a stainless-steel spacer and a cone spring. Finally, the cell is capped with the anode casing and sealed using a crimping machine to ensure tight contact and prevent leakage. The assembled cells

are normally rested for several hours to allow thorough wetting before electrochemical testing begins.

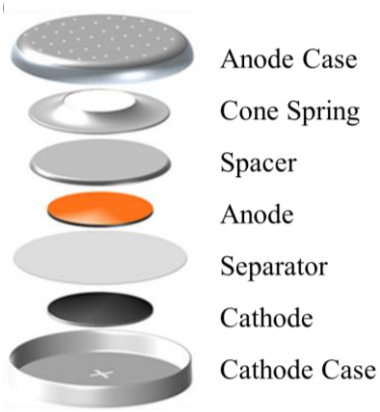


Figure 2.4 Schematic of the assembly of a coin cell.[287] Adapted from Ref. 287. Copyright © 2023, The Author(s), under exclusive license to Springer-Verlag GmbH Germany, part of Springer Nature.

2.5.3 Electrochemical Impedance Spectroscopy (EIS)

Electrochemical Impedance Spectroscopy (EIS) is a powerful and non-destructive analytical technique frequently used to explore the charge transfer and ion transport in electrochemical devices such as batteries and fuel cells. The data are commonly interpreted by fitting with an equivalent electrical circuit model (**Figure 2.5** (a)) and plotted in a Nyquist plot (**Figure 2.5** (b)).

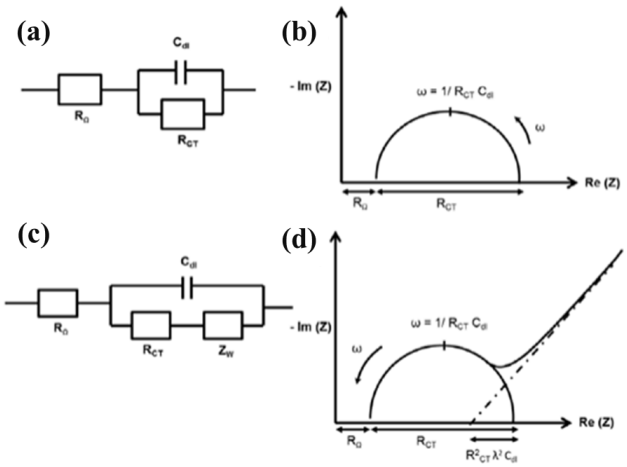


Figure 2.5 (a) Representation of Randles circuit, and (b) its characteristic Nyquist plot. (c) Randles circuit with Warburg element and (d) its characteristic Nyquist plot.[288] Reproduced from Ref. 288, used under the Creative Commons Attribution (CC BY) license.

In this study, an AC voltage signal with a small amplitude (10 mV) was applied to the batteries, and the corresponding current response was monitored to construct impedance spectra. The generated Nyquist plots, which were fitted using an equivalent circuit model as illustrated in **Figure 2.5** (c), commonly display one or two semicircles in the high-to-mid frequency region, representing charge transfer resistance and interfacial behavior. At lower frequencies, the plots show an inclined line, depicted in **Figure 2.5** (d), which corresponds to the Warburg impedance associated with lithium-ion diffusion within the electrode structure.

The measurements were conducted using a Biologic VMP-3 electrochemical workstation, and the collected impedance data were analyzed and fitted using EC-Lab software to extract key parameters such as solution resistance (R_s) and charge transfer resistance (R_{ct}).

2.5.4 Cyclic Voltammetry (CV)

Cyclic voltammetry (CV) is a widely used electrochemical technique for evaluating redox behavior, reversibility, and reaction kinetics of battery electrode materials. It is operated based on the Nernst equation and observed as a peaked current–potential curve.

A representative CV curve of a simple reversible process is shown in **Figure 2.6** (a). A linearly swept potential (the incentive) at a scan rate of v is applied to the electrode, and the redox reactions at the electrode/electrolyte interface are detected by measuring the resultant current (response). When the set potential is reached, the applied potential will be swept in the opposite direction as shown in inset of **Figure 2.6** (a). At the start of the cathodic scan (usually beginning from the open circuit voltage, OCV), the voltage is still higher than the reduction potential, so no real redox reaction occurs—only a small capacitive (non-Faradaic) current flows. As the voltage moves closer to the reduction potential, the reduction reaction begins. The reactant species at the electrode surface are consumed, creating a concentration gradient between the surface and the bulk solution, which drives diffusion toward the electrode and produces a cathodic current. As the voltage becomes more negative, more reactants are consumed at the surface, leading to the increased diffusion flux and current. When the surface concentration of reactant is nearly depleted, the current reaches a maximum (the cathodic peak current and potential). After that, the current drops because there are not enough reactants left on the surface. When the scan direction reverses (anodic scan), oxidation

reactions occur. This leads to an increase in current again, forming an anodic peak current and its corresponding potential. For an electrochemical reversible system, the current (i) is proportional to $v^{1/2}$.

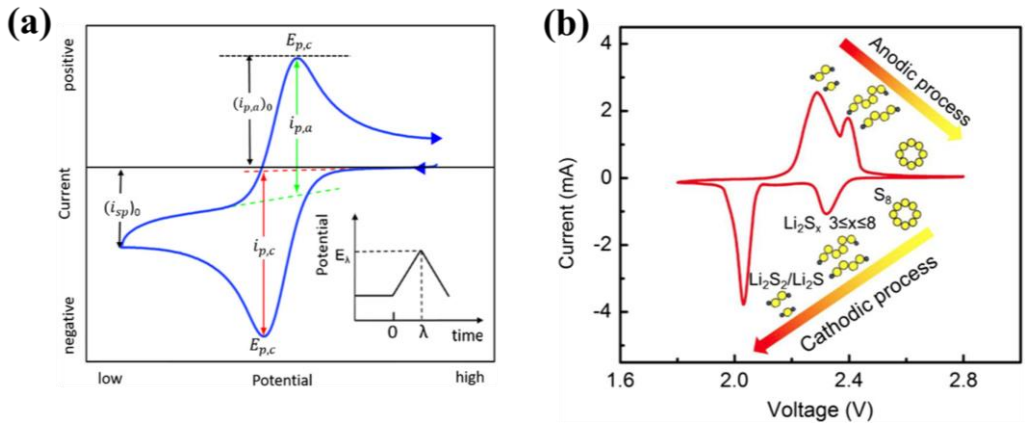


Figure 2.6 (a) A schematic CV curve for a simple reversible reaction, with the inserted showing the voltage change during the CV scan. (b) CV curves of a typical Li-S battery at a scanning rate of 0.1 mV s^{-1}.[289] Copyright © 2019 WILEY-VCH Verlag GmbH & Co. KGaA, Weinheim.

Figure 2.6 (b) exhibits a typical CV curve of Li-S batteries. The first reduction peak, typically observed between 2.4–2.2 V, corresponds to the conversion of elemental sulfur (S_8) into soluble lithium polysulfides (Li_2S_x, where $4 \leqslant x \leqslant 8$). The second reduction peak, appearing at 2.1–1.9 V, is associated with the further reduction of these polysulfides into insoluble Li_2S_2 and Li_2S. This two-step reduction is also evident in the discharge profile, which shows two distinct voltage plateaus. During the anodic scan, the oxidation of Li_2S back into polysulfides or sulfur produces a broad peak, often overlapping in the 2.2–2.6 V range.

CV measurements in this thesis were performed using a Biologic VMP-3 electrochemical workstation. For Li_2S-based batteries, the scan began with an anodic sweep from OCV up to 4.0 V, followed by a cathodic sweep down to 1.7 V, and then cycled within the voltage range of 1.7–2.8 V. In contrast, for sulfur-based batteries, the scan started with a cathodic sweep from OCV to 1.7 V, followed by an anodic sweep up to 2.8 V, with subsequent cycles also confined to the 1.7–2.8 V window. The scan rate was adjustable based on specific experimental designs.

2.5.5 Galvanostatic Charge and Discharge

Galvanostatic charge and discharge (GCD) is a pivotal electrochemical method extensively employed in battery research to assess the capacity, cycle stability, and rate performance of electrode materials. In GCD, a constant current is applied to charge and discharge the battery or half-cell, and the voltage response is recorded over time. During charging, current flows to drive Li^+ ions from the cathode to the anode, increasing the battery voltage until a set upper voltage limit is reached. In the discharging process, the current direction is reversed; Li^+ ions flow back, and the voltage drops until the lower cutoff voltage is reached.

Figure 2.7 illustrates a typical discharge/charge curve of Li-S batteries. In the initial stage of discharge, S_8 reacts with Li^+ ions and accepts electrons to form soluble long-chain lithium polysulfides. This phase consists of multiple stepwise redox reactions that collectively transfer 4 electrons per S_4 molecule. As a result, the corresponding voltage plateau is gradually sloping and accounts for approximately 25% of sulfur's theoretical capacity, yielding 418 mA h g^{-1}. In the subsequent stage, Li_2S_4 undergoes further lithiation to produce short-chain species such as Li_2S_2 and Li_2S. This transformation involves a more direct reaction that transfers the remaining 12 electrons per S_8, resulting in a flat voltage plateau that contributes to about 75% of sulfur's theoretical capacity (1255 mA h g^{-1}).

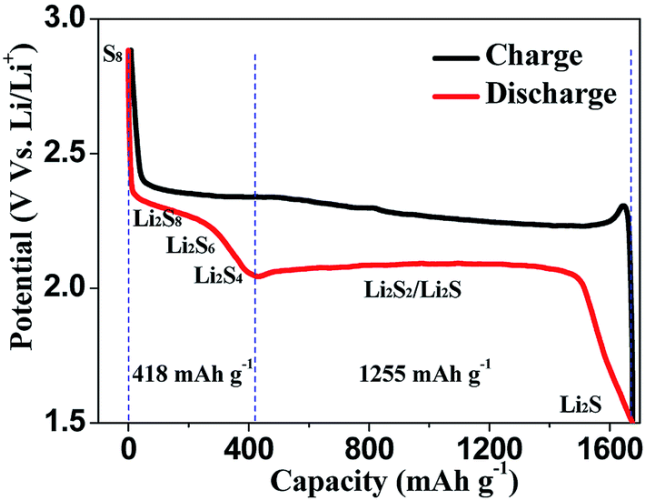


Figure 2.7 The typical discharge/charge curve of Li-S batteries.[290] Copyright © The Royal Society of Chemistry. Licensed under CC BY 3.0.

The galvanostatic charge and discharge tests in this thesis were carried on the Land 2001A battery test system. For Li_2S-based batteries, 1 C = 1166 mA g^{-1}; for Li-S batteries, 1 C = 1672 mA

g^{-1}. Additionally, evaluating rate performance at different currents (e.g., 0.1 C, 0.2 C, 0.5 C, 1.0 C and 2.0 C) using this type of plot enables assessment of how the capacity responds to varying charge/discharge speeds over repeated cycles.

Chapter 3 Mitigating First Charge Overpotential of Li_2S-Based Lithium-Sulfur Batteries by Leveraging PVDF Reaction with the LiOH/Li_2O Layer

This chapter is based on the following publication:

Z. Huang, X. Gao, Y. Wang, Y. Li, *Journal of Power Sources*, **2023**, 582: 233530.

3.1 Introduction

Lithium-ion batteries (LIBs) have been widely used since their commercial introduction in the 1990s,[291] and their demand has grown exponentially over the past decade as they entered the electric vehicle and smart grid markets.[31] However, the low energy density and high cost of LIBs limit their further applications.[292] Therefore, other batteries with higher potential energy density and lower cost have been vigorously explored in recent years.[293] Among them, lithium-sulfur batteries (LSBs) have a theoretical specific energy of 2,600 W h kg^{-1}, which is about five times that of LIBs,[293] and are inexpensive,[294] making them a promising next-generation battery technology.[108,235,295–297]

The most widely investigated LSBs use elemental sulfur cathodes and lithium metal anodes, namely S-LSBs, which tend to form lithium dendrites that cause short circuits, a common problem associated with all types of lithium metal batteries.[298] To address this issue, efforts have been made to use the discharge product Li_2S as the cathode material in conjunction with more stable anode host materials such as graphite,[144] silicon,[155] and tin.[163] This approach eliminates the requirement for lithium metal, thus enabling the development of safer Li_2S-based LSBs, or Li_2S-LSBs. Li_2S-LSBs are also more compatible with the existing manufacturing processes for conventional LIBs. An additional advantage of using Li_2S as the starting material is that the volume of active material does not increase further during charge/discharge. This property enables the active material to remain confined within the carbon host, leading to a more stable cycling performance compared to S-LSBs.[299]

Nonetheless, the development of Li_2S-LSBs has proven to be non-trivial.[165,168] Li_2S has a theoretical redox potential of ~2.4 V (*vs.* Li^+/Li) and the electrochemical behavior of Li_2S-LSBs

was expected to be similar to that of S-LSBs.[104] However, when using the same operating voltage window between 1.7 and 2.8 V applicable to S-LBSs, no appreciable battery performance was observed for Li_2S-LSBs since Li_2S could not be charged.[176] To make a Li_2S-LSB work, a potential higher than 2.8 V (up to ~4 V) is usually needed in the first charging process[175,300] and the entire first charge curve appears to be dramatically different from that of a typical S-LSB as shown in **Figure 3.1**.

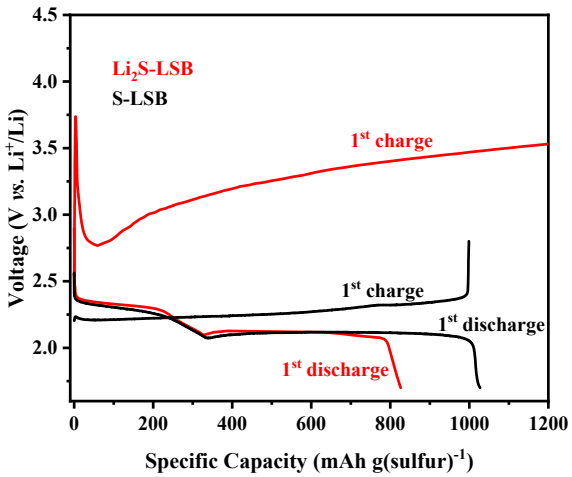


Figure 3.1 The first cycle galvanostatic charge/discharge characteristics of a typical Li_2S-LSB and the first discharge-charge cycle of a typical S-LSB, where the specific capacities were normalized to be based on sulfur for a clearer comparison. Data for the S-LSB are reproduced with permission.[295]

Copyright © 2021 American Chemical Society.

First, the Li_2S-LSB shows an overpotential spike (typically ~3.6–4 V at a rate of 0.1 C) at the very beginning of the first charging process, whereas a typical S-LSB only requires a low potential of ~2.2–2.3 V at this stage. After the overpotential spike, the charging potential drops rapidly, but remains much higher than the charging potential of the S-LSB. Then, the potential increases gradually over a prolonged period. If the battery is not forced to stop, the first charging process can often exceed the theoretical specific capacity of Li_2S due to the occurrence of some irreversible side reactions under excessively high charging voltages. For instance, ether-based electrolytes would decompose at working voltages > 3.6 V (*vs.* Li^+/Li).[177,300,301] The subsequent first discharge curve and charge/discharge cycles become similar to those of S-LSB, although the specific capacity is generally lower.

The anomalous first charge cycle observed for Li_2S-LSBs has been the subject of extensive research and numerous theories have been proposed.[165,168,302,303] For example, the high crystallinity of the starting material Li_2S has been thought to be responsible for the overpotential because Li_2S has an antifluorite crystal structure with strong bond energy and high standard enthalpy of formation, which makes the delithiation of Li_2S very difficult.[169,170] On the other hand, the Li_2S formed in typical S-LSBs after the first discharge is of poor crystallinity, because the discharge is often incomplete, and the discharge products contain Li_2S_2 and some polysulfides besides Li_2S, so the first charging process of S-LSBs is less energetically demanding.[104,304] The size of Li_2S particles is also considered to be related to the height of the potential barrier, that is, the smaller particles, the larger surface area, the shorter Li^+ diffusion length, and the smaller overpotential.[166,168] The particle size of commercially available Li_2S is usually large, which has been considered to be another reason for the high overpotential of some Li_2S-LSBs. Furthermore, during storage and/or processing of Li_2S, an insulating LiOH/Li_2O layer is inevitably formed on the surface of Li_2S particles by absorbing moisture, which is also responsible for the high potential, especially the initial spike, during the first charge.[165,175,176,200] Accordingly, various approaches have been explored to address this overpotential issue associated with Li_2S-LSBs such as extensive ball milling to reduce the Li_2S particle size,[166] addition of additives such as lithium polysulfides[104] to destroy the Li_2S crystal structure to lower the charging barrier,[165] dissolution of Li_2S to remove the LiOH/Li_2O layer,[188,305] *in-situ* preparation of Li_2S,[306] *etc.* Despite these efforts, the mechanism behind the high first charge overpotential of Li_2S-LSBs remains controversial, mainly due to the difficulty in handling Li_2S which is extremely sensitive to moisture, and effective and simple methods to solve this problem are still lacking.

Polyvinylidene fluoride (PVDF) has been widely used as a binder for LIB, S-LSB, and Li_2S-LSB electrodes and is generally considered to be stable both chemically and electrochemically. However, previous studies showed that PVDF can undergo dehydrofluorination in the presence of strong bases such as LiOH, NaOH, and KOH[307–311] and metal oxides such as Li_2O_2, $Li_7La_3Zr_2O_{12}$ (LLZO) and $Li_{6.75}La_3Zr_{1.75}Ta_{0.25}O_{12}$ (LLZTO).[312–315] Inspired by these studies, we decided to intentionally exploit the reaction between PVDF and the basic LiOH/Li_2O layer on the surface of the Li_2S particles to reduce the first charge overpotential of Li_2S-LSBs. This was achieved by

simply stirring the cathode slurry consisting of Li_2S and PVDF in anhydrous *N*-methyl-2-pyrrolidone (NMP) at room temperature for a period of time (24 or 48 h). One of the products is LiF, which has been reported to be able to effectively enhance the performance of S-LSBs.[316] As expected, the first charge overpotential spike was significantly reduced from 3.74 V for the Li_2S-LSB fabricated using the freshly prepared slurry to 3.37 V and 2.75 V for the batteries fabricated using slurries stirred for 24 h and 48 h, respectively. Additionally, the charging potential after the initial spike also decreased notably. Fourier-transform infrared spectroscopy (FTIR) analysis of PVDF treated with LiOH or Li_2O indicated that both LiOH and Li_2O can readily react with PVDF in NMP, forming unsaturated C=C bonds through dehydrofluorination. Unexpectedly, it was found that the subsequent first discharge capacity notably decreased from 576 mA h g^{-1} for the Li_2S-LSB fabricated using the freshly prepared slurry to 508 mA h g^{-1} and 479 mA h g^{-1} for the batteries fabricated using slurries stirred for 24 h and 48 h, respectively. FTIR analysis revealed that PVDF can react with Li_2S at an even faster rate than with LiOH or Li_2O, which is responsible for the reduced specific capacity of the batteries fabricated using the stirred slurries. In fact, dehydrofluorination of PVDF also occurred notably during a typical cathode fabrication process (30 min grinding of the slurry and 12 h vacuum drying of the slurry coated on a substrate at 50 °C), leading to partial removal of the LiOH/Li_2O layer on the Li_2S particle surface. This resulted in a slight reduction in overpotential (to 3.74 V) of the Li_2S-LSB battery using the freshly prepared slurry containing PVDF binder compared to the high overpotential of 3.92 V observed for the cell using a polyvinylpyrrolidone (PVP) binder that is inert to LiOH/Li_2O. This study provides new insights into the origin of the overpotential during the first charging process of Li_2S-LSBs and a simple additional slurry stirring step could effectively reduce the first charge overpotential of Li_2S-LSBs using a commercial Li_2S and a PVDF binder through the removal of the LiOH/Li_2O layer on the surface of the Li_2S particles.

3.2 Experimental Section

3.2.1 Materials

Lithium sulfide (Li_2S) (99.98 % trace metals basis) and lithium hydroxide monohydrate ($LiOH·H_2O$) (99.95 % trace metals basis), polyvinylpyrrolidone (PVP, M_W ~1,300,000), anhydrous *N*-methyl-2-pyrrolidone (NMP, 99.5 %) were purchased from Sigma-Aldrich. Lithium oxide (Li_2O) (99.5 % metals basis) was purchased from Alfa Aesar. Super P (SP) was purchased from IMERYS. Polyvinylidene fluoride (PVDF, M_W ~1,000,000) was purchased from Kynar. Other chemicals were obtained from various commercial sources. The anhydrous NMP was further dried using lithium metal and filtered using a PTFE syringe filter. All other chemicals were used without further purification.

3.2.2 Reactions between Lithium Compounds and Binders

$LiOH·H_2O$, Li_2O, and Li_2S, were weighed and mixed with PVDF at a molar ratio Li:F (n_{Li}:n_F) = 1:1 ($LiOH·H_2O$, Li_2O or Li_2S) or 10:1 (Li_2S) using anhydrous NMP as the solvent. The mixture was stirred for 24 or 48 h. After NMP was removed under vacuum at room temperature, the treated PVDF samples were washed three times with deionized water and once with acetone and then dried under vacuum at room temperature.

3.2.3 Fabrication of Lithium Sulfide Electrodes

Three slurries were prepared by grinding a mixture of Li_2S, SP, and PVDF at mass ratios of Li_2S:SP:PVDF = 70:20:10 in NMP for 30 min inside an argon (Ar)-filled glove box with O_2 and H_2O concentrations below 0.5 ppm. One slurry was immediately coated on a carbon-coated aluminum current collector and dried, which was used to fabricate the electrode labeled **PVDF-0h**. Two other slurries were stirred in sealed vials with a magnetic stirrer for 24 and 48 h before being used to fabricate electrodes labeled **PVDF-24h** and **PVDF-48h**, respectively. The PVP binder-based electrode, **PVP-48h**, was prepared in a similar manner to that used for **PVDF-48h**, except that PVP was used as the binder. The electrode, **PVDF5%-48h-5%**, was fabricated using a slurry prepared by grinding a mixture of Li_2S, SP and PVDF at a mass ratio of 70:20:5 in anhydrous NMP for 30 min, stirred in a vial for 48 h, followed by adding another 5 wt.% PVDF and stirring for an additional 10 min. All the coated electrodes were vacuum dried at 50 °C in an oven inside the glovebox overnight. The electrodes were finally cut into discs with a diameter of 12 mm. The

average lithium sulfide loading on electrodes was 1.0 ~ 1.2 mg cm^{-2}. The punched electrodes were stored in sealed vials inside the glovebox. Some electrodes were stored (aged) in the glovebox for 24 h prior to cell assembly and were labeled **PVDF-0h-A**, **PVDF-24h-A** and **PVDF-48h-A**.

3.2.4 Electrochemical Measurements

2032 coin Li_2S-LSBs with above Li_2S cathodes, lithium metal anodes, Celgard 2400 as separators, and 1.0 M lithium bis(trifluoromethanesulfonyl)imide (LiTFSI) in DOL/DME (*v*:*v* = 1:1) containing 2 wt.% $LiNO_3$ as the electrolyte were assembled in an argon-filled glovebox. The electrochemical performance of batteries was measured galvanostatically on a Land 2001A battery test system. Electrochemical impedance spectra (EIS) were recorded at the open-circuit potential (OCP) using a Bio-logic electrochemical potentiostat/galvanostat (VSP) in a frequency range from 1000 kHz to 0.1 Hz with an AC amplitude of 10 mV.

3.2.5 Characterization

XRD measurements of Li_2S samples were carried out on a Bruker D8 Discover X-ray diffractometer using Cu K_α radiation (λ=1.5418 Å). XRD samples were covered with Kapton tape to prevent them from absorbing moisture in the ambient air. Attenuated total reflectance Fourier transform infrared (ATR-FTIR) spectroscopy measurements were performed on a Bruker VERTEX 70 FT-IR Spectrometer.

3.3 Results and Discussion

3.3.1 Reaction between PVDF and LiOH or Li_2O

Since this work aims to remove the LiOH/Li_2O layer on the surface of the commercial Li_2S by using the PVDF binder during the slurry preparation process, the reaction between PVDF and LiOH or Li_2O was first carried out in anhydrous NMP solvent. Similar reactions between PVDF and LiOH or other bases under different conditions have been studied, which involve dehydrofluorination of PVDF to form unsaturated C=C bonds (**Figure 3.2** (a)).[310,317,318] The formation of C=C bonds can be confirmed by measuring the FTIR spectra of the product.

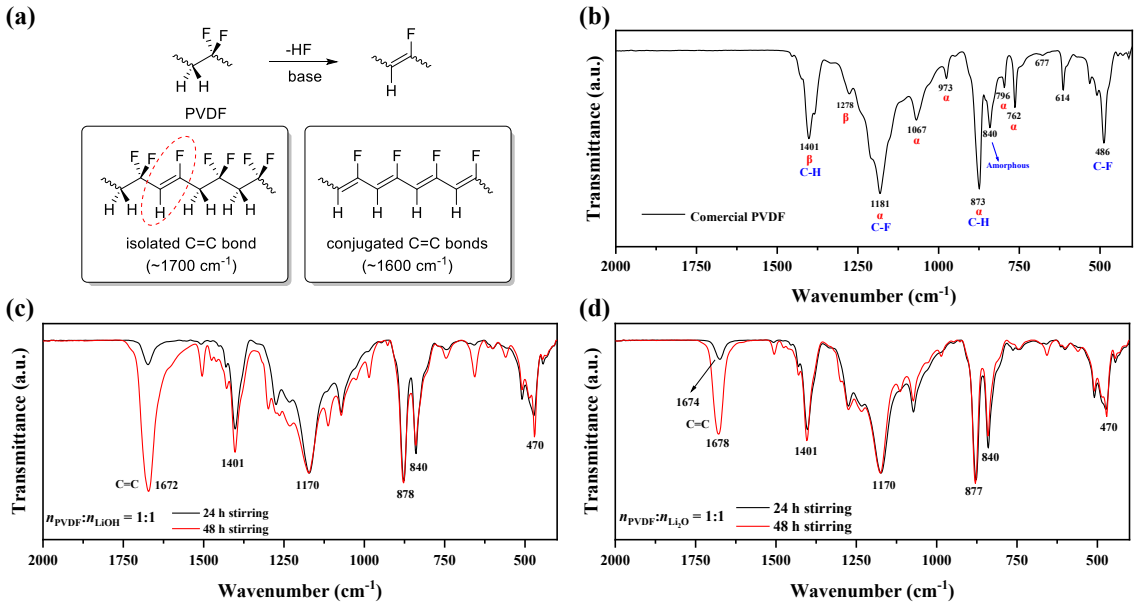


Figure 3.2 (a) Dehydrofluorination of PVDF in the presence of a base to form unsaturated C=C bonds. FTIR spectra of (b) commercial PVDF, (c) PVDF reacted with LiOH (n_{Li}:n_F = 1:1) in NMP for 24 and 48 h, and (d) PVDF reacted with Li_2O (n_{Li}:n_F = 1:1) in NMP for 24 and 48 h.

Specifically, LiOH or Li_2O was added to a PVDF solution in anhydrous NMP at a Li/F molar ratio n_{Li}:n_F of 1:1 and stirred at room temperature for 24 h or 48 h in a sealed vial in an argon-filled glove box. The obtained reaction mixture was vacuum dried at room temperature to remove NMP, washed with DI-water and then acetone to remove impurities, and dried thoroughly under vacuum at room temperature. Then the sample was measured using attenuated total reflection Fourier-transform infrared (ATR-FTIR) spectroscopy. As a comparison, the untreated commercial PVDF was also measured.

As shown **Figure 3.2** (b), the commercial PVDF sample showed peaks at 762, 796, 873, 973, 1067, and 1181 cm^{-1}, which are attributed to the α-phase, and peaks at 1278 and 1401 cm^{-1}, which are characteristic of the β-phase. There is also a peak at 840 cm^{-1}, which represents the amorphous phase.[310,317,318] The data indicate that the PVDF used in this study is mainly composed of the α phase. The very weak band at 677 cm^{-1} can be attributed to the head-to-head and tail-to-tail linkages.[319] More specifically, the bands at 1181 and 486 cm^{-1} can be indexed to C-F stretching and wagging vibration modes, respectively, while other bands at 1401 and 873 cm^{-1} are ascribed to C-H deformation.[318]

As shown in **Figure S 3.1**, at the beginning of the reaction, both PVDF/LiOH and PVDF/Li_2O mixtures were white. After stirring for 24 h, the mixtures turned dark purple and black, respectively, indicating that some reaction had occurred.

As shown in **Figure 3.2** (c) and (d), the PVDF samples treated with LiOH and Li_2O for 24 h showed a new peak at 1672 cm^{-1} and 1674 cm^{-1}, respectively. This peak intensified dramatically after stirring for 48 h for both samples. The peak position remained at 1672 cm^{-1} for the PVDF sample treated with LiOH, and shifted slightly to 1678 cm^{-1} for the sample treated with Li2O. It has been reported that the characteristic bands of C=C bonds formed through dehydrofluorination in PVDF appear in the range of ∼1600–1700 cm^{-1}.[308–310,320] Isolated C=C bonds appear at ∼1700 cm^{-1}, while conjugated C=C bonds (with two or more C=C bonds connected as shown in **Figure 3.2** (a)) appear at a shorter wavenumber towards ∼1600 cm^{-1}.[308] Accordingly, it seems that the conjugation length in both samples is rather short. Since the two samples appear dark due to their absorption of visible light, they likely contain extended π-conjugated segments with relatively narrow band gaps. Their different colors, dark purple (LiOH-treated) *vs.* black (Li_2O-treated), may be due to their different average conjugation lengths. The differences in the C=C bond peak position and color of the LiOH and Li_2O treated samples indicate that the dehydrofluorination mechanism of the two reactions may be different.

Changes also occurred in the C-F stretching and wagging frequencies from 1181 to 486 cm^{-1} for the commercial PVDF to lower wavenumbers of 1170 and 470 cm^{-1} for the LiOH or Li_2O treated samples. On the other hand, the C-H deformation bands remained at 1401 and 873 cm^{-1}. As the

reaction time increases, both the C-F and C-H peaks are significantly weakened relative to the C=C bond peak.

The above results show that PVDF can significantly react with LiOH or Li_2O in NMP when stirred at room temperature for 24–48 h, suggesting that it seems feasible to simply stir the Li_2S cathode slurry in the presence of PVDF to activate Li_2S.

3.3.2 First Charge/Discharge Cycle of Li_2S Cathodes

Next, three Li_2S cathode slurries were prepared by grinding Li_2S, Super P, and PVDF (at a mass ratio of Li_2S:SP:PVDF = 70:20:10) in anhydrous NMP inside an argon-filled glove box for 30 min. One slurry was immediately coated on a carbon-coated Al substrate and dried in a vacuum oven at 50 °C for 12 h inside the glove box. The cathode, named **PVDF-0h**, was used to assemble a Li_2S-LSB using a lithium foil as the anode and 1.0 M LiTFSI in DOL/DME (*v*/*v* = 1:1) containing 2 wt.% $LiNO_3$ as an electrolyte. Two other slurries were stirred in sealed vials inside the glove box for 24 h and 48 h, and subsequently used to fabricate Li_2S cathodes, **PVDF-24h** and **PVDF-48h**, and their Li_2S-LSBs, respectively. Since the Li_2S used in the work is highly pure (99.98%), the amount of PVDF used (Li_2S:PVDF mass ratio = 70:10) in the slurry should be adequate for the removal of the trace amount of LiOH/Li_2O on the surface of the Li_2S particles.

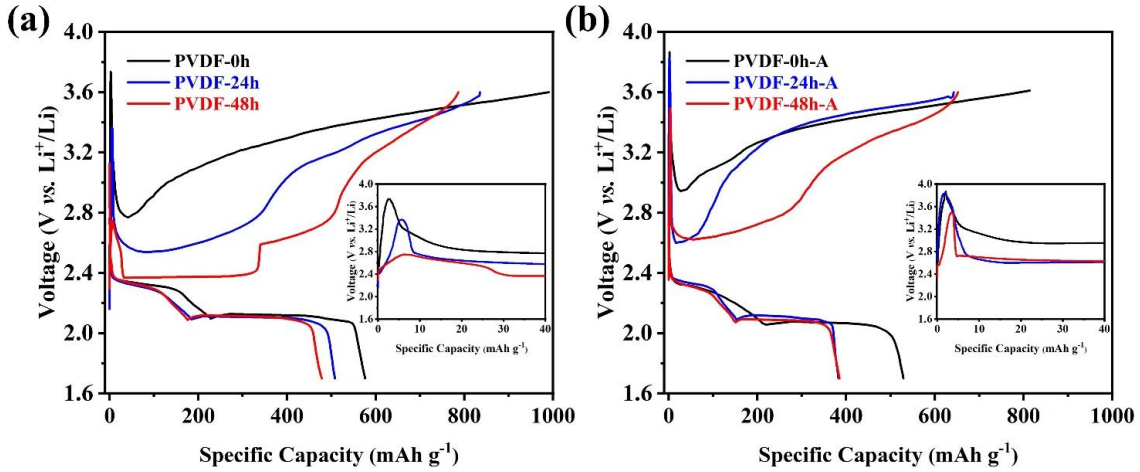


Figure 3.3 First charge/discharge curves of (a) **PVDF-0h**, **PVDF-24h** and **PVDF-48h**, and (b) **PVDF-0h-A**, **PVDF-24h-A**, and **PVDF-48h-A** batteries. Inserts are the zoomed initial charging stage of the batteries. All the electrochemical tests were carried out at 0.1 C (1 C = 1166 mA g^{-1} (Li_2S)) with an upper cut-off voltage of 3.6 V.

The first charge/discharge curves of the three electrodes at 0.1 C (1 C = 1166 mA g^{-1} (Li_2S)) are shown in **Figure 3.3** (a). For the **PVDF-0h** cathode, a high overpotential spike at 3.74 V appeared at a charging capacity of 2.5 mA h g^{-1} immediately after charging started, which is typical for Li_2S-LSBs using commercial Li_2S powers and is believed to be due to the presence of the insulating LiOH/Li_2O layer[176] and the low delithiation kinetics of pure Li_2S.[104] The charging voltage rapidly dropped and reached a low potential of 2.77 V at a capacity of 41.4 mA h g^{-1}. Then, the charging voltage gradually increased and reached a cut-off voltage of 3.6 V at a capacity of 990.8 mA h g^{-1}, completing the first charging process.

The shape of the subsequent first discharge curve is comparable to that of typical S-LSBs, exhibiting a first plateau within the voltage range of ~2.4–2.1 V, followed by a second plateau at discharge voltages of ~2.1 V. The appearance of these two distinct discharge regions are known to be due to the formation of soluble polysulfides Li_2S_y (y = 4–8) from elemental sulfur (S_8) and the formation of shorter sulfides (Li_2S_2 and Li_2S), which contribute 25% and 75% of the theoretical capacity for a complete discharge reaction from S_8 to Li_2S, respectively.[108] The discharge capacities of these two regions of the **PVDF-0h** cathode are 227.8 and 348.5 mA h g^{-1} with a total discharge capacity of 576.3 mA h g^{-1}, which is 49.4% of the theoretical specific capacity of Li_2S (1166 mA h g^{-1}). Since the capacity ratio of the second plateau to the first plateau is only 1.53, much lower than the theoretical ratio of 3, it appears that only 26.5% of Li_2S_2 were converted to the final discharge product Li_2S in the second plateau, which is much lower compared to conventional S-LSBs.[176] The **PVDF-0h** cathode slurry was prepared by manually grinding the commercial Li_2S with Super P, so the Li_2S particles and their charged product, elemental sulfur, would have a large size and stay outside the carbon black particles, which would result in poor charge transfer. On the other hand, the sulfur cathode in typical S-LSBs is prepared by thermal infiltration of sulfur into the nanopores of mesoporous carbon, which can effectively improve the charge transfer. Based on the discharge capacity of the first plateau, the sulfur utilization is calculated to be 78.1% based on the theoretical value of 291.5 mA h g^{-1} for a 100% sulfur utilization. This means that 78.1% of Li_2S were converted to sulfur in the first charging process, which would require a charging capacity of 910.6 mA h g^{-1}. Because the actual capacity of the first charge is 990.8 mA h g^{-1}, 91.9% of the charge in the first

charging process was used to convert Li_2S to elemental sulfur, indicating that 8.1% of the charge was lost due to some irreversible side reactions occurred under high charging voltages.

For the **PVDF-24h** cell, a significant decrease in the initial overpotential spike to 3.37 V was observed, followed by a low potential valley with a minimum voltage of 2.54 V at 80.8 mA h g^{-1}. The voltages of the overpotential spike and the potential valley are much lower than those of the **PVDF-0h** cell, which is most likely due to the removal of the LiOH/Li_2O layer on the surface of the Li_2S particles by PVDF during the 24 h stirring process according to the FTIR data (**Figure 3.2**). The charging voltage remained relatively low until reaching a capacity of ~340 mA h g^{-1}, then rapidly increased from ~2.8 V to ~3.1 V. Then, the voltage increased at a slower rate and reached a charge capacity of 835 mA h g^{-1} at the cut-off voltage of 3.6 V, which is lower than that (990.8 mA h g^{-1}) of the **PVDF-0h** cell.

The discharge capacity of the **PVDF-24h** cell is 508.2 mA h g^{-1}, which can be broken down to capacities of 184.4 mA h g^{-1} and 323.8 mA h g^{-1} for the first and the second plateaus, respectively. The capacity ratio of the second plateau to the first plateau is 1.76, which indicates that conversion of Li_2S_2 to Li_2S is more efficient compared to the **PVDF-0h** cell. However, the elemental sulfur involved in the first discharge is only 63.3%, resulting in a lower overall discharge capacity of the **PVDF-24h** cell compared to the **PVDF-0h** cell. Since converting 63.3% of Li_2S into sulfur requires a charge capacity of 738.1 mA h g^{-1}, 88.4% of the charge was used to convert Li_2S to elemental sulfur (capacity loss 11.6%) in the **PVDF-24h** cell during the first charge, which is slightly lower than that (91.9%) of the **PVDF-0h** cell.

The **PVDF-48h** cell showed a further decrease in the overpotential spike to 2.75 V. After the spike, the potential dropped to a very low level of 2.37 V and changed little until reaching a capacity of ~334 mA h g^{-1}, where the potential suddenly jumped to ~2.6 V. Then the charging potential experienced a slow increase period to ~2.7 V (~334–500 mA h g^{-1}), a sharp increase to ~3.1 V (~500–580 mA h g^{-1}), and finally a slow increase period to the cut-off voltage of 3.6 V (~580–786.3 mA h g^{-1}). Compared with the **PVDF-24h** cell, the overall charging potential of the **PVDF-48h** cell is further reduced, which is most likely due to the further removal of the LiOH/Li_2O layer on the surface of Li_2S particles by PVDF.

The discharge capacities of the first and second discharge plateaus of the **PVDF-48h** cell are 175.5 mA h g^{-1} and 303.1 mA h g^{-1}, respectively, with a capacity ratio of 1.73, reaching an overall discharge capacity of 478.6 mA h g^{-1}. The content of elemental sulfur involved in the first discharge is calculated similarly based on the first discharge plateau to be 60.2% of the theoretical value, indicating that a further decrease in the amount of sulfur formed in the **PVDF-48h** cell during the first charging process. The charge used to convert Li_2S into sulfur in the first charging process for the **PVDF-48h** cell is 702.0 mA h g^{-1} based on the first discharge capacity (175.5 mA h g^{-1}). So the charging efficiency is calculated to be 89.3% (with a capacity loss of 11.7%) according to the actual first charge capacity (786.3 mA h g^{-1}), which is similar to that of the **PVDF-24h** cell.

The above first cycle curves of the three Li_2S-LSBs showed that simple stirring of the Li_2S cathode slurry in the presence of PVDF could effectively reduce the overpotential spike as well as the overall charging potential. The results showed that not only the initial overpotential spike, but also the high charging voltages throughout the first charging process seem to be related to the presence of a layer of LiOH/Li_2O on the surface of the Li_2S particles. To further validate this hypothesis, the dried fresh **PVDF-0h**, **PVDF-24h**, and **PVDF-48h** cathodes were stored inside the argon-filled glove box for an additional 24 h and then assembled into cells, named **PVDF-0h-A**, **PDVF-24h-A**, and **PVDF-48h-A**, respectively, where "A" denotes "aged". It was expected that the trace amount of moisture present in the glove box would be able to react with the exposed Li_2S in the **PVDF-24h** and **PVDF-48** cathodes to form a new layer of LiOH/Li_2O on the surface of the Li_2S particles,[176] which would increase the charging potential of these aged cathodes.

As shown in **Figure 3.3** (b), compared with the **PVDF-0h** cell, the **PVDF-0h-A** cell showed higher overall charge voltages with an overpotential spike of 3.87 V and a potential valley of 2.94 V. For the **PVDF-24h-A** cell, the first charge curve exhibited a significantly increased overpotential spike (3.83 V) and a shortened post-spike potential valley compared to the **PDVF-24h** cell. The charge curve of this cell is very similar to that of the **PVDF-0h** cell prepared with a non-stirred slurry. As for the **PVDF-48h-A** cell, the overpotential spike dramatically increased to 3.49 V and the post-spike potential region became an ascending slope starting from a minimum potential of 2.62 V, rather than a low potential plateau observed for the **PVDF-48h** cell. The first charge curve of the **PVDF-48h-A** is very similar to the **PVDF-24h** cell, which indicates that the thickness of the

LiOH/Li_2O layer on the Li_2S particles in the **PVDF-48-A** cathode is similar to that of the **PVDF-24h** cell. All the cells using the aged cathodes showed lower charge and discharge capacities due to the consumption of some Li_2S by the moisture inside the glovebox. The charge/discharge data obtained for the cells using the cathodes aged in the glove box confirm that the presence of LiOH/Li_2O layer is the root cause of the observed high charging voltages throughout the first charging process of Li_2S-LSBs, and not just the initial overpotential spike.

3.3.3 Reaction of Li_2S with PVDF

The above observed reduction in first discharge capacity of the **PVDF-24h** and **PVDF-48h** cathodes suggests that some of their Li_2S may be consumed. To confirm if reaction between Li_2S and PVDF occurred during the slurry stirring, the commercial Li_2S was mixed with PVDF at an n_{Li}:n_F of 1:1 in NMP and stirred in a sealed vial for 24 h at room temperature in an Ar-filled glove box. As shown in **Figure S 3.1**, the color of the sample changed from white before stirring to dark purple after stirring for 24 h. The reaction mixture was dried under vacuum, washed with DI water and acetone, and dried under vacuum at room temperature. The ATR-FTIR spectrum of the sample showed an obvious peak at 1668 cm^{-1} (**Figure 3.4** (a)), which can be assigned to the C=C bonds as previously discussed. Compared to the PVDF sample treated with LiOH or Li_2O at n_{Li}:n_F = 1:1, the Li_2S-treated PVDF showed a stronger C=C peak, indicating the higher degree of dehydrofluorination of PVDF in the presence of Li_2S (see **Figure S 3.2** for a clearer comparison of their FTIR spectra). Therefore, the order of reactivity with PVDF is Li_2S > LiOH > Li_2O. The smaller wavenumber (1668 cm^{-1}) of the C=C bond peak of the Li_2S treated PVDF sample compared to the LiOH (1672 cm^{-1}) and Li_2O (1678 cm^{-1}) treated samples indicates that the former contains more extended π-conjugation segments. No discernible peaks related to LiOH, LiOH·H_2O, and Li_2O were detected in the FTIR spectra,[321–323] affirming that both LiOH and Li_2O were effectively washed away by DI water.

To simulate the preparation conditions of the cathode slurries, mixtures of commercial Li_2S and PVDF at a mass ratio of 70:10 (equivalent to a molar ratio of n_{Li}:n_F = 10:1) were stirred in NMP for 24 h and 48 h, respectively. After stirring for 24 h, the sample showed a very strong peak at a shorter wavenumber of 1658 cm^{-1} (**Figure 3.4** (b)), indicating a higher degree of

dehydrofluorination of this sample compared to the Li_2S-treated PVDF at n_{Li}:n_F = 1:1. After stirring for 48 h, the C=C peak became stronger, indicating that further dehydrofluorination occurred.

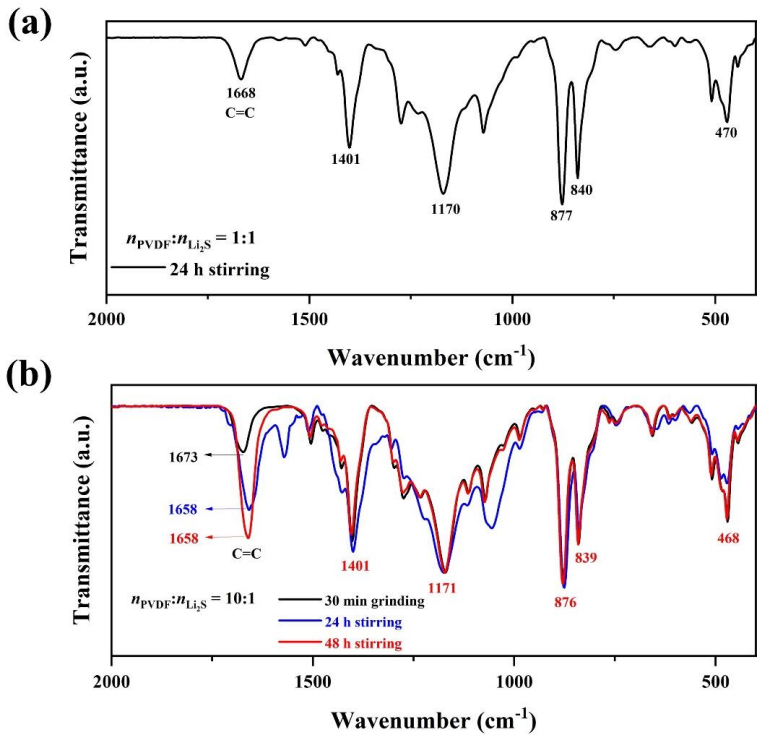
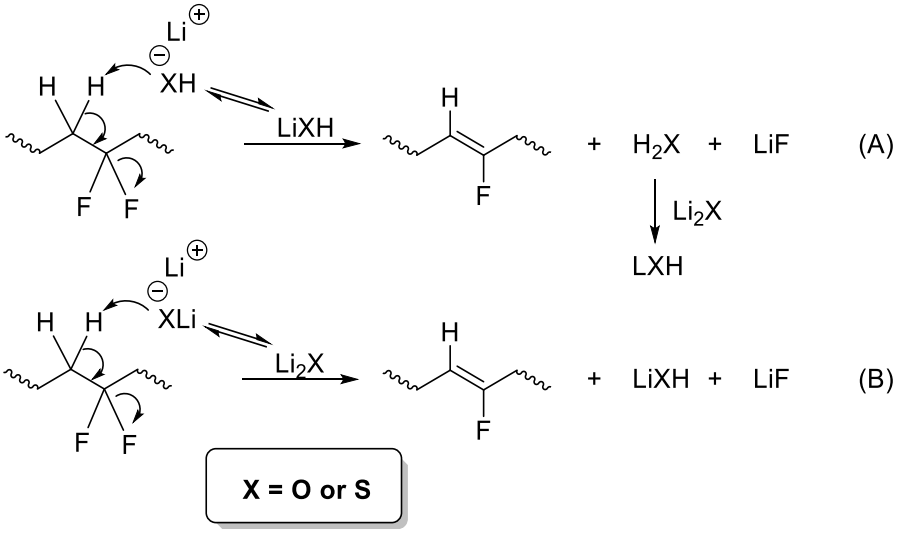


Figure 3.4 ATR-FTIR spectra of (a) PVDF treated Li_2S (molar ratio n_{Li}:n_F =1:1) in in anhydrous NMP by stirring for 24 h and (b) PVDF samples treated with Li_2S (molar ratio n_{Li}:n_F = 10:1 or mass ratio m_{Li2S}:m_{PVDF}=70:10) in anhydrous NMP by grinding for 30 min (and 12 h drying at 50 °C under vacuum) and stirring for 24 h and 48 h, respectively.

Since the reaction between Li_2S and PVDF seems to be very fast, it may also occur appreciably in the normal cathode fabrication process, which involves 30-min slurry grinding at room temperature and drying for 12 h at 50 °C in vacuum. Therefore, we grinded a mixture of Li_2S and PVDF at a mass ratio of 70:10 (or n_{Li}:n_F = 10:1) in NMP in a mortar inside the glove box. The mixture changed from white to light purple after 30-min grinding. After drying for 12 h at 50 °C in a vacuum oven to remove NMP, the mixture became dark purple, indicating that the reaction continued during drying (**Figure S 3.3**). This sample showed a strong peak at 1673 cm^{-1} originated from the C=C bonds, indicating that notable dehydrofluorination also occurred with this sample (**Figure 3.4** (b)). Therefore, it is reasonable to assume that significant dehydrofluorination occurs in the cathode composite having the same Li_2S:PVDF ratio (Li_2S:SP:PVDF mass ratio = 70:20:10)

under same processing conditions (30-min grinding at room temperature and 12-h drying under vacuum at 50 °C).

The above ATR-FTIR results showed unambiguous evidence that commercial Li_2S can readily react with PVDF, even more aggressively than LiOH and Li_2O. The reaction between LiOH and PVDF in anhydrous NMP may proceed via a bimolecular elimination (E2) mechanism.[310] For the reaction between Li_2O and PVDF, Li_2O may directly initiate dehydrofluorination through Reaction B via an E2 mechanism similar to the proposed reactions between PVDF and other metal oxides Li_2O2, LLZO and LLZTO in polar organic solvents such as DMAc, NMP and DMF (Reaction A in **Scheme 3.1**).[176,313–315] The byproduct LiOH in Reaction B may undergo dehydrofluorination via Reaction A, in which H_2O forms and reacts with Li_2O to regenerate LiOH. It is also possible that the trace amount of LiOH inevitably present in Li_2O may start dehydrofluorination and the entire reaction proceeds without the direct reaction of Li_2O with PVDF shown in Reaction B. However, the FTIR data showed that the C=C bond peak position (1672 cm^{-1}) of the LiOH-treated PVDF is quite different from that (1678 cm^{-1}) of the Li_2O-treated sample, which suggests that the formation of a new C=C bond to an existing C=C bond is more preferred in the case of using LiOH. Because the amount of LiOH present in Li_2O should be very small, it is more likely that Li_2O directly reacts with PVDF and largely contributes to the formation of C=C bonds through Reaction B.



Scheme 3.1 Possible reactions of PVDF with commercial Li_2S.

The reaction between the commercial Li_2S and PVDF may be more complicated. Since the commercial Li_2S inevitably absorbs some moisture, LiOH, LiSH, and Li_2O are formed and present on the surface of the Li_2S particles.[165] LiOH and LiSH may dissociate into OH- and SH- anions in the polar NMP solvent and initiate dehydrofluorination of PVDF via an E2 reaction (Reaction A in **Scheme 3.1**). The byproduct of H_2O or H_2S formed in Reaction A can react with Li_2O or Li_2S to regenerate LiOH or LiSH, which further reacts with PVDF to continue dehydrofluorination. However, as mentioned above, the amounts of LiOH and LiSH present in the commercial Li_2S should be very small, which cannot explain the very fast reaction between Li_2S and PVDF if Reaction A is dominant. Hence, it is more reasonable to consider that Li_2S can directly involve in dehydrofluorination through Reaction B and the formed product LiSH also reacts with PVDF via Reaction A. Because the PVDF sample treated with Li_2S is more conjugated, it seems that dehydrofluorination in the presence of Li_2S is more regioselective to form a C=C bond next to an existing C=C bond compared to the reaction in the presence of LiOH or Li_2O.

3.3.4 Effects of Stirring on the Crystallinity of the Li_2S Particles

Since the size of the Li_2S particles also influences the height of the charging potential barrier,[166,168] there is a possibility that stirring or the action of PVDF helps break down the Li_2S particles to improve the charge transfer and thus reduce the overpotential of **PVDF-24h** and **PVDF-48h** cells.

To examine the effect of stirring, a commercial Li_2S powder sample was mixed with the solvent NMP only and stirred for 24 h in an argon-filled glove box. Then, NMP was removed under vacuum, and the dried sample was sealed with Kapton tape to prevent exposure of the highly hygroscopic Li_2S to ambient air during sample transfer and XRD measurements.[324] A commercial Li_2S powder sample without treatment was also measured for comparison.

The XRD patterns of the commercial Li_2S powder sample are shown in **Figure 3.5** (a). Three broad peaks at 14 °, 22 °, and 26 ° are originated from the Kapton tape, while other peaks can be ascribed to the crystalline Li_2S with a cubic space group $Fm\bar{3}m$ structure (JCPDS card No. 81-1173). The average crystal particle size of this Li_2S sample was calculated using the *Scherrer* equation[266] to be 29 nm. The sample ground for 2 h exhibited a slightly smaller average particle

size of 27 nm. The Li_2S sample stirred in NMP for 24 h showed sharper diffraction peaks and the average crystal particle size is 34 nm. The slight increase in particle size compared to the as-received commercial Li2S sample might be due to the *Ostwald* ripening effect caused by stirring.[325] The results showed that stirring Li_2S in NMP did not decrease but slightly increased the particle size of Li_2S.

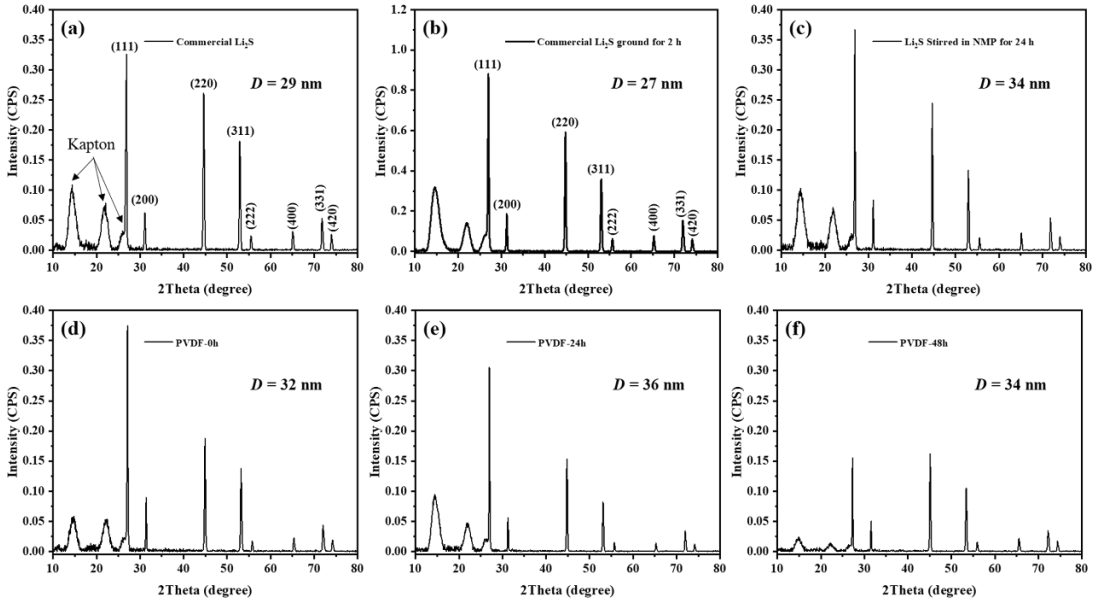


Figure 3.5 XRD patterns of (a) commercial Li_2S powders, (b) commercial Li_2S ground for 2 h, (c) commercial Li_2S powders stirred in NMP for 24 h, dried electrode slurries based on (d) **PVDF-0h**, (e) **PVDF-24h** and (f) **PVDF-48h**. The average Li_2S crystal size (*D*) values of the samples calculated using XRD data with the *Scherrer* equation are shown in the graphs. Peak (111) was excluded for the average crystal size calculation since this peak overlaps with one of the peaks from the Kapton tape.

To investigate whether the reaction of PVDF with Li_2S changes the Li_2S particle size, the dried electrode slurries of **PVDF-0h**, **PVDF-24h** and **PVDF-48h** were measured. As shown in **Figure 3.5** (d), the **PVDF-0h** sample showed stronger and sharper peaks than the commercial sample. The crystal size (32 nm) slightly increased probably due to the similar *Ostwald* ripening effect observed for the sample stirred in NMP for 24 h. The **PVDF-24h** sample showed a further increase in the crystal size (36 nm). However, intensities of all the diffraction peaks decreased compared to the **PVDF-0h** sample, indicating that stirring may reduce the amount of Li_2S. The crystal size of the **PVDF-48h** sample with a longer stirring time (48 h) is 34 nm, which is a slightly smaller than that

of the **PVDF-24h** sample, but still larger than that of the **PVDF-0h** sample. However, the Li_2S diffraction peak intensities of the **PVDF-48h** sample decreased further, suggesting a further reduction in the amount of Li_2S in this sample.

Because the Li_2S crystal particle size of the **PVDF-24h** and **PVDF-48h** samples is larger than that of the **PVDF-0h** sample, the crystal particle size factor alone would make the charging of these two cathodes more difficult. Therefore, the particle size change in Li_2S due to stirring or reaction with PVDF is unlikely to cause the decrease of overpotential with increasing stirring time.

Since the commercial Li_2S particle aggregates are large (0.5–1 μm),[157] while the crystal particle size of this commercial Li_2S is rather small (~29 nm), each aggregate may contain numerous Li_2S crystal particles. Therefore, the decrease in the first charge potential of the cathode with stirred slurry may be due to better dispersion of Li_2S particles by stirring. Electrochemical impedance spectroscopy (EIS) was used to probe this possibility. The EIS results showed that **PVDF-24h** and **PVDF-48h** electrodes had a similar charge transfer resistance (R_{ct}) (25 Ω for **PVDF-24h** and 26 Ω for **PVDF-48h**) compared to **PVDF-0h** (27 Ω) (**Figure S 3.4** and **Table S 3.1**), indicating that the additional stirring step does not appear to improve the homogeneity of the slurry to the extent that it leads to a significant reduction in overpotential. This was further verified by the battery fabricated using a Li_2S slurry stirred for 48 h in the presence of a polyvinylpyrrolidone (PVP) binder, which showed no reduction in the first charge potential (to be discussed later).

3.3.5 Impacts of the Reaction of PVDF with Commercial Li_2S on the First Cycle of Li_2S-LSBs

Since PVDF can significantly react with the commercial Li_2S under the normal cathode fabrication conditions (30 min grinding and 12 h vacuum drying at 50 °C) (**Figure 3.4** (b)), some $LiOH/Li_2O$ on the surface of the Li_2S particles in the **PVDF-0h** cathode would be removed. Therefore, the overpotential observed for the **PVDF-0h** cathode may not reflect the effect of the pristine $LiOH/Li_2O$ layer on the commercial Li_2S particle surface. Indeed, as mentioned earlier, the initial overpotential spike for the **PVDF-0h** cathode is 3.74 V, while this spike increased to 3.87 V for the **PVDF-0h-A** with the aged **PVDF-0h** cathode due to the re-growth of the $LiOH/Li_2O$ layer (**Figure 3.3**). Furthermore, as illustrated in **Figure S 3.5** (d), the battery utilizing Li_2S ground for 2

h without the presence of PVDF did not exhibit a decrease in the overpotential spike. This observation indicates that grinding Li_2S for 2 h or less has a minimal effect on reducing the overpotential or, in other words, it could not remove the $LiOH/Li_2O$ layer.

To explore the effect of the pristine $LiOH/Li_2O$ layer, we used another binder, PVP, to fabricate a cathode **PVP-48h** using the same conditions as for the **PVDF-48h** cathode. PVP is inert to LiOH and Li_2O, so the original $LiOH/Li_2O$ layer on the surface of Li_2S particles will be preserved. The **PVDF-48h** cell exhibited a high initial overpotential spike of 3.92 V and no obvious potential valley after the spike (**Figure 3.6** (a) and **Figure S 3.7** (a)). This first charge profile may reflect the effect of the pristine $LiOH/Li_2O$ layer on the first charge potential. On the other hand, it was reported that a cathode using the *in-situ* synthesized nanosphere Li_2S and PVP binder showed a low overpotential spike of ~2.9 V.[175] Therefore, it seems that the overpotential spike of the cathode using the pristine commercial Li_2S used in our study is about 3.92 V.

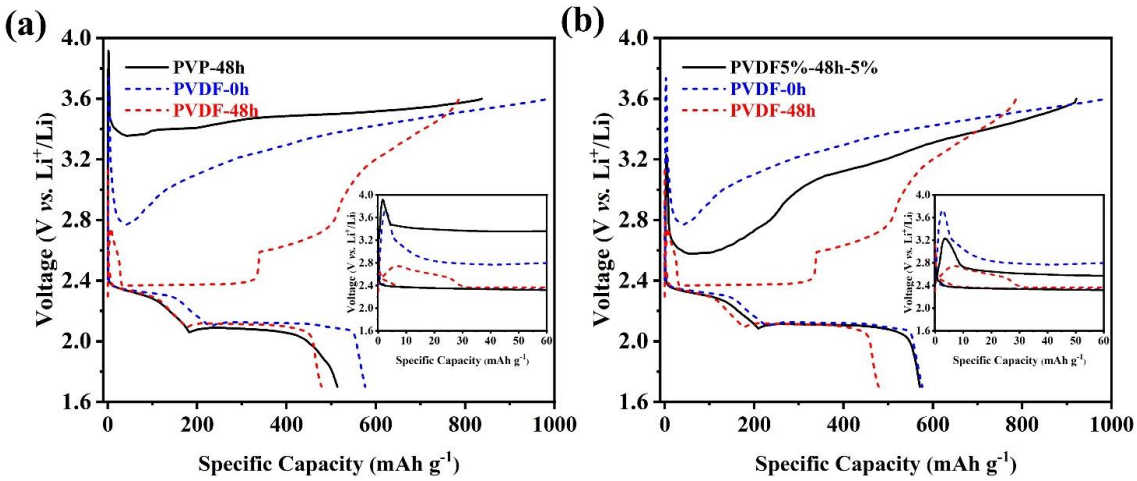


Figure 3.6 First charge/discharge curves of (a) **PVP-48h** and (b) **PVDF5%-48h-5%** batteries. Inserts are the zoomed initial charging stage of the batteries. The first charge/discharge curves of **PVDF-0h** and **PVDF-48h** are incorporated for comparison. All the electrochemical tests were carried out at 0.1 C (1 C = 1166 mA g^{-1} (Li_2S)) with an upper cut-off voltage of 3.6 V.

Based on the above experimental data, the effect of PVDF on the Li_2S particles and the initial charging of the battery under different slurry stirring times is described as follows.

1) The pristine commercial Li_2S particles in the **PVP-48h** cathode are covered with a relatively thick layer of $LiOH/Li_2O$ (**Figure 3.7**). The very low electronic and ionic

conductivities of the LiOH/Li_2O layer require a high voltage to initiate the oxidation (charging) of Li_2S. Studies show that at a low electrolyte/sulfur ratio, a direct conversion of Li_2S to S_8 occurs, which is kinetically largely hindered.[168,174] The presence of the LiOH/Li_2O layer prevents the underlying Li_2S from contacting the electrolyte solution, so direct conversion of Li_2S to S_8 may occur in the solid state, which makes the reaction of Li_2S even harder. The combined effects of the LiOH/Li_2O layer and the inaccessibility to electrolyte result in a high overpotential spike of 3.92 V for the **PVP-48h** cathode. Once some S_8 formed, the crystal structure of Li_2S adjacent to S_8 changes, which lowers the activation energy of the further conversion of Li_2S to S_8, and a small potential valley appears, but the voltage remains high since the resistance of the LiOH/Li_2O layer still exists. As the reaction proceeds deeper into the core, the insulating S_8 layer becomes thicker, and the total resistance increases. Therefore, the charging voltage continues to increase until reaching the cut-off voltage of 3.6 V. Since oxidation of LiOH/Li_2O can occur significantly at > 3.5 V (*vs.* Li^+/Li),[326,327] the LiOH/Li_2O layer may crack at the later stage of the first charge, which can facilitate the subsequent discharge. As shown in **Figure S 3.7** (a), compared with the discharge curves of the 2nd and subsequent discharge curves, the late stage of the 1st discharge curve showed lower voltages, which may be due to the presence of some LiOH/Li_2O on the surface of the S_8 particles at the end of the first charging process.

2) For the Li_2S particles in the **PVDF-0h** cathode, the LiOH/Li_2O layer becomes slightly thinner due to its reaction with PVDF during the grinding and drying processes, which results in the lowering of the overpotential spike to 3.74 V. Some areas of the Li_2S particle surface may be damaged and exposed to the electrolyte, which is caused either by the reaction with PVDF during the slurry grinding and drying processes or under the high potential at the spike. The direct contact of the exposed Li_2S with the liquid electrolyte facilitates charge transfer,[104,168,174] bringing the potential down to 2.77 V after the spike. However, the areas with exposed Li_2S are limited, so the charging voltage gradually increases until it reaches the cut-off voltage of 3.6 V. This part of the charge curve

resembles the cathode with Li_2S directly exposed to low amounts of electrolyte, where direct conversion of Li_2S to S_8 is still dominant.[174]

3) For the Li_2S particles in the **PVDF-24h** cathode, the LiOH/Li_2O layer becomes even thinner and more underlying Li_2S is exposed in some regions due to the severe dehydrofluorination with PVDF during stirring for 24 h. The overpotential spike decreases further to 3.37 V, then a long voltage valley with a minimum charge voltage of 2.54 V appears and lasts up to ~400 mA h g^{-1}. The drop in overall charging potential is attributed to the lower resistance of the thinned LiOH/Li_2O layer as well as the exposure of more Li_2S to the electrolyte solution.[104,168,174] However, as some areas on the surface of the Li_2S particles are still covered with LiOH/Li_2O, diffusion of the electrolyte into the particles becomes increasingly difficult and the charging potential increases as the reaction proceeds. At the later stage of the potential valley (~400 mA h g^{-1}), the reaction occurs through the direct conversion of Li_2S to S_8 due to the lack of electrolyte in a similar manner as in the **PVDF-0h** cell and the charging voltage rises significantly. Since the dehydrofluorination reactivity follows the order of Li_2S > LiOH > Li_2O, some Li_2S involves in dehydrofluorination of PVDF through the exposed regions. So, the charge and discharge capacities of the first cycle of the **PVDF-24h** cell are lower than those of the **PVDF-0h** cell.

4) Prolonged stirring of the slurry for 48 h is able to completely eliminate LiOH/Li_2O on the surface of the Li_2S particles (**Figure 3.7**). The overpotential spike of the **PVDF-48h** cell is very low at 2.75 V and a long flat plateau at a very low voltage of 2.37 V lasts until ~334 mA h g^{-1}. This first charge profile is characteristic of the conversion of pure activated Li_2S to S_8 with the exposure of the surface of the Li_2S particles to the sufficient liquid electrolyte.[104,157,174–176,200,301,328] The reaction is believed to involve (1) the formation of lithium deficient solid $Li_{2-x}S$ (s), which is kinetically hindered and results in the overpotential spike, (2) the formation of soluble intermediate polysulfides Li_2S_y (*l*) (y < 8), and (3) the conversion of Li_2S_y (*l*) (y = 8) to S_8.[104] After the low potential plateau, the charging voltage sharply rises to ~2.6 V and then gradually increases until it reaches the cut-off potential of 3.6 V. While this high charge potential tail usually appears on the

first charge of cathodes using activated Li_2S having a fairly large particle size,[104,174–176,200,301,328] it has not been observed for the cathodes using activated Li_2S nanoparticles.[157] Therefore, this high-potential tail may be due to the solid-phase direct conversion of Li_2S to S_8 at the particle core covered by a solid sulfur layer formed at the end of the low-potential plateau. Based on the overpotential spike (2.75 V) of the **PVDF-48h** cell and the potential after the spike (2.37 V), the overpotential (or activation barrier) of the pure crystalline Li_2S without a LiOH/Li_2O layer seems to be 0.38 V. It was found that the difference of the overpotential spike and the potential after the spike for the **PVP-48h** cell is ~0.4 V, which can be accounted for the overpotential caused by the high crystallinity of the pure Li_2S. Therefore, the overpotential contributed by the pristine LiOH/Li_2O layer of the commercial Li_2S in the **PVP-48h** cell is probably ~1.2 V (**Figure 3.7**).

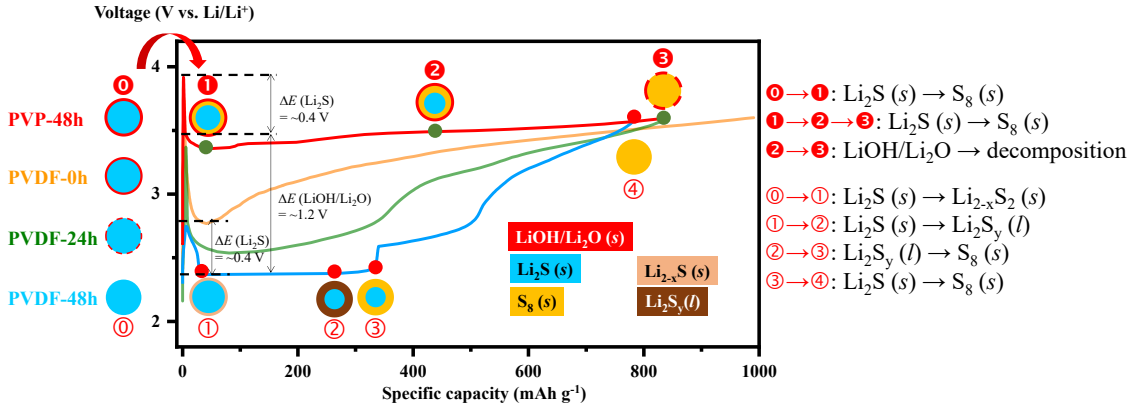


Figure 3.7 Schematic first charging processes of Li_2S particles in different Li_2S-LSBs at a rate of 0.1 C. ΔE (Li_2S) and ΔE (LiOH/Li_2O) are the overpotentials contributed by the pure crystalline Li_2S (~0.4 V) and the LiOH/Li_2O layer (~1.2 V for the **PVP-48h** cell with the pristine commercial Li_2S), respectively.

Since PVDF can remove the LiOH/Li_2O layer but also consumes the exposed Li_2S, we modified the slurry preparation process to balance these two effects. First, Li_2S, Super P and PVDF at a mass ratio of 70:20:5 were mixed in NMP and stirred for 48 h. The use of a smaller amount of PVDF is intended to minimize the unwanted reaction of PVDF with Li_2S during stirring. Then 5% more parts of PVDF were added and the mixture was stirred briefly for 10 min. The resulting **PVDF5%-48h-5%** slurry was used to make the cathode and the battery in the same manner as for other batteries. As shown in **Figure 3.6** (b) and **Figure S 3.7** (b), the initial charging potential spike

of this cathode was reduced to 3.23 V, which is lower than that of the **PVDF-0h** (3.74 V) and **PVDF-24h** (3.37 V) cathodes but higher than that of the **PVDF-48h** cathode (2.75 V). This shows that stirring with 5 wt.% PVDF for 48 h is more effective in removing the LiOH/Li_2O layer than stirring with 10% PVDF for 24 h. On the other hand, the **PVDF5%-48h-5%** cathode achieved a discharge capacity of 571.0 mA h g^{-1}, which is much higher than that of the **PVDF-24h** (508.2 mA h g^{-1}) and **PVDF-48h** (478.6 mA h g^{-1}) cathodes and very close to that of the **PVDF-0h** cathode (576.3 mA h g^{-1}) (**Table S 3.2**).

As observed for other batteries discussed above, the **PVDF5%-48h-5%** cell also suffers a high potential tail and a relatively low first/second discharge capacity ratio (1.73) due to the large particle size of the commercial Li_2S. Techniques such as extensive ball milling[157,329] and formation of Li_2S nanocomposites[322] may be used to reduce the Li_2S particle size to solve these issues.

3.4 Conclusions

Lithium-sulfur batteries (LSBs) have potential as an alternative to lithium-ion batteries (LIBs) due to their higher energy density and lower cost. However, developing LSBs with Li_2S as the cathode material faces certain challenges including the high overpotential required during the first charging process. This study proposes a simple solution by allowing the PVDF binder to react with the LiOH/Li_2O layer on the surface of the Li_2S particles during the cathode slurry preparation process, effectively reducing the first charge overpotential of Li_2S-LSBs. The study shows that the reaction between PVDF and LiOH/Li_2O in anhydrous NMP solvent can effectively activate the Li_2S particles in the cathode slurry when stirred for 48 h at room temperature. The battery **PVDF-48h** made using this slurry exhibits a significantly reduced initial overpotential spike of 2.75 V and a long low potential plateau of ~2.4 V, resembling fully activated Li_2S-based LSBs. However, we found that exposed Li_2S can also readily react with PVDF through dehydrofluorination, leading to a decrease in capacity. Our results show that the LiOH/Li_2O layer on the surface of the Li_2S particles prevents direct contact with the electrolyte, resulting in the highly energetically demanding solid phase direct conversion of Li_2S to S_8. This is the primary cause of the initial overpotential spike (contributing up to ~1.2 V to the overpotential spike at 0.1 C) and overall high charging voltages afterwards. The high crystallinity of Li_2S appears to only minimally contribute (~0.4 V at 0.1 C) to the initial overpotential spike. Furthermore, the relatively large crystal size of commercial Li_2S makes later-stage charging difficult, resulting in a gradual increase in charging voltage, even after complete removal of the surface LiOH/Li_2O layer. Overall, this study provides new insights into the origin of the first charge overpotential of Li_2S-LSBs and suggests a simple method to reduce it. To improve the performance of Li_2S-LSBs, further optimization is required, including optimizing dehydrofluorination conditions to address the issue of reduced specific capacity and decreasing Li_2S particle size to reduce high later-stage charging voltages.

3.5 Supporting Information

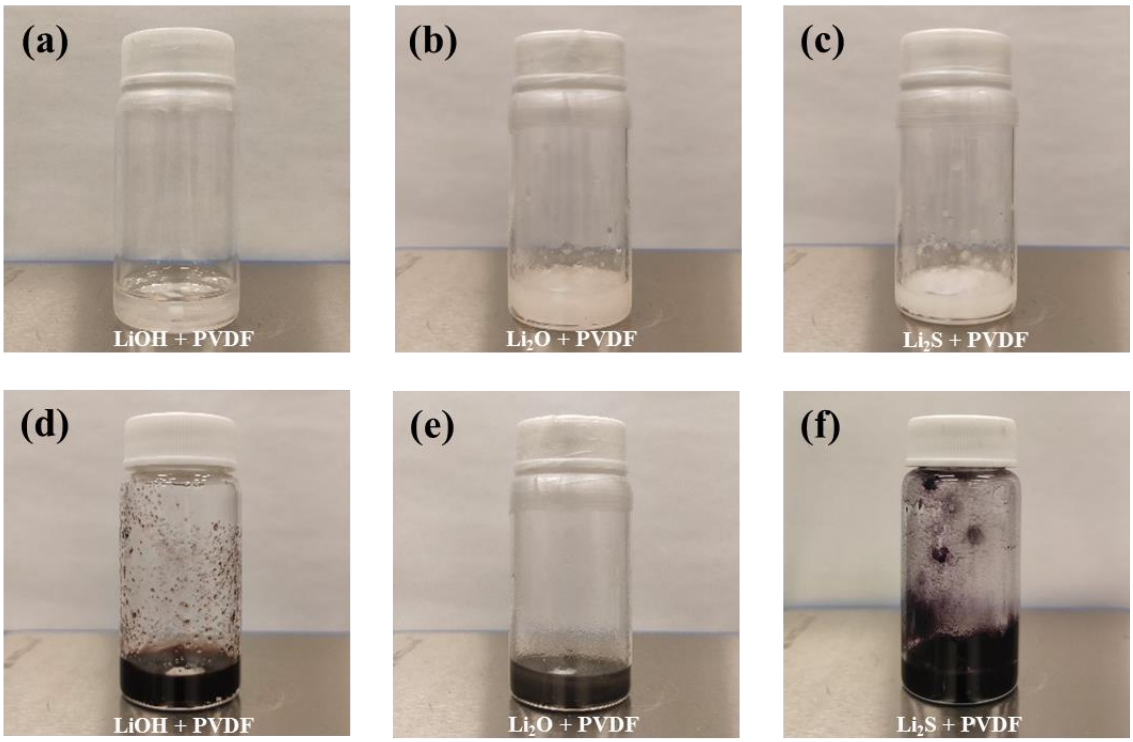


Figure S 3.1 The mixture of PVDF with (a and d) LiOH, (b and e) Li_2O and (c and f) Li_2S in molar ration n_{Li}:n_F = 1:1 in NMP in the beginning and after 24 h. The white particles in (a), (b), and (c) are the unreacted LiOH, Li_2O, and Li_2S, respectively, while the unreacted PVDF dissolved in NMP is colorless.

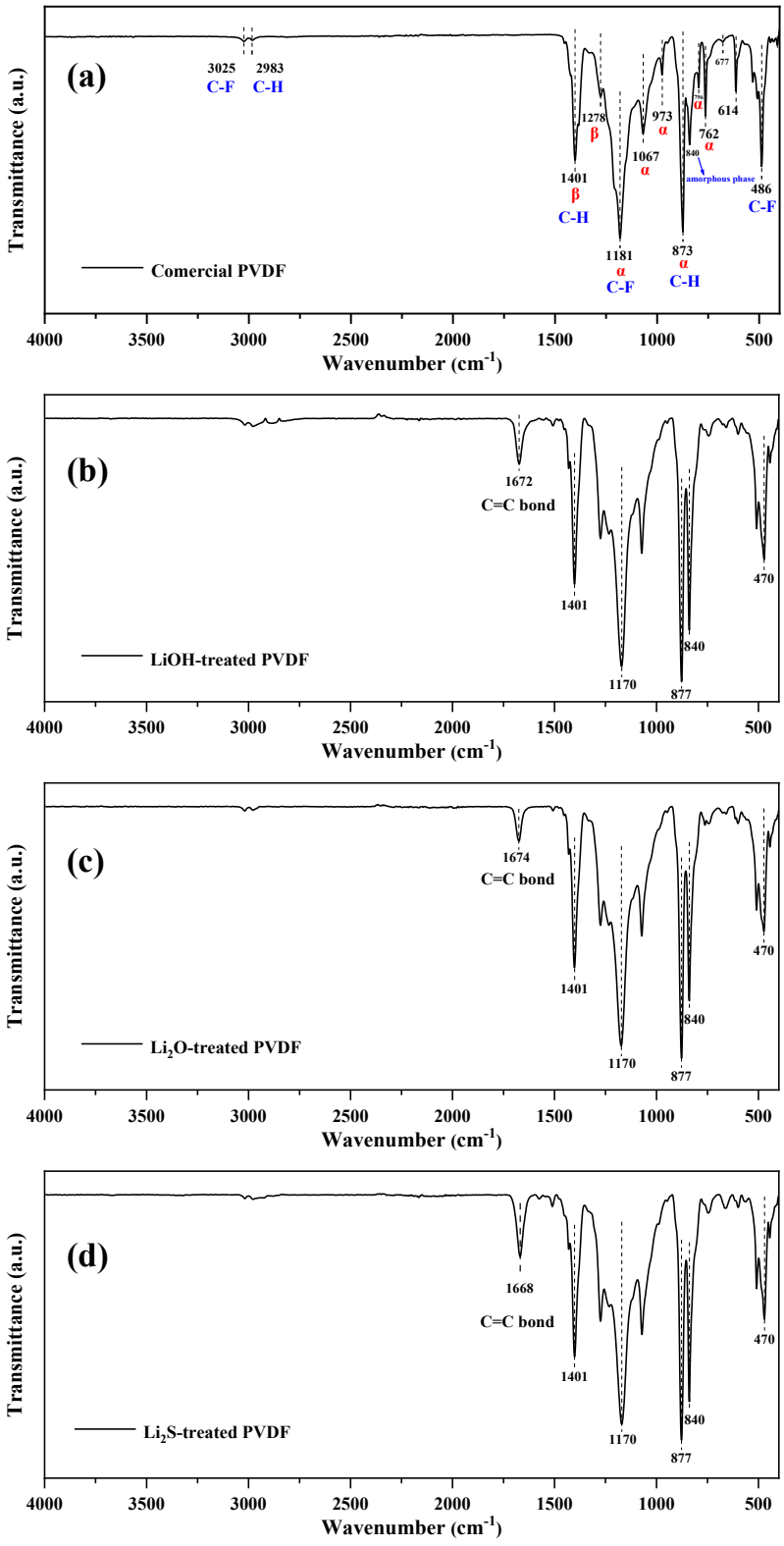


Figure S 3.2 Full ATR-FTIR spectra of (a) the commercial PVDF sample without treatment and PVDF samples treated (b) LiOH, (c) Li_2O, and (d) Li_2S (molar ratio n_{Li}:n_F=1:1) in anhydrous NMP by stirring for 24 h.

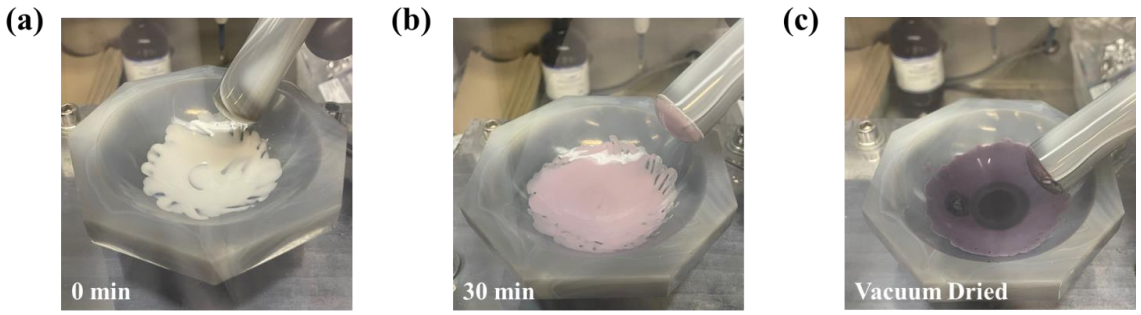


Figure S 3.3 Progress of the reaction between Li_2S powders and PVDF (m_{Li2S}:m_{PVDF} = 70:10 or n_{Li}:n_F = 10:1) with NMP as the solvent by hand grinding for 30 min. Experiments were carried out in an Ar-filled glove box. (a) The mixture of Li_2S and PVDF before being ground, (b) the mixture after being ground for 30 min, and (c) the mixture after being vacuum dried for 12 h at 50 °C.

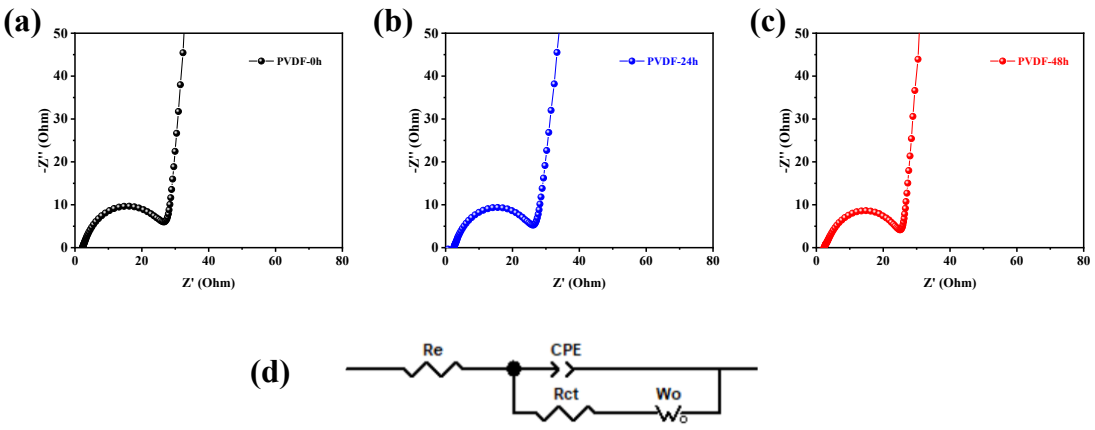


Figure S 3.4 The Nyquist plots of experimentally measured data (dots) and fitting results (lines) of (a) **PVDF-0h**, (b) **PVDF-24h**, and (c) **PVDF-48h**. (d) shows the equivalent Randles circuit used for the fitting, where R_e is the resistance of the electrolyte solution, R_{ct} is the charge transfer resistance, *CPE* is the capacitance, and W_o is the Warburg impedance.

Table S 3.1 Resistances of cathodes calculated from the EIS data in **Figure S 3.4**.

Cathode	Resistance (Ω)	
	R_e	R_{ct}
PVDF-0h	2.3	27.0
PVDF-24h	2.5	25.7
PVDF-48h	2.5	24.9

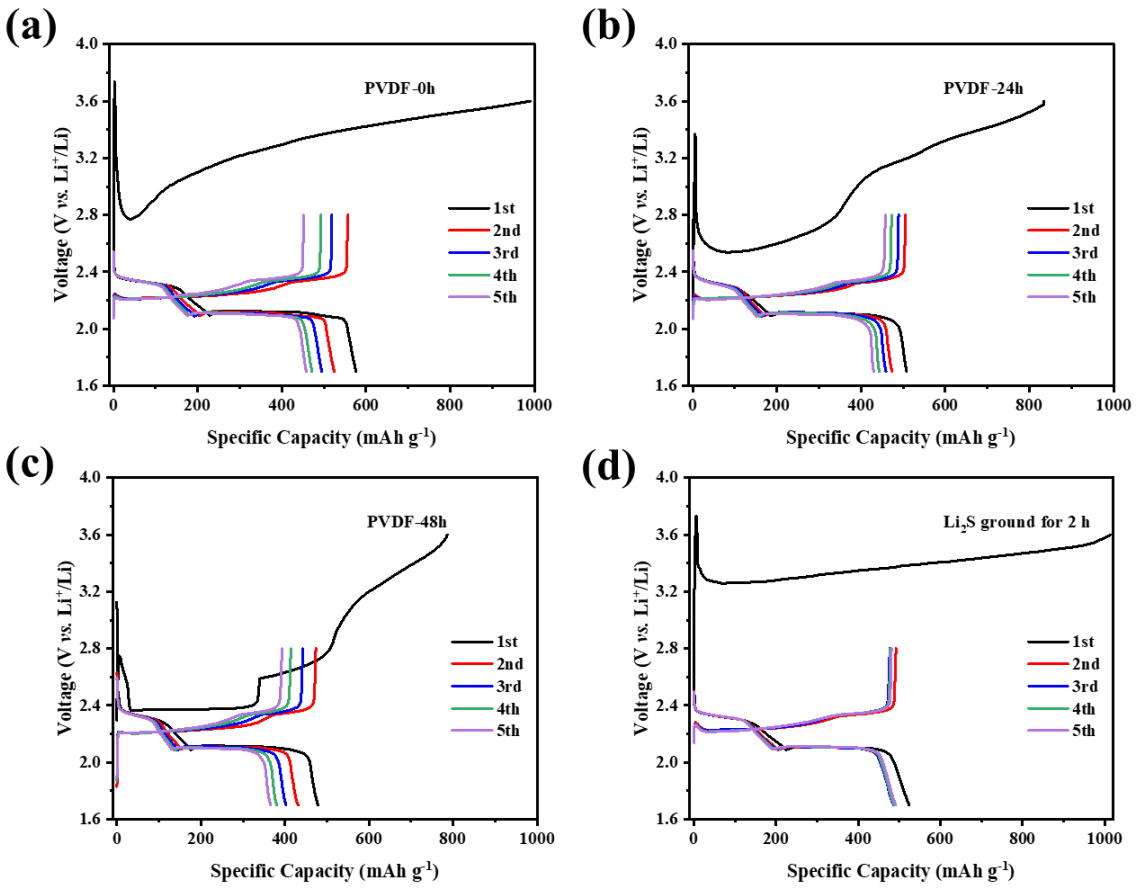


Figure S 3.5 The charge/discharge curves of the first five cycles of (a) **PVDF-0h**, (b) **PVDF-24h**, (c) **PVDF-48h** and (d) a battery using Li_2S ground for 2 h. All the electrochemical tests were carried out at 0.1 C (1 C = 1166 mA g^{-1} (Li_2S)) with upper cut-off voltage of 3.6 V for the first charge process and voltage window of 1.7–2.8 V for the following cycles.

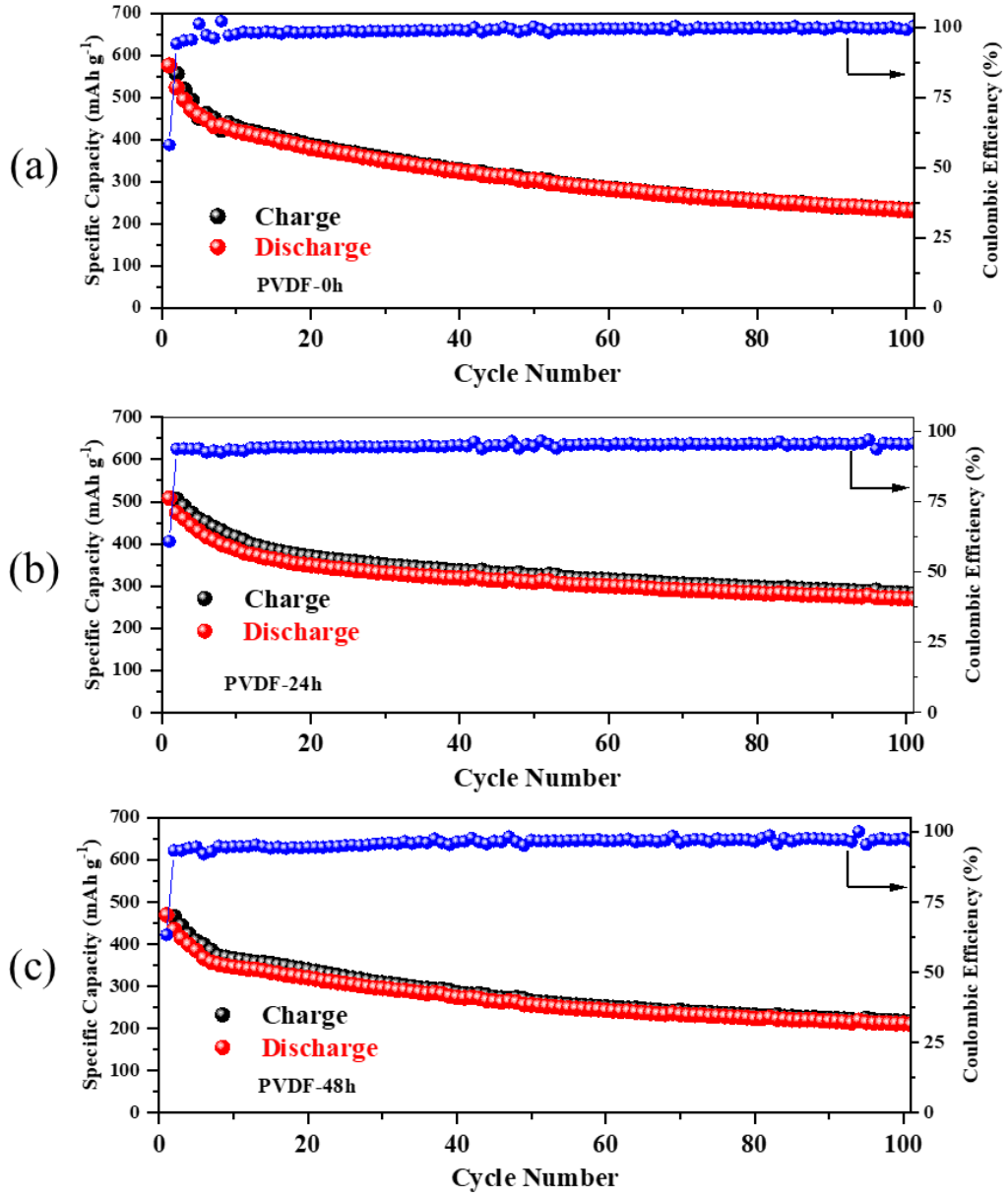


Figure S 3.6 Cycling performance of cathodes at 0.1 C over 100 cycles: (a) **PVDF-0h**, (b) **PVDF-24h**, and (c) **PVDF-48h**.

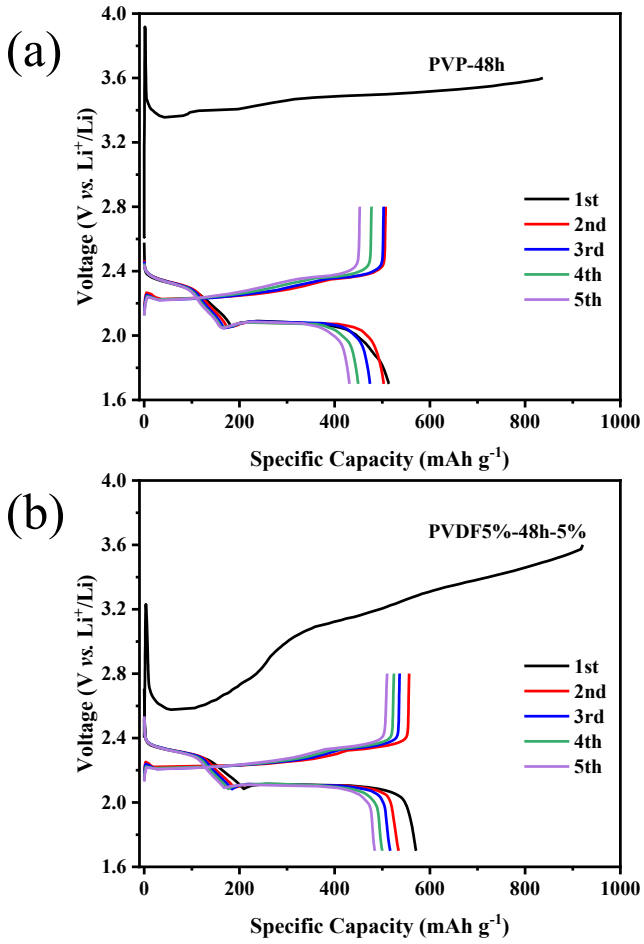


Figure S 3.7 The charge/discharge curves of the first five cycles of (a) **PVP-48h** and (b) **PVDF5%-48h-5%**. All the electrochemical tests were carried at 0.1 C (1 C = 1166 mA g^{-1} (Li_2S)) with upper cut-off voltage of 3.6 V for the first charge process and voltage window of 1.7–2.8 V for the following cycles.

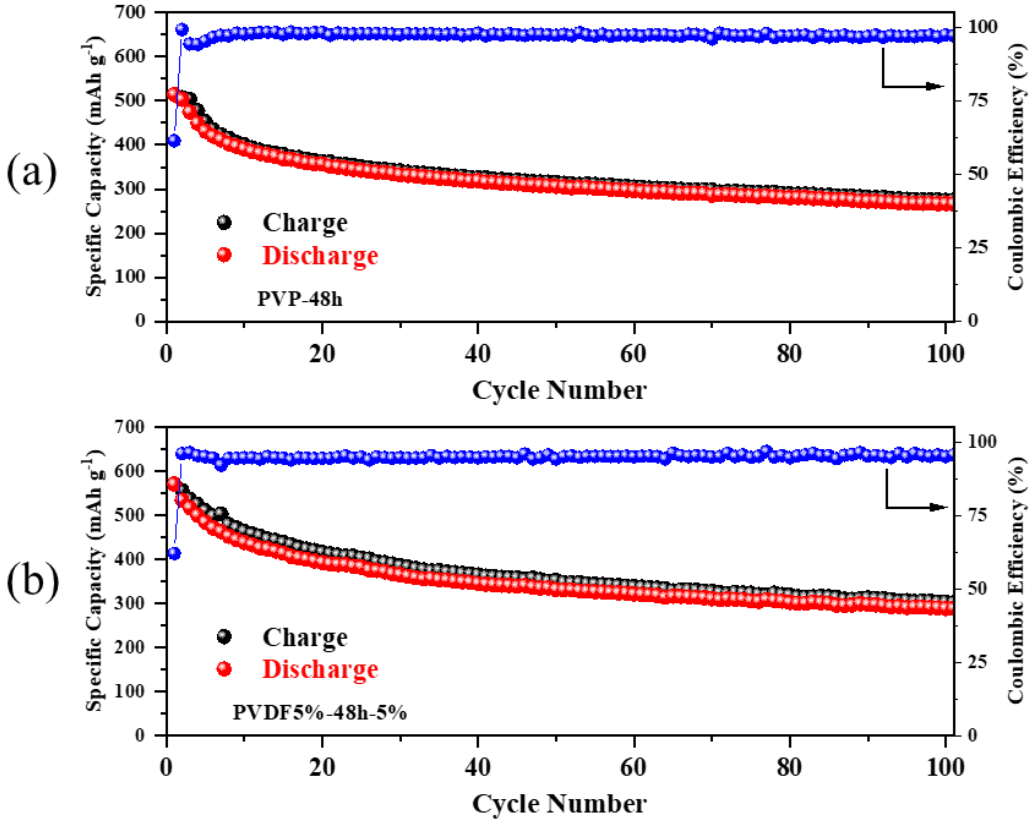


Figure S 3.8 Cycling performance of cathodes at 0.1 C over 100 cycles: (a) **PVP-48h** and (b) **PVDF5%-48h-5%**.

Table S 3.2 Summary of first cycle capacity breakdown for different batteries.

Battery	Charge capacity, mA h g^{-1}	Discharge capacity (2^{nd} plateau/1^{st} plateau), mA h g^{-1}	Theoretical charge capacity required,[a] mA h g^{-1}	Charging efficiency, [b] %	Charging loss, %
PVDF-0h	990.8	576.3 (227.8/348.5 = 1/1.53)	910.6	91.9	8.1
PVDF-24	835.0	508.2 (184.4/323.8 = 1/1.76)	738.1	88.4	11.6
PVDF-48h	786.3	478.6 (175.5/303.1 = 1/1.73)	702.0	89.3	11.7
PVDF5%-48h-5%	921.3	570.8 (208.9/361.9) = 1/1.73)	835.6	90.7	9.3
PVP-48	837.1	531.8 (182.4/349.4 = 1/1.92)	729.6	87.2	12.8

a. Calculated based on the first plateau capacity (× 4);

b. (theoretical charge capacity required/charge capacity) × 100%.

Chapter 4 Zinc Complex-Based Multifunctional Binders for Lithium Sulfide-Based Lithium-Sulfur Batteries

This chapter is based on the following publication:

Z. Huang, Y. Wang, Y. Zhao, Y. Li, *Nanoscale*, **2025**, 17, 18744-18755.

4.1 Introduction

The increasing demand for high-energy-density rechargeable batteries has driven significant efforts to improve conventional lithium-ion batteries (LIBs) and to develop next-generation battery technologies.[34,330–337] Among emerging candidates, lithium-sulfur batteries (LSBs) have attracted considerable attention due to sulfur's natural abundance and their exceptional theoretical specific energy of 2600 W h kg^{-1}, which is approximately five times that of LIBs.[87,338]

Conventional LSBs that use elemental sulfur as the cathode active material, referred to as S-LSBs, rely on metallic lithium or lithium alloy anodes,[297] which are highly reactive with oxygen, nitrogen, and moisture, posing serious safety concerns during manufacturing and raising the production cost of these batteries. Moreover, lithium metal anodes are prone to dendrite formation, which can lead to short circuits, thermal runaway, and even explosions.[339–341] To overcome these limitations, Li_2S has been explored as an alternative cathode material. Its use enables pairing with safer Li-free anode hosts like graphite,[342] silicon,[155] and tin,[163] while offering greater compatibility with existing LIB manufacturing processes, making Li_2S-based LSBs (Li_2S-LSBs) more viable for commercial application.[141,165,343]

Despite these advantages, Li_2S-LSBs introduce new challenges. Notably, Li_2S is highly sensitive to moisture and has a high melting point, which complicates electrode fabrication compared to elemental sulfur-based cathodes.[112,195,344] One critical component affected by these constraints is the binder. Due to the hydrolytic reactivity and basicity of Li_2S, water- or acid-based binders commonly used in S-LSBs are unsuitable. Consequently, the number of binders reported for Li_2S-LSBs remains limited (**Table S 4.1**) in contrast to the wide array available for S-LSBs.[262,345,346] Poly(vinylidene fluoride) (PVDF), the most widely used binder for S-LSBs,[253] is also

the most commonly adopted for Li_2S-LSBs due to its excellent electrochemical stability. However, our recent findings revealed that PVDF undergoes dehydrofluorination when mixed with Li_2S during slurry processing. This reaction consumes Li_2S and degrades PVDF's binding performance, leading to poor electrochemical performance.[344] Furthermore, growing environmental concerns have prompted regulatory bodies, such as the European Union, to propose restrictions or bans on fluorinated polymers including PVDF and PTFE,[273,347] emphasizing the urgent need for fluorine-free binder alternatives for Li_2S-LSBs.

Li_2S-LSBs also face several challenges similar to S-LSBs, including the formation of soluble lithium polysulfides (LPSs) that induce a shuttle effect and result in rapid capacity fading, as well as the inherently poor electronic and ionic conductivities of solid sulfur species, which lead to sluggish reaction kinetics.[112,341] Although various strategies, such as incorporating functional additives into the cathode, have been developed to address these issues in S-LSBs, many are not directly applicable to Li_2S-LSBs due to the above-mentioned high chemical reactivity of Li_2S.[348–354]

In recent years, the design and development of functional binders have been recognized as a critical strategy to address the challenges of both S-LSBs and Li_2S-LSBs. Beyond providing mechanical integrity, advanced binders play an active role in enhancing cathode performance by improving electronic conductivity, immobilizing LPSs, and catalyzing redox reactions. Various innovative approaches, such as chemical functionalization, incorporation of polar or redox-active groups, and the development of hybrid binder systems, have been explored to achieve these goals.[243,355,356] Despite these advances, current binder systems still face significant limitations such as insufficient mechanical resilience at high sulfur loadings, limited long-term chemical stability, and trade-offs between adhesion strength and flexibility. These progresses and remaining challenges have been thoroughly reviewed in a recent article,[295] which highlight the importance of multifunctional binder design for improving the electrochemical stability and cycling life of S-LSBs and Li_2S-LSBs.

Previously, our group demonstrated that zinc acetate diethanolamine ($Zn(OAc)_2$·DEA) complex can serve as a low-cost, fluorine-free binder in both lithium iron phosphate (LFP) batteries

and S-LSBs.[295,357] Its strong binding capability arises from the flexible DEA ligand and multiple hydrogen bonding sites. Importantly, this complex can also function as a LPS trapper to suppress shuttle effect and a catalyst to promote redox reactions in S-LSBs, enhancing cycling stability and rate capability.[295]

Motivated by these results, we explored the feasibility of applying $Zn(OAc)_2$·DEA complex as a binder in Li_2S-LSBs. However, the hydrolytic nature of Li_2S necessitates strictly anhydrous processing with dry reagents and solvents. Initially, we synthesized a $Zn(OAc)_2$·DEA solution in anhydrous ethanol and used it to prepare Li_2S slurries. This approach proved unsuitable, as partially dissolved Li_2S in ethanol rapidly reacted with the $Zn(OAc)_2$·DEA complex, leading to immediate gelation. To resolve this, we attempted to use anhydrous *N*-methyl-2-pyrrolidone (NMP), a widely used battery processing solvent and is known for its stability with Li_2S.[344] However, $Zn(OAc)_2$·DEA exhibited poor solubility in NMP. To address this, we substituted DEA with triethanolamine (TEA), introducing an additional $–CH_2CH_2OH$ group. This modification enabled successful synthesis of $Zn(OAc)_2$·TEA directly in anhydrous NMP, and the resulting solution can be used directly as a binder solution to prepare the Li_2S cathode composite. The $Zn(OAc)_2$·TEA-based cathode demonstrated markedly improved cycling stability at 0.1 C upon initial activation and high rate performance compared to the PVDF-based electrode.

To further improve the solution stability of $Zn(OAc)_2$·TEA and mechanical robustness of the Li_2S-based electrodes, a small amount (10 wt.%) of polyethylenimine (PEI) was added into the $Zn(OAc)_2$·TEA solution. The resulting $Zn(OAc)_2$·TEA/PEI (10%) complex serves as an efficient, fluorine-free binder for Li_2S-LSBs, enabling improved electrode integrity, excellent cycling stability, and high-rate performance.

4.2 Experimental Section

4.2.1 Materials

Lithium sulfide (Li_2S, 99.98% trace metals basis), zinc acetate dihydrate ($Zn(OAc)_2·2H_2O$, ACS reagent, ≥98%), diethanolamine (DEA, ACS reagent, ≥98.5%), triethanolamine (TEA, ≥99.5%), polyethylenimine (PEI, M_w ~25,000 by LS, M_n ~10,000 by GPC, branched), anhydrous ethanol (EtOH, ≤0.003% water), and anhydrous *N*-methyl-2-pyrrolidone (NMP, 99.5%) were purchased from Sigma-Aldrich. Super P (SP) was purchased from IMERYS. Polyvinylidene fluoride (PVDF, M_w ~1,000,000) was from Kynar. The commercial anhydrous EtOH was further dried using 3 Å molecular sieves. Anhydrous NMP was further dried using lithium metal and filtered through a PTFE syringe filter before use. All other chemicals were used as received without further purification.

4.2.2 Synthesis of $Zn(OAc)_2$·DEA, $Zn(OAc)_2$·TEA and $Zn(OAc)_2$·TEA/PEI Complex Solution

Zinc acetate dihydrate ($Zn(OAc)_2·2H_2O$) was first vacuum-dried heated at 100 °C for 12 h under vacuum to remove coordinated water, yielding anhydrous $Zn(OAc)_2$.

To prepare the $Zn(OAc)_2$·DEA complex, 459 mg (2.50 mmol) of $Zn(OAc)_2$ was dissolved in 5 mL of anhydrous EtOH. Separately, a DEA solution was prepared by dissolving 263 mg (2.50 mmol) of DEA in 2 mL of EtOH, which was added dropwise to the $Zn(OAc)_2$/EtOH solution under stirring at 50 °C. After complete dissolution and formation of a clear, colorless solution, EtOH was added to bring the final volume to 10 mL, yielding a 0.25 M $Zn(OAc)_2$·DEA complex solution.

To prepare the $Zn(OAc)_2$·TEA complex, 459 mg (2.50 mmol) of $Zn(OAc)_2$ was dispersed in 5 mL of NMP ($Zn(OAc)_2$ is insoluble on NMP). Separately, a TEA solution was prepared by dissolving 373 mg (2.50 mmol) of TEA in 2 mL of NMP, which was added dropwise to the $Zn(OAc)_2$ mixture under stirring at room temperature for 2 h. A clear, colorless $Zn(OAc)_2$·TEA complex solution was obtained, which was then diluted with additional NMP to a total volume of 10 mL to achieve a concentration of 0.25 M.

To prepare $Zn(OAc)_2$·TEA/PEI complex solutions with varying PEI contents (5, 10, 15, and 25 wt.% based on the total mass of $Zn(OAc)_2$·TEA + PEI), designated as $Zn(OAc)_2$·TEA/PEI (5%),

$Zn(OAc)_2$·TEA/PEI (10%), $Zn(OAc)_2$·TEA/PEI (15%) and $Zn(OAc)_2$·TEA/PEI (25%), the appropriate amount of PEI solution in NMP was added to the $Zn(OAc)_2$·TEA complex solution, followed by stirring for 12 h.

All the procedures were carried out inside an argon-filled glove box with O_2 and H_2O concentrations maintained below 0.5 ppm.

4.2.3 Synthesis of Li_2S_6

The Li_2S_6 solution was obtained by heating a mixture of Li_2S and elemental sulfur (S) with a molar ratio of 1:5 in a mixture solvent of 1,2-dimethoxyethane (DME) and 1,3-dioxolane (DOL) (*v*/*v* = 1:1) at 80 °C for 12 h under stirring. The Li_2S_6 solution was diluted to 0.5 M for further use.

4.2.4 Fabrication of Lithium Sulfide Electrodes

A mixture of Li_2S, Super P, and $Zn(OAc)_2$·TEA or $Zn(OAc)_2$·TEA/PEI at a mass ratio of 70:20:10 in anhydrous NMP was manually ground using a mortar for 30 min inside an argon-filled glove box with O_2 and H_2O concentrations maintained below 0.5 ppm. The resulting slurry was then applied to a carbon-coated aluminum foil using bar coating and dried at 50 °C under reduced pressure for 12 h inside the glovebox. After drying, the coated foil was punched into 12 mm diameter discs with a diameter of 12 mm and stored in sealed vials inside the glovebox. The Li_2S loading was 1.0–1.2 mg cm^{-2} for typical cells and ~4 mg cm^{-2} for high loading cells.

For comparison, control electrodes were fabricated using PVDF as the binder instead of $Zn(OAc)_2$·TEA or $Zn(OAc)_2$·TEA/PEI, following the same procedure.

4.2.5 Electrochemical Measurements

2032 coin-type Li_2S-LSBs were assembled using the above prepared Li_2S cathodes, lithium metal anodes (0.45 mm thick foils with a diameter of 15.6 mm), Celgard 2400 separators, and an electrolyte consisting of 1.0 M lithium bis(trifluoromethanesulfonyl)imide (LiTFSI) in a 1:1 volume ratio of 1,3-dioxolane (DOL) and dimethoxyethane (DME), containing 2 wt.% $LiNO_3$ as the electrolyte inside an argon-filled glovebox. The electrolyte volume was 24 μL. For high-loading Li_2S electrochemical performance tests, carbon paper was used as the substrate, and the electrolyte volume was 60 μL. The batteries were assembled using a manual hydraulic press at 1000 psi for 5 seconds. The electrochemical performance of the batteries was assessed through galvanostatic

measurements performed on a Land 2001A battery test system. All capacities and cycling rates are calculated based on the mass of Li_2S, with 1 C defined as 1166 mA g^{-1} based on the theoretical capacity of Li_2S. Electrochemical impedance spectra (EIS) were recorded at the open-circuit potential (OCP) using a Bio-logic electrochemical potentiostat/galvanostat (VSP) over a frequency range of 1000 kHz to 0.1 Hz, with an alternating current (AC) amplitude of 10 mV. Cyclic voltammetry (CV) tests were carried out by initial charging between 1.7 and 4.0 V for the first cycle and the following cycles between 1.7 and 2.8 V at a scan rate of 0.025 mV s^{-1}.

4.2.6 Characterization

XRD measurements of Li_2S samples were carried out on a Bruker D8 Discover X-ray diffractometer using Cu K_α radiation (λ=1.5418 Å). XRD samples were covered with Kapton tape to prevent them from absorbing moisture in the ambient air. UV-Vis absorption spectra were measured on a Cary 7000 universal measurement spectrophotometer (UMS). SEM images were taken using a Zeiss Sigma HD microscope.

4.3 Results and Discussion

4.3.1 Preparation of $Zn(OAc)_2$·TEA Complex

Previously, the $Zn(OAc)_2$·DEA complex, synthesized from $Zn(OAc)_2·2H_2O$ in a mixture of ethanol and water, was utilized as a multifunctional binder for S-LSBs, demonstrating superior LPS trapping capability for maintaining long-term cycling stability and an effective catalytic effect on the redox reactions of sulfur species to achieve high specific capacity and high rate capacibity.[295] However, this binder solution cannot be directly applied to Li_2S cathode preparation due to the high moisture sensitivity of Li_2S, which readily hydrolyzes to form LiOH. This necessitates the use of an anhydrous solvent to make the binder solution. While the $Zn(OAc)_2$·DEA complex can be dissolved in anhydrous ethanol at elevated temperatures (~50 °C), its limited solubility at room temperature presents practical difficulties. Moreover, Li_2S exhibits partial solubility in ethanol, and the resulting dissolved species react rapidly with Zn^{2+} in the complex, displacing acetate ligands and forming insoluble Zn-S species.[295] This leads to immediate gelation of the slurry, severely impairing electrode fabrication and processing.

To overcome these limitations, NMP was selected as the processing solvent due to its chemical inertness toward Li_2S.[344] However, $Zn(OAc)_2$·DEA is insoluble in NMP, limiting its practical use under these conditions. To address this issue, triethanolamine (TEA) was employed as an alternative ligand. The presence of an additional hydroxyl group in TEA renders the resulting $Zn(OAc)_2$·TEA complex soluble in NMP, as shown **Figure 4.1** (a). The XRD pattern of the vacuum-dried $Zn(OAc)_2$·TEA sample displayed distinct diffraction peaks, indicating its high crystallinity (**Figure 4.1** (b)). The XRD pattern of the Li_2S/SP/$Zn(OAc)_2$·TEA sample obtained by drying the slurry (**Figure 4.1** (c)) further confirms the homogeneous dispersion of $Zn(OAc)_2$·TEA within the composite.

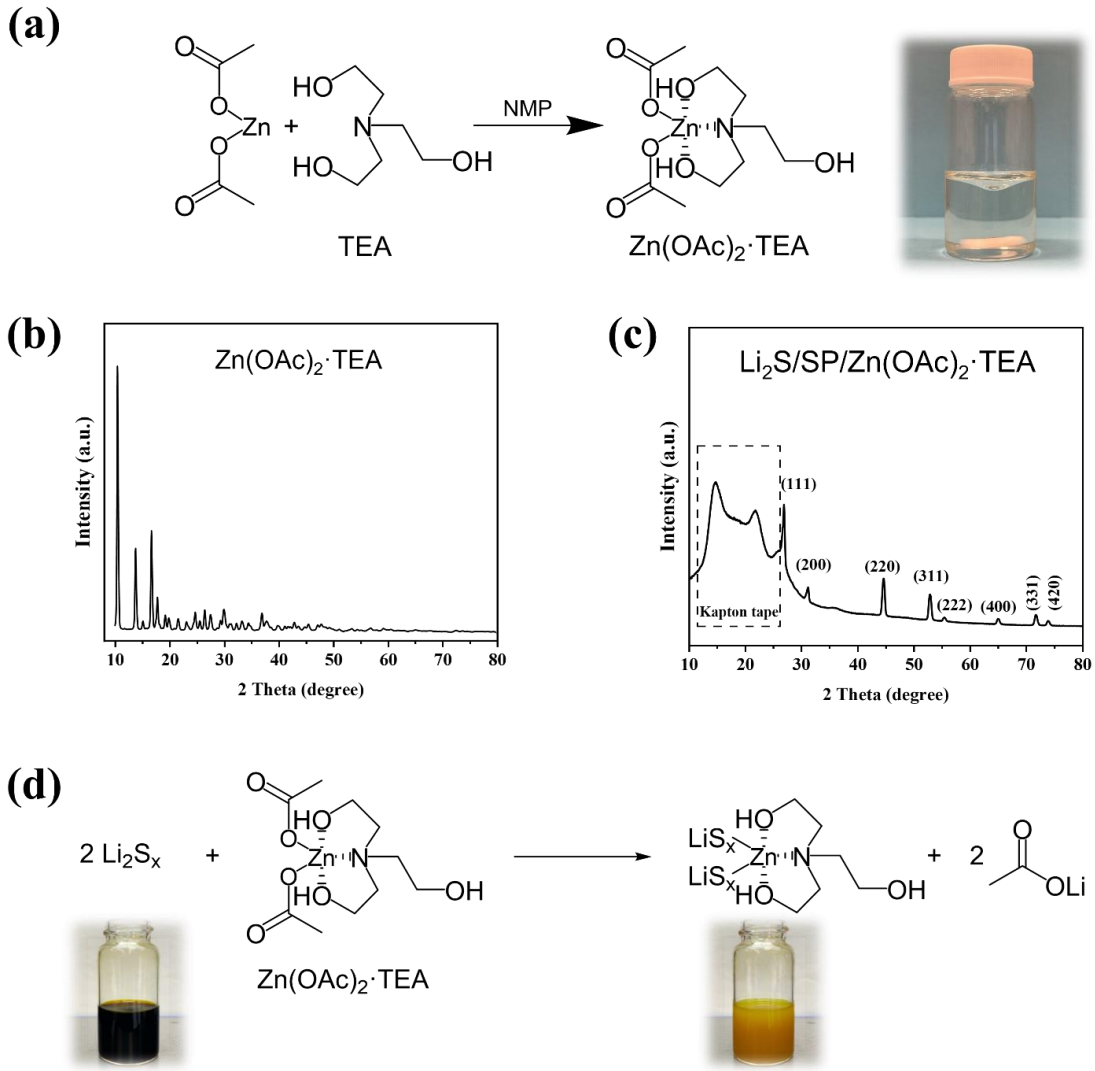


Figure 4.1 (a) $Zn(OAc)_2$·TEA prepared by mixing anhydrous $Zn(OAc)_2$ and TEA mixed in NMP. (b) XRD pattern of vacuum-dried $Zn(OAc)_2$·TEA. (c) XRD pattern of Kapton tape-covered dried Li_2S/SP/$Zn(OAc)_2$·TEA mixture. (d) Reaction between $Zn(OAc)_2$·TEA and lithium polysulfides (Li_2S_x, where x = 4–8), with photographs showing a Li_2S_6 solution before and after the addition of 0.5 molar equivalents of $Zn(OAc)_2$·TEA inside a glove box. The dark red Li_2S_6 solution turned into a suspension with brown precipitates, indicating complete reaction.

The reaction between $Zn(OAc)_2$·DEA and LPSs has been documented in the previous study, which demonstrated that two polysulfide chains can replace the two acetate groups coordinated to Zn^{2+} in $Zn(OAc)_2$·DEA.[295] Given the close structural similarity between $Zn(OAc)_2$·TEA and $Zn(OAc)_2$·DEA, it is reasonable to expect comparable polysulfide-trapping capability from $Zn(OAc)_2$·TEA. To confirm this, an LPS trapping experiment was conducted by adding 2 molar equivalents of $Zn(OAc)_2$·TEA to 1 molar equivalent of Li_2S_6 dissolved in a DOL/DME (v/v = 1 : 1)

electrolyte solvent (**Figure 4.1** (d)). Upon the addition of $Zn(OAc)_2$·TEA, the characteristic dark color of Li2S6 quickly faded, accompanied by the formation of brown precipitates. This behavior closely resembles the previously observed reaction between $Zn(OAc)_2$·DEA and LPSs, suggesting that $Zn(OAc)_2$·TEA readily captures LPSs through a similar mechanism. The formation of insoluble $Zn(S_xLi)_2$·TEA species (x = 4–8) is expected to effectively suppress the polysulfide shuttle effect. The molar trapping capacity of $Zn(OAc)_2$·TEA toward LPS was determined via UV-vis spectroscopy to be 1.98 mol LPS per mol $Zn(OAc)_2$·TEA as detailed in **Figure S 4.1** and **Table S 4.2** This result confirms the strong LPS-trapping capability of $Zn(OAc)_2$·TEA, with each binder unit effectively coordinating with two LPS species via interactions with Zn^{2+} centers—consistent with previous findings for the $Zn(OAc)_2$·DEA system.[295]

4.3.2 Electrochemical Performance of $Zn(OAc)_2$·TEA-Based Li_2S Electrode

The galvanostatic cycling performance of Li_2S batteries employing $Zn(OAc)_2$·TEA and PVDF as binders is presented in **Figure 4.2** (a–e). During the initial activation process, the cells were cycled at a current density of 0.05 C (1 C = 1166 mA g^{-1}) (**Figure 4.2** (a)). Both electrodes exhibited a pronounced overpotential spike at the onset of charging, followed by a gradual voltage decline, a behavior characteristic of Li_2S-LSBs.[344] The $Zn(OAc)_2$·TEA-based electrode displayed a lower activation spike of 3.55 V compared to that of the PVDF-based electrode (3.69 V), indicating that $Zn(OAc)_2$·TEA catalyzes Li_2S activation by lowering the energy barrier. Additionally, the $Zn(OAc)_2$·TEA-based electrode exhibited higher post-spike voltages compared to the PVDF-based counterpart. This is attributed to the strong LPS-trapping ability of $Zn(OAc)_2$·TEA, which immobilizes LPSs generated on the surface of Li_2S particles, preventing exposure of interior Li_2S to the electrolyte. As a result, further oxidation of Li_2S in the particle interior is hindered. In contrast, in the PVDF-based electrode, LPSs dissolve into the electrolyte, absorbing solvent to lower the activation barrier,[104] and diffuse away from the particle surface, thereby exposing fresh Li_2S for continued oxidation.

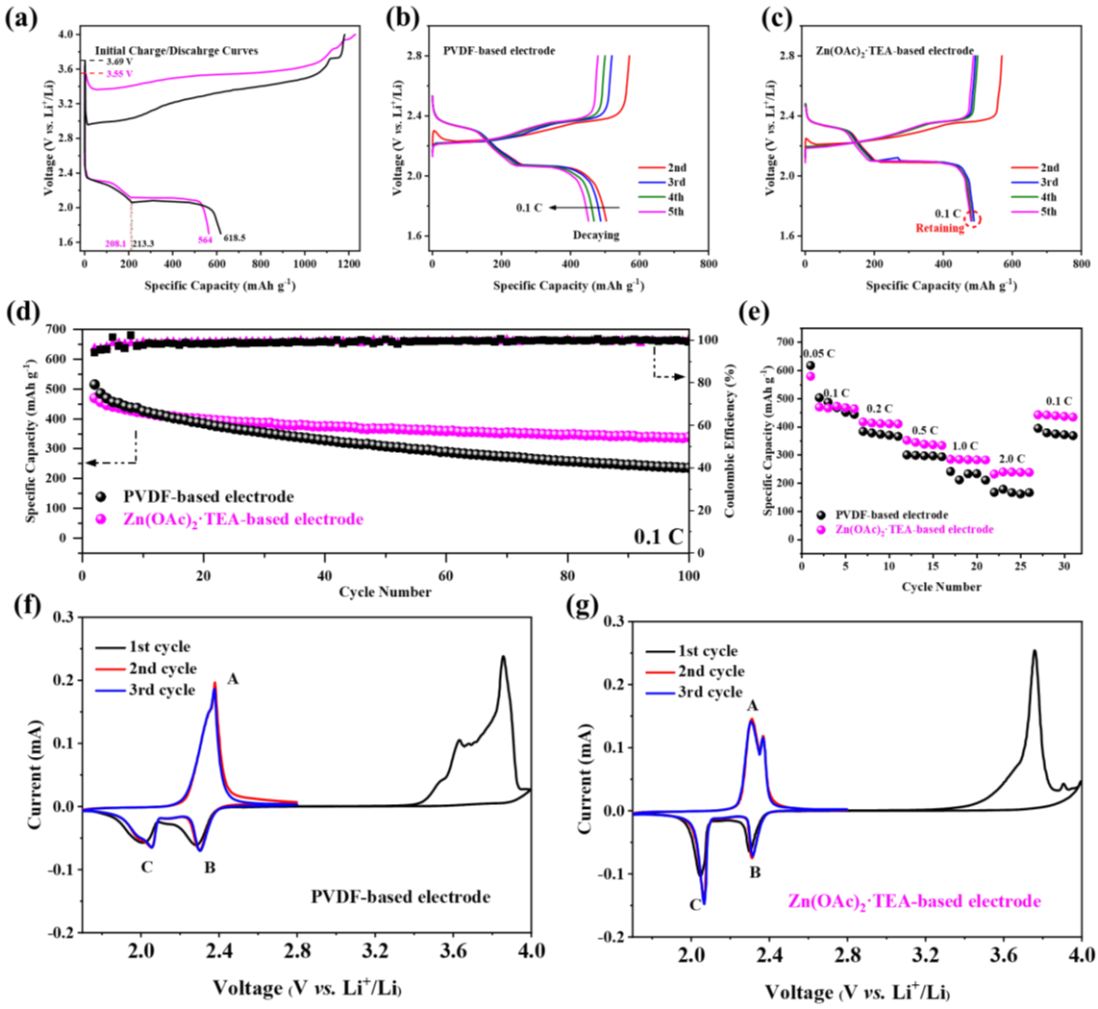


Figure 4.2 Electrochemical performance of Li_2S electrodes using PVDF and $Zn(OAc)_2$·TEA as binders. (a) First-cycle charge/discharge curves at 0.05 C. (b, c) Initial five charge/discharge cycles of PVDF- and $Zn(OAc)_2$·TEA-based electrodes, respectively. (d) Cycling performance at 0.1 C. (e) Rate performance at various current densities. (f, g) Cyclic voltammetry (CV) curves of PVDF- and $Zn(OAc)_2$·TEA-based electrodes, respectively. Electrodes were scanned from 1.7 to 4.0 V for the first cycle, and from 1.7 to 2.8 V for subsequent cycles at a scan rate of 0.025 mV s^{-1}.

During the subsequent discharge, both electrodes delivered similar capacities in the first plateau (208.1 and 213.3 mA h g^{-1} for $Zn(OAc)_2$·TEA and PVDF, respectively), corresponding to the reduction of S_8 into long-chain polysulfides (Li_2S_x, x = 4–8). However, in the second plateau, which involves the stepwise conversion of Li_2S_4 to Li_2S_2 and finally Li_2S, the $Zn(OAc)_2$·TEA-based cathode exhibited a significantly shorter plateau and a lower overall discharge capacity (564.0 mA h g^{-1} *vs.* 618.5 mA h g^{-1} for PVDF). This lower capacity is attributed to the immobilization of long-

chain LPSs by $Zn(OAc)_2$·TEA, which restricts their diffusion and uniform distribution within the cathode, thereby impeding the solid-state conversion of Li_2S_2 to Li_2S. In contrast, in the PVDF-based cathode, the dissolved LPSs diffuse more freely, enabling better distribution and more complete conversion of Li_2S_2 to Li_2S. Unlike the thermally infiltrated S@SP nanocomposites used in $Zn(OAc)_2$·DEA-based S-LSBs, where sulfur is uniformly confined within mesoporous carbon, facilitating the Li_2S_2-to-Li_2S conversion,[295] the present study uses Li_2S/SP mixture made from physically ground commercial Li_2S powders and Super P, resulting in micrometer-sized Li_2S particles located outside the Super P network. In this case, the inability of PVDF to trap LPSs incidentally assists in Li_2S particle size reduction and a more complete discharge.

Despite its lower initial discharge capacity, the $Zn(OAc)_2$·TEA-based cathode demonstrated markedly improved cycling stability at 0.1 C in subsequent cycles (**Figure 4.2** (b) and (c)). While the PVDF-based cathode experienced a sharp decline from 515.4 mA h g^{-1} in the second cycle to 235.8 mA h g^{-1} by the 100th cycle (45.8% retention), the $Zn(OAc)_2$·TEA-based electrode showed a much slower decay, decreasing from 470.3 to 339.2 mA h g^{-1} (72.1% retention), highlighting the stabilizing effect of $Zn(OAc)_2$·TEA through effective LPS trapping.

Additionally, the $Zn(OAc)_2$·TEA-based electrode exhibited superior rate performance compared to its PVDF-based counterpart, as shown in **Figure 4.2** (g). Specifically, the capacity retention at 2 C relative to 0.1 C was 51% for the $Zn(OAc)_2$·TEA-based electrode, significantly higher than the value of 33% observed for the PVDF-based electrode. This enhanced rate capability suggests improved redox kinetics in the $Zn(OAc)_2$·TEA-based system, likely attributed to the catalytic effect of the complex, similar to the behavior previously reported for its analogue, $Zn(OAc)_2$·DEA.[295]

The cyclic voltammetry (CV) profiles of the $Zn(OAc)_2$·TEA-based and PVDF-based Li_2S electrodes are shown in **Figure 4.2** (f) and (g). Notably, their initial CV curves differ significantly from those observed in subsequent cycles. In both cases, the first CV scan was performed from the open-circuit voltage (OCV) up to 4.0 V to initiate the electrochemical activation of the Li_2S cathode. Due to the presence of a passivating Li_2O/LiOH surface layer and the high crystallinity and purity of Li_2S, the initial charge process exhibits a distinct electrochemical signature characterized by a

high overpotential.[165,175,176,200] This activation behavior is characteristic of Li_2S-LSBs and is not observed in conventional S-LSBs. During the first charge, the PVDF-based electrode exhibited an onset potential of 3.45 V, followed by a broad peak at 3.63 V, and reached a maximum current at 3.86 V. In contrast, the $Zn(OAc)_2$·TEA-based electrode showed a lower onset potential of 3.34 V and a sharper oxidation peak at 3.76 V, indicating a reduced energy barrier for Li_2S activation. This improvement is likely due to the catalytic effect of Zn^{2+} centers in the $Zn(OAc)_2$·TEA complex, which can accommodate LPS intermediates and facilitate their oxidation.[295] However, unlike the PVDF-based electrode, this electrode lacked a distinct first oxidation peak and instead displayed a shoulder before the main peak, consistent with LPS immobilization raising the activation energy for oxidation of Li_2S near the surface.

In the subsequent discharge process, the $Zn(OAc)_2$·TEA-based electrode exhibited much sharper and slightly higher-voltage reduction peaks (2.31 and 2.07 V) compared to the PVDF-based electrode (2.30 and 2.05 V), indicating lower polarization and enhanced redox kinetics. During the second charge, the PVDF electrode exhibited a broad, merged oxidation peak at 2.38 V, whereas the $Zn(OAc)_2$·TEA-based electrode displayed two distinct peaks at lower potentials of 2.31 and 2.37 V. Notably, the first peak, corresponding to the oxidation of Li_2S to long-chain polysulfides (Li_2S_x), was more prominent than the second, associated with the further conversion of Li_2S_x to elemental sulfur (S_8), suggesting that the $Zn(OAc)_2$·TEA binder effectively promotes the initial oxidation step.

Overall, the CV results demonstrate that the $Zn(OAc)_2$·TEA binder exhibits notable catalytic effects, effectively lowering the activation barrier during the initial charge and accelerating the redox reactions of sulfur species in subsequent cycles. Compared to the PVDF binder, it results in reduced polarization and more well-defined redox features, underscoring its superior ability to facilitate conversion reactions of sulfur species.

To evaluate the redox catalytic activity of $Zn(OAc)_2$·TEA, Tafel slope analysis was performed using CV data. This technique is widely used to assess the kinetics of electrochemical reactions and estimate charge-transfer resistance by analyzing the relationship between overpotential and logarithmic current density.[358,359] The second CV cycle was selected for analysis, as the first cycle

in Li_2S-based batteries typically involves an activation process that does not reflect stabilized electrochemical behavior. Tafel slopes were extracted from the linear regions of the overpotential versus log(current) plots near the major redox peaks, as shown in **Figure S 4.2** and summarized in **Table S 4.3**. The results clearly demonstrate that the $Zn(OAc)_2$·TEA-based electrode exhibits significantly lower Tafel slopes compared to the control, indicating improved charge-transfer kinetics and enhanced redox catalytic activity.

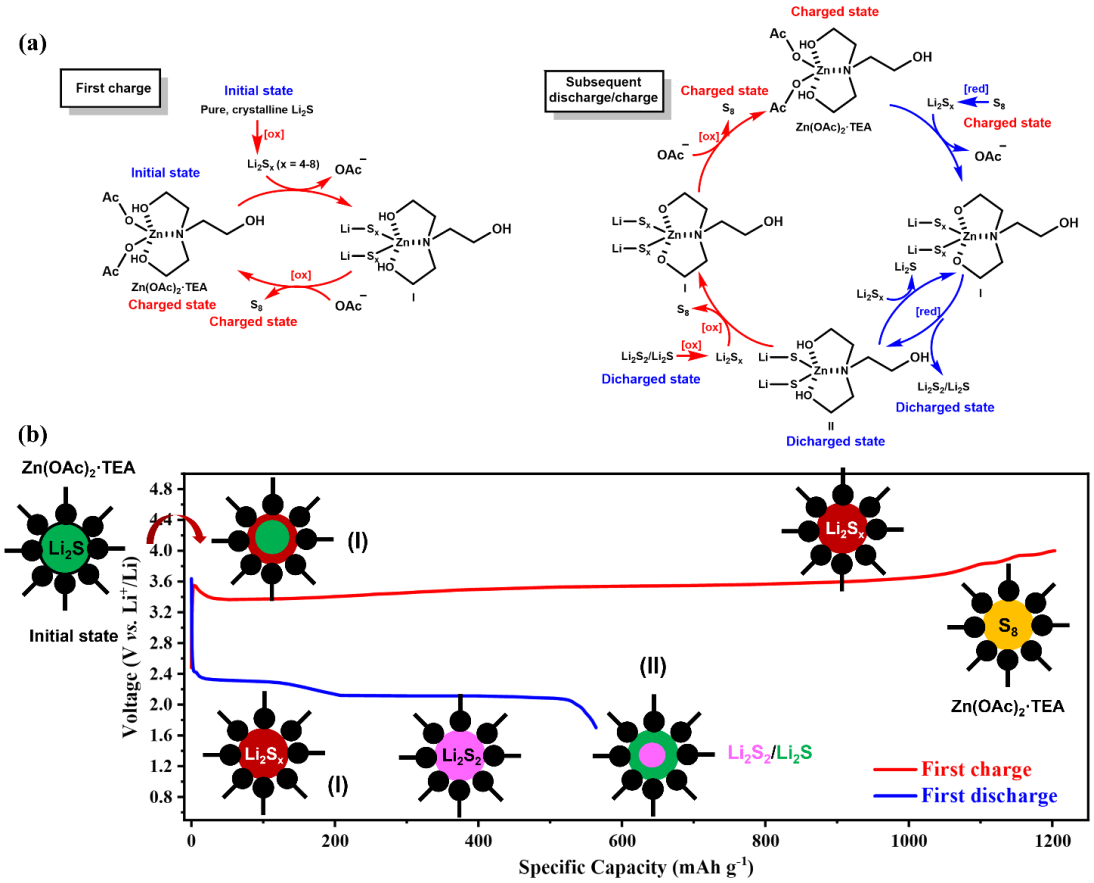


Figure 4.3 (a) Proposed polysulfide trapping cycles of $Zn(OAc)_2$·TEA during the initial charge and subsequent discharge/charge processes in the $Zn(OAc)_2$·TEA-based Li_2S electrode ([red]: reduction; [ox]: oxidation). (b) Schematic representation of the structural evolution of Li_2S particles during the first charge/discharge cycle, corresponding to the stages illustrated in (a).

These results collectively demonstrate that $Zn(OAc)_2$·TEA serves not only as a structural binder but also as a multifunctional additive that enhances battery performance through LPS trapping and redox catalysis. Its ability to immobilize LPSs helps suppress the shuttle effect and improves cycling stability, while its redox-active Zn^{2+} centers promote the initial activation of Li_2S

and facilitate subsequent redox reactions. These combined effects provide significant advantages over the conventional PVDF binder. The improved electrochemical behavior of $Zn(OAc)_2$·TEA-based electrodes is believed to follow a mechanism analogous to that previously proposed for $Zn(OAc)_2$·DEA in S-LSBs.[295] A modified version tailored to the $Zn(OAc)_2$·TEA-based Li_2S cathode is illustrated in **Figure 4.3** (a), highlighting the trapping and release of sulfur species by the Zn^{2+} centers during the charge and discharge processes.

A key distinguishing feature of Li_2S-based cells is the initial charging process, which requires overcoming a high activation barrier due to the material's intrinsic crystallinity and the presence of a passivating LiOH/Li_2O surface layer (**Figure 4.3** (b)). The $Zn(OAc)_2$·TEA molecules in contact with Li_2S particles can react with nascent LPSs and catalyze their oxidation, thereby reducing the overpotential compared to PVDF. However, because the trapped LPSs remain immobilized and do not dissolve into the electrolyte, subsequent oxidation of interior Li_2S becomes difficult, leading to elevated post-spike charging voltages.

During discharge, particularly in the later stage of the second plateau, significant volume expansion occurs as Li_2S_2 is reduced to Li_2S. The structural preservation effect of the $Zn(OAc)_2$·TEA binder inhibits this conversion near the particle core, where the intrinsically low electronic and ionic conductivity of Li_2S_2 limits charge transport. As a result, the full transformation to Li_2S is impeded, leading to a lower discharge capacity compared to the PVDF-based electrode.

4.3.3 Modification of $Zn(OAc)_2$·TEA with PEI

Although $Zn(OAc)_2$·TEA exhibits significantly improved solubility in NMP compared to $Zn(OAc)_2$·DEA, it was observed to crystallize upon standing for more than 12 h (**Figure S 4.3**). This instability presents challenges for practical application and may compromise cathode quality due to potential aggregation of $Zn(OAc)_2$·TEA during electrode drying. In fact, at high current rates (e.g., 2 C), the battery exhibited signs of overcharging (**Figure S 4.4**), suggesting poor structural integrity of the cathode.

To address this issue, polyethylenimine (PEI) was introduced into the $Zn(OAc)_2$·TEA solution in NMP at various wt.% relative to $Zn(OAc)_2$·TEA/PEI (5%), $Zn(OAc)_2$·TEA/PEI (10%), $Zn(OAc)_2$·TEA/PEI (15%), and $Zn(OAc)_2$·TEA/PEI (25%). The rationale is that the nitrogen atoms

in PEI can coordinate with Zn^{2+} centers in $Zn(OAc)_2$·TEA, analogous to the coordination observed with the nitrogen atoms in TEA and DEA. Since Zn^{2+} ions can accommodate up to six ligands,[360] it is plausible that one or two PEI-derived nitrogen atoms can bind to Zn^{2+}. In solution and during electrode drying, PEI may inhibit the crystallization or aggregation of $Zn(OAc)_2$·TEA. In the solid state, its polymeric structure can act as a cross-linker, facilitating the formation of a robust three-dimensional binder network that reinforces the structural integrity and stability of the cathode (**Figure 4.4**).

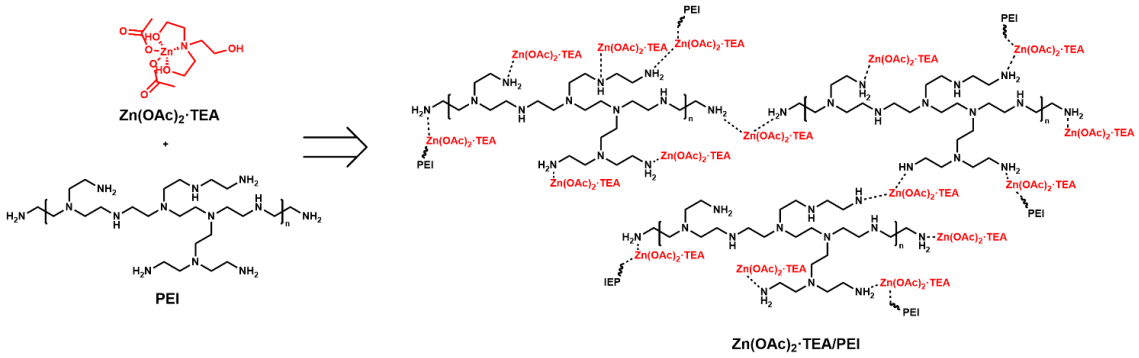


Figure 4.4 Schematic illustration of the formation of the $Zn(OAc)_2$·TEA/PEI binder, where the addition of PEI enables the establishment of a three-dimensional (3D) network through coordination between Zn^{2+} ions in $Zn(OAc)_2$·TEA and nitrogen atoms in PEI.

It was found that white precipitates still formed in the $Zn(OAc)_2$·TEA/PEI (5%) solution after 12 h of storage, whereas solutions containing 10% or more PEI showed no visible precipitation after 12 h, as shown in **Figure S 4.3**, and remained stable even upon storage for several months.

4.3.4 Electrochemical Performance of $Zn(OAc)_2$·TEA/PEI-Based Li_2S Electrodes

Li_2S electrodes were fabricated using three binder solutions with varying PEI content: $Zn(OAc)_2$·TEA/PEI (10%), $Zn(OAc)_2$·TEA/PEI (15%), and $Zn(OAc)_2$·TEA/PEI (25%). Their galvanostatic charge/discharge profiles are shown in **Figure 4.5** (a-c). During the initial activation at 0.05 C, all three electrodes exhibited charge curves similar to that of the $Zn(OAc)_2$·TEA-based system (**Figure 4.2** (c)). However, in the subsequent discharge, they delivered specific capacities of 596.7, 590.0, and 610.0 mA h g^{-1}, respectively, each exceeding the 564.0 mA h g^{-1} capacity observed for the $Zn(OAc)_2$·TEA-based electrode. This improvement may be attributed to improved contact between Li_2S and Super P particles in the presence of flexible PEI chains.

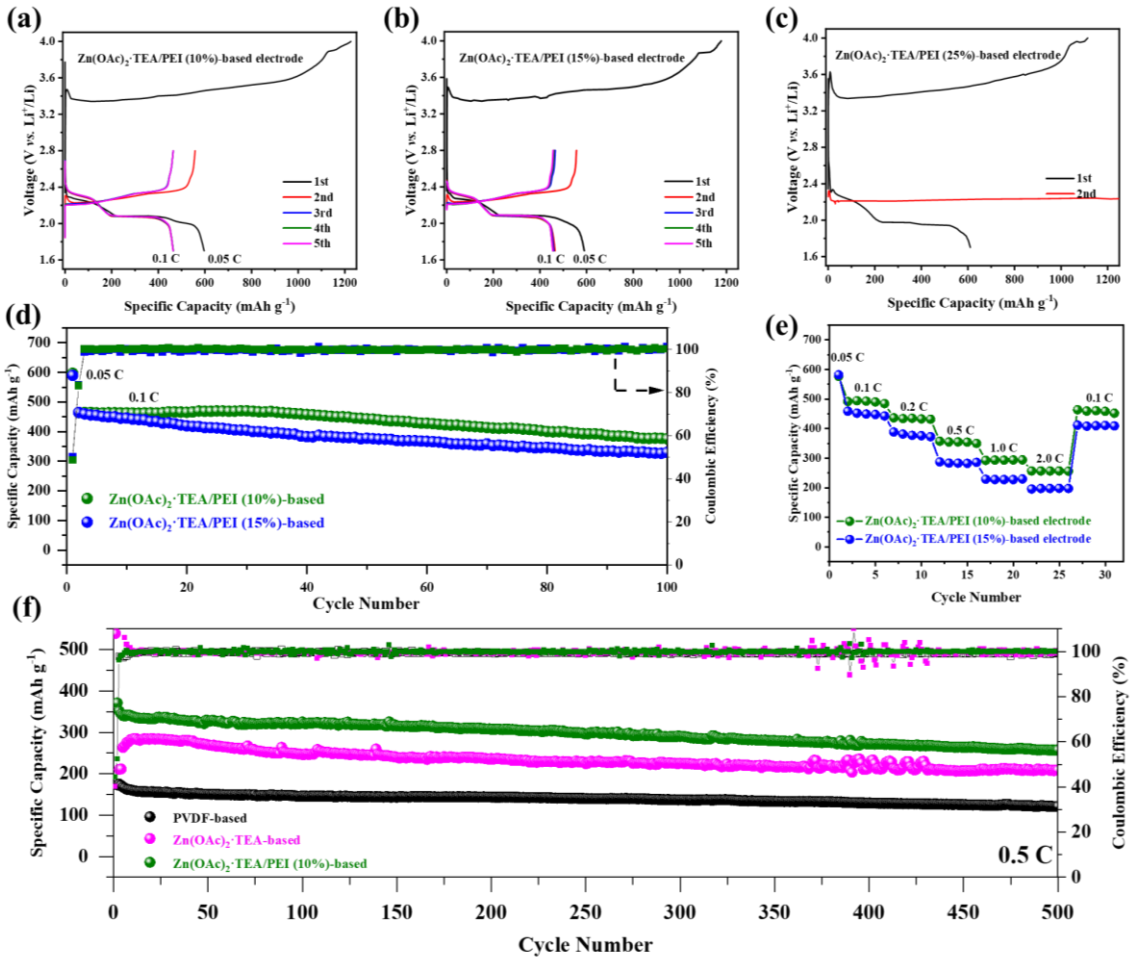


Figure 4.5 Electrochemical performance of Li_2S electrodes using PVDF and various $Zn(OAc)_2$·TEA/PEI binders. (a) Initial five charge/discharge curves of $Zn(OAc)_2$·TEA/PEI (10%)-based electrode. (b) Initial five charge/discharge curves of $Zn(OAc)_2$·TEA/PEI (15%)-based electrode. (c) Initial charge/discharge curves $Zn(OAc)_2$·TEA/PEI (25%)-based electrode. (d) Cycling performance of the $Zn(OAc)_2$·TEA/PEI (10%)- and $Zn(OAc)_2$·TEA/PEI (15%)-based electrodes at 0.1 C. (e) Rate performance of the $Zn(OAc)_2$·TEA/PEI (10%)- and $Zn(OAc)_2$·TEA/PEI (15%)-based electrodes at various rates. (f) Long-term cycling performance of PVDF-, $Zn(OAc)_2$·TEA-, and $Zn(OAc)_2$·TEA/PEI (10%)-based electrodes at 0.5 C, which were all activated at 0.05 C in the first cycle.

At 0.1 C in the second cycle, the $Zn(OAc)_2$·TEA/PEI (10%)- and $Zn(OAc)_2$·TEA/PEI (15%)-based electrodes exhibited discharge profiles comparable to the $Zn(OAc)_2$·TEA-based electrode. However, the $Zn(OAc)_2$·TEA/PEI (25%)-based electrode showed signs of overcharging, suggesting mechanical or structural degradation within the cathode. A similar overcharging behavior was

observed in the electrode using PEI alone as the binder (**Figure S 4.5**), indicating that PEI lacks sufficient binding strength to preserve cathode integrity. In the 25% PEI formulation, excess or weakly crosslinked PEI may fail to adequately anchor Li_2S and Super P particles under a higher current density, leading to electrode instability and overcharging during charging.

Figure 4.5 (d) shows the cycling stability of the $Zn(OAc)_2$·TEA/PEI (10%)- and $Zn(OAc)_2$·TEA/PEI (15%)-based electrodes at 0.1 C. The $Zn(OAc)_2$·TEA/PEI (15%)-based electrode retained 70.3% of its initial capacity (in the second cycle) after 100 cycles, comparable to the 72.1% retention observed for the $Zn(OAc)_2$·TEA-based electrode. In contrast, the $Zn(OAc)_2$·TEA/PEI (10%)-based electrode exhibited improved stability, maintaining 81.0% of its capacity after 100 cycles.

The $Zn(OAc)_2$·TEA/PEI (10%)-based electrode also exhibited better high-rate capability than the $Zn(OAc)_2$·TEA/PEI (15%)-based electrode, as shown in **Figure 4.5** (e) and **Figure S 4.6**. The capacity retention at 2 C relative to 0.1 C was 52% for the 10% PEI formulation, compared to 43% for the 15% PEI counterpart. Notably, the rate capacity of the $Zn(OAc)_2$·TEA/PEI (10%)-based electrode is comparable to the $Zn(OAc)_2$·TEA-based electrode, indicating that the incorporation of 10% PEI (or a reduced content of Zn in the cathode) does not comprise the redox kinetics. As shown in **Figure S 4.7**, the PVDF- and $Zn(OAc)_2$·TEA-based electrodes exhibited relatively unstable Coulombic efficiencies during rate performance testing, especially when switching from low to high C-rates, indicating incomplete redox reactions or sluggish kinetics. In contrast, incorporating PEI into the $Zn(OAc)_2$·TEA binder markedly stabilized the coulombic efficiency across varying rates. This enhancement highlights PEI's role in improving charge transfer kinetics and maintaining reaction reversibility during rapid cycling.

The long-term cycling performance of the PVDF-, $Zn(OAc)_2$·TEA- and $Zn(OAc)_2$·TEA/PEI (10%)-based electrodes at a rate of 0.5 C is shown in **Figure 4.5** (f). After 500 cycles, the $Zn(OAc)_2$·TEA/PEI (10%)-based electrode retained a capacity of 256 mA h g^{-1} with a retention rate of 69.3%. In contrast, although the $Zn(OAc)_2$·TEA-based electrode initially delivered higher discharge capacities than the PVDF-based electrode, its capacity and Coulombic efficiency showed noticeable fluctuations between the 370^{th} and 430^{th} cycles, indicating structural degradation of the

cathode. This instability is likely due to the limited binding strength of $Zn(OAc)_2 \cdot TEA$ alone. The incorporation of 10% PEI significantly improved cathode stability, enabling sustained cycling and the highest overall discharge capacity among the three batteries. To evaluate the long-term cycling performance of high-loading Li_2S cathodes, two electrodes with areal loadings of 3.72 and 4.51 mg cm^{-2} were tested at 0.5 C as shown in **Figure S 4.8**. For the 3.72 mg cm^{-2} electrode, the initial capacity was only 143 mA h g^{-1}, indicating incomplete activation of Li_2S likely due to increased internal resistance associated with higher loading. With continued cycling, gradual activation occurred, and the capacity increased to 187 mA h g^{-1} after 500 cycles. Similarly, the 4.51 mg cm^{-2} electrode exhibited a lower initial capacity of 95 mA h g^{-1}, but also showed continuous activation, reaching 147 mA h g^{-1} by the 500^{th} cycle. These results highlight the challenges of fully activating Li_2S under high mass loading and high current density, while also demonstrating the structural and electrochemical robustness of the electrode during extended cycling.

Electrochemical impedance spectroscopy (EIS) results for freshly prepared PVDF-, $Zn(OAc)_2 \cdot TEA$-, $Zn(OAc)_2 \cdot TEA$/PEI (10%)-, and $Zn(OAc)_2 \cdot TEA$/PEI (15%)-, $Zn(OAc)_2 \cdot TEA$/PEI (25%)-based electrodes are presented in **Figure S 4.9** and **Table S 4.4**. Among the $Zn(OAc)_2 \cdot TEA$ and PEI-modified systems, the $Zn(OAc)_2 \cdot TEA$/PEI (10%)-based electrode exhibited the lowest charge transfer resistance (R_{ct} = 61.1 Ω), indicating improved interfacial charge transport. For comparison, the PVDF-based electrode showed the lowest R_{ct} value of 52.4 Ω, which is attributed to the removal of the insulating $LiOH/Li_2O$ layer on the Li_2S surface through its reaction with PVDF during slurry processing.[344]

EIS was also conducted on cycled electrodes using different binders as shown in **Figure S 4.10** and **Table S 4.5**. All three electrodes exhibited Nyquist plots featuring two semicircles: the high-frequency semicircle associated with charge-transfer resistance (R_{ct}), and the medium-frequency semicircle corresponding to interfacial resistance (R_{int}) arising from Li_2S deposition and formation of other interfacial layers. Among the tested electrodes, the $Zn(OAc)_2 \cdot TEA$/PEI (10%)-based electrode exhibited the smallest R_{int}, followed by the $Zn(OAc)_2 \cdot TEA$-based electrode. In contrast, the PVDF-based electrode showed the largest impedance, reflecting poorer interfacial charge transfer and less effective suppression of polysulfide diffusion. These results suggest that the introduction of PEI into the $Zn(OAc)_2 \cdot TEA$ matrix significantly improves the electrochemical

environment at the electrode-electrolyte interface, likely due to enhanced ionic transport, better Li_2S redox reversibility, and stronger interactions with soluble polysulfides.

4.3.5 Mechanical Integrity and Structural Evolution of PVDF-, $Zn(OAc)_2$·TEA-, and $Zn(OAc)_2$·TEA/PEI (10%)-Based Li_2S Electrodes

To evaluate the mechanical integrity and structural evolution of Li_2S cathodes with different binder systems, we performed both tape peeling tests and scanning electron microscopy (SEM) analysis.

As shown in **Figure S 4.11**, the tape peeling tests provide a qualitative assessment of electrode adhesion and cohesion. The PVDF-based electrode exhibited strong adhesion to the current collector and good internal cohesion, with only minimal amounts of fine black powder transferred to the tape. In contrast, the $Zn(OAc)_2$·TEA-based electrode showed weaker mechanical integrity, likely due to the limited strength of hydrogen bonding between binder molecules. However, incorporating 10% PEI into the $Zn(OAc)_2$·TEA binder significantly improved mechanical stability, as evidenced by fewer and larger detached particles compared to both the $Zn(OAc)_2$·TEA- and PVDF-based electrodes. The high molecular weight PEI not only provides intrinsic mechanical strength but also introduces abundant amine groups capable of coordinating with Zn^{2+}, forming a denser and more cohesive network that reinforces internal bonding and improves adhesion to the current collector. This enhanced binding capability of the $Zn(OAc)_2$·TEA/PEI (10%) system directly correlates with the markedly improved electrochemical performance and cycling stability of the corresponding Li_2S cathodes.

SEM analysis was conducted to observe the morphological features of the electrodes before and after cycling in **Figure 4.6**. In the fresh state, all electrodes show the presence of large Li_2S particles, consistent with the commercial Li_2S used. After 100 cycles at 0.5 C, clear differences were observed. The PVDF-based electrode retained numerous large, agglomerated particles, likely unreacted Li_2S, indicating poor sulfur utilization and limited structural stabilization. The $Zn(OAc)_2$·TEA-based electrode exhibited fewer large particles after cycling, suggesting improved Li_2S dispersion and utilization due to the strong interactions between the sulfur species and $Zn(OAc)_2$·TEA. Notably, the $Zn(OAc)_2$·TEA/PEI (10%)-based electrode showed the most

homogeneous surface morphology, with finely distributed sulfur species and minimal residual large Li_2S particles. This reflects the synergistic effect of PEI, whose high molecular weight and abundant amine groups strengthen the binder network, enhancing structural integrity, suppressing particle aggregation, and improving Li_2S reversibility.

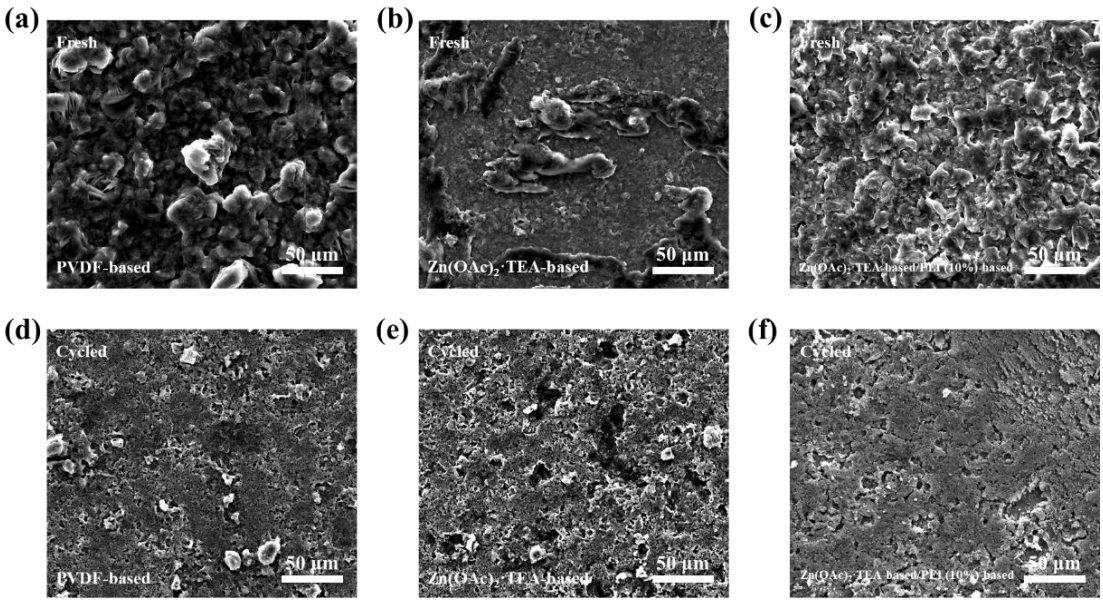


Figure 4.6 SEM images of (a, d) PVDF-, (b, e) $Zn(OAc)_2$·TEA-, and (c, f) $Zn(OAc)_2$·TEA/PEI (10%)-based electrodes before and after 100 cycles.

4.4 Conclusions

In this study, we developed a multifunctional, fluorine-free binder system based on a $Zn(OAc)_2$·TEA/PEI complex for high-performance lithium sulfide (Li_2S) cathodes in lithium–sulfur batteries. The $Zn(OAc)_2$·TEA complex exhibited strong lithium polysulfide (LPS) trapping capability and redox catalytic activity, which are critical for suppressing the polysulfide shuttle effect and promoting efficient Li_2S activation and conversion. However, the standalone use of $Zn(OAc)_2$·TEA posed issues related to crystallization and insufficient mechanical integrity during extended cycling. To address this, polyethylenimine (PEI) was introduced as a co-binder to form a stable hybrid binder network. The PEI not only enhanced solution processability and prevented binder crystallization, but also reinforced the structural integrity of the cathode through potential crosslinking with Zn^{2+} centers.

Electrochemical evaluations revealed that the optimized binder containing 10 wt.% PEI, $Zn(OAc)_2$·TEA/PEI (10%), outperformed the widely used PVDF binder in terms of long-term cycling stability and rate capability. Overall, this work presents a rational binder design strategy that integrates chemical functionality with mechanical robustness to overcome the unique challenges of Li_2S cathodes. The successful use of a fluorine-free, metal–organic binder paves the way for more environmentally sustainable and scalable solutions for Li_2S-based lithium–sulfur batteries.

4.5 Supporting Information

Table S 4.1 Different binder materials applied in Li_2S-based Li-S batteries.

Binder	Li_2S Materials	Li_2S Loading	Initial Capacity	Stability	Ref.
PVDF	Commercial Li_2S	1.0–1.2 mg cm^{-2}	576.3 mA h g^{-1}	40%@100Cycles	[344]
PVDF	Ball-milled Li_2S	1–1.5 mg cm^{-2}	950 mA h g^{-1}	85%@40Cycles	[104]
PVDF	Li_2S@C-Co-N	2 mg cm^{-2}	1137.1 mA h g^{-1}	81.7%@300Cycles	[234]
PVDF	Graphene-NanoLi$_2$S@C	1.0–1.5 mg cm^{-2}	1040 mA h g^{-1}	97%@700Cycles	[227]
PVP	Ball-milled Li_2S	2 mg cm^{-2}	760 mA h g^{-1}	69%@500Cycles	[257]
PVP	Li_2S@Super P	1.0–1.2 mg cm^{-2}	821 mA h g^{-1}	82.5%@400Cylces	[195]
PVP	Graphene-Li_2S	1.3 mg cm^{-2}	~800 mA h g^{-1}	97%@700Cycles	[227]
PVP	Li_2S/Graphene	1 mg cm^{-2}	~530 mA h g^{-1}	96%@10Cycles	[361]
PTFE	Commercial Li_2S	2–2.2 mg cm^{-2}	~500 mA h g^{-1}	N/A	[176]
PAA	Li_2S-LiEX with Ni-NC Catalysis	~3 mg cm^{-2}	~1100 mA h g^{-1}	~73%@1400Cycles	[263]
CMC	Li_2S-PAN	1.0–2.5 mg cm^{-2}	675.4 mA h g^{-1}	90.6%@250Cycles	[271]

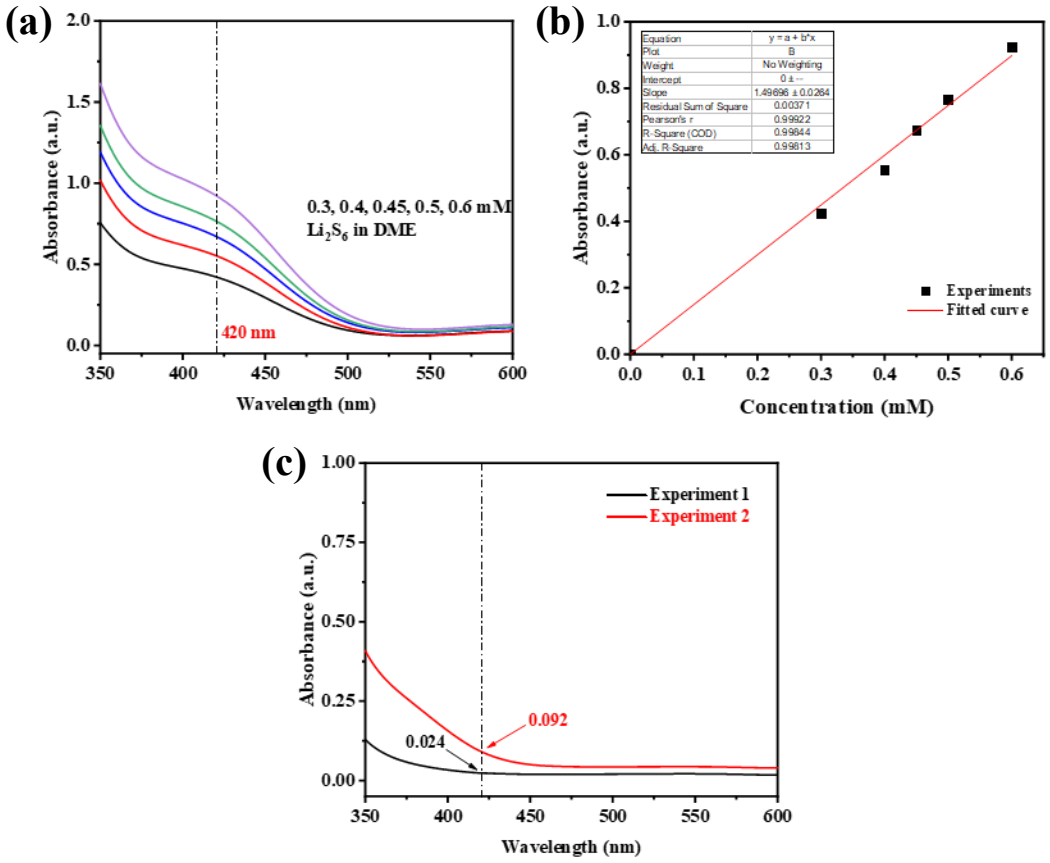


Figure S 4.1 UV-vis spectroscopy analysis of LPS trapping by $Zn(OAc)_2$·TEA using Li_2S_6 as a representative polysulfide species, following a previously reported procedure.[295] (a) UV-vis spectra of Li_2S_6 in DME at various known concentrations. (b) Calibration curve of absorbance at 420 nm *vs.* Li_2S_6 concentration, with a linear fit given by **Equation S4.1**:

$$A = 1.497c \qquad \textbf{(Equation S4.1)}$$

where A is the absorbance and c are the Li_2S_6 concentration (mM).

(c) UV-Vis spectra of the supernatant solutions from $Zn(OAc)_2$·TEA and Li_2S_6 mixtures in DME from two independent experiments.

Experimental Procedure:

Li_2S_6 solutions at known concentrations were first analyzed by UV-vis to construct the calibration curve. To assess LPS trapping, $Zn(OAc)_2$·TEA was added to Li_2S_6 solution in DME and stirred for 3 hours. After filtration, the supernatants were analyzed by UV-Vis spectroscopy, and the residual Li_2S_6 concentrations were determined using **Equation S4.1**.

Trapping Efficiency Calculation:

The molecular (or molar) trapping efficiency η was defined as the number of Li_2S_6 molecules trapped per $Zn(OAc)_2$·TEA molecule shown in **Equation S4.2**:

$$\eta = \frac{(C_0 - C_f) \times V}{n_{\text{trapper}}} \text{ (mol LPS per mol trapper)} \qquad \textbf{(Equation S4.2)}$$

where C_0 and C_f are the initial and final Li_2S_6 concentrations, V is the solution volume, and $n_{trapper}$ is the number of moles of $Zn(OAc)_2$·TEA used.

Results:

As summarized in **Table S 4.2**, the η values for two independent trials were 1.97 and 1.98, yielding an average trapping efficiency of 1.98 mol LPS per mol $Zn(OAc)_2$·TEA. This suggests that each $Zn(OAc)_2$·TEA molecule can chemically adsorb ~2 polysulfide anions, likely through coordination with Zn^{2+}, as illustrated in **Figure 4.3** (a).

Table S 4.2 Summary of LPS trapping experiment results corresponding to **Figure S 4.1**.

Initial LPS Concentration, mM	Volume of LPS Solution, mL	$Zn(OAc)_2$·TEA used, μmol	Final LPS, mM	η, mol LPS per mol $Zn(OAc)_2$·TEA	Average η, mol LPS per mol $Zn(OAc)_2$·TEA
1.20	5.0	3.0	0.0160	1.97	1.98
1.25			0.0615	1.98	

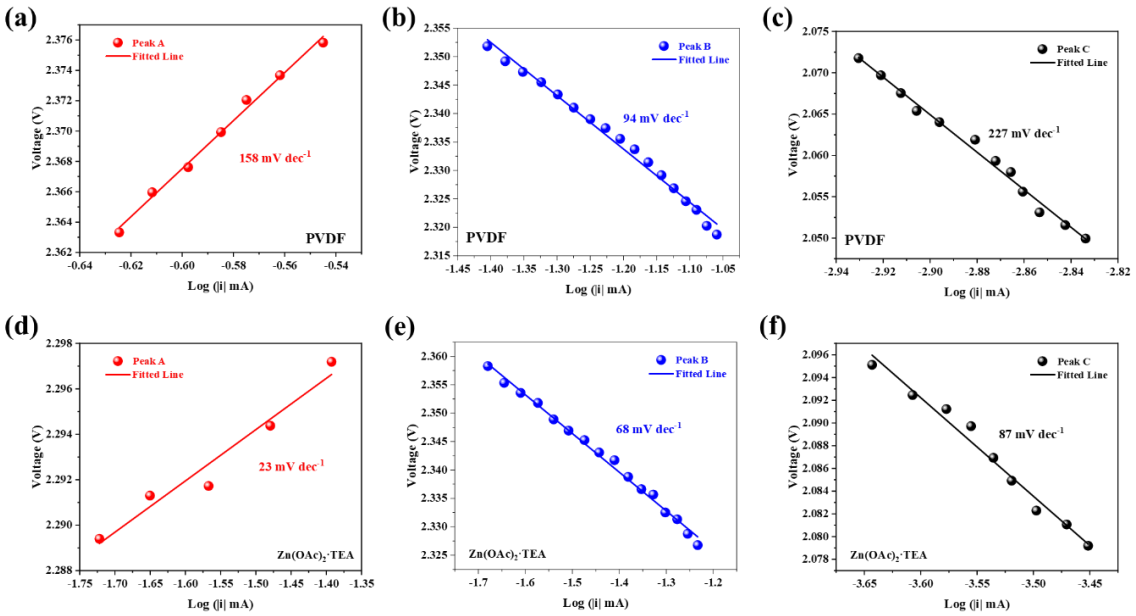


Figure S 4.2 Tafel plots derived from CV data at Peak A, B and C for Li_2S cathode using (a,b,c) PVDF and (d,e,f) $Zn(OAc)_2$·TEA, based on the CV curves shown in **Figure 4.2** (f) and (g).

Table S 4.3 Tafel slopes (mV dec^{-1}) extracted from the second-cycle CV curves at Peak A, B and C for Li_2S cathode using PVDF and $Zn(OAc)_2$·TEA complex.

	Peak A (mV dec^{-1})	**Peak B** (mV dec^{-1})	**Peak C** (mV dec^{-1})
PVDF	158	94	227
$Zn(OAc)_2$·TEA	23	68	87

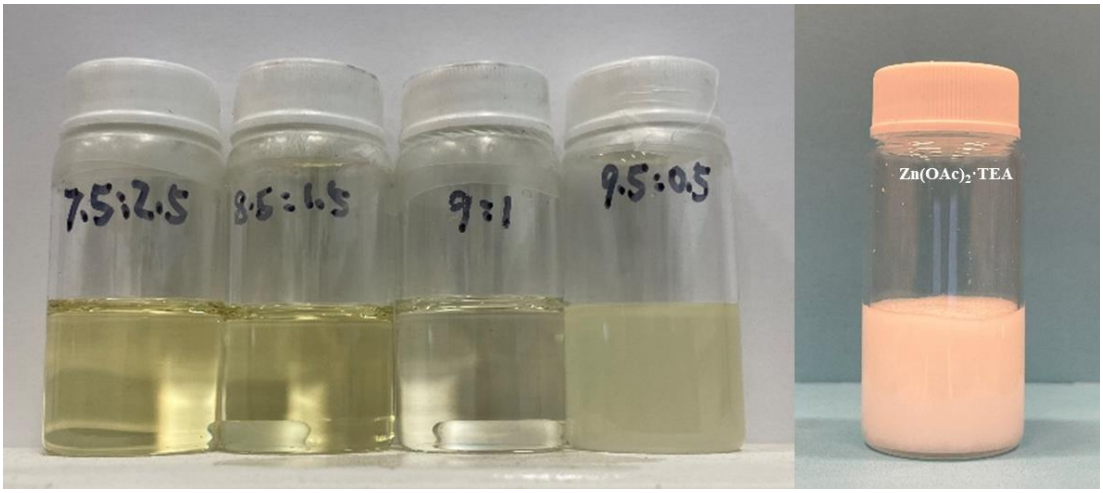


Figure S 4.3 $Zn(OAc)_2$·TEA and different $Zn(OAc)_2$·TEA/PEI solutions after storage at room temperature for 12 h following preparation.

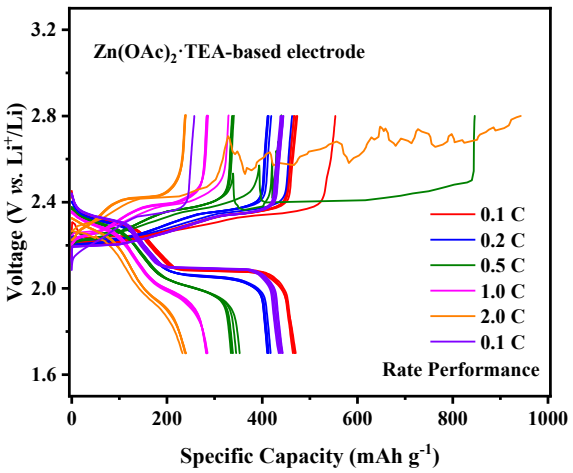


Figure S 4.4 Charge/discharge curves of $Zn(OAc)_2$·TEA-based electrodes corresponding to their rate performance data in **Figure 4.2** (g).

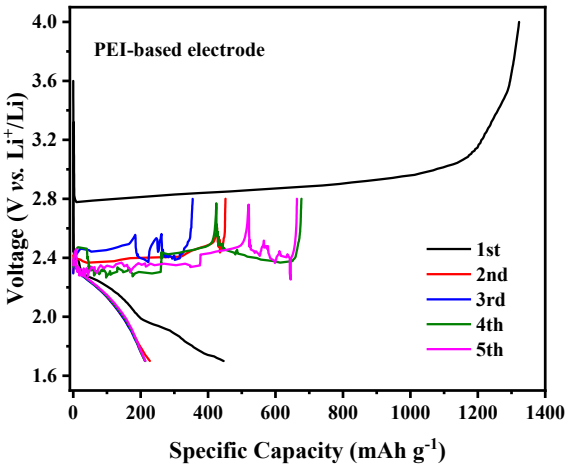


Figure S 4.5 Charge/discharge curves of the PEI-based electrode during the initial five cycles: the first cycle at 0.05 C and subsequent cycles at 0.1 C.

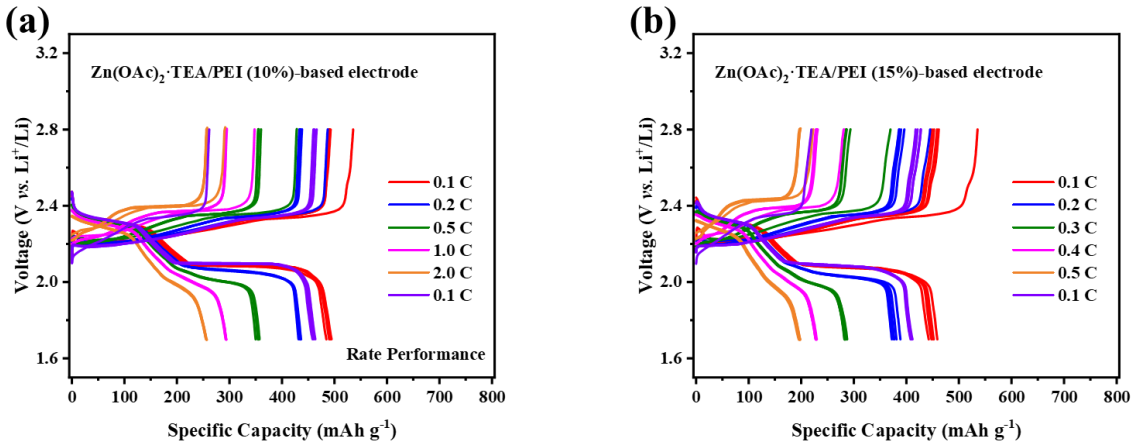


Figure S 4.6 Charge/discharge curves of (a) $Zn(OAc)_2$·TEA/PEI (10%)- and (b) $Zn(OAc)_2$·TEA/PEI (15%)-based electrodes corresponding to their rate performance data in **Figure 4.5** (e).

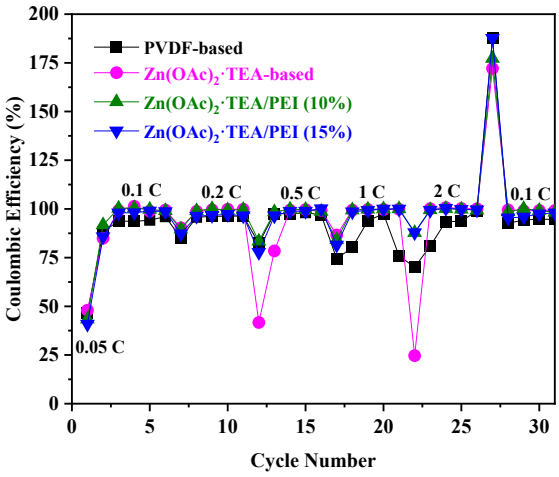


Figure S 4.7 Coulombic efficiencies of the electrodes corresponding to the rate performance tests presented in **Figure 4.2** (e) and **Figure 4.5** (e).

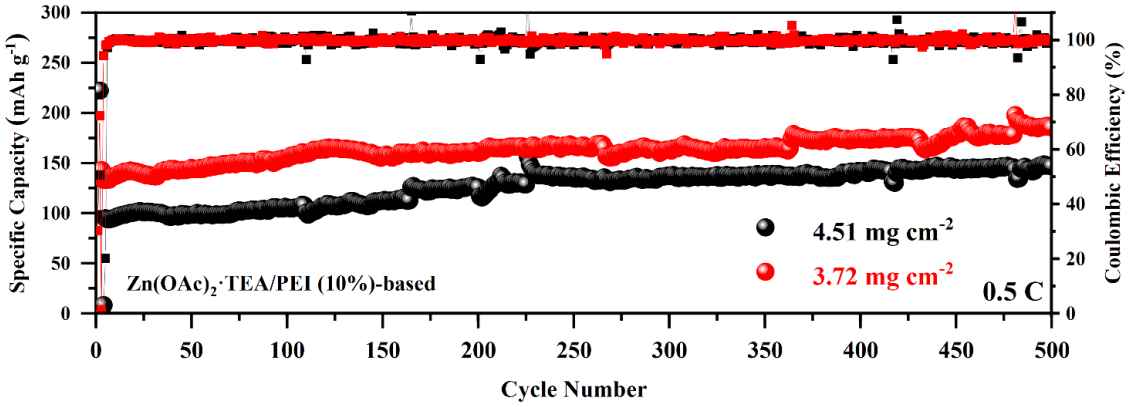


Figure S 4.8 Electrochemical performance of $Zn(OAc)_2$·TEA/PEI (10%)-based Li_2S cathodes with high areal loadings (3.72 and 4.51 mg cm^{-2}) on carbon paper current collectors at 0.5 C. The initial cycle was activated at 0.05 C.

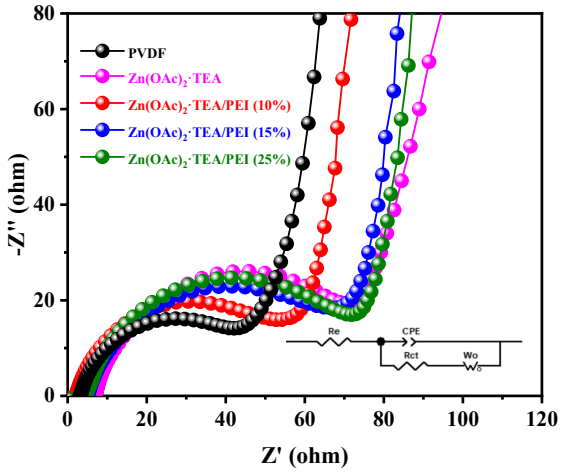


Figure S 4.9 Nyquist plots from electrochemical impedance spectroscopy (EIS) of freshly prepared electrodes using PVDF, $Zn(OAc)_2$·TEA, $Zn(OAc)_2$·TEA/PEI (10%), $Zn(OAc)_2$·TEA/PEI (15%), $Zn(OAc)_2$·TEA/PEI (25%) binders. The inset shows the equivalent Randles circuit used for fitting, where R_e is the resistance of the electrolyte solution, R_{ct} is the charge transfer resistance, *CPE* is the capacitance, and W_o is the Warburg impedance.

Table S 4.4 Resistances of cathodes calculated from the EIS data in **Figure S 4.9**.

Cathode	**Resistance (Ω)**	
	R_e	R_{ct}
PVDF-based	3.2	52.4
$Zn(OAc)_2$·TEA-based	7.1	83.6
$Zn(OAc)_2$·TEA/PEI (10%)-based	2.1	61.1
$Zn(OAc)_2$·TEA/PEI (15%)-based	5.1	78.4
$Zn(OAc)_2$·TEA/PEI (25%)-based	4.6	82.8

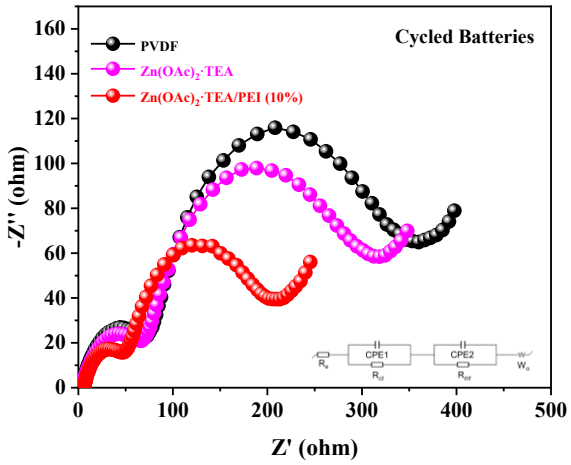


Figure S 4.10 Nyquist plots from electrochemical impedance spectroscopy (EIS) of freshly prepared electrodes using PVDF, $Zn(OAc)_2$·TEA, $Zn(OAc)_2$·TEA/PEI (10%) binders. The inset shows the equivalent Randles circuit used for fitting, where R_e is the resistance of the electrolyte solution, R_{ct} is the charge transfer resistance, R_{int} is the interphase resistance, *CPE* is the capacitance, and W_o is the Warburg impedance.

Table S 4.5 Resistances of cathodes calculated from the EIS data in **Figure S 4.10**.

Cathode	**Resistance (Ω)**	
	R_{ct}	R_{int}
PVDF-based	70.8	289.2
$Zn(OAc)_2$·TEA-based	66.8	251.2
$Zn(OAc)_2$·TEA/PEI (10%)-based	45.6	163.7

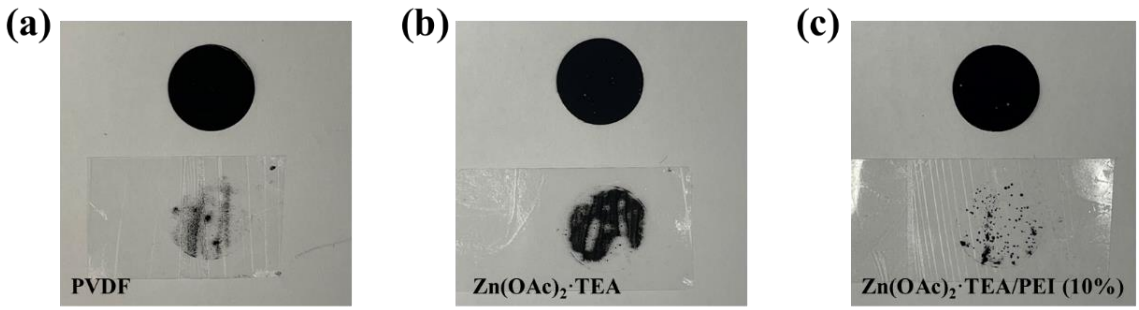


Figure S 4.11 Tape peeling test results of Li_2S cathodes with different binders. Photographs showing the electrode surfaces and corresponding adhesive tapes after peeling: (a) PVDF, (b) $Zn(OAc)_2$·TEA, and (c) $Zn(OAc)_2$·TEA/PEI (10%). Tests were conducted inside an argon-filled glovebox by firmly pressing adhesive tape onto the electrode surface, then slowly peeling it off to assess adhesion and cohesion.

Chapter 5 Facile Synthesis of Li_2S@Carbon Nanocomposite via Precursor Solution Infiltration-Decomposition for High-Performance Lithium Sulfide Batteries

This chapter is based on the following publication:

Z. Huang, Y. Wang, Y. Li, *ACS Applied Energy Materials*, **2025**, 8, 5759-5769.

5.1 Introduction

The rising demand for electric vehicles and other energy storage devices has accelerated the development of high-energy-density, long-lasting, and cost-effective rechargeable batteries.[334,335] While lithium-ion batteries (LIBs) dominate the market and are being extensively researched to boost energy density through the use of new solid electrolytes and higher-capacity anode materials,[333,336,362] their cathode materials are nearing their theoretical limits. This has spurred global efforts to find alternative cathode materials for next-generation ultrahigh-energy-density batteries.[34,337]

Lithium-sulfur batteries (LSBs) have gained significant attention over the past decade due to their high theoretical specific capacity of 1675 mA h g^{-1} for the sulfur cathode, translating to a specific energy of 2600 W h kg^{-1}.[87] In addition to their impressive high energy density potential, LSBs offer the benefits of lower manufacturing costs and reduced environmental impact, owing to sulfur's abundance and nontoxicity. However, several challenges hinder their commercialization: the extremely low electrical conductivity of sulfur and lithium sulfide, the high solubility of lithium polysulfide intermediates, and the substantial volume changes of the cathode during charging and discharging. These issues impact the overall performance and practicality of LSBs.

LSBs are typically categorized into two types based on the sulfur cathode used: elemental sulfur-based (S-LSBs)[236] and lithium sulfide-based (Li_2S-LSBs).[165,343] Both S-LSBs and Li_2S-LSBs operate based on the reversible conversion between sulfur (S_8) and Li_2S via lithium polysulfide intermediates. In S-LSBs, discharging begins with lithium oxidation at the anode and reduction of sulfur at the cathode, forming soluble lithium polysulfides and eventually solid Li_2S. Charging

reverses this process, converting Li_2S back to sulfur. In Li_2S-LSBs, the process starts from the fully lithiated state. An initial activation step is required during the first charge, typically around 3.6 V,[165,343] to overcome the high resistance of insulating Li_2S. Once activated, soluble polysulfides are generated, which improve conductivity and facilitate further conversion to sulfur. After activation, the battery follows the same redox pathway as in S-LSBs.

S-LSBs are more widely studied due to the ease of handling elemental sulfur, but they typically employ highly reactive metallic lithium or lithium alloys as the anode. The reactivity of metallic lithium with moisture, oxygen, and nitrogen increases costs and raises safety concerns during manufacturing, while there is also the risk of lithium dendrite formation during operation, which can lead to fires or explosions.[341] Additionally, sulfur's significant volume expansion (78%) when converting to Li_2S during discharge can damage the cathode structure, affecting cycle performance. In contrast, Li_2S-LSBs can utilize more stable and safer, lithium-free anode materials such as graphite,[144] silicon,[157] and tin.[161] The Li_2S-based cathode starts from a state of low density, experiencing volume reduction during charging and volume recovery during discharging, which helps maintain the structural integrity of the cathode.

Pioneering work by Nazar *et al.*[89] (16) highlighted the importance of forming sulfur-infiltrated carbon nanocomposites (S@C) to enhance S-LSB performance. Sulfur's low melting point allows for easy melt infiltration into mesoporous carbon, such as CMK-3, creating nanocomposites that trap soluble polysulfides and enhance electrical conductivity. This melt infiltration technique has enabled the development of high-performance S-LSBs using various porous carbon host materials.[363]

However, replicating this melt infiltration process for Li_2S-infiltrated carbon (Li_2S@C) nanocomposites is challenging due to Li_2S's high melting point (938 °C). As a result, alternative strategies have been explored. For example, Cai *et al.*[166] (18) used high-energy ball milling to create a nanostructured Li_2S@C composite, although this method faces challenges in reducing the Li_2S particle size below 100 nm and efficiently infiltrating Li_2S into the carbon matrix. The solution infiltration method has also been utilized, but the limited solubility of Li_2S in solvents (e.g., 25 mg

mL^{-1} in ethanol)[234] makes it difficult to achieve desirable Li_2S@C nanocomposites, as most Li_2S particles agglomerate outside the carbon host.

To overcome poor dispersion of Li_2S, sulfiphilic carbon co-doped with heteroatoms and transition metals have been used as hosts to form Li_2S@C nanocomposites, coupled with the solution filtration process. For instance, co-doped graphitic carbon (C-Co-N),[234] nickel phosphosulfide-modified 3D graphene (Ni-P-S@G),[232] and N-rich carbon (NRC) derived from polyacrylonitrile[364] have been proposed as effective hosts. Another approach to enhancing Li_2S solubility involves adding elemental sulfur to form Li_2S_3, which is slightly more soluble in ethanol (34 mg mL^{-1}) than Li_2S. This facilitates the preparation of Li_2S_3@C nanocomposites that can be thermally treated to remove excess sulfur, yielding Li_2S@C nanocomposites.[268,365]

Lithiation of sulfur-carbon nanocomposites has been reported for producing Li_2S@C nanocomposites. For instance, Yang *et al.*[157] lithiated a sulfur-carbon composite to create a Li_2S@CMK-3 composite with Li_2S particles in the carbon pores. Zhang *et al.*[156] used lithium triethylborohydride to create Li_2S particles on graphene nanosheets, while Liu *et al.*[355] formed a Li_2S@Co-C@MHF nanocomposite by infiltrating sulfur into a Co nanoparticle-decorated carbon structure and reacting it with lithium naphthalide. Yan *et al.*[366] synthesized a Li_2S@C nanocomposite by reacting lithium with carbon disulfide at 300 °C, producing Li_2S particles 50–100 nm in diameter.

Despite these advancements, an efficient, safe, facile, and low-cost method for synthesizing Li_2S@C nanocomposites is still lacking. In this study, we introduced a new method for synthesizing Li_2S@C nanocomposites under relatively mild conditions. We prepared a lithium trithiocarbonate (Li_2CS_3) solution by stirring commercial Li_2S with carbon disulfide (CS_2) in anhydrous ethanol (EtOH) at room temperature, which was mixed with mesoporous conductive carbon Super P (SP). After drying, the resulting Li_2CS_3@SP composite was heated at temperatures $\geqslant$200 °C to thermally decompose Li_2CS_3, leading to the formation of Li_2S@SP nanocomposites.

Due to Li_2CS_3's high solubility in ethanol and its amorphous state after drying, efficient infiltration into the nanopores of SP was achieved. Subsequent thermal treatment produced small Li_2S particles (~11 nm) confined within SP's mesopores. Li_2S-LSBs using the Li_2S@SP

nanocomposite, prepared at 400 °C, exhibited a discharge capacity of up to 821 mA h g^{-1} (Li_2S) at 0.1 C, equivalent to 1190 mA h g^{-1} (S) in S-LSBs. The battery also demonstrated excellent cycle stability, retaining 82.5% of its capacity after 400 cycles at 2.0 C. It outperforms both Li_2S-LSBs with physically mixed Li_2S/SP cathodes and S-LSBs with S@SP nanocomposites prepared by melt infiltration. This simple precursor solution infiltration-decomposition method shows promise for fabricating high-energy-density and cost-effective Li_2S-LSBs.

5.2 Experimental Section

5.2.1 Materials

Chemicals were obtained from Sigma-Aldrich: Li_2S (99.98%) (labeled as cLi_2S), ethanol (anhydrous, ≤ 0.003% water), carbon disulfide (≥ 99.9%), elemental sulfur (99.98%), anhydrous NMP (99.5%), and PVP (M_w ~1,300,000). Ethanol and NMP were further dried with molecular sieves. All other chemicals were used as received.

5.2.2 Preparation of Li_2CS_3

Li_2S (60 mg, 1.31 mmol) and CS_2 (100 μL, 126 mg, 1.65 mmol) were mixed in 1 mL of ethanol (EtOH) in an Ar-filled glovebox (< 0.5 ppm O_2 and H_2O). The mixture was stirred for 15 min at room temperature to form an orange Li_2CS_3 solution in EtOH. After vacuum drying, a bright yellow Li_2CS_3 powder (~160 mg, 100% theoretical yield) was obtained.

5.2.3 Preparation of Nano Li_2S

The Li_2CS_3 powder (150 mg) was heated at 200 °C under vacuum for 3 h to yield a Li_2S-200 powder (~56 mg, 100% theoretical yield). Similarly, Li_2S-400 was prepared by heating at 400 °C for 3 h, also yielding ~56 mg.

5.2.4 Preparation of Li_2CS_3@SP Precursor Composite

Li_2S (60 mg), CS_2 (100 μL), and Super P (SP) (40 mg) were mixed in EtOH (1 mL) and stirred for 6 hours at room temperature in an Ar-filled glove box. The resulting mixture was then vacuum dried at room temperature to remove EtOH and excess CS_2, yielding the Li_2CS_3@SP precursor composite.

5.2.5 Preparation of Li_2S@SP Precursor Nanocomposite

The Li_2CS_3@SP precursor was heated at 200, 350, 400, and 450 °C for 3 hours under vacuum to produce Li_2S@SP nanocomposites, labeled as Li_2S@SP-200, Li_2S@SP-350, Li_2S@SP-400, and Li_2S@SP-450, with 60 wt.% Li_2S.

Note: The symbol "@" indicates that Li_2S is infiltrated inside SP and will be used to represent other nanocomposites prepared using infiltration methods. This distinguishes them from batteries prepared by physical mixing, which are denoted with the symbol "/", such as cLi_2S/SP and Li_2S-400/SP.

5.2.6 Preparation of S@SP Nanocomposite

For comparison, a S@SP composite was prepared by grinding 126 mg sulfur (S) with 120 mg SP and heating at 155 °C for 12 h. the nanocomposite has 42 wt.% S, which is equivalent to 60 wt.% Li_2S.

5.2.7 Fabrication of Cathodes

Li_2S@SP or S@SP, SP, and PVP were mixed in a mass ratio of 80:10:10 for Li_2S@SP electrodes and 65.49:10:10 for S@SP electrodes in NMP. The slurry was coated onto carbon-coated aluminum current collectors, vacuum dried at 50 °C overnight and cut into 12 mm discs. Li_2S (or Li_2S equivalent for the S cathode) loading was ~1.0–1.2 mg cm^{-2}. Cathodes using Nano Li_2S and cLi_2S were prepared similarly.

5.2.8 Electrochemical Measurements

2032 coin cells were assembled with Li_2S@SP cathode (or other cathodes), lithium metal anodes, Celgard 2400 separators, and 1 M LiTFSI electrolyte in a 1:1 DOL/DME with 2 wt.% $LiNO_3$, all inside an Ar-filled glovebox. Electrochemical performance was evaluated using galvanostatic tests on a Land 2001A battery tester, EIS with a Bio-logic VSP (1000 kHz to 0.1 Hz, 10 mV AC), and CV in the 1.7–4.0 V and 1.7–2.8 V range at 0.1 mV s^{-1}.

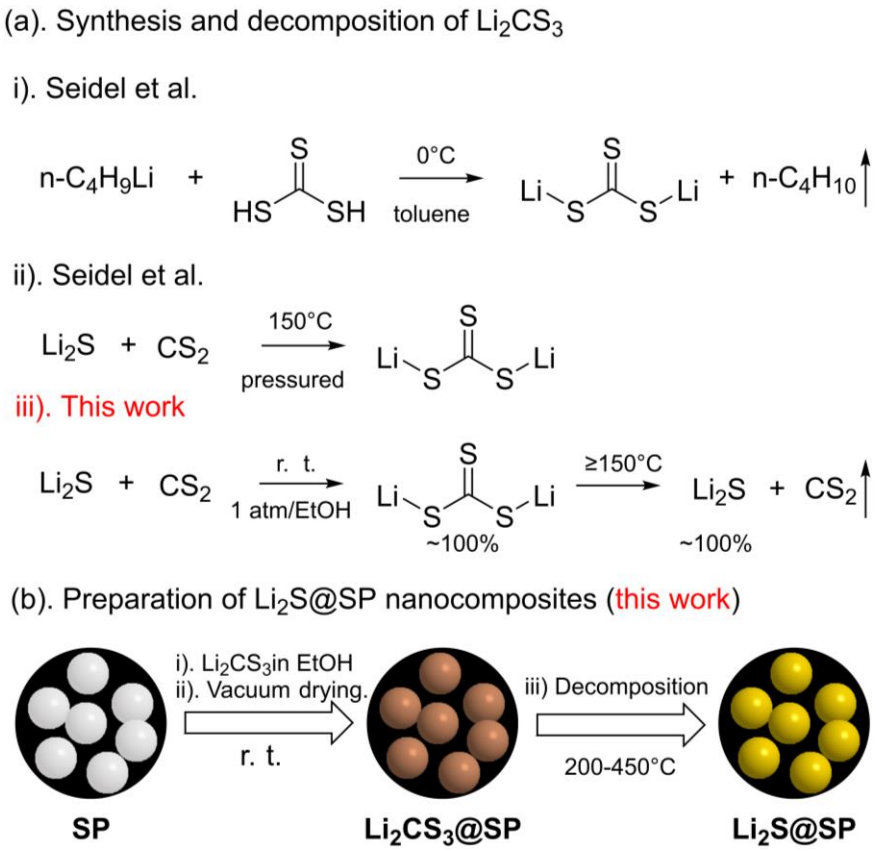
5.2.9 Characterizations

XRD was performed on a Bruker D8 Discover diffractometer with Cu Kα radiation (λ=1.5418 Å). Samples were covered with Kapton tape to avoid moisture absorption. SEM images were taken using a Zeiss Sigma HD microscope.

5.3 Results and Discussion

5.3.1 Preparation and Characterization of Li_2CS_3 and Nano Li_2S

The synthesis of Li_2CS_3 was first reported in 1971 by Seidel *et al.* via the reaction of *n*-butyllithium with trithiocarbonic acid (H_2CS_3) in toluene at 0 °C or the reaction between Li_2S and CS_2 at 150 °C in a bomb tube (**Scheme 5.1** (a)).[367]



Scheme 5.1 (a) Synthesis methods for Li_2CS_3 reported in the literature and this work and thermal decomposition of Li_2CS_3 to form Li_2S, (b) Preparation of Li_2S@SP nanocomposites through a precursor solution infiltration-decomposition method: (i) Mixing SP with a Li_2CS_3 solution in anhydrous ethanol at room temperature, (ii) Vacuum drying at room temperature, and (iii) Thermal decomposition at 200–450 °C.

In this study, we synthesized Li_2CS_3 in a more straightforward manner under mild conditions by simply mixing a slight excess of CS_2 with commercial Li_2S in anhydrous ethanol for 15 min at room temperature inside an argon-filled glovebox (**Figure S 5.1**). The white Li_2S particles were dissolved rapidly once CS_2 was added, and the mixture turned into an orange solution after a few

minutes, indicating the formation of Li_2CS_3. Upon removal of ethanol and excess CS_2 under vacuum, a bright yellow powder was obtained in a quantitative yield based on Li_2CS_3 (~100%). The resulting Li_2CS_3 has exceptional solubility in anhydrous ethanol, readily forming a homogeneous solution at any concentration. This is very desirable for infiltration of Li_2CS_3 into mesoporous carbon using a solution infiltration method. Conversely, Li_2CS_3 is insoluble in DOL, DME, and NMP (**Figure S 5.2**).

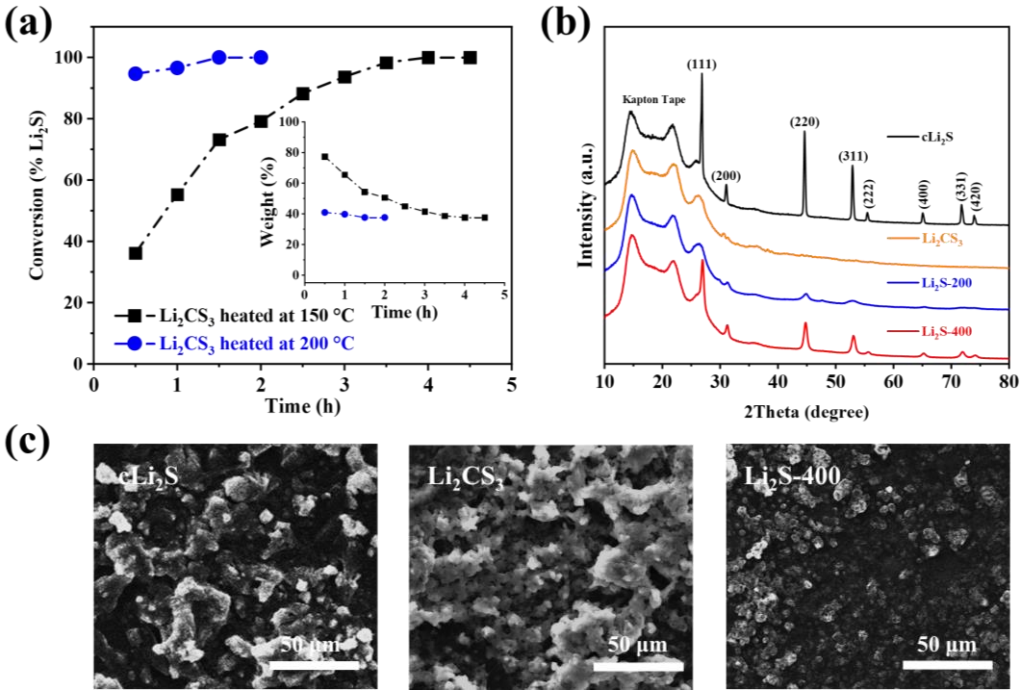


Figure 5.1 (a) Conversion of Li_2CS_3 to Li_2S over time at 150 and 200 °C under vacuum. The inset shows the corresponding weight change of Li_2CS_3 samples as a function of time at different temperatures. (b) XRD patterns of cLi_2S, Li_2CS_3, Li_2S-200, and Li_2S-400. (c) SEM images of cLi_2S, Li_2CS_3 and Li_2S-400.

To determine the thermal decomposition temperature of Li_2CS_3 for recovering Li_2S, Li_2CS_3 was heated under vacuum at temperatures from 100 to 200 °C. At 100 °C, there was no significant weight loss after overnight heating. Decomposition began at 150 °C, with Li_2S forming and CS_2 evaporating, consistent with the literature.[367] As shown in **Figure 5.1** (a), at 150 °C, 21% of Li_2CS_3 decomposed after 2 h, and complete conversion to Li_2S required 4 h. At 200 °C, 95% conversion was achieved in 30 min, with full conversion occurring after 1.5 h. A heating time of 3 h was chosen to ensure complete conversion of Li_2CS_3 to Li_2S. The Li_2S sample obtained at 200 °C was labeled

as Li_2S-200. Additionally, a sample was prepared at 400 °C for 3 h and labeled as Li_2S-400 to assess the impact of treatment temperature on the crystallinity of the resulting Li_2S.

X-ray diffraction (XRD) measurements were performed to assess the crystallinity of Li_2CS_3 and the recovered Li_2S at different temperatures, and to compare them with a commercial Li_2S powder sample. Due to the moisture sensitivity of Li_2S and Li_2CS_3, the samples were covered with Kapton tape inside a glovebox before being removed for XRD analysis. As shown in **Figure 5.1** (b), the Li_2CS_3 powder sample exhibits only the broad diffraction peak, representing its amorphous state, without any characteristic peak present in the XRD pattern for the commercial Li_2S sample, indicating the complete reaction of Li_2S with CS_2. Three broad peaks at 14, 22, and 26° are originated from the Kapton tape, while the remaining peaks of cLi_2S can be attributed to crystalline Li_2S with a cubic structure (space group $Fm\bar{3}m$; JCPDS card no. 81-1173). For Li_2S-200, rather broad peaks corresponding to Li_2S appeared, suggesting that the sample is composed of very small crystalline particles and possibly amorphous phases. Li_2S-400 shows intensified peaks, indicating its increased crystallinity at a higher temperature. Its average crystallite size is 12.6 nm, calculated using the Scherrer equation, which is much smaller than that of the commercial Li_2S sample (29.0 nm). The parameters used for calculation are listed in **Table S 5.1**.

The SEM images in **Figure 5.1** (c) show distinct changes in particle size and morphology of Li_2S-400 compared to the starting commercial Li_2S and its precursor Li_2CS_3. Commercial Li_2S forms large aggregates, up to 10 μm. In contrast, Li_2CS_3 has a porous structure with smaller agglomerates (a zoomed-in view is shown in **Figure S 5.3** (a)). Li_2S-400 displays a substantial reduction in particle size and significantly reduced aggregation compared to commercial Li_2S.

5.3.2 Preparation and Characterization of Li_2CS_3@SP Precursor and Li_2S@SP Nanocomposite

The Li_2CS_3@SP precursor nanocomposite was prepared through a liquid infiltration-evaporation process (**Scheme 5.1** (b), steps i and ii. Super P, at a Li_2S/SP ratio of 6:4, was mixed with a Li_2CS_3 solution in EtOH under stirring for 6 h at room temperature, followed by vacuum drying, inside a glovebox. Capillary forces and vacuum facilitated the infiltration of Li_2CS_3 into Super P pores.

The Li_2CS_3@SP precursor was heated in vacuo to produce the Li_2S@SP nanocomposite. While pure Li_2CS_3 decomposes completely at 150 °C in 4 h, 19% of Li_2CS_3 in the nanocomposite sample remained after 9 h at this temperature (**Figure 5.2** (a)), likely due to entrapment of Li_2CS_3 in Super P pores. Complete decomposition occurred at 200 °C in 2 h. Consequently, Li_2S@SP nanocomposites were synthesized by heating the Li_2CS_3@SP precursor at 200, 350, 400, and 450 °C for 3 h, resulting in Li_2S@SP-200, Li_2S@SP-350, Li_2S@SP-400, and Li_2S@SP-450, respectively.

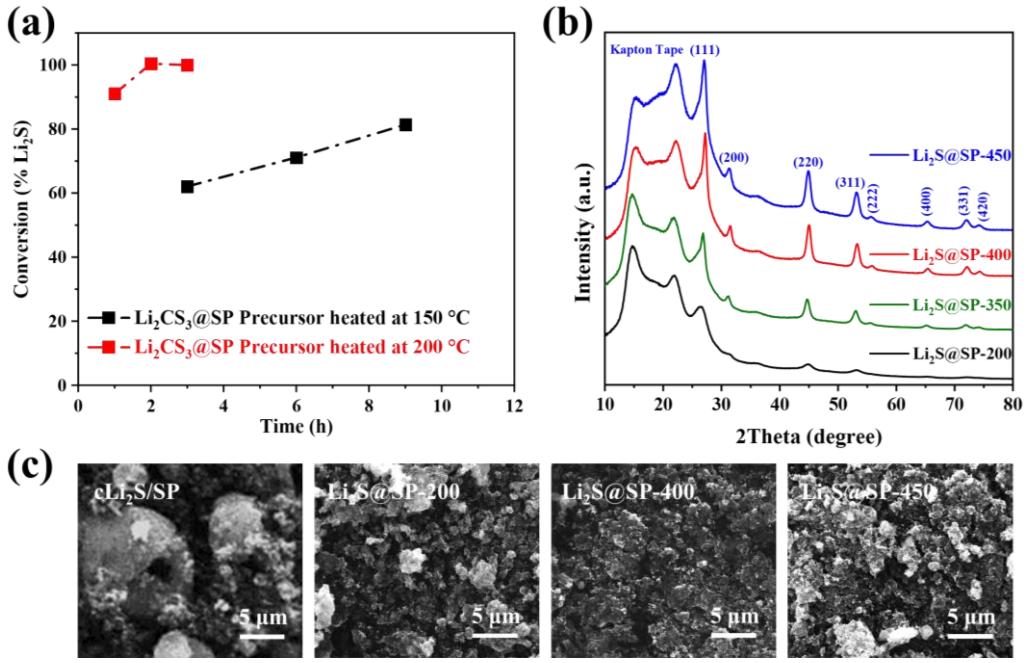


Figure 5.2 (a) Conversion of Li_2CS_3@SP precursor to Li_2S@SP nanocomposites over time at 150 and 200 °C in vacuo. (b) XRD patterns of Li_2S@SP-200, Li_2S@SP-350, Li_2S@SP-400 and Li_2S@SP-450. (c) SEM images of cLi_2S/SP (commercial Li_2S mixed with SP at a 6:4 mass ratio), Li_2S@SP-200, Li_2S@SP-400 and Li_2S@SP-450.

X-ray diffraction (XRD) analysis results of the obtained Li_2S@SP nanocomposites are shown in **Figure 5.2** (b). The XRD patterns reveal that the crystalline peaks of Li_2S become more pronounced with increasing annealing temperature from 200 to 450 °C, indicating enhanced crystallinity. The average Li_2S crystallize size calculated using the *Scherrer* equation increases from 8.5 nm at 200 °C to 11.0 nm at 350 °C, reaching 11.4 nm at 400 °C (**Table S 5.1**). At 450 °C, the crystallite size stays similar at 11.2 nm. This trend suggests that crystallinity improves with temperature but plateaus beyond 400 °C.

Notably, the crystallite sizes of Li_2S@SP-400 (11.4 nm) and Li_2S@SP-450 (11.2 nm) are smaller than that of Li_2S-400 (~12.6 nm), despite being annealed at the same or higher temperatures. This size difference is likely due to the spatial confinement effect of the Super P pores, which restrict the amount of Li_2CS_3 and limit the mobility of the formed Li_2S, thereby inhibiting further crystallite growth.

SEM images in **Figure 5.2** (c) highlight the morphological differences between physically mixed commercial Li_2S with Super P (cLi_2S/SP) and Li_2S@SP nanocomposites. The cLi_2S/SP mixture shows large Li_2S particles clumped with Super P, with clear boundaries between them. In contrast, Li_2S@SP nanocomposites show a uniform appearance with Li_2S effectively filling the Super P pores, unlike the hollow Super P structures observed in **Figure S 5.3** (b). Among the Li_2S@SP nanocomposites, Li_2S@SP-400 has the most uniform morphology and smooth surface. Li_2S@SP-200, produced at a lower temperature of 200 °C, reveals more visible Super P particles, indicating poor contacts between Super P and Li_2S particles, while Li_2S@SP-450 shows larger, poorly interconnected grains due to further grain growth at 450 °C.

5.3.3 Electrochemical Performance of Li_2S@SP Nanocomposites

To evaluate the electrochemical performance of Li_2S@SP nanocomposites synthesized at various temperatures, Li_2S-LSBs were constructed using these nanocomposites. The cathode slurry was prepared with polyvinylpyrrolidone (PVP) as the binder, avoiding poly(vinylidene fluoride) (PVDF) due to its potential reaction with Li_2S, which could reduce capacity.[344]

Electrochemical impedance spectroscopy (EIS) was used to assess battery resistance (**Figure S 5.4** and **Table S 5.2**). The charge-transfer resistance (R_{ct}) decreased as the annealing temperature increased from 200 to 400 °C, which might be due to the increased crystallinity of Li_2S and improved morphology of the nanocomposite. However, as the annealing temperature increased further to 450 °C, the battery with the resulting Li_2S@SP-450 has a slightly higher R_{ct} (49.3 Ω) compared to the Li_2S@SP-400-based battery (43.6 Ω), likely due to the deteriorated morphology of Li_2S@SP-450, as well as the formation of an insulating LiOH/Li_2O layer on the surface of Li_2S particles (discussed later).

Compared to S-LSBs, Li_2S-LSBs typically require a higher overpotential of up to 4 V (or more) and a low current density for the initial charge due to the insulating LiOH/Li_2O layer on the Li_2S particle surface and the high crystallinity of Li_2S.[165,175,176,200] The electrolyte used, 1.0 M LiTFSI in DOL/DME with 2 wt.% $LiNO_3$, demonstrated stability up to ~4.3 V, as indicated by linear sweep voltammetry (LSV) measurements (**Figure S5**). Therefore, the galvanostatic charge/discharge characteristics of Li_2S-LSBs using Li_2S@SP nanocomposites were evaluated at a rate of 0.1 C (1 C = 1166 mA g^{-1}) within a voltage range of 1.7 to 4.0 V for the first cycle, and 1.7 to 2.8 V for subsequent cycles.

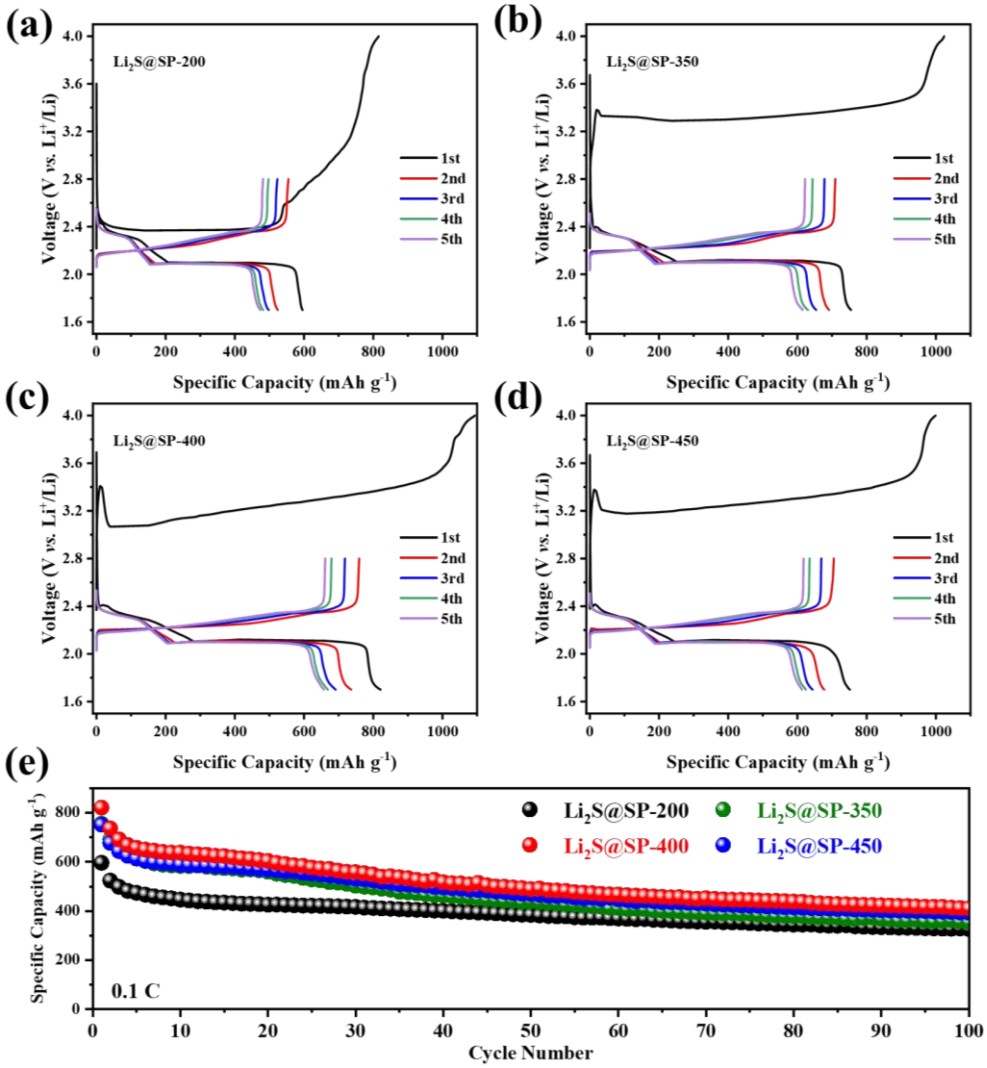


Figure 5.3 Initial charge/discharge curves at 0.1 C for batteries with PVP binder and cathode materials of (a) Li_2S@SP-200, (b) Li_2S@SP-350, (c) Li_2S@SP-400, and (d) Li_2S@SP-450. The voltage range

was set to 1.7–4.0 V for the first cycle and 1.7–2.8 V for subsequent cycles. (e) Cycling performance of the batteries at 0.1 C.

Figure 5.3 (a–d) show the initial charge/discharge curves at 0.1 C for batteries using Li_2S@SP-200, Li_2S@SP-350, Li_2S@SP-400, and Li_2S-450. Notably, the Li_2S@SP-200 battery displays no overpotential spike and a low charge voltage around 2.4 V up to approximately 500 mA h g^{-1}. This absence of an overpotential spike and the low charge voltage can be attributed to the low crystallinity and lack of a LiOH/Li_2O layer on the Li_2S particle surface, which facilitates the delithiation process. Since trace amounts of LiOH and Li_2O present on the surface of commercial Li_2S particles can dissolve in ethanol, they become uniformly distributed within the Li_2CS_3@SP precursor. As a result, in the Li_2S@SP-200 composite, LiOH and Li_2O are more evenly dispersed within the Li_2S particles rather than accumulating on the surface. This absence of a LiOH/Li_2O layer allows the surface Li_2S to make direct contact with the electrolyte, facilitating easier delithiation. Nonetheless, the charging potential rises rapidly after 500 mA h g^{-1}, likely due to poor contact between Li_2S and Super P in the Li_2S@SP-200 sample (as shown by SEM), leading to the presence of some "dead" Li_2S particles.

Intriguingly, batteries with Li_2S@SP-350, Li_2S@SP-400, and Li_2S@SP-450 all exhibit overpotential spikes around 3.4 V. This is likely due to the migration of LiOH/Li_2O from within the Li_2S particles to the surface as the crystallinity of Li_2S increases with higher annealing temperatures, which hinders delithiation. Notably, the post-spike potential for the Li_2S@SP-350 battery is the highest among all batteries. Compared to Li_2S@SP-200, ion transport within the relatively disordered Li_2S particles covered by a LiOH/Li_2O shell is significantly poorer, resulting in a higher charging potential. In the Li_2S@SP-400 battery, ion transport improves due to increased Li_2S crystallinity. However, further raising the annealing temperature to 450 °C increases crystallinity further, making ion transport difficult once again. Consequently, the charge capacities follow an ascending-then-descending trend of 816, 1024, 1094, and 998 mA h g^{-1} for Li_2S@SP-200, Li_2S@SP-350, Li_2S@SP-400, and Li_2S@SP-450, respectively. Notably, the Li_2S@SP-400 battery exhibits the highest initial charge capacity due to its optimal moderate crystallinity.

The initial discharge curves for all batteries resemble those of typical S-LSBs: long-chain polysulfides formed quickly at the voltage of ~2.4 V. The first discharge plateau capacity represents

the reduction of S_8 to Li_2S_4, which accounts for 25% of the total theoretical discharge capacity of S_8 (292 mA g^{-1} based on Li_2S). The first discharge plateau capacities are 207, 254, 283, and 249 mA h g^{-1} for Li_2S@SP-200, Li_2S@SP-350, Li_2S@SP-400, and Li_2S@SP-450, respectively (**Table S 5.3**), corresponding to approximately 25% of their respective initial charge capacities. These values indicate that all sulfur formed during the initial charge is fully utilized and that minimal side reactions occurred during the first charging process, consistent with the LSV results on the electrolyte (**Figure S 5.5**). As the discharge process progresses further, long-chain polysulfides are reduced to shorter-chain polysulfides, with the second discharge plateau (~2.1 V) corresponding to the formation and precipitation of solid discharge products, namely Li_2S_2 and Li_2S. The small tail at the end of discharge, which becomes more pronounced with increasing annealing temperature, suggests further transformation from Li_2S_2 to Li_2S due to the tight contact between Li_2S_2 and Super P, making charge transfer more efficient. However, the confinement of Li_2S_2 in the Super P pores at the end of the discharging process also impedes its further reduction to form Li_2S, causing a discharge voltage drop.[368] Among all batteries, the Li_2S@SP-400 cell delivers the highest first discharge capacity of 821 mA h g^{-1}, followed by Li_2S@SP-350 (755 mA h g^{-1}), Li_2S@SP-450 (751 mA h g^{-1}), and Li_2S@SP-200 (596 mA h g^{-1}).

From the second cycle onward, all batteries exhibit typical charge/discharge curves observed for typical LSBs. The cycling performances of the batteries at 0.1 C over 100 cycles are shown in **Figure 5.3** (e). The Li_2S@SP-400 battery demonstrates the best performance, with a discharge capacity of 411 mA h g^{-1} after 100 cycles.

5.3.4 Performance comparison of Li_2S@SP Nanocomposite with Commercial Li_2S and Nano Li_2S

Since Li_2S is electrically insulating, its particle size and contact with the conductive additive, Super P, are crucial for efficient electronic transport, which affects charge transfer between Li_2S and the electrolyte, ultimately influencing battery performance. Confining Li_2S within mesoporous conductive carbon improves electronic conduction and charge transfer through close contact between Li_2S and carbon, while also reducing particle size, which is determined by the pore size of the mesoporous carbon.

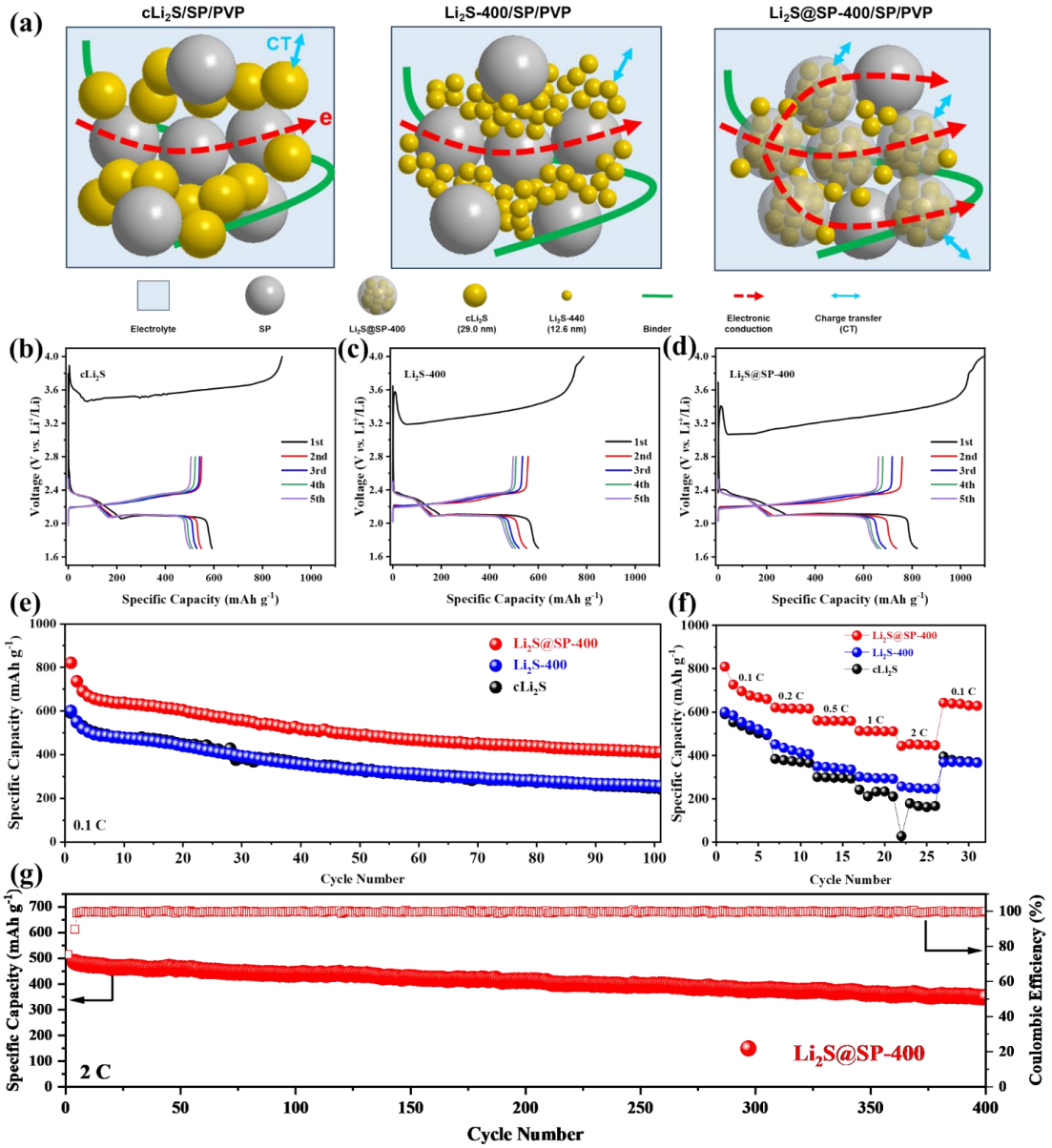


Figure 5.4 (a) Schematic illustration of the cathode structures for cLi_2S/SP/PVP, Li_2S-400/SP/PVP, and Li_2S@SP-400/SP/PVP. Initial charge/discharge curves at 0.1 C for batteries with the active material of: (b) cLi_2S, (c) Li_2S-400, and (d) Li_2S@SP-400. The first charge voltage was set to 4.0 V and the following electrochemical processes were in the voltage window between 1.7 and 2.8 V. (e) Cycling performance of batteries based on cLi_2S, Li_2S-400, and Li_2S@SP-400 at 0.1 C. (f) Rate performance of batteries based on cLi_2S, Li_2S-400, and Li_2S@SP-400. (g) Cycling performance of batteries based on Li_2S@SP-400 at 2 C.

To evaluate the impact of Li_2S confinement on battery performance, commercial Li_2S (cLi_2S) with an average crystallite size of 29.0 nm and Nano Li_2S, Li2S-400, with an average crystallite size of 12.6 nm were used to fabricate cathodes for comparison with the Li_2S@SP-400

nanocomposite, which has a Li_2S crystallite size of 11.4 nm. **Figure S 5.6** presents the TEM images of cLi_2S, Li_2S-400, and Li_2S@SP-400. Compared to cLi_2S, Li_2S-400 exhibits a substantial reduction in particle size. In the case of Li_2S@SP-400, only Super P particles are visible, suggesting that nearly all Li_2S is effectively confined within the hollow Super P structure, leading to a pronounced decrease in its particle size. It was expected that the confinement of insulating Li_2S in Super P would promote the electronic conduction and charge transfer in the Li_2S@SP-400-based cathode as schematically illustrated in **Figure 5.4** (a). The EIS in **Figure S 5.7** and **Table S 5.4** clearly demonstrate that Li_2S@SP-400 exhibits the lowest internal resistance compared to Li_2S-400 and cLi_2S batteries.

Figure 5.4 (b–d) compare the initial charge/discharge curves at 0.1 C for batteries using cLi_2S, Li_2S-400, and Li_2S@SP-400 as cathode materials, with exact capacities detailed in **Table S 5.5**. All batteries had identical amounts of Li_2S, SP, and PVP for a fair comparison.

The battery with cLi_2S shows a high overpotential of 3.89 V during the initial charge due to the LiOH/Li_2O layer on the Li_2S particle surface. The charging voltage remains above 3.4 V, attributed to the large crystal size, which hinders delithiation. In contrast, the Li_2S-400 battery shows a lower overpotential spike at 3.58 V and reduced post-spike charging potentials down to ~3.2 V due to its smaller particle size and thinner LiOH/Li_2O layer. The Li_2S@SP-400 nanocomposite exhibits an even lower overpotential spike at 3.41 V and post-spike potentials as low as ~3.1 V, with a significantly higher initial charge capacity of 1094 mA h g^{-1} compared to cLi_2S (882 mA h g^{-1}) and Li_2S-400 (788 mA h g^{-1}). Their subsequent discharge capacities consistently follow the order: cLi_2S (592 mA h g^{-1}) < Li_2S-400 (601 mA h g^{-1}) < Li_2S@SP-400 (821 mA h g^{-1}).

The confinement of Li_2S within Super P in Li_2S@SP-400 reduces the insulating Li_2S particles outside Super P, enhancing electronic conduction and charge transfer by forming conductive pathways through Super P particles. In contrast, cathodes using cLi_2S and Li_2S-400 have Li_2S particles outside Super P, making it difficult to form efficient conductive pathways, leading to some unutilized "dead" Li_2S particles (**Figure 5.4** (a)).

The Li_2S-400 battery has a shorter first discharge plateau (199.5 mA h g^{-1}) compared to the cLi_2S battery (217.8 mA h g^{-1}) but achieves a higher total discharge capacity. The cLi_2S battery also exhibits a low discharge potential valley between the first and second plateaus, indicating poor reaction kinetics, whereas this valley is absent in the Li_2S-400 battery. This suggests that although more Li_2S particles remain unutilized in Li_2S-400, the utilized particles undergo more complete reduction due to their smaller size.

The cycling curves in **Figure 5.4** (e) show that the Li_2S@SP-400 battery outperforms the other two over 100 cycles, while the cLi_2S and Li_2S-400 batteries exhibit similar cycling performance. All three batteries show comparable degradation rates, likely due to the polysulfide shuttle effect, as the mesoporous Super P has a limited capacity to trap soluble polysulfides.

The battery using Li_2S@SP-400 has the best rate performance, with 68% capacity retention in the fifth cycle at 2 C compared to the sixth 0.1 C cycle (**Figure 5.4** (f)). In comparison, cLi_2S and Li_2S-400 batteries retain only 34% and 49%, respectively. The confined Li_2S particles in Super P pores facilitate charge transfer and Li^+ ion diffusion, improving redox kinetics. While Li_2S-400 benefits from smaller particle size and outperforms cLi_2S, its loose contact with Super P results in lower conductivity and inferior rate performance compared to Li_2S@SP-400.

Notably, when the current increased to 2 C, cLi_2S showed very low capacity (~35 mA h g^{-1} charge and ~28 mA h g^{-1} discharge) in the first cycle at that rate. This is likely due to severe voltage polarization caused by the large particle size of commercial Li_2S, as well as its weak interfacial contact with the conductive Super P in the cathode composite. These structural limitations degrade the cathode's integrity when transitioning from 1 C to 2 C, leading to increased internal resistance and sluggish redox kinetics. Some capacity is recovered in later cycles, possibly due to structural adjustments that improve connectivity.

The structural stability of the cathode plays a critical role in long-term performance and is more closely related to the number of cycles than the total cycling time. As shown in **Figure 5.4** (g), the Li_2S@SP-400 battery retained 362.8 mA h g^{-1} after 400 cycles with only 0.08% degradation per cycle and 82.5% capacity retention. This excellent high-rate cycling stability indicates the robust structural integrity of the Li_2S@SP-400 cathode, likely attributed to the effective

confinement of Li_2S within the Super P host, which buffers the large volume changes during Li_2S/S_8 conversion and mitigates structural degradation.

This comparative study highlights that confining Li_2S inside mesoporous conductive carbon via the precursor solution infiltration-decomposition method effectively enhances electronic conduction and charge transfer in the Li_2S@SP nanocomposite cathode, achieving high-performance Li_2S-LSBs.

5.3.5 Performance comparison of Li_2S@SP Nanocomposite with S@SP Nanocomposite

As mentioned earlier, one key advantage of Li_2S-LSBs over S-LSBs is that Li_2S-LSBs start operation from charging, where Li_2S undergoes volume reduction rather than expansion, helping to maintain the structural integrity of the cathode. To demonstrate this advantage, we synthesized an elemental sulfur and Super P nanocomposite (S@SP) using the conventional melt infiltration method and compared it to the Li_2S@SP-400 nanocomposite. The content of the active materials (in the same state, S or Li_2S) in the cathodes was kept consistent. For easier comparison, Li_2S@SP-400 batteries were fully charged to convert Li_2S to sulfur at 0.1 C, with specific capacities calculated based on sulfur mass (mA h g^{-1} (S)).

EIS analysis reveals that the Li_2S@SP electrode, in its first charged state (sulfur state), exhibits a lower R_{ct} (45.5 Ω) than that (56.7 Ω) of the S@SP electrode, indicating more efficient charge transfer between sulfur and the electrolyte in the Li_2S@SP electrode (**Figure S 5.8** and **Table S 5.6**). This can be attributed to the formation of smaller sulfur particles from Li_2S after charging, which creates space within Super P, facilitating electrolyte diffusion. In contrast, sulfur particles in the S@SP electrode are tightly packed, making diffusion more difficult.

Cyclic voltammetry (CV) measurements at a scan rate of 0.1 mV s^{-1} (**Figure 5.5** (a) and (b)) show that both batteries exhibit two reduction peaks during the cathodic scan, corresponding to the two-step reduction of elemental sulfur to LPSs and then to Li_2S. The Li_2S@SP-400 battery shows higher peak potentials at 2.27 and 1.99 V, compared to 2.16 and 1.74 V for the S@SP electrode. In the anodic scan, both electrodes display two oxidation peaks, with the Li_2S@SP electrode showing lower peak potentials (2.34 and 2.44 V) than the S@SP electrode (2.34 and 2.53 V). The smaller

voltage difference (0.45 V) between the cathodic and anodic peaks for the Li_2S@SP electrode, compared to 0.80 V for the S@SP electrode, indicates faster kinetics for the sulfur-to-Li_2S conversion in the Li_2S@SP-400 electrode.

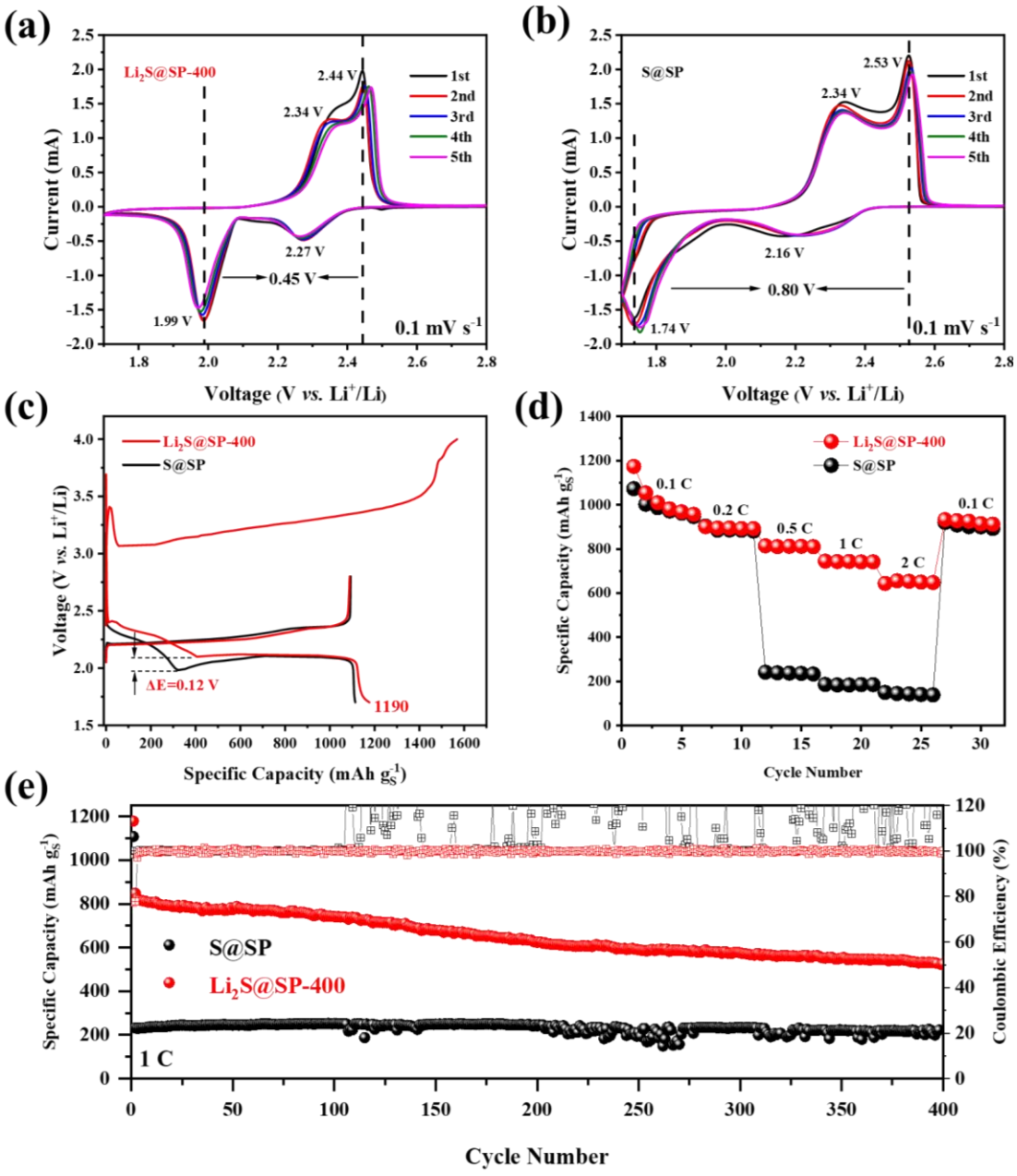


Figure 5.5 CV of (a) Li_2S@SP-400 and (b) S@SP with a scanning rate of 0.1 mV s^{-1}. (c) Initial charge/discharge curves of batteries based on Li_2S@SP-400-PVP and S@SP-PVP at 0.1 C. The first charge voltage of Li_2S@SP-400 was set to 4.0 V and the following electrochemical processes were in the voltage window between 1.7 and 2.8 V. (d) Rate performance of batteries based on Li_2S@SP-400 and S@SP. (e) Cycling performance of batteries based on S@SP and Li_2S@SP-400 at 1 C.

Figure 5.5 (c) shows the galvanostatic charge/discharge characteristics of Li_2S@SP-400 and S@SP batteries measured at 0.1 C. The Li_2S@SP-400 battery, first charged to 4.0 V for full activation, exhibited two discharge plateaus at 2.1 and 2.3 V, consistent with the two-step reaction mechanism. Additionally, a tail at the end of the discharge was observed in the Li_2S@SP-400 battery, attributed to the reduction of confined Li_2S within mesoporous carbon.[368] The Li_2S@SP-400 battery also showed a lower charging voltage in the second cycle compared to the S@SP battery, aligning with the CV results. Notably, the S@SP battery exhibited a pronounced dip between the two discharge plateaus, indicating lower reaction kinetics compared to the Li_2S@SP-400 battery.

In rate performance comparisons, both batteries show similar specific capacities at low current densities (0.1 C and 0.2 C). However, at 0.5 C, the S@SP battery's discharge capacity drops sharply due to sluggish kinetics. The charge and discharge curves (**Figure S 5.9**) show that high internal resistance in the S@SP battery causes the battery to reach the cutoff voltage prematurely.

For long-term cycling, both batteries were initially activated at 0.1 C, delivering discharge capacities of 1107 and 1179 mA h g^{-1} (S), respectively. In the subsequent cycle at 1 C, the Li_2S@SP-400 battery delivered an initial capacity of 848 mA h g^{-1} (S), while the S@SP battery delivered only 232 mA h g^{-1} (S) (**Figure 5.5** (e)). The S@SP battery also exhibited unstable cycling behavior, with notable fluctuations in both capacity and Coulombic efficiency (CE), likely due to mechanical degradation of the sulfur cathode over repeated cycling. The large volume expansion during discharge can cause structural damage and intermittent loss of contact between sulfur and the conductive Super P matrix, leading to inconsistent performance and poor CE retention.

In contrast, the Li_2S@SP-400 battery demonstrated stable cycling behavior, with consistent capacity and CE profiles. It remained operational after 400 cycles, retaining a capacity of 526 mA h g^{-1} (S). Unlike sulfur, Li_2S undergoes volume contraction during charging, which helps maintain the structural integrity of the cathode and contributes to its long-term electrochemical stability.

These results clearly demonstrate the advantages of using Li_2S as the starting cathode material in LSBs for reasons previously discussed. Specifically, sulfur, the densest of sulfur species, experiences significant volume expansion during cycling, leading to cathode structural damage, increased internal resistance, and reduced reaction kinetics. In contrast, Li_2S, with the lowest

density, undergoes volume reduction during the initial charging, which minimizes structural impact, enhances electrolyte diffusion, and improves reaction kinetics.

5.4 Conclusions

This work presents the development of a novel and efficient precursor solution infiltration-decomposition approach for the synthesis of Li_2S@C nanocomposites, achieved under mild conditions. The low solubility issue of Li_2S in EtOH was tackled by its facile reaction with CS_2 to form the amorphous and highly soluble Li_2CS_3 in EtOH, which can be easily infiltrated into mesoporous carbon SP to form a Li_2CS_3@SP nanocomposite. Upon heating above 200 °C, Li_2CS_3 quantitatively decomposed into Li_2S, forming Li_2S@SP nanocomposites. The average size of Li_2S and tight contact of the Super P's entrapment which were regulated via annealing temperature play significant roles in promoting the kinetics of Li_2S-LSBs. A discharge capacity of up to 821 mA h g^{-1} (Li_2S) is achieved in Li_2S-LSBs utilizing a Li_2S@SP-400 nanocomposite synthesized by thermal annealing at 400 °C for 3 h and PVP as a binder. The capacity is equal to a capacity of 1190 mA h g^{-1} (S) in S-LSBs. This is comparable to the values obtained by conventional S-LSBs employing S@SP nanocomposites synthesized via melt infiltration. This performance is notably superior to batteries utilizing commercial Li_2S or non-infiltrated Li_2S-400 nanoparticles of similar size. This simple, novel, and efficient method for synthesizing Li_2S@C nanocomposites overcomes a key obstacle in the commercialization of Li_2S-LSBs.

5.5 Supporting Information

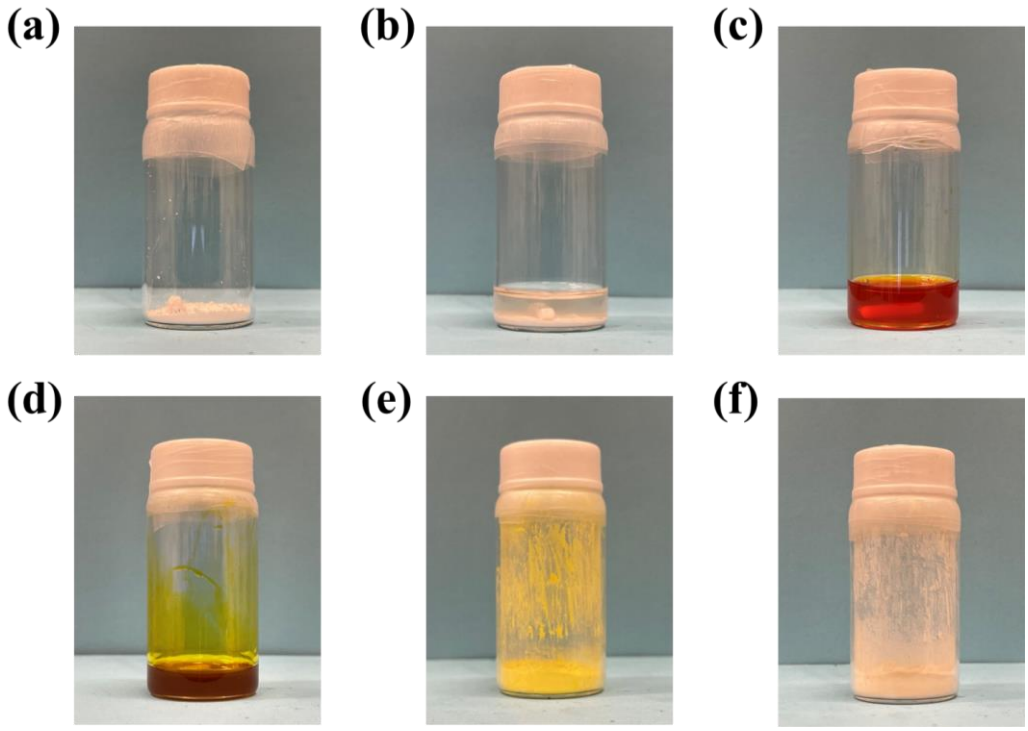


Figure S 5.1 Photos of (a) Commercial Li_2S powders, (b) Li_2S powders in EtOH (mixed in 60 mg_{Li2S}/1 mL_{EtOH}), (c) Li_2CS_3/EtOH solution (mixed in 60 mg_{Li2S}/100 μL_{CS2}), (d) Concentrated Li_2CS_3/EtOH solution, (e) Completely dried Li_2CS_3 powders, and (f) Li_2S-400.

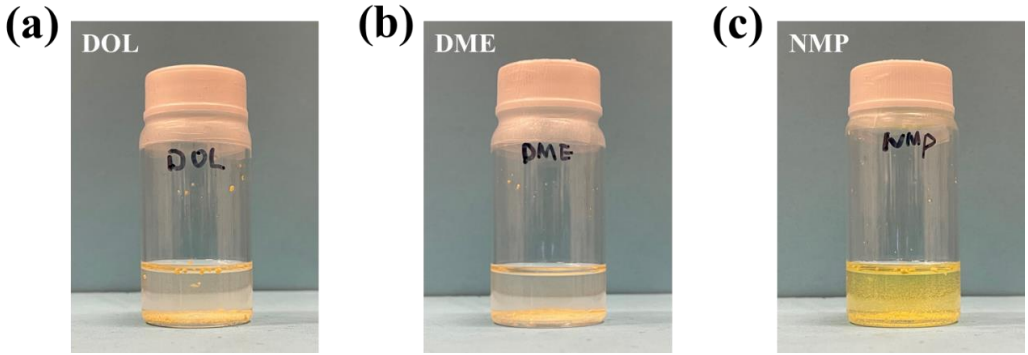


Figure S 5.2 Solubility tests of as-prepared Li_2CS_3 powders in (a) 1,3-dioxolane (DOL), (b) dimethoxyethane (DME), and (c) *N*-methyl-2-pyrrolidone (NMP).

Table S 5.1 Crystallite sizes of different Li_2S samples calculated using the *Scherrer* equation.

Sample	Peak (*hkl*)	θ (°)	FWHM (°)	*D* (nm)	Average *D* (nm)
cLi₂S	(200)	15.60	0.27	30.2	**29.0**
	(220)	22.35	0.30	28.8	
	(311)	26.45	0.31	28.0	
Li₂S-400	(200)	15.65	0.60	13.6	**12.6**
	(220)	22.43	0.69	12.3	
	(311)	26.55	0.79	11.9	
Li₂S@SP-200	(200)	16.18	0.83	9.9	**8.5**
	(220)	22.90	1.14	7.5	
	(311)	27.03	1.09	8.1	
Li₂S@SP-350	(200)	15.60	0.65	12.6	**11.0**
	(220)	22.35	0.84	10.1	
	(311)	26.53	0.85	10.3	
Li₂S@SP-400	(200)	15.78	0.62	13.1	**11.4**
	(220)	22.53	0.80	10.7	
	(311)	26.65	0.84	10.4	
Li₂S@SP-450	(200)	15.73	0.73	11.2	**11.2**
	(220)	22.45	0.68	12.6	
	(311)	26.60	0.90	9.8	

Note:

Crystallite sizes (D) were calculated using the Scherrer equation:

$$D = \frac{K\lambda}{\beta \cos\theta} \qquad \textbf{Equation S 5.1}$$

Where:

K is the shape factor (0.89, assuming spherical crystallites),

λ is the X-ray wavelength (0.154184 nm),

β is the full width at half maximum (FWHM) of the diffraction peak (in radians),

θ is the Bragg angle.

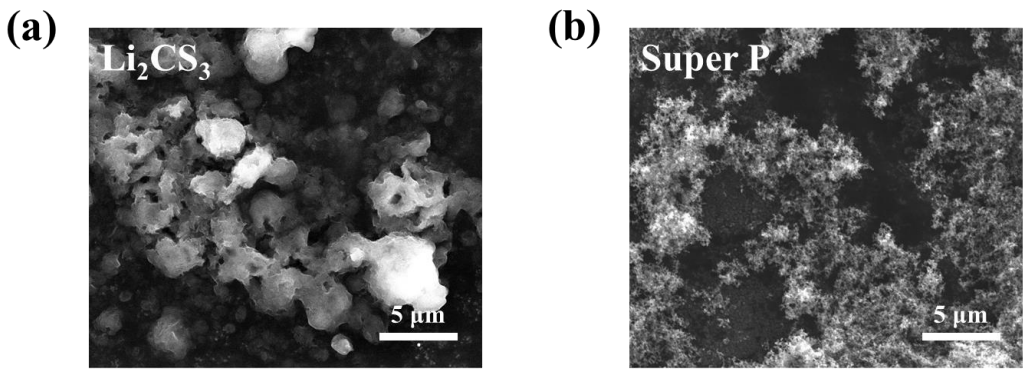


Figure S 5.3 SEM images of (a) Li_2CS_3 and (b) Super P.

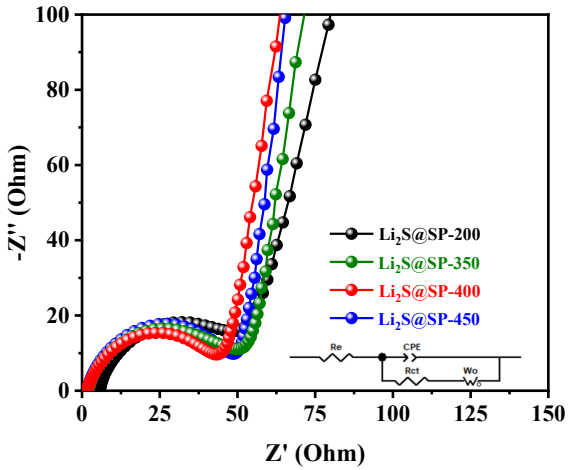


Figure S 5.4 EIS of batteries based on Li_2S@SP nanocomposites using PVP as the binder. Inserted is the equivalent Randles circuit used for the fitting, where R_e is the resistance of the electrolyte solution, R_{ct} is the charge transfer resistance, *CPE* is the capacitance, and W_o is the Warburg impedance.

Table S 5.2 Resistances of cathodes calculated from the EIS data in **Figure S 5.4**.

Cathode	Resistance (Ω)	
	R_e	R_{ct}
Li_2S@SP-200	5.6	52.5
Li_2S@SP-350	1.9	51.4
Li_2S@SP-400	1.7	43.6
Li_2S@SP-450	1.7	49.3

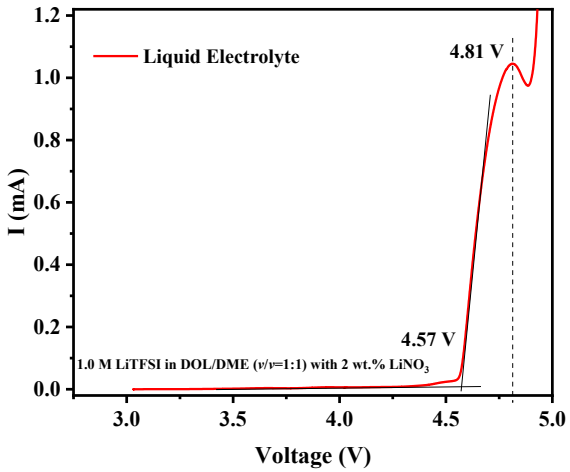


Figure S 5.5 LSV at 1.0 mV s^{-1} of battery based on carbon paper and lithium metal anode using liquid electrolyte containing 1.0 M LiTFSI in DOL/DME (*v*/*v*=1:1) with 2 wt.% $LiNO_3$ as additive.

Table S 5.3 Summary of the Initial Charge Capacity, Discharge Capacity, and 1st Discharge Plateau in **Figure 5.3**.

Battery	Charge Capacity	Discharge Capacity	1st Discharge Plateau
Li_2S@SP-200	816	595	207.5
Li_2S@SP-350	1024	755	254
Li_2S@SP-400	1094	821	283
Li_2S@SP-450	998	751	249

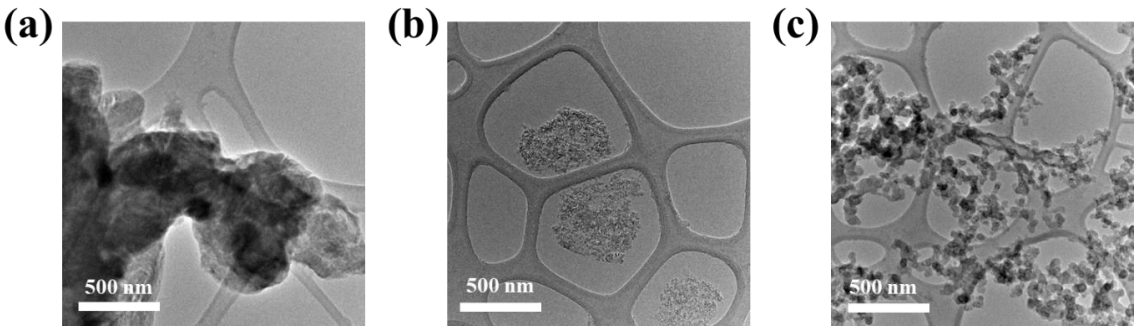


Figure S 5.6 TEM images of (a) cLi_2S, (b) Li_2S-400, and (c) Li_2S@SP-400.

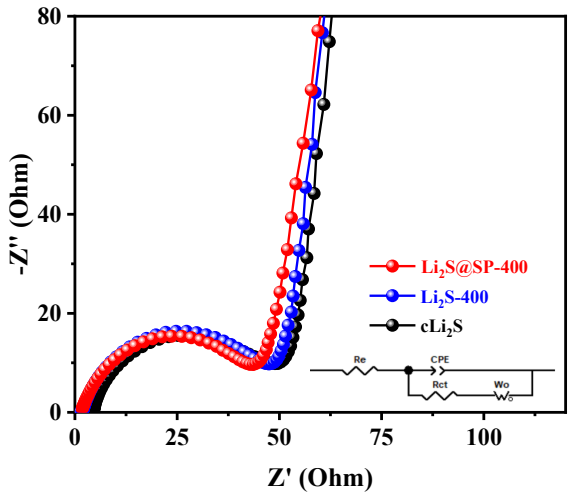


Figure S 5.7 EIS of batteries based on cLi_2S, Li_2S-400 and Li_2S@SP-400. Inserted is the equivalent Randles circuit used for the fitting, where R_e is the resistance of the electrolyte solution, R_{ct} is the charge transfer resistance, *CPE* is the capacitance, and W_o is the Warburg impedance.

Table S 5.4 Resistances of cathodes calculated from the EIS data in **Figure S 5.7**.

Cathode	Resistance (Ω)	
	R_e	R_{ct}
Li_2S@SP-400	1.7	43.6
Li_2S-400	1.8	48.7
cLi_2S	4.3	50.4

Table S 5.5 Summary of the Initial Charge Capacity, Discharge Capacity, and 1st Discharge Plateau in **Figure 5.4**.

Battery	Charge Capacity	Discharge Capacity	1st Discharge Plateau
cLi$_2$S	881	593	218
Li$_2$S-400	785	600.5	199.5
Li$_2$S@SP-400	1094	821	283

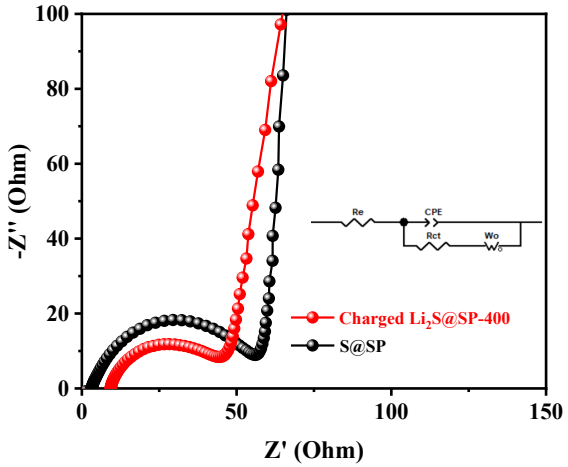


Figure S 5.8 EIS of batteries based on charged Li$_2$S@SP-400 and S@SP. Inserted is the equivalent Randles circuit used for the fitting, where R_e is the resistance of the electrolyte solution, R_{ct} is the charge transfer resistance, *CPE* is the capacitance, and W_o is the Warburg impedance.

Table S 5.6 Resistances of cathodes calculated from the EIS data in **Figure S 5.8**.

Cathode	Resistance (Ω)	
	R_e	R_{ct}
Charged Li$_2$S@SP-400	9.3	45.5
S@SP	3.1	56.7

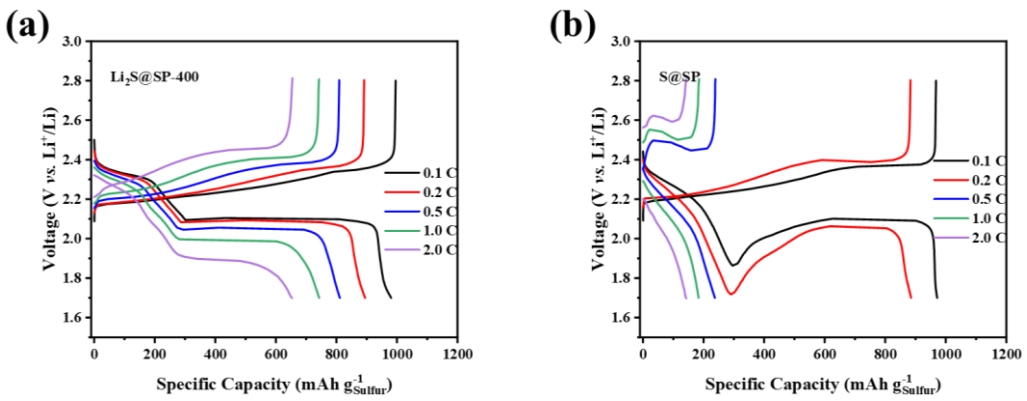


Figure S 5.9 Picked charge/discharge curves from the rate performance in **Figure 5.5** (d). The picked cycles were 4th, 9th, 14th, 19th, and 24th (the third cycle of each C-rate).

Chapter 6 Multi-Cycle Precursor Infiltration-Thermal Decomposition Achieves High In-Pore Li_2S Loading in Mesoporous Carbon for High-Performance Lithium Sulfide Batteries

This chapter is based on the following submitted manuscript:

Z. Huang, Y. Wang, Y. Zhao, Y. Li, *ACS Applied Energy Materials*.

6.1 Introduction

The accelerating demand for electric vehicles, portable electronics, and grid-scale energy storage continues to drive the development of advanced battery technologies with higher energy density, extended cycle life, and reduced cost.[31,34,334,335] While lithium-ion batteries (LIBs) dominate the current market and have seen steady improvements through innovative technologies such as solid-state electrolytes and high-capacity anode materials, their energy density remains fundamentally constrained by the limited theoretical capacities of conventional cathode materials.[333,336,369] As performance requirements grow more stringent, conventional LIBs are increasingly falling short of meeting application needs.[291] This has motivated worldwide efforts to investigate alternative cathode chemistries and next-generation battery technologies capable of delivering significantly higher energy densities.[337]

Among these alternatives, lithium-sulfur batteries (LSBs) are especially promising due to sulfur's high theoretical specific capacity (1,672 mA h g^{-1} for sulfur) and corresponding specific energy of up to 2,600 W h kg^{-1}, which far surpass those of traditional LIBs.[92,109,370] In addition to high energy density, sulfur is abundant, inexpensive, non-toxic, and environmentally benign, making LSBs a highly sustainable energy storage option.[87,90] However, several technical challenges still hinder their commercialization, including the intrinsic low electronic conductivity of both sulfur and lithium sulfide (Li_2S), the dissolution and shuttling of long-chain lithium polysulfides (LPSs), and significant cathode volume changes during cycling.[90,345,371]

LSBs are generally classified into two types based on their starting cathode materials: elemental sulfur-based (S-LSBs)[297] and lithium sulfide-based (Li_2S-LSBs).[140] While S-LSBs have

been more extensively studied, largely due to the ease of handling elemental sulfur, they suffer from practical limitations. Specifically, the reliance on highly reactive highly reactive lithium metal anodes poses serious safety risks and complicates large-scale manufacturing, while dendrite growth during cycling can lead to short circuits and thermal runaway.[341] Another major challenge is that the sulfur cathodes undergo ~78% volume expansion upon initial lithiation, causing mechanical stress and loss of structural integrity.[253] Additionally, the dissolution and migration (shuttle effect) of LPSs during cycling further compromises capacity and cycle life.[108]

Li_2S-based LSBs alleviate most of these issues. Because Li_2S is already in the fully lithiated state, it can be paired with safer, lithium-free anodes such as graphite,[144] silicon,[157] or tin,[161] improving safety and manufacturing flexibility. Moreover, the Li_2S cathode undergoes volume contraction upon initial charging, helping to retain structural integrity and physically confine LPSs within the carbon matrix.[253]

Since the seminal work by Nazar *et al.* in 2009, confining sulfur within mesoporous conductive carbon to form sulfur-carbon (S@C) nanocomposites has become a widely used strategy to overcome sulfur's intrinsic insulating nature and partially suppress polysulfide shuttling and cathode volume changes in LSBs.[89,112,168] Optimizing the sulfur loading, typically between 50 and 80 wt.%, is crucial to achieving a balance between specific capacity, electronic conductivity, and cycling stability.[372,373]

S@C nanocomposites are commonly prepared using a melt-infiltration method, where sulfur is heated with a mesoporous carbon host at temperatures above its melting point (115 °C for α-S_8), typically around 155 °C. In contrast, Li_2S has a much higher melting point (938 °C), making melt-infiltration impractical for synthesizing Li_2S@C nanocomposites. Among alternative methods (summarized in **Table S 6.1**), the Li_2S-ethanol (EtOH) solution infiltration method is widely adopted. In this method, Li_2S is dissolved in EtOH and recrystallized within a carbon matrix upon solvent evaporation.[112,224] However, due to the low solubility of Li_2S in ethanol (~25 mg mL^{-1}),[224,227,228] a large portion of Li_2S crystallizes outside the mesopores, leading to low in-pore Li_2S loading.

To improve Li_2S infiltration, Nan *et al.* synthesized nano-Li_2S spheres via lithiation of sulfur using $LiEt_3BH$, followed by carbon coating through CVD.[215] Alternatively, graphene has been used in place of mesoporous carbon to disperse Li_2S. For example, Tan *et al.* ignited lithium metal in CS_2 gas to synthesize Li_2S@graphene nanocapsules.[145] Zhang *et al.* used lithiothermic reduction of MoS_2 followed by CS_2 treatment to prepare a Mo-Li_2S-graphene composite.[277] However, these methods involve hazardous chemicals, high temperatures, or complex procedures, limiting their scalability and practicality. Moreover, in graphene-based composites, Li_2S is not as effectively confined within nanopores as in mesoporous carbon, reducing their ability to suppress polysulfide shuttling and accommodate volume changes. Additionally, graphene is significantly more expensive than conventional carbon materials such as Super P (SP).

To mitigate these issues, we previously developed a mild and scalable precursor infiltration-thermal decomposition strategy to synthesize Li_2S@C nanocomposites using Super P as a carbon host.[195] In this approach, lithium trithiocarbonate (Li_2CS_3) is formed by reacting commercial Li_2S with CS_2 in EtOH at room temperature. The highly soluble Li_2CS_3 is then infused into Super P and decomposed at ≥ 200 °C to yield Li_2S@SP. Compared to physical mixtures of commercial Li_2S and Super P (cLi_2S/SP), Li_2S@SP exhibited markedly enhanced electrochemical performance. However, thermal decomposition of Li_2CS_3 releases a large amount of CS_2 gas (~62 wt.% of the precursor), which creates internal voids and limits the in-pore Li_2S loading. To overcome this limitation, here we introduce a multi-cycle infiltration-decomposition strategy. In each cycle, a portion of the Li_2CS_3 precursor is infiltrated into the carbon host to maximize pore utilization and decomposed to form Li_2S within the pores. Repeating this process gradually refills the voids generated by CS_2 release, significantly increasing in-pore Li_2S loading.

Specifically, Li_2S@SP nanocomposites with an overall Li_2S loading of 70 wt.% were synthesized by three (Li_2S@SP-3) and five (Li_2S@SP-5) infiltration-decomposition cycles, yielding pore filling factors (FF; fraction of pore volume filled by Li_2S) of 76% and 91% and in-pore loadings (IPL: Li_2S confined in pores over total Li_2S) of 61% and 73%, respectively, substantially higher than the single-cycle values (Li_2S@SP-1: FF 38%, IPL 30%). Structural characterizations such as X-ray diffraction (XRD) and scanning electron microscopy (SEM) confirm that more Li_2S is gradually infiltrated into the carbon host with increasing cycle number,

leading to a more uniform and confined Li_2S distribution. Cyclic voltammetry (CV) results further support this trend: the Li_2S@SP-5 electrode exhibits an earlier onset of oxidation, more distinct charging peaks, and notably lower charge overpotential, indicating improved redox kinetics. As a result, the electrochemical performance improves significantly, particularly for the Li_2S@SP-5 sample, which demonstrates more efficient activation, higher specific capacity, and better cycling stability than Li_2S@SP-1 and Li_2S@SP-3. Compared to a conventional S@SP cathode prepared by thermal infiltration, the Li_2S@SP-5 electrode exhibits not only higher specific capacity, lower polarization, and better rate capability, but also superior structural integrity during prolonged cycling. This improvement is largely attributed to the initial volume contraction during Li_2S activation, which helps confine sulfur species and mitigate cathode damage. These results demonstrate the effectiveness of the multi-cycle infiltration-decomposition strategy in achieving high in-pore Li_2S loading and enabling LSBs with enhanced electrochemical performance.

6.2 Experimental Section

6.2.1 Materials

Chemicals were obtained from Sigma-Aldrich: Li_2S (99.98%) (denoted as cLi_2S), ethanol (EtOH, anhydrous, ⩽ 0.003% water), carbon disulfide (CS_2) (⩾ 99.9%), elemental sulfur (99.98%), anhydrous *N*-methyl pyrrolidone (NMP) (99.5%), and polyvinylpyrrolidone (PVP) (M_w ~1,300,000). Ethanol and NMP were further dried with molecular sieves. Super P (SP) was purchased from IMERYS. Polyvinylidene fluoride (PVDF) (M_w ~1,000,000) was from Kynar. Si/C powders (GS60, ⩾ 600 mA h g^{-1}) were purchased from Shanshan Technology, which were used to prepare anodes. All other chemicals were used as received.

6.2.2 Preparation of Li_2CS_3 Solution

The synthesis followed a previously reported method.[195] Li_2S (280 mg, 6.1 mmol) and CS_2 (386.5 μL, 487 mg, 6.4 mmol; 5% excess) were mixed in 3 mL of anhydrous ethanol (EtOH) in an Ar-filled glovebox (< 0.5 ppm O_2 and H_2O). The mixture was stirred for 30 min at room temperature to form a clear orange Li_2CS_3 solution (containing ~745 mg Li_2CS_3). Excess CS_2 was removed by brief evacuation under reduced pressure, then additional anhydrous EtOH was added to adjust the total volume to 5 mL.

6.2.3 Preparation of Li_2S@SP-1 Nanocomposite

A Li_2CS_3 solution (5 mL, composed of 280 mg Li_2S or ~745 mg Li_2CS_3) was mixed with Super P (120 mg) and stirred for 6 h at room temperature in an Ar-filled glove box. The resulting mixture was first vacuum-dried at room temperature, followed by further drying at 100 °C to ensure complete removal of residual solvent. The prepared Li_2CS_3@SP precursor was first heated at 200 °C for 2 h under vacuum and then annealed at 400 °C for 1 h to produce Li_2S@SP-1 nanocomposite with a total Li_2S loading of 70 wt.%.

6.2.4 Preparation of Li_2S@SP-3 and Li_2S@SP-5 Nanocomposites

A Li_2CS_3 solution (5 mL, containing 280 mg Li_2S or ~745 mg Li_2CS_3) was divided into three (2/1.5/1.5 mL; 40/30/30%) or five portions (2/1.25/0.75/0.5/0.5 mL; 40/25/15/10/10%) and infiltrated into Super P (120 mg) in successive steps. In each cycle, a certain amount of the precursor solution was mixed with Super P for 6 h at room temperature in an Ar-filled glove box under stirring, followed by vacuum drying at room temperature and then at 100 °C to remove residual solvent. The

resulting Li_2CS_3@SP composite was then thermally treated in vacuo at 200 °C for 2 h to decompose the precursor into Li_2S. This infiltration-decomposition cycle was repeated to achieve a total of three or five cycles. After the final cycle, the samples were annealed at 400 °C for 1 h, yielding the final nanocomposites denoted as Li_2S@SP-3, and Li_2S@SP-5, respectively.

6.2.5 Synthesis of S@SP Nanocomposite

For comparison, an S@SP composite was prepared by grinding 195 mg sulfur (S) with 120 mg Super P and heating at 155 °C for 12 h. The nanocomposite contains 62 wt.% sulfur, corresponding to the sulfur loading equivalent to 70 wt.% Li_2S in Li_2S@SP.

6.2.6 Fabrication of Cathodes

Li_2S@SP or S@SP, Super P, and PVP were ground for 30 min in NMP at a mass ratio of 80:10:10 for Li_2S@SP electrodes and 63.07:10:10 for S@SP electrodes. The resulting slurry was coated onto carbon-coated aluminum foil and vacuum dried at 50 °C overnight. The dried films were then punched into 12 mm discs. The active material loading (Li_2S, or Li_2S equivalent for the S cathode) loading was ~1.0–1.2 mg cm^{-2}.

6.2.7 Electrochemical Measurements

CR2032 half cells were assembled inside an Ar-filled glovebox using Li_2S@SP cathode (or other cathodes), lithium metal anodes, Celgard 2400 separators, and 1 M LiTFSI electrolyte in a 1:1 (*v*/*v*) DOL/DME with 2 wt.% $LiNO_3$. Galvanostatic charge-discharge measurements were conducted using a Land 2001A battery tester. Electrochemical impedance spectroscopy (EIS) was performed using a Bio-logic VSP (1000 kHz to 0.1 Hz, 10 mV AC), and CV in the 1.7−4.0 V and 1.7−2.8 V range at different scan rate of 0.025 and 0.1 mV s^{-1}.

6.2.8 Characterizations

XRD was performed on a Bruker D8 Discover diffractometer with Cu Kα radiation (λ = 1.5418 Å). Samples were covered with Kapton tape to avoid moisture uptake. SEM images were acquired using a Zeiss Sigma HD microscope.

6.3 Results and Discussion

6.3.1 Synthesis of Li_2S@SP Nanocomposites

The Li_2CS_3 precursor solution readily infiltrates the mesopores of Super P by capillary force, forming a Li_2CS_3@SP composite. Upon heating, Li_2CS_3 thermally decomposes at $\geqslant$ 150 °C to produce Li_2S and release CS_2 gas.[195] Because Li_2S accounts for only 37.6 wt.% of Li_2CS_3, a single infiltration-decomposition cycle yields a maximum pore-filling factor (FF) of ~38%. To fully confine Li_2S within the pores or reach complete (100%) in-pore Li_2S loading (IPL) for a Li_2S@C nanocomposite with a total Li_2S loading of 70 wt.%, the carbon host would need a minimum mesopore volume ($V_{pore,min}$) of 3.74 $cm^3\ g^{-1}$ (**Table S 6.2** and **Equation S 6.1**). While some porous carbons with mesopore volumes approaching or exceeding this value have been reported, most commercially available mesoporous carbons fall far below this threshold.[374,375] For example, Super P can achieve up to 70 wt.% in-pore sulfur loading in S@SP composite,[87] but its effective pore volume is estimated to be only ~1.13 $cm^3\ g^{-1}$. (The pristine, unfilled material has an even lower reported value of 0.24 $cm^3\ g^{-1}$,[376] likely due to collapse of its mesoporous structure). Assuming equal densities for Li_2CS_3 and Li_2S (1.66 g cm^{-3}), the maximum achievable IPL with Super P in a single cycle is ~41 wt.%, corresponding to complete pore filling by Li_2CS_3 without any excess precursor outside the pores. When the total Li_2S loading of the Li_2S@SP nanocomposite exceeds this limit, the excess precursor forms Li_2S on the external surface of Super P or as isolated aggregates. Such external Li_2S particles suffer from poor charge transfer, pronounced polysulfide shuttling, and severe volume changes compared with Li_2S confined within the conductive matrix. To overcome this limitation, we propose a multi-cycle infiltration-decomposition strategy (**Figure 6.1**). A carbon host with mesopore volume V_{pore} ($cm^3\ g^{-1}$(C)) can accommodate a maximum mass $V_{pore}\rho_1$ (g g^{-1}(C)) of Li_2CS_3.

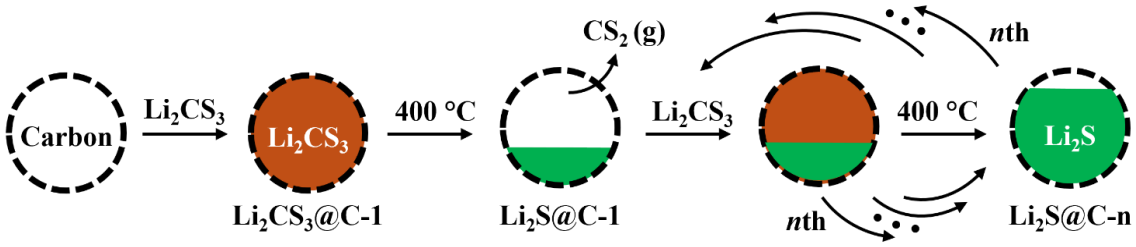


Figure 6.1 Schematic illustration of the synthesis of Li_2S@C nanocomposites with high in-pore Li_2S loading via multi-cycle Li_2CS_3 infiltration-decomposition strategy.

In the first cycle, $V_{pore}\rho_1$ of Li_2CS_3 is infiltrated to form a nanocomposite Li_2CS_3@C-1. Thermal decomposition yields a nanocomposite Li_2S@C-1 with $V_{pore}\rho_1 x$ Li_2S and generates a new void pore volume $V_{pore}\left(1 - x(\rho_1/\rho_2)\right)$, where x the Li_2S mass fraction in Li_2CS_3 is (0.376) and ρ_1 and ρ_2 are densities of Li_2CS_3 and Li_2S, respectively. For simplicity, we take $\rho_1 = \rho_2 = 1.66$ g cm^{-3}. Each subsequent cycle fills the newly generated voids with Li_2CS_3, depositing Li_2S and generating voids (see details in **Table S 6.2**). After n cycles, the cumulative in-pore Li_2S mass $m_{Li_2S,ip}$ (g g^{-1}(C)) in the Li_2S@C-n nanocomposite is given by **Equation 6.1**:

$$m_{Li_2S,ip} = V_{pore}\rho_2\left(1 - \left(1 - x\frac{\rho_1}{\rho_2}\right)^n\right) \qquad \textbf{Equation 6.1}$$

and the pore-filling factor (FF) by **Equation 6.2**:

$$\mathrm{FF} = 1 - \left(1 - x\frac{\rho_1}{\rho_2}\right)^n \qquad \textbf{Equation 6.2}$$

The in-pore Li_2S loading (IPL) for a Li_2S@C nanocomposite with total Li_2S loading y (fractional) can be calculated using **Equation 6.3**:

$$\mathrm{IPL} = V_{pore}\rho_2\left(1 - \left(1 - x\frac{\rho_1}{\rho_2}\right)^n\right)\left(\frac{1}{y} - 1\right) \qquad \textbf{Equation 6.3}$$

To validate this strategy, we used Super P as a carbon host to prepare Li_2S@SP nanocomposites with 70 wt.% total Li_2S loading using one, three, and five infiltration-decomposition cycles, denoted Li_2S@SP-1, Li_2S@SP-3, and Li_2S@SP-5, respectively. The Li_2CS_3 solution was introduced in the following proportions: 100% in a single step for Li_2S@SP-1; 40%, 30%, and 30% for Li_2S@SP-3; and 40%, 25%, 15%, 10%, and 10% for Li_2S@SP-5. Since the total amount of Li_2CS_3 used exceeds the V_{pore} of Super P, and each infiltration step supplied more than required to refill the voids generated by CS_2 release, the FF values for Li_2S@SP-1, Li_2S@SP-3, and Li_2S@SP-5 are estimated to be 38%, 76%, and 91%, respectively (**Table S 6.2**). The corresponding

IPL values estimated from **Equation 6.3** were 30% for Li_2S@SP-1, 61% for Li_2S@SP-3, and 73% for Li_2S@SP-5, confirming the high effectiveness of the multi-cycle infiltration-decomposition strategy in increasing in-pore loading.

As established in our previous study, Li_2CS_3 confined in Super P can be fully converted to Li_2S after heating at 200 °C for 2 h, while annealing at 400 °C improves electrochemical performance by enhancing interfacial contact and crystallinity.[195] Accordingly, each infiltration-decomposition cycle was conducted at 200 °C for 2 h, followed by final sintering at 400 °C for 1 h to prepare the Li_2S@SP nanocomposites.

6.3.2 Characterization of Li_2S@SP Nanocomposites

X-ray diffraction (XRD) was conducted to assess the confinement of Li_2S within the Super P pores, as in-pore Li_2S is expected to be less crystalline or even amorphous compared to external Li_2S.[195,368] As shown in **Figure 6.2** (a), the control sample, prepared by manually grinding commercial Li_2S with Super P (70:30 wt.%; cLi_2S/SP), exhibited intense, sharp Li_2S peaks, characteristic of large, unconfined crystallites. In contrast, the Li_2S@SP samples showed significantly weaker and broader Li_2S peaks, with intensity decreasing progressively from Li_2S@SP-1 to Li_2S@SP-5 as the cycle number increased. This trend indicates a reduction in crystallite size and improved dispersion of Li_2S within the carbon host. Notably, Li_2S@SP-5 exhibited the weakest peaks, suggesting the highest degree of in-pore Li_2S loading, while the residual peaks correspond to external Li_2S (~27%, **Table S 6.2**). Crystallite sizes estimated from the *Scherrer* equation also decrease with increasing infiltration cycles, as shown in **Figure 6.2** (b) and summarized in **Table S 6.3**.

These results demonstrate the effectiveness of the multi-cycle infiltration-decomposition approach in achieving uniform nanoscale dispersion of Li_2S with high in-pore loading, key factors for high-performance Li_2S cathodes.

Scanning electron microscopy (SEM) was performed to examine morphological differences among the samples, as varying amounts of external Li_2S were expected to affect their surface features. However, because all samples contained external Li_2S that readily hydrolyzed upon exposure to ambient moisture, direct SEM comparison of the as-prepared materials proved challenging (**Figure S 6.1**). To address this, the composites were fabricated into cathodes,

assembled into cells, and charged to convert Li_2S into air-stable elemental sulfur prior to SEM imaging. Because polysulfide shuttling during the initial charging process is minimal, the morphologies of the charged samples are representative of the pristine materials.

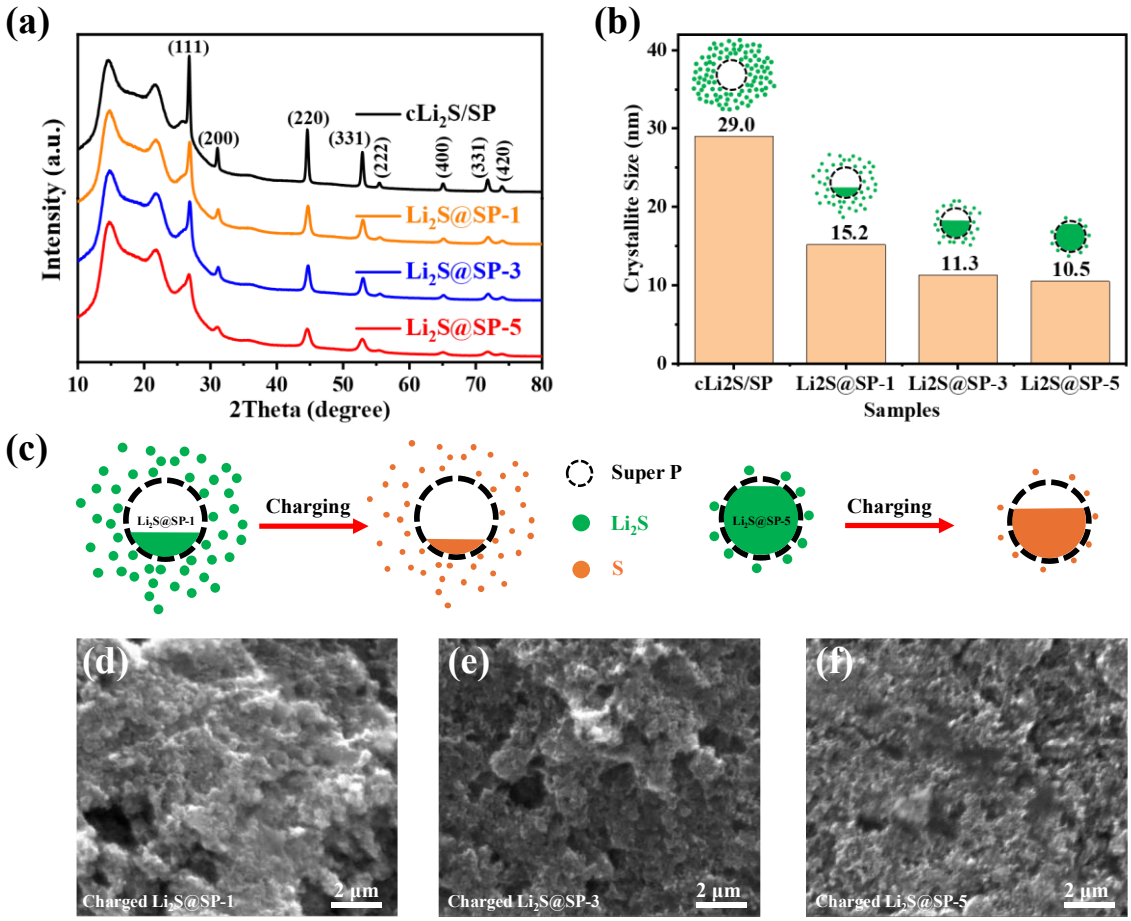


Figure 6.2 (a) XRD patterns of cLi_2S/SP (manually ground mixture, 70:30 wt.%), Li_2S@SP-1, Li_2S@SP-3, and Li_2S@SP-5. (b) Crystallite sizes derived from XRD. (c) Schematic illustration of sulfur species evolution and volume change during charging process of Li_2S@SP-1 and Li_2S@SP-5. SEM images of charged electrodes: (d) Li_2S@SP-1/SP/PVP, (e) Li_2S@SP-3/SP/PVP, and (f) Li_2S@SP-5/SP/PVP (Li_2S@SP:SP:PVP = 8:1:1 by weight), each charged from open circuit voltage (OCV) to 4.0 V.

As shown in **Figure 6.2** (d–f), distinct morphological differences were observed among the charged samples. In Li_2S@SP-1 (**Figure 6.2** (d)), bright, continuous sulfur networks obscure the carbon particles, indicating extensive external sulfur. In Li_2S@SP-3 (**Figure 6.2** (e)), some surface sulfur remains, but the spherical morphology of Super P is partially visible. In stark contrast, Li_2S@SP-5 (**Figure 6.2** (f)) exhibits clearly defined, isolated carbon spheres with the lowest

fraction of external sulfur, consistent with efficient Li_2S confinement within the pores as expected (**Table S 6.2**).

Collectively, these findings confirm that increasing the number of infiltration-decomposition cycles enhances in-pore Li_2S loading, reducing surface deposition and improving the uniformity of the nanocomposites.

6.3.3 Electrochemical Performance of Li_2S@SP Nanocomposites

To evaluate the impact of the number of infiltration-decomposition cycles on electrochemical performance, Li_2S-LSBs were assembled using Li_2S@SP nanocomposites as the cathode materials. Polyvinylpyrrolidone (PVP) was used as the binder instead of poly(vinylidene fluoride) (PVDF) that is commonly used for S-LSBs, since PVDF can react with Li_2S and lead to capacity loss.[344] Cyclic voltammetry (CV) profiles (**Figure 6.3** (a–c)) show initial anodic peaks at ~3.59 V for Li_2S@SP-1 and Li_2S@SP-3, and ~3.55 V for Li_2S@SP-5, indicating similar $Li_2S \rightarrow$ LPSs $\rightarrow S_8$ redox chemistry across all samples. However, the anodic onset potential progressively decreases from 3.25 V (Li_2S@SP-1) to 3.20 V (Li_2S@SP-3), and 3.04 V (Li_2S@SP-5), reflecting a reduced activation overpotential. This improvement is attributed to enhanced Li_2S confinement within the Super P matrix and more intimate Li_2S-carbon contact, which together promote more efficient electron and ion transport with increasing infiltration-decomposition cycles.

Subsequent cathodic scans reveal two peaks at ~2.30 V and ~2.05 V, corresponding to the stepwise reduction of sulfur species to LPSs and Li_2S. Li_2S@SP-5 exhibits the sharpest and most intense peaks, indicating more efficient reduction reactions, while Li_2S@SP-1 shows broader, weaker peaks due to kinetic limitations.

In the second CV cycle (1.7–2.8 V), Li_2S@SP-1 exhibits poorly resolved anodic peaks, indicating sluggish oxidation kinetics. In contrast, Li_2S@SP-3 shows two distinct anodic peaks at 2.31 and 2.39 V, reflecting improved reaction resolution. Li_2S@SP-5 further enhances this trend, which shows more sharply defined peaks at slightly lower potentials of 2.30 and 2.38 V. The dominant peak at 2.30 V in Li_2S@SP-5 suggests more efficient conversion of Li_2S to short-chain polysulfides, confirming the enhanced redox kinetics achieved through increased Li_2S infiltration.

In the third cycle, the anodic peaks of Li_2S@SP-1 shift to higher potentials, indicating deteriorated reaction kinetics, likely caused by the diffusion of sulfur species initially deposited

outside the Super P particles, leading to poorer contact with conductive pathways. In contrast, the anodic peaks of Li_2S@SP-3 and Li_2S@SP-5 remain stable and become more clearly resolved, suggesting that the confinement of sulfur species within the pores of Super P effectively maintains favorable redox environments.

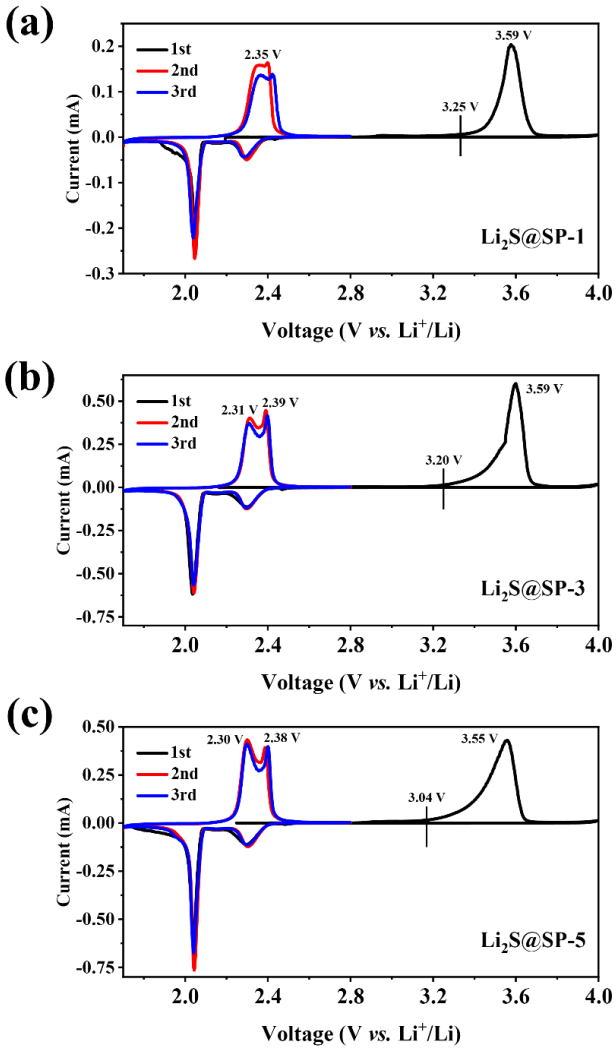


Figure 6.3 Cyclic voltammetry (CV) profiles of freshly assembled Li_2S-LSBs based on (a) Li_2S@SP-1, (b) Li_2S@SP-3, and (c) Li_2S@SP-5 nanocomposites, recorded at a scan rate of 0.025 mV s^{-1}. The initial CV scan was performed anodically from open-circuit voltage (OCV) to a cutoff of 4.0 V, followed by cyclic scans within the voltage window of 1.7–2.8 V.

Electrochemical impedance spectroscopy (EIS) (**Figure S 6.2** and **Table S 6.4**) reveals decreasing charge transfer resistance (R_{ct}) with increasing number of infiltration-decomposition cycles: 29.6 Ω (Li_2S@SP-1), 27.7 Ω (Li_2S@SP-3), and 25.0 Ω (Li_2S@SP-5). This trend is

consistent with the CV results, confirming enhanced interfacial contact with greater Li_2S confinement.

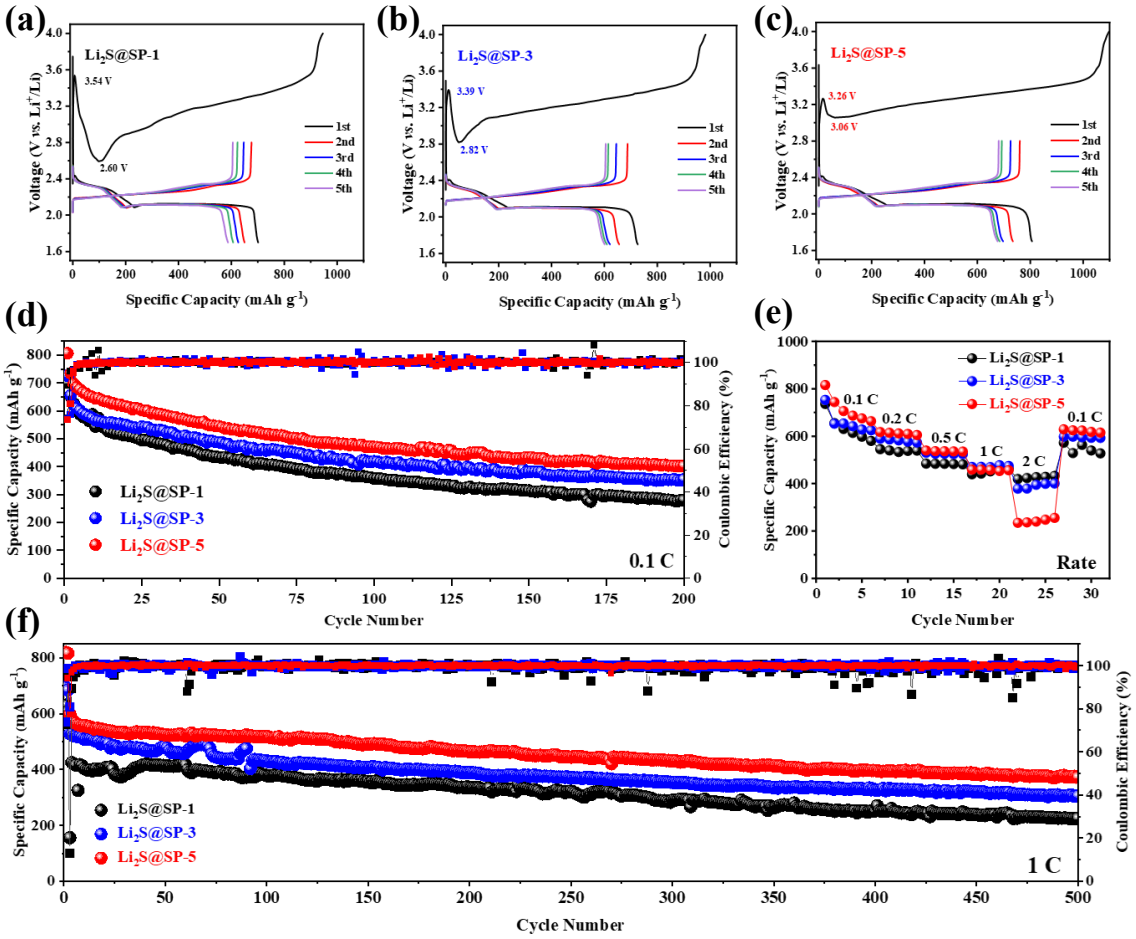


Figure 6.4 Galvanostatic charge-discharge (GCD) performance of Li_2S@SP electrodes. (a–c) Initial charge/discharge profiles; (d) long-term cycling at 0.1 C; (e) rate performance; and (f) long-term cycling at 1.0 C. The initial charge was performed at 0.1 C to 4.0 V, followed by cycling within 1.7–2.8 V.

To assess the practical electrochemical performance of the Li_2S@SP electrodes, galvanostatic charge-discharge (GCD) tests were conducted (**Figure 6.4** (a–c)). Li_2S-LSBs typically exhibit a high overpotential during the initial charging process, primarily due to the substantial activation energy required to decompose the passivating LiOH/Li_2O layer on the Li_2S surface and the limited ion diffusivity associated with highly pure and crystalline bulk Li_2S.[140,168] It is observed that the overpotential decreases progressively with increasing infiltration-decomposition cycles: 3.54 V for Li_2S@SP-1, 3.39 V for Li_2S@SP-3, and 3.26 V for Li_2S@SP-5. This trend is consistent with the

CV and EIS results and can be attributed to enhanced interfacial electron transfer enabled by improved Li_2S dispersion within the conductive Super P network.

After the initial overpotential spike, the cells displayed markedly different voltage profiles. Li_2S@SP-1 exhibits the steepest voltage drop to 2.60 V, followed by Li_2S@SP-3 (2.82 V) and Li_2S@SP-5 (3.06 V). In Li_2S@SP-1, most Li_2S resides outside the Super P matrix, allowing easy access to the electrolyte and facilitating rapid conversion to polysulfides. Additionally, the residual void space inside Super P enables electrolyte penetration, further accelerating Li_2S oxidation. In contrast, Li_2S@SP-5 features densely packed Li_2S domains confined within Super P, leaving minimal void volume. The limited space restricts electrolyte diffusion and the insulating Li_2S impedes ion transport. As a result, oxidation proceeds from the outer surface inward, requiring higher voltages for continued Li^+ extraction. Li_2S@SP-3 displays intermediate behavior, consistent with its partial infiltration level.

The initial charging capacities increase with the level of in-pore Li_2S loading, reaching 946 mA h g^{-1} (Li_2S@SP-1), 983 mA h g^{-1} (Li_2S@SP-3), and 1098 mA h g^{-1} (Li_2S@SP-5). During the subsequent discharge, Li_2S@SP-5 delivers the highest discharge capacity (807 mA h g^{-1}), followed by Li_2S@SP-3 (726 mA h g^{-1}) and Li_2S@SP-1 (701 mA h g^{-1}), indicating enhanced active material utilization with increasing in-pore Li_2S loading.

Long-term cycling at 0.1 C (**Figure 6.4** (d)) reveals enhanced stability with increasing in-pore Li_2S loading, with capacity retention after 200 cycles following the order: 280 mA h g^{-1} (40%) for Li_2S@SP-1, retains 350 mA h g^{-1} (48%) for Li_2S@SP-3, and 402.5 mA h g^{-1} (50%) for Li_2S@SP-5 after 200 cycles. Li_2S@SP-1 exhibits substantial fluctuations in both discharge capacity and Coulombic efficiency (CE), Li_2S@SP-3 shows moderate stability, and Li_2S@SP-5 remains the most stable throughout cycling. The poor stability of Li_2S@SP-1 arises from its low in-pore loading and substantial fraction of external Li_2S, which promote polysulfide diffusion, intensify shuttle effects, and accelerate cathode degradation. In contrast, Li_2S@SP-5, with the highest in-pore Li_2S loading, effectively confines polysulfides within Super P pores, thereby suppressing shuttle effects and maintaining cathode integrity.

The rate performance of the Li_2S@SP cells is shown in **Figure 6.4** (e). At low rates ($\leqslant$ 0.5 C), the discharge capacities follow the order: Li_2S@SP-5 > Li_2S@SP-3 > Li_2S@SP-1. As the

current increases, the capacity differences diminish, and at 2.0 C, Li_2S@SP-1 outperforms the other samples, likely due to its predominantly surface-deposited Li_2S. This trend may arise from increasing ion-transport limitations of the confined sulfur species within the Super P mesopores as in-pore Li_2S loading increases.

To evaluate high-rate durability, long-term cycling at 1.0 C was conducted following an initial activation cycle at 0.1 C (**Figure 6.4** (f)). Li_2S@SP-5 again shows the best performance, delivering 598 mA h g^{-1} in the first 1.0 C cycle and retaining 376 mA h g^{-1} after 500 cycles. Li_2S@SP-3 showed intermediate performance, with an initial capacity of 529 mA h g^{-1} and retaining 305 mA h g^{-1} after 500 cycles. Li_2S@SP-1 exhibited unstable capacity during the initial cycles, indicating poor structural stability of the electrode. Its capacity gradually declined to 225 mA h g^{-1} after 500 cycles, the lowest among the three samples.

Overall, these results highlight the critical role of Li_2S infiltration in governing electrochemical performance. Increasing the number of infiltration-decomposition cycles increases in-pore Li_2S loading, resulting in higher capacity, reduced polysulfide shuttling, and improved structural stability of the cathode. However, while a higher degree of infiltration benefits capacity and cycling life, it also imposes ion-transport limitations at high rates due to restricted diffusion pathways within the confined Super P pores.

6.3.4 Performance Comparison of Li_2S@SP-5 and S@SP Nanocomposites

To assess the advantages of Li_2S@SP-5 over its sulfur counterpart, a reference S@SP nanocomposite was prepared by conventional melt infiltration with the same active material content (equivalent sulfur or Li_2S content) to ensure a fair comparison. For consistency, the electrochemical performance of Li_2S@SP-5 was evaluated after an initial activation cycle (charged to 4.0 V at 0.1 C).

EIS analysis reveals that the Li_2S@SP-5 electrode, in its first charged state (sulfur state), exhibits a significantly lower R_{ct} (48.2 Ω) than that (66.3 Ω) of the S@SP electrode, indicating more efficient charge transfer between sulfur and the electrolyte in the Li_2S@SP-5 electrode (**Figure S 6.3** and **Table S 6.5**). This improvement can be attributed to the formation of less crystalline sulfur particles from Li_2S in Li2S@SP-5 after first charging, facilitating ion transport. In contrast, sulfur particles in the S@SP electrode are tightly packed, limiting ion transport.

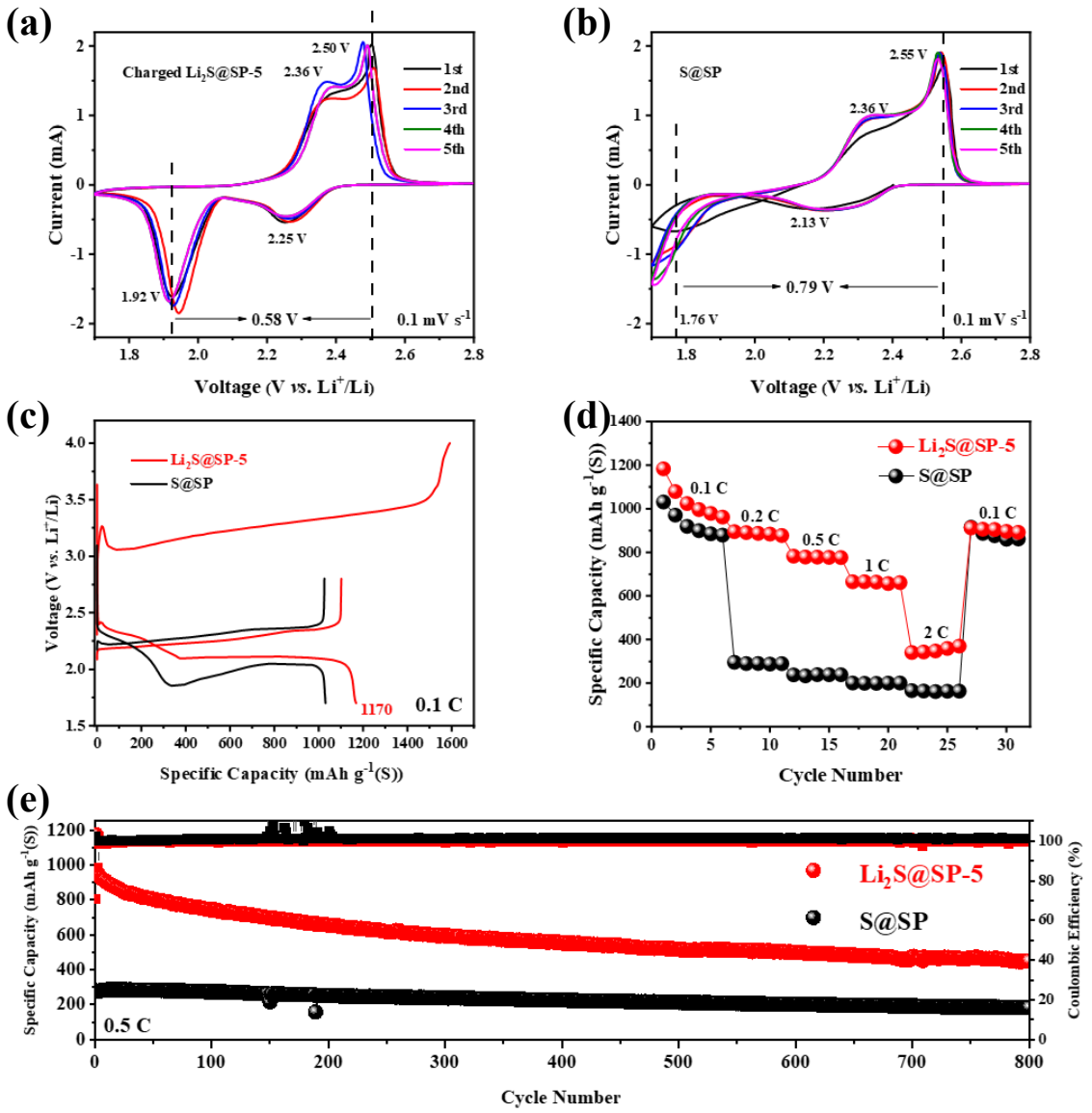


Figure 6.5 CV profiles of (a) Li_2S@SP-5 and (b) S@SP at a rate of 0.1 mV s^{-1}. (c) Initial charge/discharge curves of Li_2S@SP-5 and S@SP cells at 0.1 C. The first charge of Li_2S@SP-5 was carried out to 4.0 V, followed by cycling within 1.7–2.8 V. (d) Rate performance of Li_2S@SP-5 and S@SP cells. (e) Long-term cycling performance of Li_2S@SP-5 and S@SP cells at 0.5 C.

CV measurements at a scan rate of 0.1 mV s^{-1} (**Figure 6.5** (a) and (b)) show that both batteries exhibit two reduction peaks during the cathodic scan, corresponding to the two-step reduction of elemental sulfur to LPSs and then to Li_2S. The Li_2S@SP-5 battery shows higher peak potentials at 2.25 V and 1.92 V, compared to 2.13 V and 1.76 V for the S@SP electrode. In the anodic scan, both electrodes display a first peak at 2.36 V, with Li_2S@SP-5 showing higher intensity, while the second oxidation peak of Li_2S@SP-5 appears at 2.50 V, lower than that of the S@SP electrode

(2.55 V), indicating a reduced oxidation barrier. Furthermore, the smaller voltage difference between the cathodic and anodic peaks for Li_2S@SP-5 (0.58 V) relative to S@SP (0.79 V) indicates faster sulfur-to-Li_2S kinetics in the Li_2S@SP-5 electrode.

Figure 6.5 (c) shows the initial discharge/charge characteristics of Li_2S@SP-5 and S@SP batteries measured at 0.1 C. For comparison, the capacities of the Li_2S@SP-5 battery were normalized to sulfur mass (mA h g^{-1}(S)). The Li_2S@SP-5 battery exhibited two discharge plateaus at 2.1 V and 2.3 V, corresponding to the stepwise reduction of sulfur to long-chain polysulfides and then to Li_2S, and delivers a high initial discharge capacity of 1170 mA h g^{-1}(S). In contrast, the S@SP battery shows markedly lower discharge voltages and a pronounced voltage dip between the two plateaus, indicative of sluggish reduction kinetics, and achieves a lower initial discharge capacity of only 1030 mA h g^{-1}(S). In the subsequent charge cycle, the Li_2S@SP-5 cell exhibits a lower charging voltage than the S@SP cell, reflecting its more favorable oxidation kinetics.

Rate capability results (**Figure 6.5** (d)) show that the Li_2S@SP-5 cell delivers slightly lower capacities (~100 mA h g^{-1}(S)) at 0.1 C but suffers sharp decline at 0.2 C and higher rates. This performance degradation is likely due to sluggish kinetics and compromised cathode structural integrity, which result in disconnected sulfur species and reduced active material utilization at elevated rates. For long-term cycling (**Figure 6.5** (e)), both electrodes were pre-activated at 0.1 C in the initial cycle, delivering discharge capacities of 1170 mA h g^{-1}(S) for Li_2S@SP-5) and 1030 mA h g^{-1}(S) for S@SP. At 0.5 C, Li_2S@SP-5 retained 945 mA h g^{-1}(S) in the first cycle, whereas S@SP fell to only 279 mA h g^{-1}(S). The S@SP battery displayed unstable cycling behavior and erratic Coulombic efficiency between the 150^{th} and 200^{th} cycles, likely due to severe electrode structural degradation from volumetric expansion, polysulfide shuttling, and lithium anode passivation. In contrast, the Li_2S@SP-5 cell maintained stable cycling, retaining 450 mA h g^{-1}(S) after 800 cycles.

The morphologies of the Li_2S@SP-5 and S@SP electrodes before and after 100 cycles were examined by SEM (**Figure 6.6**). Because of the high moisture sensitivity of Li_2S, all electrodes were characterized in their charged (sulfur) state. For the fresh Li_2S@SP-5 electrode, an initial charge to 4.0 V was performed to convert Li_2S into sulfur prior to SEM observation.

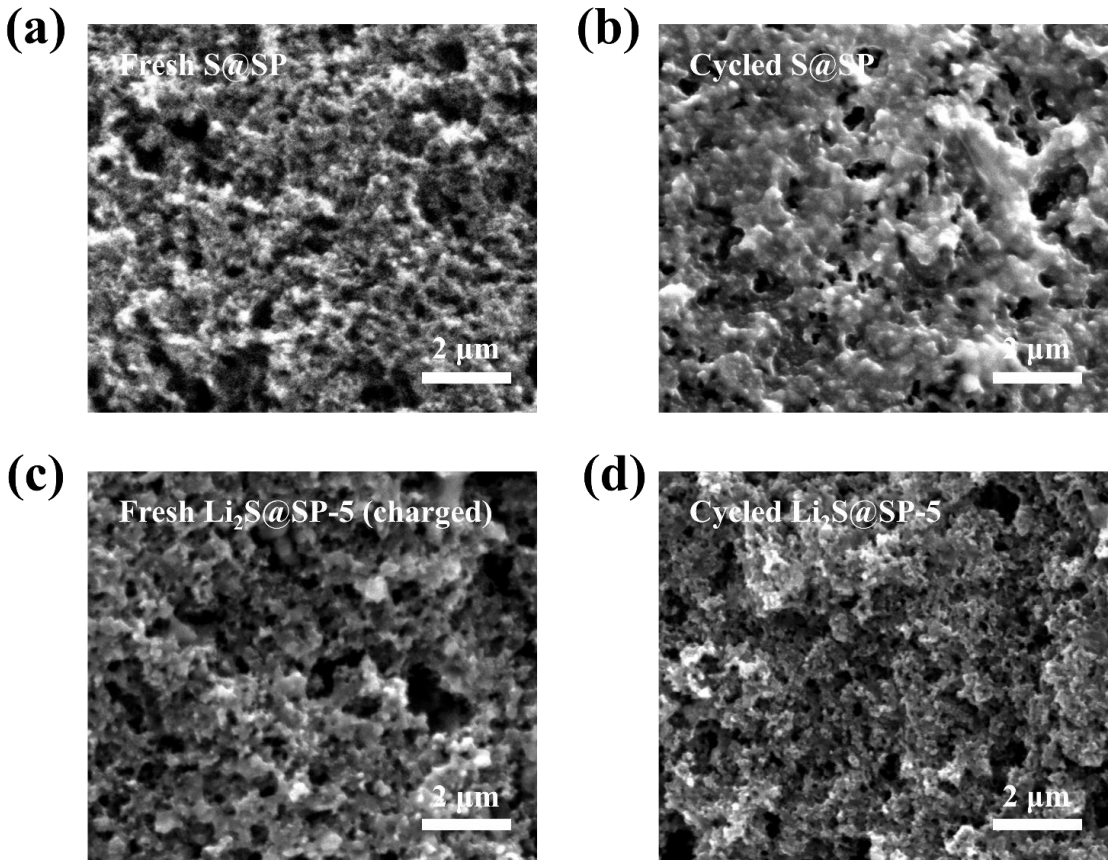


Figure 6.6 SEM images of (a) fresh S@SP electrode, (b) cycled S@SP electrode in the charged state after 100 cycles at 0.5 C, (c) fresh Li_2S@SP-5 electrode after initial charging, and (d) cycled Li_2S@SP-5 electrode in the charged state after 100 cycles at 0.5 C.

Both fresh electrodes exhibit distinct nanoparticles with uniform distribution, but the particles in the fresh S@SP electrode appear more interconnected (**Figure 6.6** (a) and (c)). This difference likely originates from variations in nanocomposite-binder interactions: in S@SP, PVP interacts more strongly with residual sulfur on the Super P surface, forming a more robust network than in Li_2S@SP-5, where PVP interacts less effectively with external Li_2S during electrode fabrication.

After 100 cycles at 0.5 C, pronounced differences emerge between the two electrodes. In the cycled S@SP (**Figure 6.6** (b)), particles are coated and interconnected by lighter-colored films, most likely sulfur that migrated out of the Super P pores as polysulfides during discharge and redeposited on particle surfaces during charge. In contrast, the cycled Li_2S@SP-5 electrode (**Figure 6.6** (d)) largely retains its initial morphology, with well-defined carbon particle boundaries and no

significant sulfur accumulation between particles, indicating that sulfur species remain confined within the Super P pores even after prolonged cycling.

These observations highlight the advantages of Li_2S@SP-5 over its sulfur-based counterpart. In S@SP, volume expansion during discharge pushes polysulfides out of the pores, where they redeposit externally, exert mechanical stress on the electrode framework, promote polysulfide shuttling, and form isolated sulfur domains, which lead to reduced capacity, sluggish kinetics, and faster degradation. By contrast, Li_2S@SP-5 undergoes volume contraction upon initial oxidation, which suppresses the escape of sulfur species from the pores and ensures much stronger confinement. Consequently, Li_2S@SP-5 achieves superior electrochemical performance and long-term cycling stability.

6.4 Conclusions

In this work, we developed a facile and scalable strategy to synthesize Li_2S@C nanocomposites with high in-pore Li_2S loading via multi-cycle precursor infiltration–decomposition. Commercial mesoporous Super P was employed as the conductive carbon host to accommodate the precursor Li_2CS_3. By dividing the precursor into multiple portions and infiltrating it through successive cycles, a series of Li_2S@SP nanocomposites with an overall Li_2S loading of 70 wt.% was obtained. XRD and SEM analyses confirmed that increasing the number of cycles enhanced in-pore Li_2S confinement. Notably, Li_2S@SP-5 achieved a pore filling factor of 91% and an in-pore loading of 73% and exhibited superior structural integrity and electrochemical performance, delivering an initial discharge capacity of 807 mA h g^{-1} at 0.1 C and excellent cycling stability compared to Li_2S@SP-1 and Li_2S@SP-3. These results demonstrate the effectiveness of the multi-cycle approach and highlight the critical role of maximizing in-pore Li_2S loading in improving Li_2S-LSB performance.

In addition, Li_2S@SP-5 significantly outperformed its sulfur-based counterpart (S@SP). Unlike S-LSBs, which begin from discharge and undergo volume expansion that drives sulfur out of the pores and compromises cathode integrity, Li_2S-LSBs start from charge and undergo volume contraction, thereby suppressing polysulfide escape, mitigating shuttling, and preserving the electrode structure.

Looking ahead, further increasing in-pore Li_2S loading will require alternative carbon hosts with larger pore volumes (**Table S 6.2**). Moreover, long-term cycling stability could be further enhanced by introducing chemical confinement strategies to complement the physical trapping of polysulfides in Super P, whose adsorption capability is limited. Incorporating functional interlayers, redox mediators, or heteroatom-doped carbon frameworks may further suppress shuttle effects, accelerate redox kinetics, and stabilize cycling. The integration of these chemical approaches with our scalable multi-cycle infiltration-decomposition method offers a promising pathway toward next-generation Li_2S cathodes that combine high loading, high utilization, and long-term durability for practical high-energy-density batteries.

6.5 Supporting Information

Table S 6.1 Reported methods for synthesizing Li_2S@C nanocomposites.

Composite	Li_2S Loading in Composite	Preparation Method	Li_2S Loading in Cathode	Initial Capacity (mAh g^{-1})	Ref.
Graphene-Li_2S	~55 wt.%	Li_2S-EtOH solution infiltration and CVD	1.3 mg cm^{-2}	~960@0.1 C	[227]
3D Li_2S/graphene hierarchical architecture	50 wt.%	Li_2S-EtOH solution infiltration and CVD	1 mg cm^{-2}	894.7@0.1 C	[231]
Li_2S-coated 3D doped graphene aerogels	50-55 wt.%	Liquid infiltration-evaporation coating	2 mg cm^{-2}	801@0.3 C	[230]
Li_2S/Graphene	66 wt.%	Li_2S/NMP mixture-evaporating	1 mg cm^{-2}	600@0.1 A g^{-1}	[361]
Nano-Li_2S/MWCNT	30 and 47 wt.%	Li_2S-EtOH solution infiltration	1.8 mg cm^{-2}	860@0.1 C	[377]
In-situ TG-Li_2S	67 wt.%	Sulfur thermal infiltration and chemical lithiation by lithium triethylborohydride ($LiEt_3BH$)	1 mg cm^{-2}	1119@0.1 C	[156]
Nanostructured-Li_2S-C	67.5 wt.%	Ball milling	0.54 mg cm^{-2}	1144@0.02 C	[166]
Li_2S-C	~70 wt.%	Li salt infiltration and H_2S gas sulfuration	~1.4 mg cm^{-2}	~650@0.1 C	[218]
Li_2S/C/G	~67.7 wt.%	Carbothermal Reduction	0.345 mg cm^{-2}	778@0.1 A g^{-1}	[279]
Li_2S/CB@NC	70 wt.%	Ball milling and carbothermal reduction	0.8 mg cm^{-2}	1020@0.1 C	[167]
Li_2S@C	88 wt.%	Chemical lithiation and CVD	1.0-1.5 mg cm^{-2}	972@0.2 C	[215]
Li_2S@graphene	~88.5 wt.%	Burning lithium in CS_2	~5 mg cm^{-2}	1160@0.1 C	[145]
Li_2S/GO@C	60 wt.%	Chemical lithiation by triethylborohydride ($LiEt_3BH$) and CVD	0.7-0.9 mg cm^{-2}	964@0.2 C	[214]
Li_2S@graphene	N/A	Lithiothermic reaction by Li and CS_2 gas	~3 mg cm^{-2}	714.6@0.1 C	[378]
Mo-Li_2S-graphene	~76 wt.%	Two-stage lithiothermic reduction with lithium and CS_2, respectively	3.5 mg cm^{-2}	815@1.0 C	[277]

Table S 6.2 Calculated parameters for multi-cycle precursor infiltration-decomposition processes to make Li_2S@C nanocomposites at different cycle number.

Cycle n	$m_{Li_2CS_3}(n)$, g g^{-1}(C)	$m_{Li_2S}(n)$, g g^{-1}(C)	$V_{pore}(n)$, cm^3 g^{-1}(C)	$m_{Li_2S,ip}$, g g^{-1}(C)	FF	IPL (y = 70%)	$V_{pore,min}$ (y = 70%), cm^3 g^{-1}(C)
0			V_{pore}				
1	$V_{pore}\rho_1$	$V_{pore}\rho_1 x$	$V_{pore}\left(1-x\frac{\rho_1}{\rho_2}\right)$	$V_{pore}\rho_1 x$	$x = 0.376$	0.302	3.74
2	$V_{pore}\rho_1\left(1-x\frac{\rho_1}{\rho_2}\right)$	$V_{pore}\rho_1 x\left(1-x\frac{\rho_1}{\rho_2}\right)$	$V_{pore}\left(1-x\frac{\rho_1}{\rho_2}\right)^2$	$V_{pore}\rho_2\left(1-\left(1-x\frac{\rho_1}{\rho_2}\right)^2\right)$	$1-\left(1-x\frac{\rho_1}{\rho_2}\right)^2 = 0.611$	0.491	2.30
3	$V_{pore}\rho_1\left(1-x\frac{\rho_1}{\rho_2}\right)^2$	$V_{pore}\rho_1 x\left(1-x\frac{\rho_1}{\rho_2}\right)^2$	$V_{pore}\left(1-x\frac{\rho_1}{\rho_2}\right)^3$	$V_{pore}\rho_2\left(1-\left(1-x\frac{\rho_1}{\rho_2}\right)^3\right)$	$1-\left(1-x\frac{\rho_1}{\rho_2}\right)^3 = 0.757$	0.609	1.86
4	$V_{pore}\rho_1\left(1-x\frac{\rho_1}{\rho_2}\right)^3$	$V_{pore}\rho_1 x\left(1-x\frac{\rho_1}{\rho_2}\right)^3$	$V_{pore}\left(1-x\frac{\rho_1}{\rho_2}\right)^4$	$V_{pore}\rho_2\left(1-\left(1-x\frac{\rho_1}{\rho_2}\right)^4\right)$	$1-\left(1-x\frac{\rho_1}{\rho_2}\right)^4 = 0.848$	0.682	1.66
5	$V_{pore}\rho_1\left(1-x\frac{\rho_1}{\rho_2}\right)^4$	$V_{pore}\rho_1 x\left(1-x\frac{\rho_1}{\rho_2}\right)^4$	$V_{pore}\left(1-x\frac{\rho_1}{\rho_2}\right)^5$	$V_{pore}\rho_2\left(1-\left(1-x\frac{\rho_1}{\rho_2}\right)^5\right)$	$1-\left(1-x\frac{\rho_1}{\rho_2}\right)^5 = 0.905$	0.728	1.55
…	…	…	…	…	…	…	…
n	$V_{pore}\rho_1\left(1-x\frac{\rho_1}{\rho_2}\right)^{n-1}$	$V_{pore}\rho_1 x\left(1-x\frac{\rho_1}{\rho_2}\right)^{n-1}$	$V_{pore}\left(1-x\frac{\rho_1}{\rho_2}\right)^n$	$V_{pore}\rho_2\left(1-\left(1-x\frac{\rho_1}{\rho_2}\right)^n\right)$	$1-\left(1-x\frac{\rho_1}{\rho_2}\right)^n$		

Note

V_{pore}: pore volume of carbon host, cm^3 per g of carbon (C) (cm^3 g^{-1} (C)) (1.13 cm^3 g^{-1} for Super P in this study);

x: Li_2S wt.% (or fraction) in Li_2CS_3 (x = 0.376);

ρ_1 and ρ_2: densities (g cm^{-3}) of Li_2CS_3 and Li_2S, respectively, assumed to be equal at 1.66 g cm^{-3};

$m_{\mathrm{Li_2CS_3}}(n)$: mass of Li_2CS_3 infiltrated in mesopores at the nth cycle;

$m_{\mathrm{Li_2S}}(n)$: mass of Li_2S deposited in mesopores after thermal decomposition of Li_2CS_3 at the nth cycle;

$V_{\mathrm{pore}}(n)$: available pore volume at the nth cycle;

$m_{Li_2S,ip} = \sum_1^n m_{\mathrm{Li_2S}}(n)$: accumulated mass of Li_2S after n cycles;

$\mathrm{FF} = m_{\mathrm{Li_2S,ip}}/m_{\mathrm{Li_2S,ip,max}} = m_{\mathrm{Li_2S,ip}}/\left(V_{\mathrm{pore}}\rho_2\right)$: pore filling factor;

$\mathrm{IPL} = m_{\mathrm{Li_2S,ip}}/m_{\mathrm{Li_2S,total}} = V_{pore}\rho_2\left(1-\left(1-x\frac{\rho_1}{\rho_2}\right)^n\right)\left(\frac{1}{y}-1\right)$: in-pore Li_2S loading, where $m_{\mathrm{Li_2S,total}}$ is the total Li_2S mass and y is the Li_2S wt.% (or fraction) loading of the Li_2S@C nanocomposite (y = 70wt.% in this study);

$V_{pore,min}$: minimum mesopore volume (cm^3 g^{-1} (C)) of the carbon host required to obtain a Li_2S@C nanocomposite with 70 wt.% total Li_2S loading, where all Li_2S is confined (infiltrated) in the mesopores (IPL = 1) after n cycles. It is calculated using **Equation S 6.1**, derived from **Equation 6.3:**

$$V_{pore,min}\rho_2\left(1-\left(1-x\frac{\rho_1}{\rho_2}\right)^n\right)\left(\frac{1}{y}-1\right) = 1 \qquad \textbf{Equation S 6.1}$$

where y = 0.7, and ρ_1 (Li_2CS_3) = ρ_2 (Li_2S) = 1.66 g cm^{-3}.

Table S 6.3 Crystallite sizes of Li_2S in different samples determined by the *Scherrer* equation.

Sample	Peak (*hkl*)	θ (°)	FWHM (°)	*D* (nm)	Average *D* (nm)
cLi_2S/SP	(200)	15.60	0.27	30.2	29.0
	(220)	22.35	0.30	28.8	
	(311)	26.45	0.31	28.0	
Li_2S@SP-1	(200)	15.6	0.48	19.2	15.2
	(220)	22.35	0.61	13.9	
	(311)	26.48	0.65	11.9	
Li_2S@SP-3	(200)	15.80	0.63	13.1	11.3
	(220)	22.55	0.82	10.4	
	(311)	26.7	0.86	10.3	
Li_2S@SP-5	(200)	15.55	0.68	12.0	10.5
	(220)	22.35	0.88	9.7	
	(311)	26.45	0.90	9.8	

Note:

Crystallite sizes (D) were calculated using the *Scherrer* equation:

$$D = \frac{K\lambda}{\beta \cos\theta} \qquad \textbf{Equation S 6.2}$$

Where:

K is the shape factor (0.89, assuming spherical crystallites),

λ is the X-ray wavelength (0.154184 nm),

β is the full width at half maximum (FWHM) of the diffraction peak (in radians),

θ is the Bragg angle.

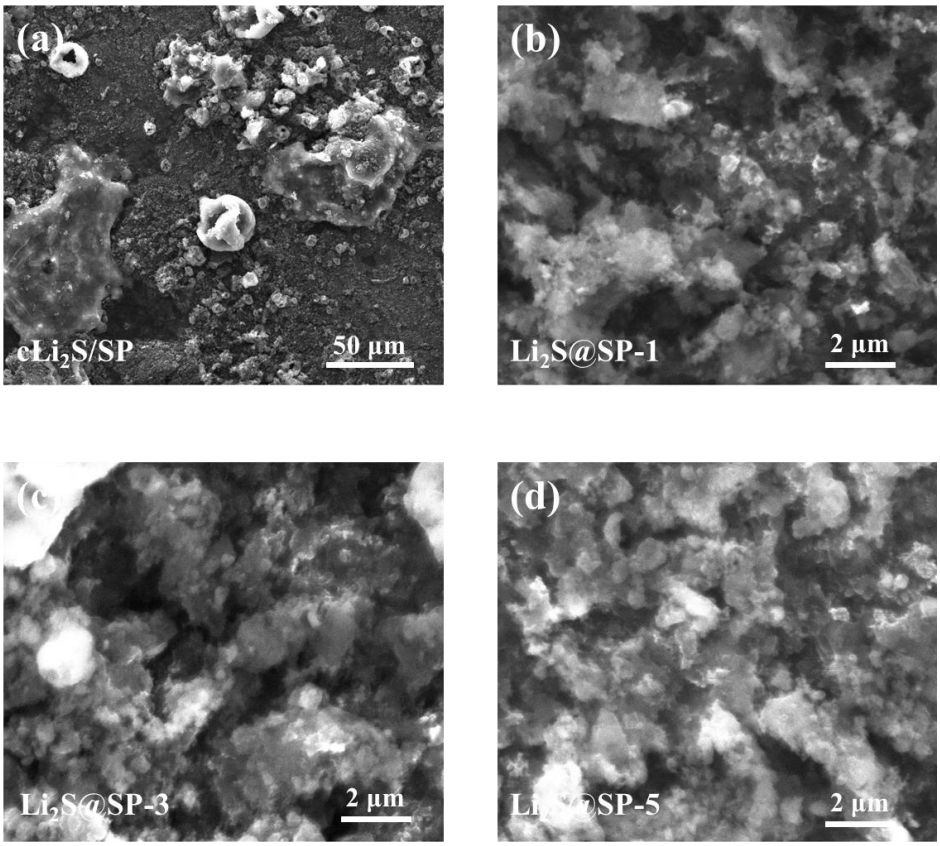


Figure S 6.1 SEM images of the as-prepared nanocomposites: (a) cLi_2S/SP (b) $Li_2S@SP-1$, (c) $Li_2S@SP-3$, and (d) $Li_2S@SP-5$.

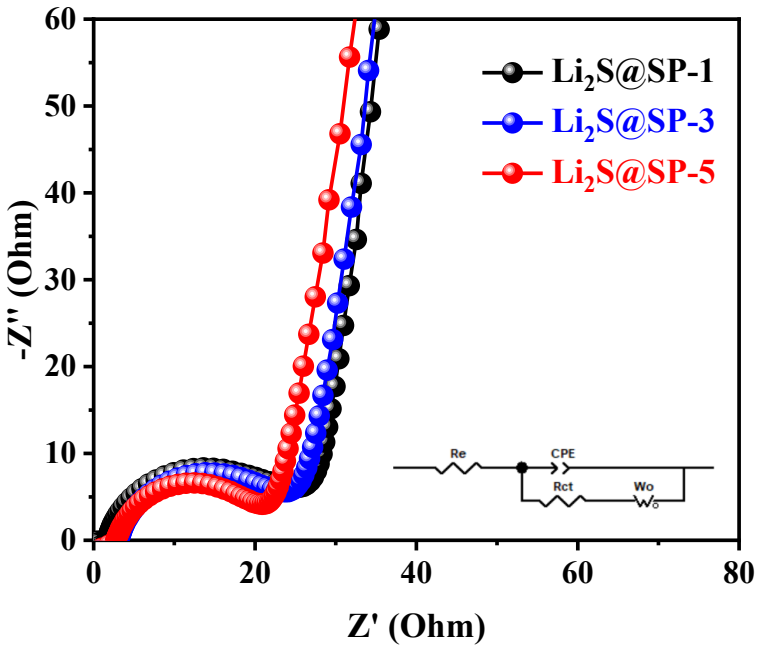


Figure S 6.2 EIS Nyquist plots of fresh Li_2S@SP-1, Li_2S@SP-3, and Li_2S@SP-5 electrodes. The inset shows the equivalent Randles circuit used for fitting, where R_e is the electrolyte resistance, R_{ct} is the charge transfer resistance, *CPE* is the capacitance, and W_o is the Warburg impedance.

Table S 6.4 Cathode resistances derived from the EIS data in **Figure S 6.2**.

Cathode	Resistance (Ω)	
	R_e	R_{ct}
Li_2S@SP-1	1.7	29.6
Li_2S@SP-3	3.1	27.7
Li_2S@SP-5	2.8	25.0

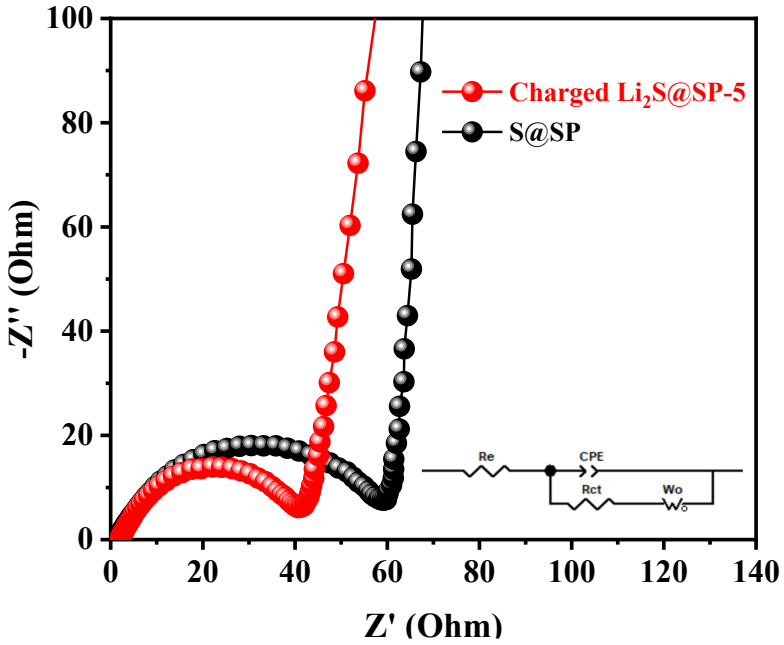


Figure S 6.3 EIS Nyquist plots of fresh S@SP and initially charged Li_2S@SP-5 electrodes. The inset shows the equivalent Randles circuit used for fitting, where R_e is the electrolyte resistance, R_{ct} is the charge transfer resistance, *CPE* is the capacitance, and W_o is the Warburg impedance.

Table S 6.5 Cathode resistances derived from the EIS data in **Figure S 6.3**.

Cathode	Resistance (Ω)	
	R_e	R_{ct}
Charged Li_2S@SP-5	2.1	48.2
S@SP	1.7	66.3

Table S 6.6 Performance of representative Li_2S-LSB full cells reported in the literature.

Cathode	Anode	Electrolyte	Voltage Range	Initial Capacity	Capacity Retention	Ref.
Mo/Li_2S	Si/C	1 M $LiPF_6$ in EC/DMC (*v*/*v*, 1:1)	0.2–2.5 V	788 mA h g^{-1}@0.1C	52%@0.5C@150	[278]
Li_2S+C	Si/C	1 M LiTFSI in DOL/DME (*v*/*v*, 1:1) + 0.5 M $LiNO_3$	1.3–2.8 V	~540 mA h g^{-1}@0.1C	~50%@0.2C@70	[276]
Li_2S/C/G	Si/C	1 M LiTFSI in DOL/DME (*v*/*v*, 1:1) + 1wt.% $LiNO_3$	1.2–3.5 V	593 mA h g^{-1}@100 mA g^{-1}	61%@0.1C@30	[279]
Mo-Li_2S-graphene	Si/C	1 M LiTFSI in DOL/DME (*v*/*v*, 1:1) + 1wt.% $LiNO_3$	1.5–3.5 V	545 mA h g^{-1}@1C	85.6%@0.1C@200	[277]
l-Li_2S/KB	Graphite	LiTFSI in G1/G3 (*v*/*v*, 1:1)	1.0–3.3 V	~600 mA h g^{-1}@0.1C	~100%@0.1C@30	[148]
Li_2S@Li_4SnS_4	Graphite	1 M LiTFSI in DOL/DME (*v*/*v*, 1:1) + 1wt.% $LiNO_3$ + AN + TTE	1.0–3.5 V	634 mA h g^{-1}@0.05C	N/A	[149]
Li_2S/MWCNT	Cu	2 M $LiCF_3SO_3$ in DOL/DME (1:1) + 0.2 M $LiNO_3$	1.8–2.8 V	919 mA h g^{-1}@0.1C	51.5%@0.1C@100	[280]
Li_2S/CFs	Cu	1 M LiTFSI in DOL/DME (1:1) + 0.75 M $LiNO_3$	1.7–2.8 V	639 mA h g^{-1}@0.1C	40%@0.1C@150	[281]
Li_2S/CFs	Cu/Au	1 M LiTFSI in DOL/DME (1:1) + 0.75 M $LiNO_3$	1.7–2.8 V	770 mA h g^{-1}@0.1C	53%@0.1C@150	[281]
Li_2S@MXene/graphene	Fe_3O_4	1 M LiTFSI in DOL/DME (1:1) + 2wt.% $LiNO_3$	1.7–2.8 V	600 mA h g^{-1}@0.2C	78%@0.2C@50	[282]
Li_2S@NCNF	Fe_3O_4/CNs	1 M LiTFSI in DOL/DME (1:1) + 2wt.% $LiNO_3$	1.5–2.8 V	576 mA h g^{-1}@0.2C	60%@0.2C@50	[209]
Li_2S-rGO	MnO_2-rGO	1 M LiTFSI in DOL/DME (1:1)	0.2–2.6 V	587.5 mA h g^{-1}@0.2C	80.5%@0.2C@150	[283]
Li_2S@SP-5	Si/C	1 M LiTFSI in DOL/DME (1:1) + 2wt.% $LiNO_3$	1.5–3.0 V	673 mA h g^{-1}@0.05C	43%@0.1C@100	This study

Chapter 7 Crosslinked Polyethylenimine-Epoxy Resin Binder for High-Performance Li_2S@C Nanocomposite Cathodes

7.1 Introduction

The accelerating demand for high-performance energy storage in electric vehicles, portable electronics, and grid-scale systems is pushing lithium-ion batteries (LIBs) toward their practical energy density limit.[34,44,330,332,334,336] Lithium-sulfur batteries (LSBs) are among the most promising next-generation candidates, offering a theoretical specific capacity of 1672 mA h g^{-1} and a specific energy of 2600 W h kg^{-1}—about five times that of LIBs.[87,338] Sulfur's natural abundance, low cost, and environmental benignity further strengthen the case for LSBs as a sustainable high-energy solution.[95,370]

Conventional LSBs with elemental sulfur cathodes (S-LSBs) depend on metallic lithium anodes, which are highly reactive with air and moisture, require stringent handling, and are prone to dendrite growth that can cause short circuits and thermal runaway.[297] Replacing sulfur with lithium sulfide (Li_2S) mitigates these risks. Li_2S-based LSBs (Li_2S-LSBs) can operate with safer, lithium-free anodes such as graphite,[145,150,151] silicon,[154–156] or tin,[161–163] while their cathode fabrication is compatible with existing LIB manufacturing lines, offering a safer and more commercially viable pathway.[141,165,343]

However, Li_2S introduces stricter processing requirements. Its high moisture sensitivity and tendency to hydrolyze exclude water-based fabrication routes, placing particular constraints on the binder, a component essential for electrode integrity and cycling stability.[112,195,344] Most water- or acid-based binders used in S-LSBs are incompatible, and the most common alternative, poly(vinylidene fluoride) (PVDF), performs poorly. Our previous work showed that PVDF undergoes dehydrofluorination in the presence of Li_2S during slurry preparation, consuming active material and degrading adhesion.[344] With proposed EU restrictions on per- and polyfluoroalkyl substances (PFAS), including PVDF and PTFE,[273,347] the need for non-aqueous, fluorine-free binders for Li_2S-LSBs is increasingly urgent.

Li_2S-LSBs also inherit the key challenges of S-LSBs: the dissolution and migration of lithium polysulfides (LPSs), which trigger the shuttle effect and capacity fading, and the poor intrinsic electronic/ionic conductivities of sulfur species, which limit reaction kinetics.[112,341] These issues are even more difficult to address in Li_2S due to its higher chemical reactivity, which often renders conventional cathode modification strategies ineffective. Achieving uniform Li_2S dispersion within conductive hosts is particularly critical to maximize utilization and suppress LPS dissolution. In **Chapter 5** and **Chapter 6**, we overcame this barrier by developing Li_2S@C nanocomposites, including Li_2S@SP-400 and Li_2S@SP with high in-pore Li_2S loading, which exhibited uniform active material dispersion, strong interfacial contact, and excellent electrochemical performance.

In **Chapter 4**, we developed a multifunctional, fluorine-free binder based on a $Zn(OAc)_2$·TEA/PEI complex for bulk Li_2S cathodes.[295] $Zn(OAc)_2$·TEA provided strong LPS adsorption and redox catalytic activity, while PEI enhanced processability, suppressed crystallization, and improved mechanical strength via potential Zn^{2+} crosslinking. Given the complementary strengths of the $Zn(OAc)_2$·TEA/PEI binder and the Li_2S@SP nanocomposite, combining the two seemed a logical step toward further performance gains. However, the nano-sized Li_2S in Li_2S@SP, with its extremely high surface area, reacted directly with $Zn(OAc)_2$·TEA, consuming the complex and stripping the binder of its functional and adhesive capabilities. This led to electrode structural degradation and rapid capacity decay, highlighting a critical distinction between bulk and nanostructured Li_2S: binders optimized for the former may fail in the latter due to enhanced surface reactivity.

Building on these insights, we turned to our group's previously developed PEI-ER series binders, a class of fluorine-free, multifunctional materials originally designed for sulfur cathodes.[379] These binders, based on the covalent crosslinking between polyethyleneimine (PEI) and epoxide resin (ER), have demonstrated excellent adhesion, flexibility, and polysulfide-trapping ability, and critically show strong compatibility with nano-sulfur cathodes, where large surface areas often pose processing challenges. Given the structural and chemical similarities between nano-sulfur and the nano-Li_2S in Li_2S@SP, it was a logical step to directly employ the previously optimized PEI-$ER_{1:2}$ formulation with Li_2S@SP with high in-pore Li_2S loading.

In this chapter, we initially adopted the PEI-$ER_{1:2}$ binder formulation from our earlier study, using branched PEI with a molecular weight of ~25,000. While this binder offered good processability, it lacked sufficient mechanical strength to hold the Li_2S@SP cathode together, and the charging process showed instability. To improve structural integrity and cycling stability, we replaced the low-molecular-weight PEI with high-molecular-weight PEI (600,000–1,000,000), which yielded smoother and more stable charge-discharge curves. We then optimized the PEI-to-ER mass ratio (1:4, 1:2, 1:1, and 1:0.5) and found that 1:1 delivered the best electrochemical performance. However, preparing the binder in advance proved challenging because the crosslinking reaction was difficult to control, leaving a very short processing window. To address this, we designed an in-situ crosslinking approach: 5 wt.% PEI was first mixed with 80 wt.% Li_2S@SP and 10 wt.% Super P in *N*-methyl-2-pyrrolidone (NMP) until fully dispersed, after which 5 wt.% ER solution was added and mixed thoroughly. The slurry was then blade-coated onto carbon-coated aluminum foil, with crosslinking occurring naturally during drying. This method produced cathodes with excellent film quality and significantly enhanced electrochemical performance. Notably, the *in-situ* crosslinked PEI-$ER_{1:1}$-based Li_2S@SP cathodes delivered higher capacities, improved cycling stability, and better rate capability compared to PVDF- and PVP-based counterparts, underscoring the effectiveness of the PEI-ER binder system for Li_2S@SP nanocomposite electrodes with high in-pore Li_2S loading. Here, we report the design, fabrication, and electrochemical evaluation of *in-situ* crosslinked PEI-$ER_{1:1}$ binders for high in-pore Li_2S loading Li_2S@SP cathodes, demonstrating their superior performance and structural stability compared to conventional binder systems.

7.2 Experimental Section

7.2.1 Materials

All chemicals were used as received unless otherwise specified. Lithium sulfide (Li_2S, 99.98%), anhydrous ethanol (≤ 0.003% water), carbon disulfide (CS_2, ≥ 99.9%), anhydrous *N*-methyl-2-pyrrolidone (NMP, 99.5%), and polyvinylpyrrolidone (PVP, M_w ~1,300,000) were purchased from Sigma-Aldrich. Polyvinylidene fluoride (PVDF, M_w ~1,000,000) was from Kynar. Ethanol and NMP were further dried using molecular sieves prior to use. Super P conductive carbon (SP) was obtained from IMERYS. Two types of polyethyleneimine (PEI) were used: branched PEI (average M_w ~25,000 by LS, M_n ~10,000 by GPC) and PEI aqueous solution (~50% in H_2O, M_w 600,000–1,000,000). The epoxy resin (ER) used was Araldite® 506.

To obtain anhydrous high-M_w PEI, the aqueous PEI solution was first dissolved in anhydrous ethanol, then treated with anhydrous sodium sulfate (Na_2SO_4) for water absorption. The resulting mixture was subjected to rotary evaporation, followed by vacuum drying at 100 °C.

To distinguish between the two types of polyethyleneimine (PEI), the branched PEI with an average molecular weight of ~25,000 (M_w by LS, M_n ~10,000 by GPC) is referred to as PEI (LM), while the anhydrous high-molecular-weight PEI obtained from the aqueous PEI solution is simply denoted as PEI.

7.2.2 Preparation of Li_2S@SP Nanocomposite

The synthesis of Li_2S@SP nanocomposites followed a previously reported multiple infiltration-decomposition steps in **Chapter 6**. Briefly, Li_2S (280 mg, 6.1 mmol) and carbon disulfide (CS_2, 386.5 μL, 487 mg, 6.4 mmol; 5% excess) were mixed in 3 mL of anhydrous ethanol (EtOH) inside an Ar-filled glovebox (O_2 and H_2O < 0.5 ppm). The mixture was stirred at room temperature for 30 minutes to form a clear orange solution of Li_2CS_3. Additional anhydrous EtOH was added to adjust the total volume to 5 mL.

The resulting Li_2CS_3 solution was divided into five portions: 40% (2.0 mL), 25% (1.25 mL), 15% (0.75 mL), 10% (0.5 mL), and 10% (0.5 mL). In each infiltration cycle, a designated portion of the precursor solution was thoroughly mixed with Super P (120 mg) at a Li_2S:Super P mass ratio of 70:30 under continuous stirring for 6 hours at room temperature in the glovebox. The mixture

was then vacuum-dried at room temperature, followed by further drying at 100 °C to remove residual solvent. The dried Li_2CS_3@SP composite was subsequently thermally treated under vacuum at 200 °C for 2 hours to decompose Li_2CS_3 into Li_2S.

This infiltration-decomposition process was repeated in total of five times using the sequential portions of the Li_2CS_3 solution. After the final cycle, the composite was annealed at 400 °C for 1 hour under vacuum to yield the final nanocomposite, denoted as Li_2S@SP.

7.2.3 Preparation of PEI Solutions and an ER Solution in NMP

Polyethyleneimine (PEI) and epoxy resin (ER) binder solutions were prepared separately using anhydrous NMP as the solvent. To ensure uniform dispersion and facilitate subsequent mixing, each component was dissolved in NMP to achieve a concentration of 200 mg mL^{-1}.

7.2.4 Preparation of Pre-crosslinked PEI-ER Binder-based Li_2S Electrodes

The pre-crosslinked PEI-ER binder solution was prepared following a previously reported method by stirring the mixture of PEI (LM) and ER at a mass ratio of 1:2. The resulting PEI(LM)-$ER_{2:1}$ binder solution was considered ready for use once it formed a gel-like consistency while remaining flowable.

An electrode slurry was prepared by thoroughly grinding Li_2S@SP (80 wt.%), Super P (10 wt.%), and the pre-crosslinked PEI(LM)-$ER_{1:2}$ binder (10 wt.%) using NMP as the solvent. The resulting slurry was then blade-coated onto a carbon-coated aluminum foil, followed by drying at 50 °C overnight. To ensure complete removal of residual NMP, the coated electrodes were further vacuum dried at 100 °C.

To further investigate the impact of PEI molecular weight and the mass ratio between PEI and ER on battery performance, PEI was used in place of PEI (LM), and the PEI:ER mass ratio was systematically varied (1:4, 1:1, 1:0.5). Electrode preparation followed the same procedure as described above, with the only difference being the use of binder solutions with different PEI-ER mass ratios.

7.2.5 Preparation of *In-Situ*-Crosslinked PEI-ER Binder-based Li_2S Electrodes

The electrode slurry was prepared by thoroughly grinding Li_2S@SP (80 wt.%), Super P (10 wt.%), and PEI (5 wt.%) in NMP for 15 minutes. Subsequently, ER (5 wt.%) was added to the

mixture, followed by an additional 15 minutes of grinding. The resulting slurry was then blade-coated onto a carbon-coated aluminum foil, followed by drying at 50 °C overnight. To ensure complete removal of residual NMP, the coated electrodes were further vacuum dried at 100 °C.

7.2.6 Preparation of PVDF- and PVP-based Li_2S Electrodes

For comparison, PVDF- and PVP-based Li_2S electrodes were prepared following the same procedure, except that PVDF or PVP was used as the binder material in place of PEI-ER.

All the dried films were then punched into 12 mm discs. The active material loading (Li_2S) was ~1.0–1.2 mg cm^{-2}.

7.2.7 Electrochemical Measurements

CR2032 half cells were assembled inside an Ar-filled glovebox using Li_2S@SP cathode (or other cathodes), lithium metal anodes, Celgard 2400 separators, and 1.0 M LiTFSI electrolyte in a 1:1 (*v*/*v*) DOL/DME with 2 wt.% $LiNO_3$. Galvanostatic charge-discharge measurements were conducted using a Land 2001A battery tester. Electrochemical impedance spectroscopy (EIS) was performed using a Bio-logic VSP (1000 kHz to 0.1 Hz, 10 mV AC), and CV in the 1.7−4.0 V and 1.7−2.8 V range at different scan rate of 0.025 mV s^{-1}.

7.2.8 Characterizations

SEM images were acquired using a Zeiss Sigma HD microscope.

7.3 Results and Discussion

7.3.1 Selection of PEI and ER as Binder Raw Materials

An initial approach involved applying the previously developed $Zn(OAc)_2$·TEA/PEI binder (in **Chapter 4**) to Li_2S@SP nanocomposites with high in-pore Li_2S loading (hereafter referred to simply as Li_2S@SP), given its proven ability to improve polysulfide confinement and interfacial stability in conventional Li_2S cathodes. However, this strategy was unsuccessful. The nano-sized Li_2S in Li_2S@SP possesses an extremely high specific surface area and strong chemical reactivity, leading to undesirable side reactions between the exposed Li_2S surface and the $Zn(OAc)_2$·TEA species in the binder.[380] These reactions consumed the binder's functional components, weakened its adhesive and cohesive network, and ultimately resulted in poor electrode integrity and unstable electrochemical performance.

To address this incompatibility, the focus shifted to the earlier PEI-ER series binders, which had demonstrated excellent performance in sulfur-based cathodes with nano-sized sulfur particles.[379] In those systems, the PEI-ER binders provided strong mechanical adhesion, effective chemical anchoring of polysulfides, and stable cycling behavior, proving its capability to work with high-surface-area active materials. This prior success suggested that PEI-ER could also be effective for Li_2S@SP nanocomposites, provided that no reactive interference occurred with Li_2S.

In the PEI-ER system, polyethylenimine (PEI) serves as the functional backbone. As shown in **Figure 7.1**, PEI contains a high density of primary, secondary, and tertiary amine groups capable of forming strong Lewis acid-base interactions and hydrogen bonds with lithium polysulfides, while also coordinating transiently with Li^+ to promote ionic conduction. Computational simulation studies have shown that nitrogen and oxygen atoms possess strong binding energies toward lithium polysulfides by forming coordination bonds between the heteroatoms (N or O) and lithium atoms in LPSs, which effectively suppresses their migration.[381] The highly branched PEI structure further enables extensive physical entanglement with conductive carbon networks, thereby improving slurry cohesion and adhesion to the current collector. For Li_2S cathodes, which undergo significant volume shrinkage during the initial activation from Li_2S to S_8, such strong initial cohesion is critical. A tightly bound electrode architecture at the outset minimizes the risk of interparticle separation and void formation as the active material contracts. This ensures that the conductive carbon

framework remains in intimate contact with the shrinking Li_2S particles, preserving continuous electron transport pathways and facilitating full electrochemical activation.

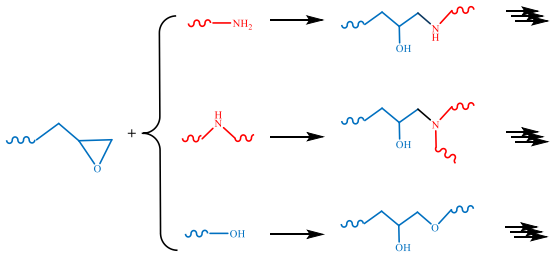


Figure 7.1 Schematics of reaction between polyethylenimine (PEI) and epoxy resin (ER).

Epoxy resins have been widely used for many years in paints, coatings, adhesives, engineering plastics, and numerous other industrial and consumer applications due to their superb mechanical properties, ease of processing, and low cost. In this study, an oligomeric bisphenol A diglycidyl ether (ER) was selected, which can react with a polyamine hardener such as PEI through a well-known epoxide-amine ring-opening reaction. Because PEI contains multiple primary, secondary, and tertiary amine groups along its branched backbone, and ER contains multiple epoxide groups per chain, this reaction proceeds at numerous sites simultaneously. The result is an extensive three-dimensional crosslinked polymer network, where each PEI molecule can be connected to multiple ER chains and vice versa, producing a large, mechanically robust network throughout the electrode film.[379] When combined with ER, the resulting crosslinked network further "locks in" this tightly packed electrode structure, effectively resisting mechanical disruption during activation and subsequent cycling. This synergistic structural stabilization is a key reason for selecting the PEI-ER system for high-loading Li_2S@SP electrodes.

The flexibility of the PEI-ER system, through adjustments in PEI molecular weight and PEI-to-ER ratio, allows its mechanical strength, ionic pathways, and polysulfide confinement ability to be optimized for the specific structural and electrochemical requirements of high-loading Li_2S@SP electrodes. This combination of chemical compatibility, mechanical robustness, and proven performance with nano-sized sulfur cathodes formed the basis for its selection in this work.

7.3.2 Impact of PEI Molecular Weight on the Electrochemical Performance of PEI-ER Binders in Li_2S@SP Cathode

To evaluate the applicability of our previously developed PEI-ER binder formulation for Li_2S@SP cathodes, we first employed the same recipe from our earlier work—branched PEI with a molecular weight of ~25,000 and epoxide resin (ER) at a mass ratio of 1:2. The binder was prepared by dissolving PEI in NMP and ER in NMP separately, then mixing the two solutions to initiate the crosslinking reaction. The reaction rate varied with the PEI-to-ER ratio, and the mixture was usable only during a narrow "gel-like" stage before full crosslinking. Once crosslinking was complete, the binder lost its processability and could no longer be incorporated into a slurry. Therefore, the PEI-ER mixture was applied to prepare the electrode slurry while still in this limited crosslinking window. The resulting slurry, containing 80 wt.% Li_2S@SP, 10 wt.% Super P, and 10 wt.% PEI-ER binder, was coated onto carbon-coated aluminum foil, during which the crosslinking reaction proceeded to completion, yielding a fully cured binder network within the electrode film.

The electrochemical impedance results (**Figure S 7.1** and **Table S 7.1**) show that the PEI(LM)-$ER_{1:2}$-based electrode exhibits a lower charge-transfer resistance (24.5 Ω) compared with the PEI-$ER_{1:2}$-based electrode (33.1 Ω), indicating that the molecular weight of PEI plays a decisive role in interfacial kinetics. In the low-M_w system, the shorter polymer chains reduce entanglement during crosslinking with ER, leading to greater exposure of nitrogen-containing functional groups at the electrode/electrolyte interface. These accessible amine groups promote polysulfide adsorption, thereby accelerating redox conversion and lowering

The initial charge/discharge curves of the Li_2S@SP cathode employing the PEI(LM)-$ER_{1:2}$ binder are shown in **Figure 7.2** (a). During the first charge, the battery exhibited an overpotential spike and high charging voltage, despite the use of nanoscale Li_2S. This behavior can be attributed to the presence of a LiOH/Li_2O passivation layer that naturally forms on commercial Li_2S powders. Although the commercial Li_2S powders were subjected to dissolution and subsequent thermal treatment, the LiOH/Li_2O layer readily re-forms during decomposition and annealing, hindering the initial activation process. Nevertheless, the battery delivered an initial charging capacity as high as 1168 mA h g^{-1} at 0.05 C, close to the theoretical value. Upon discharge, a well-defined first plateau corresponding to the reduction of S_8 to Li_2S_4 was observed at 286 mA h g^{-1}, indicating that Li_2S had

been fully activated and ~98.1% of sulfur was electrochemically utilized. The battery achieved an initial discharge capacity of 885 mA h g^{-1}, which is notably higher than the 807 mA h g^{-1} previously reported for Li_2S@SP cathodes using PVP as the binder, highlighting the beneficial effect of the PEI-ER system.

However, when the second charging process was carried out at 0.1 C, the voltage profile displayed significant instability. Instead of rising smoothly at the tail end of charging, the curve exhibited irregular "ups-and-downs". This fluctuation likely originated from insufficient electrode cohesion provided by the low-molecular-weight PEI, whose shorter chains and weaker entanglement reduce the binder's ability to maintain intimate contact between Li_2S particles, conductive carbon, and the current collector. Furthermore, PEI can interact with Li_2S surfaces, and the strongly basic environment of Li_2S accelerates the PEI-ER crosslinking reaction. Such accelerated and uneven crosslinking leads to poor binder distribution, reduced flexibility, and weakened adhesion, ultimately promoting intermittent disconnection and reconnection events during the sluggish final stage of Li_2S oxidation. Despite these issues, the battery was still able to sustain cycling and delivered a discharge capacity of 687 mA h g^{-1} at the 5^{th} cycle. Moreover, a small voltage tail at the end of discharge became increasingly evident, suggesting that Li_2S located deep within the carbon pores was gradually activated and utilized, confirming that the PEI-ER binder facilitated access to confined active material even under suboptimal binding conditions.

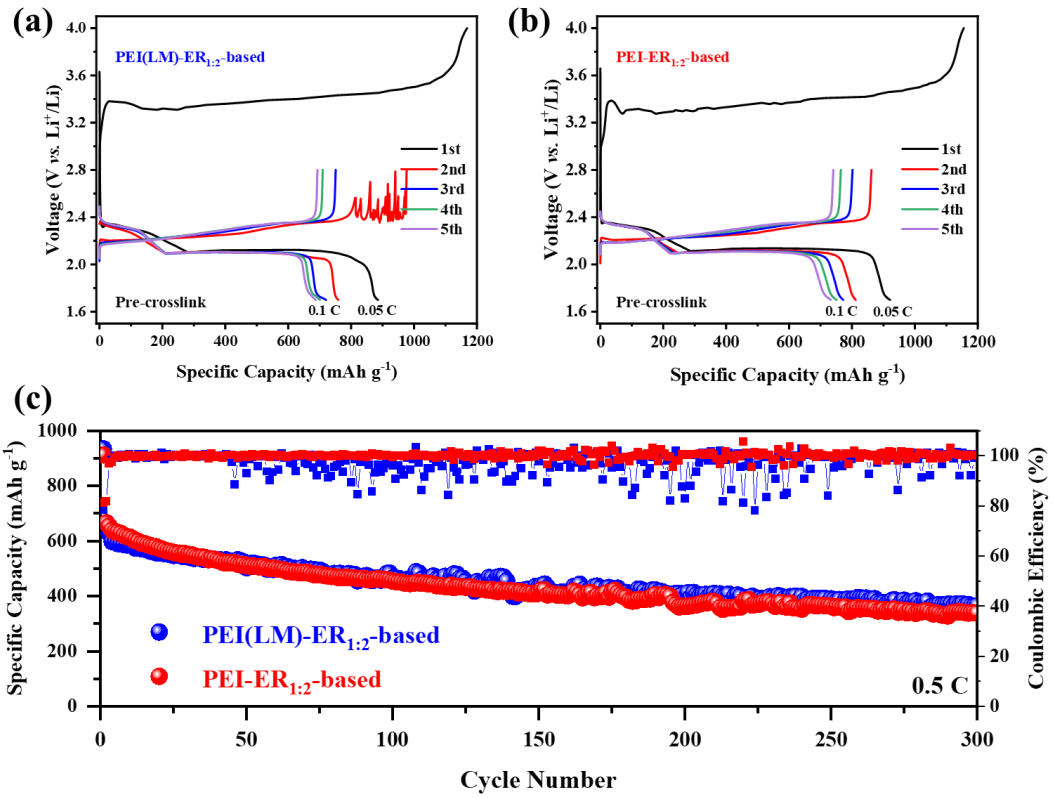


Figure 7.2 Charge/Discharge curves of (a) PEI(LM)-$ER_{1:2}$-based and (b) PEI-$ER_{1:2}$-based electrodes at 0.05 C for the initial cycle and 0.1 C for the following ones. (c) Long-term cycling comparison between these two electrodes at 0.5 C.

To address the instability observed with the low-molecular-weight PEI (~25,000) binder, we employed a high-molecular-weight PEI (600,000–1,000,000) while maintaining the ER content and the PEI-to-ER mass ratio at 1:2. The choice of high-M_w PEI (hereafter referred to simply as PEI) was motivated by its significantly longer polymer chains, which provide extensive physical entanglement within the conductive carbon network and stronger adhesion to Li_2S particles. These features allow the binder to better accommodate structural stress during Li_2S conversion and mitigate the microstructural disruption that led to unstable charging in the low-M_w system. Moreover, the higher molecular weight slows down the crosslinking kinetics in the basic Li_2S environment, avoiding the premature gelation that plagued the low-Mw binder and enabling a more uniform distribution of the binder throughout the slurry.

The initial charge/discharge behavior of the Li_2S@SP cathode with the PEI-$ER_{1:2}$ binder is shown in **Figure 7.2** (b). At 0.05 C, the battery also exhibited a characteristic overpotential spike of ~3.5 V during the first charge, lower than that observed for PVP-based electrodes, confirming

that PEI, regardless of molecular weight, helps reduce the activation barrier of Li_2S. The charging voltage remained relatively high, but the battery still delivered an initial charging capacity of 1155 mA h g^{-1}, close to the theoretical value. Upon discharge, a distinct first plateau appeared at ~286 mA h g^{-1}, corresponding to the reduction of sulfur to Li_2S_4 and indicating nearly complete sulfur utilization (~99.0%). The overall initial discharge capacity reached 921 mA h g^{-1}, which is higher than that obtained with the low-M_w PEI-ER binder, despite both systems showing the same first plateau value. This enhancement can be attributed to the superior binding strength and electrode cohesion provided by the high-M_w PEI, which allows for better electrical contact and deeper utilization of active material within the porous carbon host. Consistent with this interpretation, the discharge curve displayed a more pronounced "tiny tail" beyond the main plateau in the initial discharge, signaling that Li_2S confined within the micropores of the Super P framework was further accessed and converted. More importantly, the second charging process at 0.1 C proceeded smoothly without any of the voltage oscillations observed in the low-Mw system, confirming the stabilizing effect of the high-M_w PEI on the binder network. By the 5th cycle, the electrode still delivered a discharge capacity of 732 mA h g^{-1} at 0.1 C, notably higher than that achieved with the low-M_w PEI-ER binder, further demonstrating the robustness and improved reversibility enabled by the high-M_w formulation.

To further evaluate the impact of PEI molecular weight on cycling stability, the long-term performance of Li_2S@SP cathodes employing PEI(LM)-$ER_{1:2}$ and PEI-$ER_{1:2}$ binders was compared at 0.5 C, following an initial activation cycle at 0.05 C (**Figure 7.2** (c)). Although the PEI(LM)-$ER_{1:2}$-based battery exhibited instability during its second charging process, it was still tested at 0.5 C to probe its behavior under practical cycling conditions, since subsequent cycles showed smoother profiles. Both batteries delivered the same second-cycle discharge capacity of 666 mA h g^{-1}, indicating comparable initial reversibility. However, the PEI(LM)-$ER_{1:2}$-based battery quickly exhibited instability: the Coulombic efficiency fluctuated erratically and frequently dropped below 80%, reflecting the binder's poor ability to maintain structural cohesion. In contrast, the PEI-$ER_{1:2}$-based battery displayed significantly improved stability, with Coulombic efficiency consistently ~100% throughout extended cycling. The superior performance arises from the longer polymer chains of high-M_w PEI, which provide stronger entanglement with conductive carbon and Li_2S

particles, thereby resisting electrode fracture and particle detachment during volume changes. Nonetheless, even with this improvement, the Coulombic efficiency gradually became unstable after ~150 cycles, likely due to persistent polysulfide shuttling and side reactions, which cannot be fully suppressed by binder reinforcement alone.

These results indicate that, while the high-M_w PEI-$ER_{1:2}$ binder offers improved stability compared to its low-M_w counterpart, the 1:2 mass ratio is not optimal for Li_2S@SP cathodes. To further enhance electrochemical performance, we next investigated the effect of varying the PEI-to-ER mass ratio.

7.3.3 Optimization of PEI-ER Mass Ratio and Development of *In-Situ* Crosslinking Strategy

Building on the insights gained from the PEI-$ER_{1:2}$ formulation, we next focused exclusively on high-M_w PEI and systematically investigated the influence of different PEI-to-ER mass ratios on the performance of Li_2S@SP cathodes. For binder preparation, PEI and ER were first dissolved separately in NMP, and then mixed together at prescribed mass ratios of 1:0.5, 1:1, 1:2 (as already discussed in the previous section), and 1:4. Upon mixing, the PEI-ER crosslinking reaction began immediately, and the mixture was applied as binder during its gel-like state within the narrow crosslinking time window. Importantly, the duration of this window varied significantly depending on the mass ratio. Accordingly, the slurry preparation process had to be carefully adjusted for each ratio to ensure proper coating quality. In all cases, the electrode slurry consisted of 80 wt.% Li_2S@SP, 10 wt.% Super P, and 10 wt.% PEI-ER binder, with the PEI and ER fractions tuned according to the selected ratio.

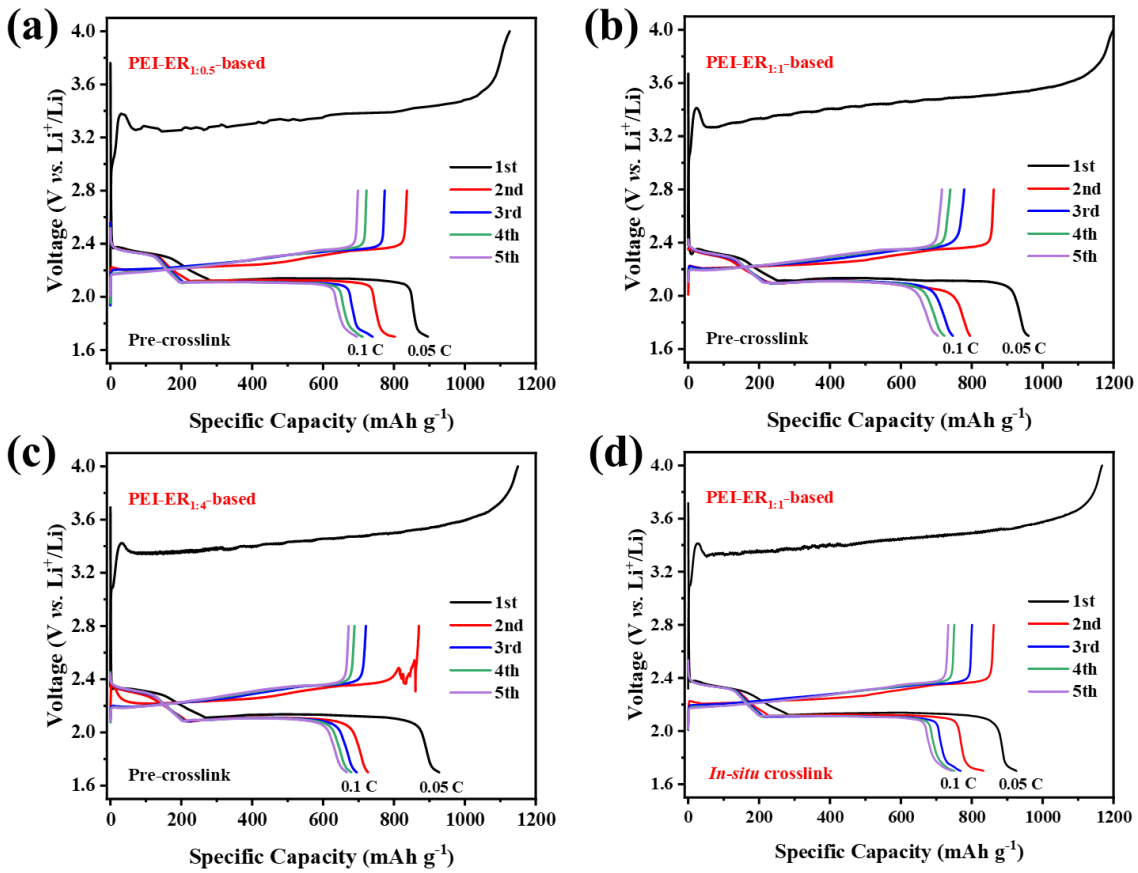


Figure 7.3 Initial charge/discharge curves of (a) PEI-ER$_{1:0.5}$- (b) PEI-ER$_{1:1}$- (c) PEI-ER$_{1:4}$-, and (d) *in-situ* crosslinked PEI-ER$_{1:1}$-based electrodes at 0.05 C for the initial cycle and 0.1 C for the following ones.

Figure 7.3 (a-c) show the initial charge/discharge curves of Li_2S@SP cathodes with PEI-ER binders at mass ratios of 1:0.5, 1:1, and 1:4. For the PEI-rich binder (PEI-ER$_{1:0.5}$, **Figure 7.3** (a)), the battery delivered an initial charging capacity of 1126 mA h g^{-1}, with a first discharge plateau of 285 mA h g^{-1} corresponding to nearly 100% sulfur utilization. The initial discharge capacity was 896 mA h g^{-1}, and a pronounced low-voltage tail was observed, indicating that the excess PEI helped confine polysulfides within the porous Super P framework for extended utilization. The PEI-ER$_{1:1}$-based cathode (**Figure 7.3** (b)) showed a slightly overcharged first charge, likely due to increased polarization during activation. However, it achieved a total initial discharge of 960 mA h g^{-1}, with the first plateau at 250 mA h g^{-1} and nearly 96% utilization of the second plateau, demonstrating more efficient confinement and reutilization of LPSs than the 1:0.5 case. By contrast, the ER-rich binder (PEI-ER$_{1:4}$, **Figure 7.3** (c)) exhibited unstable charging behavior from the second cycle

onward, similar to the irregular ups-and-downs seen with low-M_w PEI-ER binders, reflecting poor cohesion and uncontrolled crosslinking in ER-dominant systems.

The following cycle performance further underscores these differences: at the 5th cycle (0.1 C), the discharge capacities were 695 mA h g^{-1} for 1:0.5, 704 mA h g^{-1} for 1:1, and only 666 mA h g^{-1} for 1:4. Mechanistically, the 1:0.5 formulation is limited by excess PEI introducing kinetic penalties: the amine-rich polymer partially coats conductive carbon, narrows mesopores, and increases charge-transfer/ionic transport resistance. Stronger LPS adsorption also slows their re-oxidation, stretching capacity into a low-voltage tail rather than a high-efficiency plateau. In contrast, the balanced 1:1 ratio supplies enough PEI for adhesion and LPS management while retaining sufficient ER to form a robust, well-percolated network. While PEI-$ER_{1:2}$-based battery shows decent performance, the PEI-$ER_{1:1}$ formulation achieves the best balance between capacity, polysulfide confinement, and cycling stability. Taken together, these results establish PEI-$ER_{1:1}$ as the optimal composition for Li_2S@SP cathodes, outperforming PEI-rich and ER-rich extremes as well as the initially adopted PEI-$ER_{1:2}$ recipe.

However, one persistent drawback of the pre-mixed PEI-ER approach is the narrow and unpredictable crosslinking window: once gelation progresses too far, the binder loses processability and can no longer be used for slurry preparation. Moreover, premature crosslinking in solution prevents PEI from fully coating the Li_2S and conductive carbon, leading to uneven binder distribution and weaker interfacial contact. This issue is further exacerbated by Li_2S itself, whose strongly basic environment accelerates the crosslinking reaction between PEI and ER, shortening the gelation window and making slurry processing even more difficult. To address these challenges while preserving the advantages of the optimized 1:1 ratio, we next developed an in-situ crosslinking strategy. In this method, PEI was first mixed with Li_2S@SP and Super P, allowing it to uniformly coat and bind the active material and conductive network. ER was then introduced afterward, with crosslinking initiated and gradually completed during the electrode drying step. This approach effectively transformed the accelerated reactivity of Li_2S from a processing obstacle into a controlled advantage, ensuring uniform binder distribution, strong interfacial adhesion, and enhanced electrode integrity.

The initial charge/discharge behavior of the battery employing the *in-situ* crosslinked PEI-$ER_{1:1}$ binder is presented in **Figure 7.3** (d). During the first charge at 0.05 C, the electrode delivered a capacity of 1168 mA h g^{-1}, essentially matching the theoretical value of 1166 mA h g^{-1}. This indicates that the Li_2S active material was fully converted to elemental sulfur (S_8), confirming efficient activation. Upon discharge, the first plateau appeared at 284 mA h g^{-1}, corresponding to the $S_8 \rightarrow Li_2S_4$ transition and representing 97.3% sulfur utilization in this step. The total initial discharge capacity reached 928 mA h g^{-1}, notably accompanied by a pronounced tail at the end of the curve. Similar to the behavior observed for the PEI-rich PEI-$ER_{1:0.5}$ binder, this extended tail reflects the progressive reduction of polysulfides to Li_2S within the confined pores of the Super P framework. However, while the 1:0.5 formulation achieved an initial discharge of 896 mA h g^{-1} and only 695 mA h g^{-1} at the 5th cycle, the *in-situ* crosslinked PEI-$ER_{1:1}$-based battery delivered a higher initial discharge of 928 mA h g^{-1} and maintained 743 mA h g^{-1} at the 5th cycle. This comparison highlights that the *in-situ* strategy not only replicates the beneficial confinement effect of PEI-rich systems but also achieves superior capacity retention and cycling stability.

Mechanistically, this improvement arises because PEI can first coat and bind Li_2S@SP surfaces, forming a uniform network, before ER is introduced to strengthen the matrix during drying. This sequence is critical because Li_2S inherently creates a strongly basic environment that accelerates PEI-ER crosslinking. In the pre-crosslinked approach, this acceleration leads to premature gelation and uneven binder distribution, leaving parts of the electrode poorly integrated. By shifting crosslinking into the electrode drying step, the *in-situ* method accommodates Li_2S's reactivity, ensures controlled gelation, and delivers a more uniform, mechanically robust, and electrochemically effective binder network.

The EIS results of these different binder-based electrodes are shown in **Figure S 7.2** and **Table S 7.2**. The R_{ct} shows a pattern of PEI-$ER_{1:0.5}$-based (48.3 Ω) > *in-situ* crosslinked PEI-$ER_{1:1}$-based (42.2 Ω) > PEI-$ER_{1:4}$-based (35.8 Ω) > PEI-$ER_{1:1}$-based (34.2 Ω) > PEI-$ER_{1:2}$-based (33.1 Ω). And this pattern agrees with the appearance of tiny tails at the end of the discharge. A higher degree of crosslinking, as in the PEI-$ER_{1:0.5}$ and *in-situ* crosslinked PEI-$ER_{1:1}$ binders, creates a denser network that limits ion transport and restricts the accessibility of nitrogen functional groups. While such dense crosslinking enhances mechanical robustness, it simultaneously increases interfacial

resistance, causing sluggish reaction kinetics. These kinetic limitations manifest as longer discharge tails, since the electrode requires additional polarization to drive the sluggish Li_2S redox conversion to completion. At the same time, strong crosslinking can effectively lock the pores of the Super P carbon host, which confines soluble intermediates more efficiently and promotes deeper sulfur utilization. This pore-locking effect extends the discharge process, reinforcing the correlation between higher degrees of crosslinking, longer discharge tails, and improved depth of reaction.

Overall, the PEI-$ER_{1:1}$ binder with *in-situ* crosslinking proved to be the most effective strategy for Li_2S@SP cathodes. Unlike PEI-rich or ER-rich formulations, this approach balanced adhesion, flexibility, and confinement of polysulfides, while avoiding the drawbacks of premature gelation.

7.3.4 Performance Benchmarking: *In-Situ* Crosslinked PEI-$ER_{1:1}$ Binder versus Conventional PVDF and PVP Binders

To further highlight the advantages of the optimized *in-situ* crosslinked PEI-$ER_{1:1}$ binder, its performance was benchmarked against conventional binders, namely poly(vinylidene fluoride) (PVDF) and poly(vinylpyrrolidone) (PVP). PVDF has long been used in LIBs owing to its nominal electrochemical stability, yet it belongs to the class of per- and polyfluoroalkyl substances (PFAS) currently facing regulatory restrictions and is known to undergo dehydrofluorination in the presence of Li_2S, consuming active material. By contrast, PVP is widely regarded as an inert, fluorine-free binder in Li_2S-based batteries and has been extensively adopted in literature, primarily serving as a benchmark material without offering active chemical interactions. For a fair comparison, all electrodes were prepared with the same composition of 80 wt.% Li_2S@SP, 10 wt.% Super P, and 10 wt.% binder material. This direct side-by-side evaluation provides a clear evaluation of how the multifunctional PEI-ER binder design outperforms both conventional binders in Li_2S@SP cathodes.

The adhesive strength of different binder systems was further evaluated through a simple peeling test using adhesive tape, following the same protocol reported in our previous study. As shown in **Figure S 7.3**, clear differences were observed in the amount of active materials detached from the electrodes. Among the three binders, the *in-situ* crosslinked PEI-$ER_{1:1}$-based electrode exhibited the strongest binding effect, with only a negligible amount of black powder adhering to the tape (**Figure S 7.3** (c)). In contrast, the PVDF-based electrode displayed moderate binding

performance (**Figure S 7.3** (a)), while the PVP-based electrode showed the weakest adhesion, with a significant fraction of materials peeled off (**Figure S 7.3** (b)).

The superior binding of the *in-situ* crosslinked PEI-$ER_{1:1}$-based binder can be attributed to the formation of robust chemical crosslinks between the polyamine-rich PEI and the epoxy resin, which provide a three-dimensional network to strongly anchor both Li_2S particles and conductive carbon within the electrode. PVDF demonstrates better adhesion than PVP because Li_2S can partially react with the fluoropolymer to induce additional crosslinking, thereby enhancing cohesion within the electrode film. In contrast, PVP acts primarily through physical adsorption and hydrogen bonding, which are insufficient to maintain strong adhesion during peeling. These results highlight the critical role of binder chemistry in determining electrode integrity, with the in-situ crosslinked PEI-ER binder offering a distinct advantage in maintaining structural robustness.

The EIS results of the fresh electrodes based on different binders are summarized in **Figure S 7.4** and **Table S 7.3**. The PVDF-based electrode exhibits the lowest, which can be attributed to the partial reaction between PVDF and surface LiOH/Li_2O species on Li_2S particles. This reaction induces a degree of crosslinking that enhances interparticle contact and reduces the interfacial barrier for charge transfer. By contrast, the PVP-based electrode shows an intermediate as PVP is electrochemically inert toward Li_2S, and it provides only physical adhesion without forming interfacial bonds, resulting in moderate interfacial resistance. The *in-situ* crosslinked PEI-$ER_{1:1}$ binder, however, yields the highest R_{ct}. Although abundant amine groups in PEI can strongly interact with polysulfides, the dense crosslinked network formed upon in situ reaction partially covers conductive carbon surfaces and blocks electrolyte infiltration into the electrode pores.

The initial charge/discharge curves of the PVDF-based Li_2S@SP battery are shown in **Figure 7.4** (d). The first charge exhibits a reduced overpotential spike of 3.05 V, noticeably lower than that observed in PEI-ER systems. This reduction arises because, during slurry preparation, PVDF reacts with the LiOH/Li_2O layer on the Li_2S surface, exposing fresh Li_2S and thereby facilitating activation. As a result, the post-spike charging plateau also shifts downward to ~2.36 V. Such behavior has likewise been reported in commercial Li_2S batteries that were stirred with PVDF binders for extended periods (e.g., 48 h), where sufficient interfacial contact promoted the same reaction. In

the present work, the effect is even more pronounced because the nanosized Li_2S accelerates the dehydrofluorination process more efficiently, driving the characteristic voltage reduction. However, this apparent advantage comes at the cost of irreversible side reactions: PVDF undergoes dehydrofluorination in the strongly basic environment of Li_2S, consuming both PVDF and active Li_2S. Consequently, the charging capacity is significantly diminished, reaching only 864 mA h g^{-1}, and the corresponding first discharge delivers just 672 mA h g^{-1}—substantially lower than the values obtained with PEI-ER binders.

Interestingly, the discharge profile still exhibits a subtle tail feature at the end of the plateau, similar to that observed in PEI-rich PEI-$ER_{1:0.5}$ and *in-situ* crosslinked PEI-$ER_{1:1}$-based batteries. This tail likely originates from the immediate reaction between nanosized Li_2S and PVDF, which accelerates the dehydrofluorination process. The resulting PVDF fragments strongly adhere to Li_2S particle surfaces and can crosslink across the conductive carbon matrix as shown in **Figure 7.4** (a). While this process undesirably consumes Li_2S, it simultaneously creates a physical barrier that blocks pores in the Super P network. Such blockage restricts LPS diffusion, effectively confining LPSs within the pores. As a result, the PVDF-based battery exhibits relatively stable cycling behavior despite its lower capacity, highlighting the trade-off between chemical stability and long-term confinement when PVDF is used as a binder in Li_2S cathodes.

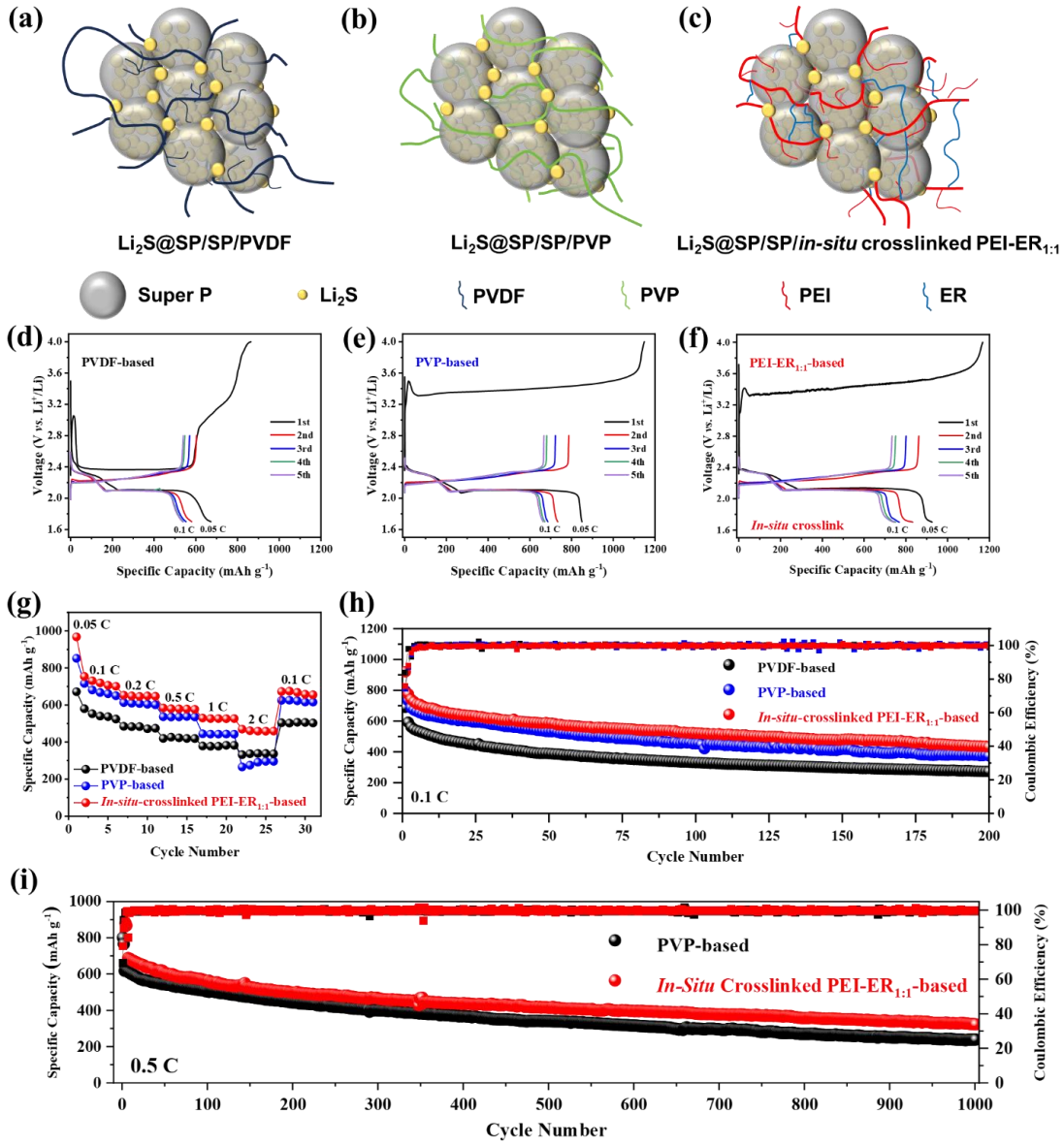


Figure 7.4 Schematic illustration of (a) Li_2S@SP/SP/PVDF (b) Li_2S@SP/SP/PVP and (c) Li_2S@SP/SP/*in-situ* crosslinked PEI-$ER_{1:1}$ electrodes. Initial charge/discharge curves of (d) PVDF- (e) PVP- and (f) *in-situ* crosslinked PEI-$ER_{1:1}$-based electrodes. (g) Rate performance comparison among PVDF-, PVP- and *in-situ* crosslinked PEI-$ER_{1:1}$-based electrodes. (h) Long-term cycling performance comparison among PVDF-, PVP- and *in-situ* crosslinked PEI-$ER_{1:1}$-based electrodes at 0.1 C. (i) Long-term cycling performance comparison between PVP- and *in-situ* crosslinked PEI-$ER_{1:1}$-based electrodes at 0.5 C.

The initial charge/discharge curves of the PVP-based Li_2S@SP battery are presented in **Figure 7.4** (e). Since PVP does not chemically interact with Li_2S, it is generally regarded as an inert binder, and thus the electrode reflects the intrinsic performance of the Li_2S@SP composite. The initial

charging capacity reached 1149 mA h g^{-1}, close to the theoretical value, mainly due to the nanoscale confinement effect of Super P. Upon discharge, the first plateau was observed at 270 mA h g^{-1}, corresponding to ~94% utilization of the transformed S_8. However, the overall initial discharge capacity was 850 mA h g^{-1}, which is lower than that of the *in-situ* crosslinked PEI-$ER_{1:1}$ binder-based battery. Notably, the discharge curve exhibited no pronounced tail at the end. This absence arises as shown in **Figure 7.4** (b) because, without a reactive binder-Li_2S interaction, PVP cannot block or seal the pores of Super P. As a result, LPSs diffuse out of the pores more freely, preventing the gradual deep-conversion signal (the "tail") that was evident in the PEI-rich and PVDF-based systems. In the *in-situ* crosslinked PEI-ER1:1 binder-based battery as shown in **Figure 7.4** (c), the pores of Super P have been blocked by the branched PEI in advance and deepened by the crosslinking reaction with ER. Over cycling, however, the electrode structure becomes more activated, and the Super P gradually confines polysulfides more effectively, leading to the emergence of a visible tail. By the 5th cycle, the discharge capacity stabilized at 664 mA h g^{-1}, still lower than that of the *in-situ* crosslinked PEI-$ER_{1:1}$-based battery.

The rate performance of Li_2S@SP batteries employing PVDF, PVP, and *in-situ* crosslinked PEI-$ER_{1:1}$ binders is shown in **Figure 7.4** (d). All batteries were first activated at 0.05 C, after which the current density was stepwise increased from 0.1 to 2 C and then returned to 0.1 C. Among the three binder systems, the *in-situ* crosslinked PEI-$ER_{1:1}$-based battery consistently delivered the highest reversible capacities across all current densities. At 0.1 C, it achieved ~755 mA h g^{-1}, significantly higher than PVDF (~580 mA h g^{-1}) and PVP (~717 mAh g^{-1}). Even at 1 C and 2 C, the *in-situ* crosslinked PEI-$ER_{1:1}$-based battery retained ~530 and ~470 mA h g^{-1}, respectively, whereas the PVDF- and PVP-based batteries both showed stronger capacity fading, dropping below 450 mA h g^{-1} at 1 C and approaching ~330 mA h g^{-1} at 2 C. Importantly, when the current density was reduced back to 0.1 C, the *in-situ* crosslinked PEI-$ER_{1:1}$ system recovered to ~673 mA h g^{-1}, demonstrating excellent structural resilience and reversibility, while PVDF and PVP only partially recovered to ~600 and ~550 mA h g^{-1}, respectively.

Interestingly, the PVP-based battery initially outperformed the PVDF-based one at lower rates. This can be attributed to PVP's inert nature, which preserves the intrinsic electrochemical activity of Li_2S@SP without consuming active material through side reactions. However, at higher rates in

Figure 7.4 (g) (e.g., 2 C), the PVP-based electrode underperformed even relative to PVDF. This decline reflects PVP's weak mechanical and interfacial binding strength: without chemical interaction with Li_2S or carbon, the electrode structure suffers from poor electronic connectivity and accelerated polysulfide shuttling at high current densities. In contrast, although PVDF reacts with Li_2S and sacrifices some initial capacity, the resulting reaction layer provides stronger adhesion and partial pore-blocking, enabling better structural retention under fast cycling.

The long-term cycling performance of Li_2S@SP batteries with PVDF, PVP, and *in-situ* crosslinked PEI-$ER_{1:1}$ binders at 0.1 C is presented in **Figure 7.4** (h). The *in-situ* crosslinked PEI-$ER_{1:1}$-based battery exhibited the best overall performance, delivering a high initial discharge capacity of ~780 mA h g^{-1} at 0.1 C and retaining ~435 mAh g^{-1} after 200 cycles (~55.8% retention). More importantly, its Coulombic efficiency remained remarkably stable and close to 100% throughout the cycling test. This stability can be attributed to the in-situ crosslinking process: PEI first coats and binds Li_2S@SP and Super P, effectively blocking polysulfide escape pathways, while subsequent ER crosslinking further strengthens the network. This dual effect not only improves sulfur utilization but also ensures excellent reversibility. The PVP-based battery, by contrast, exhibited moderate cycling stability, starting at 742 mA h g^{-1} at 0.1 C and declining to 374 mA h g^{-1} by the 200th cycle. Its Coulombic efficiency, however, displayed noticeable disturbances rather than smooth stability. Since PVP does not chemically interact with Li_2S, the binder cannot fully prevent LPS dissolution, leading to intermittent shuttling and fluctuating efficiency. The PVDF-based battery showed the lowest specific capacity (~592 mA h g^{-1} initially at 0.1 C, fading to ~379 mA h g^{-1} at 200 cycles), but its Coulombic efficiency was relatively stable. This paradoxical stability may be explained by the dehydrofluorination reaction between PVDF and Li_2S, which creates a crosslinked network on the Li_2S surface. While this reaction consumes active material and lowers capacity, the resulting crosslinked structure physically blocks polysulfides and prevents efficiency fluctuations.

The long-term cycling performance at 0.5 C is shown in **Figure 7.4** (i). Because PVDF has already been shown to be unsuitable for Li_2S-based batteries—where it reacts with active materials, causes rapid capacity fading, and loses structural integrity—it was not included in the 0.5 C long-term cycling tests. The *in-situ* crosslinked PEI-$ER_{1:1}$-based electrode consistently outperformed the

PVP-based electrode over long-term cycling. At the beginning of the 0.5 C test, the *in-situ* crosslinked PEI-$ER_{1:1}$-based electrode delivered a discharge capacity of 688 mA h g^{-1}, compared with 618 mA h g^{-1} for the PVP-based electrode. After 1000 cycles, the *in-situ* crosslinked PEI-$ER_{1:1}$-based electrode maintained 325 mA h g^{-1} (47% capacity retention), while the PVP-based electrode decreased to 238 mA h g^{-1} (39% retention). Thus, the in-situ crosslinked PEI-$ER_{1:1}$-based system not only started with higher capacity but also demonstrated slower fading during extended cycling. The Coulombic efficiency of the in-situ crosslinked PEI-ER1:1-based electrode remained relatively stable throughout cycling, whereas the PVP-based electrode exhibited noticeable fluctuations. This difference can be ascribed to the *in-situ* crosslinking reaction between PEI and ER, which forms a robust network that anchors Li_2S nanoparticles and seals the porous carbon framework. Such a crosslinked structure effectively mitigates polysulfide dissolution and shuttle effects, thereby reducing parasitic side reactions and ensuring stable Coulombic efficiency. In contrast, PVP relies mainly on physical adsorption, which weakens over time as the binder structure deteriorates and polysulfides continuously leach into the electrolyte.

At lower current density (0.1 C, **Figure 7.4** (e)), the two electrodes displayed nearly parallel capacity decay trends, indicating that both binders initially provided sufficient adhesion and polysulfide confinement. However, when cycling at higher rate (0.5 C) and for longer durations, the performance gap widened. The faster decline of the PVP-based electrode is attributed to its inferior chemical stability and weaker binding strength, which cannot sustain the repetitive charge/discharge process. As cycle number accumulates, this leads to accelerated active material loss and increasingly unstable Coulombic efficiency. In contrast, the chemically *in-situ* crosslinked PEI-$ER_{1:1}$ binder preserves electrode integrity under harsher cycling conditions, enabling superior long-term performance.

CV was shown in **Figure 7.5**. In the initial CV scan, the potential was swept from the open-circuit voltage (OCV) up to 4.0 V to activate Li_2S by oxidizing it into sulfur (S_8). A clear difference is observed in the onset of the activation process: the PVP-based electrode begins to oxidize Li_2S at 3.30 V, whereas the in-situ crosslinked PEI-$ER_{1:1}$-based electrode exhibits a much lower onset potential of 2.98 V. Moreover, the initial charging peak of the PVP-based electrode appears at 3.74 V, while the *in-situ* crosslinked PEI-$ER_{1:1}$-based electrode shows a lower charging peak at 3.57 V.

The reduction in both onset and peak potential confirms that the *in-situ* crosslinked PEI-ER$_{1:1}$ binder significantly lowers the activation barrier for Li_2S oxidation. Furthermore, when comparing the charging profiles, it is evident that the *in-situ* crosslinked PEI-ER$_{1:1}$-based electrode completes most of its oxidation reaction at lower voltages than the PVP-based electrode, reflecting a more facile and energetically favorable electrochemical process. This improvement arises from the strong chemical interactions between the amine-rich PEI-ER binder and Li_2S species, which enhance interfacial contact, stabilize polysulfide intermediates, and promote uniform oxidation.

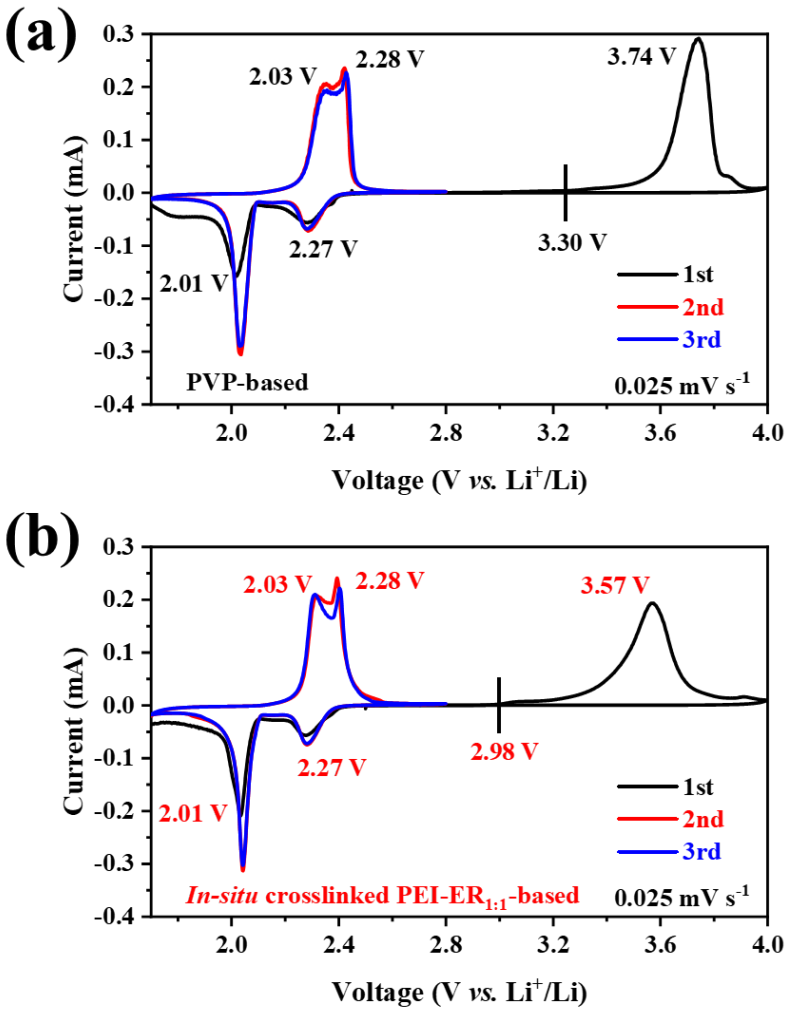


Figure 7.5 Cyclic voltammetry (CV) of (a) PVP- and (b) *in-situ* crosslinked PEI-ER$_{1:1}$-based electrodes at a scan rate of 0.025 mV s^{-1}. The initial upper scan was set to 4.0 V and the following was set between 1.7–2.8 V.

In the subsequent discharge scan to 1.7 V, both electrodes display the typical two-step sulfur reduction process: the first peak corresponds to the reduction of sulfur to soluble long-chain

polysulfides, and the second to the further conversion into insoluble Li_2S_2/Li_2S. For the PVP-based electrode, the two reduction peaks appear at 2.27 V and 2.01 V, respectively. In contrast, the *in-situ* crosslinked PEI-$ER_{1:1}$-based electrode shows slightly higher reduction peak positions at 2.28 V and 2.03 V. This small but consistent positive shift in reduction potentials indicates lower polarization and a more favorable redox environment in the PEI-ER system. Furthermore, the broader and smoother reduction peaks of the *in-situ* crosslinked PEI-$ER_{1:1}$-based electrode suggest a more gradual and uniform reaction pathway, compared with the sharper, localized processes in the PVP-based electrode. These results highlight that the *in-situ* crosslinked PEI-$ER_{1:1}$ binder not only facilitates easier activation during the initial charge but also ensures a more stable and energetically efficient reduction pathway during discharge, in sharp contrast to the inert PVP binder.

In the 2nd CV cycle, both electrodes again exhibit the expected redox features, but distinct differences emerge. For the discharge scan, the PVP-based electrode shows two peaks at 2.28 V and 2.03 V, while the *in-situ* crosslinked PEI-$ER_{1:1}$-based electrode shifts slightly higher to 2.29 V and 2.04 V, confirming consistently lower discharge polarization. During the 2nd charging scan, the PVP-based electrode displays two oxidation peaks at 2.35 V and 2.42 V, whereas the *in-situ* crosslinked PEI-$ER_{1:1}$-based electrode exhibits corresponding peaks at 2.32 V and 2.39 V. These negative shifts in charging potentials demonstrate that the *in-situ* crosslinked PEI-$ER_{1:1}$ binder facilitates faster kinetics and reduces the energy barrier for polysulfide oxidation. Moreover, the excellent overlap between the 2nd and 3rd scans in the *in-situ* crosslinked PEI-$ER_{1:1}$-based electrode underscores its high reversibility and structural stability, while the PVP-based electrode shows minor shifts indicative of greater polarization buildup.

In the 3rd cycle, a divergence in stability becomes more apparent. For the PVP-based electrode, the first charging peak shifts to a higher voltage, reflecting increasing polarization and deteriorating kinetics. By contrast, the *in-situ* crosslinked PEI-$ER_{1:1}$-based electrode maintains nearly identical peak positions to the 2nd cycle, highlighting its excellent reversibility and stable interfacial chemistry. Moreover, the two oxidation peaks of the *in-situ* crosslinked PEI-$ER_{1:1}$-based electrode become more separated in the 3rd cycle, indicating that the two-step sulfur oxidation pathway (Li_2S/Li_2S_2 → polysulfides → S_8) becomes increasingly well-defined with cycling. This enhanced resolution of redox processes suggests that the *in-situ* crosslinked PEI-$ER_{1:1}$-based binder

provides a stable framework that promotes distinct and reproducible reaction pathways, whereas the PVP binder allows greater polarization and less-controlled redox evolution.

Taken together, the *in-situ* crosslinked PEI-$ER_{1:1}$-based electrode operates with reduced polarization, enhanced reversibility, and more pronounced redox pathways compared with the inert PVP binder.

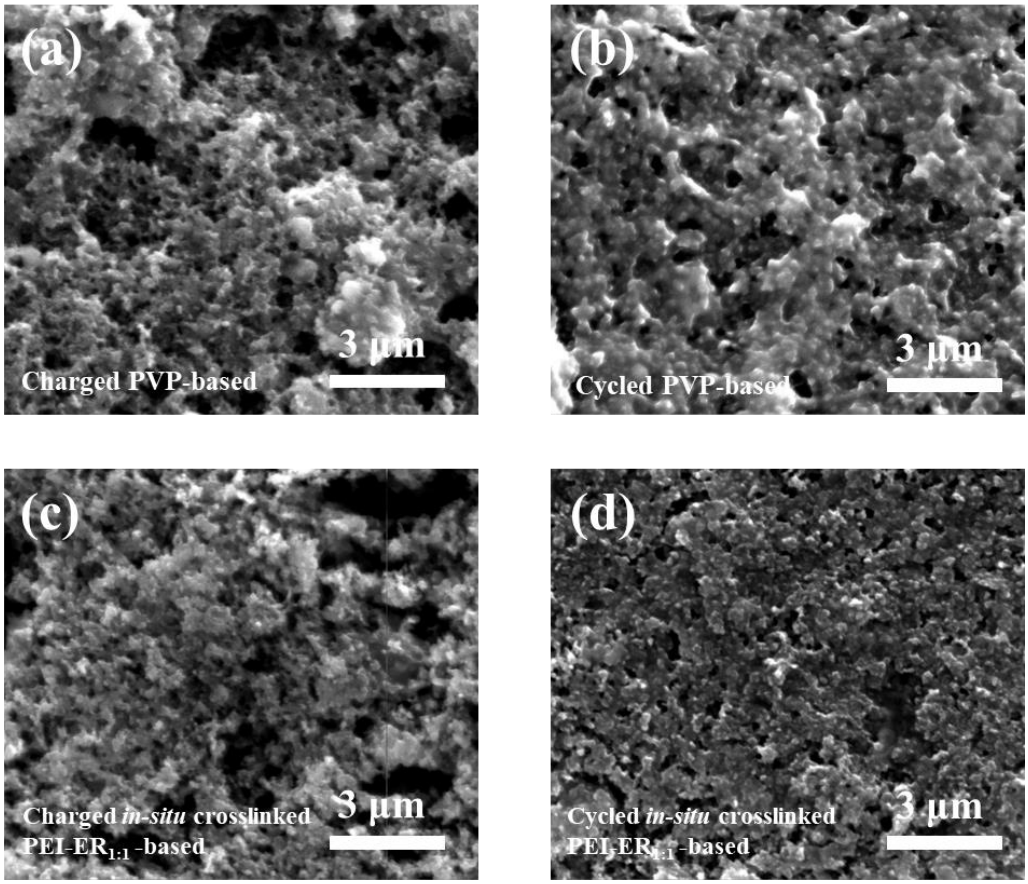


Figure 7.6 SEM images of (a) fresh PVP-based Li_2S@SP electrode after initial charging, (b) cycled PVP-based Li_2S@SP electrode in the charged state after 500 cycles at 0.5 C, (c) fresh *in-situ* crosslinked PEI-$ER_{1:1}$-based Li_2S@SP electrode after initial charging, and (d) cycled *in-situ* crosslinked PEI-$ER_{1:1}$-based Li_2S@SP electrode in the charged state after 500 cycles at 0.5 C.

The morphologies of PVP-based and *in-situ* crosslinked PEI-$ER_{1:1}$-based electrodes before and after 500 cycles were examined by SEM (**Figure 7.6**). Owing to the high moisture sensitivity of Li_2S, all electrodes were characterized in their charged (sulfur) state. To ensure consistency, the fresh electrodes were initially charged to 4.0 V to fully convert Li_2S into sulfur prior to SEM

observation, while the cycled electrodes were examined after the final charge to 2.8 V, maintaining them in the sulfur state.

The SEM images of fresh electrodes prepared with PVP and *in-situ* crosslinked PEI-$ER_{1:1}$ binders exhibit relatively similar morphologies, characterized by uniformly distributed Li_2S@SP particles. This indicates that, at the initial stage, both binders can effectively disperse active materials and ensure sufficient contact with the conductive network. Notably, by employing the *in-situ* crosslinking method, where PEI is first mixed with Li_2S@SP followed by ER addition, the morphology of the Li_2S@SP remains unchanged. This preservation of the original composite structure is critical for maintaining the intrinsic conductivity of the carbon matrix and the pore accessibility of the Li_2S@SP host, thereby ensuring efficient charge transport and sulfur utilization.

After 500 cycles at 0.5 C, clear differences emerge. The PVP-based electrode shows pronounced structural degradation: the surface becomes densely connected by sulfur deposits, with particles bridged together through permeated sulfur. This phenomenon occurs because PVP cannot effectively lock the pores of Super P, allowing dissolved polysulfides to diffuse through the carbon matrix and redeposit on the electrode surface. Combined with the volume shrinkage of Li_2S during activation, this weak binding effect accelerates electrode deterioration, resulting in particle agglomeration and electrical disconnection despite the apparent connectivity.

In contrast, the *in-situ* crosslinked PEI-$ER_{1:1}$-based electrode retains a more compact and integrated morphology after 500 cycles, without the severe sulfur bridging observed in the PVP-based electrode. This relatively unchanged morphology can be attributed to the *in-situ* crosslinking process: branched PEI is first applied, where its abundant amine groups block the pores of the Li_2S@SP nanocomposite and prevent sulfur outflow. Subsequent addition of ER further strengthens the binding effect by forming a robust crosslinked network that enhances adhesion among Li_2S particles and the conductive carbon matrix. In addition, the polar functional groups within the *in-situ* crosslinked PEI-$ER_{1:1}$ binder can effectively anchor soluble polysulfides, suppressing their migration. As a result, the electrode architecture remains well preserved during long-term cycling, which underpins the superior cycling stability and Coulombic efficiency of the *in-situ* crosslinked PEI-$ER_{1:1}$-based binder compared with its PVP-based counterpart.

The SEM observations correlate well with the electrochemical results obtained at 0.5 C for 1000 cycles. After 500 cycles, the PVP-based Li_2S@SP electrode exhibits severe sulfur permeation and particle bridging, which compromises electrical connectivity and accelerates performance decay. This structural deterioration explains the faster capacity decline observed for the PVP-based electrode in the latter half of the cycling test. In contrast, the *in-situ* crosslinked PEI-$ER_{1:1}$-based electrode maintains a compact and integrated morphology after 500 cycles, consistent with its more gradual capacity fading and higher Coulombic efficiency throughout 1000 cycles. These findings highlight that the *in-situ* crosslinked PEI-$ER_{1:1}$ binder not only preserves electrode architecture but also directly contributes to the long-term electrochemical stability of Li_2S@SP cathodes.

7.4 Conclusions

In summary, polyethylenimine-epoxy resin (PEI-ER) binders were developed and systematically evaluated for Li_2S@SP nanocomposite cathodes. The abundant nitrogen functional groups in branched PEI provide strong chemical affinity to anchor soluble lithium polysulfides and catalyze their redox conversion, thereby enhancing kinetics and mitigating shuttle effects. Crosslinking with epoxy resin produces a robust polymeric network that reinforces particle adhesion and preserves electrode integrity during cycling. Importantly, the in-situ crosslinking method enables uniform network formation without altering the intrinsic Li_2S@SP morphology, while also avoiding the narrow time window and poor reproducibility associated with pre-crosslinking.

Electrochemical results confirm that all PEI-ER systems outperform conventional PVP binders, delivering higher capacities and improved stability. The optimized *in-situ* crosslinked PEI-$ER_{1:1}$ binder exhibited the best overall performance, achieving an initial capacity of 928 mA h g^{-1} at 0.05 C, 688 mA h g^{-1} at 0.5 C, and maintaining 325 mA h g^{-1} after 1000 cycles with stable Coulombic efficiency. Morphological analyses further revealed that the PEI-ER binder maintained a compact and integrated electrode structure, in contrast to the severe degradation observed with PVP.

This study highlights the synergistic advantages of combining catalytically active, polysulfide-affinitive PEI with mechanically robust ER, and underscores the unique merits of *in-situ* crosslinking for stabilizing high-loading Li_2S electrodes. Looking ahead, further optimization of the PEI/ER ratio, scale-up of electrode fabrication, and integration with lithium-free anodes will be critical steps toward the practical realization of Li_2S-based rechargeable batteries.

7.5 Supporting Information

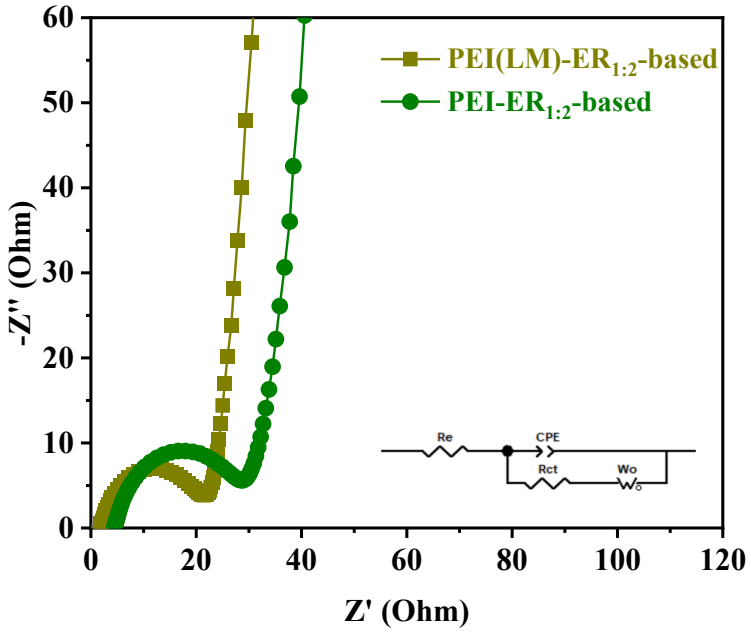


Figure S 7.1 EIS of fresh pre-mixed PEI(LM)-$ER_{1:2}$- and PEI-$ER_{1:2}$-based Li_2S@SP electrodes. Inserted is the equivalent Randles circuit used for the fitting, where R_e is the resistance of the electrolyte solution, R_{ct} is the charge transfer resistance, *CPE* is the capacitance, and W_o is the Warburg impedance.

Table S 7.1 Resistances of cathodes calculated from the EIS data in **Figure S 7.1**.

Cathode	Resistance (Ω)	
	R_e	R_{ct}
PEI(LM)-$ER_{1:2}$-based	2.1	24.5
PEI-$ER_{1:2}$-based	4.5	33.1

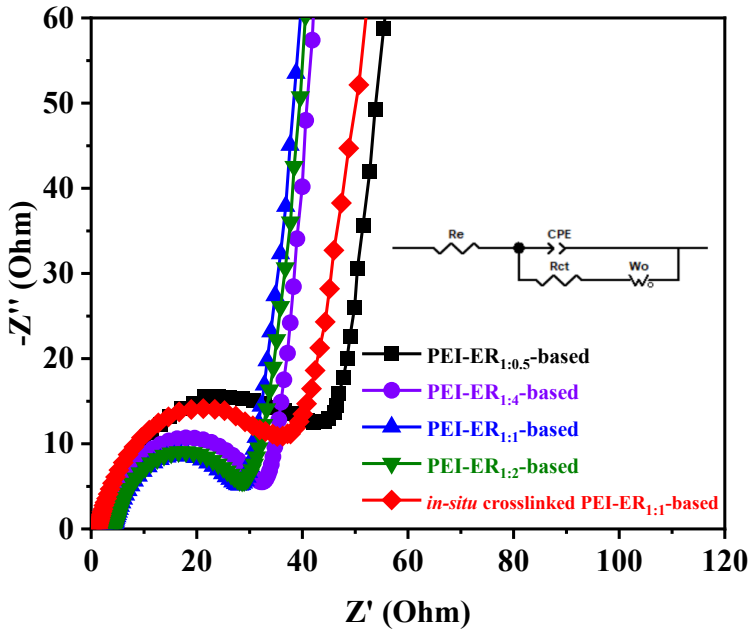


Figure S 7.2 EIS of fresh pre-mixed PEI-ER$_{1:0.5}$-, PEI-ER$_{1:1}$-, PEI-ER$_{1:2}$-, PEI-ER$_{1:4}$- and *in-situ* crosslinked PEI-ER$_{1:1}$-based Li_2S@SP electrodes. Inserted is the equivalent Randles circuit used for the fitting, where R_e is the resistance of the electrolyte solution, R_{ct} is the charge transfer resistance, *CPE* is the capacitance, and W_o is the Warburg impedance.

Table S 7.2 Resistances of cathodes calculated from the EIS data in **Figure S 7.2**.

Cathode	Resistance (Ω)	
	R_e	R_{ct}
PEI-ER$_{1:0.5}$-based	2.9	48.3
PEI-ER$_{1:1}$-based	4.2	34.2
PEI-ER$_{1:2}$-based	4.5	33.1
PEI-ER$_{1:4}$-based	2.6	35.8
***In-situ* crosslinked PEI-ER$_{1:1}$-based**	1.3	42.2

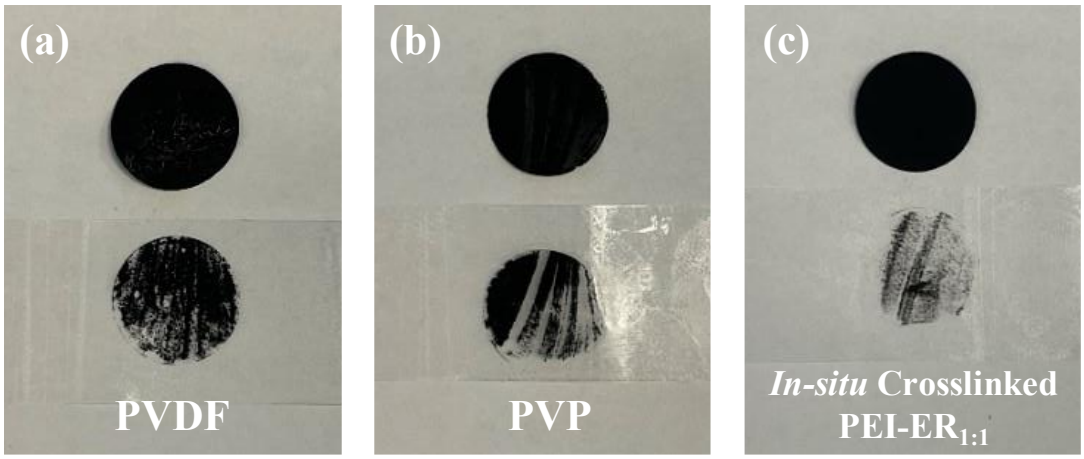


Figure S 7.3 Tape peeling test comparison of Li_2S@SP electrodes using different binders: (a) PVDF, (b) PVP, and (c) In-situ crosslinked PEI-$ER_{1:1}$.

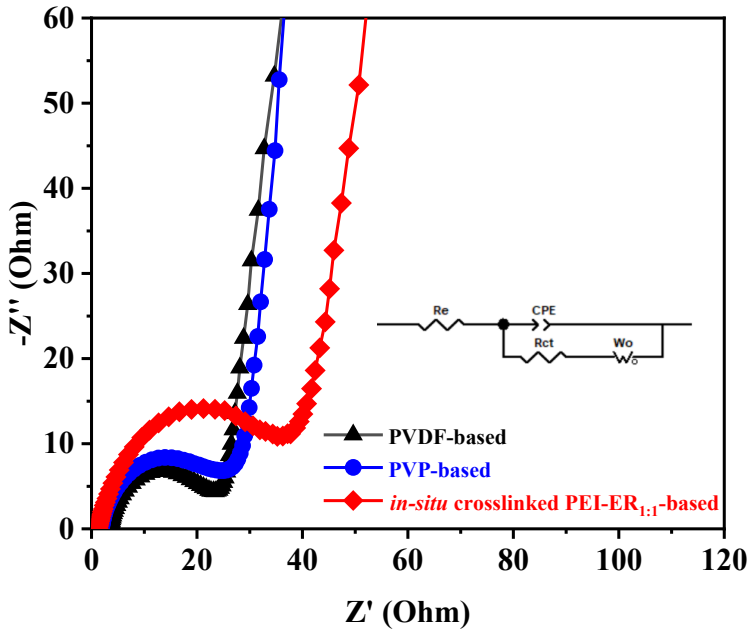


Figure S 7.4 EIS of fresh PVDF-, PVP- and *in-situ* crosslinked PEI-$ER_{1:1}$-based Li_2S@SP electrodes. Inserted is the equivalent Randles circuit used for the fitting, where R_e is the resistance of the electrolyte solution, R_{ct} is the charge transfer resistance, *CPE* is the capacitance, and W_o is the Warburg impedance.

Table S 7.3 Resistances of cathodes calculated from the EIS data in **Figure S 7.4**.

Cathode	Resistance (Ω)	
	R_e	R_{ct}
PVDF-based	3.5	26.7
PVP-based	1.9	27.9
***In-situ* crosslinked PEI-$ER_{1:1}$-based**	1.3	42.2

Chapter 8 Integration of High In-Pore Li_2S Loading Li_2S@Carbon Cathode with Si/C Anode for Lithium-Metal-Free Full Cells

This chapter is partially based on the following submitted manuscripts:

Z. Huang, Y. Wang, Y. Zhao, Y. Li, *ACS Applied Materials & Interfaces.*

8.1 Introduction

As previously discussed, lithium sulfide (Li_2S) cathodes prepared from Li_2S@SP nanocomposites with high in-pore Li_2S loading exhibit excellent electrochemical performance in half-cell configurations. However, the ultimate goal of developing Li_2S-based electrodes is to pair this lithium-rich cathode with a high-capacity, non-lithium-metal anode to assemble safe and practical full batteries, thereby eliminating the safety hazards associated with metallic lithium anodes. To further assess the practical applicability of Li_2S cathodes, it is therefore essential to move beyond half-cell testing and evaluate their electrochemical performance in full-cell systems. Full cells provide a more realistic evaluation platform by coupling Li_2S cathodes with commercially relevant anodes, thereby addressing both the energy density and stability requirements for practical applications.

Li_2S possesses a high theoretical capacity of 1166 mA h g^{-1}, making it one of the most promising cathode candidates for next-generation high-energy batteries. To fully exploit this advantage, the anode must also deliver a comparably high capacity so that the overall energy density of the full cell is not limited by the anode side. Pure silicon, despite its ultrahigh theoretical capacity (3579 mA h g^{-1}), suffers from extreme volume expansion (> 300%) upon cycling, leading to severe mechanical degradation and poor cycle life. Pure carbon, in contrast, offers excellent stability but has a much lower capacity (~372 mA h g^{-1} for graphite), which cannot effectively balance the high capacity of Li_2S. Silicon/carbon (Si/C) composites combine the merits of both: they buffer the large volume changes of Si with the structural stability and conductivity of C, while still providing a practical reversible capacity of ~600–800 mA h g^{-1}. This makes Si/C particularly well matched to the 1166 mA h g^{-1} capacity of Li_2S, enabling balanced full cells with high energy density, good stability, and strong commercial potential.

In this chapter, full-cell batteries were therefore assembled using commercial Si/C anodes and high in-pore Li_2S loading Li_2S@SP cathodes developed in **Chapter 6**. The *in-situ* crosslinked PEI-$ER_{1:1}$ binder, demonstrated in **Chapter 7** to be the most effective among the studied systems, was employed as the ultimate optimized binder. For reference, a second set of cells employing polyvinylpyrrolidone (PVP) was also assembled to provide a baseline comparison. This chapter thus represents the culmination of the research presented in this thesis: integrating advanced Li_2S@SP nanocomposites with an optimized functional binder into a realistic lithium-metal-free full-cell system. The primary objective is to validate the feasibility and performance of Li_2S@SP||Si/C full cells, with the comparison against PVP highlighting the improvements achieved by the optimized binder design. Through this study, the cycling stability, Coulombic efficiency, rate capability, and capacity retention of the full cells are systematically evaluated, underscoring the importance of full-cell demonstration as the critical step toward translating material-level innovations into practical and commercially relevant lithium-sulfide batteries.

8.2 Experimental Section

8.2.1 Materials

All chemicals were used as received unless otherwise specified. Lithium sulfide (Li_2S, 99.98%), anhydrous ethanol (≤ 0.003% water), carbon disulfide (CS_2, ≥ 99.9%), anhydrous *N*-methyl-2-pyrrolidone (NMP, 99.5%), polyvinylpyrrolidone (PVP, M_w ~1,300,000) and polyethyleneimine (PEI) aqueous solution (~50% in H_2O, M_w 600,000–1,000,000) were purchased from Sigma-Aldrich. Polyvinylidene fluoride (PVDF, M_w ~1,000,000) was from Kynar. Ethanol and NMP were further dried using molecular sieves prior to use. Super P conductive carbon (SP) was obtained from IMERYS. The epoxy resin (ER) used was Araldite® 506. Si/C powders (GS60, ⩾ 600 mA h g^{-1}) were purchased from Shanshan Technology, which were used to prepare anodes.

To obtain anhydrous PEI, the aqueous PEI solution was first dissolved in anhydrous ethanol, then treated with anhydrous sodium sulfate (Na_2SO_4) for water absorption. The resulting mixture was subjected to rotary evaporation, followed by vacuum drying at 100 °C.

8.2.2 Preparation of Li_2S@SP Nanocomposite

The synthesis of Li_2S@SP nanocomposites followed a previously reported multiple infiltration-decomposition steps in **Chapter 6**. Briefly, Li_2S (280 mg, 6.1 mmol) and carbon disulfide (CS_2, 386.5 μL, 487 mg, 6.4 mmol; 5% excess) were mixed in 3 mL of anhydrous ethanol (EtOH) inside an Ar-filled glovebox (O_2 and H_2O < 0.5 ppm). The mixture was stirred at room temperature for 30 minutes to form a clear orange solution of Li_2CS_3. Additional anhydrous EtOH was added to adjust the total volume to 5 mL.

The resulting Li_2CS_3 solution was divided into five portions: 40% (2.0 mL), 25% (1.25 mL), 15% (0.75 mL), 10% (0.5 mL), and 10% (0.5 mL). In each infiltration cycle, a designated portion of the precursor solution was thoroughly mixed with Super P (120 mg) at a Li_2S:SP mass ratio of 70:30 under continuous stirring for 6 hours at room temperature in the glovebox. The mixture was then vacuum-dried at room temperature, followed by further drying at 100 °C to remove residual solvent. The dried Li_2CS_3@SP composite was subsequently thermally treated under vacuum at 200 °C for 2 hours to decompose Li_2CS_3 into Li_2S.

This infiltration-decomposition process was repeated in total of five times using the sequential portions of the Li_2CS_3 solution. After the final cycle, the composite was annealed at 400 °C for 1 hour under vacuum to yield the final nanocomposite, denoted as Li_2S@SP.

8.2.3 Preparation of PEI solutions and an ER solution in NMP

Polyethyleneimine (PEI) and epoxy resin (ER) binder solutions were prepared separately using anhydrous NMP as the solvent. To ensure uniform dispersion and facilitate subsequent mixing, each component was dissolved in NMP to achieve a concentration of 200 mg mL^{-1}.

8.2.4 Preparation of *In-situ* crosslinked PEI-ER binder-based Li_2S electrode

The electrode slurry was prepared by thoroughly grinding Li_2S@SP (80 wt.%), Super P (10 wt.%), and PEI (5 wt.%) in NMP for 15 minutes as discussed in **Chapter 7**. Subsequently, ER (5 wt.%) was added to the mixture, followed by an additional 15 minutes of grinding. The resulting slurry was then blade-coated onto a carbon-coated aluminum foil, followed by drying at 50 °C overnight. To ensure complete removal of residual NMP, the coated electrodes were further vacuum dried at 100 °C.

8.2.5 Preparation of PVP-based Li_2S electrodes

For comparison, PVP-based Li_2S electrodes were prepared following the same procedure, except that PVP was used as the binder material in place of PEI-ER. All the dried films were then punched into 12 mm discs. The active material loading (Li_2S) was ~1.0–1.2 mg cm^{-2}.

8.2.6 Preparation of Si/C Anode

Si/C, Super P and PVDF were ground for 30 min at a mass ratio of 80:5:15 in NMP. The resulting slurry was coated onto copper current collectors and vacuum dried at 120 °C overnight. The dried films were then punched into 16 mm discs. The Si/C loading was ~5.5–6.0 mg cm^{-2}.

8.2.7 Electrochemical Measurements

For anode preparation, CR2032 coin cells were assembled using Si/C anodes and lithium metal counter electrodes, with Celgard 2400 separators and 1 M LiTFSI in 1:1 (*v*/*v*) DOL/DME electrolyte with 2 wt.% $LiNO_3$. The Si/C anodes were electrochemically activated cycling between 0.01 and 2.0 V (discharge-charge-discharge). The cells were then disassembled to retrieve the activated anodes. Full cells were assembled using Li_2S@SP-5 cathodes and the pre-activated Si/C anodes,

with the same 1 M LiTFSI in 1:1 DOL/DME electrolyte with 2 wt.% $LiNO_3$. Galvanostatic charge-discharge measurements were conducted using a Land 2001A battery tester. The voltage range was set between 1.5–3.0 V after the initial activation to 4.0 V.

8.3 Results and Discussion

To evaluate the practical applicability of the Li_2S@SP nanocomposite cathode, full cells were assembled using commercial Si/C composite as anodes. Capacity matching between the two electrodes is indispensable to achieve balanced utilization and maintain a high operating voltage. The Si/C anode was aimed to be optimized to deliver an areal capacity of ~1166 mA h cm^{-2} within the narrow 0–0.1 V (*vs.* Li^+/Li) window, closely matching the theoretical specific capacity of the Li_2S cathode (1166 mA h g^{-1}). Considering that the anode disk was slightly larger than the cathode disk, this balance ensured efficient utilization of the Li_2S@SP cathode with an active material loading of ~1.0–1.2 mg cm^{-2}.

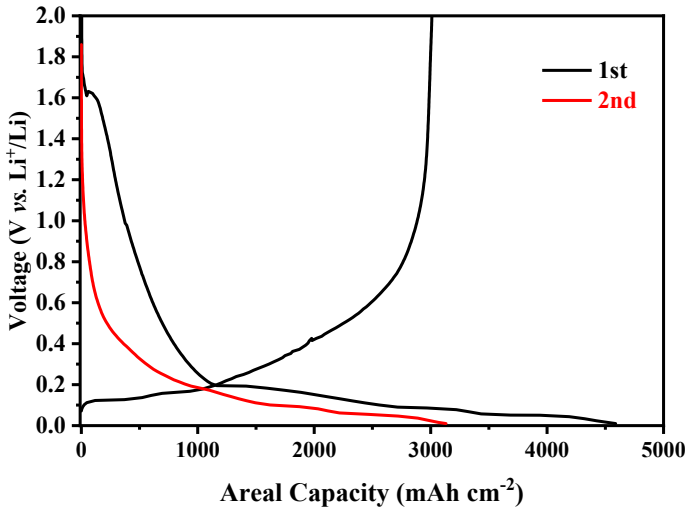


Figure 8.1 Activation of Si/C anode via discharge-charge-discharge processes at 0.25 mA between 0.01–2.0 V.

Equally critical was the pre-lithiation of the Si/C anode. Before full-cell assembly, the Si/C electrodes underwent a controlled discharge–charge–discharge process in half-cells against lithium metal (**Figure 8.1**). In the first discharge, the Si/C electrode delivered an areal capacity of 4588 mA h cm^{-2}, followed by a charge capacity of 3010 mA h cm^{-2}. The difference between these two values reflects the irreversible lithium consumption associated with SEI formation and electrolyte decomposition during the initial lithiation process. On the subsequent discharge, the capacity stabilized at 3130 mA h cm^{-2}, nearly matching the preceding charge capacity, which indicates that the SEI was largely established after the first cycle. Importantly, in the second discharge, the areal

capacity within the practical potential window of 0–0.1 V was ~1500 mA h cm^{-2}, providing an excellent match with the Li_2S cathode.

The electrolyte used during this activation process contained $LiNO_3$, and its decomposition products further reinforced SEI formation on the Si/C surface. While $LiNO_3$ is conventionally applied in Li-S batteries to passivate lithium metal and suppress polysulfide shuttle, in this work it also played a crucial role in stabilizing the Si/C interface. The pre-lithiation process therefore not only established a robust SEI but also preserved the lithium source from the Li_2S cathode. Overall, the close match between the stabilized Si/C anode capacity (~1500 mA h cm^{-2} within 0–0.1 V) and the theoretical capacity of the Li_2S cathode (~1166 mA h g^{-1} at ~1.0–1.2 mg cm^{-2} loading) highlights the careful electrode design and underpins the practical feasibility of the full-cell system.

After completing the discharge–charge–discharge activation process, the half-cells were carefully disassembled in an argon-filled glovebox, and the pre-lithiated Si/C anodes were retrieved. These activated anodes, equipped with a stable SEI and balanced lithium inventory, were then paired with Li_2S@SP cathodes to assemble full cells. To demonstrate the practical applicability of the Li_2S@SP cathodes, electrodes prepared with two representative binders—conventional PVP and the *in-situ* crosslinked PEI-$ER_{1:1}$ binder—were employed. The initial charge/discharge profiles of these full cells (**Figure 8.2**) provide critical insights into the electrochemical activation of Li_2S in a lithium-metal-free configuration, highlighting the feasibility of pairing Li_2S cathodes with Si/C anodes for practical next-generation battery systems.

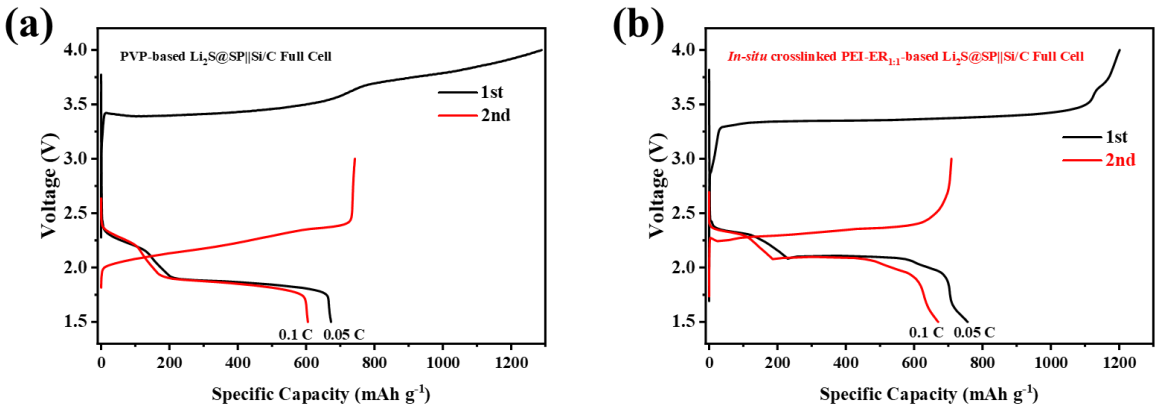


Figure 8.2 Initial charge/discharge curves of Li_2S@SP||Si/C full cells using (a) PVP and (b) *in-situ* crosslinked PEI-$ER_{1:1}$ binders in the cathodes.

For the PVP-based full cell as shown in **Figure 8.2** (a), the first charging process exhibits a small overpotential spike at ~3.42 V, followed by a slight drop to 3.39 V before steadily increasing to the cutoff at 4.0 V. This feature is commonly associated with the sluggish activation of Li_2S, where significant polarization is required to initiate the oxidation of Li_2S into soluble polysulfides and eventually elemental sulfur. The cell delivered a total charging capacity of ~1290 mA h g^{-1}, which is somewhat higher than the theoretical capacity of Li_2S (1166 mA h g^{-1}), likely due to side reactions during the initial activation. The subsequent discharge reached 673 mA h g^{-1}, reflecting incomplete utilization of active material and highlighting the limitations of PVP as a binder in facilitating efficient Li_2S conversion.

In contrast, the *in-situ* crosslinked PEI-$ER_{1:1}$-based full cell displayed distinctly different behavior as shown in **Figure 8.2** (b). No sharp overpotential spike was observed during the initial charging, and the charging plateau remained stable around 3.35 V over an extended capacity range, indicative of improved reaction kinetics. This catalytic effect can be attributed to the abundant nitrogen functional groups in PEI, which provide strong chemical affinity toward polysulfides and promote their redox conversion. The charge plateau extended until ~1000 mA h g^{-1} before rising to the 4.0 V cutoff, resulting in a total charging capacity of ~1200 mA h g^{-1}, much closer to the theoretical value of 1166 mA h g^{-1}. On discharge, the *in-situ* crosslinked PEI-$ER_{1:1}$-based cell delivered a higher capacity of 757 mA h g^{-1} compared to the PVP-based cell, along with a higher discharge voltage profile, further confirming the enhanced kinetics imparted by the functional binder.

Notably, a small tail feature was observed in the discharge curve of the *in-situ* crosslinked PEI-$ER_{1:1}$-based cell, which can be ascribed to the pore-locking effect of the crosslinked binder network. The tight interfacial binding and physical confinement provided by the *in-situ* crosslinked PEI-$ER_{1:1}$ structure facilitate deeper reduction of sulfur species, thereby contributing to additional capacity at lower voltages. This dual role—catalyzing redox reactions through nitrogen sites and stabilizing the electrode structure through crosslinking—not only reduces polarization but also enables more complete Li_2S utilization. Importantly, these improvements in the full cell are consistent with the half-cell results presented earlier in **Chapter 7**, where PEI-ER-based electrodes also exhibited lower activation barriers, higher discharge voltages, and superior utilization compared with PVP.

This coherence across both systems underscores the robustness of the binder design and highlights its practical potential for advancing Li_2S-based full cells.

Furthermore, when the current density was increased to 0.1 C in the second cycle, the PVP-based full cell delivered 605 mA h g^{-1}, while the *in-situ* crosslinked PEI-$ER_{1:1}$-based full cell achieved a higher capacity of 670 mA h g^{-1}. The latter also maintained a higher discharge voltage profile, demonstrating that the kinetic and structural advantages of the *in-situ* crosslinked PEI-$ER_{1:1}$ binder persist beyond the activation stage and continue to benefit the cell under practical cycling conditions.

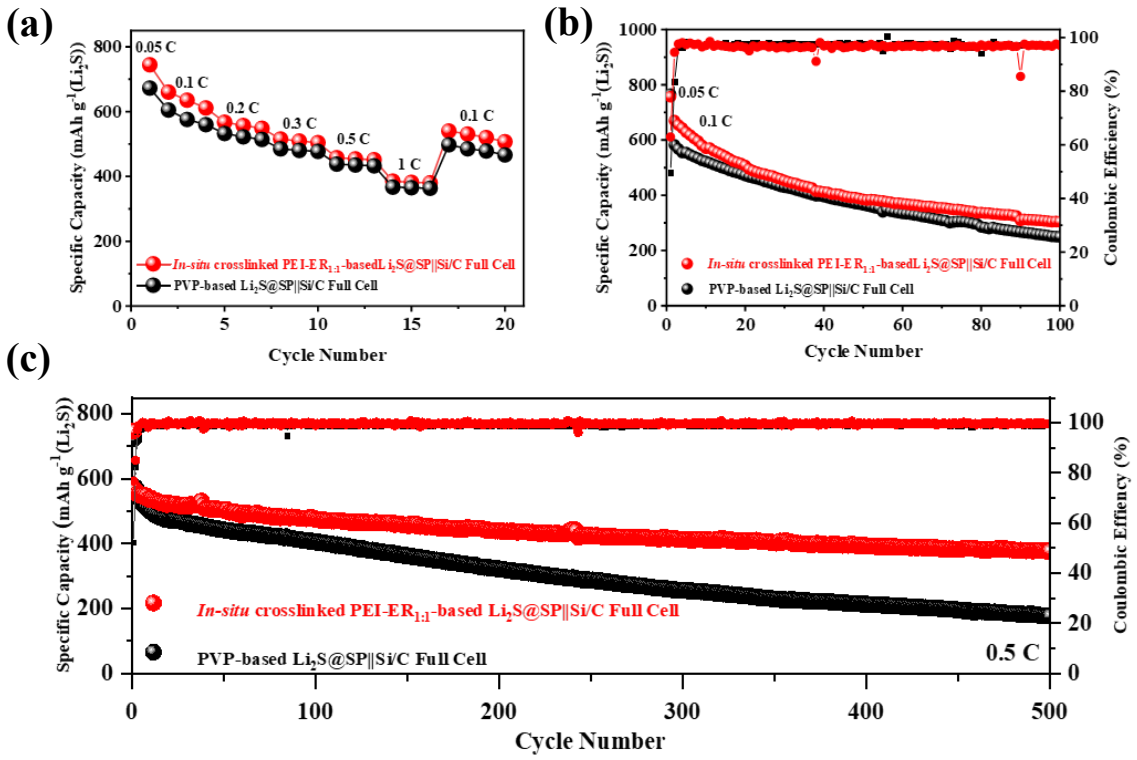


Figure 8.3 Electrochemical performance of Li_2S@SP||Si/C full cell: (a) Rate performance. (b) Cycling performance at 0.1 C. (c) Long-term cycling performance at 0.5 C. The voltage range was set to 1.5–3.0 V after the initial activation to 4.0 V.

The rate performance of the full cells is presented in **Figure 8.3** (a). For the PVP-based full cell, the discharge capacity reached 605 mA h g^{-1} at 0.1 C and remained at 367 mA h g^{-1} when the rate increased to 1 C. Upon returning to 0.1 C, the capacity recovered to 497 mA h g^{-1}, demonstrating that the Li_2S@SP nanocomposite possesses inherent structural stability and electrochemical reversibility, even when combined with a conventional, inert binder such as PVP.

In contrast, the *in-situ* crosslinked PEI-$ER_{1:1}$-based full cell delivered 660 mA h g^{-1} at 0.1 C and maintained 385 mA h g^{-1} at 1 C. When the current density was reduced back to 0.1 C, the capacity recovered to 540 mA h g^{-1}. This superior reversibility highlights not only the stability of the Li_2S@SP framework but also the additional benefits imparted by the functional binder. The abundant nitrogen groups in PEI and the crosslinked PEI-ER network provide strong polysulfide affinity, catalytic activity, and robust mechanical adhesion, enabling improved electrochemical kinetics and more efficient utilization of active material compared with the PVP-based system.

The long-term cycling performance at 0.1 C is presented in **Figure 8.3** (b). The PVP-based full cell delivered an initial discharge capacity of 582 mA h g^{-1} and retained 250 mA h g^{-1} after 100 cycles, corresponding to a capacity retention of ~43%. This result suggests that even when combined with a conventional, inert binder, the Li_2S@SP nanocomposite framework can provide a degree of structural stability during extended cycling. By contrast, the *in-situ* crosslinked PEI-$ER_{1:1}$-based full cell exhibited a higher initial capacity of 670 mA h g^{-1} and maintained 304 mA h g^{-1} after 100 cycles, corresponding to ~45% retention. Although the percentage retention values are comparable, the *in-situ* crosslinked PEI-$ER_{1:1}$-based system consistently delivered higher absolute capacities and exhibited more stable Coulombic efficiency throughout the test. These improvements can be attributed to the functional binder, whose nitrogen-rich sites and crosslinked network effectively suppress polysulfide migration and reinforce electrode integrity. Overall, these results demonstrate that while the Li_2S@SP nanocomposite itself ensures basic structural stability, the incorporation of the *in-situ* crosslinked PEI-$ER_{1:1}$ binder provides additional electrochemical durability, underscoring its practical value for Li_2S full-cell applications.

The long-term cycling performance of the Li_2S@SP||Si/C full cells at 0.5 C is presented in **Figure 8.3** (c). The results clearly highlight the advantages of the *in-situ* crosslinked PEI-$ER_{1:1}$ binder in sustaining stable operation over extended cycles. After the activation process, the *in-situ* crosslinked PEI-$ER_{1:1}$-based full cell delivered an initial discharge capacity of 564 mA h g^{-1}. Remarkably, after 500 cycles, it still retained 377 mA h g^{-1}, corresponding to a capacity retention of 66.8%. In contrast, the PVP-based full cell, although starting with a slightly higher initial discharge capacity of 573 mA h g^{-1}, suffered from severe capacity fading, retaining only 176 mA h g^{-1} after 500 cycles, which corresponds to a retention of just 30.7%. This sharp divergence in cycling

stability demonstrates the critical role of the binder in maintaining electrode integrity under realistic full-cell conditions. The weak interaction of PVP with Li_2S and polysulfides leads to poor structural stabilization, continuous loss of active material, and accelerated side reactions, all of which contribute to rapid capacity fading. By comparison, the *in-situ* crosslinked PEI-$ER_{1:1}$ binder forms a robust crosslinked network with abundant polar groups that can chemically anchor soluble polysulfides and catalyze their redox conversion, thereby suppressing the shuttle effect and improving reaction kinetics.

The Coulombic efficiency (CE) results further reinforce this conclusion. Both full cells maintained relatively stable CE during long-term cycling, which can be attributed to the robust structural design of the Li_2S@SP cathode framework that helps suppress severe LPS shuttle effect even in the PVP-based system. However, the *in-situ* crosslinked PEI-$ER_{1:1}$-based full cell consistently exhibited slightly higher CE values than the PVP-based one. This difference suggests that the optimized binder not only preserves electrode integrity but also more effectively suppresses side reactions, thereby improving the reversibility of polysulfide conversion.

These electrochemical findings are consistent with the SEM observations of cycled electrodes, where the *in-situ* crosslinked PEI-$ER_{1:1}$-based cathodes maintained a more compact and integrated morphology, while the PVP-based electrodes exhibited severe cracking and particle detachment after prolonged cycling.

8.4 Conclusions

In this chapter, the practical applicability of Li_2S cathodes was demonstrated by assembling lithium-metal-free full cells using the Li_2S@SP cathodes with high in-pore Li_2S loading developed in **Chapter 6**, paired with commercial Si/C anodes. This configuration eliminates the safety risks associated with lithium metal.

Two types of binders were employed in the cathodes for comparison. The in-situ crosslinked PEI-$ER_{1:1}$ binder, previously optimized in **Chapter 7**, was selected as the ultimate binder, while polyvinylpyrrolidone (PVP) served as a reference. The results clearly demonstrate the superior long-term cycling stability of the *in-situ* crosslinked PEI-$ER_{1:1}$-based full cells, which retained 377 mA h g^{-1} after 500 cycles at 0.5 C (66.8% retention), compared with only 176 mA h g^{-1} (30.7% retention) for the PVP-based system. Both systems exhibited stable Coulombic efficiencies throughout cycling, but the *in-situ* crosslinked PEI-$ER_{1:1}$-based full cell consistently achieved slightly higher values, highlighting its effectiveness in suppressing side reactions and improving reversibility.

The enhanced performance of the *in-situ* crosslinked PEI-$ER_{1:1}$-based full cell is attributed to the multifunctional nature of the binder, which combines chemical polysulfide anchoring, catalytic activity, and a mechanically robust crosslinked network. These advantages were supported by morphological analyses, which showed that the *in-situ* crosslinked PEI-$ER_{1:1}$ binder preserved electrode integrity and maintained lower charge-transfer resistance during cycling, in stark contrast to the structural degradation observed in PVP-based electrodes in **Chapter 7**.

Overall, this chapter represents the culmination of the work presented in this thesis by integrating the high in-pore loading Li_2S@SP cathodes developed in **Chapter 6** with the optimized functional binder from **Chapter 7** into a realistic full-cell system. The results confirm that Li_2S@SP||Si/C full cells can achieve high capacity, stable cycling, and good reversibility, paving the way toward the development of safe, high-energy, lithium-metal-free Li_2S batteries suitable for practical applications.

Chapter 9 Conclusions and Outlook

9.1 Conclusions

This thesis investigates the design and optimization of functional binders and Li_2S@Carbon nanocomposite engineering strategies to address critical challenges in Li_2S batteries. At the outset, the background of lithium-sulfur batteries was comprehensively reviewed, highlighting the unique advantages of Li_2S cathodes and the fundamental challenges associated with their development. State-of-the-art strategies were also summarized, with emphasis on binder materials, nanostructured Li_2S composites, and examples of different anode materials to illustrate the feasibility of full-cell configurations. Building on this foundation, the research systematically tackled the obstacles: the large particle size of commercial Li_2S, the high melting point and poor solubility hinder conventional Li_2S@Carbon composite fabrication, while the limitations of binders also appear when applied to nanoscale Li_2S. Each of these issues is identified and addressed sequentially in the course of this research, ultimately paving the way toward the realization of practical lithium-anode-free full cell batteries.

The large first-charge overpotential due to the insulating LiOH/Li_2O surface layer in Li_2S-LSBs hinders activation and induces irreversible side reactions. **Chapter 3** proposes mitigating the activation barrier by exploiting the reaction between polyvinylidene fluoride (PVDF) binder and LiOH/Li_2O through dehydrofluorination. Model reactions confirmed that both LiOH and Li_2O readily react with PVDF at room temperature. Electrochemical testing showed that electrodes prepared with commercial Li_2S via conventional 30 min slurry grinding exhibited a high first-charge overpotential of 3.74 V. In contrast, extending slurry stirring to 48 h reduced the overpotential spike to 2.75 V, demonstrating that prolonged mixing facilitates the interfacial reaction and lowers activation barriers. However, PVDF was also found to react with Li_2S itself, partially consuming active material and lowering discharge capacity. Overall, this study provides mechanistic insights into the origin of Li_2S activation overpotential and demonstrates the dual role of conventional PVDF binders, where slurry processing with PVDF can effectively reduce the first-charge barrier, while also highlighting the limitations of PVDF as a binder for Li_2S electrodes.

Based on the discovery from **Chapter 3** that PVDF might be unsuitable for Li_2S electrodes, **Chapter 4** investigates alternative binders capable of enhancing the electrochemical performance of Li_2S-LSBs. A binder based on a zinc acetate triethanolamine ($Zn(OAc)_2$·TEA) complex was developed. This complex not only provides strong polysulfide-trapping ability but also exhibits redox catalytic activity, leading to markedly improved capacity, rate capability, and cycling stability compared with PVDF. To further reinforce electrode integrity and improve dispersion stability, polyethylenimine (PEI) was incorporated to form a $Zn(OAc)_2$·TEA/PEI hybrid binder. Electrochemical testing showed that Li_2S cathodes employing $Zn(OAc)_2$·TEA/PEI with 10 wt.% PEI achieved superior rate performance, high discharge capacity, and excellent long-term cycling stability. An additional advantage of $Zn(OAc)_2$·TEA-based series of binders is their fluorine-free composition, which aligns with environmental sustainability requirements and complies with emerging regulatory frameworks, including the European Union's restrictions on per- and polyfluoroalkyl substances (PFAS).

In **Chapter 5**, an efficient precursor solution infiltration-decomposition strategy was invented to synthesize Li_2S@Carbon nanocomposites under mild conditions, overcoming the challenges posed by the high melting point and poor solubility of Li_2S. In this approach, Li_2S was first reacted with carbon disulfide (CS_2) in anhydrous ethanol at ambient temperature to form a highly soluble lithium trithiocarbonate (Li_2CS_3) precursor, which was readily infiltrated into mesoporous Super P carbon (SP). Subsequent thermal decomposition of Li_2CS_3@SP at 400 °C produced Li_2S@SP-400 nanocomposites with a Li_2S:SP mass ratio of 60:40, containing finely dispersed Li_2S particles (~11 nm) uniformly confined within the Super P matrix. Electrochemical testing demonstrated that these nanocomposites delivered a high discharge capacity of 821 mA h g^{-1} (Li_2S), equivalent to 1190 mA h g^{-1} (S), and exhibited superior rate capability and cycling stability compared to commercial Li_2S, non-infiltrated Li_2S nanoparticles, and melt-infiltrated sulfur composites (S@SP). This simple and scalable method provides a practical pathway for producing Li_2S@Carbon nanocomposites, thereby advancing the commercialization prospects of high-energy-density Li_2S-LSBs.

The thermal decomposition of Li_2CS_3 precursor releases a large amount of CS_2 gas (~62 wt.% of the precursor), which creates internal voids and limits the in-pore Li_2S loading. To address this, **Chapter 6** builds upon precursor infiltration-decomposition method with a multi-cycle strategy to

achieve high Li_2S content and high in-pore loading simultaneously. Using mesoporous Super P as the conductive host and Li_2CS_3 as the precursor, repeated infiltration-decomposition cycles progressively increased the pore filling factor (FF) and in-pore Li_2S loading (IPL), from FF = 38% and IPL = 30% for Li_2S@SP-1 (one cycle) to FF = 91% and IPL = 73% for Li_2S@SP-5 (five cycles), while also raising the overall Li_2S content to 70 wt.%. Direct structural evidence from XRD and SEM confirmed reduced crystallite size, suppressed external deposition, and uniform Li_2S distribution in the optimized Li_2S@SP-5. Complementary circumstantial evidence from CV profiles and charge/discharge curves further supported that increasing the number of infiltration-decomposition cycles resulted in greater in-pore Li_2S loading and more efficient electrochemical utilization. Electrochemical testing demonstrated that Li_2S@SP-5 with 70 wt.% Li_2S loading delivered an initial discharge capacity of 807 mA h g^{-1} (Li_2S) at 0.1 C, 598 mA h g^{-1} (Li_2S) in the first cycle at 1.0 C, and retained 376 mA h g^{-1} (Li_2S) after 500 cycles at 1.0 C. This work establishes multi-cycle infiltration-decomposition as a scalable and broadly applicable strategy to achieve both high in-pore loading and high overall Li_2S content, and the approach can be extended to other porous carbon hosts, thereby advancing Li_2S cathodes toward practical, high-energy-density battery systems.

After developing functional binders in **Chapter 4** and high in-pore loading Li_2S@SP nanocomposites in **Chapter 6**, these components were combined in an effort to construct high-performance cathodes. However, this attempt revealed a critical limitation: owing to the nanoscale Li_2S particles and the high reactivity of the $Zn(OAc)_2$·TEA complex, the binder rapidly lost its binding effect. This finding highlights that such binder strategies are inadequate for nanoscale, highly reactive Li_2S composites and underscores the need to design new binders tailored for nanostructured materials. To address this challenge, **Chapter 7** introduces a functional binder based on polyethylenimine-epoxy resin (PEI-ER) networks. Branched PEI provides abundant nitrogen-containing functional groups that chemically interact with soluble lithium polysulfides (LPS) to suppress shuttle effects and catalyze their redox conversion, thereby enhancing reaction kinetics. Initially, pre-mixed PEI-ER binders were tested, but their application was hindered by a short and difficult-to-control reaction window. To overcome this limitation, an *in-situ* crosslinking method was developed, which enabled uniform network formation during electrode fabrication without

disturbing the original Li_2S@SP morphology. Electrochemical evaluations demonstrated that all PEI-ER binders, whether pre-mixed or *in-situ* crosslinked, outperformed the conventional PVP binder. Among them, the optimized *in-situ* crosslinked PEI-$ER_{1:1}$ binder delivered an initial capacity of 928 mA h g^{-1} at 0.05 C, 688 mA h g^{-1} at 0.5 C, and retained 325 mA h g^{-1} after 1000 cycles with stable Coulombic efficiency, surpassing both PVP- and PVDF-based electrodes. SEM analyses further confirmed that the *in-situ* crosslinked PEI-$ER_{1:1}$-based electrode maintained a compact, integrated structure, whereas PVP-based electrodes exhibited severe sulfur migration and particle detachment. Together, these results demonstrate the unique advantages of *in-situ* PEI-ER crosslinking and establish it as a versatile binder strategy for stabilizing nanoscale, high-loading Li_2S cathodes, thereby advancing lithium-metal-free LSBs toward practical applications.

To construct high-performance cathodes, the functional binder from **Chapter 4** was combined with the high in-pore loading Li_2S@SP from **Chapter 6**. This attempt failed because $Zn(OAc)_2$·TEA/PEI-based binders exhibited limitations with highly reactive nanoscale Li_2S, resulting in diminished binding effectiveness. **Chapter 7** therefore introduces a series of polyethylenimine-epoxy resin (PEI-ER) binders, where high-molecular-weight PEI anchors and catalyzes polysulfides while epoxy crosslinking reinforces mechanical stability. The *in-situ* crosslinking method further improved processing by removing the short crosslinking window and enabling uniform networks without altering Li_2S@SP morphology. Electrochemical tests showed the optimized *in-situ* crosslinked PEI-$ER_{1:1}$ binder achieved 928 mA h g^{-1} at 0.05 C, 688 mA h g^{-1} in the first cycle at 0.5 C and retained 325 mA h g^{-1} after 1000 cycles at 0.5 C with stable Coulombic efficiency. SEM confirmed its compact structure, establishing *in-situ* PEI-ER crosslinking as a robust binder strategy for nanoscale, high-loading Li_2S cathodes.

Building on the advances achieved in the preceding chapters, **Chapter 8** focuses on the assembly and evaluation of full-cell configurations to demonstrate the practical feasibility of lithium-anode-free Li_2S-based batteries. High in-pore loading Li_2S@SP nanocomposites developed in **Chapter 6** (70 wt.% Li_2S) were employed as the cathode active material, while commercial Si/C composites served as the anode. For the binders, two systems were compared: PVP as a baseline and the optimized *in-situ* crosslinked PEI-$ER_{1:1}$ developed in **Chapter 7**, which had previously shown strong polysulfide-trapping ability, catalytic activity, and superior mechanical robustness.

Electrochemical testing revealed that full cells with *in-situ* crosslinked PEI-$ER_{1:1}$-based cathodes delivered an initial discharge capacity of 670 mA h g^{-1} at 0.1 C and retained 304 mA h g^{-1} after 100 cycles (~45% retention), outperforming the PVP-based counterpart, which started at 582 mA h g^{-1} and fell to 250 mA h g^{-1} (~43% retention). More importantly, at 0.5 C, the *in-situ* crosslinked PEI-$ER_{1:1}$-based full cell delivered 564 mA h g^{-1} after activation and retained 377 mA h g^{-1} after 500 cycles, corresponding to 66.8% capacity retention. In contrast, the PVP-based full cell, although starting slightly higher at 573 mA h g^{-1}, faded rapidly to only 176 mA h g^{-1} after 500 cycles (30.7% retention). This stark divergence demonstrates the critical role of the binder in sustaining structural integrity and suppressing side reactions under realistic full-cell conditions. Overall, this chapter demonstrates the successful integration of nanostructured Li_2S cathodes and functional binder design with commercial Si/C anodes, marking a significant step toward the realization of practical, high-energy-density lithium-metal-free LSBs.

In summary, this thesis addresses the critical challenges of Li_2S cathodes, including the large first-charge overpotential, the drawback of PVDF consuming Li_2S, the large particle size of commercial Li_2S, the high melting point and poor solubility that hinder conventional Li_2S@Carbon composite fabrication, and the limitations of binders when applied to nanoscale Li_2S, each identified in the process of resolving the preceding issue. By systematically investigating these problems, this thesis advances functional binder design, exploits precursor chemistry, and engineers nanostructured composites, concluding with the successful demonstration of lithium-anode-free full cell batteries.

9.2 Outlook

The research presented in this thesis establishes foundational strategies for advancing Li_2S-LSBs, particularly through the scalable fabrication of Li_2S@Carbon nanocomposites and the development of functional binders tailored for practical electrode processing. These contributions provide a platform for moving beyond laboratory-scale demonstrations toward device-relevant configurations. To translate these advances into commercially viable systems, future studies must bridge materials innovation with cell-level engineering, including integration with lithium-free anodes and adaptation to industrial fabrication protocols. Building upon these findings, several promising directions emerge for future research:

Exploration of advanced Li_2S@Carbon nanocomposites. Super P remains the most widely used carbon material in Li_2S cathodes because of its availability, conductivity, and reliable performance, yet it represents only a baseline. The real potential lies in engineering functional carbon hosts that can form optimized Li_2S@Carbon nanocomposites. A wide range of advanced carbons—such as hollow nanospheres, carbon nanotube scaffolds, and 3D graphene architectures—offer tunable pore structures, hierarchical frameworks, and interconnected conductive networks. These features not only improve pore accessibility and electronic transport but also provide robust mechanical buffering during cycling. By carefully tailoring the structure and surface chemistry of these hosts, Li_2S can be uniformly incorporated at the nanoscale, enabling high loading, efficient utilization, and superior long-term stability. Thus, the future development of Li_2S cathodes will strongly depend on rational nanocomposite design that integrates both carbon architecture and Li_2S distribution to surpass the limitations of conventional Super P systems.

Integration of electrocatalysts. Electrocatalysts have been extensively developed in S-LSBs to accelerate polysulfide redox reactions, and given the shared reaction mechanisms, many of these strategies can be directly adapted to Li_2S-LSBs. Embedding catalytic species such as transition metal sulfides, nitrides, or even single-atom catalysts into the carbon host or binder matrix can effectively enhance the sluggish Li_2S conversion kinetics. Rational catalyst design has the potential to reduce charge-transfer resistance, lower the first-charge overpotential, and improve rate performance. Moreover, the integration of electrocatalysts with advanced carbon host materials can

couple catalytic activity with optimized pore accessibility and conductivity, offering a synergistic pathway to maximize Li_2S utilization and cycling stability.

Incorporation of solid electrolytes. Despite the progress achieved in this thesis, the lithium polysulfide (LPS) shuttle effect remains unresolved and continues to be a critical barrier to the practical deployment of both S-LSBs and Li_2S-LSBs. The dissolution and migration of LPS not only cause severe capacity fading but also lead to low Coulombic efficiency and shortened cycle life. The adoption of solid or hybrid solid-liquid electrolytes offers a promising route to mitigate these issues. In particular, sulfide- and polymer-based solid electrolytes can physically block polysulfide diffusion, suppress shuttle effects, and stabilize electrode-electrolyte interfaces. Integrating Li_2S cathodes with such electrolytes may therefore enable safer, more durable, and truly lithium-anode-free battery systems.

Advancement of binder systems. While this thesis has demonstrated the potential of functional binders to improve Li_2S cathode performance, binder design remains a relatively underexplored yet crucial aspect for Li_2S-LSBs. Future work should focus on multifunctional binders that not only provide mechanical cohesion but also contribute to ion transport, polysulfide confinement, and catalytic activity. For instance, incorporating redox-active moieties, ionic conductive segments, or dynamic covalent crosslinks may further accelerate Li_2S conversion while preserving electrode integrity. In addition, the compatibility of binders with nanoscale Li_2S, high-loading electrodes, and lean-electrolyte operation must be systematically evaluated.

Device-level optimization. To achieve energy densities comparable to state-of-the-art lithium-ion batteries, it is essential to increase the loading of active materials in Li_2S cathodes. Future research should therefore focus on scaling Li_2S electrodes to high areal capacities while operating under lean-electrolyte conditions. At the same time, attention must be paid to ensuring compatibility with practical electrode fabrication methods used in industry, such as slurry casting and roll-to-roll processing. On the anode side, integrating Li_2S cathodes with lithium-free anodes such as Si/C composites or graphite is equally critical to realizing truly lithium-anode-free systems. Ultimately, demonstrating pouch-cell prototypes that combine high-loading Li_2S cathodes with compatible anodes, long cycle life, and high energy density will be a decisive step toward the commercialization of Li_2S-based batteries for portable electronics and electric vehicles.

In summary, future progress in Li_2S-LSBs will require synergistic advances across multiple dimensions. Rational nanocomposite engineering can maximize Li_2S utilization, while solid or hybrid electrolytes are key to addressing the persistent polysulfide shuttle effect. Electrocatalyst integration offers pathways to accelerate sluggish redox kinetics, and next-generation binders can provide multifunctional roles beyond mechanical cohesion. At the device level, achieving high active-material loading under lean-electrolyte conditions and coupling Li_2S cathodes with lithium-free anodes will be indispensable for practical deployment. Collectively, these research directions highlight a roadmap by which the concepts developed in this thesis may evolve into viable, high-energy-density, and safer next-generation energy storage technologies.

References

[1] Chen, H.; Ding, Y.; Pan, X.; Wu, H.; Song, J.; Shui, S. Integrated Multi-Time Scale Sustainable Scheduling of Wind Power Incorporating Combined High Energy Demand and Energy Storage. *J. Energy Storage* **2024**, *97*, 112792. https://doi.org/10.1016/j.est.2024.112792.

[2] Overland, I.; Juraev, J.; Vakulchuk, R. Are Renewable Energy Sources More Evenly Distributed than Fossil Fuels? *Renewable Energy* **2022**, *200*, 379–386. https://doi.org/10.1016/j.renene.2022.09.046.

[3] Wang, J.; Azam, W. Natural Resource Scarcity, Fossil Fuel Energy Consumption, and Total Greenhouse Gas Emissions in Top Emitting Countries. *Geosci. Front.* **2024**, *15* (2), 101757. https://doi.org/10.1016/j.gsf.2023.101757.

[4] Yi, S.; Raza Abbasi, K.; Hussain, K.; Albaker, A.; Alvarado, R. Environmental Concerns in the United States: Can Renewable Energy, Fossil Fuel Energy, and Natural Resources Depletion Help? *Gondwana Res.* **2023**, *117*, 41–55. https://doi.org/10.1016/j.gr.2022.12.021.

[5] Li, S.; Gao, L. Greenhouse Gas Emissions from Synthetic Natural Gas Production. *Nat. Clim. Change* **2016**, *6* (3), 220–221. https://doi.org/10.1038/nclimate2887.

[6] Kittner, N.; Lill, F.; Kammen, D. M. Energy Storage Deployment and Innovation for the Clean Energy Transition. *Nat. Energy* **2017**, *2* (9), 17125. https://doi.org/10.1038/nenergy.2017.125.

[7] Chu, S.; Cui, Y.; Liu, N. The Path towards Sustainable Energy. *Nat. Mater.* **2017**, *16* (1), 16–22. https://doi.org/10.1038/nmat4834.

[8] Tavoni, M.; De Cian, E.; Luderer, G.; Steckel, J. C.; Waisman, H. The Value of Technology and of Its Evolution towards a Low Carbon Economy. *Climatic Change* **2012**, *114* (1), 39–57. https://doi.org/10.1007/s10584-011-0294-3.

[9] Wang, Q.; Pornrungroj, C.; Linley, S.; Reisner, E. Strategies to Improve Light Utilization in Solar Fuel Synthesis. *Nat. Energy* **2022**, *7* (1), 13–24. https://doi.org/10.1038/s41560-021-00919-1.

[10] Sun, X.; Jiang, S.; Huang, H.; Li, H.; Jia, B.; Ma, T. Solar Energy Catalysis. *Angew. Chem.* **2022**, *134* (29), e202204880. https://doi.org/10.1002/ange.202204880.

[11] Roga, S.; Bardhan, S.; Kumar, Y.; Dubey, S. K. Recent Technology and Challenges of Wind Energy Generation: A Review. *Sustain. Energy Technol. Assess.* **2022**, *52*, 102239. https://doi.org/10.1016/j.seta.2022.102239.

[12] Khare, V.; Bhuiyan, M. A. Tidal Energy—Path towards Sustainable Energy: A Technical Review. *Cleaner Energy Syst.* **2022**, *3*, 100041. https://doi.org/10.1016/j.cles.2022.100041.

[13] Kiss, V. M.; Hetesi, Z.; Kiss, T. The Effect of Time Resolution on Energy System Simulation in Case of Intermittent Energies. *Renew. Sustain. Energy Rev.* **2024**, *191*, 114099. https://doi.org/10.1016/j.rser.2023.114099.

[14] Mlilo, N.; Brown, J.; Ahfock, T. Impact of Intermittent Renewable Energy Generation Penetration on the Power System Networks—A Review. *Technol. Econ. Smart Grids Sustain. Energy* **2021**, *6* (1), 25. https://doi.org/10.1007/s40866-021-00123-w.

[15] Mitali, J.; Dhinakaran, S.; Mohamad, A. A. Energy Storage Systems: A Review. *Energy Storage Sav.* **2022**, *1* (3), 166–216. https://doi.org/10.1016/j.enss.2022.07.002.

[16] Hannan, M. A.; Wali, S. B.; Ker, P. J.; Rahman, M. S. A.; Mansor, M.; Ramachandaramurthy, V. K.; Muttaqi, K. M.; Mahlia, T. M. I.; Dong, Z. Y. Battery Energy-Storage System: A Review of Technologies, Optimization Objectives, Constraints, Approaches, and Outstanding Issues. *J. Energy Storage* **2021**, *42*, 103023. https://doi.org/10.1016/j.est.2021.103023.

[17] Zhang, Z.; Ding, T.; Zhou, Q.; Sun, Y.; Qu, M.; Zeng, Z.; Ju, Y.; Li, L.; Wang, K.; Chi, F. A Review of

Technologies and Applications on Versatile Energy Storage Systems. *Renew. Sustain. Energy Rev.* **2021**, *148*, 111263. https://doi.org/10.1016/j.rser.2021.111263.

[18] Dunn, B.; Kamath, H.; Tarascon, J.-M. Electrical Energy Storage for the Grid: A Battery of Choices. *Science* **2011**, *334* (6058), 928–935. https://doi.org/10.1126/science.1212741.

[19] Nasajpour-Esfahani, N.; Garmestani, H.; Bagheritabar, M.; Jasim, D. J.; Toghraie, D.; Dadkhah, S.; Firoozeh, H. Comprehensive Review of Lithium-Ion Battery Materials and Development Challenges. *Renew. Sustain. Energy Rev.* **2024**, *203*, 114783. https://doi.org/10.1016/j.rser.2024.114783.

[20] Dincer, I.; Acar, C. A Review on Clean Energy Solutions for Better Sustainability. *Int. J. Energy Res.* **2015**, *39* (5), 585–606. https://doi.org/10.1002/er.3329.

[21] Haines, A.; Smith, K. R.; Anderson, D.; Epstein, P. R.; McMichael, A. J.; Roberts, I.; Wilkinson, P.; Woodcock, J.; Woods, J. Policies for Accelerating Access to Clean Energy, Improving Health, Advancing Development, and Mitigating Climate Change. *Lancet* **2007**, *370* (9594), 1264–1281. https://doi.org/10.1016/S0140-6736(07)61257-4.

[22] Nishi, Y. The Development of Lithium Ion Secondary Batteries. *Chem. Rec.* **2001**, *1* (5), 406–413. https://doi.org/10.1002/tcr.1024.

[23] Hemavathi, S.; Srirama, S.; Prakash, A. S. Present and Future Generation of Secondary Batteries: A Review. *ChemBioEng Rev.* **2023**, *10* (6), 1123–1145. https://doi.org/10.1002/cben.202200040.

[24] Kennedy, B.; Patterson, D.; Camilleri, S. Use of Lithium-Ion Batteries in Electric Vehicles. *J. Power Sources* **2000**, *90* (2), 156–162. https://doi.org/10.1016/S0378-7753(00)00402-X.

[25] Duan, J.; Tang, X.; Dai, H.; Yang, Y.; Wu, W.; Wei, X.; Huang, Y. Building Safe Lithium-Ion Batteries for Electric Vehicles: A Review. *Electrochem. Energy Rev.* **2020**, *3* (1), 1–42. https://doi.org/10.1007/s41918-019-00060-4.

[26] Cano, Z. P.; Banham, D.; Ye, S.; Hintennach, A.; Lu, J.; Fowler, M.; Chen, Z. Batteries and Fuel Cells for Emerging Electric Vehicle Markets. *Nat. Energy* **2018**, *3* (4), 279–289. https://doi.org/10.1038/s41560-018-0108-1.

[27] Xu, J.; Cai, X.; Cai, S.; Shao, Y.; Hu, C.; Lu, S.; Ding, S. High-Energy Lithium-Ion Batteries: Recent Progress and a Promising Future in Applications. *Energy Environ. Mater.* **2023**, *6* (5), e12450. https://doi.org/10.1002/eem2.12450.

[28] Deng, J.; Bae, C.; Denlinger, A.; Miller, T. Electric Vehicles Batteries: Requirements and Challenges. *Joule* **2020**, *4* (3), 511–515. https://doi.org/10.1016/j.joule.2020.01.013.

[29] Au, H.; Crespo-Ribadeneyra, M.; Titirici, M.-M. Beyond Li-Ion Batteries: Performance, Materials Diversification, and Sustainability. *One Earth* **2022**, *5* (3), 207–211. https://doi.org/10.1016/j.oneear.2022.02.014.

[30] Banerjee, A. N.; Joo, S. W. "Beyond Li-Ion Technology"—A Status Review. *Nanotechnology* **2024**, *35* (47), 472001. https://doi.org/10.1088/1361-6528/ad690b.

[31] Li, M.; Lu, J.; Chen, Z.; Amine, K. 30 Years of Lithium-Ion Batteries. *Adv. Mater.* **2018**, *30* (33), 1800561. https://doi.org/10.1002/adma.201800561.

[32] Crabtree, G.; Kócs, E.; Trahey, L. The Energy-Storage Frontier: Lithium-Ion Batteries and Beyond. *MRS Bull.* **2015**, *40* (12), 1067–1078. https://doi.org/10.1557/mrs.2015.259.

[33] Diouf, B.; Pode, R. Potential of Lithium-Ion Batteries in Renewable Energy. *Renewable Energy* **2015**, *76*, 375–380. https://doi.org/10.1016/j.renene.2014.11.058.

[34] Grey, C. P.; Hall, D. S. Prospects for Lithium-Ion Batteries and Beyond—A 2030 Vision. *Nat. Commun.* **2020**, *11* (1), 6279. https://doi.org/10.1038/s41467-020-19991-4.

[35] Berzelius, J. J. Ein Neues Mineralisches Alkali Und Ein Neues Metall. *J. Chem. Phys.* **1817**, *21*, 44–48.

[36] Arfwedson, A. Untersuchung Einiger Bei Der Eisen-Grube von Utö Vorkommenden Fossilien Und von Einem

Darin Gefundenen Neuen Feuerfesten Alkali. *J. Chem. Phys.* **1818**, *22*, 93–117.

[37] Xu, K. A Long Journey of Lithium: From the Big Bang to Our Smartphones. *Energy Environ. Mater.* **2019**, *2* (4), 229–233. https://doi.org/10.1002/eem2.12057.

[38] Brande, W. T. *A Manual of Chemistry*; J. W. Parker, 1848.

[39] Lewis, G. N.; Keyes, F. G. The Potential of the Lithium Electrode. *J. Am. Chem. Soc.* **1913**, *35* (4), 340–344.

[40] Arora, P.; Zhang, Z. (John). Battery Separators. *Chem. Rev.* **2004**, *104* (10), 4419–4462. https://doi.org/10.1021/cr020738u.

[41] Meng, Y. S.; Srinivasan, V.; Xu, K. Designing Better Electrolytes. *Science* **2022**, *378* (6624), eabq3750. https://doi.org/10.1126/science.abq3750.

[42] Li, M.; Lu, J.; Ji, X.; Li, Y.; Shao, Y.; Chen, Z.; Zhong, C.; Amine, K. Design Strategies for Nonaqueous Multivalent-Ion and Monovalent-Ion Battery Anodes. *Nat. Rev. Mater.* **2020**, *5* (4), 276–294. https://doi.org/10.1038/s41578-019-0166-4.

[43] Manthiram, A. A Reflection on Lithium-Ion Battery Cathode Chemistry. *Nat. Commun.* **2020**, *11* (1), 1550. https://doi.org/10.1038/s41467-020-15355-0.

[44] Sun, Y.; Liu, N.; Cui, Y. Promises and Challenges of Nanomaterials for Lithium-Based Rechargeable Batteries. *Nat. Energy* **2016**, *1* (7), 16071. https://doi.org/10.1038/nenergy.2016.71.

[45] Jeong, E.-D.; Won, M.-S.; Shim, Y.-B. Cathodic Properties of a Lithium-Ion Secondary Battery Using $LiCoO_2$ Prepared by a Complex Formation Reaction. *J. Power Sources* **1998**, *70* (1), 70–77. https://doi.org/10.1016/S0378-7753(97)02667-0.

[46] Lyu, Y.; Wu, X.; Wang, K.; Feng, Z.; Cheng, T.; Liu, Y.; Wang, M.; Chen, R.; Xu, L.; Zhou, J.; Lu, Y.; Guo, B. An Overview on the Advances of $LiCoO_2$ Cathodes for Lithium-Ion Batteries. *Adv. Energy Mater.* **2021**, *11* (2), 2000982. https://doi.org/10.1002/aenm.202000982.

[47] Tarascon, J.-M.; Armand, M. Issues and Challenges Facing Rechargeable Lithium Batteries. *Nature* **2001**, *414* (6861), 359–367. https://doi.org/10.1038/35104644.

[48] Baazouzi, S.; Feistel, N.; Wanner, J.; Landwehr, I.; Fill, A.; Birke, K. P. Design, Properties, and Manufacturing of Cylindrical Li-Ion Battery Cells—A Generic Overview. *Batteries* **2023**, *9* (6), 309. https://doi.org/10.3390/batteries9060309.

[49] Kayyar, A.; Huang, J.; Samiee, M.; Luo, J. Construction and Testing of Coin Cells of Lithium Ion Batteries. *J. Vis. Exp.* **2012**, *66*, 4104. https://doi.org/10.3791/4104.

[50] Murray, V.; Hall, D. S.; Dahn, J. R. A Guide to Full Coin Cell Making for Academic Researchers. *J. Electrochem. Soc.* **2019**, *166* (2), A329. https://doi.org/10.1149/2.1171902jes.

[51] Sahraei, E.; Keshavarzi, M. M.; Zhang, X.; Lai, B. Mechanical Properties of Prismatic Li-Ion Batteries—Electrodes, Cells, and Stacks. *J. Electrochem. Energy Convers. Storage* **2022**, *19*, 041008. https://doi.org/10.1115/1.4054823.

[52] Cousseau, J.-F.; Siret, C.; Biensan, P.; Broussely, M. Recent Developments in Li-Ion Prismatic Cells. *J. Power Sources* **2006**, *162* (2), 790–796. https://doi.org/10.1016/j.jpowsour.2005.02.095.

[53] An, S. J.; Li, J.; Daniel, C.; Kalnaus, S.; Wood, D. L. Design and Demonstration of Three-Electrode Pouch Cells for Lithium-Ion Batteries. *J. Electrochem. Soc.* **2017**, *164* (7), A1755. https://doi.org/10.1149/2.0031709jes.

[54] Gopinadh, S. V.; Anoopkumar, V.; Ansari, Md. J. N.; Srivastava, D.; Raj M., A.; John, B.; Samridh, A.; Vijayakumar, P. S.; Mercy, T. D. Lithium-Ion Pouch Cells: An Overview. In *Energy Harvesting and Storage: Fundamentals and Materials*; Jayaraj, M. K., Antony, A., Subha, P. P., Eds.; Springer Nature: Singapore, 2022; pp 209–224. https://doi.org/10.1007/978-981-19-4526-7_7.

[55] Li, W.; Xia, Y.; Chen, G.; Sahraei, E. Comparative Study of Mechanical-Electrical-Thermal Responses of Pouch, Cylindrical, and Prismatic Lithium-Ion Cells under Mechanical Abuse. *Sci. China Technol. Sci.* **2018**, *61* (10),

1472–1482. https://doi.org/10.1007/s11431-017-9296-0.

[56] Ma, X.; Wang, J.; Wang, Z.; Wang, L.; Xu, H.; He, X. Engineering Strategies for High-Voltage $LiCoO_2$ Based High-Energy Li-Ion Batteries. *Electron* **2024**, *2* (3), e33. https://doi.org/10.1002/elt2.33.

[57] Padhi, A. K.; Nanjundaswamy, K. S.; Goodenough, J. B. Phospho-Olivines as Positive-Electrode Materials for Rechargeable Lithium Batteries. *J. Electrochem. Soc.* **1997**, *144* (4), 1188. https://doi.org/10.1149/1.1837571.

[58] Wang, Y.; He, P.; Zhou, H. Olivine $LiFePO_4$: Development and Future. *Energy Environ. Sci.* **2011**, *4* (3), 805–817. https://doi.org/10.1039/C0EE00176G.

[59] Kwak, W.-J.; Park, N.-Y.; Sun, Y.-K. ICAC 2018: The First International Conference Focused on NCM & NCA Cathode Materials for Lithium Ion Batteries. *ACS Energy Lett.* **2018**, *3* (11), 2757–2760. https://doi.org/10.1021/acsenergylett.8b01926.

[60] Yan, J.; Huang, H.; Tong, J.; Li, W.; Liu, X.; Zhang, H.; Huang, H.; Zhou, W. Recent Progress on the Modification of High Nickel Content NCM: Coating, Doping, and Single Crystallization. *Interdiscip. Mater.* **2022**, *1* (3), 330–353. https://doi.org/10.1002/idm2.12043.

[61] Ammundsen, B.; Paulsen, J. Novel Lithium-Ion Cathode Materials Based on Layered Manganese Oxides. *Adv. Mater.* **2001**, *13* (12–13), 943–956. https://doi.org/10.1002/1521-4095(200107)13:12/13<943::AID-ADMA943>3.0.CO;2-J.

[62] Huang, Y.; Dong, Y.; Li, S.; Lee, J.; Wang, C.; Zhu, Z.; Xue, W.; Li, Y.; Li, J. Lithium Manganese Spinel Cathodes for Lithium-Ion Batteries. *Adv. Energy Mater.* **2021**, *11* (2), 2000997. https://doi.org/10.1002/aenm.202000997.

[63] Liu, S.; Xiong, L.; He, C. Long Cycle Life Lithium Ion Battery with Lithium Nickel Cobalt Manganese Oxide (NCM) Cathode. *J. Power Sources* **2014**, *261*, 285–291. https://doi.org/10.1016/j.jpowsour.2014.03.083.

[64] Belharouak, I.; Sun, Y.-K.; Liu, J.; Amine, K. $Li(Ni_{1/3}Co_{1/3}Mn_{1/3})O_2$ as a Suitable Cathode for High Power Applications. *J. Power Sources* **2003**, *123* (2), 247–252. https://doi.org/10.1016/S0378-7753(03)00529-9.

[65] Lin, Y.; Gao, M. X.; Zhu, D.; Liu, Y. F.; Pan, H. G. Effects of Carbon Coating and Iron Phosphides on the Electrochemical Properties of $LiFePO_4$/C. *J. Power Sources* **2008**, *184* (2), 444–448. https://doi.org/10.1016/j.jpowsour.2008.03.026.

[66] Zhang, W.-J. Structure and Performance of $LiFePO_4$ Cathode Materials: A Review. *J. Power Sources* **2011**, *196* (6), 2962–2970. https://doi.org/10.1016/j.jpowsour.2010.11.113.

[67] Lin, Y.; Li, F.; Zhao, K.; Zou, S.; Tan, X.; Shi, Z.; Fan, J.; Ouyang, L.; Zhu, M.; Liu, J. Earth-Abundant Spinel $LiMn_2O_4$ Cathode for Lithium-Ion Batteries: Challenges, Strategies, and Perspectives. *Small Methods* **2024**, *n/a* (n/a), 2402233. https://doi.org/10.1002/smtd.202402233.

[68] Zheng, J.; Myeong, S.; Cho, W.; Yan, P.; Xiao, J.; Wang, C.; Cho, J.; Zhang, J.-G. Li- and Mn-Rich Cathode Materials: Challenges to Commercialization. *Adv. Energy Mater.* **2017**, *7* (6), 1601284. https://doi.org/10.1002/aenm.201601284.

[69] Wang, X.; Ding, Y.-L.; Deng, Y.-P.; Chen, Z. Ni-Rich/Co-Poor Layered Cathode for Automotive Li-Ion Batteries: Promises and Challenges. *Adv. Energy Mater.* **2020**, *10* (12), 1903864. https://doi.org/10.1002/aenm.201903864.

[70] Cao, W.; Zhang, J.; Li, H. Batteries with High Theoretical Energy Densities. *Energy Storage Mater.* **2020**, *26*, 46–55. https://doi.org/10.1016/j.ensm.2019.12.024.

[71] Callegari, D.; Coduri, M.; Fracchia, M.; Ghigna, P.; Braglia, L.; Tamburini, U. A.; Quartarone, E. Lithium Intercalation Mechanisms and Critical Role of Multi-Doping in $LiFe_xMn_{2-x-y}Ti_yO_4$ as High-Capacity Cathode Material for Lithium-Ion Batteries. *J. Mater. Chem. C* **2022**, *10* (23), 8994–9008. https://doi.org/10.1039/D2TC00573E.

[72] Gao, Y.; Pan, Z.; Sun, J.; Liu, Z.; Wang, J. High-Energy Batteries: Beyond Lithium-Ion and Their Long Road to

Commercialisation. *Nano-Micro Lett.* **2022**, *14* (1), 94. https://doi.org/10.1007/s40820-022-00844-2.

[73] Huie, M. M.; Bock, D. C.; Takeuchi, E. S.; Marschilok, A. C.; Takeuchi, K. J. Cathode Materials for Magnesium and Magnesium-Ion Based Batteries. *Coord. Chem. Rev.* **2015**, *287*, 15–27. https://doi.org/10.1016/j.ccr.2014.11.005.

[74] Leisegang, T.; Meutzner, F.; Zschornak, M.; Münchgesang, W.; Schmid, R.; Nestler, T.; Eremin, R. A.; Kabanov, A. A.; Blatov, V. A.; Meyer, D. C. The Aluminum-Ion Battery: A Sustainable and Seminal Concept? *Front. Chem.* **2019**, *7*. https://doi.org/10.3389/fchem.2019.00268.

[75] Gummow, R. J.; Vamvounis, G.; Kannan, M. B.; He, Y. Calcium-Ion Batteries: Current State-of-the-Art and Future Perspectives. *Adv. Mater.* **2018**, *30* (39), 1801702. https://doi.org/10.1002/adma.201801702.

[76] Ming, J.; Guo, J.; Xia, C.; Wang, W.; Alshareef, H. N. Zinc-Ion Batteries: Materials, Mechanisms, and Applications. *Mater. Sci. Eng., R* **2019**, *135*, 58–84. https://doi.org/10.1016/j.mser.2018.10.002.

[77] Biemolt, J.; Jungbacker, P.; van Teijlingen, T.; Yan, N.; Rothenberg, G. Beyond Lithium-Based Batteries. *Materials* **2020**, *13* (2), 425. https://doi.org/10.3390/ma13020425.

[78] Olabi, A. G.; Sayed, E. T.; Wilberforce, T.; Jamal, A.; Alami, A. H.; Elsaid, K.; Rahman, S. M. A.; Shah, S. K.; Abdelkareem, M. A. Metal-Air Batteries—A Review. *Energies* **2021**, *14* (21), 7373. https://doi.org/10.3390/en14217373.

[79] Grande, L.; Paillard, E.; Hassoun, J.; Park, J.-B.; Lee, Y.-J.; Sun, Y.-K.; Passerini, S.; Scrosati, B. The Lithium/Air Battery: Still an Emerging System or a Practical Reality? *Adv. Mater.* **2015**, *27* (5), 784–800. https://doi.org/10.1002/adma.201403064.

[80] Wang, Q.; Kaushik, S.; Xiao, X.; Xu, Q. Sustainable Zinc–Air Battery Chemistry: Advances, Challenges and Prospects. *Chem. Soc. Rev.* **2023**, *52* (17), 6139–6190. https://doi.org/10.1039/D2CS00684G.

[81] Islam, S.; Nayem, S. M. A.; Anjum, A.; Shaheen Shah, S.; Ahammad, A. J. S.; Aziz, Md. A. A Mechanistic Overview of the Current Status and Future Challenges in Air Cathode for Aluminum Air Batteries. *Chem. Rec.* **2024**, *24* (1), e202300017. https://doi.org/10.1002/tcr.202300017.

[82] Hwang, J.-Y.; Myung, S.-T.; Sun, Y.-K. Sodium-Ion Batteries: Present and Future. *Chem. Soc. Rev.* **2017**, *46* (12), 3529–3614. https://doi.org/10.1039/C6CS00776G.

[83] Gao, Y.; Zhang, H.; Peng, J.; Li, L.; Xiao, Y.; Li, L.; Liu, Y.; Qiao, Y.; Chou, S.-L. A 30-Year Overview of Sodium-Ion Batteries. *Carbon Energy* **2024**, *6* (6), e464. https://doi.org/10.1002/cey2.464.

[84] Xu, Y.; Du, Y.; Chen, H.; Chen, J.; Ding, T.; Sun, D.; Ha Kim, D.; Lin, Z.; Zhou, X. Recent Advances in Rational Design for High-Performance Potassium-Ion Batteries. *Chem. Soc. Rev.* **2024**, *53* (13), 7202–7298. https://doi.org/10.1039/D3CS00601H.

[85] Sada, K.; Darga, J.; Manthiram, A. Challenges and Prospects of Sodium-Ion and Potassium-Ion Batteries for Mass Production. *Adv. Energy Mater.* **2023**, *13* (39), 2302321. https://doi.org/10.1002/aenm.202302321.

[86] Raza, H.; Bai, S.; Cheng, J.; Majumder, S.; Zhu, H.; Liu, Q.; Zheng, G.; Li, X.; Chen, G. Li-S Batteries: Challenges, Achievements and Opportunities. *Electrochem. Energy Rev.* **2023**, *6* (1), 29. https://doi.org/10.1007/s41918-023-00188-4.

[87] Manthiram, A.; Fu, Y.; Chung, S.-H.; Zu, C.; Su, Y.-S. Rechargeable Lithium–Sulfur Batteries. *Chem. Rev.* **2014**, *114* (23), 11751–11787. https://doi.org/10.1021/cr500062v.

[88] Sun, J.; Wang, T.; Gao, Y.; Pan, Z.; Hu, R.; Wang, J. Will Lithium-Sulfur Batteries Be the next beyond-Lithium Ion Batteries and Even Much Better? *InfoMat* **2022**, *4* (9), e12359. https://doi.org/10.1002/inf2.12359.

[89] Ji, X.; Lee, K. T.; Nazar, L. F. A Highly Ordered Nanostructured Carbon–Sulphur Cathode for Lithium–Sulphur Batteries. *Nat. Mater.* **2009**, *8* (6), 500–506. https://doi.org/10.1038/nmat2460.

[90] Peng, H.-J.; Huang, J.-Q.; Cheng, X.-B.; Zhang, Q. Review on High-Loading and High-Energy Lithium–Sulfur Batteries. *Adv. Energy Mater.* **2017**, *7* (24), 1700260. https://doi.org/10.1002/aenm.201700260.

[91] Zhao, F.; Xue, J.; Shao, W.; Yu, H.; Huang, W.; Xiao, J. Toward High-Sulfur-Content, High-Performance Lithium-Sulfur Batteries: Review of Materials and Technologies. *J. Energy Chem.* **2023**, *80*, 625–657. https://doi.org/10.1016/j.jechem.2023.02.009.

[92] Li, T.; Bai, X.; Gulzar, U.; Bai, Y.-J.; Capiglia, C.; Deng, W.; Zhou, X.; Liu, Z.; Feng, Z.; Proietti Zaccaria, R. A Comprehensive Understanding of Lithium–Sulfur Battery Technology. *Adv. Funct. Mater.* **2019**, *29* (32), 1901730. https://doi.org/10.1002/adfm.201901730.

[93] Bruce, P. G.; Freunberger, S. A.; Hardwick, L. J.; Tarascon, J.-M. Li–O_2 and Li–S Batteries with High Energy Storage. *Nat. Mater.* **2012**, *11* (1), 19–29. https://doi.org/10.1038/nmat3191.

[94] Zhang, T.; Wu, N.; Zhao, Y.; Zhang, X.; Wu, J.; Weng, J.; Li, S.; Huo, F.; Huang, W. Frontiers and Structural Engineering for Building Flexible Zinc–Air Batteries. *Adv. Sci.* **2022**, *9* (6), 2103954. https://doi.org/10.1002/advs.202103954.

[95] Boyd, D. A. Sulfur and Its Role in Modern Materials Science. *Angew. Chem., Int. Ed.* **2016**, *55* (50), 15486–15502. https://doi.org/10.1002/anie.201604615.

[96] Ji, X.; Nazar, L. F. Advances in Li–S Batteries. *J. Mater. Chem.* **2010**, *20* (44), 9821–9826. https://doi.org/10.1039/B925751A.

[97] Steudel, R. *Elemental Sulfur and Sulfur-Rich Compounds II*; Springer Science & Business Media: 2003.

[98] Fang, R.; Zhao, S.; Sun, Z.; Wang, D.-W.; Cheng, H.-M.; Li, F. More Reliable Lithium-Sulfur Batteries: Status, Solutions and Prospects. *Adv. Mater.* **2017**, *29* (48), 1606823. https://doi.org/10.1002/adma.201606823.

[99] Mikhaylik, Y. V.; Akridge, J. R. Polysulfide Shuttle Study in the Li/S Battery System. *J. Electrochem. Soc.* **2004**, *151* (11), A1969. https://doi.org/10.1149/1.1806394.

[100] Barchasz, C.; Leprêtre, J.-C.; Alloin, F.; Patoux, S. New Insights into the Limiting Parameters of the Li/S Rechargeable Cell. *J. Power Sources* **2012**, *199*, 322–330. https://doi.org/10.1016/j.jpowsour.2011.07.021.

[101] Ahn, J. H.; Lim, D.-A.; Kim, J.; You, T.-S.; Kim, D.-W. Enhancement of the Cycling Stability of Lithium-Sulfur Batteries by Using a Reactive Additive for Blocking Dissolution of Lithium Polysulfides. *J. Ind. Eng. Chem.* **2022**, *108*, 484–492. https://doi.org/10.1016/j.jiec.2022.01.025.

[102] Hou, L.-P.; Zhang, X.-Q.; Li, B.-Q.; Zhang, Q. Challenges and Promises of Lithium Metal Anode by Soluble Polysulfides in Practical Lithium–Sulfur Batteries. *Mater. Today* **2021**, *45*, 62–76. https://doi.org/10.1016/j.mattod.2020.10.021.

[103] Sadd, M.; De Angelis, S.; Colding-Jørgensen, S.; Blanchard, D.; Johnsen, R. E.; Sanna, S.; Borisova, E.; Matic, A.; Bowen, J. R. Visualization of Dissolution-Precipitation Processes in Lithium–Sulfur Batteries. *Adv. Energy Mater.* **2022**, *12* (10), 2103126. https://doi.org/10.1002/aenm.202103126.

[104] Yang, Y.; Zheng, G.; Misra, S.; Nelson, J.; Toney, M. F.; Cui, Y. High-Capacity Micrometer-Sized Li_2S Particles as Cathode Materials for Advanced Rechargeable Lithium-Ion Batteries. *J. Am. Chem. Soc.* **2012**, *134* (37), 15387–15394. https://doi.org/10.1021/ja3052206.

[105] Wang, Z.; Li, Y.; Ji, H.; Zhou, J.; Qian, T.; Yan, C. Unity of Opposites between Soluble and Insoluble Lithium Polysulfides in Lithium–Sulfur Batteries. *Adv. Mater.* **2022**, *34* (47), 2203699. https://doi.org/10.1002/adma.202203699.

[106] Li, H.; Ma, S.; Li, J.; Liu, F.; Zhou, H.; Huang, Z.; Jiao, S.; Kuang, Y. Altering the Reaction Mechanism to Eliminate the Shuttle Effect in Lithium-Sulfur Batteries. *Energy Storage Mater.* **2020**, *26*, 203–212. https://doi.org/10.1016/j.ensm.2020.01.002.

[107] Hofmann, A. F.; Fronczek, D. N.; Bessler, W. G. Mechanistic Modeling of Polysulfide Shuttle and Capacity Loss in Lithium–Sulfur Batteries. *J. Power Sources* **2014**, *259*, 300–310. https://doi.org/10.1016/j.jpowsour.2014.02.082.

[108] Huang, Y.; Lin, L.; Zhang, C.; Liu, L.; Li, Y.; Qiao, Z.; Lin, J.; Wei, Q.; Wang, L.; Xie, Q.; Peng, D.-L. Recent

Advances and Strategies toward Polysulfides Shuttle Inhibition for High-Performance Li–S Batteries. *Adv. Sci.* **2022**, *9* (12), 2106004. https://doi.org/10.1002/advs.202106004.

[109] Li, J.; Gao, L.; Pan, F.; Gong, C.; Sun, L.; Gao, H.; Zhang, J.; Zhao, Y.; Wang, G.; Liu, H. Engineering Strategies for Suppressing the Shuttle Effect in Lithium–Sulfur Batteries. *Nano-Micro Lett.* **2023**, *16* (1), 12. https://doi.org/10.1007/s40820-023-01223-1.

[110] Wang, J.; Wang, H.; Jia, S.; Zhao, Q.; Zheng, Q.; Ma, Y.; Ma, T.; Li, X. Recent Advances in Inhibiting Shuttle Effect of Polysulfide in Lithium-Sulfur Batteries. *J. Energy Storage* **2023**, *72*, 108372. https://doi.org/10.1016/j.est.2023.108372.

[111] Chung, S.-H.; Manthiram, A. Current Status and Future Prospects of Metal–Sulfur Batteries. *Adv. Mater.* **2019**, *31* (27), 1901125. https://doi.org/10.1002/adma.201901125.

[112] Luo, S.; Wu, F.; Yushin, G. Strategies for Fabrication, Confinement and Performance Boost of Li_2S in Lithium-Sulfur, Silicon-Sulfur & Related Batteries. *Mater. Today* **2021**, *49*, 253–270. https://doi.org/10.1016/j.mattod.2021.03.017.

[113] Peng, L.; Wei, Z.; Wan, C.; Li, J.; Chen, Z.; Zhu, D.; Baumann, D.; Liu, H.; Allen, C. S.; Xu, X.; Kirkland, A. I.; Shakir, I.; Almutairi, Z.; Tolbert, S.; Dunn, B.; Huang, Y.; Sautet, P.; Duan, X. A Fundamental Look at Electrocatalytic Sulfur Reduction Reaction. *Nat. Catal.* **2020**, *3* (9), 762–770. https://doi.org/10.1038/s41929-020-0498-x.

[114] Lee, S.; Sim, K.; Kwon, J.; Seok, D.; Eom, K. Unraveling the Effect of Disproportionation of Lithium Polysulfides on the Electrochemical Reaction and S Utilization in Lithium-Sulfur Battery. *Electrochim. Acta* **2022**, *412*, 140092. https://doi.org/10.1016/j.electacta.2022.140092.

[115] Waluś, S.; Offer, G.; Hunt, I.; Patel, Y.; Stockley, T.; Williams, J.; Purkayastha, R. Volumetric Expansion of Lithium-Sulfur Cell during Operation—Fundamental Insight into Applicable Characteristics. *Energy Storage Mater.* **2018**, *10*, 233–245. https://doi.org/10.1016/j.ensm.2017.05.017.

[116] Brieske, D. M.; Warnecke, A.; Sauer, D. U. Modeling the Volumetric Expansion of the Lithium-Sulfur Battery Considering Charge and Discharge Profiles. *Energy Storage Mater.* **2023**, *55*, 289–300. https://doi.org/10.1016/j.ensm.2022.11.053.

[117] See, K. A.; Jun, Y.-S.; Gerbec, J. A.; Sprafke, J. K.; Wudl, F.; Stucky, G. D.; Seshadri, R. Sulfur-Functionalized Mesoporous Carbons as Sulfur Hosts in Li–S Batteries: Increasing the Affinity of Polysulfide Intermediates to Enhance Performance. *ACS Appl. Mater. Interfaces* **2014**, *6* (14), 10908–10916. https://doi.org/10.1021/am405025n.

[118] Xia, S.; Zhang, X.; Liang, C.; Yu, Y.; Liu, W. Stabilized Lithium Metal Anode by an Efficient Coating for High-Performance Li–S Batteries. *Energy Storage Mater.* **2020**, *24*, 329–335. https://doi.org/10.1016/j.ensm.2019.07.042.

[119] Foroozan, T.; Sharifi-Asl, S.; Shahbazian-Yassar, R. Mechanistic Understanding of Li Dendrites Growth by in-Situ/Operando Imaging Techniques. *J. Power Sources* **2020**, *461*, 228135. https://doi.org/10.1016/j.jpowsour.2020.228135.

[120] Gireaud, L.; Grugeon, S.; Laruelle, S.; Yrieix, B.; Tarascon, J.-M. Lithium Metal Stripping/Plating Mechanisms Studies: A Metallurgical Approach. *Electrochem. Commun.* **2006**, *8* (10), 1639–1649. https://doi.org/10.1016/j.elecom.2006.07.037.

[121] Dornbusch, D. A.; Hilton, R.; Lohman, S. D.; Suppes, G. J. Experimental Validation of the Elimination of Dendrite Short-Circuit Failure in Secondary Lithium-Metal Convection Cell Batteries. *J. Electrochem. Soc.* **2015**, *162* (3), A262. https://doi.org/10.1149/2.0021503jes.

[122] Huang, L.; Liu, L.; Lu, L.; Feng, X.; Han, X.; Li, W.; Zhang, M.; Li, D.; Liu, X.; Sauer, D. U.; Ouyang, M. A Review of the Internal Short Circuit Mechanism in Lithium-Ion Batteries: Inducement, Detection and Prevention.

Int. J. Energy Res. **2021**, *45* (11), 15797–15831. https://doi.org/10.1002/er.6920.

[123] Wu, H.; Jia, H.; Wang, C.; Zhang, J.-G.; Xu, W. Recent Progress in Understanding Solid Electrolyte Interphase on Lithium Metal Anodes. *Adv. Energy Mater.* **2021**, *11* (5), 2003092. https://doi.org/10.1002/aenm.202003092.

[124] Ramasubramanian, A.; Yurkiv, V.; Foroozan, T.; Ragone, M.; Shahbazian-Yassar, R.; Mashayek, F. Stability of Solid-Electrolyte Interphase (SEI) on the Lithium Metal Surface in Lithium Metal Batteries (LMBs). *ACS Appl. Energy Mater.* **2020**, *3* (11), 10560–10567. https://doi.org/10.1021/acsaem.0c01605.

[125] Wu, B.; Chen, C.; Raijmakers, L. H. J.; Liu, J.; Danilov, D. L.; Eichel, R.-A.; Notten, P. H. L. Li-Growth and SEI Engineering for Anode-Free Li-Metal Rechargeable Batteries: A Review of Current Advances. *Energy Storage Mater.* **2023**, *57*, 508–539. https://doi.org/10.1016/j.ensm.2023.02.036.

[126] Zhao, H.; Wang, J.; Shao, H.; Xu, K.; Deng, Y. Gas Generation Mechanism in Li-Metal Batteries. *Energy Environ. Mater.* **2022**, *5* (1), 327–336. https://doi.org/10.1002/eem2.12180.

[127] Wang, Y.; Huang, X.; Zhang, S.; Hou, Y. Sulfur Hosts against the Shuttle Effect. *Small Methods* **2018**, *2* (6), 1700345. https://doi.org/10.1002/smtd.201700345.

[128] Zhou, L.; Danilov, D. L.; Eichel, R.-A.; Notten, P. H. L. Host Materials Anchoring Polysulfides in Li–S Batteries Reviewed. *Adv. Energy Mater.* **2021**, *11* (15), 2001304. https://doi.org/10.1002/aenm.202001304.

[129] Wu, C.; Lai, W.-H.; Cai, X.; Chou, S.-L.; Liu, H.-K.; Wang, Y.-X.; Dou, S.-X. Carbonaceous Hosts for Sulfur Cathode in Alkali-Metal/S (Alkali Metal = Lithium, Sodium, Potassium) Batteries. *Small* **2021**, *17* (48), 2006504. https://doi.org/10.1002/smll.202006504.

[130] Deng, S.; Guo, T.; Heier, J.; Zhang, C. (John). Unraveling Polysulfide's Adsorption and Electrocatalytic Conversion on Metal Oxides for Li-S Batteries. *Adv. Sci.* **2023**, *10* (5), 2204930. https://doi.org/10.1002/advs.202204930.

[131] Zeng, P.; Zhou, X.; Peng, J.; Huang, X.; Chang, B.; Chen, G.; Chen, M.; Zheng, L.; Pei, Y.; Su, J.; Wang, X. Promoting "Strong Adsorption" and "Fast Conversion" of Polysulfides in Li-S Batteries Based on Conductive Sulfides Host with Hollow Prism Structure and Surface Defects. *Adv. Funct. Mater.* **2023**, *33* (4), 2211818. https://doi.org/10.1002/adfm.202211818.

[132] Chen, X.; Zhao, C.; Yang, K.; Sun, S.; Bi, J.; Zhu, N.; Cai, Q.; Wang, J.; Yan, W. Conducting Polymers Meet Lithium–Sulfur Batteries: Progress, Challenges, and Perspectives. *Energy Environ. Mater.* **2023**, *6* (5), e12483. https://doi.org/10.1002/eem2.12483.

[133] Shafique, A.; Vanhulsel, A.; Rangasamy, V. S.; Safari, M.; Bragaggia, G.; Gross, S.; Adriaensens, P.; Van Bael, M. K.; Hardy, A.; Sallard, S. Impact of Different Conductive Polymers on the Performance of the Sulfur Positive Electrode in Li–S Batteries. *ACS Appl. Energy Mater.* **2022**, *5* (4), 4861–4876. https://doi.org/10.1021/acsaem.2c00270.

[134] Yang, H.; Chen, J.; Yang, J.; Wang, J. Prospect of Sulfurized Pyrolyzed Poly(Acrylonitrile) (S@pPAN) Cathode Materials for Rechargeable Lithium Batteries. *Angew. Chem.* **2020**, *132* (19), 7374–7386. https://doi.org/10.1002/ange.201913540.

[135] Jeong, Y. C.; Kim, J. H.; Nam, S.; Park, C. R.; Yang, S. J. Rational Design of Nanostructured Functional Interlayer/Separator for Advanced Li–S Batteries. *Adv. Funct. Mater.* **2018**, *28* (38), 1707411. https://doi.org/10.1002/adfm.201707411.

[136] Zhai, P.; Liu, L.; Gu, X.; Wang, T.; Gong, Y. Interface Engineering for Lithium Metal Anodes in Liquid Electrolyte. *Adv. Energy Mater.* **2020**, *10* (34), 2001257. https://doi.org/10.1002/aenm.202001257.

[137] He, X.; Zhang, K.; Zhu, Z.; Tong, Z.; Liang, X. 3D-Hosted Lithium Metal Anodes. *Chem. Soc. Rev.* **2024**, *53* (1), 9–24. https://doi.org/10.1039/D3CS00495C.

[138] Tan, J.; Ye, M.; Shen, J. Deciphering the Role of $LiNO_3$ Additives in Li–S Batteries. *Mater. Horiz.* **2022**, *9* (9), 2325–2334. https://doi.org/10.1039/D2MH00469K.

[139] Zhang, S. S. Role of $LiNO_3$ in Rechargeable Lithium/Sulfur Battery. *Electrochim. Acta* **2012**, *70*, 344–348. https://doi.org/10.1016/j.electacta.2012.03.081.

[140] Ting, L. K. J.; Gao, Y.; Wang, H.; Wang, T.; Sun, J.; Wang, J. Lithium Sulfide Batteries: Addressing the Kinetic Barriers and High First Charge Overpotential. *ACS Omega* **2022**, *7* (45), 40682–40700. https://doi.org/10.1021/acsomega.2c05477.

[141] Jiang, J.; Fan, Q.; Chou, S.; Guo, Z.; Konstantinov, K.; Liu, H.; Wang, J. Li_2S-Based Li-Ion Sulfur Batteries: Progress and Prospects. *Small* **2021**, *17* (9), 1903934. https://doi.org/10.1002/smll.201903934.

[142] Offermann, J.; Paolella, A.; Adelung, R.; Abdollahifar, M. Rising Anode-Free Lithium-Sulfur Batteries. *Chem. Eng. J.* **2024**, *502*, 157920. https://doi.org/10.1016/j.cej.2024.157920.

[143] Su, D.; Zhou, D.; Wang, C.; Wang, G. Toward High Performance Lithium–Sulfur Batteries Based on Li_2S Cathodes and Beyond: Status, Challenges, and Perspectives. *Adv. Funct. Mater.* **2018**, *28* (38), 1800154. https://doi.org/10.1002/adfm.201800154.

[144] Li, Z.; Zhang, S.; Terada, S.; Ma, X.; Ikeda, K.; Kamei, Y.; Zhang, C.; Dokko, K.; Watanabe, M. Promising Cell Configuration for Next-Generation Energy Storage: Li_2S/Graphite Battery Enabled by a Solvate Ionic Liquid Electrolyte. *ACS Appl. Mater. Interfaces* **2016**, *8* (25), 16053–16062. https://doi.org/10.1021/acsami.6b03736.

[145] Tan, G.; Xu, R.; Xing, Z.; Yuan, Y.; Lu, J.; Wen, J.; Liu, C.; Ma, L.; Zhan, C.; Liu, Q.; Wu, T.; Jian, Z.; Shahbazian-Yassar, R.; Ren, Y.; Miller, D. J.; Curtiss, L. A.; Ji, X.; Amine, K. Burning Lithium in CS_2 for High-Performing Compact Li_2S–Graphene Nanocapsules for Li–S Batteries. *Nat. Energy* **2017**, *2* (7), 1–10. https://doi.org/10.1038/nenergy.2017.90.

[146] Tan, L.; Li, A.; Yang, Y.; Zhang, J.; Niu, X.; Li, N.; Liu, L.; Guo, L.; Zhu, Y. Highly Active and Stable Li_2S–Cu Nanocomposite Cathodes Enabled by Kinetically Favored Displacement Interconversion between Cu2S and Li_2S. *Angew. Chem.* **2022**, *134* (31), e202206012. https://doi.org/10.1002/ange.202206012.

[147] Zheng, S.; Chen, Y.; Xu, Y.; Yi, F.; Zhu, Y.; Liu, Y.; Yang, J.; Wang, C. In Situ Formed Lithium Sulfide/Microporous Carbon Cathodes for Lithium-Ion Batteries. *ACS Nano* **2013**, *7* (12), 10995–11003. https://doi.org/10.1021/nn404601h.

[148] Momma, T.; Wu, Y.; Mikuriya, H.; Nara, H.; Osaka, T. In-Situ Lithiation through an "Injection" Strategy in the Pouch Type Sulfur-Graphite Battery System. *J. Power Sources* **2019**, *430*, 228–232. https://doi.org/10.1016/j.jpowsour.2019.05.033.

[149] Meng, X.; Liu, Y.; Yu, L.; Qiu, J.; Wang, Z. Air-Stable Li_2S Cathode for Quasi-Solid-State Anode-Free Batteries with High Volumetric Energy. *Adv. Funct. Mater.* **2023**, *33* (11), 2211062. https://doi.org/10.1002/adfm.202211062.

[150] Ye, F.; Liu, M.; Yan, X.; Li, J.; Pan, Z.; Li, H.; Zhang, Y. In Situ Electrochemically Derived Amorphous-Li_2S for High Performance Li_2S/Graphite Full Cell. *Small* **2018**, *14* (17), 1703871. https://doi.org/10.1002/smll.201703871.

[151] Wang, N.; Zhao, N.; Shi, C.; Liu, E.; He, C.; He, F.; Ma, L. In Situ Synthesized Li_2S@Porous Carbon Cathode for Graphite/Li_2S Full Cells Using Ether-Based Electrolyte. *Electrochim. Acta* **2017**, *256*, 348–356. https://doi.org/10.1016/j.electacta.2017.10.053.

[152] Kim, H.; Min, K.-J.; Bang, S.; Hwang, J.-Y.; Kim, J. H.; Yoon, C. S.; Sun, Y.-K. Long-Lasting, Reinforced Electrical Networking in a High-Loading Li_2S Cathode for High-Performance Lithium–Sulfur Batteries. *Carbon Energy* **2023**, *5* (8), 308. https://doi.org/10.1002/cey2.308.

[153] Wu, Y.; Yokoshima, T.; Nara, H.; Momma, T.; Osaka, T. A Pre-Lithiation Method for Sulfur Cathode Used for Future Lithium Metal Free Full Battery. *J. Power Sources* **2017**, *342*, 537–545. https://doi.org/10.1016/j.jpowsour.2016.12.101.

[154] Fan, Q.; Si, Y.; Zhu, F.; Guo, W.; Fu, Y. Activation of Bulk Li_2S as Cathode Material for Lithium-Sulfur

Batteries through Organochalcogenide-Based Redox Mediation Chemistry. *Angew. Chem., Int. Ed.* **2023**, *62* (32), e202306705. https://doi.org/10.1002/anie.202306705.

[155] Hao, Z.; Chen, J.; Yuan, L.; Bing, Q.; Liu, J.; Chen, W.; Li, Z.; Wang, F. R.; Huang, Y. Advanced Li_2S/Si Full Battery Enabled by TiN Polysulfide Immobilizer. *Small* **2019**, *15* (50), 1902377. https://doi.org/10.1002/smll.201902377.

[156] Zhang, K.; Wang, L.; Hu, Z.; Cheng, F.; Chen, J. Ultrasmall Li_2S Nanoparticles Anchored in Graphene Nanosheets for High-Energy Lithium-Ion Batteries. *Sci. Rep.* **2014**, *4* (1), 6467. https://doi.org/10.1038/srep06467.

[157] Yang, Y.; McDowell, M. T.; Jackson, A.; Cha, J. J.; Hong, S. S.; Cui, Y. New Nanostructured Li_2S/Silicon Rechargeable Battery with High Specific Energy. *Nano Lett.* **2010**, *10* (4), 1486–1491. https://doi.org/10.1021/nl100504q.

[158] Yu, M.; Zhou, S.; Wang, Z.; Pei, W.; Liu, X.; Liu, C.; Yan, C.; Meng, X.; Wang, S.; Zhao, J.; Qiu, J. A Molecular-Cage Strategy Enabling Efficient Chemisorption–Electrocatalytic Interface in Nanostructured Li_2S Cathode for Li Metal-Free Rechargeable Cells with High Energy. *Adv. Funct. Mater.* **2019**, *29* (46), 1905986. https://doi.org/10.1002/adfm.201905986.

[159] Agostini, M.; Hassoun, J.; Liu, J.; Jeong, M.; Nara, H.; Momma, T.; Osaka, T.; Sun, Y.-K.; Scrosati, B. A Lithium-Ion Sulfur Battery Based on a Carbon-Coated Lithium-Sulfide Cathode and an Electrodeposited Silicon-Based Anode. *ACS Appl. Mater. Interfaces* **2014**, *6* (14), 10924–10928. https://doi.org/10.1021/am4057166.

[160] Mollania, H.; Zhang, C.; Du, R.; Qi, X.; Li, J.; Horta, S.; Ibañez, M.; Keller, C.; Chenevier, P.; Oloomi-Buygi, M.; Cabot, A. Nanostructured Li_2S Cathodes for Silicon–Sulfur Batteries. *ACS Appl. Mater. Interfaces* **2023**, *15* (50), 58462–58475. https://doi.org/10.1021/acsami.3c14072.

[161] Hassoun, J.; Sun, Y.-K.; Scrosati, B. Rechargeable Lithium Sulfide Electrode for a Polymer Tin/Sulfur Lithium-Ion Battery. *J. Power Sources* **2011**, *196* (1), 343–348. https://doi.org/10.1016/j.jpowsour.2010.06.093.

[162] Liu, M.; Ren, Y. X.; Jiang, H. R.; Luo, C.; Kang, F. Y.; Zhao, T. S. An Efficient Li_2S-Based Lithium-Ion Sulfur Battery Realized by a Bifunctional Electrolyte Additive. *Nano Energy* **2017**, *40*, 240–247. https://doi.org/10.1016/j.nanoen.2017.08.017.

[163] Hassoun, J.; Scrosati, B. A High-Performance Polymer Tin Sulfur Lithium Ion Battery. *Angew. Chem.* **2010**, *122* (13), 2421–2424. https://doi.org/10.1002/ange.200907324.

[164] Obrovac, M. N.; Dahn, J. R. Electrochemically Active Lithia/Metal and Lithium Sulfide/Metal Composites. *Electrochem. Solid-State Lett.* **2002**, *5* (4), A70. https://doi.org/10.1149/1.1452482.

[165] Son, Y.; Lee, J.-S.; Son, Y.; Jang, J.-H.; Cho, J. Recent Advances in Lithium Sulfide Cathode Materials and Their Use in Lithium Sulfur Batteries. *Adv. Energy Mater.* **2015**, *5* (16), 1500110. https://doi.org/10.1002/aenm.201500110.

[166] Cai, K.; Song, M.-K.; Cairns, E. J.; Zhang, Y. Nanostructured Li_2S–C Composites as Cathode Material for High-Energy Lithium/Sulfur Batteries. *Nano Lett.* **2012**, *12* (12), 6474–6479. https://doi.org/10.1021/nl303965a.

[167] Chen, L.; Liu, Y.; Zhang, F.; Liu, C.; Shaw, L. L. PVP-Assisted Synthesis of Uniform Carbon Coated Li_2S/CB for High-Performance Lithium–Sulfur Batteries. *ACS Appl. Mater. Interfaces* **2015**, *7* (46), 25748–25756. https://doi.org/10.1021/acsami.5b07331.

[168] Ye, H.; Li, M.; Liu, T.; Li, Y.; Lu, J. Activating Li_2S as the Lithium-Containing Cathode in Lithium–Sulfur Batteries. *ACS Energy Lett.* **2020**, *5* (7), 2234–2245. https://doi.org/10.1021/acsenergylett.0c00936.

[169] Wang, L.; Zhang, T.; Yang, S.; Cheng, F.; Liang, J.; Chen, J. A Quantum-Chemical Study on the Discharge Reaction Mechanism of Lithium-Sulfur Batteries. *J. Energy Chem.* **2013**, *22* (1), 72–77. https://doi.org/10.1016/S2095-4956(13)60009-1.

[170] Kim, D.-H.; Lee, M.-S.; Park, K.-Y.; Kang, K. First-Principles Study on the Charge Transport Mechanism of

Lithium Sulfide (Li_2S) in Lithium-Sulfur Batteries. *Chem. Asian J.* **2016**, *11* (8), 1288–1292. https://doi.org/10.1002/asia.201600007.

[171] Park, H.; Koh, H. S.; Siegel, D. J. First-Principles Study of Redox End Members in Lithium–Sulfur Batteries. *J. Phys. Chem. C* **2015**, *119* (9), 4675–4683. https://doi.org/10.1021/jp513023v.

[172] Wagemaker, M.; Mulder, F. M.; Van der Ven, A. The Role of Surface and Interface Energy on Phase Stability of Nanosized Insertion Compounds. *Adv. Mater.* **2009**, *21* (25–26), 2703–2709. https://doi.org/10.1002/adma.200803038.

[173] Wang, L.; Wang, Y.; Xia, Y. A High Performance Lithium-Ion Sulfur Battery Based on a Li_2S Cathode Using a Dual-Phase Electrolyte. *Energy Environ. Sci.* **2015**, *8* (5), 1551–1558. https://doi.org/10.1039/C5EE00058K.

[174] Vizintin, A.; Chabanne, L.; Tchernychova, E.; Arčon, I.; Stievano, L.; Aquilanti, G.; Antonietti, M.; Fellinger, T.-P.; Dominko, R. The Mechanism of Li_2S Activation in Lithium-Sulfur Batteries: Can We Avoid the Polysulfide Formation? *J. Power Sources* **2017**, *344*, 208–217. https://doi.org/10.1016/j.jpowsour.2017.01.112.

[175] Zhang, L.; Sun, D.; Feng, J.; Cairns, E. J.; Guo, J. Revealing the Electrochemical Charging Mechanism of Nanosized Li_2S by in Situ and Operando X-Ray Absorption Spectroscopy. *Nano Lett.* **2017**, *17* (8), 5084–5091. https://doi.org/10.1021/acs.nanolett.7b02381.

[176] Jung, Y.; Kang, B. Understanding Abnormal Potential Behaviors at the 1st Charge in Li_2S Cathode Material for Rechargeable Li–S Batteries. *Phys. Chem. Chem. Phys.* **2016**, *18* (31), 21500–21507. https://doi.org/10.1039/C6CP03146C.

[177] Meini, S.; Elazari, R.; Rosenman, A.; Garsuch, A.; Aurbach, D. The Use of Redox Mediators for Enhancing Utilization of Li_2S Cathodes for Advanced Li–S Battery Systems. *J. Phys. Chem. Lett.* **2014**, *5* (5), 915–918. https://doi.org/10.1021/jz500222f.

[178] Huang, R.; Wang, F.; Han, W.; Wang, Y.; You, D.; Deng, B.; Yang, W.; Dong, P.; Zhang, Y.; Li, X. Investigation of the Corrosion Behavior Influence of Carbon Interlayer on Aluminum Collector in Lithium-Sulfur Battery System. *Electrochim. Acta* **2023**, *469*, 143033. https://doi.org/10.1016/j.electacta.2023.143033.

[179] Zhou, G.; Chen, H.; Cui, Y. Formulating Energy Density for Designing Practical Lithium–Sulfur Batteries. *Nat. Energy* **2022**, *7* (4), 312–319. https://doi.org/10.1038/s41560-022-01001-0.

[180] Zhou, Y.; Wu, C.; Zhang, H.; Wu, X.; Fu, Z. Electrochemical Reactivity of Co–Li_2S Nanocomposite for Lithium-Ion Batteries. *Electrochim. Acta* **2007**, *52* (9), 3130–3136. https://doi.org/10.1016/j.electacta.2006.09.054.

[181] Luo, G.; Zhao, J.; Wang, B. First-Principles Study of Transition Metal Doped Li_2S as Cathode Materials in Lithium Batteries. *J. Renewable Sustainable Energy* **2012**, *4* (6), 063128. https://doi.org/10.1063/1.4768814.

[182] Hong, T. H.; Min, W.; Choi, G.; Kim, J. D.; Lee, J. T.; Kim, D. Unified Interplay of Chemical Bond and Solid-State Kinetics in Lithium–Sulfur Batteries. *Adv. Energy Mater.* **2023**, *13* (25), 2300636. https://doi.org/10.1002/aenm.202300636.

[183] Gao, J.; Gao, Y.; Hao, J.; Sun, X.; Zhao, F.; Zhang, Y.; Si, W.; Wu, J. Activating Redox Kinetics of Li_2S via Cu^+, I^- Co-Doping toward High-Performance All-Solid-State Lithium Sulfide-Based Batteries. *Small* **2024**, *20* (47), 2404171. https://doi.org/10.1002/smll.202404171.

[184] Babu, G.; Masurkar, N.; Al Salem, H.; Arava, L. M. R. Transition Metal Dichalcogenide Atomic Layers for Lithium Polysulfides Electrocatalysis. *J. Am. Chem. Soc.* **2017**, *139* (1), 171–178. https://doi.org/10.1021/jacs.6b08681.

[185] Zhou, G.; Tian, H.; Jin, Y.; Tao, X.; Liu, B.; Zhang, R.; Seh, Z. W.; Zhuo, D.; Liu, Y.; Sun, J.; Zhao, J.; Zu, C.; Wu, D. S.; Zhang, Q.; Cui, Y. Catalytic Oxidation of Li_2S on the Surface of Metal Sulfides for Li–S Batteries. *Proc. Natl. Acad. Sci. U. S. A.* **2017**, *114* (5), 840–845. https://doi.org/10.1073/pnas.1615837114.

[186] Yuan, H.; Chen, X.; Zhou, G.; Zhang, W.; Luo, J.; Huang, H.; Gan, Y.; Liang, C.; Xia, Y.; Zhang, J.; Wang, J.; Tao, X. Efficient Activation of Li_2S by Transition Metal Phosphides Nanoparticles for Highly Stable Lithium–

Sulfur Batteries. *ACS Energy Lett.* **2017**, *2* (7), 1711–1719. https://doi.org/10.1021/acsenergylett.7b00465.

[187] Liang, X.; Yun, J.; Xu, K.; Xiang, H.; Wang, Y.; Sun, Y.; Yu, Y. A Multi-Layered Ti_3C_2/Li_2S Composite as Cathode Material for Advanced Lithium-Sulfur Batteries. *J. Energy Chem.* **2019**, *39*, 176–181. https://doi.org/10.1016/j.jechem.2019.02.002.

[188] Liang, X.; Yun, J.; Xu, K.; Shi, P.; Sun, Y.; Chen, C.; Xiang, H. Trace Ethanol as an Efficient Electrolyte Additive to Reduce the Activation Voltage of the Li_2S Cathode in Lithium-Ion–Sulfur Batteries. *Chem. Commun.* **2019**, *55* (68), 10088–10091. https://doi.org/10.1039/C9CC04877D.

[189] Lin, Z.; Liu, Z.; Fu, W.; Dudney, N. J.; Liang, C. Phosphorous Pentasulfide as a Novel Additive for High-Performance Lithium-Sulfur Batteries. *Adv. Funct. Mater.* **2013**, *23* (8), 1064–1069. https://doi.org/10.1002/adfm.201200696.

[190] Zu, C.; Klein, M.; Manthiram, A. Activated Li_2S as a High-Performance Cathode for Rechargeable Lithium–Sulfur Batteries. *J. Phys. Chem. Lett.* **2014**, *5* (22), 3986–3991. https://doi.org/10.1021/jz5021108.

[191] Tsao, Y.; Lee, M.; Miller, E. C.; Gao, G.; Park, J.; Chen, S.; Katsumata, T.; Tran, H.; Wang, L.-W.; Toney, M. F.; Cui, Y.; Bao, Z. Designing a Quinone-Based Redox Mediator to Facilitate Li_2S Oxidation in Li-S Batteries. *Joule* **2019**, *3* (3), 872–884. https://doi.org/10.1016/j.joule.2018.12.018.

[192] Jiang, Y.; Liao, Y.; Yu, J.; Li, X.; Jin, T.; Xu, Y.; Li, W.; Huang, S.; Xia, S.; Zhao, B.; Sun, X.; Zhang, J. Multi-Effect Ionic Liquid Additives Achieve High Cycle Stability Lithium-Sulfur Batteries by Constructing an Electrostatic Shielding Layer and Eliminating "Dead Sulfur." *Adv. Funct. Mater.* **2025**, *n/a* (n/a), 2500077. https://doi.org/10.1002/adfm.202500077.

[193] Wu, F.; Lee, J. T.; Nitta, N.; Kim, H.; Borodin, O.; Yushin, G. Lithium Iodide as a Promising Electrolyte Additive for Lithium–Sulfur Batteries: Mechanisms of Performance Enhancement. *Adv. Mater.* **2015**, *27* (1), 101–108. https://doi.org/10.1002/adma.201404194.

[194] Meng, X.; Comstock, D. J.; Fister, T. T.; Elam, J. W. Vapor-Phase Atomic-Controllable Growth of Amorphous Li_2S for High-Performance Lithium–Sulfur Batteries. *ACS Nano* **2014**, *8* (10), 10963–10972. https://doi.org/10.1021/nn505480w.

[195] Huang, Z.; Wang, Y.; Li, Y. Facile Synthesis of Lithium Sulfide@Carbon Nanocomposite via Precursor Solution Infiltration-Decomposition for High-Performance Lithium Sulfide Batteries. *ACS Appl. Energy Mater.* **2025**, *8* (9), 5759–5769. https://doi.org/10.1021/acsaem.5c00102.

[196] Dudina, D. V.; Bokhonov, B. B. Materials Development Using High-Energy Ball Milling: A Review Dedicated to the Memory of M. A. Korchagin. *J. Compos. Sci.* **2022**, *6* (7), 188. https://doi.org/10.3390/jcs6070188.

[197] Stein, M., IV; Chen, C.-F.; Mullings, M.; Jaime, D.; Zaleski, A.; Mukherjee, P. P.; Rhodes, C. P. Probing the Effect of High Energy Ball Milling on the Structure and Properties of $LiNi_{1/3}Mn_{1/3}Co_{1/3}O_2$ Cathodes for Li-Ion Batteries. *J. Electrochem. Energy Convers. Storage* **2016**, *13*, 031001. https://doi.org/10.1115/1.4034755.

[198] Zhou, L.; Zhang, W.; Wang, Y.; Liang, S.; Gan, Y.; Huang, H.; Zhang, J.; Xia, Y.; Liang, C. Lithium Sulfide as Cathode Materials for Lithium-Ion Batteries: Advances and Challenges. *J. Chem.* **2020**, *2020* (1), 6904517. https://doi.org/10.1155/2020/6904517.

[199] Chen, L.; Liu, Y.; Ashuri, M.; Liu, C.; Shaw, L. L. Li_2S Encapsulated by Nitrogen-Doped Carbon for Lithium Sulfur Batteries. *J. Mater. Chem. A* **2014**, *2* (42), 18026–18032. https://doi.org/10.1039/C4TA04103H.

[200] Li, X.; Gao, M.; Du, W.; Ni, B.; Wu, Y.; Liu, Y.; Shang, C.; Guo, Z.; Pan, H. A Mechanochemical Synthesis of Submicron-Sized Li_2S and a Mesoporous Li_2S/C Hybrid for High Performance Lithium/Sulfur Battery Cathodes. *J. Mater. Chem. A* **2017**, *5* (14), 6471–6482. https://doi.org/10.1039/C7TA00557A.

[201] Ansell, T. Y.; Hanneman, T.; Gonzalez-Perez, A.; Park, C.; Nieto, A. Effect of High Energy Ball Milling on Spherical Metallic Powder Particulates for Additive Manufacturing. *Part. Sci. Technol.* **2021**, *39* (8), 981–989. https://doi.org/10.1080/02726351.2021.1876192.

[202] Le Bolay, N. On Agglomeration Phenomena in Ball Mills: Application to the Synthesis of Composite Materials. *Powder Technol.* **2003**, *130* (1), 450–455. https://doi.org/10.1016/S0032-5910(02)00249-8.

[203] Shi, J.; Zhang, J.; Zhao, Y.; Yan, Z.; Hart, N.; Guo, J. Synthesis of Li_2S-Carbon Cathode Materials via Carbothermic Reduction of Li_2SO4. *Front. Energy Res.* **2019**, *7*, 53. https://doi.org/10.3389/fenrg.2019.00053.

[204] Ye, F.; Noh, H.; Lee, J.; Lee, H.; Kim, H.-T. Li_2S/Carbon Nanocomposite Strips from a Low-Temperature Conversion of Li_2SO4 as High-Performance Lithium–Sulfur Cathodes. *J. Mater. Chem. A* **2018**, *6* (15), 6617–6624. https://doi.org/10.1039/C8TA00515J.

[205] Wu, Z.; Han, C.; Wang, J.; Li, X.; Fei, H.; Wang, D. Low-Cost Synthesis of High-Purity Li_2S for Sulfide Solid State Electrolytes Enabled by Polyvinyl Alcohol. *J. Cent. South Univ.* **2024**, *31* (12), 4449–4459. https://doi.org/10.1007/s11771-024-5824-z.

[206] Yang, Z.; Guo, J.; Das, S. K.; Yu, Y.; Zhou, Z.; Abruña, H. D.; Archer, L. A. In Situ Synthesis of Lithium Sulfide–Carbon Composites as Cathode Materials for Rechargeable Lithium Batteries. *J. Mater. Chem. A* **2013**, *1* (4), 1433–1440. https://doi.org/10.1039/C2TA00779G.

[207] Kohl, M.; Brückner, J.; Bauer, I.; Althues, H.; Kaskel, S. Synthesis of Highly Electrochemically Active Li_2S Nanoparticles for Lithium–Sulfur-Batteries. *J. Mater. Chem. A* **2015**, *3* (31), 16307–16312. https://doi.org/10.1039/C5TA04504E.

[208] Yang, S.; Hu, X.; Xu, S.; Han, A.; Zhang, X.; Zhang, N.; Chen, X.; Tian, R.; Song, D.; Yang, Y. Synthesis of Deliquescent Lithium Sulfide in Air. *ACS Appl. Mater. Interfaces* **2023**, *15* (34), 40633–40647. https://doi.org/10.1021/acsami.3c08506.

[209] Yu, M.; Wang, Z.; Wang, Y.; Dong, Y.; Qiu, J. Freestanding Flexible Li_2S Paper Electrode with High Mass and Capacity Loading for High-Energy Li–S Batteries. *Adv. Energy Mater.* **2017**, *7* (17), 1700018. https://doi.org/10.1002/aenm.201700018.

[210] Nasouri, K.; Shoushtari, A. M.; Mojtahedi, M. R. M. Thermodynamic Studies on Polyvinylpyrrolidone Solution Systems Used for Fabrication of Electrospun Nanostructures: Effects of the Solvent. *Adv. Polym. Technol.* **2015**, *34* (3). https://doi.org/10.1002/adv.21495.

[211] Malara, A. Environmental Concerns on the Use of the Electrospinning Technique for the Production of Polymeric Micro/Nanofibers. *Sci. Rep.* **2024**, *14* (1), 8293. https://doi.org/10.1038/s41598-024-58936-5.

[212] Şenol, N.; Akkoyun, Ş. Effect of Processing Conditions on the Electrospinning Behavior of Polyvinylpyrrolidone with Lower Toxicity Solvents. *EJOSAT* **2020**, *121*–128. https://doi.org/10.31590/ejosat.819593.

[213] Zhang, X.; Yang, H.; Sun, Y.; Yang, Y. Lithium Sulfide: Magnesothermal Synthesis and Battery Applications. *ACS Appl. Mater. Interfaces* **2022**, *14* (36), 41003–41012. https://doi.org/10.1021/acsami.2c11196.

[214] Hwa, Y.; Zhao, J.; Cairns, E. J. Lithium Sulfide (Li_2S)/Graphene Oxide Nanospheres with Conformal Carbon Coating as a High-Rate, Long-Life Cathode for Li/S Cells. *Nano Lett.* **2015**, *15* (5), 3479–3486. https://doi.org/10.1021/acs.nanolett.5b00820.

[215] Nan, C.; Lin, Z.; Liao, H.; Song, M.-K.; Li, Y.; Cairns, E. J. Durable Carbon-Coated Li_2S Core–Shell Spheres for High Performance Lithium/Sulfur Cells. *J. Am. Chem. Soc.* **2014**, *136* (12), 4659–4663. https://doi.org/10.1021/ja412943h.

[216] Wu, Y.; Momma, T.; Ahn, S.; Yokoshima, T.; Nara, H.; Osaka, T. On-Site Chemical Pre-Lithiation of S Cathode at Room Temperature on a 3D Nano-Structured Current Collector. *J. Power Sources* **2017**, *366*, 65–71. https://doi.org/10.1016/j.jpowsour.2017.08.113.

[217] Wang, Z.; Xu, C.; Chen, L.; Si, J.; Li, W.; Huang, S.; Jiang, Y.; Chen, Z.; Zhao, B. In-Situ Lithiation Synthesis of Nano-Sized Lithium Sulfide/Graphene Aerogel with Covalent Bond Interaction for Inhibiting the Polysulfides Shuttle of Li-S Batteries. *Electrochim. Acta* **2019**, *312*, 282–290. https://doi.org/10.1016/j.electacta.2019.04.169.

[218] Hart, N.; Shi, J.; Zhang, J.; Fu, C.; Guo, J. Lithium Sulfide–Carbon Composites via Aerosol Spray Pyrolysis as

Cathode Materials for Lithium–Sulfur Batteries. *Front. Chem.* **2018**, *6*, 476. https://doi.org/10.3389/fchem.2018.00476.

[219] Dressel, C. B.; Jha, H.; Eberle, A.-M.; Gasteiger, H. A.; Fässler, T. F. Electrochemical Performance of Lithium–Sulfur Batteries Based on a Sulfur Cathode Obtained by H_2S Gas Treatment of a Lithium Salt. *J. Power Sources* **2016**, *307*, 844–848. https://doi.org/10.1016/j.jpowsour.2015.12.140.

[220] Liang, S.; Xia, Y.; Liang, C.; Gan, Y.; Huang, H.; Zhang, J.; Tao, X.; Sun, W.; Han, W.; Zhang, W. A Green and Facile Strategy for the Low-Temperature and Rapid Synthesis of Li_2S@PC–CNT Cathodes with High Li_2S Content for Advanced Li–S Batteries. *J. Mater. Chem. A* **2018**, *6* (21), 9906–9914. https://doi.org/10.1039/C8TA01342J.

[221] Miyashita, N. Method for Producing Lithium Sulfide for Lithium Ion Cell Solid Electrolyte Material. EP 2698856 A1, February 19, 2014. https://patents.google.com/patent/EP2698856A1/en.

[222] Chen, C.; Li, D.; Gao, L.; Harks, P. P. R. M. L.; Eichel, R.-A.; Notten, P. H. L. Carbon-Coated Core–Shell Li_2S@C Nanocomposites as High Performance Cathode Materials for Lithium–Sulfur Batteries. *J. Mater. Chem. A* **2017**, *5* (4), 1428–1433. https://doi.org/10.1039/C6TA09146F.

[223] Italiano, G.; Galliou, P.; Kerleau, P. Method for Producing Lithium Sulfide in a Circulating Bed Reactor. WO 2024 134055 A1, June 27, 2024. https://patents.google.com/patent/WO2024134055A1/en (accessed 2025-07-15).

[224] Wu, F.; Lee, J. T.; Magasinski, A.; Kim, H.; Yushin, G. Solution-Based Processing of Graphene–Li_2S Composite Cathodes for Lithium-Ion and Lithium–Sulfur Batteries. *Part. Part. Syst. Charact.* **2014**, *31* (6), 639–644. https://doi.org/10.1002/ppsc.201300358.

[225] Wang, C.; Wang, X.; Yang, Y.; Kushima, A.; Chen, J.; Huang, Y.; Li, J. Slurryless Li_2S/Reduced Graphene Oxide Cathode Paper for High-Performance Lithium Sulfur Battery. *Nano Lett.* **2015**, *15* (3), 1796–1802. https://doi.org/10.1021/acs.nanolett.5b00112.

[226] He, J.; Chen, Y.; Lv, W.; Wen, K.; Xu, C.; Zhang, W.; Qin, W.; He, W. Three-Dimensional CNT/Graphene–Li_2S Aerogel as Freestanding Cathode for High-Performance Li–S Batteries. *ACS Energy Lett.* **2016**, *1* (4), 820–826. https://doi.org/10.1021/acsenergylett.6b00272.

[227] Wu, F.; Lee, J. T.; Zhao, E.; Zhang, B.; Yushin, G. Graphene–Li_2S–Carbon Nanocomposite for Lithium–Sulfur Batteries. *ACS Nano* **2016**, *10* (1), 1333–1340. https://doi.org/10.1021/acsnano.5b06716.

[228] Wu, F.; Zhao, E.; Gordon, D.; Xiao, Y.; Hu, C.; Yushin, G. Infiltrated Porous Polymer Sheets as Free-Standing Flexible Lithium-Sulfur Battery Electrodes. *Adv. Mater.* **2016**, *28* (30), 6365–6371. https://doi.org/10.1002/adma.201600757.

[229] Wu, F.; Kim, H.; Magasinski, A.; Lee, J. T.; Lin, H.-T.; Yushin, G. Harnessing Steric Separation of Freshly Nucleated Li_2S Nanoparticles for Bottom-Up Assembly of High-Performance Cathodes for Lithium-Sulfur and Lithium-Ion Batteries. *Adv. Energy Mater.* **2014**, *4* (11), 1400196. https://doi.org/10.1002/aenm.201400196.

[230] Zhou, G.; Paek, E.; Hwang, G. S.; Manthiram, A. High-Performance Lithium-Sulfur Batteries with a Self-Supported, 3D Li_2S-Doped Graphene Aerogel Cathodes. *Adv. Energy Mater.* **2016**, *6* (2), 1501355. https://doi.org/10.1002/aenm.201501355.

[231] He, J.; Chen, Y.; Lv, W.; Wen, K.; Li, P.; Qi, F.; Wang, Z.; Zhang, W.; Li, Y.; Qin, W.; He, W. Highly-Flexible 3D Li_2S/Graphene Cathode for High-Performance Lithium Sulfur Batteries. *J. Power Sources* **2016**, *327*, 474–480. https://doi.org/10.1016/j.jpowsour.2016.07.088.

[232] Zhou, G.; Sun, J.; Jin, Y.; Chen, W.; Zu, C.; Zhang, R.; Qiu, Y.; Zhao, J.; Zhuo, D.; Liu, Y.; Tao, X.; Liu, W.; Yan, K.; Lee, H. R.; Cui, Y. Sulfiphilic Nickel Phosphosulfide Enabled Li_2S Impregnation in 3D Graphene Cages for Li–S Batteries. *Adv. Mater.* **2017**, *29* (12), 1603366. https://doi.org/10.1002/adma.201603366.

[233] Wu, F.; Lee, J. T.; Fan, F.; Nitta, N.; Kim, H.; Zhu, T.; Yushin, G. A Hierarchical Particle–Shell Architecture for Long-Term Cycle Stability of Li_2S Cathodes. *Adv. Mater.* **2015**, *27* (37), 5579–5586.

https://doi.org/10.1002/adma.201502289.

[234] He, J.; Chen, Y.; Lv, W.; Wen, K.; Xu, C.; Zhang, W.; Li, Y.; Qin, W.; He, W. From Metal–Organic Framework to Li_2S@C–Co–N Nanoporous Architecture: A High-Capacity Cathode for Lithium–Sulfur Batteries. *ACS Nano* **2016**, *10* (12), 10981–10987. https://doi.org/10.1021/acsnano.6b05696.

[235] Pope, M. A.; Aksay, I. A. Structural Design of Cathodes for Li-S Batteries. *Adv. Energy Mater.* **2015**, *5* (16), 1500124. https://doi.org/10.1002/aenm.201500124.

[236] Kong, L.-L.; Wang, L.; Ni, Z.-C.; Liu, S.; Li, G.-R.; Gao, X.-P. Lithium–Magnesium Alloy as a Stable Anode for Lithium–Sulfur Battery. *Adv. Funct. Mater.* **2019**, *29* (13), 1808756. https://doi.org/10.1002/adfm.201808756.

[237] Wu, F.; Qian, J.; Chen, R.; Lu, J.; Li, L.; Wu, H.; Chen, J.; Zhao, T.; Ye, Y.; Amine, K. An Effective Approach To Protect Lithium Anode and Improve Cycle Performance for Li–S Batteries. *ACS Appl. Mater. Interfaces* **2014**, *6* (17), 15542–15549. https://doi.org/10.1021/am504345s.

[238] Fazaeli, R.; Aliyan, H.; Javadi, M.; Huang, Z.; Wang, Y.; Li, Y. Modification of Glass Fiber Separators with a Ternary V_2O_5/Cys/FeNi-LDH Composite to Enhance the Performance of Lithium-Sulfur Batteries. *Inorg. Chem. Commun.* **2025**, *178*, 114418. https://doi.org/10.1016/j.inoche.2025.114418.

[239] Fazaeli, R.; Huang, Z.; Wang, Y.; Aliyan, H.; Li, Y. Enhanced Cycling Stability in Li-S Batteries: CR-CTA Modified GF Separators with Mechanistic Insights and Performance Evaluation. *J. Power Sources* **2025**, *644*, 237097. https://doi.org/10.1016/j.jpowsour.2025.237097.

[240] Fazaeli, R.; Huang, Z.; Wang, Y.; Li, Y. Enhancing Lithium-Sulfur Battery Performance through the Synergistic Effects of Congo Red and SnO_2 Nanoparticles in Separator Modification Layers. *Surf. Interfaces* **2025**, *64*, 106465. https://doi.org/10.1016/j.surfin.2025.106465.

[241] Fazaeli, R.; Aliyan, H.; Huang, Z.; Wang, Y.; Li, Y. Advancements in Glass Fiber Separator Technology for Lithium-Sulfur Batteries: The Role of Transport, Material Properties, and Modifications. *ACS Omega* **2025**, *10* (4), 3228–3261. https://doi.org/10.1021/acsomega.4c07070.

[242] Zeng, F.-L.; Li, N.; Shen, Y.-Q.; Zhou, X.-Y.; Jin, Z.-Q.; Yuan, N.-Y.; Ding, J.-N.; Wang, A.-B.; Wang, W.-K.; Yang, Y.-S. Improve the Electrodeposition of Sulfur and Lithium Sulfide in Lithium-Sulfur Batteries with a Comb-like Ion-Conductive Organo-Polysulfide Polymer Binder. *Energy Storage Mater.* **2019**, *18*, 190–198. https://doi.org/10.1016/j.ensm.2018.09.018.

[243] Gong, Q.; Hou, L.; Li, T.; Jiao, Y.; Wu, P. Regulating the Molecular Interactions in Polymer Binder for High-Performance Lithium–Sulfur Batteries. *ACS Nano* **2022**, *16* (5), 8449–8460. https://doi.org/10.1021/acsnano.2c03059.

[244] Lu, Y.-Q.; Li, J.-T.; Peng, X.-X.; Zhang, T.; Deng, Y.-P.; Wu, Z.-Y.; Deng, L.; Huang, L.; Zhou, X.-D.; Sun, S.-G. Achieving High Capacity Retention in Lithium-Sulfur Batteries with an Aqueous Binder. *Electrochem. Commun.* **2016**, *72*, 79–82. https://doi.org/10.1016/j.elecom.2016.09.004.

[245] Chen, Z.; Lu, M.; Qian, Y.; Yang, Y.; Liu, J.; Lin, Z.; Yang, D.; Lu, J.; Qiu, X. Ultra-Low Dosage Lignin Binder for Practical Lithium–Sulfur Batteries. *Adv. Energy Mater.* **2023**, *13* (17), 2300092. https://doi.org/10.1002/aenm.202300092.

[246] Feng, K.; Li, M.; Liu, W.; Kashkooli, A. G.; Xiao, X.; Cai, M.; Chen, Z. Silicon-Based Anodes for Lithium-Ion Batteries: From Fundamentals to Practical Applications. *Small* **2018**, *14* (8), 1702737. https://doi.org/10.1002/smll.201702737.

[247] Li, J.-T.; Wu, Z.-Y.; Lu, Y.-Q.; Zhou, Y.; Huang, Q.-S.; Huang, L.; Sun, S.-G. Water Soluble Binder, an Electrochemical Performance Booster for Electrode Materials with High Energy Density. *Adv. Energy Mater.* **2017**, *7* (24), 1701185. https://doi.org/10.1002/aenm.201701185.

[248] Guo, R.; Zhang, S.; Wang, J.; Ying, H.; Han, W. One-Pot Synthesis of a Copolymer Micelle Crosslinked Binder with Multiple Lithium-Ion Diffusion Pathways for Lithium–Sulfur Batteries. *ChemSusChem* **2020**, *13* (4), 819–

826. https://doi.org/10.1002/cssc.201902772.

[249] Hencz, L.; Chen, H.; Ling, H. Y.; Wang, Y.; Lai, C.; Zhao, H.; Zhang, S. Housing Sulfur in Polymer Composite Frameworks for Li–S Batteries. *Nano-Micro Lett.* **2019**, *11* (1), 17. https://doi.org/10.1007/s40820-019-0249-1.

[250] Choi, Y.-J.; Kim, K.-W.; Ahn, H.-J.; Ahn, J.-H. Improvement of Cycle Property of Sulfur Electrode for Lithium/Sulfur Battery. *J. Alloys Compd.* **2008**, *449* (1), 313–316. https://doi.org/10.1016/j.jallcom.2006.02.098.

[251] Cheon, S.-E.; Ko, K.-S.; Cho, J.-H.; Kim, S.-W.; Chin, E.-Y.; Kim, H.-T. Rechargeable Lithium Sulfur Battery: I. Structural Change of Sulfur Cathode during Discharge and Charge. *J. Electrochem. Soc.* **2003**, *150* (6), A796. https://doi.org/10.1149/1.1571532.

[252] Yi, H.; Lan, T.; Yang, Y.; Zeng, H.; Zhang, T.; Tang, T.; Wang, C.; Deng, Y. A Robust Aqueous-Processable Polymer Binder for Long-Life, High-Performance Lithium Sulfur Battery. *Energy Storage Mater.* **2019**, *21*, 61–68. https://doi.org/10.1016/j.ensm.2018.12.009.

[253] Guo, R.; Yang, Y.; Huang, X. L.; Zhao, C.; Hu, B.; Huo, F.; Liu, H. K.; Sun, B.; Sun, Z.; Dou, S. X. Recent Advances in Multifunctional Binders for High Sulfur Loading Lithium-Sulfur Batteries. *Adv. Funct. Mater.* **2024**, *34* (1), 2307108. https://doi.org/10.1002/adfm.202307108.

[254] Yuan, H.; Huang, J.-Q.; Peng, H.-J.; Titirici, M.-M.; Xiang, R.; Chen, R.; Liu, Q.; Zhang, Q. A Review of Functional Binders in Lithium–Sulfur Batteries. *Adv. Energy Mater.* **2018**, *8* (31), 1802107. https://doi.org/10.1002/aenm.201802107.

[255] Liu, J.; Zhang, Q.; Sun, Y.-K. Recent Progress of Advanced Binders for Li-S Batteries. *J. Power Sources* **2018**, *396*, 19–32. https://doi.org/10.1016/j.jpowsour.2018.05.096.

[256] Qi, Q.; Lv, X.; Lv, W.; Yang, Q.-H. Multifunctional Binder Designs for Lithium-Sulfur Batteries. *J. Energy Chem.* **2019**, *39*, 88–100. https://doi.org/10.1016/j.jechem.2019.02.001.

[257] Seh, Z. W.; Zhang, Q.; Li, W.; Zheng, G.; Yao, H.; Cui, Y. Stable Cycling of Lithium Sulfide Cathodes through Strong Affinity with a Bifunctional Binder. *Chem. Sci.* **2013**, *4* (9), 3673–3677. https://doi.org/10.1039/C3SC51476E.

[258] Li, M.; Zhang, J.; Gao, Y.; Wang, X.; Zhang, Y.; Zhang, S. A Water-Soluble, Adhesive and 3D Cross-Linked Polyelectrolyte Binder for High-Performance Lithium–Sulfur Batteries. *J. Mater. Chem. A* **2021**, *9* (4), 2375–2384. https://doi.org/10.1039/D0TA09859K.

[259] Liu, J.; Galpaya, D. G. D.; Yan, L.; Sun, M.; Lin, Z.; Yan, C.; Liang, C.; Zhang, S. Exploiting a Robust Biopolymer Network Binder for an Ultrahigh-Areal-Capacity Li–S Battery. *Energy Environ. Sci.* **2017**, *10* (3), 750–755. https://doi.org/10.1039/C6EE03033E.

[260] Qiao, X.; Wang, C.; Zang, J.; Guo, B.; Zheng, Y.; Zhang, R.; Cui, J.; Fang, X. Conductive Inks Composed of Multicomponent Carbon Nanomaterials and Hydrophilic Polymer Binders for High-Energy-Density Lithium-Sulfur Batteries. *Energy Storage Mater.* **2022**, *49*, 236–245. https://doi.org/10.1016/j.ensm.2022.04.022.

[261] Sun, K.; Cama, C. A.; Huang, J.; Zhang, Q.; Hwang, S.; Su, D.; Marschilok, A. C.; Takeuchi, K. J.; Takeuchi, E. S.; Gan, H. Effect of Carbon and Binder on High Sulfur Loading Electrode for Li-S Battery Technology. *Electrochim. Acta* **2017**, *235*, 399–408. https://doi.org/10.1016/j.electacta.2017.03.023.

[262] Yuan, H.; Huang, J.-Q.; Peng, H.-J.; Titirici, M.-M.; Xiang, R.; Chen, R.; Liu, Q.; Zhang, Q. A Review of Functional Binders in Lithium–Sulfur Batteries. *Adv. Energy Mater.* **2018**, *8* (31), 1802107. https://doi.org/10.1002/aenm.201802107.

[263] Wu, J.; Ye, H.; Hu, Y.; Huang, W.; Zhu, X.; Chang, W.; Li, Y.; Pan, B.; Li, Y.; Lu, J. Xanthate-Mediated Oxidation of Li_2S as the Lithium-Containing Cathode in Lithium–Sulfur Batteries with Extremely Low Overpotential. *Adv. Mater.* **2024**, *36* (48), 2411525. https://doi.org/10.1002/adma.202411525.

[264] Chen, Y.; Lu, S.; Zhou, J.; Qin, W.; Wu, X. Synergistically Assembled Li_2S/FWNTs@Reduced Graphene Oxide Nanobundle Forest for Free-Standing High-Performance Li_2S Cathodes. *Adv. Funct. Mater.* **2017**, *27* (25),

1700987. https://doi.org/10.1002/adfm.201700987.

[265] Li, Z.; Luo, C.; Zhang, S.; Sun, G.; Ma, J.; Wang, X.; He, Y.-B.; Kang, F.; Yang, Q.-H.; Lv, W. Co-Recrystallization Induced Self-Catalytic Li_2S Cathode Fully Interfaced with Sulfide Catalyst toward a High-Performance Lithium-Free Sulfur Battery. *InfoMat* **2022**, *4*, e12361. https://doi.org/10.1002/inf2.12361.

[266] Brune, V.; Bohr, C.; Ludwig, T.; Wilhelm, M.; Hirt, S. D.; Fischer, T.; Wennig, S.; Oberschachtsiek, B.; Ichangi, A.; Mathur, S. A Novel Molecular Synthesis Route to Li_2S Loaded Carbon Fibers for Lithium–Sulfur Batteries. *J. Mater. Chem. A* **2022**, *10* (18), 9902–9910. https://doi.org/10.1039/D2TA00369D.

[267] Ye, F.; Noh, H.; Lee, H.; Kim, H.-T. An Ultrahigh Capacity Graphite/Li_2S Battery with Holey-Li_2S Nanoarchitectures. *Adv. Sci.* **2018**, *5* (7), 1800139. https://doi.org/10.1002/advs.201800139.

[268] Qiu, Y.; Rong, G.; Yang, J.; Li, G.; Ma, S.; Wang, X.; Pan, Z.; Hou, Y.; Liu, M.; Ye, F.; Li, W.; Seh, Z. W.; Tao, X.; Yao, H.; Liu, N.; Zhang, R.; Zhou, G.; Wang, J.; Fan, S.; Cui, Y.; Zhang, Y. Highly Nitridated Graphene–Li_2S Cathodes with Stable Modulated Cycles. *Adv. Energy Mater.* **2015**, *5* (23), 1501369. https://doi.org/10.1002/aenm.201501369.

[269] Li, Z.; Zhang, S.; Zhang, C.; Ueno, K.; Yasuda, T.; Tatara, R.; Dokko, K.; Watanabe, M. One-Pot Pyrolysis of Lithium Sulfate and Graphene Nanoplatelet Aggregates: In Situ Formed Li_2S/Graphene Composite for Lithium–Sulfur Batteries. *Nanoscale* **2015**, *7* (34), 14385–14392. https://doi.org/10.1039/C5NR03201F.

[270] Lodovico, L.; Hosseini, S. M.; Varzi, A.; Passerini, S. Amorphous Lithium Sulfide as Lithium–Sulfur Battery Cathode with Low Activation Barrier. *Energy Technol.* **2019**, *7* (12), 1801013. https://doi.org/10.1002/ente.201801013.

[271] Shen, Y.; Zhang, J.; Pu, Y.; Wang, H.; Wang, B.; Qian, J.; Cao, Y.; Zhong, F.; Ai, X.; Yang, H. Effective Chemical Prelithiation Strategy for Building a Silicon/Sulfur Li-Ion Battery. *ACS Energy Lett.* **2019**, *4* (7), 1717–1724. https://doi.org/10.1021/acsenergylett.9b00889.

[272] Brunn, H.; Arnold, G.; Körner, W.; Rippen, G.; Steinhäuser, K. G.; Valentin, I. PFAS: Forever Chemicals—Persistent, Bioaccumulative and Mobile. Reviewing the Status and the Need for Their Phase out and Remediation of Contaminated Sites. *Environ. Sci. Eur.* **2023**, *35* (1), 20. https://doi.org/10.1186/s12302-023-00721-8.

[273] Spyrakis, F.; Dragani, T. A. The EU's Per- and Polyfluoroalkyl Substances (PFAS) Ban: A Case of Policy over Science. *Toxics* **2023**, *11* (9), 721. https://doi.org/10.3390/toxics11090721.

[274] Zeng, P.; Han, Y.; Duan, X.; Jia, G.; Huang, L.; Chen, Y. A Stable Graphite Electrode in Superconcentrated LiTFSI-DME/DOL Electrolyte and Its Application in Lithium-Sulfur Full Battery. *Mater. Res. Bull.* **2017**, *95*, 61–70. https://doi.org/10.1016/j.materresbull.2017.07.018.

[275] Lv, D.; Yan, P.; Shao, Y.; Li, Q.; Ferrara, S.; Pan, H.; Graff, G. L.; Polzin, B.; Wang, C.; Zhang, J.; Liu, J.; Xiao, J. High Performance Li-Ion Sulfur Batteries Enabled by Intercalation Chemistry. *Chem. Commun.* **2015**, *51* (70), 13454–13457. https://doi.org/10.1039/C5CC05171A.

[276] Jha, H.; Buchberger, I.; Cui, X.; Meini, S.; Gasteiger, H. A. Li-S Batteries with Li_2S Cathodes and Si/C Anodes. *J. Electrochem. Soc.* **2015**, *162* (9), A1829–A1835. https://doi.org/10.1149/2.0681509jes.

[277] Zhang, J.; Wang, J.; Qian, M.; Zhao, B.; Wang, R.; Hao, X.; Huang, X.; Shao, R.; Xing, Z.; Xie, J.; Xu, B.; Su, Y.; Wu, F.; Tan, G. Lithiothermic-Synchronous Construction of Mo–Li_2S–Graphene Nanocomposites for High-Energy Li_2S//Si–C Battery. *Adv. Funct. Mater.* **2022**, *32* (1), 2108305. https://doi.org/10.1002/adfm.202108305.

[278] Balach, J.; Jaumann, T.; Giebeler, L. Nanosized Li_2S-Based Cathodes Derived from MoS_2 for High-Energy Density Li–S Cells and Si–Li_2S Full Cells in Carbonate-Based Electrolyte. *Energy Storage Mater.* **2017**, *8*, 209–216. https://doi.org/10.1016/j.ensm.2017.03.013.

[279] Wang, S.; Chen, H.; Zhong, Z.; Hou, X.; Hu, S.; Wu, J. Graphene-Decorated Sphere Li_2S Composite Prepared by Spray Drying Method as Cathode for Lithium-Sulfur Full Cell. *Ionics* **2018**, *24* (11), 3385–3392. https://doi.org/10.1007/s11581-018-2493-7.

[280] Nanda, S.; Gupta, A.; Manthiram, A. A Lithium–Sulfur Cell Based on Reversible Lithium Deposition from a Li_2S Cathode Host onto a Hostless-Anode Substrate. *Adv. Energy Mater.* **2018**, *8* (25), 1801556. https://doi.org/10.1002/aenm.201801556.

[281] Chen, J.; Xiang, J.; Chen, X.; Yuan, L.; Li, Z.; Huang, Y. Li_2S-Based Anode-Free Full Batteries with Modified Cu Current Collector. *Energy Storage Mater.* **2020**, *30*, 179–186. https://doi.org/10.1016/j.ensm.2020.05.009.

[282] Wang, Z.; Zhang, N.; Yu, M.; Liu, J.; Wang, S.; Qiu, J. Boosting Redox Activity on MXene-Induced Multifunctional Collaborative Interface in High Li_2S Loading Cathode for High-Energy Li-S and Metallic Li-Free Rechargeable Batteries. *J. Energy Chem.* **2019**, *37*, 183–191. https://doi.org/10.1016/j.jechem.2019.03.012.

[283] Chen, Y.; Lu, S.; Li, Y.; Qin, W.; Wu, X. A High-Performance Li_2S/MnO_2 Rechargeable Battery. *Mater. Lett.* **2019**, *248*, 157–160. https://doi.org/10.1016/j.matlet.2019.04.018.

[284] Le Pevelen, D. D. Small Molecule X-Ray Crystallography, Theory and Workflow. **2010**, 2559–2576. https://doi.org/10.1016/B978-0-12-374413-5.00359-6.

[285] Hassanzadeh-Tabrizi, S. A. Precise Calculation of Crystallite Size of Nanomaterials: A Review. *J. Alloys Compd.* **2023**, *968*, 171914. https://doi.org/10.1016/j.jallcom.2023.171914.

[286] Chen, Y.; Zou, C.; Mastalerz, M.; Hu, S.; Gasaway, C.; Tao, X. Applications of Micro-Fourier Transform Infrared Spectroscopy (FTIR) in the Geological Sciences—A Review. *Int. J. Mol. Sci.* **2015**, *16* (12), 30223–30250. https://doi.org/10.3390/ijms161226227.

[287] Xue, Z.; Guan, D.; Zeng, J.; Cao, Y.; Peng, Z.; Hu, G.; Du, K. Research on the Assembly Process of Full Coin Cells: Key Factors Affecting Data Reliability. *Ionics* **2023**, *29* (12), 5285–5293. https://doi.org/10.1007/s11581-023-05225-2.

[288] Ramasamy, R. P.; N. S. Electrochemical Impedance Spectroscopy for Microbial Fuel Cell Characterization. *J. Microb. Biochem. Technol.* **2013**, *S6*, 004. https://doi.org/10.4172/1948-5948.S6-004.

[289] Huang, X.; Wang, Z.; Knibbe, R.; Luo, B.; Ahad, S. A.; Sun, D.; Wang, L. Cyclic Voltammetry in Lithium–Sulfur Batteries—Challenges and Opportunities. *Energy Technol.* **2019**, *7* (8), 1801001. https://doi.org/10.1002/ente.201801001.

[290] Guo, J.; Liu, J. A Binder-Free Electrode Architecture Design for Lithium–Sulfur Batteries: A Review. *Nanoscale Adv.* **2019**, *1* (6), 2104–2122. https://doi.org/10.1039/C9NA00040B.

[291] Lu, Y.; Zhang, Q.; Chen, J. Recent Progress on Lithium-Ion Batteries with High Electrochemical Performance. *Sci. China Chem.* **2019**, *62* (5), 533–548. https://doi.org/10.1007/s11426-018-9410-0.

[292] Fotouhi, A.; Auger, D. J.; Propp, K.; Longo, S.; Wild, M. A Review on Electric Vehicle Battery Modelling: From Lithium-Ion toward Lithium–Sulphur. *Renewable Sustainable Energy Rev.* **2016**, *56*, 1008–1021. https://doi.org/10.1016/j.rser.2015.12.009.

[293] Yang, Y.; Zheng, G.; Cui, Y. Nanostructured Sulfur Cathodes. *Chem. Soc. Rev.* **2013**, *42* (7), 3018–3032. https://doi.org/10.1039/C2CS35256G.

[294] Arvidsson, R.; Janssen, M.; Svanström, M.; Johansson, P.; Sandén, B. A. Energy Use and Climate Change Improvements of Li/S Batteries Based on Life Cycle Assessment. *J. Power Sources* **2018**, *383*, 87–92. https://doi.org/10.1016/j.jpowsour.2018.02.054.

[295] Ma, Z.; Zuo, Z.; Li, Y. Zinc Complex-Based Multifunctional Reactive Lithium Polysulfide Trapper Approaching Its Theoretical Efficiency. *ACS Appl. Mater. Interfaces* **2021**, *13* (20), 23936–23944. https://doi.org/10.1021/acsami.1c04483.

[296] Xing, C.; Chen, H.; Qian, S.; Wu, Z.; Nizami, A.; Li, X.; Zhang, S.; Lai, C. Regulating Liquid and Solid-State Electrolytes for Solid-Phase Conversion in Li–S Batteries. *Chem* **2022**, *8* (5), 1201–1230. https://doi.org/10.1016/j.chempr.2022.01.002.

[297] Deng, R.; Wang, M.; Yu, H.; Luo, S.; Li, J.; Chu, F.; Liu, B.; Wu, F. Recent Advances and Applications toward

Emerging Lithium–Sulfur Batteries: Working Principles and Opportunities. *Energy Environ. Mater.* **2022**, *5* (3), 777–799. https://doi.org/10.1002/eem2.12257.

[298] Yang, Y.; Wang, W.; Li, L.; Li, B.; Zhang, J. Stable Cycling of Li–S Batteries by Simultaneously Suppressing Li-Dendrite Growth and Polysulfide Shuttling Enabled by a Bioinspired Separator. *J. Mater. Chem. A* **2020**, *8* (7), 3692–3700. https://doi.org/10.1039/C9TA12921A.

[299] Yin, Y.-X.; Xin, S.; Guo, Y.-G.; Wan, L.-J. Lithium–Sulfur Batteries: Electrochemistry, Materials, and Prospects. *Angew. Chem., Int. Ed.* **2013**, *52* (50), 13186–13200. https://doi.org/10.1002/anie.201304762.

[300] Ryan, K. R.; Trahey, L.; Ingram, B. J.; Burrell, A. K. Limited Stability of Ether-Based Solvents in Lithium–Oxygen Batteries. *J. Phys. Chem. C* **2012**, *116* (37), 19724–19728. https://doi.org/10.1021/jp306797s.

[301] Zhang, J.; Shi, Y; Ding, Y.; Peng, L.; Zhang, W.; Yu, G. A Conductive Molecular Framework Derived Li_2S/N,P-Codoped Carbon Cathode for Advanced Lithium–Sulfur Batteries. *Adv. Energy Mater.* **2017**, *7* (14), 1602876. https://doi.org/10.1002/aenm.201602876.

[302] Wild, M.; O'Neill, L.; Zhang, T.; Purkayastha, R.; Minton, G.; Marinescu, M.; Offer, G. J. Lithium Sulfur Batteries, a Mechanistic Review. *Energy Environ. Sci.* **2015**, *8* (12), 3477–3494. https://doi.org/10.1039/C5EE01388G.

[303] Yan, Y.; Cheng, C.; Zhang, L.; Li, Y.; Lu, J. Deciphering the Reaction Mechanism of Lithium–Sulfur Batteries by In Situ/Operando Synchrotron-Based Characterization Techniques. *Adv. Energy Mater.* **2019**, *9* (18), 1900148. https://doi.org/10.1002/aenm.201900148.

[304] Yang, X.; Gao, X.; Sun, Q.; Jand, S. P.; Yu, Y.; Zhao, Y.; Li, X.; Adair, K.; Kuo, L.-Y.; Rohrer, J.; Liang, J.; Lin, X.; Banis, M. N.; Hu, Y.; Zhang, H.; Li, X.; Li, R.; Zhang, H.; Kaghazchi, P.; Sham, T.-K.; Sun, X. Promoting the Transformation of Li_2S_2 to Li_2S: Significantly Increasing Utilization of Active Materials for High-Sulfur-Loading Li–S Batteries. *Adv. Mater.* **2019**, *31* (25), 1901220. https://doi.org/10.1002/adma.201901220.

[305] Wu, F.; Magasinski, A.; Yushin, G. Nanoporous Li_2S and MWCNT-Linked Li_2S Powder Cathodes for Lithium-Sulfur and Lithium-Ion Battery Chemistries. *J. Mater. Chem. A* **2014**, *2* (17), 6064–6070. https://doi.org/10.1039/C3TA14161F.

[306] Fu, Y.; Zu, C.; Manthiram, A. In Situ-Formed Li_2S in Lithiated Graphite Electrodes for Lithium–Sulfur Batteries. *J. Am. Chem. Soc.* **2013**, *135* (48), 18044–18047. https://doi.org/10.1021/ja409705u.

[307] Crowe, R.; Badyal, J. P. S. Surface Modification of Poly(Vinylidene Difluoride) (PVDF) by LiOH. *J. Chem. Soc., Chem. Commun.* **1991**, *0* (14), 958–959. https://doi.org/10.1039/C39910000958.

[308] Kise, H.; Ogata, H. Phase Transfer Catalysis in Dehydrofluorination of Poly(Vinylidene Fluoride) by Aqueous Sodium Hydroxide Solutions. *J. Polym. Sci., Polym. Chem. Ed.* **1983**, *21* (12), 3443–3451. https://doi.org/10.1002/pol.1983.170211208.

[309] Dias, A. J.; McCarthy, T. J. Dehydrofluorination of Poly(Vinylidene Fluoride) in Dimethylformamide Solution: Synthesis of an Operationally Soluble Semiconducting Polymer. *J. Polym. Sci., Polym. Chem. Ed.* **1985**, *23* (4), 1057–1061. https://doi.org/10.1002/pol.1985.170230410.

[310] Ross, G. J.; Watts, J. F.; Hill, M. P.; Morrissey, P. Surface Modification of Poly(Vinylidene Fluoride) by Alkaline Treatment. 1. The Degradation Mechanism. *Polymer* **2000**, *41* (5), 1685–1696. https://doi.org/10.1016/S0032-3861(99)00343-2.

[311] Zhang, Q.; Lu, J.; Saito, F.; Baron, M. Mechanochemical Solid-Phase Reaction between Polyvinylidene Fluoride and Sodium Hydroxide. *J. Appl. Polym. Sci.* **2001**, *81* (9), 2249–2252. https://doi.org/10.1002/app.1663.

[312] Amanchukwu, C. V.; Harding, J. R.; Shao-Horn, Y.; Hammond, P. T. Understanding the Chemical Stability of Polymers for Lithium–Air Batteries. *Chem. Mater.* **2015**, *27* (2), 550–561. https://doi.org/10.1021/cm5040003.

[313] Zhang, X.; Liu, T.; Zhang, S.; Huang, X.; Xu, B.; Lin, Y.; Xu, B.; Li, L.; Nan, C.-W.; Shen, Y. Synergistic Coupling between $Li_{6.75}La_3Zr_{1.75}Ta_{0.25}O_{12}$ and Poly(Vinylidene Fluoride) Induces High Ionic Conductivity,

Mechanical Strength, and Thermal Stability of Solid Composite Electrolytes. *J. Am. Chem. Soc.* **2017**, *139* (39), 13779–13785. https://doi.org/10.1021/jacs.7b06364.

[314] Li, B.; Su, Q.; Yu, L.; Wang, D.; Ding, S.; Zhang, M.; Du, G.; Xu, B. $Li_{0.35}La_{0.55}TiO_3$ Nanofibers Enhanced Poly(Vinylidene Fluoride)-Based Composite Polymer Electrolytes for All-Solid-State Batteries. *ACS Appl. Mater. Interfaces* **2019**, *11* (45), 42206–42213. https://doi.org/10.1021/acsami.9b14824.

[315] Wu, M.; Liu, D.; Qu, D.; Xie, Z.; Li, J.; Lei, J.; Tang, H. 3D Coral-like LLZO/PVDF Composite Electrolytes with Enhanced Ionic Conductivity and Mechanical Flexibility for Solid-State Lithium Batteries. *ACS Appl. Mater. Interfaces* **2020**, *12* (47), 52652–52659. https://doi.org/10.1021/acsami.0c15004.

[316] Lin, Y.; Zhou, Y.; Huang, S.; Xiao, M.; Han, D.; Qin, J.; Wang, S.; Meng, Y. Catalytic Disproportionation for Suppressing Polysulfide Shuttle in Li–S Pouch Cells: Beyond Adsorption Interactions. *Adv. Energy Mater.* **2022**, *12* (37), 2201912. https://doi.org/10.1002/aenm.202201912.

[317] The Contrastive Study of Chemical Treatment on the Properties of Hydrophobic PVDF Membrane. *J. Appl. Sci. Process Eng.* **2021**. https://doi.org/10.33736/jaspe.163.2015.

[318] Zhao, X.; Song, L.; Fu, J.; Tang, P.; Liu, F. Experimental and DFT Investigation of Surface Degradation of Polyvinylidene Fluoride Membrane in Alkaline Solution. *Surf. Sci.* **2011**, *605* (11), 1005–1015. https://doi.org/10.1016/j.susc.2011.02.022.

[319] Lanceros-Méndez, S.; Mano, J. F.; Costa, A. M.; Schmidt, V. H. FTIR and DSC Studies of Mechanically Deformed β-PVDF Films. *J. Macromol. Sci., Part B: Phys.* **2001**, *40* (3–4), 517–527. https://doi.org/10.1081/MB-100106174.

[320] Kise, H.; Ogata, H.; Nakata, M. Chemical Dehydrofluorination and Electrical Conductivity of Poly(Vinylidene Fluoride) Films. *Angew. Makromol. Chem.* **1989**, *168* (1), 205–216. https://doi.org/10.1002/apmc.1989.051680117.

[321] Wijaya, O.; Hartmann, P.; Younesi, R.; Markovits, I. E.; Rinaldi, A.; Janek, J.; Yazami, R. A Gamma Fluorinated Ether as an Additive for Enhanced Oxygen Activity in Li–O_2 Batteries. *J. Mater. Chem. A* **2015**, *3* (37), 19061–19067. https://doi.org/10.1039/C5TA03439F.

[322] Nair, S.; Raghavan, R. A Kinetic Study of CO_2 Sorption/Desorption of Lithium Silicate Synthesized through a Ball Milling Method. *Thermochim. Acta* **2021**, *699*, 178918. https://doi.org/10.1016/j.tca.2021.178918.

[323] Tian, N.; Hua, C.; Wang, Z.; Chen, L. Reversible Reduction of Li_2CO_3. *J. Mater. Chem. A* **2015**, *3* (27), 14173–14177. https://doi.org/10.1039/C5TA02499D.

[324] Wang, D. H.; Xie, D.; Yang, T.; Zhong, Y.; Wang, X. L.; Xia, X. H.; Gu, C. D.; Tu, J. P. Conversion from Li_2SO_4 to Li_2S@C on Carbon Paper Matrix: A Novel Integrated Cathode for Lithium-Sulfur Batteries. *J. Power Sources* **2016**, *331*, 475–480. https://doi.org/10.1016/j.jpowsour.2016.09.033.

[325] Baldan, A. Progress in Ostwald Ripening Theories and Their Applications to Nickel-Base Superalloys. Part I: Ostwald Ripening Theories. *J. Mater. Sci.* **2002**, *37* (11), 2171–2202. https://doi.org/10.1023/A:1015388912729.

[326] Leskes, M.; Moore, A. J.; Goward, G. R.; Grey, C. P. Monitoring the Electrochemical Processes in the Lithium–Air Battery by Solid State NMR Spectroscopy. *J. Phys. Chem. C* **2013**, *117* (51), 26929–26939. https://doi.org/10.1021/jp410429k.

[327] Viswanathan, V.; Pande, V.; Abraham, K. M.; Luntz, A. C.; McCloskey, B. D.; Addison, D. Comment on "Cycling Li–O_2 Batteries via LiOH Formation and Decomposition." *Science* **2016**, *352* (6286), 667. https://doi.org/10.1126/science.aad8689.

[328] Yu, H.; Zeng, P.; Liu, H.; Zhou, X.; Guo, C.; Li, Y.; Liu, S.; Chen, M.; Guo, X.; Chang, B.; Wu, T.; Wang, X. Li_2S In Situ Grown on Three-Dimensional Porous Carbon Architecture with Electron/Ion Channels and Dual Active Sites as Cathodes of Li–S Batteries. *ACS Appl. Mater. Interfaces* **2021**, *13* (28), 32968–32977. https://doi.org/10.1021/acsami.1c07198.

[329] Cai, K.; Song, M.-K.; Cairns, E. J.; Zhang, Y. Nanostructured Li_2S–C Composites as Cathode Material for High-Energy Lithium/Sulfur Batteries. *Nano Lett.* **2012**, *12* (12), 6474–6479. https://doi.org/10.1021/nl303965a.

[330] Dua, R.; Almutairi, S.; Bansal, P. Emerging Energy Economics and Policy Research Priorities for Enabling the Electric Vehicle Sector. *Energy Rep.* **2024**, *12*, 1836–1847. https://doi.org/10.1016/j.egyr.2024.08.001.

[331] Yuan, H.; Ma, M.; Zhou, N.; Xie, H.; Ma, Z.; Xiang, X.; Ma, X. Battery Electric Vehicle Charging in China: Energy Demand and Emissions Trends in the 2020s. *Appl. Energy* **2024**, *365*, 123153. https://doi.org/10.1016/j.apenergy.2024.123153.

[332] Niu, H.; Zhang, N.; Lu, Y.; Zhang, Z.; Li, M.; Liu, J.; Zhang, N.; Song, W.; Zhao, Y.; Miao, Z. Strategies toward the Development of High-Energy-Density Lithium Batteries. *J. Energy Storage* **2024**, *88*, 111666. https://doi.org/10.1016/j.est.2024.111666.

[333] Albertus, P.; Babinec, S.; Litzelman, S.; Newman, A. Status and Challenges in Enabling the Lithium Metal Electrode for High-Energy and Low-Cost Rechargeable Batteries. *Nat. Energy* **2018**, *3* (1), 16–21. https://doi.org/10.1038/s41560-017-0047-2.

[334] Wu, F.; Maier, J.; Yu, Y. Guidelines and Trends for Next-Generation Rechargeable Lithium and Lithium-Ion Batteries. *Chem. Soc. Rev.* **2020**, *49* (5), 1569–1614. https://doi.org/10.1039/C7CS00863E.

[335] Zhu, Z.; Jiang, T.; Ali, M.; Meng, Y.; Jin, Y.; Cui, Y.; Chen, W. Rechargeable Batteries for Grid Scale Energy Storage. *Chem. Rev.* **2022**, *122* (22), 16610–16751. https://doi.org/10.1021/acs.chemrev.2c00289.

[336] Lu, J.; Chen, Z.; Pan, F.; Cui, Y.; Amine, K. High-Performance Anode Materials for Rechargeable Lithium-Ion Batteries. *Electrochem. Energ. Rev.* **2018**, *1* (1), 35–53. https://doi.org/10.1007/s41918-018-0001-4.

[337] Tian, Y.; Zeng, G.; Rutt, A.; Shi, T.; Kim, H.; Wang, J.; Koettgen, J.; Sun, Y.; Ouyang, B.; Chen, T.; Lun, Z.; Rong, Z.; Persson, K.; Ceder, G. Promises and Challenges of Next-Generation "Beyond Li-Ion" Batteries for Electric Vehicles and Grid Decarbonization. *Chem. Rev.* **2021**, *121* (3), 1623–1669. https://doi.org/10.1021/acs.chemrev.0c00767.

[338] Fei, Y.; Li, G. Unveiling the Pivotal Parameters for Advancing High Energy Density in Lithium-Sulfur Batteries: A Comprehensive Review. *Adv. Funct. Mater.* **2024**, *34* (21), 2312550. https://doi.org/10.1002/adfm.202312550.

[339] Yao, W.; Xu, J.; Ma, L.; Lu, X.; Luo, D.; Qian, J.; Zhan, L.; Manke, I.; Yang, C.; Adelhelm, P.; Chen, R. Recent Progress for Concurrent Realization of Shuttle-Inhibition and Dendrite-Free Lithium–Sulfur Batteries. *Adv. Mater.* **2023**, *35* (32), 2212116. https://doi.org/10.1002/adma.202212116.

[340] Hao, Z.; Zhao, Q.; Tang, J.; Zhang, Q.; Liu, J.; Jin, Y.; Wang, H. Functional Separators towards the Suppression of Lithium Dendrites for Rechargeable High-Energy Batteries. *Mater. Horiz.* **2021**, *8* (1), 12–32. https://doi.org/10.1039/D0MH01167C.

[341] Wang, J.; Yi, S.; Liu, J.; Sun, S.; Liu, Y.; Yang, D.; Xi, K.; Gao, G.; Abdelkader, A.; Yan, W.; Ding, S.; Kumar, R. V. Suppressing the Shuttle Effect and Dendrite Growth in Lithium–Sulfur Batteries. *ACS Nano* **2020**, *14* (8), 9819–9831. https://doi.org/10.1021/acsnano.0c02241.

[342] Abdollahifar, M.; Molaiyan, P.; Lassi, U.; Wu, N. L.; Kwade, A. Multifunctional Behaviour of Graphite in Lithium–Sulfur Batteries. *Renewable Sustainable Energy Rev.* **2022**, *169*, 112948. https://doi.org/10.1016/j.rser.2022.112948.

[343] Li, M.; Chen, Z.; Wu, T.; Lu, J. Li_2S- or S-Based Lithium-Ion Batteries. *Adv. Mater.* **2018**, *30* (48), 1801190. https://doi.org/10.1002/adma.201801190.

[344] Huang, Z.; Gao, X.; Wang, Y.; Li, Y. Mitigating First Charge Overpotential of Li_2S-Based Lithium–Sulfur Batteries by Leveraging PVDF Reaction with the LiOH/Li_2O Layer. *J. Power Sources* **2023**, *582*, 233530. https://doi.org/10.1016/j.jpowsour.2023.233530.

[345] Kannan, S. K.; Joseph, J.; Joseph, M. G. Review and Perspectives on Advanced Binder Designs Incorporating Multifunctionalities for Lithium–Sulfur Batteries. *Energy Fuels* **2023**, *37* (9), 6302–6322.

https://doi.org/10.1021/acs.energyfuels.3c00155.

[346] Tiwari, S.; Pal, D.; Yadav, V.; Singh, D.; Poonia, A. K. Recent Advancement in Polymeric Binder for Novel Lithium-Sulfur Batteries: A Comprehensive Review. *Inorg. Chem. Commun.* **2025**, *177*, 114332. https://doi.org/10.1016/j.inoche.2025.114332.

[347] Tyrrell, N. D. A Proposal That Would Ban Manufacture, Supply, and Use of All Fluoropolymers and Most Fluorinated Reagents within the Entire EU. *Org. Process Res. Dev.* **2023**, *27* (8), 1422–1426. https://doi.org/10.1021/acs.oprd.3c00199.

[348] Zhao, M.; Peng, H.-J.; Li, B.-Q.; Huang, J.-Q. Kinetic Promoters for Sulfur Cathodes in Lithium–Sulfur Batteries. *Acc. Chem. Res.* **2024**, *57* (4), 545–557. https://doi.org/10.1021/acs.accounts.3c00698.

[349] Zhou, L.; Danilov, D. L.; Qiao, F.; Wang, J.; Li, H.; Eichel, R.-A.; Notten, P. H. L. Sulfur Reduction Reaction in Lithium–Sulfur Batteries: Mechanisms, Catalysts, and Characterization. *Adv. Energy Mater.* **2022**, *12* (44), 2202094. https://doi.org/10.1002/aenm.202202094.

[350] Cheng, Z.; Pan, H.; Zhong, H.; Xiao, Z.; Li, X.; Wang, R. Porous Organic Polymers for Polysulfide Trapping in Lithium–Sulfur Batteries. *Adv. Funct. Mater.* **2018**, *28* (38), 1707597. https://doi.org/10.1002/adfm.201707597.

[351] Yan, L.; Gao, X.; Palathinkal Thomas, J.; Ngai, J.; Altounian, H.; Tong Leung, K.; Meng, Y.; Li, Y. Ionically Cross-Linked PEDOT:PSS as a Multi-Functional Conductive Binder for High-Performance Lithium–Sulfur Batteries. *Sustainable Energy Fuels* **2018**, *2* (7), 1574–1581. https://doi.org/10.1039/C8SE00167G.

[352] Tao, X.; Wang, J.; Liu, C.; Wang, H.; Yao, H.; Zheng, G.; Seh, Z. W.; Cai, Q.; Li, W.; Zhou, G.; Zu, C.; Cui, Y. Balancing Surface Adsorption and Diffusion of Lithium-Polysulfides on Nonconductive Oxides for Lithium–Sulfur Battery Design. *Nat. Commun.* **2016**, *7* (1), 11203. https://doi.org/10.1038/ncomms11203.

[353] Cheung, G.; Huang, C. Strategies to Suppress Polysulfide Dissolution and Its Effects on Lithium–Sulfur Batteries. *Batteries* **2025**, *11* (4), 139. https://doi.org/10.3390/batteries11040139.

[354] Liang, X.; Hart, C.; Pang, Q.; Garsuch, A.; Weiss, T.; Nazar, L. F. A Highly Efficient Polysulfide Mediator for Lithium–Sulfur Batteries. *Nat. Commun.* **2015**, *6* (1), 5682. https://doi.org/10.1038/ncomms6682.

[355] Liu, Y.; Meng, X.; Wang, Z.; Qiu, J. A Li_2S-Based All-Solid-State Battery with High Energy and Superior Safety. *Sci. Adv.* **2022**, *8* (1), eabl8390. https://doi.org/10.1126/sciadv.abl8390.

[356] Han, P.; Chung, S.-H.; Chang, C.-H.; Manthiram, A. Bifunctional Binder with Nucleophilic Lithium Polysulfide Immobilization Ability for High-Loading, High-Thickness Cathodes in Lithium–Sulfur Batteries. *ACS Appl. Mater. Interfaces* **2019**, *11* (19), 17393–17399. https://doi.org/10.1021/acsami.9b02399.

[357] Ma, Z.; Zuo, Z.; Li, L.; Li, Y. Unleash the Capacity Potential of $LiFePO_4$ through Rocking-Chair Coordination Chemistry. *Adv. Funct. Mater.* **2022**, *32* (8), 2108692. https://doi.org/10.1002/adfm.202108692.

[358] Wang, K.; Wang, Y.; Wang, J.; Wang, H.; Ding, C.; Zheng, Z.; Liu, Y.; Luo, Z.; Ding, Y. Unveiling the Curvature-Dependent Electrocatalytic Kinetics for Sulfur Redox Reaction in Li–S Chemistry. *Adv. Funct. Mater.* **2025**, *35* (26), 2422689. https://doi.org/10.1002/adfm.202422689.

[359] Xiao, H.; Li, K.; Zhang, T.; Liang, X.; Zhang, F.; Zhuang, H.; Zheng, L.; Gao, Q. High Loading Atomically Distributed Fe Asymmetrically Coordinated with Pyridinic and Pyrrolic N on Porous N-Rich Carbon Matrix Driving High Performance of Li–S Battery. *Chem. Eng. J.* **2023**, *471*, 144553. https://doi.org/10.1016/j.cej.2023.144553.

[360] Kondratenko, Y.; Fundamensky, V.; Ignatyev, I.; Zolotarev, A.; Kochina, T.; Ugolkov, V. Synthesis and Crystal Structure of Two Zinc-Containing Complexes of Triethanolamine. *Polyhedron* **2017**, *130*, 176–183. https://doi.org/10.1016/j.poly.2017.04.022.

[361] Shunxin, J.; Xiuping, C.; Fan, P.; Zhao, Z.; Chen, F.; Zhong, M. A Simple Solution-Based Method to Prepare Honeycomb-Like Li_2S/Graphene Composite for Lithium-Sulfur Batteries. *Int. J. Electrochem. Sci.* **2018**, *13* (4), 3407–3419. https://doi.org/10.20964/2018.04.44.

[362] Zheng, F.; Kotobuki, M.; Song, S.; Lai, M. O.; Lu, L. Review on Solid Electrolytes for All-Solid-State Lithium-Ion Batteries. *J. Power Sources* **2018**, *389*, 198–213. https://doi.org/10.1016/j.jpowsour.2018.04.022.

[363] Wang, M.; Xia, X.; Zhong, Y.; Wu, J.; Xu, R.; Yao, Z.; Wang, D.; Tang, W.; Wang, X.; Tu, J. Porous Carbon Hosts for Lithium–Sulfur Batteries. *Chem. Eur. J.* **2019**, *25* (15), 3710–3725. https://doi.org/10.1002/chem.201803153.

[364] Hu, C.; Chen, H.; Xie, Y.; Fang, L.; Fang, J.; Xu, J.; Zhao, H.; Zhang, J. Alleviating Polarization by Designing Ultrasmall Li_2S Nanocrystals Encapsulated in N-Rich Carbon as a Cathode Material for High-Capacity, Long-Life Li–S Batteries. *J. Mater. Chem. A* **2016**, *4* (47), 18284–18288. https://doi.org/10.1039/C6TA08572E.

[365] Ye, F.; Hou, Y.; Liu, M.; Li, W.; Yang, X.; Qiu, Y.; Zhou, L.; Li, H.; Xu, Y.; Zhang, Y. Fabrication of Mesoporous Li_2S–C Nanofibers for High Performance Li/Li_2S Cell Cathodes. *Nanoscale* **2015**, *7* (21), 9472–9476. https://doi.org/10.1039/C5NR00480B.

[366] Yan, H.; Wang, H.; Wang, D.; Li, X.; Gong, Z.; Yang, Y. In Situ Generated Li_2S–C Nanocomposite for High-Capacity and Long-Life All-Solid-State Lithium Sulfur Batteries with Ultrahigh Areal Mass Loading. *Nano Lett.* **2019**, *19* (5), 3280–3287. https://doi.org/10.1021/acs.nanolett.9b00882.

[367] Seidel, H.; Meyn, R. Notizen: Die Darstellung der Verbindung Li_2CS_3 / The Synthesis of Li_2CS_3. *Z. Naturforsch., B* **1971**, *26* (11), 1192–1192. https://doi.org/10.1515/znb-1971-1123.

[368] Li, L.; Ma, Z.; Li, Y. Accurate Determination of Optimal Sulfur Content in Mesoporous Carbon Hosts for High-Capacity Stable Lithium-Sulfur Batteries. *Carbon* **2022**, *197*, 200–208. https://doi.org/10.1016/j.carbon.2022.06.036.

[369] Xu, P.; Shuang, Z.-Y.; Zhao, C.-Z.; Li, X.; Fan, L.-Z.; Chen, A.; Chen, H.; Kuzmina, E.; Karaseva, E.; Kolosnitsyn, V.; Zeng, X.; Dong, P.; Zhang, Y.; Wang, M.; Zhang, Q. A Review of Solid-State Lithium Metal Batteries through in-Situ Solidification. *Sci. China Chem.* **2023**. https://doi.org/10.1007/s11426-023-1866-y.

[370] Manthiram, A.; Chung, S.-H.; Zu, C. Lithium–Sulfur Batteries: Progress and Prospects. *Adv. Mater.* **2015**, *27* (12), 1980–2006. https://doi.org/10.1002/adma.201405115.

[371] Barai, P.; Mistry, A.; Mukherjee, P. P. Poromechanical Effect in the Lithium–Sulfur Battery Cathode. *Extreme Mech. Lett.* **2016**, *9*, 359–370. https://doi.org/10.1016/j.eml.2016.05.007.

[372] Sevilla, M.; Carro-Rodríguez, J.; Díez, N.; Fuertes, A. B. Straightforward Synthesis of Sulfur/N,S-Codoped Carbon Cathodes for Lithium–Sulfur Batteries. *Sci. Rep.* **2020**, *10* (1), 4866. https://doi.org/10.1038/s41598-020-61583-1.

[373] Bilal, H. M.; Eroglu, D. Carbon-to-Sulfur Ratio in the Cell Controls the Discharge Capacity, Cycling Performance and Energy Density of a Lithium-Sulfur Battery. *Int. J. Energy Res.* **2022**, *46* (11), 15926–15937. https://doi.org/10.1002/er.8291.

[374] Estevez, L.; Prabhakaran, V.; Garcia, A. L.; Shin, Y.; Tao, J.; Schwarz, A. M.; Darsell, J.; Bhattacharya, P.; Shutthanandan, V.; Zhang, J.-G. Hierarchically Porous Graphitic Carbon with Simultaneously High Surface Area and Colossal Pore Volume Engineered via Ice Templating. *ACS Nano* **2017**, *11* (11), 11047–11055. https://doi.org/10.1021/acsnano.7b05085.

[375] Cox, M.; Mokaya, R. Ultra-High Surface Area Mesoporous Carbons for Colossal Pre-Combustion CO_2 Capture and Storage as Materials for Hydrogen Purification. *Sustainable Energy Fuels* **2017**, *1* (6), 1414–1424. https://doi.org/10.1039/C7SE00300E.

[376] Huang, Q.; Choi, D.; Cosimbescu, L.; Lemmon, J. P. Multi-Electron Redox Reaction of an Organic Radical Cathode Induced by a Mesopore Carbon Network with Nitroxide Polymers. *Phys. Chem. Chem. Phys.* **2013**, *15* (48), 20921–20928. https://doi.org/10.1039/C3CP54358G.

[377] Li_2S Nanocrystals Confined in Free-Standing Carbon Paper for High Performance Lithium–Sulfur Batteries. *ACS Appl. Mater. Interfaces*. https://pubs.acs.org/doi/10.1021/acsami.5b06615.

[378] Zhang, J.; Zhao, B.; Qian, M.; Yu, C.; Mao, P.; Xie, J.; Huang, J.-Q.; Wu, F.; Tan, G. Optimizing Electrocatalysis and Domain Effects of Graphene on Li_2S Cathodes for High-Efficient-Stable Li–S Batteries. *Small* **2025**, *21* (4), 2409172. https://doi.org/10.1002/smll.202409172.

[379] Yan, L.; Gao, X.; Wahid-Pedro, F.; Quinn, J. T. E.; Meng, Y.; Li, Y. A Novel Epoxy Resin-Based Cathode Binder for Low Cost, Long Cycling Life, and High-Energy Lithium–Sulfur Batteries. *J. Mater. Chem. A* **2018**, *6* (29), 14315–14323. https://doi.org/10.1039/C8TA04450C.

[380] Huang, Z.; Wang, Y.; Zhao, Y.; Li, Y. Zinc Complex-Based Multifunctional Binders for Lithium Sulfide-Based Lithium–Sulfur Batteries. *Nanoscale* **2025**. https://doi.org/10.1039/D5NR01950H.

[381] Kim, J. H.; Seo, J.; Choi, J.; Shin, D.; Carter, M.; Jeon, Y.; Wang, C.; Hu, L.; Paik, U. Synergistic Ultrathin Functional Polymer-Coated Carbon Nanotube Interlayer for High Performance Lithium–Sulfur Batteries. *ACS Appl. Mater. Interfaces* **2016**, *8* (31), 20092–20099. https://doi.org/10.1021/acsami.6b06190.